PLANET FORMATION IN THE EARLY STAGES OF STAR FORMATION

by

Patrick Duffy Sheehan

A Dissertation Submitted to the Faculty of the

DEPARTMENT OF ASTRONOMY

In Partial Fulfillment of the Requirements
For the Degree of

DOCTOR OF PHILOSOPHY
WITH A MAJOR IN ASTRONOMY AND ASTROPHYSICS

In the Graduate College

THE UNIVERSITY OF ARIZONA

2017

THE UNIVERSITY OF ARIZONA
GRADUATE COLLEGE

As members of the Dissertation Committee, we certify that we have read the dissertation prepared by Patrick Duffy Sheehan, titled Planet Formation In the Early Stages of Star Formation and recommend that it be accepted as fulfilling the dissertation requirement for the Degree of Doctor of Philosophy.

_____   Date: 31 July 2017
Josh Eisner

_____   Date: 31 July 2017
Dan Marrone

_____   Date: 31 July 2017
George Rieke

_____   Date: 31 July 2017
Yancy Shirley

_____   Date: 31 July 2017
Andrew Youdin

_____   Date: 31 July 2017

Final approval and acceptance of this dissertation is contingent upon the candidate's submission of the final copies of the dissertation to the Graduate College.

I hereby certify that I have read this dissertation prepared under my direction and recommend that it be accepted as fulfilling the dissertation requirement.

_____   Date: 31 July 2017
Dissertation Director: Josh Eisner

STATEMENT BY AUTHOR

This dissertation has been submitted in partial fulfillment of requirements for an advanced degree at the University of Arizona and is deposited in the University Library to be made available to borrowers under rules of the Library.

Brief quotations from this dissertation are allowable without special permission, provided that accurate acknowledgment of source is made. Requests for permission for extended quotation from or reproduction of this manuscript in whole or in part may be granted by the head of the major department or the Dean of the Graduate College when in his or her judgment the proposed use of the material is in the interests of scholarship. In all other instances, however, permission must be obtained from the author.

SIGNED: Patrick Duffy Sheehan

ACKNOWLEDGEMENTS

It's been a long journey to get to the point of putting this document together, and so I think this is a good time to step back and reflect on what it took to get here. While all of the work presented here is my own, none of it would have been possible without an amazing supporting cast. So, I would like to take this opportunity to express my sincerest thanks to everyone who made this possible.

First and foremost, I want to thank my advisor, Josh, for everything he's done for me during my time in graduate school. He was, of course, the one who initially gave me this project, and so I wouldn't be at this point without him. For the past six years he has pushed me to do the best work possible, and has helped to develop me into the scientist I am today. He has also constantly helped me through difficult referee reports, while writing telescope proposals, and during job application season to name just a few examples. I am indebted to him for the time he put in to my graduate career.

I am tremendously grateful to Dan Watson, who gave me my first job in astronomy and started me down this path. I can truly say that without his support and mentorship during my time at the University of Rochester, I would not be here today. Even to this day I am not sure that there is anyone in astronomy who believes in me more than he does.

I also want to thank my colleagues at Steward Observatory for giving me an opportunity to do my graduate work here, and for providing a stimulating environment to work in. The department is a great place to go to graduate school, and I benefitted greatly from daily interactions with my colleagues and the many talks, seminars, and group meetings that happen there. In particular I would like to thank Dan Marrone, who was instrumental in expediting my CARMA observing programs, and Yancy Shirley, who wrote many letters of recommendation for me this past year.

Every summer I was fortunate enough to have the opportunity to be a counselor at Astronomy Camp, and I am grateful to Don McCarthy for giving me that chance, and to all of the excellent counselors and campers who made the camps such a rewarding experience. Even during the hardest times these past six years, Astronomy Camp always reminded me why I came to graduate school and helped to reenergize and revitalize me.

I have made so many wonderful friends in Tucson, all of whom have helped in some way to get me through the past six years, and I don't have room here to thank them all. But I would like to mention a few: Christine and Justin, there's too much to say but I look forward to Margarita Mondays for a long time to come. Greg, office 214 was never quite the same without you. Every day I miss our chats about

sports, politics, or whatever else, as well as our regular trips to Chipotle. Steph, we did get through it! And Michi, you organized many adventures throughout graduate school, perhaps none grander than our hike through the German Alps just a week before I defended my thesis. To everyone on the StrOHS summer softball team, you made going outside in the heat an (almost) pleasant experience.

Ben, Corey, Matt and Claire, you have been my best friends for the past ten years (I can't believe it's been that long already!). I don't know if I would have made it through the late nights at the POA doing physics homework without you.

While I've moved around a lot in my life, family has been the one constant through it all. I owe them all, my grandparents on both sides of the family, aunts and uncles, cousins, and of course Kelly and Brady, a major thank you for always being there. I have the most supportive parents anyone could ask for, who never questioned me when I told them I would be going to graduate school in astronomy instead of getting a real job. And of course it was Pa who first took me out on the boat and taught me the constellations.

Last, but certainly not least, Wen-fai has been my biggest supporter for the past two and a half years. These last 12 months were among the busiest and most stressful of my life, and I can't thank her enough for helping shoulder the burden by preparing meals, doing laundry, and generally being my emotional support. All this (mostly) without even complaining! I'm looking forward to getting back to normal life with you and can't wait for all of our adventures to come!

DEDICATION

For Pa, who first showed me the night sky,
and for Pop-pop, who shared with me his lifelong love of learning.

TABLE OF CONTENTS

TABLE OF CONTENTS – *Continued*

TABLE OF CONTENTS – *Continued*

TABLE OF CONTENTS – *Continued*

LIST OF FIGURES

LIST OF FIGURES – *Continued*

LIST OF FIGURES – *Continued*

LIST OF FIGURES – *Continued*

LIST OF FIGURES – *Continued*

LIST OF FIGURES – *Continued*

LIST OF FIGURES – *Continued*

LIST OF FIGURES – *Continued*

LIST OF FIGURES – *Continued*

LIST OF TABLES

LIST OF TABLES – *Continued*

ABSTRACT

Recent studies suggest that many protoplanetary disks around pre-main sequence stars with inferred ages of 1-5 Myr (known as Class II protostars) may contain insufficient mass to form giant planets. This may be because by this stage much of the material in the disk has already grown into larger bodies, hiding the material from sight. If this is the case, then these older disks may not be an accurate representation of the initial mass budget in disks for forming planets.

To test this hypothesis, I have observed a sample of protostars in the Taurus star forming regions identified as Class I in multiple independent surveys, whose young (< 1 Myr old) disks are more likely to represent the initial mass budget of protoplanetary disks. For my dissertation I have used detailed radiative transfer modeling of a multi-wavelength dataset to determine the geometry of the circumstellar material and measure the mass of the disks around these protostars. I discuss how the inferred disk mass distribution for this sample compares with results for the existing 1-5 Myr old disk samples, and what these results imply for giant planet formation.

Next, I discuss the cases of three separate, individual Class I protostars discovered through my ongoing survey of Class I protostars whose disks are all of particular interest, each for its own reasons. Each of these disks may provide clues that even at the young ages of Class I protostars, planet formation may already be well underway in their disks.

Finally, large disk mass surveys of large star forming regions like the Orion Nebula Cluster may be contaminated by free-free emission from disks that are being photoevaporated by nearby massive stars. I discuss my work with the VLA to constrain the free-free emission spectra for these sources so that current and future millimeter surveys can accurately measure disk masses in the ONC.

CHAPTER 1

INTRODUCTION

1.1 Star Formation in Nearby Molecular Clouds

Stars form from clouds of gas and dust that collapse under the force of gravity (e.g. Shu et al., 1987). During the collapse, if the cloud has even a small amount of rotation, then the conservation of angular momentum forces the collapsing cloud to form into a disk rather than being accreted directly onto the central protostar (e.g. Hoyle, 1960; Cameron, 1962; Cassen and Moosman, 1981; Terebey et al., 1984). Although magnetic braking may act to inhibit disk formation and initially cause the formation of a pseudo-disk (e.g. Galli and Shu, 1993a,b; Allen et al., 2003; Mellon and Li, 2008; Li et al., 2011), some mechanism must allow this to be overcome, as several embedded disks supported by Keplerian rotation have been identified (Brinch et al., 2007b; Lommen et al., 2008; Lee, 2010; Choi et al., 2010; Takakuwa et al., 2012; Yen et al., 2013; Harsono et al., 2014; Aso et al., 2015)

Material is then accreted through the disk and onto the central protostar by viscosity, which allows mass to move inwards while angular momentum is transferred out with a small amount of material (e.g. Lynden-Bell and Pringle, 1974). Although molecular viscosity is far too small to cause accretion and disk depletion on the $\sim 5-10$ Myr timescales that are inferred for disk lifetimes (e.g. Haisch et al., 2001; Hernández et al., 2008; Mamajek, 2009), turbulence driven by the magnetorotational instability can produce effective viscosity in the disk (Balbus and Hawley, 1991) that allows the accretion of matter. Early in the lifetimes of disks when they are still very massive, gravitational instabilities may also provide a mechanism for angular momentum transport (e.g. Papaloizou and Savonije, 1991; Laughlin and Bodenheimer, 1994). It is in these disks that planet formation is expected to occur.

1.1.1 The Evolution and Classification of Young Stellar Objects

Young, forming stars are historically classified by their spectral index at infrared wavelengths (typically between 2 μm and 24μm; Myers et al., 1987; Lada, 1987) as well as by the bolometric temperature measured from their spectral energy distribution (SED; Myers and Ladd, 1993; Chen et al., 1995). These classifications also represent an evolutionary sequence from young, heavily embedded sources to mature disks, to ultimately disks with only debris from the star and planet formation process remaining (e.g. Adams et al., 1987). It is, of course, possible for a source's geometry to be incorrectly inferred from its SED (e.g. Chiang and Goldreich, 1999; Crapsi et al., 2008; McClure et al., 2010; Dunham et al., 2014), but the mapping from SED to source geometry is largely reliable as long as inclinations are not too high (e.g. Crapsi et al., 2008). We show a diagram of the typical SED of each of the standard classifications in Figure 1.1 and an illustration of the physical structure that is expected to produce those features in Figure 1.2.

Class 0 protostars are heavily embedded objects that show little or no optical or infrared emission. They were initially identified by Andre et al. (1993) as millimeter cores with no corresponding infrared detections. They typically have very steep infrared spectral indices ($\alpha_{2-24} > 0.3$) and very low bolometric temperatures ($T_{bol} <$ 70 K). These sources are also found to be young from counting statistics, with estimated lifetimes of < 0.1 Myr (Enoch et al., 2009). They are thought to be the earliest stages of disks, embedded in massive envelopes of collapsing cloud material. Although disk-like structures have been identified towards many Class 0 protostars (e.g. Looney et al., 2000; Tobin et al., 2015), only a few have been confirmed to be supported by Keplerian rotation (e.g. Tobin et al., 2012, 2013). It is possible that magnetic braking may slow the collapse and cause pseudo-disk structures to form rather than Keplerian rotating disks (e.g. Allen et al., 2003; Mellon and Li, 2008; Li et al., 2011).

Class I protostars are classified by rising emission with wavelength in the infrared ($\alpha_{2-24} > 0.3$), which peaks at mid- to far- infrared wavelengths, and bolometric
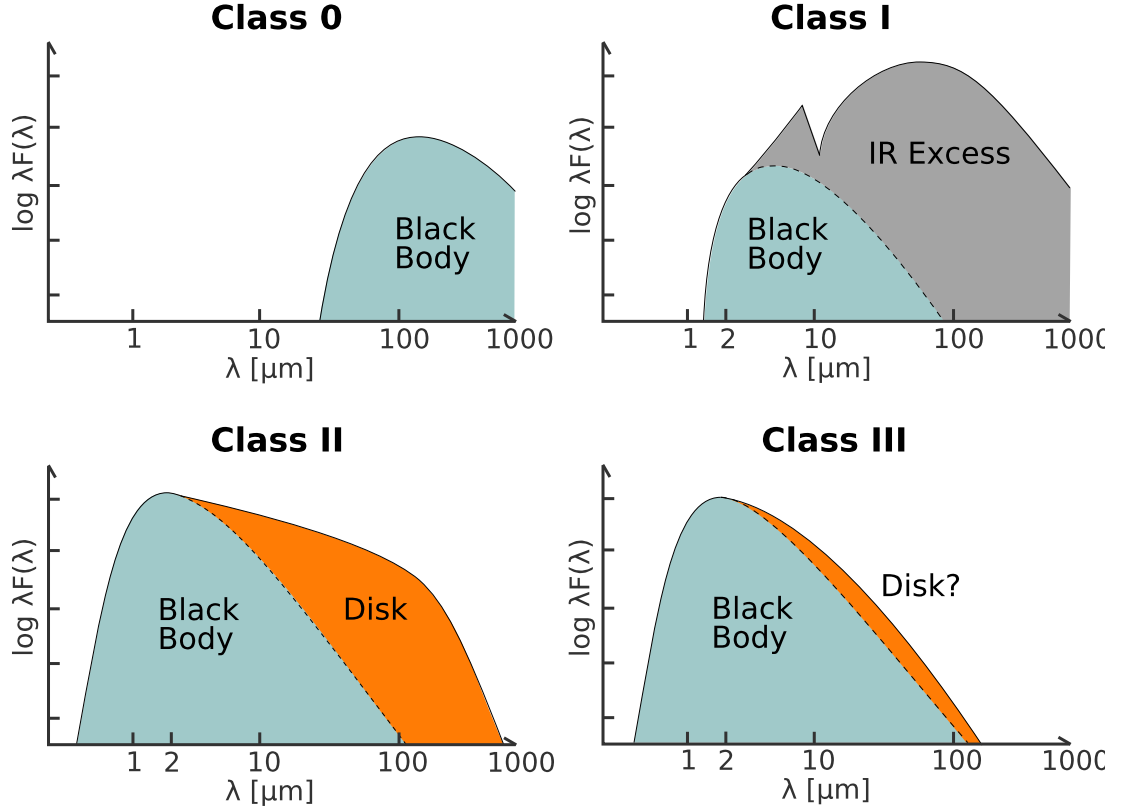
Figure 1.1: An illustration of the typical spectral energy diagram (SED) for the various classifications of young stars. Borrowed from Magnus Persson (https://figshare.com/authors/Magnus_Vilhelm_Persson/388643).

temperatures of ($T_{bol} = 70 - 650$ K). They are thought to be young (~ 0.5 Myr; Evans et al., 2009; Dunham et al., 2015) protostars, surrounded by disks that are still embedded in remnant envelope material, but they are not nearly as heavily obscured as the younger, Class 0 objects. By the Class I stage, any impediments to disk formation seem to have been circumvented, as Keplerian rotation has been observed in a number of these sources (e.g. Lommen et al., 2008; Yen et al., 2013; Harsono et al., 2014; Aso et al., 2015).

Between the Class I and II stages there is a group of objects whose underlying physical structure is somewhat ambiguous. These sources are termed "flat-spectrum" objects as they have infrared spectra that are approximately flat at near-infrared wavelengths ($-0.3 < \alpha_{2-24} < -0.3$; Greene et al., 1994). They are likely

sources with some small amount of envelope material remaining, but not enough to be classified as a Class I. They may also include a component of edge-on disks that can mimic the spectral appearance of a Class 0 or I protostar (e.g. Chiang and Goldreich, 1999; Crapsi et al., 2008).

Class II protostars are classified by infrared emission that falls with increasing wavelength ($-1.6 < \alpha_{2-24} < -0.3$) and high bolometric temperatures of $T_{bol} = 650-2800$. They are associated with protostars that have shed their envelopes, exposing the pre-main sequence star surrounded by a mature disk. They are thought to have ages of $1-10$ Myr (e.g. Strom et al., 1989; Wilking et al., 2005; Bell et al., 2013). The lack of an envelope makes these disks appealing targets for studying the properties of protoplanetary disks, and indeed their masses (e.g. Beckwith et al., 1990; Andrews and Williams, 2005; Eisner et al., 2008; Mann et al., 2014; Pascucci et al., 2016; Eisner et al., 2016), structures (e.g. Andrews et al., 2009, 2010; Guilloteau et al., 2011; Flaherty et al., 2015), and chemistries (e.g. Qi et al., 2011; Bergin et al., 2016; Schwarz et al., 2016; Huang et al., 2017), among other quantities, have been studied in detail.

A special subset of Class II protostars, known as "transition disks", has received a particularly large amount of attention in recent years. These objects were initially identified by visible photosphere emission and mid- to far- infrared emission that is similar to the standard Class II spectra, however, their spectra display a lack of near-infrared emission (e.g. Strom et al., 1989; Najita et al., 2007; Espaillat et al., 2007; Kim et al., 2009; Merín et al., 2010). These sources were suggested to have large cavities in the centers of their disks, which would lead to a lack of hot disk material that emits in the near-infrared. Recent millimeter observations have confirmed this hypothesis by directly imaging holes in a handful of these sources (e.g. Piétu et al., 2006; Hughes et al., 2007; Brown et al., 2009; Isella et al., 2010; Andrews et al., 2011a). These holes may be produced by the presence of multiple planets in the cavities (e.g. Dodson-Robinson and Salyk, 2011; Zhu et al., 2011), but may also be the result of dust grain growth in the inner disk (e.g. Tanaka et al., 2005; Dullemond and Dominik, 2005), or photoevaporation (e.g. Clarke et al., 2001; Alexander et al.,
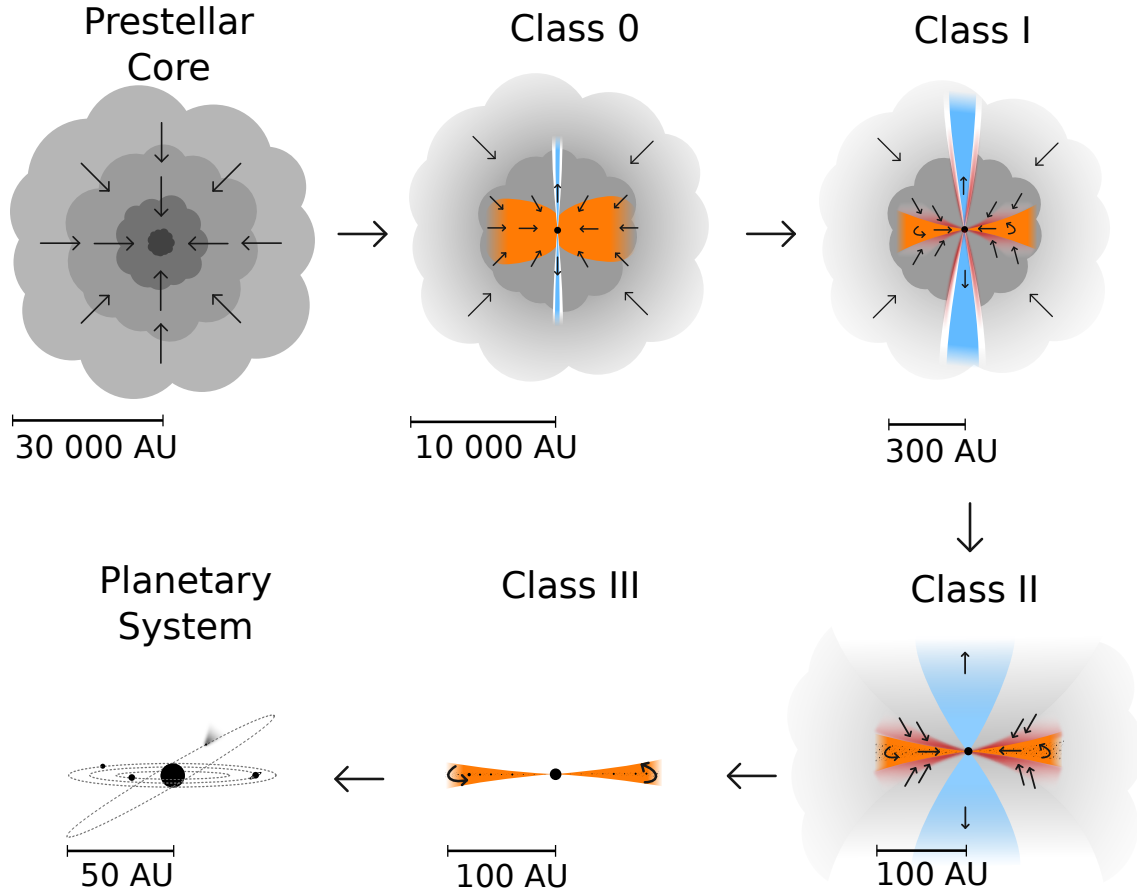
Figure 1.2: An illustration of the physical structure thought to give rise to the standard SED classifications, as seen in Figure 1.1. Borrowed from Borrowed from Magnus Persson (https://figshare.com/authors/Magnus_Vilhelm_Persson/388643).

2006; Gorti and Hollenbach, 2009a). High resolution near-infrared imaging has identified proto-planets in the gaps of a few transition disks (e.g. Kraus and Ireland, 2012; Reggiani et al., 2014; Sallum et al., 2015; Quanz et al., 2015), but it is not clear as of yet if these holes are, in general, carved by planets.

Finally, Class III young stellar objects have SEDs that appear very much like the photospheres of main sequence stars, but they have a small amount of infrared excess that indicates the remains of a protoplanetary disk. They are typically identified by steeply negative spectral indices ($\alpha_{2-24} < -1.6$) and very high bolometric

temperatures ($T_{bol} > 2800$ K). These sources likely lack massive, gaseous disks and so by this stage giant planet formation must be complete, although terrestrial planet formation may be ongoing.

1.2   Planet Formation in Protoplanetary Disks

It has now been well established by high resolution imaging that young, forming stars are surrounded by protoplanetary disks (e.g. Churchwell et al., 1987; Adams et al., 1987; Beckwith et al., 1990; O'Dell et al., 1993; Dutrey et al., 1996; McCaughrean and O'Dell, 1996; Stapelfeldt et al., 1998). It is only recently, however, with high resolution images of disks, that planet formation in disks has been studied up close.

Figure 1.3: An edge-on disk in the Orion Nebula. Images such as these from the Hubble Space Telescope demonstrated definitively that disks are present around young, forming stars.

1.2.1 A Brief Summary of the Theory of Planet Formation

The most commonly accepted process for the formation of giant planets is core accretion (e.g. Safronov and Zvjagina, 1969; Pollack et al., 1996). In the core accretion scenario, dust grains initially grow by collisions that lead to sticking as they settle towards the disk midplane under the force of gravity. Simple models of dust coagulation and settling suggest that the growth of small particles up to millimeter or centimeter sizes under these conditions can lead to rapid growth of particles up to millimeter or centimeter sizes (e.g. Dullemond and Dominik, 2005).

Growth beyond these size scales, however, tends to be problematic. On the one hand, collisions of particles of these sizes or larger tend to lead to bouncing and fragmentation back to smaller sizes rather than growth (e.g. Blum and Wurm, 2008; Zsom et al., 2010). If meter-sized bodies are, however, able to grow, they drift radially inwards due to a headwind from gas orbiting at sub-Keplerian velocities sapping their angular momentum. This radial drift inwards causes meter-sized grains to accrete onto the central protostar (Weidenschilling, 1977) at rates far faster than they can grow to larger sizes (e.g. Birnstiel et al., 2012).

The likely resolution to this problem is that in regions of high solid to gas mass ratios, perhaps in the midplane where settled particles gather, local pressure maxima that can trap dust particles (e.g. Whipple, 1972; Pinilla et al., 2012), or outside of snow-lines where solid densities can be enhanced (e.g. Ros and Johansen, 2013; Drążkowska and Dullemond, 2014; Armitage et al., 2016), the streaming instability (Youdin and Goodman, 2005) can initiate the clumping of dust particles. If the over-densities of these clumps grow large enough, gravitational instabilities could lead to the rapid formation of planetesimal sized bodies in the disk (e.g. Johansen and Youdin, 2007; Johansen et al., 2012; Simon et al., 2016).

Once planetesimals are formed in the disk, growth to larger sizes continues by way of planetesimal collisions (e.g. Safronov and Zvjagina, 1969). When planets have grown large enough that they can influence other particles through their gravitation, so called "gravitational focusing", they enter a stage of runaway growth that does not

end until they have accreted the entirety of the planetesimals within their sphere of influence. The accretion of pebble-sized objects on to planetesimals in this stage may also play a large role in the growth of these planetesimals to larger sizes (Ormel and Klahr, 2010; Lambrechts and Johansen, 2012). Eventually the core becomes massive enough to accrete a gaseous envelope. When a critical mass is reached (Mizuno et al., 1978; Mizuno, 1980), rapid accretion of gas onto the core is sustained (e.g. Pollack et al., 1996) until the planet has accreted enough material to open a gap in the disk and slow the rate of further gas accretion.

Alternatively, if disks are massive enough, it is possible for regions in the disk to be subject to gravitational instabilities that can lead to the direct formation of massive planets (e.g. Kuiper, 1951; Cameron, 1978; Boss, 2003, 2011). These instabilities can cause material in the disk to collapse directly into proto-planets in local regions of high density. This may be a method for forming giant planets quickly, as the timescale for collapse is on the order of the disk dynamical timescale. It is unclear, however, whether it is possible to stop the gravitational collapse and subsequent accretion of gas from the disk at planet masses, or whether the gravitational collapse is more likely to grow bodies to brown dwarf masses (e.g. Kratter et al., 2010).

1.2.2   Observational Evidence of Planet Formation in Disks

While observations of young stars have long shown the presence of disks, it has only been recently with large telescopes and high angular resolution that observational planet formation studies have taken dramatic steps forward.

The spectral slope of optically thin millimeter emission is related to the disk dust grain size distribution (e.g. Draine, 2006). As such, the sizes of dust grains in disks can be estimated by comparing disk fluxes at two separate millimeter wavelengths. Early studies of Class II protoplanetary disks found evidence of dust grain growth in a number of protoplanetary disks (e.g. Beckwith and Sargent, 1991), but it was only with high resolution observations of large samples that studies were able to distinguish between dust grain growth and compact, optically thick disks (e.g.
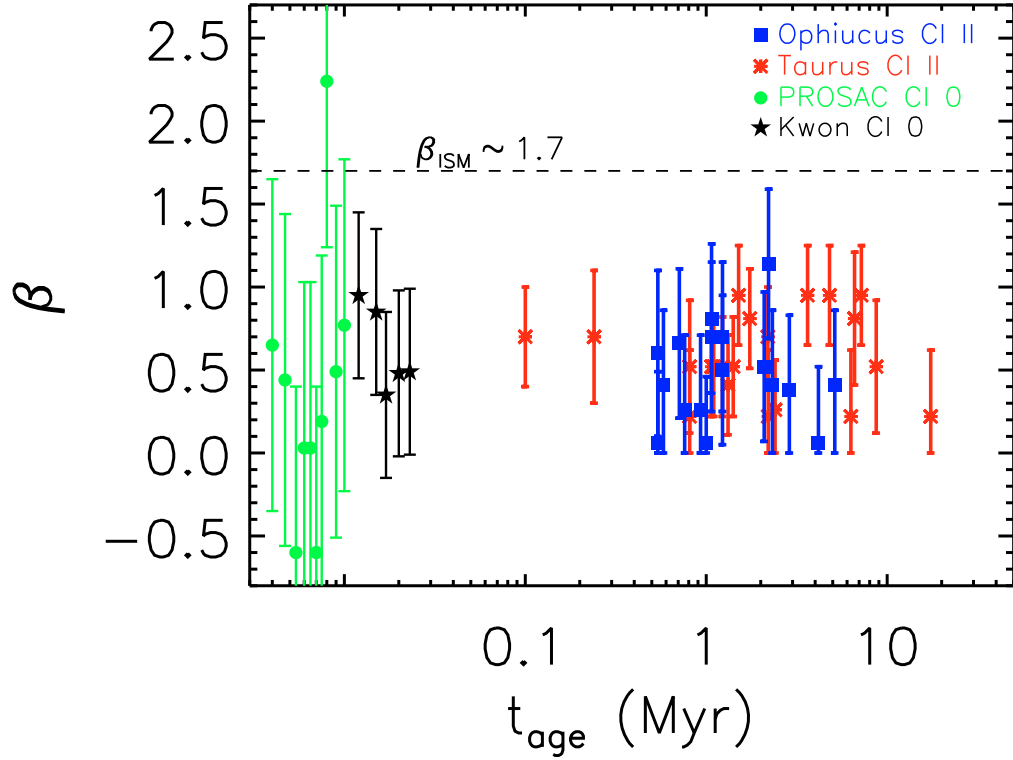
Figure 1.4: Measurements of millimeter spectral index for a range of protostars. The Class II protostars, for which the sizes are measured to break the degeneracy between dust grain growth and optically thick disks, tend to have values of β that are much less than the ISM value of 1.7. This is an indication that dust grains have grown to millimeter, or larger, sizes in these disks. Taken from Ricci et al. (2010a).

Rodmann et al., 2006; Ricci et al., 2010b,a). These studies indicate that dust grain growth has already advanced to sizes larger than a few millimeters in the majority of Class II disks. Spatially resolved studies of a few disks have also shown that the maximum size of dust grains decreases at large radii in a handful of Class II disks (Pérez et al., 2012; Trotta et al., 2013; Pérez et al., 2015). While this may be an indication that grain growth proceeds to larger sizes in the inner disk, it may also be a result of the faster radial drift of larger particles (e.g. Weidenschilling, 1977) concentrating the largest particles in the inner disk.

More recently, direct observational signatures of planets in disks have been observed with high resolution millimeter and near-infrared telescopes. These high

resolution imaging campaigns have discovered myriad features that may be associated with the planet formation process. This includes disks with multiple narrow gaps in their emission profiles (ALMA Partnership et al., 2015; Andrews et al., 2016; Isella et al., 2016; Loomis et al., 2017; Fedele et al., 2017) as well as disks with large central clearings, the so-called "transition disks" discussed above (e.g. Piétu et al., 2006; Brown et al., 2009; Isella et al., 2010; Andrews et al., 2011b; Casassus et al., 2013). Moreover a number of disks with azimuthal asymmetries (e.g. van der Marel et al., 2013; Isella et al., 2013; Rosenfeld et al., 2013; Casassus et al., 2013; Pérez et al., 2014) including the presence of spiral arms (e.g. Clampin et al., 2003; Fukagawa et al., 2004; Muto et al., 2012; Grady et al., 2013; Garufi et al., 2013; Avenhaus et al., 2014; Pérez et al., 2016) have also been found.

While these features need not be produced directly by planets, although planets have been shown to produce such features (e.g. Goldreich and Tremaine, 1980; Lin and Papaloizou, 1993; Bryden et al., 1999; Dodson-Robinson and Salyk, 2011; Dong et al., 2015; Barge and Sommeria, 1995; Regály et al., 2012; Zhu and Stone, 2014), many of the proposed drivers of these features are likely to aid in the planet formation process. These features could be produced by pressure bumps in disks, possibly caused by MRI driven zonal flows that tend to lead to an enhancement of
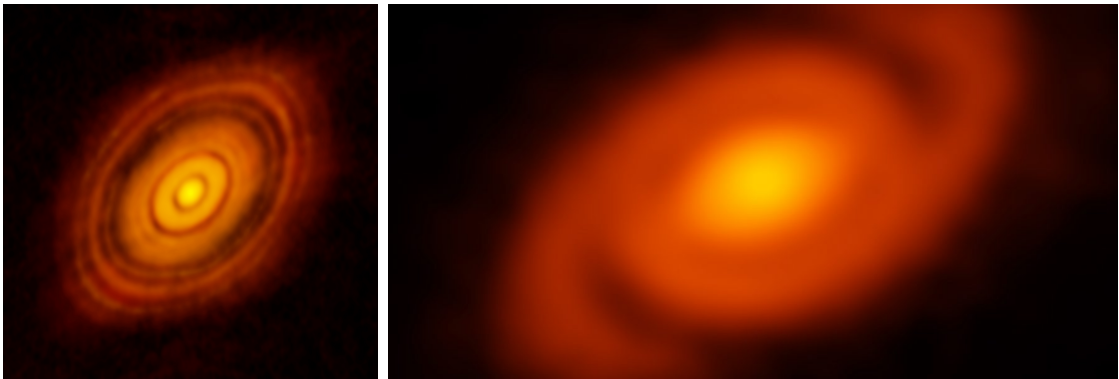
Figure 1.5: Examples of features found in high resolution images of protoplanetary disks. On the left is HL Tau, a young protoplanetary disk that appears to have a number of azimuthally symmetric dark rings that may be gaps in the disk (ALMA Partnership et al., 2015). On the right is Elias 2-27, whose disk has two spiral arms (Pérez et al., 2016).

large dust particles at the location of the pressure bump (e.g. Johansen et al., 2009; Pinilla et al., 2012; Dittrich et al., 2013; Simon and Armitage, 2014; Flock et al., 2015), or dust chemistry variations that may alter dust sticking and fragmentation properties (e.g. Ros and Johansen, 2013; Zhang et al., 2015; Banzatti et al., 2015; Okuzumi et al., 2016). In some cases, however, there is indeed direct evidence of planets forming in disks with such features (e.g. Kraus and Ireland, 2012; Reggiani et al., 2014; Sallum et al., 2015; Quanz et al., 2015).

1.2.3 The Minimum Mass Solar Nebula

An important consideration for planet formation is the amount of matter that is needed to form planets. With exoplanet studies advancing at a rapid pace, it may not be long before we have a better understanding of the amount of matter needed to form exoplanetary systems. Some early attempts at characterizing this value have already been made (Chiang and Laughlin, 2013; Raymond and Cossou, 2014). However the system for which we currently have the best mass/composition constraints is our own Solar System, and so it is commonly used to estimate the amount of matter needed to form planets.

If the amount of heavy material in each of the planets in the Solar System is augmented with hydrogen and helium to bring each planet to solar composition, and then that material is spread out over annuli marked out by the locations of the planets, the surface density distribution of the early Solar nebula can be estimated. These sorts of calculations typically find that the surface density distribution is $\Sigma \propto r^{-3/2}$, and the scaling of this relation is such that the amount of matter in the disk, i.e. the Minimum Mass Solar Nebula, is between $0.01 - 0.1$ M$_\odot$ (Weidenschilling, 1977; Hayashi, 1981; Desch, 2007).

Of course, it is important to note that this is a *minimum* mass, as the efficiency of converting solid mass into planets is likely not unity. Moreover, it is possible, if not likely, that the planets may have migrated and they were formed in a different configuration from what is seen today (e.g. Goldreich and Tremaine, 1980; Lin et al., 1996; Levison et al., 2007). Still, these estimates provide some guidance as to how

much mass may have been needed to form a planetary system like our own. In particular this should perhaps be viewed as the amount of matter needed to form giant planets, as the mass budget in the Solar System is dominated by the mass of Jupiter (Weidenschilling, 1977).

1.3 Mass Measurements of Protoplanetary Disks

Disk mass is an important driver of the evolution of protoplanetary disks. When disks are young and very massive, they may be susceptible to gravitational instabilities, which could cause disks to fragment and produce planetary, substellar, or even stellar mass companions (e.g. Boss, 2003, 2011; Kratter et al., 2010). Gravitational instabilities in the disk may also drive periods of rapid accretion of material onto the central protostar (e.g. Kenyon and Hartmann, 1995). Later, when the disk is calmer and less turbulent, the amount of matter in the disk is important for understanding the ultimate outcomes of planet formation in the disk (e.g. Alibert et al., 2005).

1.3.1 Disk Masses From Optically Thin Dust Emission

Dust emission is typically optically thin at millimeter wavelengths, so a disk's millimeter flux is proportional to the amount of dusty material present,

$$M_d = \frac{F_\nu \, d^2}{\kappa_\nu \, B_\nu(T)}, \tag{1.1}$$

(e.g. Hildebrand, 1983; Beckwith et al., 1990). Equation 1.1, along with reasonable assumptions about the opacity and temperature, typically that $\kappa_\nu = 2.3$ cm^2 g^{-1} and $T = 20$ K, can be used to estimate disk masses from a measured millimeter flux. A standard gas-to-dust ratio of 100 is also often used to quote total disk masses rather than the dust mass.

A large amount of work has gone into millimeter surveys of protoplanetary disks over the past few decades. These surveys were initially done with bolometers on single dish telescopes (e.g. Beckwith et al., 1990; Andre and Montmerle, 1994a; Osterloh and Beckwith, 1995; Andrews and Williams, 2005, 2007). Recently, however,
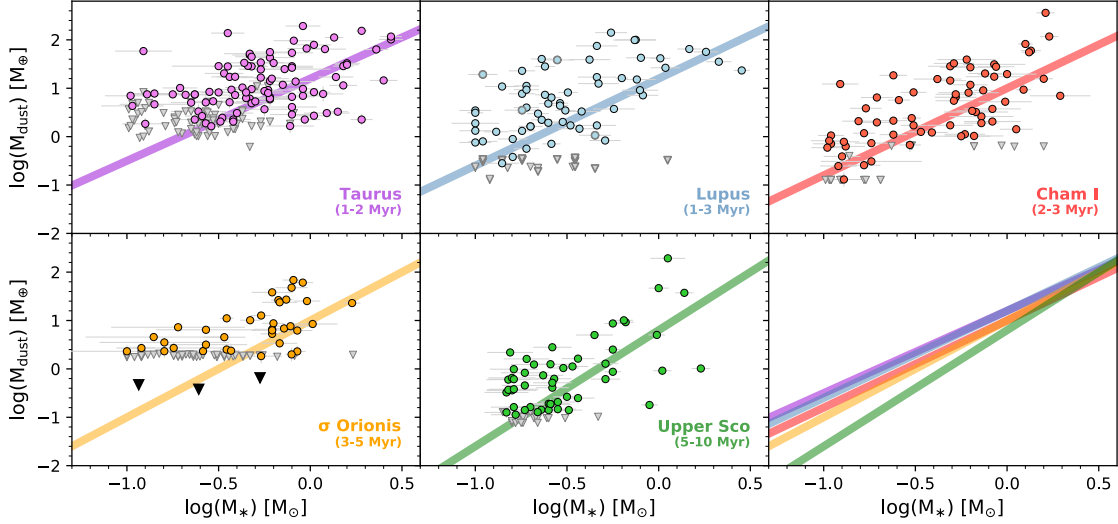
Figure 1.6: A compilation of the dust mass vs. stellar mass relationship for a number of nearby star forming regions. The oldest regions have a steeper relationship, and on average their disks are lower mass. From Ansdell et al. 2017.

large interferometers such as ALMA have become powerful enough to quickly map large samples of disks and measure their fluxes (e.g. Mundy et al., 1995; Bally et al., 1998b; Williams et al., 2005; Eisner et al., 2008; Mann and Williams, 2010; Andrews et al., 2013; Mann et al., 2014; Barenfeld et al., 2016; Eisner et al., 2016; Pascucci et al., 2016; Ansdell et al., 2016, 2017).

Because of that work, the Class II disk mass distribution has now been well studied for a number of star forming regions. Their disks are typically found to have mean masses of $0.0015 - 0.0045$ M$_\odot$. It has also recently been shown that disk mass is proportional to stellar mass (Andrews et al., 2013; Barenfeld et al., 2016; Pascucci et al., 2016; Ansdell et al., 2016, 2017), although the scatter in this relationship is also quite large. Moreover, older disks are on average less massive than younger disks (Barenfeld et al., 2016; Ansdell et al., 2016) and the disk-mass-stellar-mass scaling relationship also steepens at older ages (Pascucci et al., 2016). This latter finding is consistent with simple simulations of dust evolution in disks of different initial masses (Pascucci et al., 2016).

These estimates of disk mass are appealing in their simplicity, but they are not
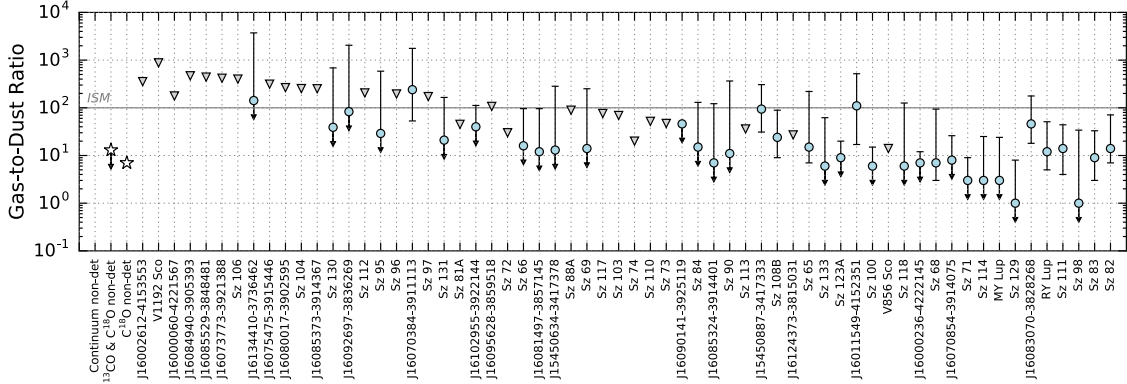
Figure 1.7: Measurements for the gas-to-dust ratio for disks in Lupus. Most of these disks have gas-to-dust ratios that fall well below the ISM value of 100, although in many cases the uncertainties are large. From Ansdell et al. 2016.

without their issues. As was mentioned above, disk mass estimates typically assume that the gas-to-dust ratio in protoplanetary disks is similar to the ISM gas-to-dust ratio, of 100. However, recent direct measurements of gas masses in protoplanetary disks have suggested that gas-to-dust ratios may be much lower than this typically assumed value (Williams and Best, 2014; Ansdell et al., 2016). It is not yet well understood whether these low measurements are due to a depletion of CO gas in Class II disks, or whether chemical processing lowers the amount of CO gas available in the gas phase (e.g. Miotello et al., 2017). Still, it may be that the above estimates of mean disk masses are overestimated by a factor of a few.

Furthermore, while millimeter emission is typically proportional to the amount of matter present in protoplanetary disks, it is possible that there can be contamination from other emission sources. In particular, free-free emission from outflows (e.g. Cohen et al., 1982; Eisloffel et al., 2000; Reipurth et al., 2004) or photoevaporation from external sources (e.g. Garay et al., 1987; Churchwell et al., 1987; O'Dell et al., 1993). Solar flares (e.g. Bower et al., 2003; Forbrich et al., 2008; Rivilla et al., 2015) can also produce strong synchrotron emission at the same millimeter wavelengths. In order to accurately measure disk masses, it is crucial that free-free emission be constrained and removed from the millimeter emission as they can contribute a significant amount of flux at millimeter wavelengths.

Fortunately, the spectral index of dust emission is quite steep, $F_\nu \propto \nu^{2-4}$, while optically thin free-free emission is approximately flat, $F_\nu \propto \nu^{-0.1}$, so at low frequencies, typically centimeter wavelengths or longer, free-free emission dominates over dust emission. Free-free emission can therefore be constrained by flux measurements at multiple radio wavelengths, and then extrapolated to millimeter wavelengths where disk mass measurements are being done.

1.3.2 Disk Masses from Radiative Transfer Modeling

Equation 1.1 is clearly an oversimplification, in particular because disks are certainly not isothermal and identifying a reasonable temperature on a case-by-case basis may not be straightforward (e.g. Hendler et al., 2017). It is also unlikely that dust opacity or gas-to-dust ratio are uniform throughout a sample or even an individual disk. Moreover, optical depth or viewing angle can also have an impact on mass measurements made this way (e.g. Chiang and Goldreich, 1999; Crapsi et al., 2008; Dunham et al., 2014). When averaged over the whole disk and over large samples of disks, these estimates are likely reasonable, but there may be large systematic errors when considering the mass of an individual disk.

In the very earliest stages of the lifetimes of disks, however, the issues can be much worse. The youngest protostellar disks are still embedded in the remnants of the initial in-falling cloud material, and so any millimeter flux measurement will include a contribution from both the disk and the envelope. Single-dish millimeter flux measurements (e.g. Andre and Montmerle, 1994b; Motte et al., 1998; Motte and André, 2001a; Stanke et al., 2006) are almost certainly primarily measuring emission from an extended envelope, and likely cannot be used to estimate the disk mass. Even high resolution millimeter observations that resolve the disk and envelope may be affected by radiative transfer effects (e.g. Crapsi et al., 2008; Dunham et al., 2014). As such, simple methods like those outlined above are difficult to use to measure disk masses for Class I protostars.

Instead, radiative transfer models can be used to model multi-wavelength datasets and infer disk and envelope properties. These procedures were initially

applied to broadband SEDs of embedded protostars (e.g. Kenyon et al., 1993; Whitney et al., 1997, 2003; Robitaille et al., 2006; Furlan et al., 2008; Robitaille, 2017). Resolved observations at additional wavelengths, particularly near-infrared scattered light or millimeter images, however, provide more direct information about disk and envelope geometry. Modeling these resolved images in combination with broadband SEDs can help to break model degeneracies and better constrain disk and envelope properties (e.g. Wolf et al., 2003; Osorio et al., 2003; Eisner et al., 2005; Gramajo et al., 2007, 2010; Eisner, 2012). Resolved millimeter observations are of particular importance because the emission should be largely optically thin, and therefore the images are a good probe of disk structure.

1.4   The Initial Mass Budget for Forming Planets and the Role of this Thesis

Estimates of the Class II disk mass distribution suggest that Class II disks are, on average, too low mass to form giant planets as determined by the Minimum Mass Solar Nebula. It is also not clear whether the Class II disk mass distribution can reproduce the observed frequency of giant planets around FGK stars (e.g. Cumming et al., 2008). However, it may simply be that at this advanced state, dust processing has depleted the dust in the disk by accretion or growth into larger bodies to which millimeter observations are not sensitive. If this is the case, it may be that the younger Class I disks are a better representation of the initial mass budget in protoplanetary disks. Some previous studies have attempted to measure Class I disk masses (e.g. Jørgensen et al., 2009; Eisner, 2012), and these studies have suggested that they are indeed higher on average than Class II disk masses, however sample sizes for these studies remain small (Eisner, 2012) or use flawed disk mass estimates (Jørgensen et al., 2009; Dunham et al., 2014).

In this dissertation I will discus my work to study planet formation in the early, Class I phase, of protoplanetary disks. In Chapter 2, I give a brief overview of two techniques that are prevalent throughout this work, millimeter interferometry

and Monte Carlo radiative transfer. In Chapter 3, I will discuss a survey of Class I protoplanetary disks done with the CARMA array to measure masses for a sample of Class I disks in the Taurus Molecular Clouds, and how these disk masses compare to the older Class II sample. In Chapters 4, 5, and 6, I discuss three particular individual objects that all have interesting features in their disks, some of which may be indications that planets are already forming. In order to understand our Class I disk masses, understanding Class II disk masses is important for providing context. In Chapter 7, I present my work to constrain free-free emission from photoevaporating disks in the Orion Nebula. This free-free emission can be bright at the radio wavelengths where disk masses are typically measured, and so it is important to understand it's properties when measuring disk masses. Finally, I summarize my work and present an outlook for the future in Chapter 8.

CHAPTER 2

METHODOLOGY

2.1 Introduction

The research presented in this document relies on a number of different astronomical techniques, however there are two in particular that play key roles in the work being done and are prevalent throughout my body of work. As such, it is worthwhile to introduce each before I delve into my work. In particular, those techniques are millimeter interferometry, which is key to imaging the structure of protoplanetary disks, and Monte Carlo radiative transfer, which is crucial for interpreting those observations. We discuss each in further detail below.

2.2 Monte Carlo Radiative Transfer Codes

As discussed above, radiative transfer is important for interpreting multi-wavelength observations of protoplanetary disks. Moreover, the full three-dimensional solution to the radiative transfer equation in protoplanetary disks and envelopes is not analytically tractable, so numerical solutions are needed.

Monte Carlo radiative transfer has become increasingly popular as a method for solving the radiative transfer equations because of it's algorithmic simplicity and easy portability to higher dimensions and complex geometries. The method was initially developed several decades ago (e.g. Witt, 1977; Lefevre et al., 1982, 1983), but various optimizations and improvements have been introduced since its initial conception (e.g. Code and Whitney, 1995; Lucy, 1999; Yusef-Zadeh et al., 1984; Bjorkman and Wood, 2001; Min et al., 2009; Robitaille, 2010). In the Monte Carlo radiative transfer algorithm, photon packets are emitted from energetic sources and propagated through a grid of cells with constant densities. Each photon packet is

randomly assigned an optical depth and direction to travel through the grid before being absorbed or scattered. When a photon packet is absorbed, it deposits its energy into the cell, before being reemitted as a new photon. A large number of photon packets are propagated through the grid, being absorbed and re-emitted until they escape from the grid. Once all of the photons have escaped, the temperature in each cell is calculated from the energy absorbed, and the simulation is repeated, with the temperatures from the previous run used as initial conditions, until some convergence criterion for the temperature has been met. In the final run, photons escaping from the grid are captured and binned into images and SEDs (e.g. Lucy, 1999).

This Monte Carlo radiative transfer method, in it's most basic form, is embarrassingly parallel. Each photon packet is completely independent of the other photon packets. The total number of photon packets can be split up among any number of computer cores and propagated through the grid. Once all of the photon packets have escaped, the energies absorbed in each cell across the cores can be merged and the temperature throughout the grid can be calculated. This provides an additional incentive for these methods, as parallelization is trivial.

The simplest form of Monte Carlo radiative transfer, however, can still be quite slow, particularly if there are a large number of cells (e.g. for more than one dimension) because it can take a large number of photons to ensure that enough photons are absorbed in each grid cell to beat down the noise. To counteract this, Lucy (1999) suggested a method of continuous absorption. Rather than depositing all of a photon packets energy in the cell it is absorbed in, energy is deposited in all of the cells along the photon packets path according to the optical depth traveled through the cell. This method allows every cell to be sampled more quickly.

An alternative formulation by Bjorkman and Wood (2001) updates the temperature in a cell at the same time that the photon is absorbed in the cell. Photons are then reemitted from a modified emissivity function to account for the fact that earlier photons were emitted from cells with different temperatures. As the temperature is constantly being updated throughout the grid, multiple iterations of

this calculation are not needed. Instead, enough photons must be run through the grid such that the temperature has converged after all of the photons have passed through. As cell temperatures are constantly being updated, this algorithm is also much more difficult to parallelize.

One potential drawback to Monte Carlo radiative transfer is that runtimes depend strongly on the input density distribution; simulations can be slowed down significantly by high density cells with optical depths across the cell. In these high optical depth cells, photons can become trapped, needing a large number of steps to reach the edge of the cells. This can be mitigated to some degree by the Modified Random Walk method (MRW; Min et al., 2009; Robitaille, 2010). In a code using MRW, if a cell reaches a certain density and a photon becomes trapped, then the photon is allowed to diffuse to the edge of the cell in large steps. This avoids the calculation of millions of individual absorption and scattering events by grouping them into larger steps. For cells that are so optically thick and hidden that few photons reach them, the Partial Diffusion Approximation can be used to update the temperature in the cells based on the temperatures in neighboring cells (Min et al., 2009).

Moreover, producing images can also be slow, as a large number of photons are needed to produce high fidelity images. A number of methods have been developed to speed up the collection of photons to produce images and spectra, such as "peeling off" photons every time that they are absorbed and re-emitted and binning those peeled off photons in the final image (Yusef-Zadeh et al., 1984). Raytracing is a much more efficient method for computing images and spectra. However, knowledge of the scattering phase function is still needed to produce accurate synthetic observations. This is typically solved by running a short scattering simulation to calculate the scattering phase function throughout the density distribution, and then raytracing can be used to produce images.

Although many Monte Carlo radiative transfer codes have been written, there are currently two publicly available codes that are in widespread use. `RADMC-3D` (Dullemond, 2012) employs the algorithm of Bjorkman and Wood (2001) to update

cell temperatures as photons are absorbed and reemitted and uses raytracing to produce synthetic observations. Because it incorporates the Bjorkman and Wood (2001) algorithm, it is not parallelized. `Hyperion` (Robitaille, 2011), on the other hand, employs an iteration based scheme to calculate the temperature throughout the grid, and so it has been parallelized effectively. Synthetic observations, however, are made using the "peeling-off" method and so they can be time-consuming to compute. Raytracing is available for thermal dust emission, however the ability to raytrace scattered light has not yet been implemented. I will make use of both codes throughout this work.

2.3   Millimeter Interferometry

Because thermal dust emission is largely optically thin at millimeter wavelengths, radio telescopes provide an excellent probe of the bulk material in a protoplanetary disk (Andrews, 2015). While single-dish radio telescopes can provide useful information about disks, they are quickly limited by their resolution. At their nearest, $d \sim 140$ pc (e.g. Ortiz-León et al., 2017), these disks only subtend $\sim 1 - 2$" on the sky. The resolution of a single telescope is limited by diffraction, and can be approximated by $\Delta\theta \sim \lambda/D$. At radio wavelengths, this implies that enormous radio dishes are needed to well resolve the majority of protoplanetary disks.

Millimeter interferometers are the solution to this problem. Instead of using a single large telescope to collect light, light from an array of smaller telescopes is combined by interfering the light from pairs of telescopes. According to the van Cittert-Zernicke theorem, the spatial coherence function of radiation from two apertures at $\vec{r_1}$ and $\vec{r_2}$ is

$$V_\lambda(\vec{B}) \propto \int I_\lambda(\vec{s}) \exp\left[-\frac{i2\pi}{\lambda}\vec{B}\cdot\vec{s}\right] d\Omega. \tag{2.1}$$

where $\vec{B} = \vec{r_1} - \vec{r_2}$ is the baseline vector between two antennas and $\vec{s} = \vec{s_0} + \vec{\sigma}$ is the position of the source in the sky. $\vec{s_0}$ is the vector to the center of the source and $\vec{\sigma}$ is the sky offset from the source center. The dot product $\vec{B}\cdot\vec{s_0}$ is the geometric delay,

and can be tracked and nulled by adding an instrumental delay so that $\vec{B}\cdot\vec{s} \to \vec{B}\cdot\vec{\sigma}$. It is also useful to work in terms of spatial frequencies, i.e. $\vec{B}/\lambda$. We can write $\vec{B}/\lambda$ and $\vec{\sigma}$ in a coordinate system such that $\vec{s_0} = \hat{k}$, and $\hat{i}$ and $\hat{j}$ are East and North. In this system we can write that

$$\vec{\sigma} = \alpha\,\hat{i} + \delta\,\hat{j} + (\sqrt{1-\alpha^2-\delta^2}-1)\,\hat{k}, \tag{2.2}$$

$$\frac{\vec{B}}{\lambda} = u\,\hat{i} + v\,\hat{j} + w\,\hat{k}. \tag{2.3}$$

If α and δ are small enough that $\frac{1}{2}(\alpha^2+\delta^2)\,w \approx 0$, meaning if the field of view is small enough, then the response can be written as

$$V(u,v) \propto \int\int I_\lambda(\alpha,\delta)\,\exp[-i2\pi(\alpha u + \delta v)]\,d\alpha\,d\delta. \tag{2.4}$$

In other words, an interferometer measures the Fourier transform of the sky emission distribution. Each pair of antennas in an interferometer corresponds to a fixed position (u, v) in the Fourier plane, so each baseline measures a single Fourier component of the sky emission distribution.

By observing with a large number of pairs of antennae, the Fourier plane is filled in and a large telescope aperture can be synthesized. Images of the source structure can be made by Fourier transforming the measured source visibilities back to the image plane. For interferometers, the spatial resolution is determined by $\Delta\theta \sim \lambda/B_{\max}$, where $B_{\max}$ is the maximum "baseline," or maximum separation between antennas in the array. $B_{\max}$ sets the approximate size of the synthesized aperture. So, instead of building enormous single dish telescopes, many smaller telescopes can be combined in an array to work as one large telescope.

Of course, millimeter interferometry isn't without its issues as well. Interferometers spatially filter information, and so while the resolution is roughly determined by $\lambda/B_{\max}$, they are also not sensitive to scales larger than $\sim \lambda/B_{\min}$. This is not always a negative, as it means that interferometers naturally resolve out large scale emission from molecular clouds that protoplanetary disks are embedded in. This will be particularly useful in Chapter 7, where background free-free emission from the ONC is very bright. However, with the large baselines that are available in

modern day interferometers, remaining sensitive to all of the relevant spatial scales, including both disk and envelope, of Class I protostar systems in a single array configuration is rarely possible. Because of this, it is often necessary to take observations with multiple array configurations, both compact and extended, in order to be sensitive to emission on all relevant scales.

Radio interferometers have now been developed sufficiently, with large enough baselines and high enough sensitivity, to be used to study protoplanetary disks in great detail. Although a number of interferometers paved the way and provided initial insights into disk structures (SMA, CARMA, PdBI, ATCA; baselines up to $\sim 1-2$ km, spatial resolutions up to ~ 0.15"), the crown jewels are the Atacama Large Millimeter Array (ALMA) and the Very Large Array (VLA). These instruments have maximum baselines of ~ 15 km (ALMA) and ~ 35 km (VLA), large numbers of dishes, and have taken some of the sharpest ever images of protoplanetary disks (ALMA Partnership et al., 2015; Andrews et al., 2016).

CHAPTER 3

Disk Masses for Embedded Class I Protostars in the Taurus Molecular Cloud[†]

Class I protostars are thought to represent an early stage in the lifetime of protoplanetary disks, when they are still embedded in their natal envelope. Here we measure the disk masses of 10 Class I protostars in the Taurus Molecular Cloud to constrain the initial mass budget for forming planets in disks. We use radiative transfer modeling to produce synthetic protostar observations and fit the models to a multi-wavelength dataset using a Markov Chain Monte Carlo fitting procedure. We fit these models simultaneously to our new CARMA 1.3 mm observations that are sensitive to the wide range of spatial scales that are expected from protostellar disks and envelopes so as to be able to distinguish each component, as well as broadband spectral energy distributions compiled from the literature. We find a median disk mass of 0.018 $M_{\odot}$ on average, more massive than the Taurus Class II disks, which have median disk mass of ~ 0.0025 $M_{\odot}$. This indicates that by the Class II stage, at a few Myr, a significant amount of dust grain processing has occurred. However, there is evidence that significant dust processing has occurred even during the Class I stage, so it is likely that the initial mass budget is higher than the value quoted here.

3.1 Introduction

Stars form from clouds of gas and dust that collapse under the strength of gravity. Conservation of angular momentum causes the majority of the material to be deposited into a circumstellar disk. Viscosity in the disk causes material to accrete onto the star. The viscous time in these disks is comparable to theoretical

---

[†]This chapter has been submitted for publication as Sheehan & Eisner 2017b.

expectations of planet formation timescales.

Young stars have historically been classified by their near-infrared spectral index (Lada, 1987; Myers et al., 1987; Andre et al., 1993) and bolometric temperature (e.g. Myers and Ladd, 1993; Chen et al., 1995). Class 0 protostars are characterized by a lack of optical and near-/mid-infrared emission, and low bolometric temperatures, suggesting that the central source is highly extincted. They are thought to represent the earliest stage of star formation, where a massive protostellar envelope shrouds the central protostar, obscuring it's light from view. They are likely forming disks as material from the envelope is funneled onto the protostar (Ulrich, 1976; Terebey et al., 1984). It is not clear whether these sources have rotationally supported disks, or whether magnetic braking at these early ages inhibits disk formation (e.g. Allen et al., 2003; Mellon and Li, 2008; Li et al., 2013). Rotationally supported disks have been observed around some Class 0 protostars (Tobin et al., 2012, 2013; Murillo et al., 2013; Codella et al., 2014; Lindberg et al., 2014; Aso et al., 2015).

Class I protostars are characterized by steeply rising near-infrared emission that peaks at mid-infrared wavelengths, and have bolometric temperatures of a few hundred Kelvin. They are likely sources with mature protoplanetary disks that are still being fed by a collapsing envelope of material (e.g. Harsono et al., 2014; Aso et al., 2015).

Class II YSO's have SEDs that are flat or declining at near-infrared wavelengths, with some light from the central star visible. By this stage the material in the envelope is thought to have been depleted onto the disk and protostar, exposing the stellar photosphere to observers. Finally Class III protostars are dominated by the light of the central protostar with a small amount of infrared excess, and are thought to be disks in which the gas has been depleted and only a small amount of rocky material remains.

Previous studies have shown this classification scheme to be prone to errors. For example it is possible to mistake an edge-on disk as a highly obscured Class I protostar (e.g. Chiang and Goldreich, 1999; Crapsi et al., 2008). Disks that are highly obscured by foreground material have also been mistaken for Class I disks (e.g.

Brown et al., 2012). More recent studies have attempted to define other metrics for determining the evolutionary state of protostars, for example, based on bolometric temperatures and the strength of HCO^+ emission towards the source (e.g. van Kempen et al., 2009). The best way, however, to probe the underlying density distribution is through spatially resolved observations of optically thin matter. Detailed radiative transfer modeling of datasets at multiple wavelengths can be used to break model degeneracies, constrain parameters like temperature and opacity, and determine physical properties of the system (e.g. Osorio et al., 2003; Wolf et al., 2003; Eisner et al., 2005; Lommen et al., 2008; Gramajo et al., 2010; Eisner, 2012; Sheehan and Eisner, 2014, 2017).

The masses of protoplanetary disks are an important driver for the processes of star and planet formation. Early in the lifetime of protostars disks are thought to be massive and turbulent, and accretion from the envelope onto these massive disks could cause gravitational instabilities that drive high accretion rates in young sources (e.g. Kenyon and Hartmann, 1987). The disk mass also sets a limit on the amount of material available for forming planets and the ultimate outcomes of the planet formation process (e.g. Alibert et al., 2005).

Disk masses are typically measured from their sub-millimeter flux, which if tracing optically thin matter, is directly proportional to the amount of material present in the disk (e.g. Beckwith et al., 1990). Class II disks are the easiest to study because, without a protostellar envelope, the entirety of the sub-millimeter flux can be attributed to disk emission. In the past decade there has been a large effort, particularly with interferometers like CARMA, the SMA, and now ALMA, towards measuring Class II disk masses (Andrews and Williams, 2005, 2007; Eisner et al., 2008; Mann and Williams, 2010; Mann et al., 2014; Ansdell et al., 2016; Barenfeld et al., 2016; Pascucci et al., 2016; Ansdell et al., 2017). These studies typically find that the majority of these disks fall well below the $0.01 - 0.1$ M$_\odot$ needed to form planetary systems like our own (e.g. Weidenschilling, 1977; Desch, 2007).

It may be that by the typical age of Class II disks ($1 - 5$ Myr; Andre and Montmerle, 1994a; Barsony, 1994), dust grain growth has locked up large amounts

of mass in large bodies to which sub-millimeter observations are not sensitive. If this is the case, then studying the disks around the younger ($\sim$ 0.5 Myr; Evans et al., 2009) Class I disks, which have had less significant dust processing, may give a better picture of the initial mass budget for forming planets. The masses of these disks are more difficult to determine because they are still embedded in their natal envelope, and any millimeter flux measurement will include a contribution from both the disk and envelope. Masses for Class I disks have been measured from high resolution millimeter visibilities by using radiative transfer modeling to separate disk and envelope contributions (Eisner et al., 2005; Eisner, 2012; Sheehan and Eisner, 2014), but sample sizes for these surveys are small.

In this paper we present a study of a sample of 10 Class I protostars in the Taurus Molecular Cloud, expanding on our previous work by including new, high resolution CARMA 1.3 mm maps for an expanded sample of objects. We use radiative transfer modeling and employ a fitting method that uses Markov Chain Monte Carlo simulations to fit models simultaneously to a 1.3 mm visibilities + broadband SED dataset and measure physical properties of the systems such as disk masses and radii. We discuss how these measurements of Class I disk masses compare to measurements of Class II disk masses, and what this means for the formation of planets.

3.2   Observations & Data Reduction

3.2.1   Sample Selection

Our sample includes 10 protostars in Taurus that are consistently identified as Class I across multiple independent studies (e.g. Myers et al., 1987; Kenyon et al., 1993; Motte and André, 2001a; Andrews and Williams, 2005; Furlan et al., 2008; Eisner, 2012). All of our targets fit standard criteria for selecting Class I protostars: all have an infrared spectral index of $\alpha > 0.15$ and a bolometric temperature of $70 < T_{bol} < 650$ (e.g. Myers et al., 1987; Chen et al., 1995; Motte and André, 2001a; Andrews and Williams, 2005). Furthermore, all of our targets have been observed with the

Spitzer IRS spectrograph and most have silicate and/or CO_2 ice absorption in their spectra, commonly associated with embedded sources (e.g. Alexander et al., 2003; Watson et al., 2004; Boogert et al., 2004; Pontoppidan et al., 2008).

In this sample we have excluded Class I objects that have been identified as compact binaries because the modeling of close separation binaries can be more challenging (e.g. Sheehan and Eisner, 2014). In all, our sample contains 10 of 12 companionless bona fide Class I protostars in Taurus. We were unable to observe the remaining 2, which were left for last because they were expected to be faint, before CARMA was decommissioned. Our targets do, however, span a wide range of millimeter fluxes (Motte and André, 2001a; Jørgensen et al., 2009; Eisner, 2012) so they should span a range of masses of circumstellar material. They also span a range of spectral types (M6-K4; White and Hillenbrand, 2004; Doppmann et al., 2005; Connelley and Greene, 2010) and scattered light morphologies (e.g. Padgett et al., 1999; Stark et al., 2006; Gramajo et al., 2010).

3.2.2 CARMA 1.3 mm Observations

We obtained 230 GHz Combined Array for Research in Millimeter-wave Astronomy (CARMA) dust continuum observations of our sample from September 3, 2012 until January 15, 2015. The observations were taken with CARMA's B, C, D, and E configurations (baselines ranging from ∼5 m to ∼1 km) so that our data would be sensitive to both large and small scale structures from the protostellar disks and envelopes. The observations were set up with 14 of CARMA's 16 spectral windows in wideband continuum mode from 216.798 GHz to 233.296 GHz with 500 MHz of bandwidth per-spectral window. The continuum observations had a mean frequency of 222.242 GHz and a total of 7 GHz of continuum bandwidth. The remaining two spectral windows were configured for spectral line observations, which we will discuss in a separate paper. We show a log of our observations in Table 3.1.

Table 3.1. Log of CARMA Observations

Source	Observation Date (UT)	Configuration	Baselines (m)
IRAS 04016+2610	Sep. 3 2012, Jan. 22 2013, Mar. 17, 19, 19, Oct. 3, Dec. 29 2014	E, B, C, C, C, E, D	4 - 982
IRAS 04108+2803B	Mar. 20, Jun. 19, Oct. 3 2014, Jan. 15 2015	C, E, E, D	6 - 386
IRAS 04158+2805	Sep. 3 2012, Jan. 21, Feb. 1 2013, Mar. 20, Oct. 3, Dec. 30 2015	E, B, B, C, E, D	5 - 982
IRAS 04166+2706	Oct. 3 2012, Jan. 2, 21, Feb 1 2013	E, C, B, B	5 - 982
IRAS 04169+2702	Oct. 3 2012, Jan. 2, 22 2013	E, C, B	5 - 982
IRAS 04181+2654A	Oct. 5 2014, Jan. 2 2015	E, D	7 - 152
IRAS 04181+2654B	Mar. 17, 19, 19, Oct. 3 2014, Jan. 3 2015	C, C, C, E, D	7 - 386
IRAS 04263+2426	Mar. 17, 19, 19, Jun. 19, Oct. 3, Dec. 29 2014	C, C, C, E, E, D	5 - 386
IRAS 04295+2251	Oct. 4 2014, Jan. 2 2015	E, D	7 - 153
IRAS 04302+2247	Sep. 3 2012, Jan. 2 2013, Jan. 3 2015	E, C, D	1 - 386
IRAS 04365+2535	Sep. 3 2012, Jan. 15 2015	E, D	5 - 152
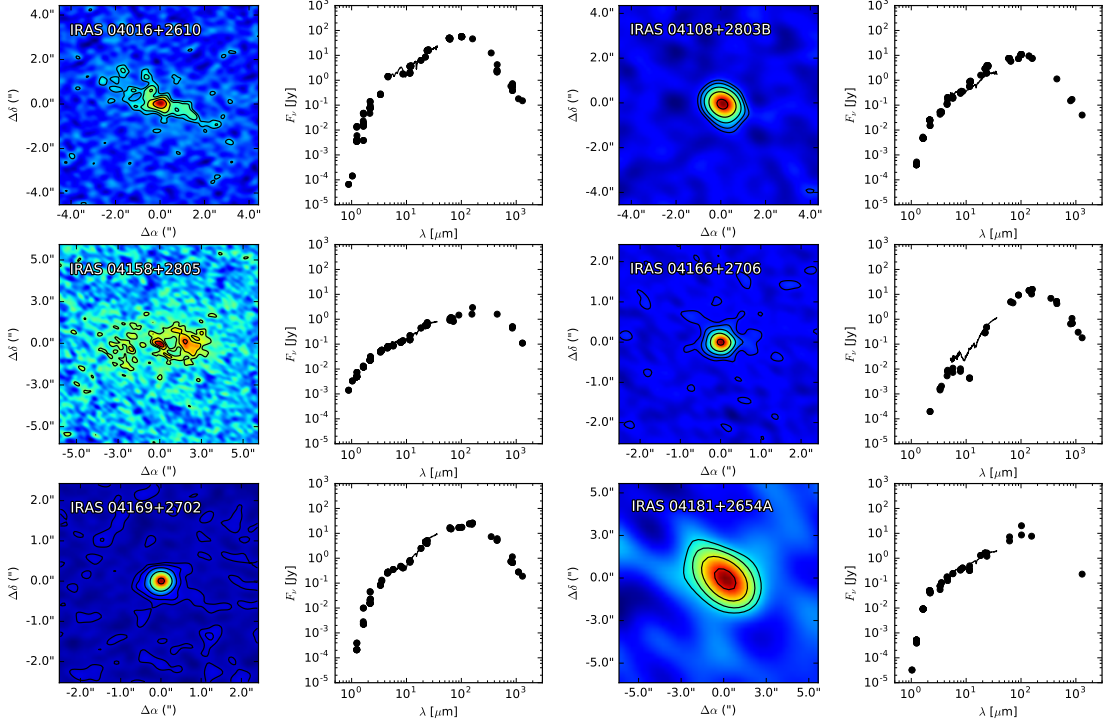
Figure 3.1: We show the 1.3 mm CARMA maps (first and third columns) and broadband SEDs (second and fourth columns) for each of the sources in our sample. Many of our sources were observed with high enough spatial resolution to resolve structure in their disks and envelopes. Only one source, I04181B is undetected in our maps. For all sources the SED is sampled across the electromagnetic spectrum and includes a high resolution Spitzer IRS spectrum.

The CARMA data were reduced using the `CASA` software package in the standard way. For the majority of the tracks Uranus was used as the flux calibrator, the quasar 3C84 as the bandpass calibrator, and 3C111 and QSO 0510+180 as the gain calibrators. For a few tracks, QSO 0530+135 was also used as the gain calibrator when 3C111 or QSO 0510+180 were unavailable. For tracks where Uranus was unavailable to use as the flux calibrator we used 3C84 instead with measured fluxes from the SMA calibrator catalog.

Following calibration, the data were imaged by Fourier transforming the visibilities with `CASA`'s *clean* routine to produce images of our targets. For each source we combine all of the available tracks and configurations to produce a single image. We use the multi-frequency synthesis mode and the Briggs weighting scheme with
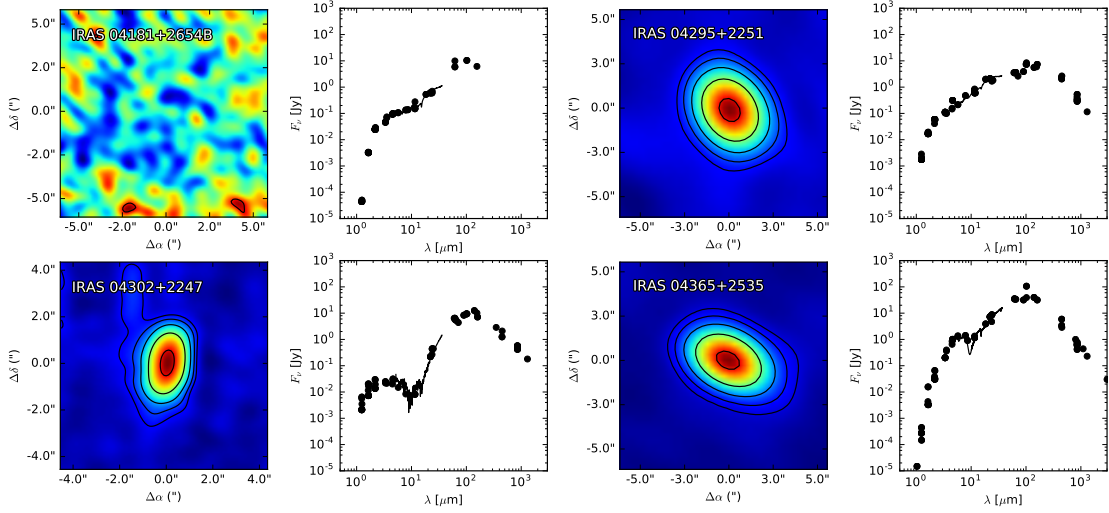
Figure 3.2: Continued.

a robust parameter of 0.5. Because CARMA is a heterogeneous array, mosaicking mode is needed to correctly image the data. We show images of our targets in Figures 3.1 & 3.2. Although we show images of the data, we do all of our analysis and modeling directly with the visibilities.

3.2.3   SEDs from the Literature

For each of our sources we compiled a broadband SED using data from the literature. This data includes photometry from Spitzer IRAC and MIPS, WISE, 2MASS, and IRAS as well as other infrared and millimeter surveys (Ladd et al., 1991; Barsony and Kenyon, 1992; Moriarty-Schieven et al., 1994; Ohashi et al., 1996; Chandler and Richer, 2000; Motte and André, 2001a; Young et al., 2003; Andrews and Williams, 2005, 2007; Eisner, 2012). In addition to this photometry, we downloaded a calibrated Spitzer IRS spectrum with wavelength coverage from $5 - 30$ μm from the CASSIS database to include in our SED (Lebouteiller et al., 2011, 2015).

In order to assess the quality of our model fits through metrics such as χ^2, which we describe in Section 3.3.6, we assume a uniform 10% flux uncertainty on all photometry from the literature. We also sample the IRS spectrum at 25 points spaced uniformly over the spectral range to include in our SED. We do this because

calculating fluxes at the several hundred IRS spectrum channels with our radiative transfer modeling routines is computationally expensive, and it is not a goal of this paper to model in extreme detail the IRS spectrum.

3.2.4 HST Scattered Light Images

Five of our sources (IRAS 04016+2610, IRAS 04108+2803B, IRAS 04158+2805, IRAS 04295+2251 and IRAS 0302+2247) have near-infrared Hubble Space Telescope scattered light images with the Wide-field Planetary Camera available, although IRAS 04108+2803 is a non-detection. We downloaded calibrated versions of these images from the Hubble Legacy Archive for comparison with our models.

3.3 Modeling

We use detailed radiative transfer modeling to produce synthetic observations of a protostar model that can be matched to our millimeter visibilities + broadband SED dataset. The model includes a central star, protoplanetary disk, and a rotating collapsing envelope, following the modeling scheme of Eisner et al. (2005), Eisner (2012), and Sheehan and Eisner (2014). These previous studies ran large grids of radiative transfer models and fit those grids to multi-wavelength datasets to determine system parameters. The availability of computational resources, however, limited those previous studies to a small set of discrete values for each parameter. Here we have developed a Markov Chain Monte Carlo procedure to more completely explore parameter space, particularly in the vicinity of the best fit model. We describe the components and free parameters of the model as well as our modeling technique below.

3.3.1 Pre-Main-Sequence Star

Our Class I model includes a central protostar with a temperature of 4000 K and a luminosity, $L_\odot$, that is left as a free parameter. The majority of the sources in our system are K- or M-type stars (White and Hillenbrand, 2004; Doppmann et al., 2005;

Connelley and Greene, 2010), so a temperature of 4000 K is a reasonable assumption. We may, however, explore varying the protostellar temperature in future works.

3.3.2 Disk

Our model also includes a protoplanetary disk that uses the standard density profile of a flared power-law disk,

$$\rho = \rho_0 \left(\frac{R}{R_0}\right)^{-\alpha} \exp\left(-\frac{1}{2}\left[\frac{z}{h(R)}\right]^2\right), \tag{3.1}$$

where R and z are in cylindrical coordinates. $h(R)$ is the disk scale height at a given radius,

$$h(R) = h_0 \left(\frac{R}{1\ \text{AU}}\right)^{\beta}. \tag{3.2}$$

The surface density profile is

$$\Sigma = \Sigma_0 \left(\frac{R}{R_0}\right)^{-\gamma}, \ \gamma = \alpha - \beta. \tag{3.3}$$

We truncate the disk at a specified inner and outer disk radius, R_{in} and R_{disk}, that are allowed to vary in our fit. The surface density power law exponent, γ, and the scale height power law exponent, β, are also left as free parameters in our model. We leave the disk mass, M_{disk}, and scale height at 1 AU, h_0, as free parameters. The density at the inner radius, ρ_0 can be calculated from the disk mass by integrating equation 1 over all space.

3.3.3 Envelope

Our sources are young and likely embedded in an envelope of material remaining from the initial cloud from which they formed, so we also include an envelope component in our protostar model. We use the density profile for a rotating collapsing envelope from Ulrich (1976),

$$\rho = \frac{\dot{M}}{4\pi}\left(GM_*r^3\right)^{-\frac{1}{2}}\left(1+\frac{\mu}{\mu_0}\right)^{-\frac{1}{2}}\left(\frac{\mu}{\mu_0}+2\mu_0^2\frac{R_c}{r}\right)^{-1} \tag{3.4}$$

where $\mu = \cos\theta$, and r and θ are defined in the typical sense for spherical coordinates. We truncate the envelope at the same inner radius, R_{in}, as the disk and at an outer radius, R_{env}, that is left as a free parameter. We require that the envelope radius be larger than the disk radius. R_c is the critical radius, inside of which the envelope begins to flatten due to rotation, and is the location where the majority of material is accreting onto the disk (Ulrich, 1976; Terebey et al., 1984). This makes the most sense physically if the critical radius is equal to the disk radius, so in our model we specify that $R_c = R_{disk}$. The envelope mass, M_{env}, is also a free parameter, and the density normalization can again be calculated by integrating equation 4 over all space.

We give the envelope an outflow cavity. In regions where

$$z > 1 \text{ AU} + r^\zeta \tag{3.5}$$

we reduce the envelope density by the factor f_{cav}. We leave both ζ and f_{cav} as free parameters to be varied in our modeling routines.

3.3.4 Dust

We provide our disk model with dust opacities that are the same as those used by Sheehan and Eisner (2014), that for small maximum dust grain sizes, are similar to the icy dust grains from Ossenkopf and Henning (1994). The opacities have a composition that is 40% astronomical silicate, 30% organics, and 30% water ice, roughly following the recipe from Pollack et al. (1994) but adjusted to match the dense protostellar core opacities from Ossenkopf and Henning (1994) (see Sheehan and Eisner 2014 for a more thorough discussion). We use a gain size distribution with $n \propto a^{-p}$ with $p = 3.5$ (Mathis et al., 1977), and dust grains ranging from 0.005 μm to a_{max}. In the envelope, where dust grain growth is likely to be less advanced, we fix $a_{max} = 1$ μm. In the disk, however, we leave a_{max} as a free parameter.

3.3.5 Radiative Transfer Modeling + Synthetic Images

We use the 3D Monte Carlo radiative transfer modeling codes `RADMC-3D` (Dulle-mond, 2012) and `Hyperion` (Robitaille, 2011) to produce synthetic observations of our protostar model that can subsequently be compared with our combined mil-limeter visibilities + broadband SED dataset. We use the radiative transfer codes to run a simulation to calculate the temperature everywhere throughout the disk and envelope by propagating photon packets through the model and updating the temperature in each model cell every time a photon is absorbed and then reemit-ted. In most cases we use `RADMC-3D` to do the temperature calculation, however for protostars with a particularly high density, i.e. small disk or envelope radii or large disk or envelope masses, we use `Hyperion` because it can be run in parallel to speed up the computation. We have compared the results from `RADMC-3D` and `Hyperion` when running the same input model and find that the codes are consistent. Fol-lowing the radiative transfer simulation we use raytracing in `RADMC-3D` to produce synthetic SEDs and millimeter images, and we Fourier transform the millimeter im-ages to produce synthetic visibilities. The viewing angle parameters, inclination and position angle (i and $p.a.$), are free parameters in our fitting procedure.

3.3.6 Fitting Procedure

We fit our model to the data by comparing synthetic visibilities and SEDs to our millimeter visibilities + broadband SED dataset with the Markov Chain Monte Carlo (MCMC) code `emcee` (Foreman-Mackey et al., 2013). For each source in our sample we run a MCMC fit in which we spread out 200 walkers randomly with a uniform distribution over a large volume of parameter space and allow the walkers to collectively move towards regions of parameters space that represent the best fits to the data.

In these simulations the walkers are seeking to maximize the log-likihood of the model, which is directly proportional to χ^2. Here we are simultaneously fitting to the millimeter visibilities and the broadband SED, which are separate datasets with

heteroscedastic error bars, so specifying a goodness-of-fit metric is challenging. For simplicity we use the weighted sum of the χ^2 values for our individual datasets,

$$X^2 = w_{vis}\, \chi^2_{vis} + w_{SED}\, \chi^2_{SED}, \tag{3.6}$$

to provide a log-likihood to our fits, and we seek to maximize $-X^2/2$. We can vary the weights of each dataset (w_*) to increase the contribution of that dataset to the fit. As resolved images provide more direct information about source geometry than unresolved SEDs, we typically weight up the visibilities to ensure that they are fit well.

Each individual radiative transfer model is computationally intensive to run and can take anywhere from a few minutes to a few hours. `emcee` uses MPI to spread the calculations out over a large number of cores, with each core computing the models for a subset of walkers, to significantly speed up the computation. In principle the calculations can be spread over any number of nodes, but we find that fits typically converge over reasonable timescales of a few weeks when spread over 28 cpus. We can then simultaneously run fits to many sources on individual nodes of a supercomputer.

3.4   Results

We list the best fit parameters in Table 3.2 and show the best fit models compared with the data for each source in Figures 3.3-3.12. We are able to find models that reproduce the combined 1.3 mm visibilities + broadband SED dataset for each of our sources. We note that the masses (both disk and envelope) listed here assume a standard gas-to-dust ratio of 100. Dust masses, which are the values that are directly constrained by our modeling, are a factor of 100 lower. We list total mass for ease of comparing with the Minimum Mass Solar Nebula, which is typically quoted in terms of total mass.

Table 3.2. Best-fit Model Parameters

Source	L_* [$L_\odot$]	M_{disk} [$M_\odot$]	R_{in} [AU]	R_{disk} [AU]	h_0 [AU]	γ	β	M_{env} [$M_\odot$]	R_{env} [AU]	f_{cav}	ξ	a_{max} [μm]	i [°]	$P.A.$ [°]	A_K
IRAS 04016+2610	$6.5^{+1.1}_{-0.9}$	$0.012^{+0.007}_{-0.004}$	$1.2^{+0.4}_{-0.3}$	491^{+24}_{-23}	$0.12^{+0.03}_{-0.03}$	$0.66^{+0.04}_{-0.04}$	$0.99^{+0.08}_{-0.08}$	$0.023^{+0.005}_{-0.004}$	1373^{+145}_{-131}	$0.74^{+0.25}_{-0.25}$	$1.19^{+0.33}_{-0.33}$	492^{+378}_{-214}	68^{+1}_{-1}	65^{+1}_{-1}	$1.4^{+0.2}_{-0.2}$
IRAS 04108+2803B	$0.6^{+0.2}_{-0.1}$	$0.011^{+0.008}_{-0.005}$	$0.8^{+0.4}_{-0.3}$	49^{+15}_{-12}	$0.09^{+0.02}_{-0.02}$	$1.30^{+}_{-0.47}$	$0.89^{+0.15}_{-0.15}$	$0.005^{+0.007}_{-0.003}$	399^{+403}_{-201}	$0.50^{+0.10}_{-0.10}$	$0.84^{+0.20}_{-0.20}$	116^{+431}_{-92}	38^{+8}_{-8}	117^{+30}_{-30}	$\cdots$
IRAS 04158+2805	$0.4^{+0.1}_{-0.1}$	$0.116^{+0.027}_{-0.022}$	$0.1^{+0.0}_{-0.0}$	566^{+13}_{-12}	$0.19^{+0.02}_{-0.02}$	$-0.27^{+0.06}_{-0.06}$	$0.88^{+0.03}_{-0.03}$	$0.084^{+0.032}_{-0.052}$	3602^{+1637}_{-1126}	$0.00^{+0.00}_{-0.00}$	$0.92^{+0.01}_{-0.01}$	661^{+160}_{-129}	65^{+1}_{-1}	94^{+1}_{-1}	$\cdots$
IRAS 04166+2706	$0.3^{+0.0}_{-0.0}$	$0.024^{+0.012}_{-0.008}$	$1.2^{+0.4}_{-0.3}$	188^{+13}_{-12}	$0.05^{+0.02}_{-0.02}$	$1.93^{+0.05}_{-0.05}$	$0.93^{+0.12}_{-0.12}$	$0.090^{+0.028}_{-0.021}$	1204^{+179}_{-156}	$0.79^{+0.10}_{-0.10}$	$1.00^{+0.05}_{-0.05}$	5405^{+12023}_{-3729}	40^{+4}_{-4}	153^{+2}_{-2}	$\cdots$
IRAS 04169+2702	$0.8^{+0.2}_{-0.2}$	$0.012^{+0.002}_{-0.002}$	$0.2^{+0.2}_{-0.1}$	40^{+3}_{-3}	$0.05^{+0.03}_{-0.03}$	$0.75^{+0.14}_{-0.14}$	$1.12^{+0.10}_{-0.10}$	$0.036^{+0.011}_{-0.008}$	668^{+66}_{-60}	$0.13^{+0.07}_{-0.07}$	$1.02^{+0.02}_{-0.02}$	9316^{+3725}_{-2661}	34^{+2}_{-3}	2^{+3}_{-3}	$\cdots$
IRAS 04181+2654A	$0.4^{+0.1}_{-0.1}$	$0.005^{+0.001}_{-0.001}$	$0.2^{+0.1}_{-0.0}$	49^{+23}_{-16}	$0.11^{+0.04}_{-0.04}$	$0.15^{+0.57}_{-0.57}$	$0.88^{+0.19}_{-0.19}$	$0.695^{+0.377}_{-0.244}$	16351^{+7019}_{-4911}	$0.61^{+0.23}_{-0.23}$	$1.14^{+0.17}_{-0.17}$	8^{+46}_{-6}	15^{+13}_{-13}	98^{+53}_{-53}	$\cdots$
IRAS 04181+2654B	$0.2^{+0.0}_{-0.0}$	$0.000^{+0.000}_{-0.000}$	$0.1^{+0.0}_{-0.0}$	21^{+6}_{-4}	$0.10^{+0.01}_{-0.01}$	$0.64^{+0.17}_{-0.17}$	$0.63^{+0.04}_{-0.04}$	$0.003^{+0.002}_{-0.001}$	436^{+387}_{-205}	$0.50^{+0.09}_{-0.09}$	$1.39^{+0.08}_{-0.08}$	66^{+39}_{-25}	4^{+3}_{-3}	80^{+26}_{-26}	$\cdots$
IRAS 04295+2251	$0.5^{+0.0}_{-0.0}$	$0.027^{+0.004}_{-0.004}$	$0.2^{+0.1}_{-0.1}$	152^{+10}_{-9}	$0.29^{+0.09}_{-0.09}$	$0.00^{+0.13}_{-0.13}$	$0.58^{+0.09}_{-0.09}$	$0.043^{+0.032}_{-0.018}$	2862^{+2635}_{-1372}	$0.77^{+0.21}_{-0.21}$	$1.38^{+0.11}_{-0.11}$	1443^{+1075}_{-616}	56^{+2}_{-2}	66^{+2}_{-2}	$\cdots$
IRAS 04302+2247	$0.4^{+0.0}_{-0.0}$	$0.107^{+0.017}_{-0.015}$	$2.6^{+0.7}_{-0.6}$	243^{+7}_{-6}	$0.04^{+0.04}_{-0.04}$	$-0.39^{+0.10}_{-0.10}$	$0.82^{+0.19}_{-0.19}$	$0.019^{+0.009}_{-0.006}$	1137^{+414}_{-304}	$0.81^{+0.20}_{-0.20}$	$1.22^{+0.25}_{-0.25}$	17181^{+12730}_{-7312}	78^{+1}_{-1}	172^{+1}_{-1}	$\cdots$
IRAS 04365+2535	$3.7^{+0.7}_{-0.6}$	$0.027^{+0.003}_{-0.003}$	$0.6^{+0.3}_{-0.2}$	111^{+12}_{-11}	$0.09^{+0.03}_{-0.03}$	$0.72^{+0.24}_{-0.24}$	$0.86^{+0.15}_{-0.15}$	$0.167^{+0.053}_{-0.040}$	2119^{+209}_{-191}	$0.23^{+0.10}_{-0.10}$	$0.86^{+0.03}_{-0.03}$	1440^{+588}_{-418}	59^{+2}_{-2}	78^{+3}_{-3}	$0.8^{+0.3}_{-0.3}$

We list error bars derived from the standard deviation of the positions of the walkers at the end of our MCMC fit. While they are a reasonable representation of the range of allowed values for each parameter, our weighted sum of χ^2 likely makes it such that these are not rigorous uncertainties. We have, however, compared the error bars we measure on inclination with the results of a simple uniform disk geometrical fit and find that the magnitudes of the errors are generally in agreement. As such, the errors we list are likely reasonable estimates of how well constrained our models are.

Our sample has a range of inferred properties, including disk radii ranging from $50 - 560$ AU and disk masses ranging from $0.0002 - 0.1$ M$_\odot$. Our sample also has a diversity of envelope properties, with masses ranging from $0.003 - 0.35$ M$_\odot$ and radii from $400 - 10000$ AU. The ratio of disk-to-envelope masses ranges from $0.2 - 5$. We discuss each of the sources below.

3.4.1   IRAS 04016+2610

IRAS 04016+2610 has one of the largest disks in our sample, with a radius of about 500 AU. For such a large disk, though, it is relatively low mass, at 0.01 M$_\odot$. The disk is highly inclined, with an inclination of 65°. Although we did not include scattered light imaging in our fit, our best fit model nicely reproduces the observed HST scattered light image of the system (see Figure 3.13). The envelope is about twice as massive as the disk, indicating that IRAS 04016+2610 is a well-embedded source.

Our base model is not able to fully reproduce both the millimeter visibilities and the SED for IRAS 04016+2610 simultaneously. Any fit that reproduces the millimeter visibilities does not provide enough extinction to match the SED at near-infrared wavelengths (see Figure 3.3), so some additional source of extinction is needed. To remedy this, we have run a fit that includes an additional parameter, the K-band extinction (A_K) that we use to redden the SED using the McClure et al. (2010) extinction law, and find that both datasets can be reproduced with $A_K \sim 1.5$.

Although this extinction could simply be from the large scale cloud in the fore-
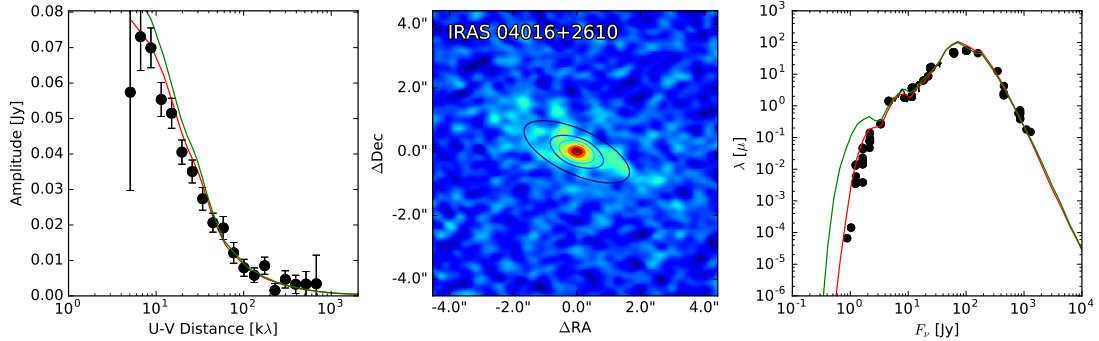
Figure 3.3: We show the 1.3 mm visibility profile (*left*), 1.3 mm image (*center*), and broadband SED (*right*) for IRAS 04016+2610 with the best-fit disk+envelope model curves over-plotted. The green curve shows our base model, which matches the visibilities but does not extinct the spectrum sufficiently at short wavelengths. If we include some foreground extinction in the fit (the red line), however, the models fit the data. Parameters for these models can be found in Table 3.2.

ground of IRAS 04016+2610, previous studies of the system have suggested other possibilities. Hogerheijde and Sandell (2000) found that IRAS 04016+2610 is in close proximity to a neighboring starless dark cloud, and Brinch et al. (2007a) found that they could only fit their models if IRAS 04016+2610 was located behind the edge of that dark cloud. If this dark cloud is indeed in the foreground, as Brinch et al. (2007a) suggest, it could be the source of the extinction. Alternatively, it may be that this large amount of extinction could come from large scale, constant density material from the cloud that has not yet begun to collapse, but could collapse sometime in the future (e.g. Jayawardhana et al., 2001).

IRAS 04016+2610 was previously studied using a similar procedure to our own modeling by Eisner (2012), but using a grid rather than an MCMC fit. The parameters for the best fits IRAS 04016+2610 are similar to what we find here, with a typical disk mass of 0.005 $M_\odot$ and a disk radius of 250 - 450 AU. Most of the best fit models from Eisner (2012) for IRAS 04016+2610, however, are found to have $i \sim 35 - 40°$, much smaller than what we find here. The exception to this a model in which the scattered light image is given more weight, and as a result the best fit inclination is 65°. This is also consistent with the inclination Stark et al. (2006)

found, of $i \sim 65°$ by modeling only the near-infrared scattered light image. Measurements of the inclination from the bipolar outflow found to be associated with IRAS 04016+2610 (Gomez et al., 1997; Hogerheijde et al., 1998) find that the disk must have an inclination of 60°, in very good agreement with what we find here.

Other studies have previously modeled this source and found a range of results. Furlan et al. (2008) found a much lower inclination ($i \sim 40°$) and disk radius ($R_c \sim$ 100 AU), but only considered the SED and had no imaging constraints on the system geometry. Similarly, Robitaille et al. (2007) found low inclinations from a SED-only fit. Gramajo et al. (2010) find a higher inclination, of $50 - 63°$ by considering the Spitzer IRS spectrum and scattered light images, along with the broadband SED. Brinch et al. (2007a) found that the IRAS 04016+2610 has a slightly flattened envelope with an inclination of 74°, while Brinch et al. (2007b) suggested that the disk may be misaligned with the envelope and has an inclination of 40°, but these models were based on lower resolution observations than we present here. Inferred disk masses for this source range from $\sim 0.004 - 0.02$ M$_\odot$, and our measurement falls nicely in the middle of that range.

3.4.2   IRAS 04108+2803B

Our best fit model for IRAS 04108+2803B has both a compact disk ($R_{disk} \approx 50$ AU) and envelope ($R_{env} \approx 400$ AU), and the disk is about twice as massive as the envelope. The disk is not resolved well in our millimeter maps, nor is the system detected in scattered light, so the constraints on geometrical properties of the system are somewhat weak.

This system has been modeled previously and found to have a compact disk, with a disk radius of 30-100 AU and moderate (20-60°) inclinations (Kenyon et al., 1993; Whitney et al., 1997; Eisner et al., 2005; Furlan et al., 2008). Our best fit model is in good agreement with Eisner et al. (2005), who find a disk radius of 30 AU, an envelope radius of 500 AU, and an inclination of 24°. They find that the disk is significantly more massive than our results ($M_{disk} \sim 0.5$ M$_\odot$), but they also suggest that this is likely an overestimate.
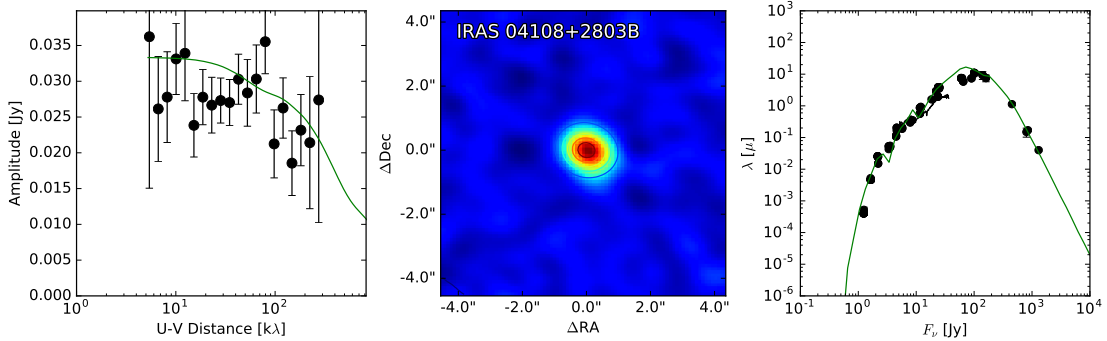
Figure 3.4: We show the 1.3 mm visibility profile (*left*), 1.3 mm image (*center*), and broadband SED (*right*) for IRAS 04108+2803B with the best-fit disk+envelope model curves over-plotted. Parameters for these models can be found in Table 3.2.

Chiang and Goldreich (1999) suggested that the SED of this source could be fit by an inclined flared accretion disk, suggesting that the disk may be an edge-on Class II disk rather than a Class I source. The large disk radius needed (~ 250 AU), though, would have been resolved in our millimeter observations, and indeed Eisner et al. (2005) find that an envelope component is needed to fit the SED. Watson et al. (2004) also suggest that the 15.2 μm ice absorption feature found in the Spitzer IRS spectrum is most likely to arise in an envelope. This is consistent with our own results that find that an envelope is needed to match the data.

Our results do, however, show that the envelope is quite low-mass compared to other Class I sources, which seems to suggest that IRAS 04108+2803B is close to dispelling its envelope and emerging as a Class II system. This is consistent with the presence of a wide-separation companion, IRAS 04108+2803A, that appears to be a more evolved, Class II system. If the binary system is approximately coeval, as might be expected, then these sources may both be young and on the boundary between Class I and II.

3.4.3 IRAS 04158+2805

IRAS 04158+2805 has the largest disk of the sample, at $R_{disk} = 560$ AU, and is the most massive disk ($M_{disk} = 0.12$ $M_{\odot}$). The disk is somewhat inclined, at about 65°.
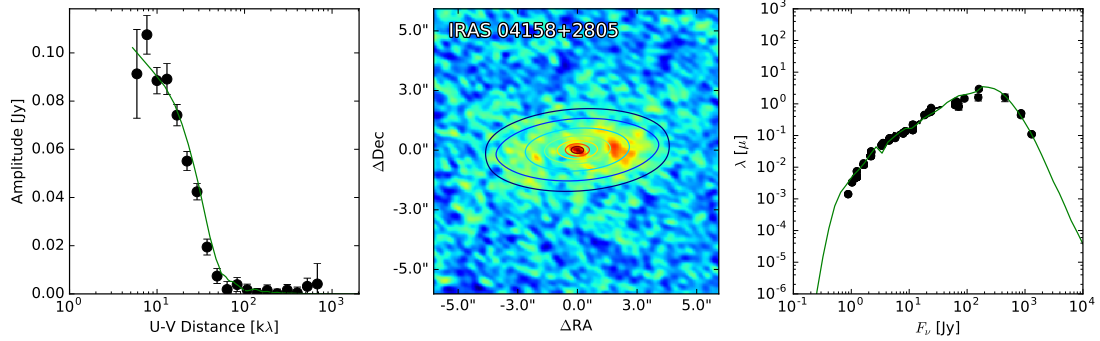
Figure 3.5: We show the 1.3 mm visibility profile (*left*), 1.3 mm image (*center*), and broadband SED (*right*) for IRAS 04158+2805 with the best-fit disk+envelope model curves over-plotted. Parameters for these models can be found in Table 3.2.

The envelope has a mass of $M_{env} = 0.084$ M$_\odot$ and a radius of $R_{env} = 3600$ AU. Like IRAS 04016+2610, we did not include the HST scattered light image in the fit, but our best fit model naturally reproduces the scattered light image without any fitting needed (see Figure 3.13).

There has been some disagreement about the nature of this object in previous studies. Most signs point to this source being a very low mass protostar, with a spectral type of M5-6 ($M_* \sim 0.1 - 0.2$) (White and Hillenbrand, 2004; Luhman, 2006; Connelley and Greene, 2010), although mass estimates from gas kinematics (Andrews et al., 2008) and other spectral typing surveys (Doppmann et al., 2005) have suggested it might be more massive. Some studies have classified IRAS 04158+2805 as a Class II disk, and indeed Glauser et al. (2008) suggested that the near-infrared scattered light image and SED for the system could be fit without an envelope component. However, their model needs a much larger disk radius ($R_{disk} \sim 1150$ AU) than what we find here. Our observations suggest that the disk is much smaller than that, although still quite large compared to typical protoplanetary disks. Moreover, the infrared spectrum exhibits absorption features of H_2O and CO_2 ices and a silicate absorption feature, all of which are more commonly associated with Class I sources embedded in envelopes (e.g. Watson et al., 2004; Pontoppidan et al., 2008). The presence of these features along with the good fit of our disk+envelope model to the combined SED and millimeter visibilities suggest that this is an embedded

source.

3.4.4 IRAS 04166+2706

Our best fit model for IRAS 04166+2706 indicates a 190 AU radius disk and an envelope that is about three times more massive than its disk. The disk and the envelope are clearly detected in our millimeter visibilities, with an apparent break at 30-80 kλ where the disk begins to dominate over the envelope. There is no apparent flattening at the shortest baselines, likely indicating that we have resolved out some of the envelope, and may be underestimating its mass. No HST scattered light image was available for the source, and Eisner et al. (2005) were unable to detect it in scattered light with Keck LRIS imaging. This is perhaps unsurprising, given how embedded the source appears to be from the SED.

IRAS 04166+2706's defining characteristic is it's bipolar outflow (Bontemps et al., 1996) that has an extremely high velocity component that is highly collimated (Tafalla et al., 2004; Santiago-García et al., 2009; Wang et al., 2014). That, coupled with its highly embedded disk, have led some to suggest that it is a Class 0 protostar. Tafalla et al. (2004) suggested based on the outflow that the disk must be highly inclined, although our high resolution millimeter observations contradict that.
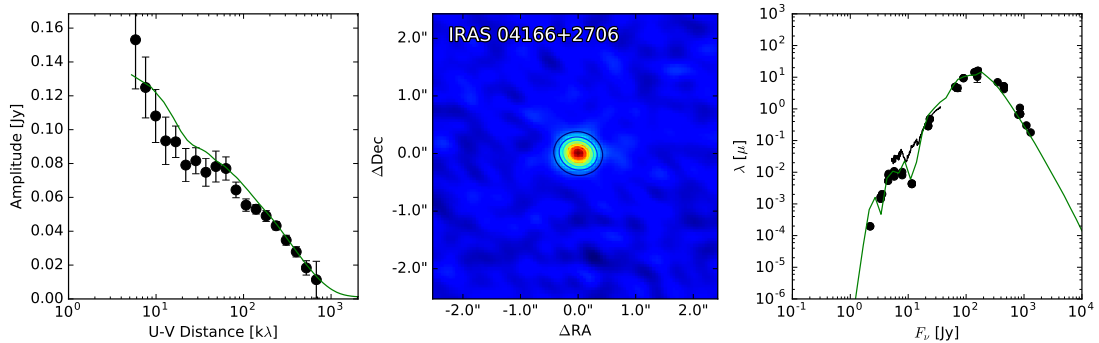
Figure 3.6: We show the 1.3 mm visibility profile (*left*), 1.3 mm image (*center*), and broadband SED (*right*) for IRAS 04166+2706 with the best-fit disk+envelope model curves over-plotted. Parameters for these models can be found in Table 3.2.

The disk mass of our best fit model for IRAS 04166+2706 is in good agreement with the results from Eisner (2012), but the disk radius we measure is much smaller (160 AU compared with 450 AU). Furlan et al. (2008) find a disk radius of 300 AU, although note that a disk of 200 AU can also provide a good fit. Kenyon et al. (1993) find a smaller disk (70 AU), but a similar inclination (30°). Our millimeter dataset, however is much higher resolution than what was available for Eisner (2012), and Kenyon et al. (1993) and Furlan et al. (2008) model only the SED, so we are able to constrain the structure of the disk.

3.4.5   IRAS 04169+2702

IRAS 04169+2702 has a compact ($R_{disk} \sim 40$ AU) disk hidden in a larger envelope that is about three times more massive than the disk. The disk has a mass of $M_{disk} \sim 0.012$, and it is being viewed at low or moderate inclinations of $\sim 30°$. The millimeter visibility amplitudes flatten out at around 50 kλ, likely where the disk begins to dominate over the envelope.

This source was modeled previously by Eisner (2012), who found a much larger disk, typically $250 - 450$ AU although weighting up the SED produces a fit with a 100 AU disk, but comparable disk masses and inclinations. Furlan et al. (2008) fit the SED with a disk about twice the size we find here, but with a high inclination,
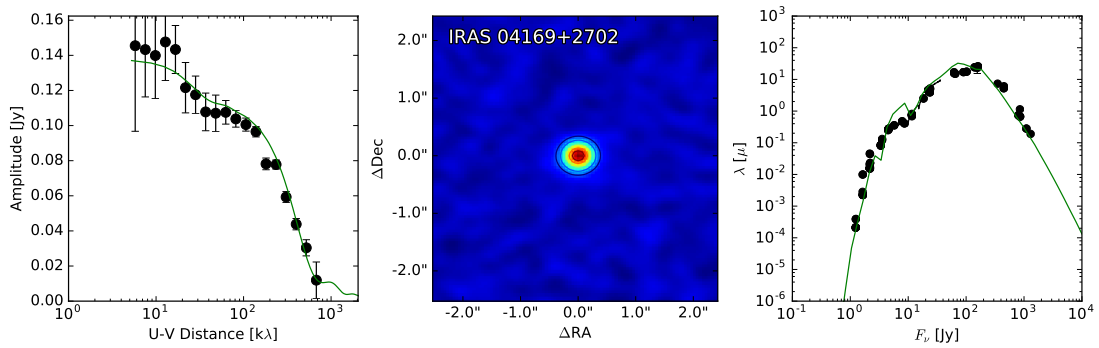
Figure 3.7: We show the 1.3 mm visibility profile (*left*), 1.3 mm image (*center*), and broadband SED (*right*) for IRAS 04169+2702 with the best-fit disk+envelope model curves over-plotted. Parameters for these models can be found in Table 3.2.

while Robitaille et al. (2007) found from SED fitting that $R_{disk} < 150$ AU and $i > 30°$, both in agreement with our results. IRAS 04169+2702 is associated with a bipolar outflow (Bontemps et al., 1996), and Ohashi et al. (1997) find that the outflow is associated with an elongated envelope structure inclined 60° with respect to our line of sight (Ohashi et al., 1997). However, compared with both of these studies we have much better resolution to study disk structure, so our measurement is likely more accurate.

3.4.6 IRAS 04181+2654A

IRAS 04181+2654A appears to be a low mass disk ($M_{disk} \sim 0.005$ M$_\odot$) embedded in a very massive envelope ($M_{env} \sim 0.7$ M$_\odot$). Although the visibilities are noisy, a clear break in the visibility profile at around 10 kλ is readily identifiable, indicating the presence of significant amounts of emission on large spatial scales. Our observations are not sensitive to large enough scales to fully determine the structure of the envelope, but it appears to be quite large ($R_{env} \sim 15000$ AU) and massive. The disk, by comparison, is quite compact, with a radius of about 50 AU and a mass of only 0.005 $M_\odot$.

Because this object has few flux measurements at millimeter wavelengths, there have been a lack of studies to determine parameters for the system, and what has
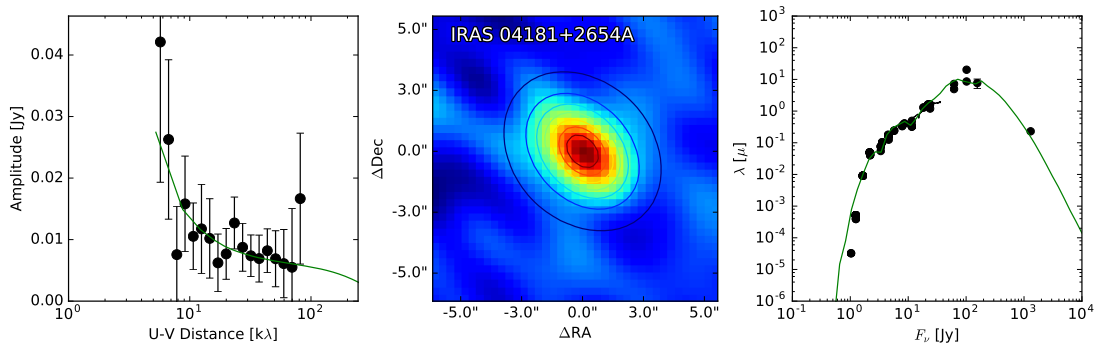
Figure 3.8: We show the 1.3 mm visibility profile (*left*), 1.3 mm image (*center*), and broadband SED (*right*) for IRAS 04181+2654A with the best-fit disk+envelope model curves over-plotted. Parameters for these models can be found in Table 3.2.

been done only considered the SED. Our results are in good agreement with what was found by Furlan et al. (2008), who find a low inclination disk with a radius of 50 AU and an envelope with a radius of 10,000 AU. Kenyon et al. (1993) also find that the disk is compact (R_{disk} = 70 AU) and low inclination (i = 30°).

3.4.7 IRAS 04181+2654B

IRAS 04181+2654B is detected in the near- to far-infrared, but has not been detected at millimeter wavelengths. This remains true of our own observations, which detect no 1.3 mm emission. It seems to be embedded based on CO_2 ice absorption in its Spitzer IRS SED and its association with the embedded source IRAS 04181+2654A. We have included the source in our modeling, but the models are not constrained well. We show that the disk is likely small and low mass, but can say little else definitively. At 31" from IRAS 04181+2654A, or 4300 AU projected separation, it falls well within the envelope we measure for IRAS 04181+2654A. As that envelope is quite large and massive, it could be that this source is simply a low mass disk hidden behind the IRAS 04181+2654A envelope.
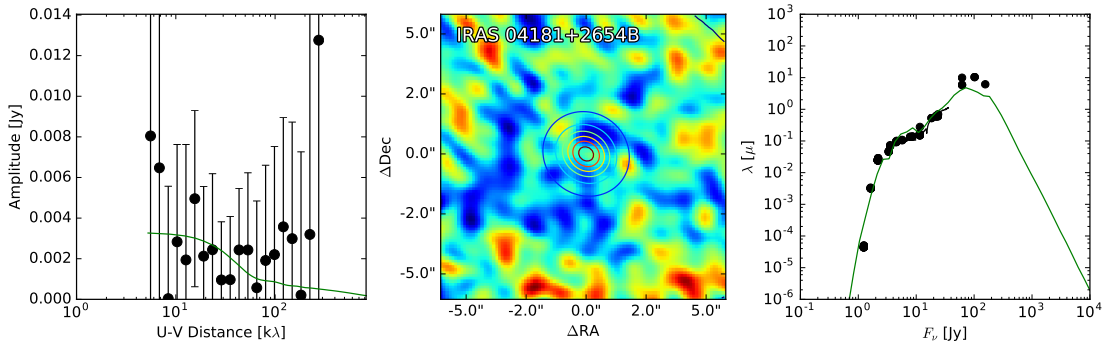
Figure 3.9: We show the 1.3 mm visibility profile (*left*), 1.3 mm image (*center*), and broadband SED (*right*) for IRAS 04181+2654B with the best-fit disk+envelope model curves over-plotted. Parameters for these models can be found in Table 3.2.

3.4.8   IRAS 04295+2251

Our model for IRAS 04295+2251 fits both the broadband SED and millimeter vis-
ibilities, and naturally reproduces the scattered light image, as seen in Figure 3.13.
We have not resolved the disk well, but it appears to have a radius of about 160 AU
and a mass of $\sim$ 0.03 M$_\odot$. The best-fit model indicates that the disk is relatively
highly inclined ($i \sim 60°$). The good match to the scattered light image, even though
the scattered light image was not used to determine the fit, validates our inferred
inclination. The envelope is of comparable mass to the disk, but the visibility profile
does not flatten at small < 10 kλ scales, which may indicate that there is large scale
envelope material that is resolved out by our observations.

   Our best fit model is generally in agreement with what is found by previous
studies. Eisner et al. (2005) found that the disk has a radius of 100 AU but that
the inclination is low ($i \sim 20°$). Eisner (2012) found that IRAS 04295+2251 has
a compact (30–100 AU) disk with a mass of 0.01 M$_\circ$ and a higher inclination, of
45–55°. Furlan et al. (2008) model the SED and find a very compact ($R_{disk} = 20$
AU) disk with an inclination of 70°. Chiang and Goldreich (1999) suggested that
IRAS 04295 could be an edge on disk, but our modeling indicates that even though
the disk is somewhat edge-on, an envelope component is still needed to reproduce
the observations.
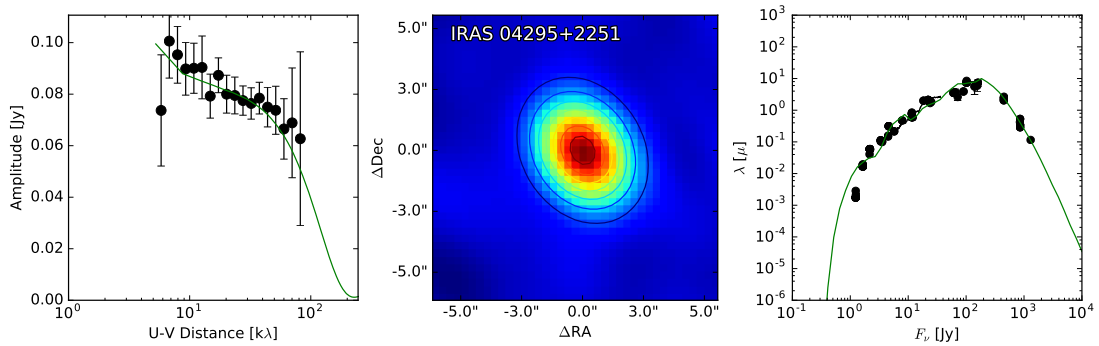
Figure 3.10: We show the 1.3 mm visibility profile (*left*), 1.3 mm image (*center*),
and broadband SED (*right*) for IRAS 04295+2251 with the best-fit disk+envelope
model curves over-plotted. Parameters for these models can be found in Table 3.2.

3.4.9 IRAS 04302+2247

IRAS 04302+2247 is a well-known edge-on disk (Wolf et al., 2003, 2008; Eisner, 2012) nicknamed the "butterfly star" by Lucas and Roche (1997) for it's scattered light morphology, and our modeling results are in agreement with that. Our results suggest that it has a massive disk, with $M_{disk} \sim 0.1$ M$_\odot$, and a radius of ~ 250 AU. Although the envelope is still comparable in mass to most of our targets ($M_{env} \sim 0.02$ M$_\odot$), it is several times less massive than the disk, possibly indicating that IRAS 04302+2247 may be in the process of shedding the final layers of it's envelope. Alternatively, it is possible that we are resolving out large scale structure in the envelope, as has been pointed out for several of our other targets.

Although the general morphology of the scattered light image is reproduced by our modeling, the scattered light image prefers a model that is even more edge on (also see Wolf et al., 2003) than what we find here ($i \sim 78 \pm 1$). Interestingly, our best fit model appears to preclude a disk that is precisely edge on, as is suggested by the scattered light morphology. This apparent misalignment of the disk, as traced by millimeter dust emission, and envelope, as traced by scattered light, has been previously noted (Eisner, 2012). We speculate that this apparent misalignment may be due to a warped disk, perhaps driven by a massive non-coplanar companion (e.g. Mouillet et al., 1997; Dawson et al., 2011), or a misalignment of the disk and
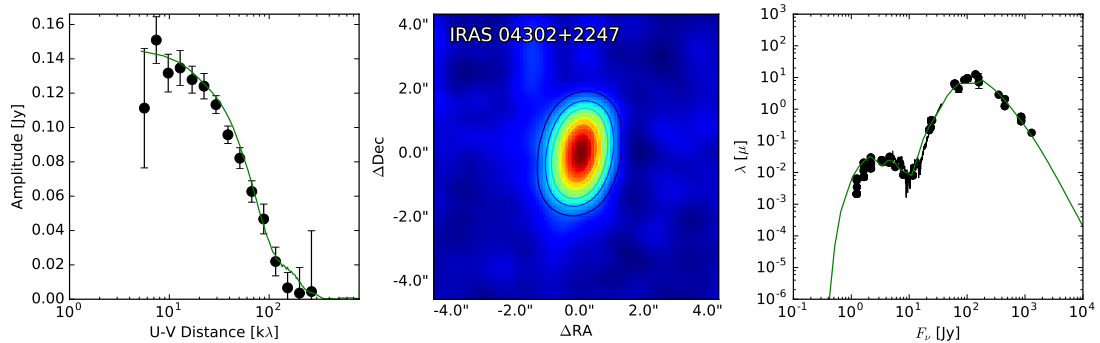
Figure 3.11: We show the 1.3 mm visibility profile (*left*), 1.3 mm image (*center*), and broadband SED (*right*) for IRAS 04302+2247 with the best-fit disk+envelope model curves over-plotted. Parameters for these models can be found in Table 3.2.

envelope, perhaps caused by a perturbation by a passing star sometime in the past (e.g. Quillen et al., 2005).

Our best fit model is in good agreement with the modeling results from Eisner (2012), which found that the disk has a radius of 250 AU and an inclination of $70 - 90°$. That said, our model suggests that the disk is more massive than their best fit models ($0.005 - 0.01$ M$_\odot$). Eisner (2012), however, argues that their grid cannot produce a model that fits all of the datasets simultaneously. Our best fit model is also in good agreement with Wolf et al. (2003), who model the SED, millimeter visibilities and scattered light imaging to find that the disk has a mass of 0.07 M$_\odot$ and a radius of 300 AU. Gramajo et al. (2010) also find a similar disk mass, radius and inclination by fitting the SED and scattered light image, but find a substantially higher envelope mass ($M_{env} \sim 0.12$ M$_\odot$). Studies that consider just the SED (Kenyon et al., 1993; Whitney et al., 1997; Furlan et al., 2008) or just the scattered light image (Lucas and Roche, 1997; Stark et al., 2006) typically find similar results.

3.4.10   IRAS 04365+2535

IRAS 04365+2535 is one of the few in our sample with a detected Keplerian rotating disk (e.g. Harsono et al., 2014; Aso et al., 2015). Our best fit model for it has a disk with a radius of $R_{disk} \sim 110$ AU and a mass of 0.025 M$_\odot$ embedded in a fairly massive, ~ 0.2 M$_\odot$ envelope of material. The disk appears to be highly inclined $i \sim 60°$. The visibility profile is flat from 50 kλ onwards, likely indicating the presence of an unresolved disk, but short-ward of this the visibilities rise and trace emission from the envelope. There's no clear evidence of a flattening of the visibilities at short baselines, so it is likely that we have resolved out large scale structure of the envelope. Like IRAS 04016+2610, we need to add a small amount of foreground extinction to fit the near-infrared photometry. This may, however, be because our millimeter visibilities resolve out large scale emission and our model is not correctly capturing the large scale envelope structure.

Our observations are generally in good agreement with results from previous
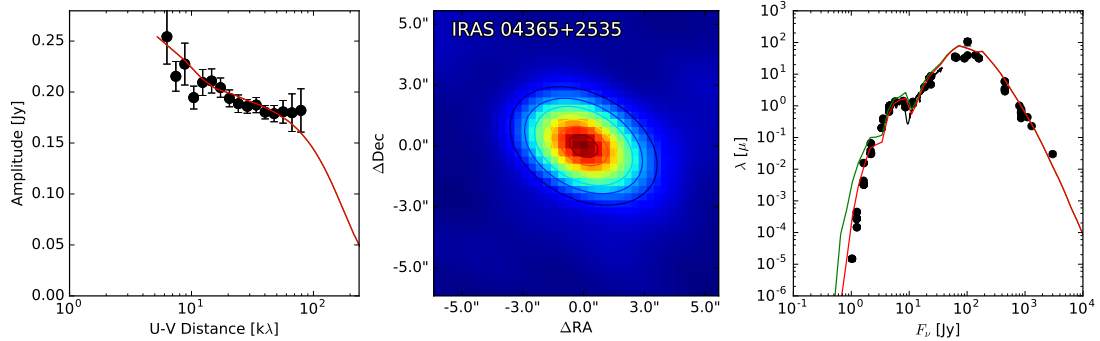
Figure 3.12: We show the 1.3 mm visibility profile (*left*), 1.3 mm image (*center*), and broadband SED (*right*) for IRAS 04365+2535 with the best-fit disk+envelope model curves over-plotted. The green curve shows our base model, which matches the visibilities but does not extinct the spectrum sufficiently at short wavelengths. If we include some foreground extinction in the fit (the red line), however, the models fit the data. Parameters for these models can be found in Table 3.2.

studies. Chandler et al. (1996) suggested that the disk must be inclined by $40 - 68°$ based on observations of IRAS 04365+2535's bipolar outflow, and Hogerheijde et al. (1998) similarly found an inclination of $55°$. Both Kenyon et al. (1993) and Whitney et al. (1997) modeled the SED and found inclinations of $60°$ and $\sim 70-90°$ respectively. Whitney et al. (1997) also found a disk radius of 50 AU, smaller than we find here. Gramajo et al. (2007) modeled scattered light images of the system and found an inclination of $\sim 70°$.

Harsono et al. (2014) observed Keplerian rotation in the IRAS 04365+2535 disk with ^{13}CO observations and modeled the disk with a radius of 80-100 AU and inclination of $55°$. Similarly, Aso et al. (2015) modeled infall and rotation detected towards the protostar in C^{18}O emission and found that the disk has an inclination of $65°$ and a radius of 100 AU. These results are both consistent with our own model fits.

Unlike these other studies, though, Robitaille et al. (2007), Furlan et al. (2008), and Eisner (2012) all find much lower disk inclinations of $i \sim 18-30°$. It is perhaps not surprising that Robitaille et al. (2007) and Furlan et al. (2008) find different inclinations, as they only consider the SED in their modeling. Our results likely
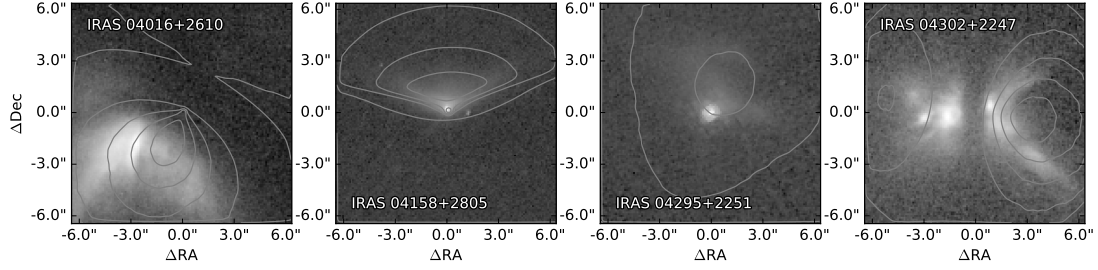
Figure 3.13: 0.8 μm scattered light images from HST for the four sources where such images were available. In all four cases, although we did not fit our model to the scattered light data, the best fit model does a reasonable job of reproducing the the scattered light distribution. IRAS 04032+2247 shows a more edge-on morphology than we find when fitting the combined millimeter visibilities and broadband SED dataset, possibly indicating a disk warp or disk/envelope misalignment (see Section 3.4.9).

differ from Eisner (2012) because their observations did not resolve the disk well. The more recent studies with higher quality millimeter data (Harsono et al., 2014; Aso et al., 2015), though, seem to agree with the results presented here.

3.5   Discussion

3.5.1   Class I vs. Class II Disk Masses

Over the past few decades, there have been numerous studies of nearby star forming regions at millimeter wavelengths with the aim of measuring disk masses for large samples of disks, and this work has been accelerated in recent years by the power of ALMA to quickly survey large numbers of sources (e.g. Beckwith et al., 1990; Osterloh and Beckwith, 1995; Dutrey et al., 1996; Andrews and Williams, 2005, 2007; Eisner et al., 2008; Mann and Williams, 2010; Andrews et al., 2013; Mann et al., 2014; Ansdell et al., 2016; Eisner et al., 2016; Pascucci et al., 2016; Barenfeld et al., 2016; Ansdell et al., 2017). These surveys have tended to target the population of Class II protostar disks because they are no longer embedded in an envelope, and so estimates of their disk masses are more straightforward. We can compare the Class I disk masses measured here with those of the older Class II disks.

We show histograms of disk masses for our sample of Class I disks compared with the sample of Class II disks in Taurus from Andrews et al. (2013) in Figure 3.14. We show the Taurus Class II disk masses because they are from the same region as our Class I sample, but Class II disks from other regions have similar distributions (see Ansdell et al., 2017). We calculate the disk masses for the Class II sample assuming optically thin dust so that,

$$M_{disk} = \frac{F_\nu \, d^2}{\kappa_\nu \, B_\nu(T)}. \tag{3.7}$$

We use standard assumptions, of $\kappa_{1.3mm} = 2.3$ cm^2 g^{-1} (e.g. Beckwith et al., 1990) and $T = 20$ K. We also assume a standard gas-to-dust ratio of 100.

We find that the median Class I disk mass is 0.018 M$_\odot$. This is several times higher than the Class II median disk mass, which we find to be 0.0024 $M_\odot$ for the Taurus sample. A more detailed study of Class II disk masses finds that the mean Class II disk mass ranges from $0.0015 - 0.0045$ M$_\odot$ for a number of nearby star
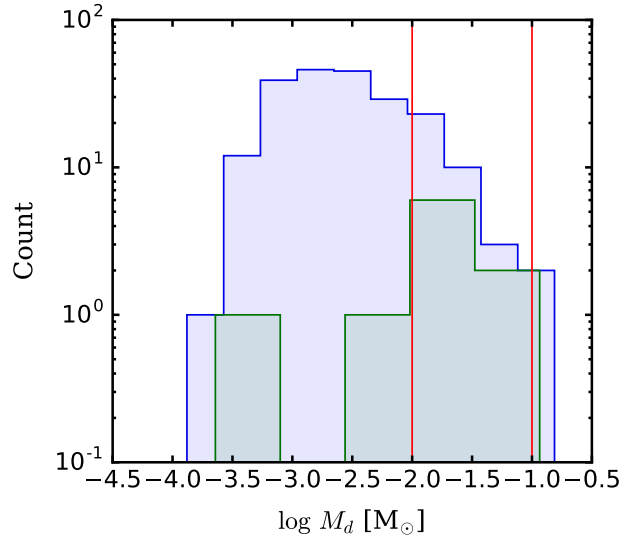
Figure 3.14: Histograms of the disk masses of Class I (*green*) sources in our sample and Class II (*blue*) sources in Taurus (Andrews et al., 2013). The red lines show the range of lower limits for the Minimum Mass Solar Nebula (e.g. Weidenschilling 1977). We find that our Class I disks, on average, are more massive than the Taurus Class II disks, likely due to dust grain processing hiding matter in larger bodies in the older Class II disks. However, there is still a lack of massive, > 0.1 M$_\odot$ disks, which may be needed to form giant planets.

forming regions (see Ansdell et al., 2017). If we assume that the disk masses for Class I and II protostars are distributed normally in log-space, then a two-sided t-test finds a probability of $p = 0.018$ that they are drawn from distributions with the same mean value. If, instead, we split each sample up into two categories, disks above and below the median Class II disk mass, then a Fisher Exact test finds a probability of $p = 0.019$ that Class I and Class II disks are drawn from the same distribution. Thus the disk mass distributions among Class I and II sources appear different, with a significance of > 2 sigma.

Our sample is missing 2 of the 12 companionless bona-fide Class I protostars in Taurus, and those two are among the faintest of our targets when observed with a single dish telescope (e.g. Motte and André, 2001a). If their faintness also corresponds to a low disk mass, it is possible that we may be artificially boosting the median disk mass of Class I sources by biasing our sample towards higher mass disks. If we assume that both sources are similar in mass to IRAS 04181+2654A, which is at the low end of our disk mass distribution, however, we still calculate a median disk mass of 0.011 $M_\odot$. It is important to note, however, that a lower single-dish millimeter flux may not indicate a low-mass disk. IRAS 04108+2803B has a comparable single dish flux to both of these objects (Motte and André, 2001a) and yet we find that its disk mass is above the median for Class I disks.

The higher average mass of Class I disks compared with Class II disks is an indication that substantial dust processing and grain growth occurs between the Class I and II stages. If dusty disk material has grown into rock, planetesimal, and planet sizes by the Class II stage, then much of this matter would be hidden from millimeter surveys, which are primarily sensitive to millimeter sized dust. This is borne out by a number of studies that have found cavities, gaps, spiral arms and other asymmetries in Class II disks that may indicate the presence of planets (Isella et al., 2010; Andrews et al., 2011a; van der Marel et al., 2013; Casassus et al., 2013; Andrews et al., 2016; Pérez et al., 2016; Isella et al., 2016; Loomis et al., 2017; Fedele et al., 2017), although planets have so far only been found in a few disks (e.g. Sallum et al., 2015).

3.5.2 Implications for Giant Planet Formation

Recent disk mass surveys of Class II protostars have raised concerns about whether their disks contain enough mass to form giant planets (e.g. Williams and Best, 2014; Eisner et al., 2016; Ansdell et al., 2016). An accounting of the material in our own Solar System, which is dominated by the mass of Jupiter, suggests that disk masses of $\gtrsim 0.01 - 0.1$ M$_\odot$ are needed to form a planetary system like our own (e.g. Weidenschilling, 1977; Hayashi, 1981; Desch, 2007). The masses inferred from sub-millimeter observations of Class II disks are, on average, below this Minimum Mass Solar Nebula. It has also been found recently that gas-to-dust ratios in Class II disks may be well below the canonical value of 100 (Williams and Best, 2014; Eisner et al., 2016; Ansdell et al., 2016). If true, this would create further discrepancies with the MMSN, although it may simply be that CO is depleted in Class II disks (e.g. Miotello et al., 2017).

Whether Class II disks have enough mass to form giant planets may, however, be irrelevant, as evidence is mounting that planets are already present in Class II disks (see above). As such, the Class I disks, which are younger (e.g. Evans et al., 2009; Dunham et al., 2015) and have had less time for dust processing and planet formation to occur, should better represent the initial mass budget of disks for forming planets. And although the Class I disk sample appears to be more massive, on average, than the Class II sample, it remains unclear from our results whether Class I disks are massive enough to form giant planets.

With a median disk mass of 0.016 M$_\odot$, Class I disks do have enough mass, on average, to form giant planets if the minimum amount of matter needed is 0.01 M$_\odot$. However this median disk mass is still well below the MMSN estimates of 0.06 M$_\odot$ (Desch, 2007) and the high end of 0.1 M$_\odot$ (Weidenschilling, 1977). A t-test shows with $> 2\sigma$ confidence ($p = 0.03$) that the mean Class I disk mass is below 0.06 M$_\odot$ and with $\sim 3\sigma$ confidence ($p = 0.007$) that the mean is below 0.1 M$_\odot$. There are two sources (i.e. 20% of the sample; IRAS 04158+2805 and IRAS 04302+2247) that have $M_{disk} \gtrsim 0.06 - 0.1$ M$_\odot$, comparable to the $\sim 20\%$ of stars with giant planets

(Cumming et al., 2008), but this is clearly not statistically significant.

If the upper end of the MMSN estimates do represent better estimates of the initial amount of matter needed to form giant planets, this may be an indication that planet formation has already begun during the Class I stage. In fact, recent observations with ALMA provide evidence that this is the case. The HL Tau system, which is now known to have a series of narrow gaps in it's disk (e.g. ALMA Partnership et al., 2015), is thought to be somewhere between the Class I and II stages and is likely ~ 1 Myr old. If the gaps are carved by planets (Dong et al., 2015), it would be an indication that planet formation must begin early enough to form Saturn-mass planets (e.g. Dong et al., 2015; Kanagawa et al., 2015) within the first $\sim$ Myr. Perhaps even more interesting, several Class I protoplanetary disks have recently been found to also exhibit similar features. This includes WL 17, which has a 12 AU-wide hole in the center of its disk (Sheehan and Eisner, 2017), and GY 91, which has three narrow dark lanes and is very similar to the HL Tau disk (Sheehan & Eisner, in prep.). Although these features could very well be produced by something other than planets, many of the likely causes are still indications that the planet formation process has begun. If planet formation occurs during the Class I stage then we would expect that disk masses are even higher at younger ages, perhaps during the Class 0 stage, before dust processing has had time to progress significantly.

3.6   Conclusions

We have presented an updated method for fitting disk+envelope radiative transfer models to a multi-wavelength dataset (e.g. Eisner et al., 2005; Eisner, 2012; Sheehan and Eisner, 2014) that uses Markov Chain Monte Carlo fitting. Although these models are computationally intensive to run, the fitting can be done in a reasonable amount of time when run in parallel on systems with a large number of cpus.

We have used this modeling infrastructure to fit disk+envelope models to a sample of 10 Class I protostars in the Taurus Molecular Cloud. These sources were

chosen because they are widely accepted to be Class I objects and also because none have been found to have close companions. We find good fits to the combined broadband SED and CARMA 1.3 mm visibilities dataset for each source. The resulting best fit models are even good matches to HST scattered light images, when such images are available, despite the fit not including these data.

From our best fit models we are able to determine the disk masses for this sample of Class I sources. We find that the median Class I disk mass is 0.018 $M_{\odot}$, which is higher than the median Class II disk mass by a factor of a few, although it remains unclear whether Class I disks have enough mass in millimeter-sized dust grains, on average, to form giant planets. Larger samples of Class I disks are needed to better nail down the Class I disk mass distribution. Moreover, we'd like to study disks in the rich clusters where most stars form (Tachibana et al., 2006; Adams, 2010), as the nearby massive stars produce significant amounts of ionizing radiation (Lada and Lada, 2003) that can photoevaporate disks (e.g. Churchwell et al., 1987) and affect their structure and masses. With ALMA now online, a much larger sample of Class I disks can be observed with higher spatial resolution and better sensitivity far more efficiently, so it is only a matter of time before these questions are answered.

CHAPTER 4

Constraining the Disk Masses of the Class I Binary Protostar GV Tau[†]

We present new spatially resolved 1.3 mm imaging with CARMA of the GV Tau system. GV Tau is a Class I binary protostar system in the Taurus Molecular Cloud, the components of which are separated by 1.2". Each protostar is surrounded by a protoplanetary disk, and the pair may be surrounded by a circumbinary envelope. We analyze the data using detailed radiative transfer modeling of the system. We create synthetic protostar model spectra, images, and visibilities and compare them with CARMA 1.3 mm visibilities, an HST near-infrared scattered light image, and broadband SEDs from the literature to study the disk masses and geometries of the GV Tau disks. We show that the protoplanetary disks around GV Tau fall near the lower end of estimates of the Minimum Mass Solar Nebula, and may have just enough mass to form giant planets. When added to the sample of Class I protostars from Eisner (2012) we confirm that Class I protostars are on average more massive than their Class II counterparts. This suggests that substantial dust grain processing occurs between the Class I and Class II stages, and may help to explain why the Class II protostars do not appear to have, on average, enough mass in their disks to form giant planets.

4.1   Introduction

The process of star formation begins with a roughly spherical cloud of gas and dust in hydrostatic equilibrium that has yet to begin collapsing under the force of gravity to form a protostar. As the collapse proceeds, conservation of angular momentum forces most of the in-falling material to form a disk rather than accrete directly

---

[†]This chapter has been published previously as Sheehan and Eisner 2014

onto the forming protostar. Viscosity in the disk then transports mass inwards and angular momentum outward, allowing matter to accrete from the disk onto the central protostar. Eventually the material from the in-falling spherical envelope is depleted onto the massive protostellar disk. In turn, the material from the disk is then deposited onto the pre-main sequence star until the disk is tenuous and the central star is exposed. At the same time dust grains in the disk coagulate to form larger and larger bodies, which eventually may grow into planets.

Young stars are typically classified according to the shape of their spectral energy distributions (SEDs) (e.g. Lada, 1987; Andre et al., 1993) and their bolometric temperatures (e.g. Enoch et al., 2009). Class 0 Young Stellar Objects (YSOs) have SEDs that are highly obscured at optical and near to mid infrared wavelengths and peak at far-infrared or sub-millimeter wavelengths, corresponding to bolometric temperatures below 100 K. These objects are believed to be young stars that are still enveloped by their natal envelopes. There is evidence suggesting that a few Class 0 protostars are surrounded by rotationally supported protostellar disks (e.g. Tobin et al., 2013). However, it is not yet clear that Class 0 YSOs in general possess disks. Class I YSO SED's rise steeply in the near-infrared, peak in the mid-infrared, and often have significant obscuration of their central protostars. They are also characterized by bolometric temperatures below about 600 K. This class likely represents protostars surrounded by massive disks still embedded in their original envelopes. Class II YSOs have SEDs that are flatter at near-infrared wavelengths and show some light from the central protostar. They are thought to represent pre-main sequence stars encompassed by massive protoplanetry disks. Class III YSO SEDs are dominated by the light from the central protostar, and have little or no infrared excess arising from an optically thin disk of matter.

The mass of the circumstellar disk at each of these stages is an important indicator for the evolution of circumstellar mass during star and planet formation. Disks that are too massive may be subject to gravitational instabilities that could help to grow protostellar mass quickly. Gravitational instabilities leading to rapid mass accretion may help to rectify the discrepancy between observed envelope-to-disk and

disk-to-star mass accretion rates (e.g. Kenyon and Hartmann, 1987). Conversely, disks with too little mass may not have enough material to form giant planets (e.g. Weidenschilling, 1977; Desch, 2007).

The masses of protostellar disks and envelopes are usually measured from millimeter wavelength observations. If the matter is optically thin, as is much of the circumstellar material around protostars, then the millimeter flux is proportional to the dust mass. In order, however, to make the conversion between millimeter flux and total mass it is necessary to know the temperature distribution throughout the disk, the opacity of the dust in the disk, as well as the gas-to-dust mass ratio. Furthermore, dense regions in the disk can be optically thick and hide material from sight. For Class I objects, which are surrounded by both a disk and its natal envelope, disentangling the disk and envelope masses is also a challenge. The best method for overcoming these difficulties and unambiguously determining the mass of the protostellar disk is through detailed radiative transfer modeling of resolved imaging.

Studies using radiative transfer modeling to match SEDs have historically been used to place constraints on the distribution of matter around young stars (e.g. Adams et al., 1987; Kenyon et al., 1993; Robitaille et al., 2007). Such modeling, however, can be subject to significant degeneracies. For example, it is difficult to use a SED to distinguish between a flattened disk-like envelope (Ulrich, 1976; Terebey et al., 1984) and flared edge-on disks (Chiang and Goldreich, 1999). To break these degeneracies, additional imaging datasets such as short wavelength scattered light images or millimeter continuum images can be modeled to provide new constraints on circumstellar structure. Modeling of multiple datasets has previously been used to determine the circumstellar mass distribution of young stars more accurately than was possible by modeling a single dataset by itself (e.g. Osorio et al., 2003; Wolf et al., 2003; Eisner et al., 2005; Eisner, 2012).

Disk masses for Class 0 protostars (ages $\lesssim 0.2$Myr), if indeed disks are present, have been suggested to be high ($\gtrsim 0.05 - 0.1$ M$_\odot$; Jørgensen et al., 2009). Mass accretion rates of Class 0 protostars have also been estimated to be high ($\gtrsim 10^{-5}$ M$_\odot$

yr^{-1}) from SED fitting (e.g. Jayawardhana et al., 2001), outflow measurements (e.g. Bontemps et al., 1996), and lifetime measurements from statistical arguments (e.g. Andre and Montmerle, 1994a; Barsony, 1994). These high disk masses and accretion rates suggest that the disks around these protostars may be gravitationally unstable. Conversely, the masses of Class II disks in Taurus and Orion (ages $\sim 1 - 5$Myr) have been well studied and are found to have a median mass of 0.001 M$_\odot$, with $\lesssim$10% of systems having disk masses higher than 0.01 M$_\odot$ and $\lesssim$1% with disk masses greater than 0.1 M$_\odot$ (e.g. Eisner et al., 2008; Andrews et al., 2013). These median masses are low compared with the amount of matter needed to form giant planets, estimated to be 0.01 - 0.1 M$_\odot$ (e.g. Weidenschilling, 1977; Desch, 2007). The millimeter wavelength observations used to make these measurements, however, are only sensitive to particles smaller than $\sim$ 1mm. It might be the case that significant dust processing and grain growth has already occurred in these systems, effectively hiding the mass in the disk in larger undetectable bodies.

Class I YSOs thus may represent a transitional stage between massive, highly unstable protoplanetary disks to stable disks in which planet formation is progressing. The disks around Class I YSOs may also more accurately represent the initial mass budget of disks for forming planets as they are younger and presumably grain growth is less advanced.

Previous radiative transfer modeling studies of the masses of Class I disks in Taurus and Ophiuchus (ages $\sim 0.2 - 0.5$ Myr) using millimeter continuum images (e.g. Jørgensen et al., 2009) or SEDs, scattered light images, and millimeter images (Osorio et al., 2003; Wolf et al., 2003; Eisner et al., 2005; Eisner, 2012) find disk masses ranging from 0.005-1 M$_\odot$. Eisner (2012) finds a median disk mass for their sample of 0.01 M$_\odot$. They also find, however, that the mass within 100 AU, where planets form, has a median of 0.008 M$_\odot$. If the mass measured using millimeter emission traces the entire disk mass, there is likely not enough matter for forming giant planets, which may require as much as 0.1 M$_\odot$ (Eisner, 2012).

Binary stars are particularly interesting candidates for disk mass studies, not only because they allow measurements of two disk masses simultaneously, but also

because a significant fraction of young stars are formed with companions (e.g. Abt and Levy, 1976; Raghavan et al., 2010), so their properties are important for understanding the evolution of disk masses and planet formation for a large portion of young stars. Furthermore, disks in young binary systems are coeval. Similarities and differences in the properties of each individual system will therefore highlight nuances in the progression of star and planet formation.

In this paper we study the Class I binary GV Tau. GV Tau (IRAS 04263-2426, Haro 6-10) is located in the Taurus Molecular Cloud Complex, at a distance of 140 pc (Mamajek, 2008). GV Tau was first discovered to be a binary by Leinert and Haas (1989) using speckle interferometry, and has since been resolved at near-infrared, millimeter, and centimeter wavelengths (Koresko et al., 1999; Reipurth et al., 2004; Roccatagliata et al., 2011; Guilloteau et al., 2011). The binary consists of a bright optical source, GV Tau S, and its companion, GV Tau N, located 1.2" north of its southern counterpart. At the distance of Taurus this projected separation corresponds to 170 AU. GV Tau N is 100 times fainter than GV Tau S at optical wavelengths but becomes bright in the near- and mid-infrared (Leinert and Haas, 1989; Koresko et al., 1999; Roccatagliata et al., 2011). Doppmann et al. (2008) find that the GV Tau N and S have stellar masses of 0.8 and 0.5 $M_\odot$ and temperatures of 3800 and 4100 K respectively.

Both components of the GV Tau binary have been found to be highly variable in the near-infrared on timescales as short as a month (Leinert et al., 2001). Leinert et al. (2001) attribute the variability of GV Tau N to variable accretion and suggest that the variability of GV Tau S is due to inhomogeneities in its accretion disk. Doppmann et al. (2008) find that GV Tau S has a variable radial velocity and suggest that GV Tau S may be a multiple system with a companion with mass $M_\star < 0.15$ $M_\odot$ (mass ratio > 3) and $a < 0.35$ AU.

A number of previous studies have attempted to constrain the distribution of material around each component of the GV Tau binary. Early near-infrared imaging studies by Menard et al. (1993) suggested that the binary pre-main sequence stars were surrounded by a flattened circumbinary envelope or disk, and potentially

circumstellar disks around each component. More recent studies have suggested that GV Tau N is surrounded by an edge on disk while GV Tau S's disk is close to face on, and that both components are surrounded by a common envelope, the composition of which is similar to that of the interstellar medium (Roccatagliata et al., 2011). Guilloteau et al. (2011) modeled Plateau de Bure Interferometer 1.3mm visibilities for the GV Tau binary and found the disks to be optically thick with radii around 15 AU.

In this work we use detailed radiative transfer modeling of new CARMA 1.3mm visibilities along with HST scattered light imaging and broadband SEDs to expand on previous works and more accurately constrain the structure and properties of the GV Tau binary young stellar objects.

4.2 Observations & Data Reduction

4.2.1 CARMA Observations & Data Reduction

We observed GV Tau on 2010 October 29 with the Combined Array for Research in Millimeter-wave Astronomy (CARMA). Our observations were taken in CARMA's C configuration, with baselines ranging from 20 - 350 m, corresponding to an angular resolution of 1" and a largest resolvable scale ($\theta_{MRS} \sim 0.5\lambda/B_{min}$) of 6.5". The CARMA correlator was in wideband mode, with a local oscillator (LO) frequency of 227 GHz, and an intermediate frequency (IF) band $\pm 1 - 9$ GHz from the LO. Eight 500 MHz bands were placed evenly spaced in each of the sidebands, for a total continuum bandwidth of 8 GHz. Our observations were taken during the same track as two other young stars in Taurus with cycles of 19 minutes consisting of 5 minute integrations for each science target and 4 minutes for our gain calibrator, 3C111. We also observed the quasar 3C84 at the beginning of the track for bandpass calibration. The total on-source integration time for GV Tau was 50 minutes, and the total length of the track was 3 hours and 15 minutes.

The calibration of our data was done using the CASA and *MIRIAD* data reduction packages. We applied a series of calibration corrections to the data, beginning
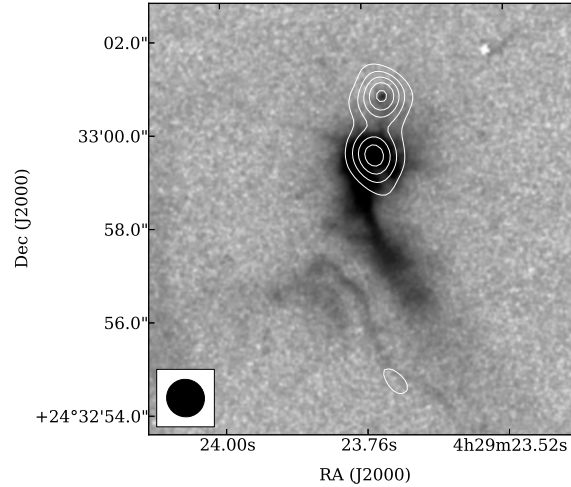
Figure 4.1: 0.8 μm HST scattered light image of GV Tau in grayscale with the 1.3 millimeter CARMA image overplotted as contours. Both images have high enough spatial resolution and sensitivity to resolve the binary. The beam size of the millimeter image is shown in the bottom left.

with a correction for instrumental phase drifts from differences in line lengths. Next, we used 3C84 to estimate the bandpass responses and correct for variations in flux across the channels of each band. Antenna 8 was used as the reference antenna throughout the calibration process. After applying the bandpass corrections to the data we used the CASA gain calibration routine on 3C111 to determine the time dependent gain corrections and interpolated to apply them to the data. No flux calibrator was observed during this track, so we scaled the visibilities using a flux of 1.94 Jy for 3C111 at 1 mm as measured by the SMA on October 28, 2010[1].

After calibrating the visibilities, we Fourier transformed our data to obtain an image, and we CLEANed the resulting image to deconvolve the image and the dirty beam. The imaging provides a nice visualization of the system, however we perform most of the analysis for this paper in the visibility plane, where we do not have to contend with beam effects. We plot the millimeter contours in Figure 4.1 and the visibilities in Figure 4.2. To better demonstrate that the target is a binary using the visibilities we plot the visibilities averaged in bins along a baseline parallel to

---

[1]Can be found at http://sma1.sma.hawaii.edu/callist/callist.html
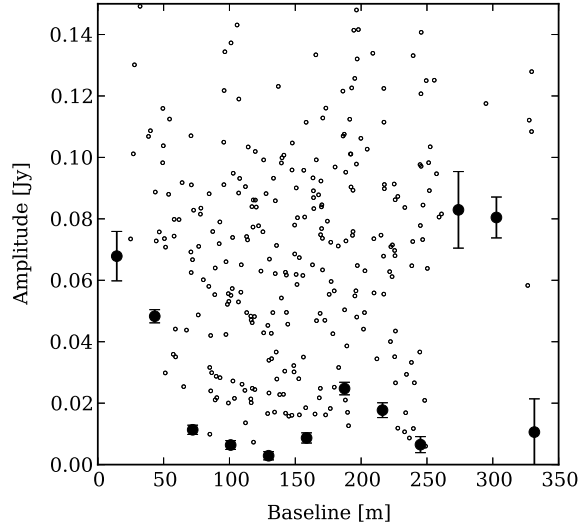
Figure 4.2: 1.3 mm visibilities for the GV Tau system. We plot the amplitudes of the one dimensional azimuthally averaged visbilities with solid points, while the open circles show the the amplitudes of the visibilities averaged using a two-dimensional grid. We average the data coherently, so phase noise in the data may result in average amplitudes which are lower than the amplitudes for the unaveraged data.

the binary in Figure 4.3.

To model our targets individually we needed to separate the contribution to the measured visibilities of each member of the binary. To do this we fit the combined visibilities with both a double point source model, leaving the centroids and fluxes as free parameters, and a double two dimensional gaussian model, with the widths, centroids, fluxes, inclination, and position angle as free parameters. From our best fit we find that both components are unresolved, or at best marginally resolved, by our observations.

We also find that our double point source models underpredict the flux of our targets at short baselines. We can improve the model fit to the data by adding a gaussian source with a large spatial extent to the model, likely representing large scale circumbinary structure. This gaussian has a FWHM of ~ 5", making it signifi-cantly larger than the binary. Given our limited coverage of short baselines, however, the outer scale of this structure is difficult to constrain. The best fit model is plotted
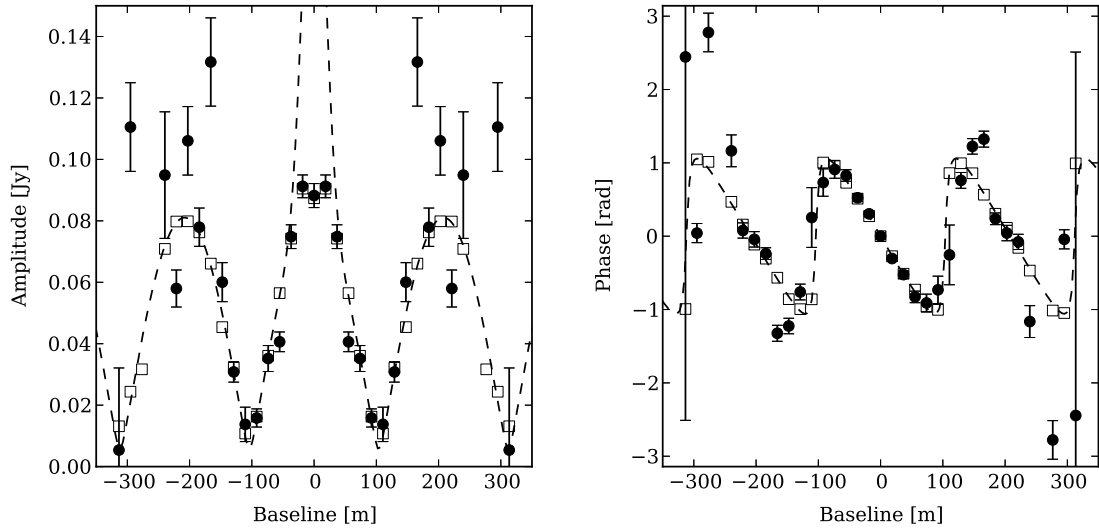
Figure 4.3: 1.3 mm visibilities, shown as filled circles, plotted and averaged along the axis of the binary. On the left we show the amplitude and on the right we show the phase of the complex visibilities. The data are perfectly symmetric across the zero-baseline line because the complex visibilities are Hermitian. We have over plotted the best fit double point source plus gaussian model as open squares and a dashed line. The open squares represent the best fit model sampled at the same binned uv points as our data, while the dashed line shows the best fit model if the uv plane were perfectly sampled.

over our data in Figure 4.3. To determine the visibilities for a single component of the binary we first remove the component arising from the large scale circumbinary material. We then subtract the best fit model for the other component from the visibilities. We do this for both the best fit point source and gaussian models and find that the difference in the resulting single component visibilities is negligible.

We binned the visibilities into both a two dimensional grid as well as an annular grid to increase the signal to noise ratio for our data. We gridded the visibilities with a weighted average of real and imaginary components of the visibilities within each grid cell, with weights determined by our calibration.

4.2.2 Scattered Light Imaging

We downloaded an archival *Hubble Space Telescope* Widefield and Planetary Camera 3 (WFPC3) near-infrared 0.8 μm scattered light image of GV Tau from the Hubble Legacy Archive (HST Program 7387, PI: Stapelfeldt). The image was previously calibrated, with the exception of cosmic ray removal so we removed the cosmic ray hits from the image using the COSMICS program (van Dokkum, 2001). Finally, we scaled the data to units of ergs cm^{-2} s^{-1} $\mathring{A}^{-1}$ using the appropriate scaling factor from the fits header. We calculated uncertainties for the image from the square root of the counts frame of the data multiplied by the scaling factor to convert the image to a real flux value.

The HST image of GV Tau lacks background stars to be used to for determining astrometry of the image. Instead we used a widefield Sloan Digital Sky Survey (SDSS), Data Release 10, 0.75 μm scattered light image of GV Tau which does have background stars to determine the astrometry and transfer it to the HST images. We used the HST image in our modeling rather than the SDSS image because the HST image has higher resolution and shows significantly more structure than the SDSS image. We used SExtractor (Bertin and Arnouts, 1996) and SCAMP (Bertin, 2006) to locate point sources in the SDSS images and find an astrometric solution for the image. We then used distinctive features of the scattered light surrounding the southern component to align the HST and SDSS images and transfer the astrometry to the HST image. Figure 4.4 shows a plot of our alignment of the SDSS and HST images, and Figure 4.1 shows the HST image with the millimeter contours overplotted. The uncertainty in the SDSS image astrometry is 0.2", and we estimate that the uncertainty in the HST image is 0.3".

4.2.3 Photometric Data from the Literature

In addition to our CARMA data and archival HST imaging data we collected photometry for GV Tau from the literature to create a spectral energy distribution (SED). Because the components of the GV Tau binary are only separated by 1.2"
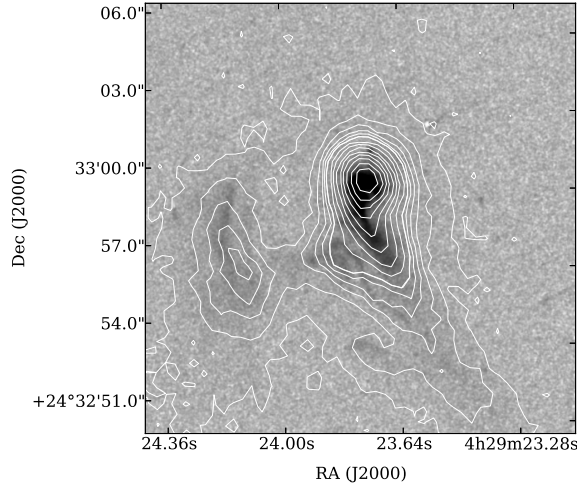
Figure 4.4: HST 0.8 μm image of GV Tau in grayscale with contours of the SDSS *i*-band image overplotted. We matched the SDSS image to the HST image based on features in the scattered light image in order to transfer astrometry from the SDSS image to the HST image. This figure shows our best match, which we used for the transfer. This figure demonstrates that the HST image has much higher spatial resolution than the SDSS image, so we use the HST image for our modeling.

the photometry from the literature for GV Tau is largely unresolved. We did however find a number of studies that spatially resolved the binary and provided photometry for each component. We also used VLT resolved near-infrared spectroscopy of the silicate feature for both components from Roccatagliata et al. (2011). We list the resolved and unresolved photometry in Tables 4.1 and 4.2 and plot the spectra in Figure 4.5. For our model fitting we ignored the uncertainties quoted in the literature and used a uniform 10% uncertainty for each data point, although this value is somewhat arbitrary.

Reipurth et al. (2004) used the Very Large Array (VLA) A configuration to observe GV Tau at 3.6 cm with 0.3" resolution and resolved the components of the binary. The 3.6 cm emission detected towards the southern component appears to trace an outflow and is likely not thermal dust emission, while the emission detected towards the northern component is consistent with thermal dust emission with a spectral index of 2. Given our current data we cannot be certain of the origin of the 3.6 cm emission from either source so we exclude the point from our modeling

for the time being. We intend to follow up on this feature in a future paper.

The left panel of figure 4.5 shows a plot of the photometry for GV Tau in which the binary was not resolved, along with the sum of the photometry for each component. The composite GV Tau N and S photometry matches the unresolved data well at wavelengths longer than 3 μm. At shorter wavelengths the composite photometry falls below the unresolved photometry. This is likely because the unresolved data use a larger aperture and thus includes more of the nebulosity that is present in near-infrared images of GV Tau. In our modeling, described below, we fit individual protostar models to the resolved photometry for each component. We also include the unresolved photometry from 12 - 100 μm as upper limits to constrain the modeling as we do not have resolved photometry in that range.
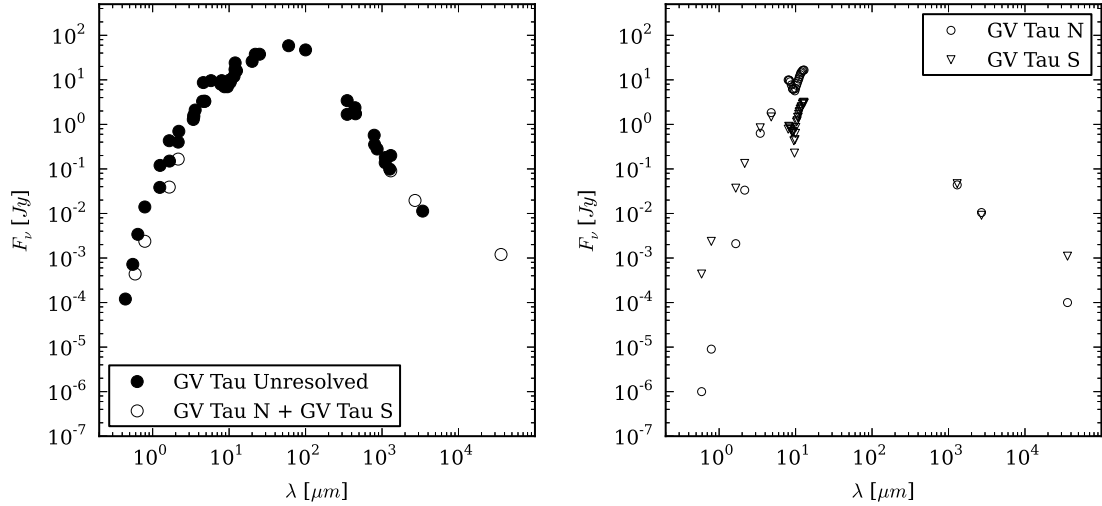
Figure 4.5: SEDs for GV Tau using data from the literature. We plot the unresolved photometry on the left as filled circles as well as the sums of the resolved photometry as open circles. At most wavelengths, these lie on top of each other. The sums of the resolved near-infrared photometry likely fall below the unresolved photometry due to the smaller aperture used for the unresolved photometry. The unresolved photometry is likely more sensitive to the extended scattered light structure. In the right panel we plot the resolved photometry for both components of the GV Tau system.

Table 4.1.   Unresolved photometry of GV Tau

λ (μm)	F_ν (Jy)	Reference
0.44	0.00012	Myers et al. (1987)
0.55	0.00072	Myers et al. (1987)
0.64	0.0034	Myers et al. (1987)
0.79	0.014	Myers et al. (1987)
1.24	0.0385	2MASS
1.25	0.12	Myers et al. (1987)
1.65	0.43	Myers et al. (1987)
1.66	0.15	2MASS
2.16	0.4	2MASS
2.20	0.7	Myers et al. (1987)
3.40	1.29038	Rebull et al. (2011)
3.45	1.6	Myers et al. (1987)
3.60	2.1	Cieza et al. (2009)
4.50	3.3	Cieza et al. (2009)
4.60	8.68941	Rebull et al. (2011)
4.80	3.3	Myers et al. (1987)
5.80	9.6	Cieza et al. (2009)
7.80	8.0	Myers et al. (1987)
8.00	9.6	Cieza et al. (2009)
8.70	7.0	Myers et al. (1987)
9.50	7.00	Myers et al. (1987)

Table 4.1 (cont'd)

λ (μm)	F_ν (Jy)	Reference
10.10	9.0	Myers et al. (1987)
10.30	10.0	Myers et al. (1987)
11.60	12.0	Myers et al. (1987)
12.00	16.6	IRAS
12.00	24.02720	Rebull et al. (2011)
12.50	16.0	Myers et al. (1987)
20.00	26.0	Myers et al. (1987)
22.00	37.5286	Rebull et al. (2011)
25.00	37.6	IRAS
60.00	58.4	IRAS
100.00	47.0	IRAS
350.00	1.68	Andrews and Williams (2005)
350.00	3.42	Dent et al. (1998)
443.00	2.37	Chandler et al. (1998)
443.00	1.81	Andrews and Williams (2005)
450.00	1.73	Dent et al. (1998)
790.00	0.571	Chandler et al. (1998)
800.00	0.353	Dent et al. (1998)
863.00	0.28	Andrews and Williams (2005)
1100.00	0.138	Dent et al. (1998)
1104.00	0.18	Chandler et al. (1998)

Table 4.1 (cont'd)

λ	F_ν	Reference
(μm)	(Jy)	
1260.00	0.099	Chandler et al. (1998)
1300.00	0.20	Motte and André (2001b)
1927.00	<0.16	Chandler et al. (1998)
3400.00	0.0113	Hogerheijde et al. (1997)

Table 4.2. Resolved photometry of GV Tau

λ	$F_{\nu,S}$	$F_{\nu,N}$	Reference
(μm)	(Jy)	(Jy)	
0.59	0.000437	0.000001	Roccatagliata et al. (2011)
0.79	0.002365	0.000009	Roccatagliata et al. (2011)
1.65	0.037	0.0021	Roccatagliata et al. (2011)
1.65	0.402	0.028	Leinert and Haas (1989)
2.16	0.1329	0.0334	Roccatagliata et al. (2011)
2.20	0.615	0.08	Leinert and Haas (1989)
3.45	0.838	0.631	Leinert and Haas (1989)
4.80	1.468	1.837	Leinert and Haas (1989)
1300	0.0404	0.0443	This work
1300	0.0467	0.0438	Guilloteau et al. (2011)
2700	0.0091	0.0105	Guilloteau et al. (2011)
36000	0.0011	0.0001	Reipurth et al. (2004)

4.3   Modeling

We follow the same modeling procedure as Eisner et al. (2005) and Eisner (2012) using a grid of models described below.

4.3.1   Input Density Distributions

Our models include a central protostar surrounded by a circumstellar disk and an envelope with an outflow cavity. We provide below further details of the structure of each component and the parameters that were varied to create our grid of models.

Protostar

We use a central protostar with a temperature of 4000 K and a mass of 0.5 M$_\odot$ for both protostars in the GV Tau system. This is consistent with previous studies of GV Tau, which find a mass and temperature of 0.5 M$_\odot$ and 3800 K for GV Tau S and of 0.8 M$_\odot$ and 4100 K for GV Tau N (Doppmann et al., 2008). We allow the luminosity of the protostar to be 1, 3 or 6 L$_\odot$, and calculate the radius of the protostar accordingly, assuming that the protostar is a spherical blackbody. Our selected luminosities are compatible with previous luminosity measurements by White and Hillenbrand (2004), Doppmann et al. (2005), and Prato et al. (2009). While Doppmann et al. (2008) measured lower luminosities for the protostars (0.3 L$_\odot$ and 0.6 L$_\odot$), the assumed age in that study may be too old, thus pushing the luminosity down. We discuss this further in Section 4.5.3. The spectrum of the protostar is also assumed to be that of a spherical blackbody with a temperature of 4000 K.

Envelope

We model the density distribution of the protostellar envelope using the solution for a rotating collapsing envelope (Ulrich, 1976),

$$\rho_{env}(r,\mu) = \frac{\dot{M}}{4\pi}\left(GM_* r^3\right)^{-\frac{1}{2}}\left(1+\frac{\mu}{\mu_0}\right)^{-\frac{1}{2}}\left(\frac{\mu}{\mu_0}+2\mu_0^2\frac{R_c}{r}\right)^{-1}, \qquad (4.1)$$

where r and θ are defined in the typical sense for spherical coordinates centered on the protostar, and $\mu = \cos\theta$. The parameter $\dot{M}$ is the accretion rate of the envelope onto the protostar, and can be calculated from the total envelope mass by integration over all space. R_c is the centrifugal radius of the envelope, interior to which the density distribution begins to significantly flatten due to rotation. $\mu_0 = \cos\theta_0$ is the initial angle of the infalling material and can be solved numerically from the equation (Ulrich, 1976),

$$\frac{r}{R_c} = \frac{1 - \mu_0^2}{1 - \mu/\mu_0}. \tag{4.2}$$

Finally, we truncate the envelope at a an outer radius, R_{env}, and at a fixed inner radius, R_{in}.

The inner radius of the envelope in our models is fixed at a distance of 0.1 AU, consistent with previously measured inner disk radii for our range of model luminosities (e.g. Eisner et al., 2007), while the total envelope mass, M_{env}, and the outer radius of the envelope, R_{env}, are left as free parameters to be varied in our grid. We allow M_{env} to take values of 1×10^{-6}, 5×10^{-6}, 1×10^{-5}, 5×10^{-5}, 1×10^{-4}, and 5×10^{-4} $M_\odot$, and R_{env} is selected from 60, 90, 300 and 1000 AU. Although the centrifugal radius, R_c, is a free parameter, we fix it to be equal to the radius of the protoplanetary disk, described below. It can take values of 30, 60, 100, or 300 AU. We allow values of R_c larger than the projected separation of the protostars (170 AU) because of the possibility that the actual separation is much larger.

We also give the envelope an outflow cavity, the location of which is determined by

$$z > 1\mathrm{AU} + r^\zeta \tag{4.3}$$

Inside the outflow cavity, the density of the envelope is reduced by a scale factor, f_{cav}. We leave f_{cav} as a free parameter which is allowed to take values of 0.05, 0.2, and 1, and hold ζ fixed at a value of 1.0. While it would be nice to vary ζ, computational limitations dictate that we hold some parameters fixed. The parameter study in Eisner (2012) suggests that ζ primarily affects the overall flux scaling of the 1.3 mm visibilities as well as the offset between the scattered light emission and the

protostar. This would suggest that ζ is degenerate with the disk mass, which is largely responsible for the overall flux scaling of the 1.3 mm visibilities, however ζ only affects this scaling on the order of 10% so we do not believe that it produces a significant error in our disk mass measurements. ζ may, however have a significant effect on inclination and position angle, but the astrometry errors of our scattered light image likely overshadow this error.

Protoplanetary Disk

To model the protoplanetary disk, we use the standard prescription for a flared viscous accretion disk,

$$\rho_{disk}(r, z) = \rho_0 \left(\frac{r}{1AU} \right)^{-\alpha} \exp \left(-\frac{1}{2} \left[\frac{z}{h(r)} \right]^2 \right), \tag{4.4}$$

$$h(r) = h_0 \left(\frac{r}{1AU} \right)^{\beta}, \tag{4.5}$$

with r and z defined in the usual sense for cylindrical coordinates. ρ_0 is the density of the disk at the midplane at a radius of 1 AU, and can be calculated from the total disk mass, M_{disk}, by integrating the disk density over all space. h_0 is the scale height of the disk at 1 AU. We truncate the disk at a given outer radius, R_{disk}, and inner radius, R_{in}.

In our models we fix β at a value of 58/45 (or 1.29) as found by Chiang and Goldreich (1997) for a flared accretion disk in hydrostatic equilibrium. Viscous accretion theory specifies that $\alpha = 3(\beta - \frac{1}{2}) = 71/30$ (or 2.37) (Shakura and Sunyaev, 1973). For these values of α and β the surface density is proportional to $r^{-1.08}$. We take the scale height at 1 AU, h_0, to be 0.15 AU, and hold the inner radius of the disk fixed at 0.1 AU, consistent with measurements of the inner disk radius of T Tauri stars for the range of luminosities we chose (e.g. Eisner et al., 2007). The total disk mass, M_{disk}, and the outer radius of the disk, R_{disk}, are left as free parameters. In our grid we allow M_{disk} to take values of 1×10^{-6}, 5×10^{-6}, 1×10^{-5}, 5×10^{-5}, and 1×10^{-4} $M_{\odot}$, and we let R_{disk} vary between 30, 60, 100 and 300 AU. We again

allow large disk radii because the actual separation of the protostars may be larger than the projected separation. We do not allow models in which $R_{\mathrm{disk}} > R_{\mathrm{env}}$.

Summary of Model Parameters

The model we employ includes a significant number of free parameters, and creating a grid of models that can fully explore the parameter space of these models is not practical. This is especially true because of the significant amount of computational time required to generate a single model, meaning that our grid must be relatively coarse out of necessity. Instead we focus on the subset of the free parameters which are particularly important for determing the best model fit to the data. We hold h_0 and ζ constant so that we can explore more values for other parameters. The parameter study from Eisner (2012) suggests that these parameters have a smaller influence on models compared with other parameters. The free parameters in our models are M_{disk}, $R_{\mathrm{disk}} = R_c$, M_{env}, R_{env}, L_{star}, and f_{cav}.

4.3.2 Opacity

We calculate the opacity of dust grains in our model following the prescription of Pollack et al. (1994). Our dust grains are composed by volume of a mixture of 38% astronomical silicates, 3% troilite, 29% organics, and 30% water ice. Optical constants for the astronomical silicates, troilite, organics, and water ice were taken from Draine (2003), Begemann et al. (1994), Pollack et al. (1994), and Hudgins et al. (1993) respectively. We reduce the amount of water ice relative to the other constituents when compared with the Pollack et al. (1994) recipe to account for the high temperatures which would vaporize much of the water ice in the inner regions of the disk. We calculate the optical properties of the mixed grains using the Bruggeman mixing rule. We calculate the absorption and scattering opacities from the optical properties of the combined grains assuming that the grains are spherical and using the code BHMIE (Bohren and Huffman, 1983).

We assume that the dust in our models follows a power law grain size distribution,
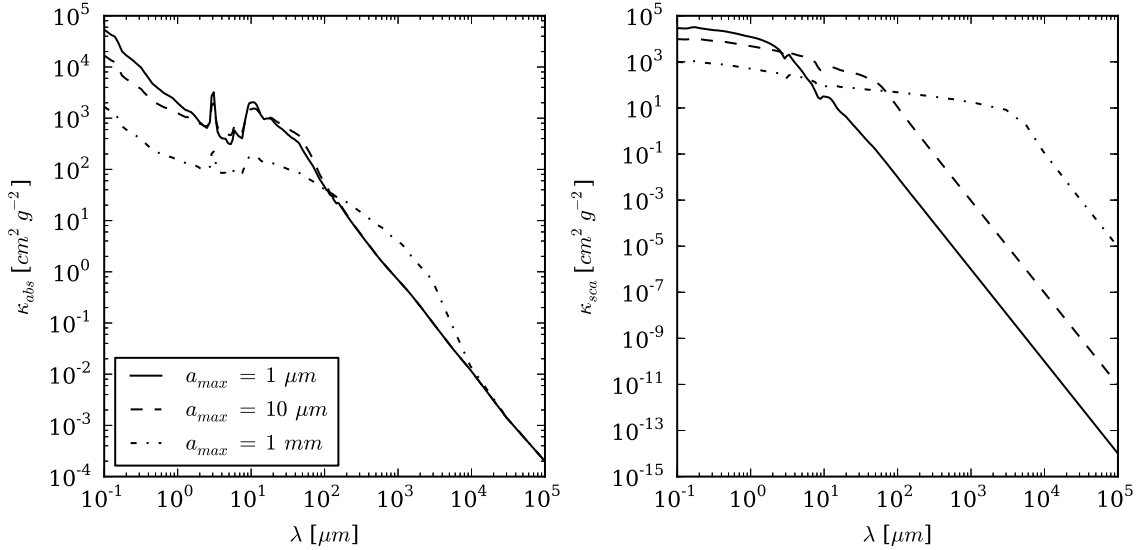
Figure 4.6: Opacities we use in our modeling, with three different maximum grain sizes. We plot the absorption and scattering coefficients for the opacities in the left and right panels respectively. The behavior of our opacities with increasing a_{max} agrees qualitatively with both the opacities used by D'Alessio et al. (2001).

$n(a) \propto a^{-p}$, between some minimum and maximum grain size. Mathis et al. (1977) find that $p = 3.5$ for the interstellar medium, and several investigators have found that the collisional cascade in debris disks also results in $p \approx 3.5$ (e.g. Dohnanyi, 1969). The power law exponent in Class I disks is not well known, so we assume $p = 3.5$. We assume a minimum grain size of 0.005 μm for all of our opacities. The dust in the envelope of our models always uses opacities with a maximum grain size of 1 μm, roughly consistent with dust grains in the interstellar medium. We, however, allow the maximum dust grain size, a_{max}, in the disk to take values of 1 μm, 10 μm, and 1 mm so that we might explore grain growth in the disk of our targets.

Our opacities for dust grains with a maximum grain size of 1 μm are in good agreement with the Ossenkopf and Henning (1994) dense ($n = 10^5$) protostellar core opacities, differing by at most a factor of two. This is well within the degree to which we know the composition of interstellar dust grains. We also compare our opacities qualitatively with the opacities of D'Alessio et al. (2001), who follow a similar recipe,

and find that our results are in good qualitative agreement for different grain size distributions. We plot the effect of changing the maximum dust grain size in Figure 4.6. Changing the relative abundances of the constituent grains produced smaller effects on the resulting opacities.

4.3.3   Radiative Transfer Codes

We use a combination of the three dimensional Monte Carlo dust radiative transfer codes Hyperion (Robitaille, 2011) and RADMC-3D to create our grid of spectra, images and visibilities of model protostars. For a given dust density distribution, we use Hyperion to perform a Monte Carlo simulation to calculate the dust temperature throughout the grid. We then use RADMC-3D raytracing to create synthetic spectra and images of the model from the density and temperature distributions. Finally, we Fourier transform synthetic 1.3mm images to create visibilities. We describe the basic functioning of these codes, as well as our rationale for using two in tandem, below.

Hyperion runs Monte Carlo simulations to determine the temperature structure of a given protostellar model using the iteration method proposed by Lucy (1999). Photons are propagated through the density grid, being absorbed and re-emitted as they go, and after all of the photons have escaped the grid, the temperature is computed, and the simulation is carried out again until the temperature converges to a satisfactory level. For our simulations, each iteration used 10^5 photons, which we found to give a good balance between accuracy in the temperature measurement and time required to run a single model simulation. Each simulation usually requires ~ 10 iterations to converge, for a total of about 10^6 photons for each thermal simulation.

Our models tend to include very high density regions (e.g. the disk midplane) into which few photons travel. To improve the signal-to-noise of the temperature measurement we allow Hyperion to use the Partial Diffusion Approximation (PDA) to more accurately calculate the temperature in these high optical depth regions following each iteration. Furthermore, if a photon does wander into these regions of the grid it can end up being trapped in the high density cell, which significantly

slows down the calculation. To circumvent this problem we employ the Modified Random Walk (MRW; Min et al., 2009; Robitaille, 2010) method which can speed up these trapped photons by allowing the photons to diffuse out of the cell in a single step rather than hundreds or thousands.

Images and SEDs are computed for our models using raytracing of the dust thermal emission. To account for scattered light emission, which can contribute a significant fraction of the signal at short wavelengths, we run scattered light simulations in which monochromatic photons are propagated through the grid and allowed to scatter until they are absorbed. The scattering phase function can then be determined by the scattering properties of the photons and included in the raytracing algorithm to quickly create images and SEDs from the models. The scattered light simulations are run with 10^4 photons at each wavelength in an SED generated and 10^5 photons for each image, which was found to give good signal-to-noise in our models. We calculate the images and SEDs for inclinations from $0°$ to $90°$ at intervals of $5°$, and we vary the position angle from $0°$ to $360°$ in intervals of $10°$.

We elected to use a combination of both codes because we frequently found that the run time for each thermal simulation was dominated by photons being trapped in high optical depth regions, so the MRW and PDA procedures significantly sped up the simulations. At the time when we created our grid of models, only Hyperion employed both of these procedures and thus we elected to use Hyperion for the thermal simulation portion of our modeling. Conversely, raytracing for both thermal emission and scattered light is the fastest method for producing spectra and images, and at the time when we created our grid of models, only RADMC-3D offered raytracing for scattered light. We note, however, that since we ran our model grid RADMC-3D has been updated to include the MRW algorithm and has a PDA module under development. Furthermore, Hyperion may include raytracing for scattered light in the future (Robitaille, 2011).

4.3.4   Model fitting

We fit our models to all three datasets (SED, HST scattered light image, and CARMA visibilities) simultaneously with a weighted least squares fit. For each individual dataset we calculate χ^2 for the corresponding component of each model. We then combine the separate χ^2 measurements into one weighted least squares parameter:

$$X^2 = \left(w_{spec} \frac{\chi^2_{spec}}{min(\chi^2_{spec})} + w_{im} \frac{\chi^2_{im}}{min(\chi^2_{im})} + w_{vis} \frac{\chi^2_{vis}}{min(\chi^2_{vis})} \right) / (w_{spec} + w_{vis} + w_{im}).$$
(4.6)

It is important to note that our goodness of fit parameter X^2 is not a true χ^2 statistic and cannot be used in a statistically rigorous way.

We use our X^2 metric rather than a true χ^2 to determine the best fit to the data so that we have the ability to change the weight given to each dataset. If we were to use a true χ^2 metric, our fits would be dominated by the imaging data, which has a significantly larger number of data points than the visibilities or SED. The primary goal of this study is to constrain disk properties from our datasets. Fitting with a true χ^2, however, would place most of the weight on the scattered light images, and scattered light images do not trace the disk properties as well as the visibilities or SED. Millimeter wavelength measurements are particularly sensitive to the dust mass of a system, so fits with larger weight given to the 1.3mm visibilities may more faithfully reproduce the distribution of denser material. Our X^2 statistic allows us to put more weight on the visibilities and make our fitting more sensitive to disk mass.

Our X^2 metric allows us to explore how consistent our best fit parameters are with each dataset individually. If a parameter remains relatively constant as we give each dataset significantly more weight than the others, that would suggest that the parameter is consistent with each of the datasets and is well constrained. Conversely, those parameters that vary significantly with different weights are likely not well constrained and may suggest that a more complex model is needed to fully explain the complete dataset.

We fit our models to the data for each component of the binary separately. In order to do this we fit the model spectrum to only the resolved spectrum of each source, while the unresolved data are used as upper limits. We also split the HST image into smaller sub-images which only contain the appropriate source, and split the visibilities as described above to obtain the visibilities for an individual source. However we do verify that our best-fit models also provide good fits to the composite imaging, visibility and photometric data.

4.4   Results

We list the best fit model parameters for GV Tau N and S in Table 4.3, ordered by increasing X^2. We plot the synthetic data for the best fit models, as described in row "a" of Table 4.3, in Figure 4.7. We also plot the sum of the best fit models against the full binary dataset to show that we fit all of the composite data. We give the mm data more weight, as described above, in our best-fit model. However we explore other weighting schemes to determine whether best-fit parameters are consistent with each dataset individually. If parameters change as weights are varied, that implies that some model parameters may produce degenerate effects, or that a more complex model may be required to fit the combined dataset well. We list all models with $X^2 < 2$ for GV Tau N and $X^2 < 1.7$ for GV Tau S in Table 4.3, and those models are plotted in Figures 4.8 & 4.9 in order of increasing X^2. In Figure 4.10 we show the models with the next-lowest X^2 values. These models are clearly unsuitable fits to the data, so we do not consider them, or models with still higher X^2 values, further.

We find that the disk dust masses of the best fit models for GV Tau N and S are each 5.0×10^{-5} M$_\odot$. By examining the fit quality across our model grid, we provide qualitative estimates of the acceptable range of parameter values. A disk mass a factor of two larger than our best fit model can still reproduce our dataset well (Figures 4.8 & 4.9), while a disk mass five times lower cannot (Figure 4.10). While not statistically rigorous, we therefore estimate that the disk masses for GV
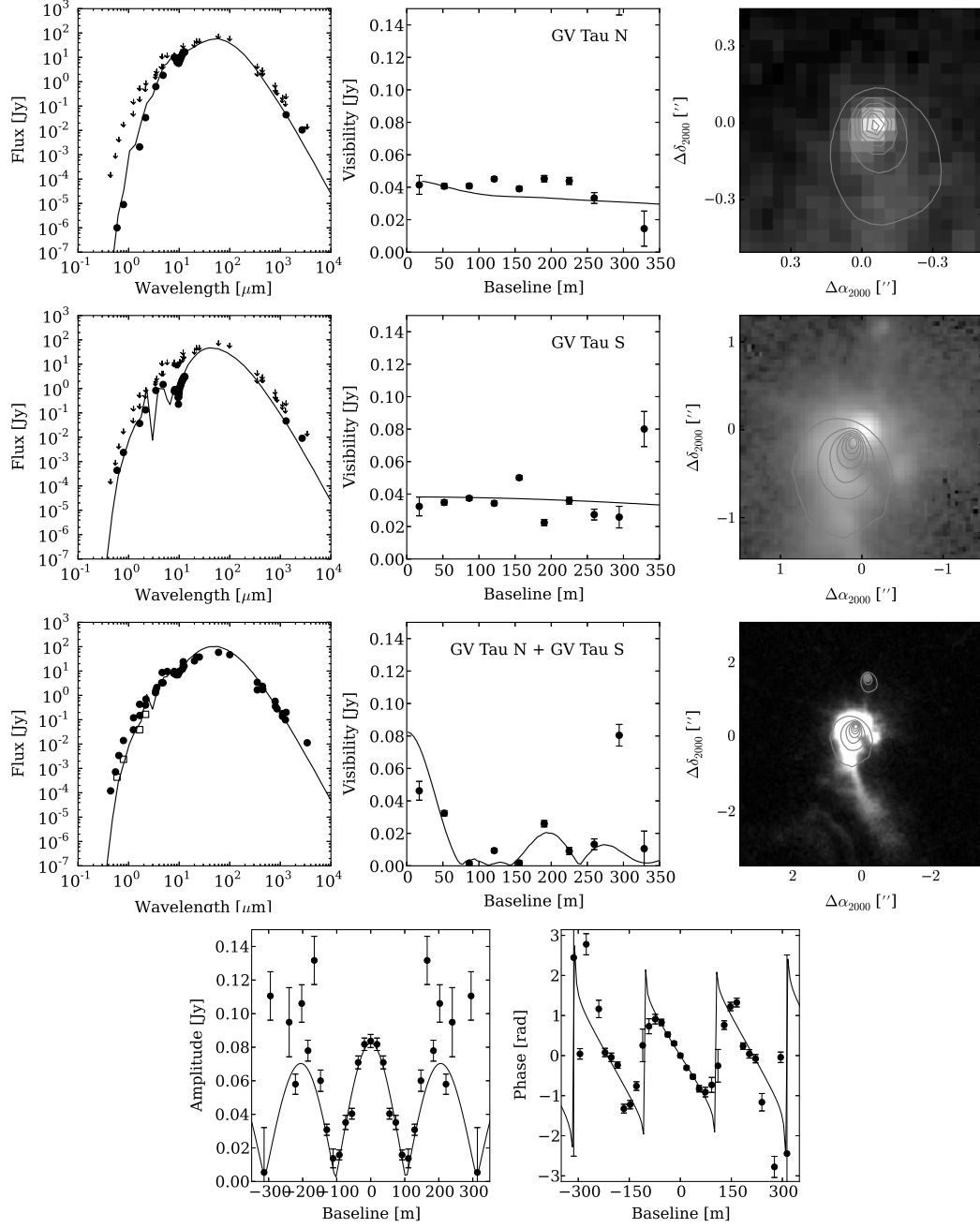
Figure 4.7: Our data, shown as solid points, with the best fit models, shown as lines, for GV Tau N and S overplotted. The first three rows show broadband SEDs in the left panel, 1.3 mm visibilities in the middle panel, and 0.8 μm scattered light images in the right panel. Panels which show the resolved spectra of GV Tau N or S also show the unresolved spectrum of the system as upper limits. The first row shows the data and model for GV Tau N, while the second row shows the same for GV Tau S. The third and fourth rows show the combined GV Tau dataset with the sum of the best fit north and south models plotted on top. The fourth row shows the visibilities, both amplitude and phase, averaged along the binary axis.
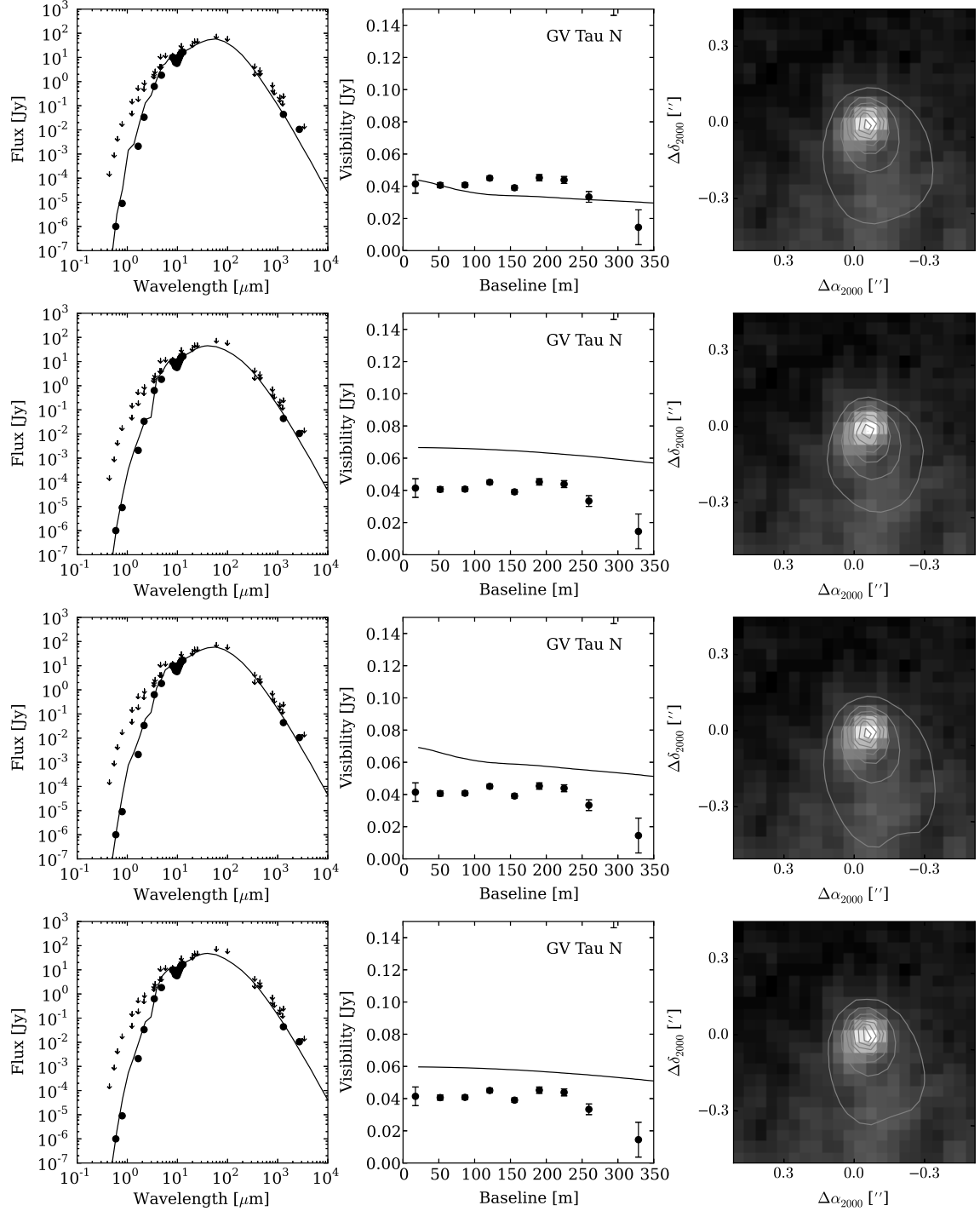
Figure 4.8: Models for GV Tau N which show good fits to the data. See Figure 4.7 for more information about each panel. Such models can be used to determine how robust our determination of each parameter is, as well as how uncertain our measurements may be. Each row shows the model for the corresponding row for GV Tau N in Table 4.3. Like Table 4.3, the plots are ordered by increasing X^2.

Table 4.3. Best fit models.

	Source	w_{mm}	w_{NIR}	w_{SED}	X^{2}[a]	M_{disk} (M$_\odot$)	R_{disk} (AU)	M_{env} (M$_\odot$)	R_{out} (AU)	a_{max}[b] (μm)	f_{cav}	L_* (L$_\odot$)	i (°)	PA (°)
a	GV Tau N	10	1	1	1.2	5×10^{-5}	30	5×10^{-5}	300	1	0.2	3	30	200
b	GV Tau N	1	1	10	1.2	1×10^{-4}	30	1×10^{-5}	90	1000	0.2	3	35	200
c	GV Tau N	1	1	1	1.5	1×10^{-4}	30	5×10^{-5}	300	1	0.2	3	30	200
d	GV Tau N	1	10	1	1.7	1×10^{-4}	30	5×10^{-5}	300	10	0.2	3	25	200
a	GV Tau S	10	1	1	1.1	5×10^{-5}	30	1×10^{-5}	300	10	1	6	55	160
b	GV Tau S	1	1	10	1.1	1×10^{-4}	30	1×10^{-5}	300	1000	1	6	55	160
c	GV Tau S	10	1	10	1.3	1×10^{-4}	30	1×10^{-5}	300	1000	1	6	55	160
d	GV Tau S	1	1	1	1.4	1×10^{-4}	30	1×10^{-5}	300	1000	1	6	55	160

[a]Note that X^2 is a measure of the goodness of fit of a model, as defined by Equation 6, and not a true χ^2.

[b]The parameter a_{max} is the maximum dust grain size for the opacity used in the disk. The maximum dust grain size in the envelope is held constant at 1 μm.

Tau N and S are constrained to within a factor of 2.

Opacity is likely a large source of additional uncertainty on our disk mass measurement because millimeter flux measurements are sensitive to the product of mass and opacity. We allowed the maximum dust grain size to vary in an attempt to constrain the opacity, but we are unable to definitively determine the properties of the opacity. Both protostars can be fit by models with maximum grain sizes that range across the spectrum of allowed values. Interestingly, regardless of which opacity law is used, the disk mass is measured to be the same. One might expect that for the larger values of a_{max} that we consider we would measure a lower M_{disk} because the 1.3mm opacity is higher. For larger values of the 1.3mm opacity however, it turns out that our best fit model disks are significantly more optically thick than for lower 1.3mm opacities. This means that more mass is needed than is otherwise expected to reproduce the 1.3mm flux. It is likely because of this high optical depth that our modeling has difficulties in constraining the opacity in the disk. Furthermore, for $a_{max} \gg 1$ mm the dust opacity at 1.3 mm will drop, also allowing for a larger inferred disk mass. Changing the opacity parameters also has different effects at different wavelengths, so models may require the mass to remain constant to fit the combined dataset, even as the opacity is varied.

We are, however, able to place a constraint on the radii of the GV Tau N and S
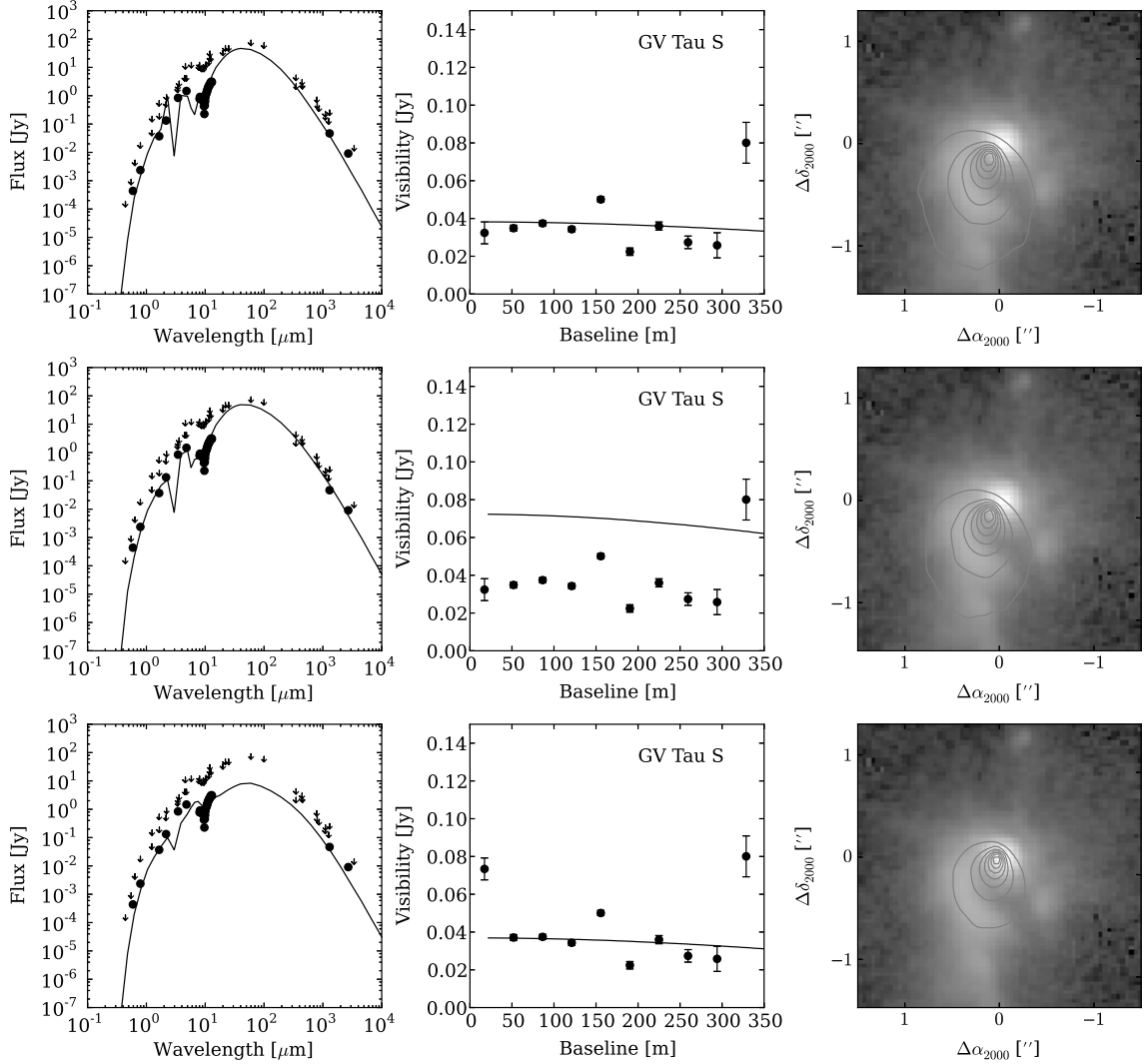
Figure 4.9: Models which fit the data for GV Tau S well. See Figure 4.7 for more information about each panel. The first row is our best fit model, as described by row "a" for GV Tau S in Table 4.3, and the second row shows the model from rows b-d, as the rows are identical. In the third row we show a good model fit which was tuned by hand to plausibly reproduce the 8-13 μm visibilities from Roccatagliata et al. (2011) while maintaining a good fit to our datasets (see Figure 4.11 for further details).

disks. Our modeling shows that both protostars strongly favor models with $R_{disk} = 30$ AU. This is the smallest radius allowed in our model grid, so it is possible the the true disk radii are, in fact, smaller than our best fit models suggest. It is also possible that the disk radius could be somewhat larger than 30 AU, as the next
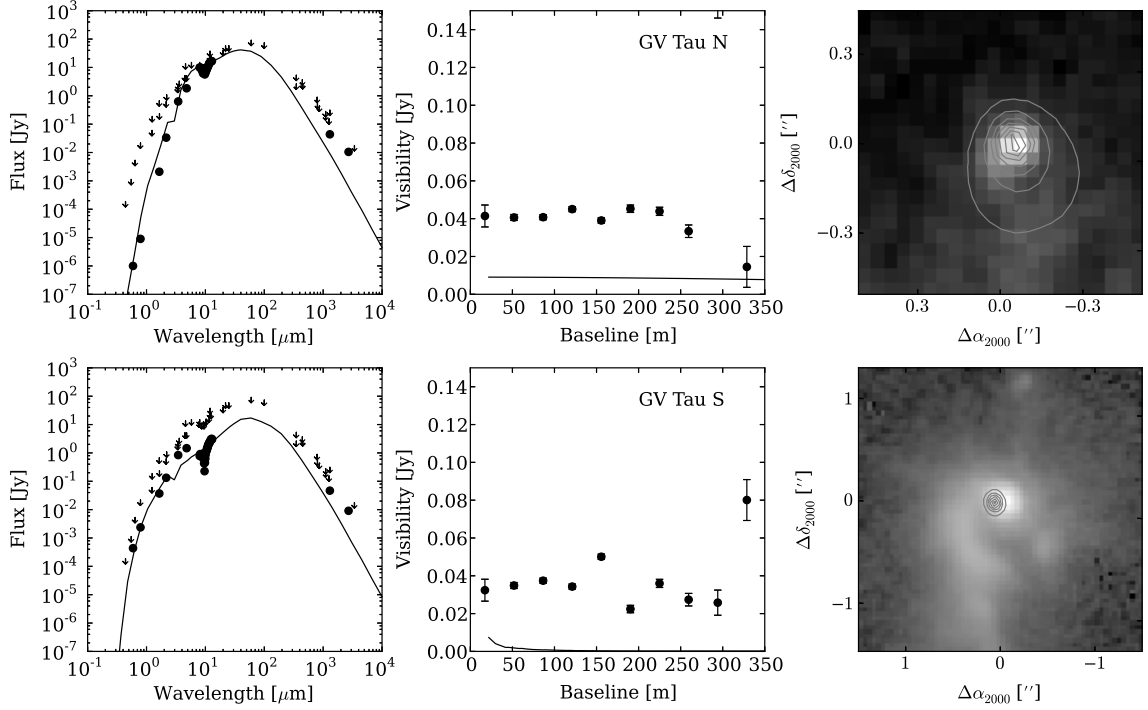
Figure 4.10: Models for both sources which do not fit the data well. See Figure 4.7 for more information about each panel. We show a model for GV Tau N with $X^2 = 2.0$ in the top row and a model for GV Tau S with $X^2 = 1.7$ in the bottom row. Models with X^2 above our thresholds, of 2 for GV Tau N and 1.7 for GV Tau S, no longer reproduce the data well, as demonstrated by the poor fits of these models.

smallest radius in our grid is $R_{disk} = 60$ AU. A disk with a radius of ~ 60 AU would have an extent of ~ 0.8" and would be marginally resolved by our 1.3 mm visibilities. Our data, however, suggest that the disks are unresolved, so we conlcude that $R_{disk} < 30$ AU.

The parameters of the envelopes also appear to be somewhat constrained by our modeling, however we also find some degeneracy between envelope mass and radius. The best fit envelope dust mass is 5.0×10^{-5} M$_\odot$ for GV Tau N and 1.0×10^{-5} M$_\odot$ for GV Tau S, and both protostars have $R_{env} = 300$ AU. Furthermore, our modeling suggests that $f_{cav} = 0.2$ for GV Tau N and $f_{cav} = 1$ for GV Tau S. It is, however, possible to decrease (or increase) both M$_{env}$ and R$_{env}$ while maintaining the quality of fit to the data. This is unsurprising because our millimeter visibilities

have very limited sensitivity to faint extended structures, particularly those close to or larger than 1000 AU. As such, we suggest that these envelope parameters should be treated with caution.

Furthermore, from our modeling we are able to marginally constrain the viewing geometry of the GV Tau system. We find that the best fit models for GV Tau N suggest an inclination of 30° while they suggest an inclination of 55° for GV Tau S. Similarly, we find a position angle of 200° for GV Tau N and 160° for GV Tau S. These parameters however, are dependent on the astrometry of the scattered light image, which we find to be quite uncertain. If we adjust the astrometry within the bounds allowed by our uncertainty, we find that the position angle of neither source is well constrained by our modeling. If we consider the uncertainty in the astrometry, as well as the variations of best fit inclinations as we change the weighting of our datasets, we estimate that we could vary our best fit inclinations by up to 20° and still find acceptable fits to the dataset. The inclination is better constrained than the position angle because the SED can provide an additional constraint only on the inclination, while the position angle is constrained almost entirely by the scattered light imaging.

Finally, we find that the luminosity of each protostar is constrained by our modeling, with an accuracy limited by the sparse sampling of the parameters in our grid. GV Tau N very strongly prefers a luminosity of 3 L$_\odot$ while GV Tau S tends to favor a luminosity of 6 L$_\odot$. We have also found a model with a $L_{star} = 1.5$ L$_\odot$ which can also reproduce our data (see Section 5.2 and Figure 4.11), so the allowed range of luminosities for GV Tau S likely spans a large range.

4.5   Discussion

4.5.1   Gas vs. dust masses

Until this point we have presented our models and results in terms of the mass of dust present in the system. Dust mass is constrained by our radiative transfer modeling, and is also the relevant quantity for understanding giant planet formation

via core accretion (e.g. Lissauer, 1993). However, disk masses are often quoted as the total of dust+gas mass. We therefore convert our dust masses into total masses using the common assumption that the gas-to-dust mass ratio is 100 times the total mass of our systems. With this assumption, the total mass in each of the GV Tau disks is 0.005 $M_\odot$. Throughout the remainder of the text we refer to the total mass rather than the dust mass.

4.5.2   Comparison with previous works

Prior to this work, several investigators have attempted to measure the disk masses of GV Tau N and S. Guilloteau et al. (2011) measured total disk masses of 0.0006 and 0.0005 $M_\odot$ for GV Tau N and S respectively, noting that the disks are likely optically thick and that these numbers are lower limits. Their results are compatible with our own as we find disk masses of 0.005 $M_\odot$ for both GV Tau N and S. Guilloteau et al. (2011) also measure disk radii of 17 and 10 AU for the disks in the system, again consistent with our constraints since neither work had a linear resolution of better than $\sim$50 AU. Furthermore, the smallest disk radius in our model grid was 30 AU, so it is possible that there is a similar or better quality fit model with a disk radius smaller than we considered in our modeling.

There have been a number of studies which have made estimates of the inclination of the GV Tau S disk. Beck et al. (2010) detected spatially extended [Fe II] and Brγ emission trailing from GV Tau S to the southwest, presumably tracing an outflow. They noted that the extent of the outflow is roughly consistent with an inclination of $60° - 70°$, as suggested by Movsessian and Magakian (1999). The same outflow is seen from GV Tau S at 3.6 cm by Reipurth et al. (2004). Conversely, Roccatagliata et al. (2011) modeled 8-13 μm VLT visibilities with a two-blackbody model and found that GV Tau S is very close to face-on, with an inclination of $10° \pm 5°$. We find that our best fit model for GV Tau S, which includes physically-motivated complexity beyond the simple geometric model of Roccatagliata et al. (2011), has a disk with an inclination of 55°. This matches the inclination found by Beck et al. (2010) but is decidedly different from that of Roccatagliata et al. (2011). We are
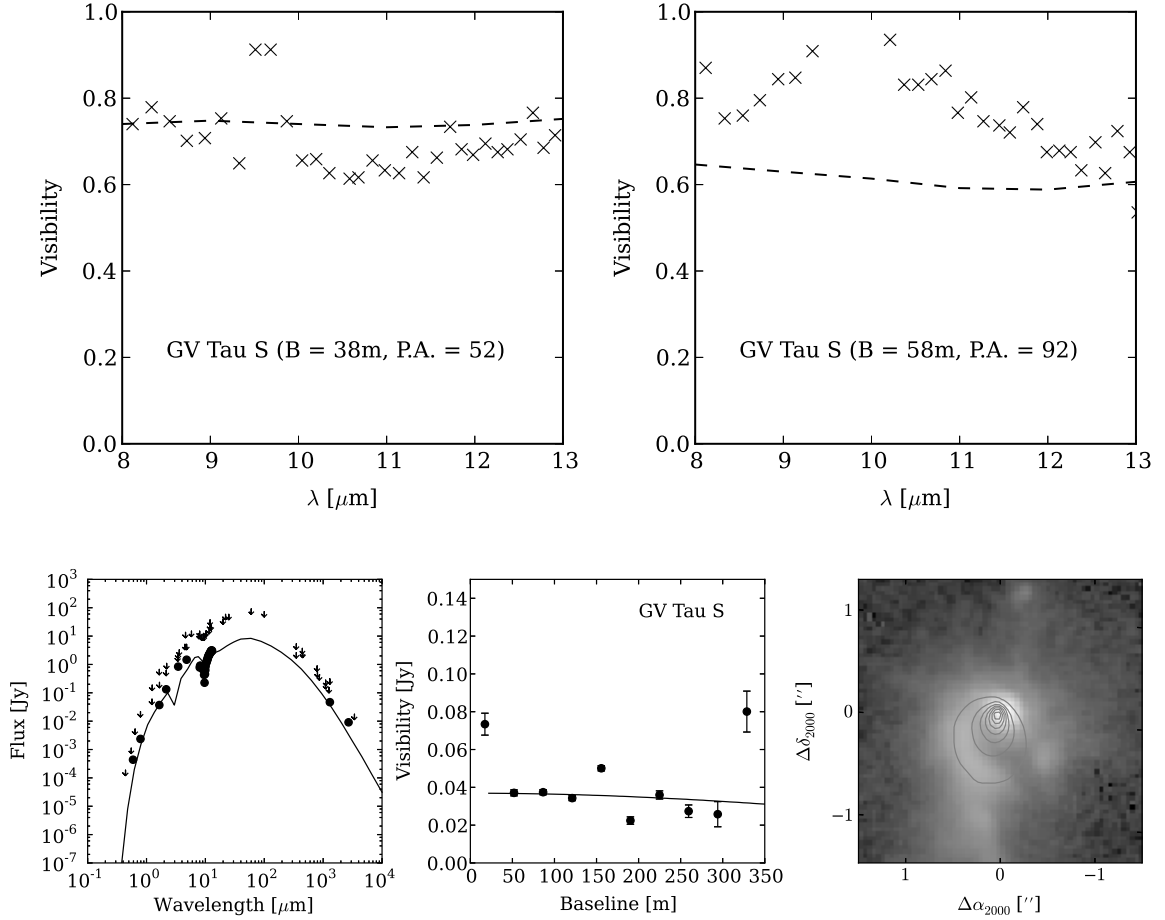
Figure 4.11: Model which can plausibly reproduce the 8-13 μm visibilities for GV Tau S while also preserving the majority of our best fit model parameters. In the first row we show the 8-13 μm visibilities for GV Tau S from Roccatagliata et al. (2011) at two baselines, with the model visibilities shown as dashed lines. See Figure 4.7 for more information about the panels in the second row. The parameters for this model are $L_{star} = 1.5$ L$_\odot$, $M_{disk} = 0.015$ M$_\odot$, $R_{disk} = 30$ AU, $h_0 = 0.01$ AU, $M_{env} = 0.002$ M$_\odot$, $R_{env} = 200$ AU, $f_{cav} = 0.2$, $\zeta = 0.7$, $R_{in} = 0.05$ AU, and $i = 55°$. Although not perfect, the plot can plausibly reproduce all of the datasets while preserving the best fit parameters that we find from our modeling, within our estimated uncertainties.

unable to find a model in our grid with an inclination consistent with Roccatagliata et al. (2011) that also fits all of the data well. We can, however, produce a model of GV Tau S that reproduces the 8-13 μm visibilities with an inclination of 55° while maintaining the other parameters within their previously discussed uncertainties, as

we demonstrate in Figure 4.11, so we believe that these measurements are in fact consistent with a non-zero inclination.

Little has been determined about the geometry of the disk of GV Tau N, although a number of studies have suggested that the disk is close to edge on based on the faintness of GV Tau N at short wavelengths. Furthermore, several investigators have reported the detection of warm HCN and/or C_2H_2 absorption in the disk of GV Tau N, which may suggest a higher inclination for the disk (Gibb et al., 2007, 2008; Doppmann et al., 2008; Fuente et al., 2012). Indeed, Roccatagliata et al. (2011) measured an inclination for GV Tau N of $80° \pm 10°$ using VLT interferometry. Our work has demonstrated, however, that an edge-on disk cannot be invoked to reproduce the observed properties of GV Tau N. We are unable to find a model in our grid that can reproduce our datasets with an inclination consistent with the one
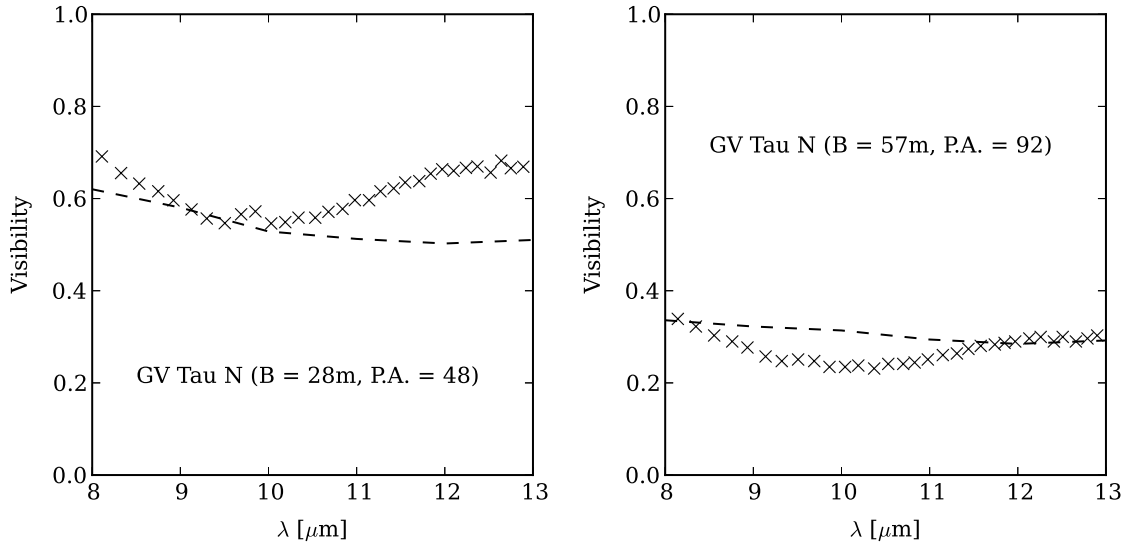
Figure 4.12: 8-13 μm visibilities measured by Roccatagliata et al. (2011) with the 8-13 μm visibilities for our best fit GV Tau N model overplotted as a dashed line. Each panel shows the visibilities at a different baseline. Our best fit model, which uses a very different inclination than is found by Roccatagliata et al. (2011) from the same data, can reproduce the best the data reasonably well, considering that the data were not included in our fitting. Indeed, the fit to the 10 um spectro-interferometry data is of comparable quality to the one presented in Roccatagliata et al. (2011).

found by Roccatagliata et al. (2011). Our best fit model for GV Tau N suggests that the system has an inclination of 30°. Our best fit model can also plausibly reproduce the 8-13 μm visibilities modeled in Roccatagliata et al. (2011), as we show in Figure 4.12. We do not attempt to model the gas in the system so we cannot determine whether our best fit models are consistent with the detections of warm molecules towards GV Tau N.

A number of studies have suggested that the GV Tau system is surrounded by a flattened circumbinary envelope (Menard et al., 1993; Koresko et al., 1999; Leinert et al., 2001). As discussed earlier, we find that our simple double point source model for GV Tau is improved by adding a Gaussian source with a FWHM of $\sim$5". This Gaussian may represent emission from this circumbinary envelope. Because our interferometry data have limited sensitivity to extended emission, however, we cannot constrain the properties of such a circumbinary envelope.

Previous studies of near-infrared photometry have measured the luminosity of GV Tau S to be 1.8 $L_\odot$ (White and Hillenbrand, 2004) and 3.3 $L_\odot$ (Doppmann et al., 2005), roughly consistent with our best fit models. Our models indicate a luminosity of 6 $L_\odot$ for GV Tau S, slightly higher than previous measurements, however we are also able to find acceptable model fits with luminosities as low as 1.5 $L_\odot$. As such, the previous measurements of the luminosity of GV Tau S fit nicely in the range allowed by our modeling.

4.5.3 The Evolutionary State of GV Tau

GV Tau N and S are classified as Class I protostars, however previous investigators have estimated that the age of the system is $\sim$ 3 Myr (e.g. Doppmann et al., 2008). That would mean that the protostars are more likely Class II pre-main sequence stars based on the ages of each stage as measured by counting statistics (e.g. Andre and Montmerle, 1994a; Barsony, 1994). If GV Tau were a Class II protostar, however, the highly obscured near infrared spectrum of GV Tau N would imply that the disk must be close to edge on, which is inconsistent with our modeling.
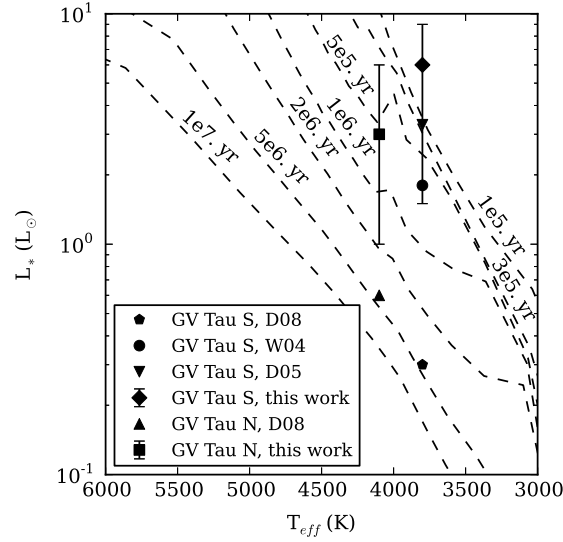
Figure 4.13: Pre-main sequence tracks from Siess et al. (2000) as dashed lines with the temperature and luminosity measurements from White and Hillenbrand (2004), Doppmann et al. (2005), Doppmann et al. (2008) and this work overplotted. The errorbars on our measurements represent the limited sampling of L_{star} in our model grid rather than actual errors. Our luminosity measurements, as well as those of White and Hillenbrand (2004) and Doppmann et al. (2005), suggest much younger ages for the protostars than what Doppmann et al. (2008) measure. Our suggested age, of ~ 0.5 Myr, is in better agreement with the ages for Class I protostars as estimated by counting statistics (e.g. Andre and Montmerle, 1994a; Barsony, 1994).

Doppmann et al. (2008) measure the age of the system by placing GV Tau N and S on an H-R diagram and comparing with pre-main sequence protostar tracks (Siess et al., 2000). They measure the temperature and surface gravity of each protostar by matching absorption line features in the near-infrared with stellar synthesis models and determine the mass by associating temperature with stellar mass. From there they use the mass and surface gravity to determine the stellar radius, and combine the radius and temperature to determine a luminosity. These measurements, however, are indirect, and are inconsistent with other measurements which use photometry and bolometric corrections to determine luminosity (White and Hillenbrand, 2004; Doppmann et al., 2005).

If we use our luminosity constraints, or those of White and Hillenbrand (2004)

or Doppmann et al. (2005), and the same evolutionary tracks to determine the age of the protostars, we find GV Tau has an age of a few hundred thousand years (see Figure 4.13). This age provides a more consistent description of the system as a pair of Class I protostars, as suggested by the geometry of our best fit models, with an age of a few hundred thousand years. If we assume that the protostars are coeval, then we estimate an age of ~ 0.5 Myr for the system.

4.5.4   Relation to the MMSN

Disk mass is an important quantity for understanding the formation of planets. In order to form giant planets a protoplanetary disk must contain more than 0.01 $M_\odot$, and likely closer to 0.1 $M_\odot$, of material (Weidenschilling, 1977; Desch, 2007). Studies of the disks around Class II YSOs in Taurus and Orion (ages $\sim 1-5$ Myr) have found that on average the disks around these stars do not contain enough material to form giant planets based on this criterion (Andrews and Williams, 2005; Eisner et al., 2008; Andrews et al., 2013). Observations at millimeter wavelengths, however, are only sensitive to dust grains smaller than a few millimeters. The insufficient mass present in the disks may be because dust grain growth in these disks hides the mass in larger bodies which are not traced by sub-millimeter observations.

We have estimated that the masses of the disks in the GV Tau system are 0.005 $M_\odot$ each, which places both disks near the lower limit to the amount of matter needed to form giant planets (Weidenschilling, 1977). Unlike the other Class I disks measured in Eisner (2012), which were found to have a median disk mass within 100 AU of 0.007 $M_\odot$ and even less within 30 AU, the entirety of the disk mass in the GV Tau system is located within $\lesssim 30$ AU of the protostars. This is important because the Minimum Mass Solar Nebula (MMSN) is defined within 30 AU. The mass within 30 AU is then the proper mass to compare with the MMSN for determining potential for planet formation. While there may be just enough mass contained in the GV Tau circumstellar disks to form giant planets, the mass is located entirely within the regions of the disks where planets are actually formed. We plot the cumulative mass distribution for the GV Tau N and S best fit models as a function of radius in
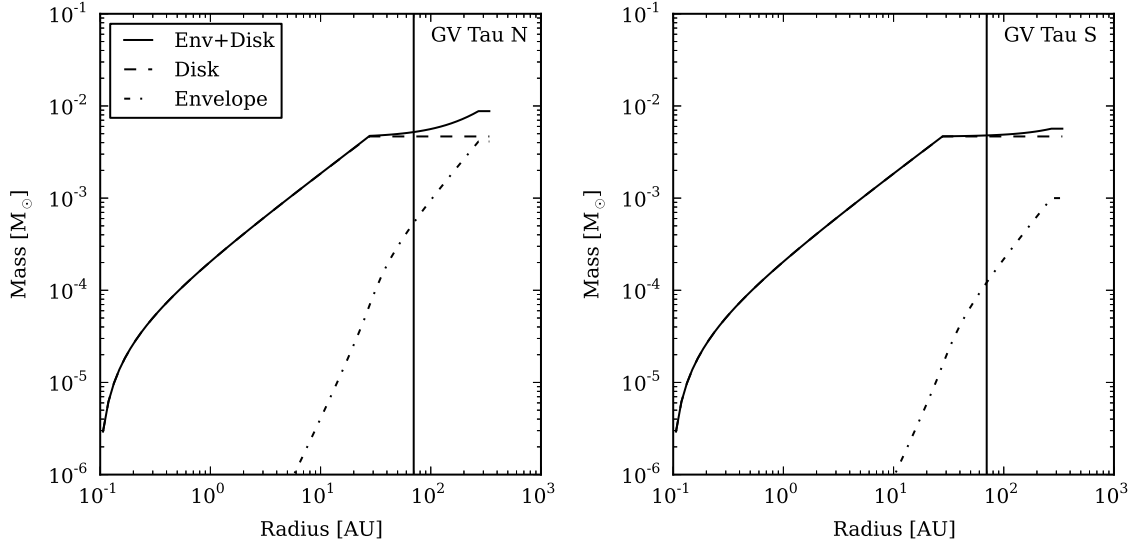
Figure 4.14: Cumulative mass distribution for each component of the GV Tau system as a function of radius. For each figure we plot the contributions from the disk and envelope, as well as the combined distribution of the two. We also plot a vertical line at a radius of 70 AU (or a 140 AU diameter) to indicate the spatial resolution of our CARMA observations. While both protostars appear to have disks that are near or just shy of the 0.01 $M_\odot$ for forming giant plantets, all of the disk mass is within 30 AU, where giant planets are expected to form.

Figure 4.14.

If we include both components of GV Tau in the sample of Class I protostars in Taurus (ages $\sim 0.1 - 1$ Myr) from Eisner (2012) we find that the median mass of the Taurus Class I sample is 0.008 $M_\odot$. For comparison, the sample of Taurus Class II protostars (ages $\sim 1 - 5$ Myr) from Andrews et al. (2013) has a median disk mass of 0.001 $M_\odot$. The sample of Orion Class II objects from Eisner et al. (2008) has a similar median disk mass. All ten of the disks in our Class I sample have a mass greater than or equal to the median mass of the sample from Andrews et al. (2013). Fisher's exact test shows that the disks around our Class I sample are more massive than the Taurus and Orion Class II disks at the 99.8% confidence level. The larger disk masses for Class I protostars likely reflects the fact that between the Class I and II stages some of the small dust particles in the disk have grown into larger bodies. Furthermore, the disk masses for both Class I and II protostars fall short

of the minimum mass solar nebula, which may indicate that significant dust grain growth has already occurred by the time a protostar reaches the Class I stage.

We can also compare the Class I and Class II samples with the exoplanet sample to determine whether either distribution can reproduce the observed fraction of stars with giant planets. Cumming et al. (2008) determined that 18% of stars have a giant planet within 20 AU, meaning that a minimum of 18% of stars have giant planets. Conversely, the sample of Taurus and Orion Class II YSOs has 11% of stars with disk masses greater than 0.01 $M_\odot$ and 0.6% of stars with disk masses greater than 0.1 $M_\odot$ (Andrews and Williams, 2005; Eisner et al., 2008; Andrews et al., 2013). If we assume that the fraction of YSOs with disk masses sufficient to form giant planets is the same as the fraction of stars with giant planets, and we take 0.01 $M_\odot$ to be the threshold for forming giant planets, then the probability of randomly selecting Class II YSOs and reproducing the observed distribution is 0.02%. If we take the threshold for forming planets to be 0.1 $M_\odot$ the probability becomes astronomically small. It would appear that the Taurus and Orion Class II disks cannot reproduce the observed fraction of stars with giant planets. For our Taurus Class I sample of 10 objects we find 2-7 objects that may have disks with masses greater than 0.01 $M_\odot$ but only 1 with a disk mass greater than 0.1 $M_\odot$. This would suggest that Class I protostars may have enough mass in their disks to form giant planets if the threshold is 0.01 $M_\odot$, but may not if the threshold is 0.1 $M_\odot$. Again, both of these comparisons neglect any disk mass in larger bodies that would not be traced well by observations.

4.5.5 Stability of the Disks

Previous studies have shown that the disk-to-star accretion rates measured for young stars are low compared with the time averaged envelope-to-disk infall rates (Kenyon and Hartmann, 1987; White and Hillenbrand, 2004; Eisner et al., 2005). One proposed solution to this discrepancy is that gravitational instabilities in the protostellar disk may lead to short bursts of gravitationally enhanced accretion in which material from the disk is rapidly accreted onto the central protostar. Such instabilities
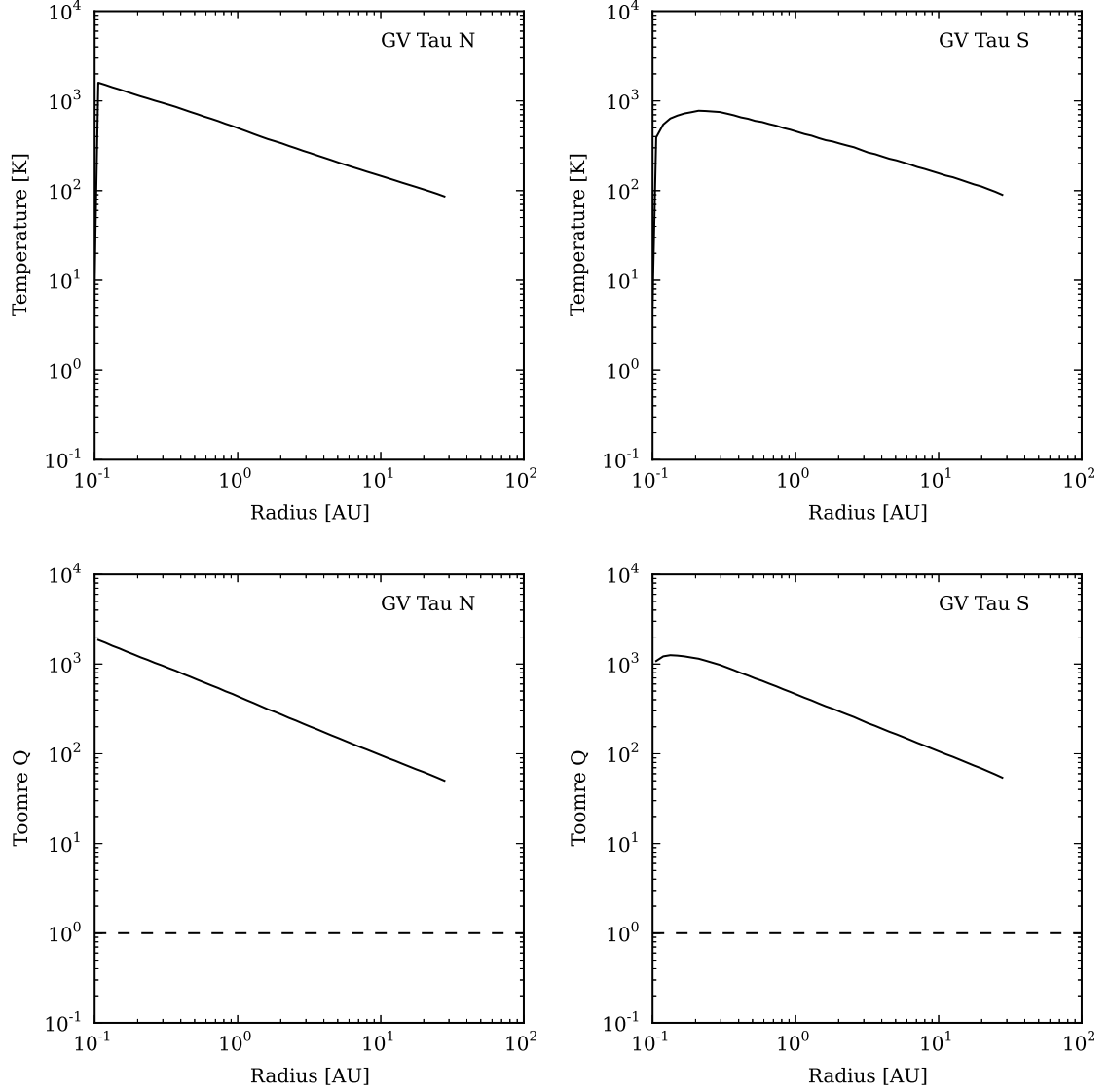
Figure 4.15: (*Top row*) Mean temperature of the disk as a function of radius for GV Tau N and S. (*Bottom row*) Toomre's Q as a function of radius for the disks of GV Tau N and S. The dashed line marks a value of Q=1. Values less than one imply that the disk is gravitationally unstable at that location, while values greater than one suggest that the disk is gravitationally stable. This shows that both disks are very stable. We do note that our millimeter-wave observations may not be sensitive to the entire mass of the disk, however we would have to be missing the majority of the total disk mass to make these disks unstable.

could be present in disks which are particularly massive, approximately one tenth the mass of the star, or dense.

Our study has suggested that the disks in the GV Tau system are quite small, on the order of 30 AU, but contain a significant amount of mass within those small disks. It might seem logical that these high density disks may be subject to gravitational instabilities. To calculate the stability of the disks we calculate Toomre's Q value as a function of radius for each disk. We assume a gas-to-dust ratio of 100 for this calculation. Values of Q > 1 imply that the disk is stable against gravitational collapse, while values of Q < 1 suggest that the disk may be susceptible to collapse under the force of gravity. We find that the best fit models for the GV Tau N and S disks are gravitationally stable throughout, with Q> 10 at all radii. Our millimeter-wave observations are likely not sensitive to all of the mass in the disk, however we would have to be missing a majority of the mass to make these disks unstable. We plot the value of Toomre's Q as well as the mean disk temperature as a function of radius for both disks in Figure 4.15.

4.5.6   Formation Mechanism

There have been a number of proposed mechanisms that may lead to the formation of a binary star. One potential route occurs when a molecular cloud core that has begun to collapse to form a protostar fragments into multiple cores, each of which in turn collapse to form individual stars in a binary system (e.g. Boss and Bodenheimer, 1979; Bate and Burkert, 1997). Alternatively, a binary star system could be formed when the protostellar disk surrounding a young star becomes gravitationally unstable and collapses to form a second star in the system (e.g. Bonnell, 1994; Bonnell and Bate, 1994a,b; Burkert et al., 1997).

Both proposed theories make predictions about the geometry of the resulting binary system that can be used to explore how a binary system formed. A binary system formed by a gravitational instability in the disk around the primary star is expected to have protoplanetary disks that are aligned. Disks that formed, however, by the fragmentation of a collapsing molecular cloud core can be misaligned (Bate

et al., 2000). Interactions with passing objects or the accretion of a small amount of material with a different angular momentum near the end of the accretion phase can also cause misalignment (Bate et al., 2000). Conversely, tidal interactions can act to align disks, as well.

Roccatagliata et al. (2011) measured the inclination of the disks in the GV Tau system to be 10° and 80° and claimed that this misalignment is evidence that the system formed as the result of molecular cloud core fragmentation. Our best fit model for each component finds inclinations of 30° and 55°, although each of these estimates may be able to vary by 20°. The mutual inclination of the disks is then close to 25°, but may vary by 30°. These results suggest that the mutual inclination of the disks in the GV Tau system may not be as high as Roccatagliata et al. (2011) found, and the disks may even be aligned. Thus we cannot distinguish between formation scenarios.

4.5.7 Future Work

While we are able to constrain the mass in the GV Tau protoplanetary disks with our current data, we have left a number of other parameters somewhat unconstrained. Higher spatial resolution millimeter observations of the binary can resolve the protoplanetary disks and more accurately measure the disk radii, inclinations, and position angles. If the disks have radii of 30 AU or smaller, as we have suggested, then a resolution of < 0.4" will allow us to resolve the disks and make these measurements. Modern interferometers, such as ALMA or the VLA, can provide high enough spatial resolution (~ 0.05" for the VLA) to resolve these disks and determine these parameters without ambiguity.

It may also be important to add observations of GV Tau with an interferometer in a more compact configuration. Such a configuration would be significantly more sensitive to the faint extended emission from the proposed circumbinary envelope. Our observations with the CARMA C-array do not include baselines shorter than ~ 20m. As such we are not very sensitive to spatial scales larger than about 1000 AU. Compact array observations would be capable of detecting the signal from this

extended envelope around GV Tau and could be important important for breaking any degeneracy between the envelope mass and radius.

Another significant source of uncertainty in our measurements comes from the opacity of the dust assumed for our model. In this study we were unable to constrain the dust grain properties in the system. One way to better constrain the opacity for the dust in the protoplanetary disks is with additional millimeter-wave observations of the system. Millimeter fluxes of dust roughly follow a power law, $F_\nu \propto \nu^{2+\beta}$, where β is related to the optical properties of the dust, with $\beta \sim 2$ corresponding to small grains and $\beta \sim 0$ relating to larger dust grains. Multiple millimeter wavelength observations can thus help to constrain the dust optical properties. There is some evidence that $\beta \approx 0$ in GV Tau N, if the 3.6cm emission seen by Reipurth et al. (2004) is from dust emission, so GV Tau N may be a particularly interesting candidate for this sort of study.

4.6   Conclusion

We have used detailed radiative transfer modeling to create synthetic model protostars to match to CARMA millimeter visibilities, HST near-infrared scattered light imaging, and broadband SEDs in order to constrain the masses of the disks around the protostars in the binary YSO system GV Tau. We find that the best fit model disks around GV Tau N and S each have gas+dust masses of 0.005 $M_\odot$ and disk radii < 30 AU, and that the age of the system is ~ 0.5 Myr. These estimates place both components near the lower end of the Minimum Mass Solar Nebula, meaning they may have just enough mass to form giant planets. We also find that both disks are gravitationally stable throughout, unless our millimeter-wave observations are missing the majority of the disk mass. Furthermore, we find that the disks of GV Tau N and S are inclined at 30° and 55° respectively, consistent with some previous studies of the system (Movsessian and Magakian, 1999; Beck et al., 2010), but inconsistent with a recent study by Roccatagliata et al. (2011). We have shown, however, that we can plausibly reproduce the 8-13 μm visibilities from Roccatagliata et al. (2011)

with our best fit model for GV Tau N and a modified version of our best fit model for GV Tau S which preserves the inclination of our best fit model.

When we include both protostars in the GV Tau system with the Class I protostars modeled by Eisner (2012) we find that the sample of 10 Class I protostars has a median disk mass of 0.008 - 0.01 $M_{\odot}$. All of the disks in our Class I sample are more massive than the median of the Class II sample of disks (of 0.001 $M_{\odot}$). These numbers suggest that, on average, the circumstellar disks of Class I protostars are more massive than those of the more evolved Class II protostars. This likely indicates that between the two stages some of the smaller dust grains in the disks have grown into larger bodies. For both samples, however, the median masses fall below the minimum mass solar nebula (Weidenschilling, 1977; Desch, 2007), and may not be able to reproduce the observed frequency of giant planets. It may be the case that significant dust grain processing has already occurred by the Class I stage, and it may be necessary to explore even younger disks to determine the initial mass budget for planet formation.

CHAPTER 5

WL 17: A Young Embedded Transition Disk[†]

We present the highest spatial resolution ALMA observations to date of the Class I protostar WL 17 in the ρ Ophiuchus L1688 molecular cloud complex, which show that it has a 12 AU hole in the center of its disk. We consider whether WL 17 is actually a Class II disk being extincted by foreground material, but find that such models do not provide a good fit to the broadband SED and also require such high extinction that it would presumably arise from dense material close to the source such as a remnant envelope. Self-consistent models of a disk embedded in a rotating collapsing envelope can nicely reproduce both the ALMA 3 mm observations and the broadband SED of WL 17. This suggests that WL 17 is a disk in the early stages of its formation, and yet even at this young age the inner disk has been depleted. Although there are multiple pathways for such a hole to be created in a disk, if this hole were produced by the formation of planets it could place constraints on the timescale for the growth of planetesimals in protoplanetary disks.

5.1 Introduction

Protoplanetary disks are the birthplaces of planets. Many protoplanetary disks have been found to have large central clearings. This was initially discovered by modeling disk SEDS (e.g. Strom et al., 1989; Espaillat et al., 2007), but more recently these holes have been directly imaged with millimeter interferometers (e.g. Isella et al., 2010; Andrews et al., 2011a). These "transition" disks have been hypothesized to be the result of planets carving holes in disks (e.g. Dodson-Robinson and Salyk, 2011), although other physical processes such as photoevaporation and dust grain

---

[†]This chapter has been published previously as Sheehan and Eisner 2017

growth can also explain these holes (e.g Dullemond and Dominik, 2005; Alexander et al., 2006). Recently planets have been found hiding in the cavities, giving credibility to the idea that the holes are carved by planets (e.g. Sallum et al., 2015). However, these transition disks have only been found in the older sample of Class II disks, which are thought to have ages greater than a million years (e.g. Andre and Montmerle, 1994a; Barsony, 1994).

WL 17 is a M3 protostar in the L1688 region of the ρ Ophiuchus molecular cloud (Doppmann et al., 2005), located a distance of 137 pc away (Ortiz-León et al., 2017). It has consistently been identified as a Class I protostar (van Kempen et al., 2009; Enoch et al., 2009), meaning it is younger than $\sim 5 \times 10^5$ years and still embedded in envelope material from the collapsing molecular cloud (e.g. Evans et al., 2009). The SED of WL 17 peaks in the mid-infrared, and shows a lack of optical emission that demonstrates that the source is highly extincted (Enoch et al., 2009). Low spatial resolution millimeter observations of WL 17 suggest the presence of large scale emission, likely from the remnants of a protostellar envelope (van Kempen et al., 2009). Moreover, these same observations detected HCO^+ $J = 4 - 3$ emission towards WL 17 that is too bright to be associated with a disk. In addition, a survey of outflows in the L1688 region of Ophiuchus found that there is a weak outflow associated with WL 17 (van der Marel et al., 2013). All of these signs point towards WL 17 being a young source that is still embedded in its natal envelope.

As such, it was observed as part of our ALMA survey of young embedded protostars in Ophiuchus (Sheehan & Eisner, in prep.). However, upon imaging WL 17 we were surprised to find that it has a large hole in its center, suggesting a transition disk. While the highly reddened SED peaking in the mid-infrared clearly shows that WL 17 is embedded, it is not unprecedented to find disks that are extincted by the large scale cloud (e.g. Boogert et al., 2002; Brown et al., 2012). Here we explore the nature of the medium extincting WL 17 to determine whether it is a young protostar still embedded in its natal envelope, which has cleared out a hole despite its young age, or whether it is an older, disk-only source that has been highly extincted by foreground dust.

Table 5.1.   Log of ALMA Observations

Observation Date (UT)	Baselines (m)	Total Integration Time (s)	Calibrators (Flux, Bandpass, Gain)
Oct. 31 2015	84 - 16,200	169	1517-2422, 1625-2527
Nov. 26 2015	68 - 14,300	169	1517-2422, 1625-2527
Apr. 17 2016	15 - 600	58	1733-1304, 1427-4206, 1625-2527

5.2   Observations & Data Reduction

5.2.1   ALMA

WL 17 was observed with ALMA in three tracks from 31 October 2015 to 17 April 2016, with baselines ranging from 14 m – 15.3 km. The observations were done with the Band 3 receivers, and the four basebands were tuned for continuum observations centered at 90.5, 92.5, 102.5, 104.5 GHz, each with 128 15.625 MHz channels for 2 GHz of continuum bandwidth per baseband. In all the observations had 8 GHz of total continuum bandwidth. We list details of the observations in Table 5.1.

We reduce the data in the standard way with the `CASA` software package and the calibrators listed in Table 5.1. After calibrating, we image the data by Fourier transforming the visibilities with the `CLEAN` routine. We use Briggs weighting with a robust parameter of 0.5, which provides a good balance between sensitivity and resolution, to weight the visibilities. The resulting image has a beam of size 0.06" by 0.05" with a P.A. of 81.9°. We show the resulting image in Figure 5.1, and the azimuthally averaged visibility amplitudes in Figure 5.2. The rms of the image is 36 μJy/beam. All analysis is done directly to the un-averaged two dimensional visibilities.
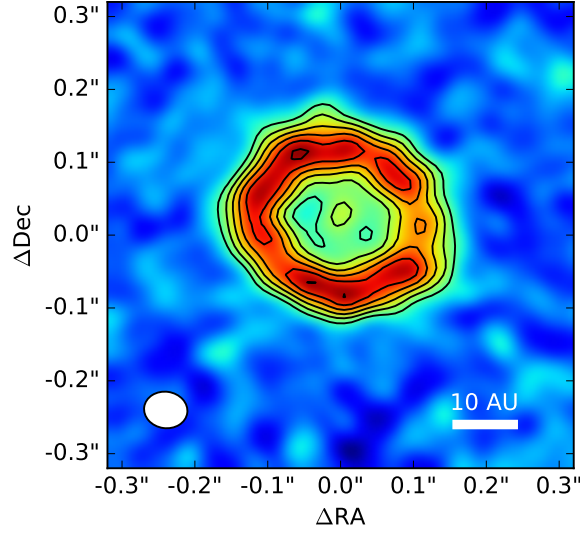
Figure 5.1: ALMA 3 mm map of WL 17 showing a clear ring-like structure. The synthesized beam size is 0.06" by 0.05" with a P.A. of 81.9°. Contours begin at 4σ and subsequent contours are every additional 2σ, with $1\sigma = 36$ μJy. The emission interior to the ring does not drop to zero, but rather falls to a 4σ level at the inner edge of the ring. At the center of the ring the emission rises to a 6σ level. This may indicate the presence of material remaining in the cleared out region.

5.2.2 SED from the Literature

We compile a broadband spectral energy distribution (SED) for WL 17 from a thorough literature search. We show the SED in Figure 5.2. The data includes *Spitzer* IRAC and MIPS photometry as well as fluxes from the literature at a range of wavelengths (Wilking and Lada, 1983; Lada and Wilking, 1984; Greene and Young, 1992; Andre and Montmerle, 1994a; Strom et al., 1995; Barsony et al., 1997; Johnstone et al., 2000; Allen et al., 2002; Natta et al., 2006; Stanke et al., 2006; Alves de Oliveira and Casali, 2008; Jørgensen et al., 2008; Padgett et al., 2008; Wilking et al., 2008; Evans et al., 2009; Gutermuth et al., 2009; Barsony et al., 2012). We exclude WISE photometry because the fluxes are inconsistent with the IRAC and MIPS fluxes. This is because the WISE beam is larger than the Spitzer beam, and may cause confusion with nearby sources. The IRAC and MIPS flux measurements were also independently reproduced by two different groups using separate datasets

(Evans et al., 2009; Gutermuth et al., 2009), so we believe these measurements to be reliable.

We also include the the SL, SH, and LH calibrated Spitzer IRS spectrum from the CASSIS database in our SED(Lebouteiller et al., 2011, 2015). We find that we need to scale the IRS spectrum by a factor of 3 to align it with the IRAC/MIPS photometry for the system. When scaled up the IRS spectrum also nicely matches ground-based 10 μm photometry of the silicate absorption feature. This factor may be needed due to issues in the flux calibration or the pointing towards the source.

For the purposes of assessing the quality of model fits to the SED we assume a 10% uncertainty on all flux measurements when computing χ^2. We also sample the IRS spectrum at 25 points evenly spaced across the spectrum to minimize the number of individual wavelengths at which radiative transfer flux calculations, which can be time intensive, must be done.

5.3   Results

Our 3 mm map of WL 17, shown in Figure 5.1, shows a well detected, compact source with a hole measuring $\sim 0.2''$ in diameter in the center. At the distance of Ophiuchus, which we assume to be 137 pc, the hole is 27 AU across ($\sim$13 AU in radius). Emission at the center of the hole peaks at $\sim$ 250 μJy, which suggests that there may still be material remaining inside the transition disk cavity. Alternatively this could be emission from magnetic activity at the surface of a young star.

Studies that have found holes in the centers of many other protoplanetary disks, dubbed "transition disks" (Espaillat et al., 2007; Isella et al., 2010; Muzerolle et al., 2010; Andrews et al., 2011a; Espaillat et al., 2014). Transition disks are typically found in the population of Class II protoplanetary disks, which represents older disks that are no longer embedded in envelopes. Unlike these previous detections, WL 17 has an SED (shown in Figure 5.2) that peaks at mid-infrared wavelengths and looks very much like a Class I source. WL 17 must be embedded in some obscuring material, but stars form in giant clouds of gas and dust, so it is reasonable

to think that WL 17 could be a Class II source made to look like a Class I by foreground extinction from this cloud. Transition disks have been previously found with significant amounts of extinction from foreground material (e.g. Boogert et al., 2002; Brown et al., 2012). It is also possible to mistake edge on Class II disks as Class I sources (e.g. Chiang and Goldreich, 1999).

As such, a disk model that includes foreground extinction is a good first guess for attempting to reproduce the combined ALMA 3 mm visibilities and broadband SED dataset. To do so we use detailed radiative transfer models, run using the Monte Carlo radiative transfer codes `RADMC-3D` and `Hyperion` (Robitaille, 2011; Dullemond, 2012), to produce synthetic visibilities and SEDs and attempt to match the data with the models. We give a brief description of the models here, but refer to Sheehan and Eisner (2014) for a more detailed account.

Our model assumes a central protostar with a M3 spectral type ($T = 3400K$; Doppmann et al., 2005), although we allow the luminosity of the protostar, L_*, to vary. We include a disk with a power law surface density,

$$\rho = \rho_0 \left(\frac{R}{R_0} \right)^{-\alpha} \exp \left(-\frac{1}{2} \left[\frac{z}{h(R)} \right]^2 \right) \tag{5.1}$$

where R and z are in cylindrical coordinates. $h(R)$ is the disk scale height at a given radius,

$$h(R) = h_0 \left(\frac{R}{1 \text{ AU}} \right)^{\beta}. \tag{5.2}$$

We truncate the disk at some outer radius, R_{disk}, and specify a gap radius, R_{gap}, inside of which the density is decreased by a multiplicative factor, δ. α, β, h_0, and the disk mass M_{disk} are also left as free parameters, as are the inclination and position angle of the system. We supply the model with dust opacities from Sheehan and Eisner (2014), but allow the maximum size of the dust grain size distribution, a_{max}, to vary. We extinct the synthetic SED by some number of K-band magnitudes, A_K, using the McClure (2009) extinction law. The model visibilities are unaffected by this extinction because extinction at millimeter wavelengths from foreground dust is negligible. Moreover, our millimeter observations resolve out large scale emission from the foreground cloud.
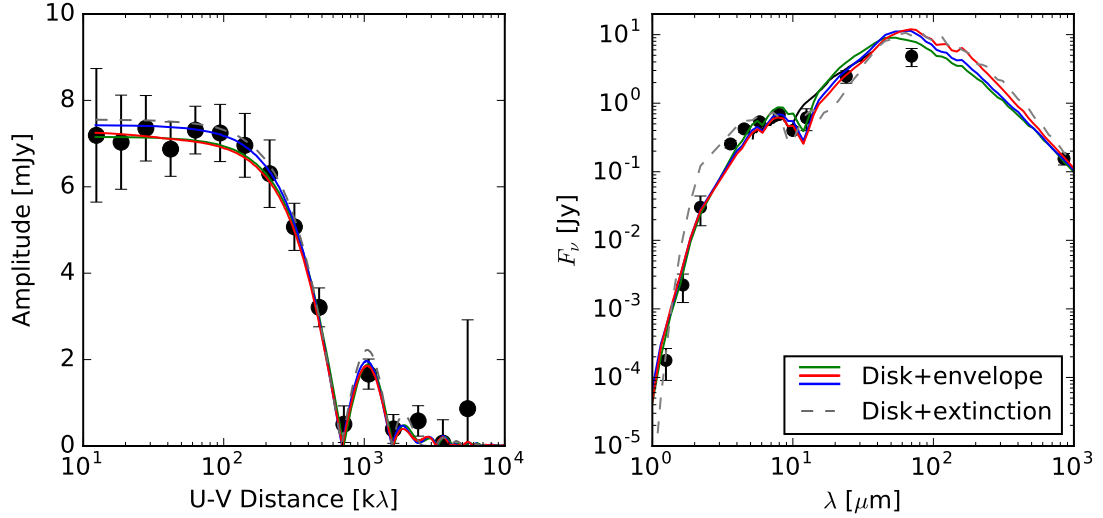
Figure 5.2: Examples of models that fit the combined WL 17 3 mm visibilities (*left*) + SED (*right*) dataset. We show our broadband SED and the 1D azimuthally averaged visibilities as black points, and the IRS spectrum is shown as a black line. In gray we show the disk+foreground extinction model that does not fit the data well. In red, green, and blue red and blue we show three possible disk+envelope models that can well fit the data with a range of values for the envelope mass and radius. Parameter values for these models, as well as metrics to assess the quality of the fits, are listed in Table 5.2.

We show the best fit disk+extinction model in Figure 5.2, and list the best fit parameter values in Table 5.2. Although the model well reproduces the 3 mm visibility profile, it cannot produce a good fit to the SED as it under-predicts the mid-infrared flux. This is because, with an inner radius of 12 AU, there is not enough hot material close to the star to overcome foreground extinction and produce the necessary mid-infrared flux. The model also slightly over-predicts the amount of near-infrared flux. Moreover, $A_K \sim 4$ ($A_V \sim 30$ for the McClure (2009) extinction law) is needed to properly extinct the near-infrared SED. Boogert et al. (2002) found two foreground clouds that contribute $A_V \sim 11$ in the region near WL 17, but this is not enough to explain the $A_V \sim 30$ needed to match the SED. Such high extinction seems unlikely to come from foreground extinction from nearby star forming regions.

A more natural explanation for the extinction towards WL 17 is that it is still a young disk embedded in its natal envelope. To test this hypothesis we consider

a disk+envelope density distribution model to see whether it can reproduce our dataset. We use the same prescription for the disk, but embed the disk in a rotating collapsing envelope (Ulrich, 1976). The density profile for the envelope is given by,

$$\rho = \frac{\dot{M}}{4\pi} \left(GM_*r^3\right)^{-\frac{1}{2}} \left(1 + \frac{\mu}{\mu_0}\right)^{-\frac{1}{2}} \left(\frac{\mu}{\mu_0} + 2\mu_0^2 \frac{R_c}{r}\right)^{-1}, \qquad (5.3)$$

where $\mu = \cos\theta$ and r and θ are in spherical coordinates. Here the mass and radius of the envelope (M_{env} and R_{env}) are left as free parameters and the envelope is truncated at an inner radius of 0.1 AU. The critical radius R_c represents the radius inside of which the density distribution flattens into a disk-like structure, with the majority of material being deposited at R_c. This makes the most sense physically if $R_c \sim R_{disk}$, so we provide this constraint to our modeling. We still allow for a small amount of extinction towards WL 17 in the disk+envelope model because of the known foreground clouds in the region.

Our disk+envelope model is able to produce good fits to the combined 3 mm visibilities and broadband SED dataset. We show a few examples of these fits in Figure 5.2. These models were found by taking the disk+extinction model disk parameters, adding an envelope, and adjusting the parameters by hand to find models that produce better χ^2 values. These models are not "best fits" because no optimization was done, but their χ^2 values (see Table 5.2) are clearly better than that of the disk+extinction model.

In Figure 5.3 we compare the 3 mm ALMA map with a representative image of the disk+envelope model, which we produced by sampling a synthetic 3 mm image from our radiative transfer model at the same spatial frequencies as the ALMA data before making the image. Unlike the disk+extinction model, which under-predicts the mid-infrared flux, the disk+envelope model is better able to fit the mid-infrared spectrum of WL 17. This is because the envelope allows for more hot material close in to the protostar, boosting the mid-infrared flux.

There is a significant degeneracy between envelope mass and radius in these models; both large, high mass and small compact envelopes can produce the extinction needed to match the SED. Our millimeter observations resolve out scales
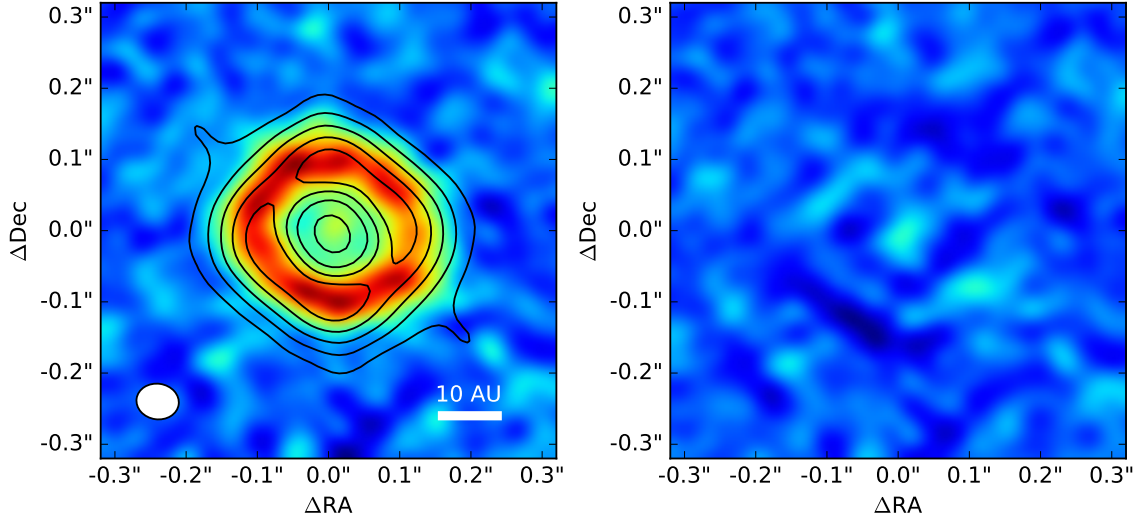
Figure 5.3: (*left*) ALMA 3 mm map of WL 17 with the best fit disk+envelope model as contours to demonstrate the good match of the model to the data in the image plane. (*right*) Residual map produced by subtracting our best fit model from the 3 mm map in the visibility plane and inverting to produce an image. The peak residual is at a 5σ level, but the rest are $< 3\sigma$. The large residual level comes from the somewhat clumpy structure seen in the image. We employ a fairly simple model that assumes the disk structure is smooth, so we cannot expect to fully reproduce this clumpy structure with our model.

larger than ~ 20", or radii larger than ~ 1300 AU, so our data is not sensitive to large scale envelope structure. Moreover, the visibilities lack the sensitivity at intermediate scales to detect faint emission from a more compact envelope. As such, our modeling cannot well distinguish between compact low mass envelopes and larger and more massive envelopes.

Table 5.2. Model Parameters

Model	L_* [$L_\odot$]	M_{disk} [$M_\odot$]	R_{in} [AU]	R_{disk} [AU]	$h_0{}^{\mathrm{a}}$ [AU]	γ^{b}	β^{c}	δ^{d}	M_{env} [$M_\odot$]	R_{env} [AU]	i [°]	$P.A.$ [°]	a_{max} [mm]	A_K [mag]	χ^2_{vis}	χ^2_{SED}
Disk+envelope (green)	0.5	0.05	11.6	22.7	0.15	0.0	0.75	0.011	3×10^{-5}	25	28	82.4	10	0.5	1067	112
Disk+envelope (blue)	0.5	0.04	11.6	22.7	0.15	0.0	0.75	0.011	3×10^{-4}	100	28	82.4	10	0.5	1070	145
Disk+envelope (red)	0.5	0.035	11.6	22.7	0.2	0.0	0.75	0.01	0.003	600	28	82.4	10	0.75	1071	172
Disk+extinction	6.2	0.06	11.6	22.7	0.11	-0.24	1.0	0.02	$\cdots$	$\cdots$	28	82.4	0.3	4.2	1078	325

[a] h_0 is the disk scale height at 1 AU.

[b] γ is the disk surface density power law exponent.

[c] β is the power law exponent which describes how the disk scale height varies with radius (see Equation 2).

[d] δ is the factor by which the disk density is reduced inside of the gap.

5.4   Discussion & Conclusion

In order to provide a quantitative assessment of the quality of fit of our models, we have computed the χ^2 value for each of the models listed in Table 5.2 for both the SED and the 3 mm visibilities. We find that for all four models, including both our disk+extinction and disk+envelope models, the quality of the fit to the 3 mm visibilities is indistinguishable; all models are able to reproduce the observed 3 mm visibilities of WL 17. The disk+extinction model, however, has a much worse χ^2 value for the SED than the disk+envelope models. Only the disk+envelope models can well reproduce both the visibilities and the broadband SED simultaneously. The disk+extinction model cannot simultaneously reproduce both datasets, and moreover the best fit disk+extinction model requires $A_V \sim 30$, which is quite high for foreground extinction.

The good fit of the disk+envelope models, as well as the high extinction required of the disk+extinction model, indicates that the extinction seen towards WL 17 is the result of it being embedded in an envelope of dusty material. This matches nicely with previous studies of the system, discussed above, that have hinted at its youth (van Kempen et al., 2009; van der Marel et al., 2013).

As such, we suggest that WL 17 is a young source still embedded in the remnants of its natal envelope. It may be, if the envelope remnants are low-mass, that the system is in the process of shedding the final layers of envelope and will soon be exposed as a more traditional transition disk system. However, the presence of even a low-mass remnant envelope indicates youth. Moreover, substantially more massive envelopes cannot be ruled out.

Regardless of the exact nature of the envelope, the discovery of a transition disk still embedded in its envelope raises interesting questions. There are a few explanations for such a hole, including photoevaporation of the inner disk by the central protostar, dust grain growth in the inner disk, and a dynamical clearing of the inner disk by large bodies (e.g Dullemond and Dominik, 2005; Alexander et al., 2006; Dodson-Robinson and Salyk, 2011). Embedded protoplanetary disks are thought

to be only a few hundred thousand years old (e.g. Andre and Montmerle, 1994a; Barsony, 1994), so any explanation of the presence of the hole must be compatible with a young age.

Photoevaporation tends to be ineffective early in the lifetimes of disks, when the accretion rate exceeds the photoevaporation rate; furthermore, once a gap is opened, the disk is dispersed quickly (e.g. Alexander et al., 2006). Photoevaporation models that include the influence of FUV and X-ray photons produce significantly higher photoevaporation rates, and could explain the presence of a large hole early in the lifetime of a disk (e.g. Gorti and Hollenbach, 2009a; Owen et al., 2010; Armitage, 2011). Still, these models require low accretion rates to be effective, and if this system is embedded in an envelope, the accretion rate is unlikely to be low.

Dust grain growth in the inner disk could be possible. Our millimeter observations show a dearth of millimeter sized bodies within the hole, but it is possible that this hole is indicating that even larger planetesimals have formed here. That said, dust grain growth may have challenges reproducing the sharp inner edge seen in Figure 5.1 (e.g. Birnstiel et al., 2012).

If the disk is dynamically cleared, it may be that WL 17 is a compact binary system. Radial velocity searches of the system have been done and no evidence of a companion has been found (Viana Almeida et al., 2012), although the limits are not strong. For a companion just inside the disk at 10 AU and a sensitivity to changes in radial velocity of $\sim 4 - 6$ km s^{-1}, we estimate an upper limit on the mass of a companion of $< 0.25 - 0.4$ M$_\odot$, although the true limit is likely worse given the sparse sampling of the data. Another, perhaps more exciting possibility, is that this hole may be cleared out by a planet or multiple planets.

It may seem surprising to find a young disk with a large hole as it may require the presence of planets at a very young age. Planets can, however, form quickly in massive disks (e.g. Pollack et al., 1996). Indeed, multiple gaps have been found in the disk of HL Tau, another young and possibly embedded protostar likely between the Class I and II stages (ALMA Partnership et al., 2015). The gaps in the HL Tau disk, however, can be produced by Saturn-mass objects (e.g. Dong et al., 2015)

whereas transition disk holes like the one seen in WL 17 may need planets of a Jupiter-mass or larger (e.g. Dodson-Robinson and Salyk, 2011). The existence of gaps and holes in young embedded disks seems to indicate that the processes that govern planet formation must happen quite quickly, as planets must grow to large enough masses to clear out holes in their disks in a short amount of time.

CHAPTER 6

Multiple Gaps in the Disk of the Class I Protostar GY 91[†]

We present the highest spatial resolution ALMA observations to date of the Class I protostar GY 91 in the ρ Ophiuchus L1688 molecular cloud complex. Our 870 μm and 3 mm dust continuum maps show that the GY 91 disk has a radius of $\sim$80 AU, and an inclination of $\sim$40°, but most interestingly that the disk has three dark lanes located at 10 AU, 40 AU, and 70 AU. We model these features assuming they are gaps in the disk surface density profile and find that their widths are 7 AU, 30 AU, and 10 AU. These gaps bear a striking resemblance to the gaps seen in the HL Tau disk, suggesting that there may be Saturn-mass planets hiding in the disk. To constrain the relative ages of GY 91 and HL Tau, we also model the disk and envelope of HL Tau; its higher disk/envelope mass ratio suggests it is somewhat older than GY 91. Although snow lines and magnetic dead zones can also produce dark lanes, if planets are indeed carving these gaps then Saturn-mass planets must form within the first $\sim$0.5 Myr of the lifetime of these protoplanetary disks.

6.1 Introduction

Planets form in protoplanetary disks. When observed at high resolution with ALMA, a number of these disks show interesting patterns in their millimeter emission profiles, in some cases including series of bright and dark rings (ALMA Partnership et al., 2015; Dong et al., 2015; Andrews et al., 2016; Isella et al., 2016; Loomis et al., 2017; Fedele et al., 2017). There are a number of explanations for such features, including chemical processes that alter dust opacities and sticking/fracturing processes near snow lines (e.g. Ros and Johansen, 2013; Zhang et al., 2015; Banzatti

---

[†]This chapter has been submitted for publication as Sheehan & Eisner 2017c.

et al., 2015) as well as vortices created at the edges of magnetic dead zones (e.g. Simon and Armitage, 2014; Flock et al., 2015), but the most exciting possibility is that these features are tracing gaps opened in disks by forming planets (e.g. Dong et al., 2015).

GY 91 is a M4 protostar (Doppmann et al., 2005) in the L1688 region of the ρ Ophiuchus molecular cloud, located at a distance of 137 pc (Ortiz-León et al., 2017). GY 91's broadband spectral energy distribution (SED) rises sharply in the infrared and appears to peak at far-infrared wavelengths, although it has not been detected between 35 μm and 870 μm. The infrared spectral index ($\alpha_{IR} = 0.45$) and bolometric temperature ($T_{bol} = 370$ K), as well as its association with a 1.1 mm core, classify GY 91 as a Class I protostar (e.g. Enoch et al., 2008; McClure et al., 2010; Dunham et al., 2015). This indicates that the protostar is surrounded by a protoplanetary disk still embedded in its natal envelope of collapsing cloud material, and is young ($\lesssim 0.5$ Myr; Evans et al., 2009). The Spitzer IRS spectrum of the source shows both silicate and ice absorption features, which are also commonly associated with embedded protostars (e.g. Watson et al., 2004).

A few studies that consider alternate classification schemes have suggested that GY 91 may not be embedded. McClure et al. (2010) find that the 5–12 μm spectral index is within the range found for disks with foreground extinction ($n_{5-12} = -0.25$). However, their measured value is also on the border between disks with foreground extinction and disks with envelopes (of $n_{5-12} = -0.2$), and the extinction corrected spectral index ($\alpha'_{IR} = 0.31$) and bolometric temperature ($T'_{bol} = 470$ K) still qualify the source as a Class I protostar (Dunham et al., 2015). van Kempen et al. (2009) also found HCO$^+$ emission towards GY 91 that was bright enough to be above the cutoff for an embedded source, but that emission seems to be associated with a patch of cloud that peaks 30" away from the source.

Here we present new ALMA data, which when combined with the observed SED, show that GY 91 is indeed a Class I protostar with a circumstellar disk embedded in an envelope. Our 3 mm and 870 μm images also reveal the presence of three narrow dark rings in its disk that resemble those seen in HL Tau and a handful

Table 6.1.   Log of ALMA Observations

Observation Date (UT)	ALMA Band	Baselines (m)	Total Integration Time (s)	Calibrators (Flux, Bandpass, Gain)
Oct. 31 2015	3	84 - 16,200	169	1517-2422, 1625-2527
Nov. 26 2015	3	68 - 14,300	169	1517-2422, 1625-2527
Apr. 17 2016	3	15 - 600	58	1733-1304, 1427-4206, 1625-2527
May 19 2016	7	15 - 640	30	J1517-2422, J1625-2527
Sep. 11, 2016	7	15 - 3140	60	J1517-2422, J1625-2527

of other disks (ALMA Partnership et al., 2015; Dong et al., 2015; Andrews et al., 2016; Isella et al., 2016; Loomis et al., 2017; Fedele et al., 2017). We compare the circumstellar structure of GY 91 to HL Tau, and argue that GY 91 is the youngest source in which disk gaps have been detected. If caused by planets, these features provide evidence for giant planet formation within 0.5 Myr.

6.2 Observations & Data Reduction

6.2.1 ALMA

GY 91 was observed with ALMA Band 3 (100 GHz/3 mm) in three tracks from 31 October 2015 to 17 April 2016, with baselines ranging from 14 m – 15.3 km. All four basebands were tuned for continuum observations centered at 90.5, 92.5, 102.5, 104.5 GHz, each with 128 15.625 MHz channels for 2 GHz of continuum bandwidth per baseband. In all the observations had 8 GHz of total continuum bandwidth. We also observed GY 91 with ALMA Band 7 (345 GHz/870 μm) on 19 May 2016 and 11 September 2016, with baselines ranging from 15 – 3140 m. Two of four basebands were configured for continuum observations centered at 343 GHz and 356.25 GHz, with a total of 4 GHz of continuum bandwidth. The remaining basebands were devoted to spectral line observations, although nothing was detected. We list details of the observations in Table 6.1.

The data were reduced in the standard way with the `CASA` pipeline and the

calibrators listed in Table 6.1. After calibrating, we imaged the data by Fourier transforming the visibilities with the `CLEAN` routine. After our initial imaging, we found that we could improve the sensitivity of the 345 GHz image by self-calibrating. We ran four iterations of phase-only self-calibration on the compact configuration track and a single iteration of phase-only self-calibration on the extended configuration track. This improved the rms in an image produced with natural weighting (i.e. a robust parameter of 2) from 0.36 mJy /beam to 0.27 mJy/beam. We were unable to improve the 100 GHz image by self-calibration.

Our final images were produced using Briggs weighting with a robust parameter of 0.5, which provides a good balance between sensitivity and resolution, to weight the visibilities for both datasets. The 3 mm image has a beam of size 0.06" by 0.05" with a P.A. of 81.9° and an rms of 36 μJy/beam. The 870 μm image nas a beam size of 0.134" by 0.129" with a P.A. of -9.4° and an rms of 0.31 mJy/beam. We show the images in Figure 6.1.

6.2.2 SED from the Literature

We compile a broadband spectral energy distribution (SED) for GY 91 from a thorough literature search. The data includes *Spitzer* IRAC and MIPS photometry as well as fluxes from the literature at a range of wavelengths (Wilking and Lada, 1983; Lada and Wilking, 1984; Greene and Young, 1992; Andre and Montmerle, 1994a; Strom et al., 1995; Barsony et al., 1997; Johnstone et al., 2000; Allen et al., 2002; Natta et al., 2006; Stanke et al., 2006; Alves de Oliveira and Casali, 2008; Jørgensen et al., 2008; Padgett et al., 2008; Wilking et al., 2008; Evans et al., 2009; Gutermuth et al., 2009; Barsony et al., 2012). When modeling the SED, as we discuss below, we assume a constant 10% uncertainty on any photometry from the literature to account for any flux calibration uncertainties between the measurements.

In addition to the broadband photometry, we also download the Spitzer IRS spectrum of GY 91 from the CASSIS database (Lebouteiller et al., 2011, 2015). Rather than consider the entire SED, which can be computationally prohibitive for the radiative transfer calculations described below, we sample the IRS spectrum at

25 points ranging from 5 to 35 μm. We also assume a 10% uncertainty on these fluxes, like we do for the broadband photometry.

6.3   Results

We show our 3mm and 870 μm images of GY 91 in Figure 6.1. The 870 μm image has a much higher signal-to-noise ratio, and it is fairly easy to identify, by-eye, two concentric dark lanes that appear in the disk. The 3 mm image, which has a factor of two better spatial resolution, also reveals a third dark lane in the inner regions of the disk. To better illustrate the presence of these features, in Figure 6.2 we show a one dimensional brightness profile for both the 870 μm and 3 mm images, averaged in ellipses defined by the position angle and inclination of the disk to be constant radius bins. The outer two dark lanes show up clearly in the 870 μm radial profile, while the inner lane shows up clearly in the 3 mm profile. Moreover, there appears to be a break in the 870 μm profile at the location of the inner dark lane, and there appears to be a dip in the 3 mm brightness profile that is consistent with
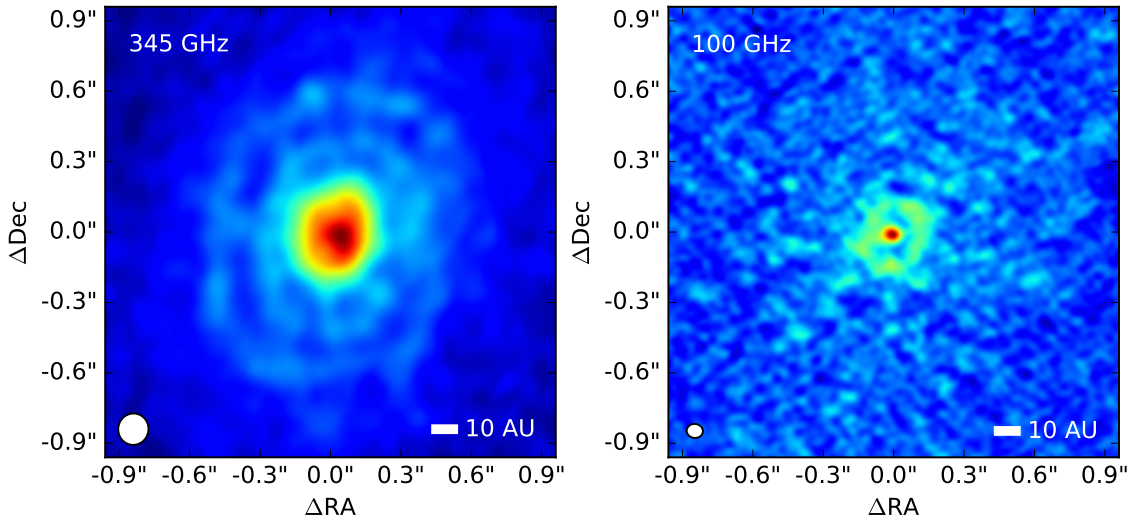
Figure 6.1: Our ALMA 345 GHz (*left*) and 100 GHz (*right*) maps of the GY 91 protoplanetary disk. Two dark lanes are readily apparent in the 345 GHz map, while a third dark lane is also apparent in inner regions of the disk at 100 GHz because of the higher resolution of our 100 GHz maps.
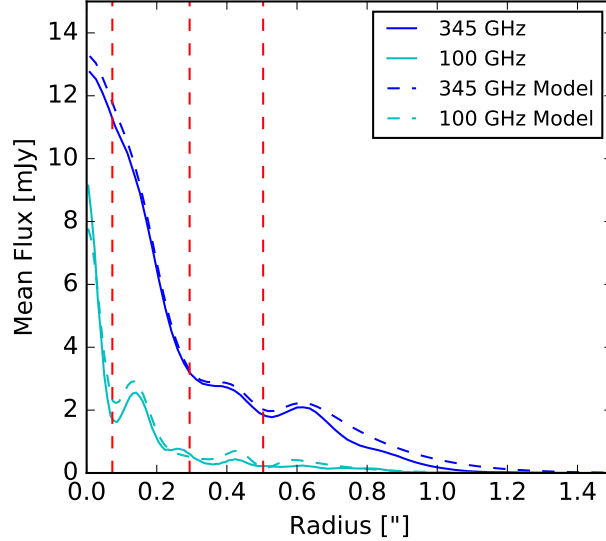
Figure 6.2: The one dimensional, azimuthally averaged, de-projected radial brightness profile of the GY 91 disk at 345 GHz and 100 GHz, with the locations of the dark lanes marked by vertical dashed lines. These gaps are readily seen in the brightness profile. We also show the azimuthally averaged brightness profile of our gapped disk+envelope model (see Figure 6.4, Table 2) at each wavelength.

the location of the middle dark lane, despite the noisiness of the 3 mm image that prevents it from being detected by eye.

In order to study these features in greater detail, we fit a model to the data to determine disk properties such as radius, position angle, and inclination, as well as the locations, widths, and depths of the gaps. We use Monte Carlo radiative transfer codes to produce synthetic observations of model protostars that can be fit to our combined millimeter visibility and broadband SED dataset of GY 91. This modeling procedure is described in further detail in Sheehan and Eisner (2014) and Sheehan & Eisner (submitted), but we give a brief overview here.

Our model includes a flared protoplanetary disk with a physically motivated surface density profile (e.g. Lynden-Bell and Pringle, 1974) surrounded by a rotating collapsing envelope (e.g. Ulrich, 1976),

$$\Sigma = \Sigma_0 \left(\frac{R}{r_c} \right)^{-\gamma} \exp\left[-\left(\frac{R}{r_c} \right)^{2-\gamma} \right], \tag{6.1}$$

$$\rho_{disk} = \frac{\Sigma}{\sqrt{2\pi}\,h} \, \exp\left(-\frac{1}{2}\left[\frac{z}{h}\right]^2\right), \tag{6.2}$$

$$h = h_0 \left(\frac{R}{1\ \text{AU}}\right)^{\beta}, \tag{6.3}$$

$$\rho_{env} = \frac{\dot{M}}{4\pi} \left(GM_* r^3\right)^{-\frac{1}{2}} \left(1 + \frac{\mu}{\mu_0}\right)^{-\frac{1}{2}} \left(\frac{\mu}{\mu_0} + 2\mu_0^2 \frac{R_c}{r}\right)^{-1}. \tag{6.4}$$

In Equations 1, 2 & 3, R and z are in cylindrical coordinates, while in Equation 4, $\mu = \cos\theta$ and r and θ are in spherical coordinates.

In this model the disk mass, M_{disk}, inner and outer radii, R_{in} & R_{disk}, surface density power-law exponent, γ, scale height power-law exponent, β, and scale height at 1 AU, h_0, are left as free parameters. We also leave the envelope mass, M_{env}, and radius, R_{env}, as free parameters, and give the envelope an outflow cavity described by f_{cav}, the fraction by which the density is reduced in the cavity, and ξ, which relates to the cavity opening angle. We supply the density structure with opacities described in Sheehan and Eisner (2014), leaving the maximum dust grain size, a_{max}, and grain size distribution power-law exponent, p, as free parameters.

We model the dark lanes as gaps in the surface density profile, which are described by their radius ($R_{gap,i}$), width ($w_{gap,i}$), and depth ($\delta_{gap,i}$). The depth of the gap is a multiplicative factor that represents the amount by which the surface density is reduced in the gap. $\delta = 0$ corresponds to a complete absence of material in the gap. Because of the computational intensity of this modeling, we make initial estimates of disk properties and the gap widths and depths by fitting a simple geometric model to the 870 μm and 3 mm visibilities (see Figure 6.3). The parameters found from this simple geometrical fit are then used as initial guesses for the radiative transfer modeling fit.

We use the Monte Carlo radiative transfer codes RADMC-3D (Dullemond, 2012) and Hyperion (Robitaille, 2011) to calculate the temperature throughout the density structure, and then produce synthetic millimeter visibilities and broadband SEDs. We fit these synthetic observations simultaneously to all three (870 μm visibilities, 3 mm visibilities, and broadband SED) of our datasets. We compare the gapped disk+envelope model to the observed visibilities and SED in Figure 6.4 and list the
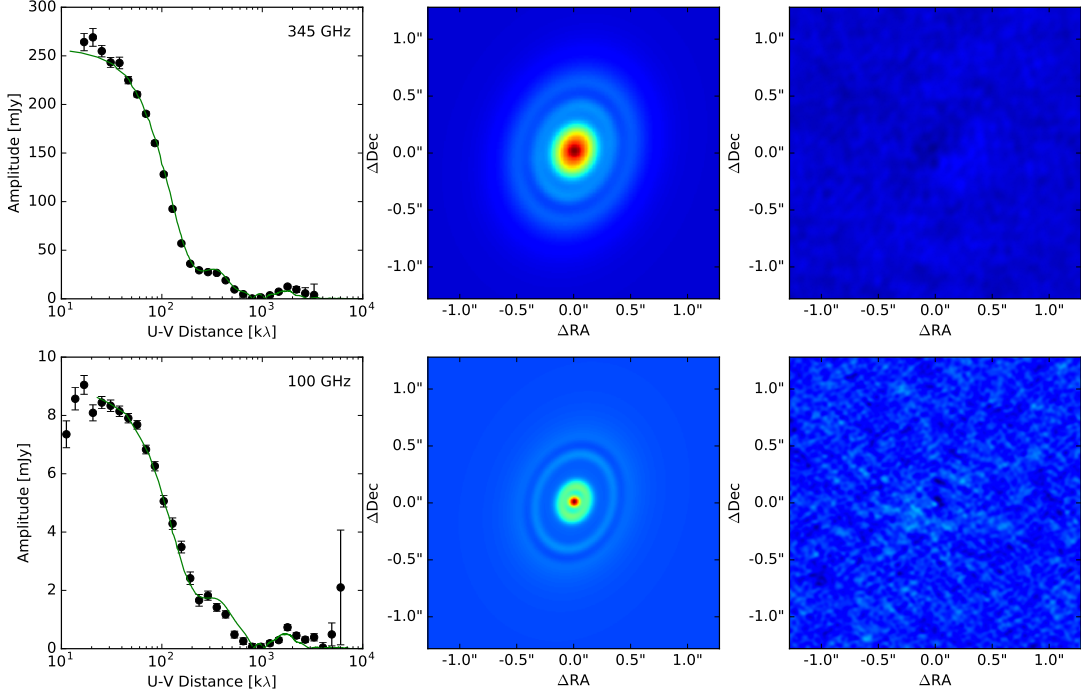
Figure 6.3: The best fit simple geometrical model for GY 91 compared with the data. The model assumes the disk is flat, with a surface density described by Equation 1 and $M_{disk} = 0.36$ M$_\odot$, $r_c = 71$ AU, $\gamma = 0.3$, $i = 39°$, and $p.a. = -19°$. The model uses a power-law temperature distribution with $T = 46(R/1\,\text{AU})^{-0.4}$. We use the power-law millimeter opacity function described in Beckwith et al. (1990), $\kappa(\nu) = 0.1\,(\nu/1000\,\text{GHz})^\beta$ cm^2 g^{-1} with $\beta = 1.8$. Our model includes three gaps with the following parameters: $R_{gap,1} = 10.4$ AU, $w_{gap,1} = 5.9$ AU, $\delta_{gap,1} \approx 0$, $R_{gap,2} = 40.3$ AU, $w_{gap,2} = 27.5$ AU, $\delta_{gap,2} = 0.15$, $R_{gap,3} = 68.9$ AU, $w_{gap,3} = 10.7$ AU, and $\delta_{gap,3} \approx 0$. Our modeling indicates that the first and third gaps are deep, however as the data is noisy and not high enough resolution to well resolve the gaps, the actual depths are quite uncertain. We show the one dimensional, azimuthally averaged, visibility amplitudes on the left, model images in the center column, and the residuals on the right. The peak residuals are 1.7σ at 345 GHz and 3.5σ at 100 GHz.

model parameters in Table 6.2. The images for our gapped disk+envelope model look almost identical to those shown in Figure 6.3, although the residuals between data and model are higher, not surprising since we are fitting the visibilities and SED simultaneously here.

This model can simultaneously reproduce the 870 μm visibilities, 3 mm visibili-
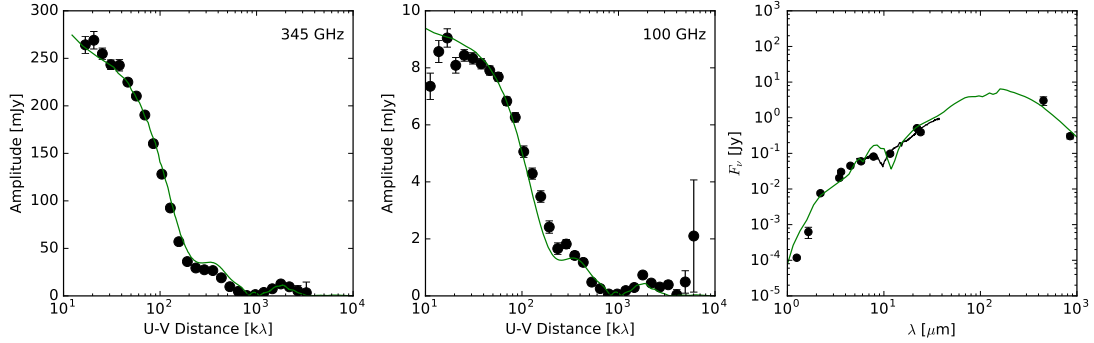
Figure 6.4: The gapped disk+envelope model for GY 91 compared with the data. We show the one dimensional, azimuthally averaged, 870 μm visibility amplitudes on the left, the 3 mm visibilities in the center, and the SED on the right.

ties, and broadband SED for GY 91. The GY 91 disk appears to be embedded in an envelope with $M_{env} = 1.35\, M_{disk}$. Gaps are found at radii of $\sim$7 AU, $\sim$40 AU, and $\sim$69 AU, with widths of $\sim$7 AU, $\sim$30 AU, and $\sim$10 AU. The gap depths for the inner and outer gaps are not well constrained because they are not resolved well by our observations. The middle gap appears to be wide and somewhat shallow, although with higher resolution it is possible that it will break up into multiple gaps.

6.4 Discussion & Conclusion

GY 91 appears to be part of a growing population of protoplanetary disks that have ring-like features in their millimeter emission profiles. The 870 μm image resembles the disks of HL Tau, AA Tau, TW Hya, HD 162953, and HD 169142, all of which have several gaps visible in their millimeter emission profiles (ALMA Partnership et al., 2015; Andrews et al., 2016; Isella et al., 2016; Loomis et al., 2017; Fedele et al., 2017). Closer inspection of these systems, however, reveals differences in the appearance of the features in each disk. The bright and dark rings seen in TW Hya are narrow (sizes < 2 AU) and shallow (Andrews et al., 2016). Only the innermost gap, at 2 AU, has a significant depth. The gaps found in AA Tau, HD 162953, and HD 169142, on the other hand, are all very wide and deep, with widths of 22 – 55 AU (Isella et al., 2016; Loomis et al., 2017; Fedele et al., 2017). The gaps found

Table 6.2.   Gapped Disk+Envelope Model Parameters

Parameters	Values
L_{star} [$L_\odot$]	0.16
M_{disk} [$M_\odot$]	0.12
R_{in} [AU]	0.3
R_{disk} [AU]	81
h_0 [AU]	0.18
γ	0.10
β	0.60
M_{env} [$M_\odot$]	0.158
R_{env} [AU]	3483
f_{cav}	1.00
ξ	0.96
i [°]	40
p.a. [°]	110
a_{max} [μm]	70481
$R_{gap,1}$ [AU]	10.0
$w_{gap,1}$ [AU]	7.0
$\delta_{gap,1}$	0.01
$R_{gap,2}$ [AU]	40.5
$w_{gap,2}$ [AU]	30.0
$\delta_{gap,2}$	0.22
$R_{gap,3}$ [AU]	69.1
$w_{gap,3}$ [AU]	10.0
$\delta_{gap,3}$	0.01
p	3.40

in HL Tau appear to be deep, with moderate widths of $\sim 5 - 20$ AU (e.g. ALMA Partnership et al., 2015; Zhang et al., 2015).

The innermost and outermost gaps we find in GY 91's disk appear to be quantitatively the most similar to the HL Tau gaps as they are somewhat narrow, with widths of $\sim$7 AU and $\sim$10 AU, while the middle gap appears to be large like the gaps found in AA Tau, HD 162953, and HD 169142.

6.4.1   Planets Carving Gaps?

Although there are a number of potential origins of these features, the most exciting possibility is, perhaps, that these gaps are carved by proto-planets embedded in the disk. Dong et al. (2015) found that the gaps in the HL Tau disk could be sculpted by planets with masses as small as a Saturn-mass. Isella et al. (2016) found similar results for HD 162953, although the gaps are much larger in that disk.

We can estimate the masses of planets that are needed to produce the gaps we see in GY 91's disk. Simulations suggest that planets should open gaps whose widths are a few times larger than the Hill radius of the planet,

$$W \approx 8 \times R_p \left(\frac{M_p}{M_*} \right)^{1/3} \tag{6.5}$$

(Rosotti et al., 2016). Although the protostellar mass of GY 91 is not constrained well, it is thought to be a M4 protostar with a temperature of 3300 K (Doppmann et al., 2005), which evolutionary models predict should have a mass of ~ 0.25 M$_\odot$ at ~ 0.5 Myr (Baraffe et al., 2015). Using these assumptions, we estimate that planets of masses ~ 0.2 M$_J$, $\sim$0.2 M$_J$, and $\sim$0.002 M$_J$ are needed to produce the observed gaps.

The mass estimated for the outermost planet highlights the limitations of these simple estimates, as it seems unlikely that an Earth-mass planet is opening such a gap. Recent studies have suggested that for low-mass planets, the gap width may be a constant multiple of the scale height and therefore independent of planet mass (e.g. Duffell and MacFadyen, 2013; Dong and Fung, 2017). Further studies suggest that the mass of a gap-opening planet is best constrained by measurements of the

gap width and depth in the gas distribution, combined with a measurement of disk viscosity (Fung et al., 2014; Kanagawa et al., 2015; Dong and Fung, 2017). Without knowledge of the gas distribution, however, we cannot place stronger constraints on the potential planet masses. It also should be noted that a single planet can open multiple gaps in a disk (Bae et al., 2017).

6.4.2 Other Causes of Dark Lanes

Planets aren't the only possible cause of these features. One alternative that should be common in protoplanetary disk is the variation in dust opacities and collisional fragmentation/coagulation properties that is expected to occur at snow lines. As dust grains radially drift inwards due to the loss of angular momentum from a headwind of sub-Keplerian gas (Weidenschilling, 1977), they will cross a series of snow lines for various volatiles. When they cross a snow line, that volatile sublimates back into the gas phase. As the sublimated gas radially diffuses, it can re-condense onto particles outside of the snow line. The icy particles outside of the snow line can efficiently grow to decimeter or larger sizes, while solids inside the snow line tend to fragment (Cuzzi and Zahnle, 2004; Ros and Johansen, 2013; Banzatti et al., 2015). The change in the optical properties of dust grains across the snow line could cause features like those seen in HL Tau or GY 91 (e.g. Zhang et al., 2015).

We compare the midplane disk temperature inferred from our model of GY 91 with the temperatures of snow lines of common volatiles as calculated by Zhang et al. (2015). The outermost gap does roughly match the freeze out region of N_2, and the middle gap may have some overlap with the snow lines of CO and CH_4. No obvious counterparts are seen for the innermost gap, although it does fall near the snow line for H_2S. These estimates are, however very sensitive to chemical models and the disk temperature profile. Without direct observations of snow lines in the disk, we cannot rule out snow lines as the drivers of these features, and even direct observations require complicated chemical models to interpret (e.g. van't Hoff et al., 2017).

Alternatively, the "sintering" of dust grains, **in which volatiles sublimate**

and re-condense to form thick necks between fused particles just below the sublimation temperature, produces brittle grains that fragment more readily and therefore grow to smaller sizes just outside the snow line. Because the sintered grains have smaller sizes, they undergo slower radial drift, causing pile ups near snow lines. This process could also produce features similar to those seen in HL Tau or GY 91 (Okuzumi et al., 2016).

Zonal flows produced by magneto-rotational instability driven turbulence (Johansen et al., 2009) have also been shown to produce axisymmetric pressure bumps that can trap large dust grains and may produce gap-like features in millimeter images (Pinilla et al., 2012; Dittrich et al., 2013; Simon and Armitage, 2014). In this case, the pressure bumps are created by large scale variations in the magnetically driven turbulence that produce variations in the mass accretion rate that in turn causes material to pile up. This effect can also be seen at the outer edge of magnetic dead zones, where there is strong radial variation in the mass accretion rate. These flows can produce gap-like features in disks (Pinilla et al., 2012; Flock et al., 2015).

6.4.3 Comparison with HL Tau

If planets are indeed carving gaps in GY 91's disk, the masses of those planets would place strong constraints on the timescales for planet formation in disks. As a Class I protostar, GY 91 likely has an age of ~ 0.5 Myr (Evans et al., 2009), so planets must grow to masses of ~ 0.2 M$_J$ on these short timescales. Similar constraints have been placed on the timescale for planet formation by the gaps in HL Tau's disk, as it is also thought to be young and possibly still embedded (e.g. Robitaille et al., 2007). To the best of our knowledge, however, a detailed radiative transfer modeling fit to the combined HL Tau millimeter visibilities and SED has not been done since the ALMA Science Verification data was acquired. We use the disk+envelope modeling procedure described above to fit a disk+envelope model to the HL Tau ALMA millimeter visibilities and SED. For simplicity, though, we ignore the gaps and consider only a smooth density distribution. The best fit model is shown in Figure 6.5.
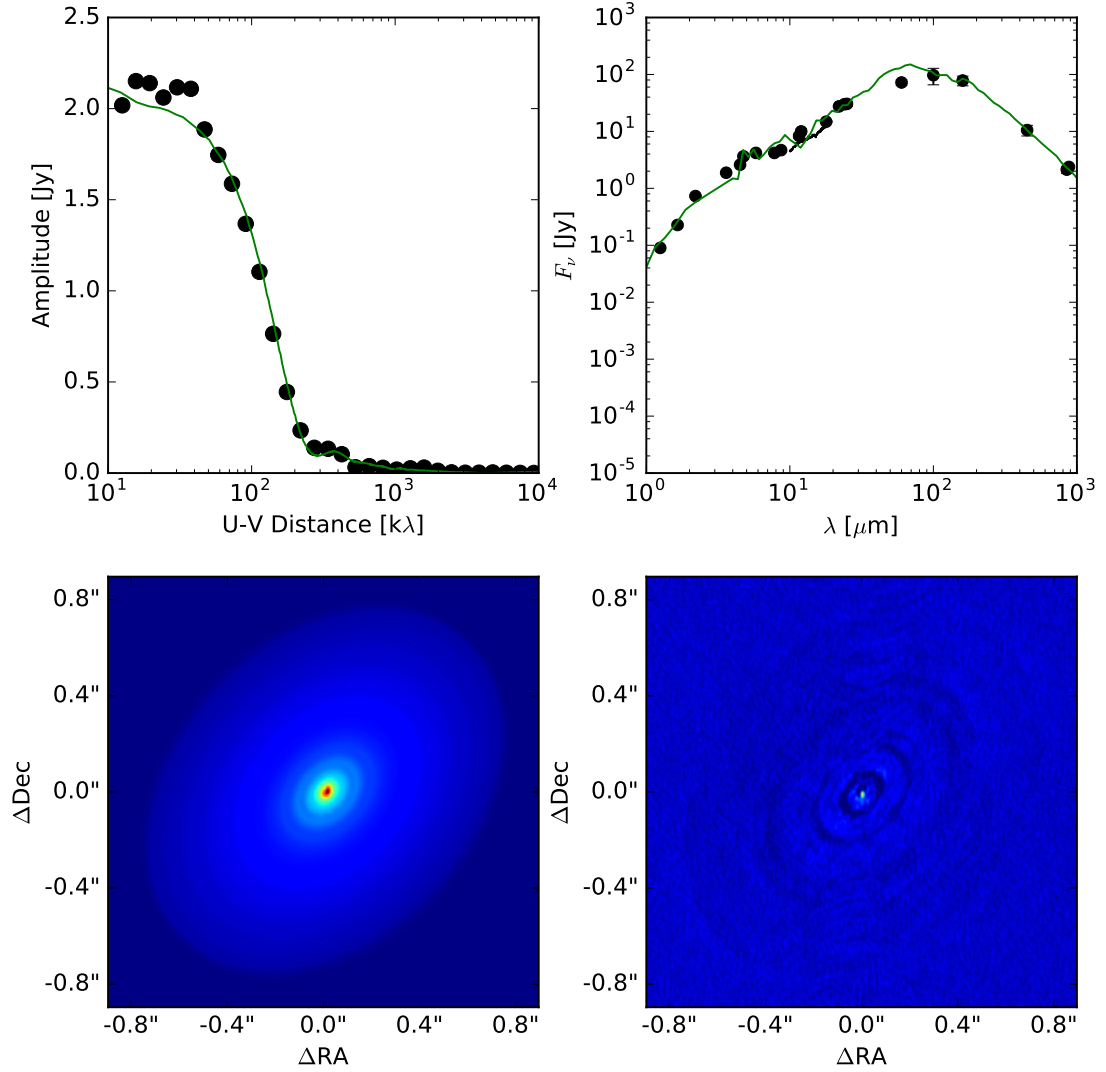
Figure 6.5: The disk+envelope model for HL Tau compared with the data. In the first row we show the one dimensional, azimuthally averaged, 870 μm visibility amplitudes on the left and the SED on the right, with the model as a green curve in both. The second row shows the 345 GHz model and residual images. We did not include gaps in this model, which is why they can be seen in the residual map. The model has a disk with a mass of 0.2 $M_\odot$ a radius of 120 AU, a surface density power law exponent of $\gamma = 1.7$, and an inclination of 44°. The envelope has a mass of 0.04 $M_\odot$ and a radius of 1800 AU.

Our model for HL Tau has $M_{env} = 0.2\,M_{disk}$, smaller than what we find for GY 91 ($M_{env} = 1.35\,M_{disk}$). This may indicate that a larger fraction of the HL Tau envelope has been depleted onto the disk or central protostar. This is in agreement with the classification of HL Tau as a "flat spectrum" object, indicating it is likely in transition from the Class I to Class II stage. In contrast, GY 91 has a more substantial envelope remaining relative to its disk mass. If we assume that M_{env}/M_{disk} is an evolutionary indicator (e.g. Crapsi et al., 2008), this suggests that GY 91 is younger than HL Tau. If planets are indeed carving the holes in GY 91's disk, measurements of their masses could place stronger constraints on the timescales of planet formation than planets in the HL Tau disk.

Regardless of whether these dark lanes are formed by planets, zonal flows, or chemical variations produced by radial drift, the presence of these features is likely an indication that planet formation is well underway at early times. Both zonal flows and chemical effects have been suggested to enhance the growth of particles in disks (e.g. Simon and Armitage, 2014; Ros and Johansen, 2013), and may be key elements in how planets are formed. Further high resolution studies of these young disks are crucial for understanding the early stages of planet formation.

CHAPTER 7

A VLA Survey For Faint Compact Radio Sources in the Orion Nebula Cluster[†]

We present Karl G. Janksy Very Large Array (VLA) 1.3 cm, 3.6 cm, and 6 cm continuum maps of compact radio sources in the Orion Nebular Cluster. We mosaicked 34 square arcminutes at 1.3 cm, 70 square arcminutes at 3.6 cm and 109 square arcminutes at 6 cm, containing 778 near-infrared detected YSOs and 190 *HST*-identified proplyds (with significant overlap between those characterizations). We detected radio emission from 175 compact radio sources in the ONC, including 26 sources that were detected for the first time at these wavelengths. For each detected source we fit a simple free-free and dust emission model to characterize the radio emission. We extrapolate the free-free emission spectrum model for each source to ALMA bands to illustrate how these measurements could be used to correctly measure protoplanetary disk dust masses from sub-millimeter flux measurements. Finally, we compare the fluxes measured in this survey with previously measured fluxes for our targets, as well as four separate epochs of 1.3 cm data, to search for and quantify variability of our sources.

7.1   Introduction

The Orion Nebular Cluster (ONC) presents an excellent example of star formation in a richly clustered environment, typical of star formation in our galaxy. Near-infrared surveys of the ONC find >700 YSOs, most of which are likely to harbor protoplanetary disks (Hillenbrand and Carpenter, 2000). *Hubble Space Telescope* (*HST*) images of the ONC also reveal ionized disks and dusty disks sillhoutetted

---

[†]This chapter has been published previously as Sheehan et al. 2016

against the backdrop of nebular emission (e.g., O'Dell and Wen, 1994; Bally et al., 1998a; Smith et al., 2005; Ricci et al., 2008).

The O6 star θ^1 Ori C, located in the central Trapezium Cluster, produces intense UV radiation that photoevaporates many of the nearby protoplanetary disks. The hot gas ionized by this intense radiation expands freely and flows away at the local sound speed into lower pressure regions (e.g., Henney and Arthur, 1998). The ionized winds from the protoplanetary disks emit strong free-free emission at radio wavelengths (e.g., Garay et al., 1987; Churchwell et al., 1987).

Compact radio sources have long been known in the ONC (e.g., Moran et al., 1982; Garay et al., 1987; Churchwell et al., 1987; Felli et al., 1993a; Zapata et al., 2004a,b). They were first identified as free-free emission by Garay et al. (1987), and suggested to be the ionized material evaporated from protostellar disks by Churchwell et al. (1987). Observations of the ONC with the *Hubble Space Telescope* firmly established these compact structures as externally ionized protoplanetary disks (e.g., O'Dell et al., 1993).

Measurements of the masses of protoplanetary disks are crucial for understanding evolution, as well as potential for planet formation. Disk mass measurements are typically made by observing dust continuum emission at long wavelengths, where the emission is optically thin and probes the entirety of the disk (e.g., Beckwith et al., 1990). Towards this end, a host of millimeter interferometric surveys of the ONC have previously been carried out (e.g Mundy et al., 1995; Bally et al., 1998b; Williams et al., 2005; Eisner and Carpenter, 2006; Eisner et al., 2008; Mann and Williams, 2009, 2010; Mann et al., 2014).

These surveys are complicated by potential contamination of the millimeter dust continuum emission by free-free emission from ionized disk winds. Disk mass measurements are facilitated at shorter wavelengths, of 1.3 mm or 870 μm, where the ratio of dust emission to free-free emission is expected to be more favorable. Even here, however, free-free emission can contribute significantly to the observed brightnesses of the sources (e.g., Eisner et al., 2008; Mann and Williams, 2009, 2010; Mann et al., 2014).

Observations at longer radio wavelengths can help to constrain the free-free contribution at shorter wavelengths. Free-free emission has a flat spectrum ($F_\nu \propto \nu^{-0.1}$) when optically thin, as is expected to be true at millimeter and centimeter wavelengths (e.g. Eisner et al., 2008; Mann and Williams, 2009, 2010; Mann et al., 2014). Optically thick free-free emission can span a range of spectral indices, but the emission usually only becomes optically thick at wavelengths longer than ~ 10 cm (e.g. Eisner et al., 2008). Dust emission, however, has a steep spectral index ($F_\nu \propto \nu^{2+\beta}$, $\beta = 0 - 2$) which falls off rapidly at longer wavelengths. Free-free emission can therefore be constrained at longer radio wavelengths where the contribution from dust emission to the flux is small. Radio fluxes may also in some cases be affected by magnetospheric flaring from young stars, exhibiting gyrosynchrotron emission with a steep negative spectral index when optically thin ($F_\nu \propto \nu^{-0.7}$; e.g. Feigelson and Montmerle, 1999; Rivilla et al., 2015), or a steep positive spectral index when optically thick at lower frequencies ($F_\nu \propto \nu^{2.5}$).

Previous studies have used the VLA to search for compact radio sources in the ONC (e.g., Felli et al., 1993a; Zapata et al., 2004a), and fluxes produced by those studies have been used to correct for free-free contamination in disk mass studies (e.g., Eisner et al., 2008; Mann and Williams, 2010; Mann et al., 2014). The expanded capabilities of the VLA correlator (Perley et al., 2009), now enable surveys of much higher sensitivity than were previously possible. More recent surveys have taken advantage of this increase in sensitivity to map star forming regions, including the ONC at 4.5 GHz and 7.5 GHz (Dzib et al., 2013; Kounkel et al., 2014; Forbrich et al., 2016). This enhanced sensitivity is well-matched to the deeper observations now enabled with ALMA.

Here we present new high resolution Karl G. Jansky Very Large Array (henceforth JVLA to avoid confusion with previous surveys using the original VLA) maps of the ONC at 1.3 cm, 3.6 cm, and 6 cm to study the free-free emission from ONC cluster members. In Section 2 we describe our observations and maps of the ONC. In Section 3 we detail our methodology for searching for compact radio sources, as well as our model for characterizing the free-free emission. In Section 4 we compare

our results to previous catalogs of compact radio sources in the ONC, discuss the nature of the sources we detect, and show that our measurements are crucial for accurately measuring disk masses of protoplanetary disks from both current and future submillimeter surveys.

7.2   Observations & Data Reduction

We imaged the Orion Nebula Cluster in 1.3 cm, 3.6 cm, and 6 cm wavelength continuum emission with the JVLA between November 2013 and May 2014. The 3.6 cm and 6 cm maps were observed using the 'A' configuration (baselines ranging from 680 m to 36 km), and the 1.3 cm data were taken in three epochs with the 'A' configuration and one epoch with the 'B' configuration (baselines ranging from 210 m to 11 km). Details of the observations and maps are provided in Table 7.1.

The 3.6 cm and 6 cm data were taken simultaneously in 32 128 MHz bands, split evenly between 3.6 cm and 6 cm. Each band contained 64 2 MHz channels, and the bands were arranged continuously from 4.488 - 6.512 GHz at 6 cm and from 8.116 - 10.012 GHz at 3.6 cm, for a total of 2 GHz of continuum bandwidth each.

The field of view of the JVLA antenna primary beam at 6 cm, FWHM of 9', encompasses all 778 YSOs from Hillenbrand and Carpenter (2000), and 196 of the 196 HST detected proplyds (Ricci et al., 2008). 141 of the 196 HST detected proplyds are also detected as sources in Hillenbrand and Carpenter (2000). We therefore use a single pointing to image the field at 6 cm. At 3.6 cm the field of view is 5', so we imaged the field with two pointings that encompassed 778 YSOs and 187 *HST*-detected proplyds.

For a rectangular mosaic the Nyquist sampling theorem suggests that a pointing spacing of FWHM/2 or better is needed (e.g. Cornwell, 1988), but since we are interested in compact sources, Nyquist sampling is not crucial (e.g. Eisner et al., 2008). At 3.6 cm the FWHM/2 is between 2.1' and 2.6' across the band. The two 3.6 cm pointings are separated by 2.4', so the map is sub-Nyquist sampled at the low frequency end of the band, but not at the high frequency end of the band.

Table 7.1.   Log of VLA Observations

Band	Configuration	Date	Int. Time [min]	RMS [μJy]	Peak RMS [μJy]	Beam	No. Beams	Total Detections	$> 6\sigma$ Detections	$> 4.5\sigma$ Detections
1.3 cm	B	Nov. 10, 2013	62	33	~ 93	0.33"$\times$0.21"	1.5×10^6	79	57	22
6 cm	A	Mar. 3, 2014	7	37	~ 150	0.40"$\times$0.28"	3.1×10^6	108	87	21
3.6 cm	A	Mar. 3, 2014	9.5	30	~ 70	0.24"$\times$0.18"	5.1×10^6	98	80	18
1.3 cm	A	Mar. 3, 2014	49	25	~ 50	0.09"$\times$0.08"	14.9×10^6	70	54	16
1.3 cm	A	Mar. 7, 2014	49	26	~ 100	0.08"$\times$0.08"	15.7×10^6	73	56	17
1.3 cm	A	May 3, 2014	36.5	22	~ 85	0.10"$\times$0.07"	14.6×10^6	89	67	22
1.3 cm	A & B combined	$\cdots$	$\cdots$	12	~ 50	0.09"$\times$0.09"	12.4×10^6	126	98	28

[a]$> 6\sigma$ Detections refers to the number of sources detected in each map because they pass the blind detection threshold. $> 4.5\sigma$ Detections refers to the additional sources detected in a catalog driven search, and Total Detections is the sum of those numbers.

The 1.3 cm data were taken in 64 128 MHz bands arranged from 17.976 - 26.024 GHz. Each band was composed of 64 2 MHz channels, for a total of 8 GHz of bandwidth. Most of the data, however, from 17.976 - 22.024 GHz is affected by significant RFI, so we exclude that data from our analysis. The 1.3 cm data therefore has an effective bandwidth of 4 GHz.

A field of view containing 778 YSOs and 193 *HST* detected proplyds was mosaicked using 7 pointings. A two dimensional map is Nyquist sampled if the pointing spacing is FWHM/$\sqrt{3}$ or better, but since we are interested here in compact sources, Nyquist sampling is, again, not crucial. At 1.3 cm FWHM/$\sqrt{3}$ is between 1.2' and 1.4' across the band. The mosaic spacings range between 1-2', so the map is largely not Nyquist sampled. We show the field of view of our observations for each band in Figure 7.1.
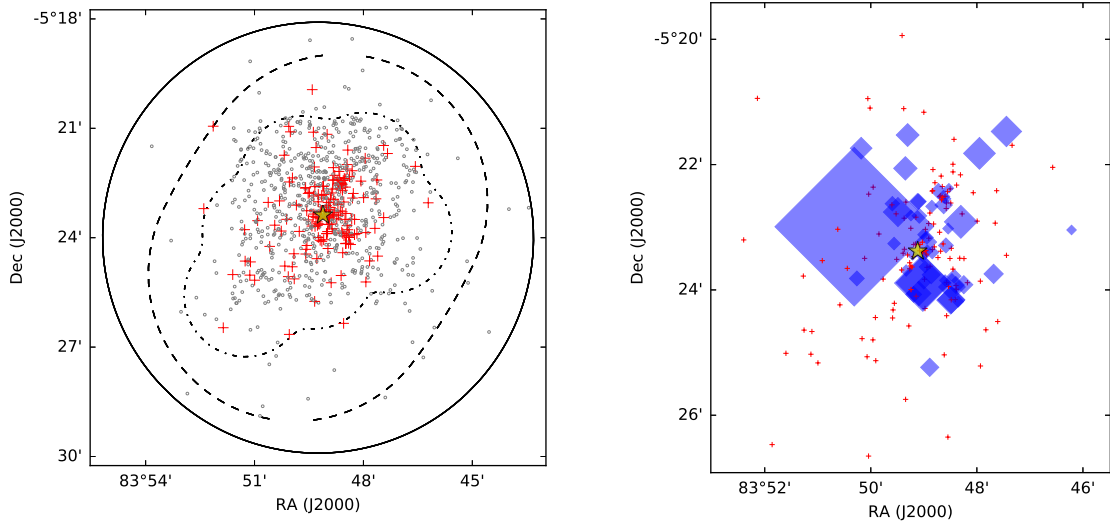
Figure 7.1: The fields we image, out to the 20% gain contour at 6 cm (solid) and the 10% gain contour at 3.6 cm (dashed) and 1.3 cm (dash-dotted) observations, with a yellow star representing the location of θ^1 Ori C. On the left we show all of the sources we detected in at least one of our bands with red plusses and the known sources surveyed but not detected with grey circles. On the right we show sources found to be variable with blue rectangles whose size is proportional to how variable the source is. The largest symbols represent a variability amplitude of 900% while the smallest represent an amplitude of 20%. The detected sources which are not variable are shown again with red plusses.

The data were calibrated and imaged using the CASA software package. Antenna-based complex gains were calculated using periodic observations of the quasar J0541-0541. Bandpass solutions for each antenna were calculated from observations of the quasar J0319+4130, and the overall flux density scale was calculated using models included in CASA for 3C48.

We produced maps of the ONC at each frequency by Fourier transforming the complex visibilities, using the mosaicking modes for the 1.3 cm and 3.6 cm maps. We weighted the data with a robust parameter of 0, which provided a good balance between the high sensitivity of normal weighting and the high spatial resolution of uniform weighting. Our goal is to search for compact structures in the Orion Nebula, so we removed baselines shorter than 100 kλ from our data before inverting the visibilities. The spatial scales eliminated by this cut correspond to structures greater than $2''$, meaning that large scale structure from the Orion Nebula has been resolved out of our maps. For these observations our reference frequencies are 5.5 GHz for the 6 cm map, 9 GHz for the 3.6 cm map, and 22.5 GHz for the 1.3 cm map. We image the 6 cm data out to the 20% gain contour at 5.5 GHz, and the smaller 3.6 cm and 1.3 cm maps out to the 10% gain contour at 9 GHz and 22 GHz respectively[1]. We imaged each 1.3 cm epoch separately to study the variability of the bright sources, and together to increase our sensitivity to look for faint sources in the map.

We CLEANed the images using the Clark algorithm (Clark, 1980). Sources above 10σ were initially identified for CLEANing by visual inspection. The maps were CLEANed down to the rms, as measured in source-free regions of the maps, listed in Table 7.1. Post-source detection, we could re-CLEAN the image using the new detections, however the sidelobes of these sources are low enough to be below the noise level, and the improvement by CLEANing them is minimal and the computational requirements are significant.

---

[1]These correspond to the 33 and 10% gain contours for the low and high frequency 6 cm band edges respectively, the 16 and 6% gain contours for the 3.6 cm band edges, and the 14 and 6% gain contours for the 1.3 cm band edges.

We used a single iteration of self-calibration on the 6 cm data, correcting for just the phases of our data from a model produced by an initial CLEANing of the data. This improved the rms (~ 50 μJy to ~ 40 μJy) in crowded regions of the map or near bright sources with significant beam artifacts.

We self-calibrated the data using a model produced from both fields simultaneously. We find that self-calibrating the fields separately and then imaging them jointly produced ringing in the image that was removed by self-calibrating the data together. We used two iterations of self-calibration, first solving for the phases from our initial model, and then solving for the amplitudes and any residual phase errors in a second iteration. We apply amplitude self-calibration because it helps to remove residual artifacts around bright sources in our map. It does not change the flux in our maps markedly. This improved the rms from ~ 80 μJy near bright sources with significant beam artifacts to ~ 45 μJy.

We self-calibrated fields including the brightest sources together, which is necessary to remove ringing like in the 3.6 cm maps, using a single iteration of self-calibration to correct phase errors in the data. The self-calibration improved the rms by as much as a factor of 3 near bright sources with significant beam artifacts (e.g. ~ 50 μJy to ~ 20 μJy for the combined 1.3 cm map, ~ 100 μJy to ~ 35 μJy for the 1.3 cm data taken on March 3, 2014).

After CLEANing, each map was corrected for attenuation by the primary beam, using the primary beam at the central frequency of each band. The bandwidth of our observations is a significant fraction of the central frequency, however, so the primary beam correction may vary significantly over the band. We have computed the error induced in wideband fluxes measured when correcting by the primary beam of the central frequency, rather than the appropriate primary beam for each channel, and find that this error is <5% for realistic spectral indices (-0.1-2).

Finally, we restored each map with a CLEAN beam whose size is determined by a Gaussian fit to the central peak of the dirty beam for that map. The size of this beam is given approximately by λ/B_{max} for the map, but the exact size and shape depend on the distribution of baselines in the uv-plane and the choice

of weighting function. We list the beam sizes for each map in Table 7.1. After our initial CLEANing of the data we self-calibrated on the brightest sources in our maps to remove residual beam structure and improve the sensitivity, particularly in crowded regions.

7.3 Analysis

7.3.1 Source Detection

In each of our VLA maps we search for sources detected above a certain signal-to-noise threshold. Our maps contain $> 10^6$ synthesized beams (see Table 7.1), so we must employ a relatively conservative threshold to ensure that we do not select noise spikes in the images as real detections. The noise in each map follows a Gaussian distribution (see Figure 7.2), so we expect $\ll 1$ noise spike to fall above a 6σ detection threshold. We therefore use 6σ as our detection limit.
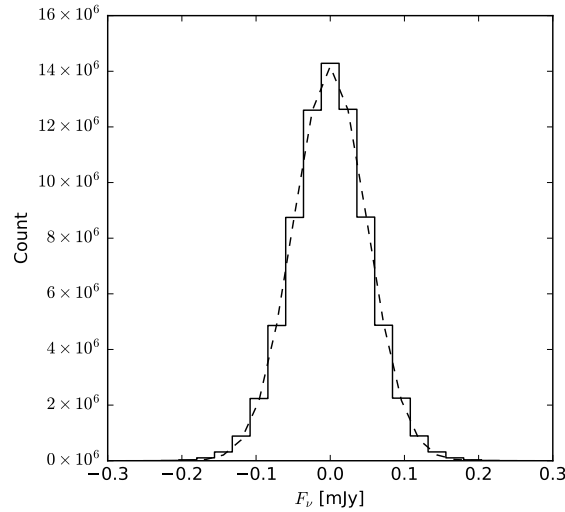
Figure 7.2: We show a histogram of all the pixel values within the 50% gain contour of our 6 cm residual map. We also show the best fit Gaussian to the distribution with the dashed line. Here we show only the 6 cm map, but we have produced similar figures for the 3.6 cm and 1.3 cm maps and find that both of those distributions are also Gaussian, so we can use a σ-cut to confidently distinguish between real sources and noise spikes in our images.

We can also use catalogs of previously known source positions to target our search. We search our maps at the positions of >700 near-infrared detected sources (Hillenbrand and Carpenter, 2000) and ~200 HST detected proplyds (Ricci et al., 2008, with an overlap of about ~150 of the near-infrared detected sources). We also search the coordinates of known submillimeter sources detected with the SMA, CARMA, and ALMA that lack counterparts at infrared wavelengths (Eisner et al., 2008; Mann and Williams, 2010; Mann et al., 2014). Finally, we search for compact radio sources which were detected with the VLA by previous surveys (Felli et al., 1993a; Kounkel et al., 2014). Due to the smaller number of synthesized beams being probed (~ 800), we expect $\ll 1$ noise spike to fall above a 4.5σ level. For each previously identified source we search for a detection above 4.5σ within a radius of 0.5", typical of the sizes of beams from these previous studies.

The rms at each pixel is calculated from a 128 by 128 pixel box surrounding that pixel in the residual map. The rms in the map is generally low (~ 25 μJy in the 1.3 cm maps, ~ 30 μJy at 3.6 cm, and ~ 37 μJy at 6 cm). However, the central region of each map exhibits beam artifacts from a cluster of bright sources and poor sampling of large scale emission. The rms in these regions can be much higher than the rest of the map (~ 100 μJy in the 1.3 cm maps, ~ 70 μJy at 3.6 cm, and ~ 150 μJy at 6 cm; see Table 7.1).

We list the total number of sources detected in each map in Table 7.1. For each map we also provide a breakdown of the number of sources detected in our blind search as well as the additional number of sources detected from the catalog driven search. We detect 108 objects in our 6 cm map, 98 objects in our 3.6 cm map, and a total of 144 objects across all of our 1.3 cm maps. In all we detect 175 distinct sources across all of our maps. We show the position of every detected source in our maps in the left panel of Figure 7.1.

Of the 175 unique compact radio sources, 120 sources are associated with YSOs detected in near-infrared surveys (e.g. Hillenbrand and Carpenter, 2000), and 67 sources are associated with HST detected proplyds. 149 have previous radio detections, and 40 have been previously detected at millimeter wavelengths. We also
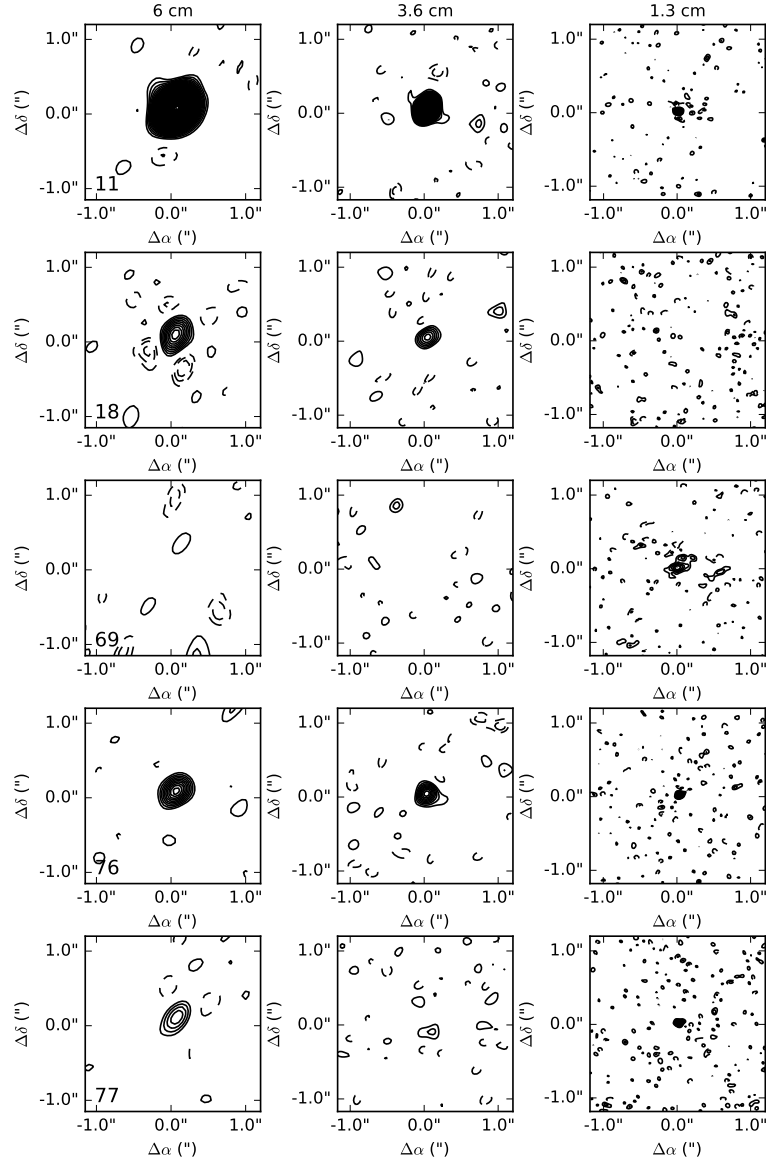
Figure 7.3: Contour images of sources detected in our 6 cm, 3.6 cm or 1.3 cm continuum maps. Each row shows a single source in each band. At 1.3 cm we show only one epoch as a representative image of the source. Contour increments are 1σ, beginning at $\pm 2\sigma$, where σ is determined locally for each object. This figure is continued at the end of the text.

report the detection of 11 sources here for the first time at any wavelength.

We fit every detected source with a two dimensional Gaussian to determine position, extent, and total source flux. For sources identified in the previously mentioned catalogs that are not detected in our maps, we also integrate over a 1" aperture centered on the known source position to produce an unbiased estimate of the signal (or noise) towards that position. We include a 10% error on the measurement to account for systematic errors in the band-to-band flux calibration. These intensities, measured towards all cataloged objects in our field of view, are presented in Table 7.2. The print version of this paper presents only the first page of that table. We also plot images of those sources in Figure 7.3.

Our catalog of sources, as presented in Table 7.2 is sorted by right ascension and then given a catalog 'ID', which we list in Table 7.2. We refer to each source by this ID throughout the remainder of the text and figures. In Table 7.2 we also list the proplyd name, identification from early ONC radio surveys (e.g., Garay et al., 1987; Felli et al., 1993b), identification from Zapata et al. (2004a), or identification from Hillenbrand and Carpenter (2000) when applicable.

7.3.2 Estimating the Free-Free Emission Spectrum

Evidence suggests that the proplyds are undergoing mass loss from photoevaporation by the nearby O star θ^1 Ori C, so the free-free emission we detect here is likely due to a wind (e.g., Churchwell et al., 1987; Henney and Arthur, 1998). For emission from a spherically symmetric wind with an arbitrary $n \propto r^{-\alpha}$ density profile the expected spectral dependence of free-free emission is

$$F_{\nu,ff} = \begin{cases} F_{\nu,turn} \left(\frac{\nu}{\nu_{turn}} \right)^{-0.1} & \nu \geq \nu_{turn} \\ F_{\nu,turn} \left(\frac{\nu}{\nu_{turn}} \right)^{(4\alpha-6.2)/(2\alpha-1)} & \nu < \nu_{turn} \end{cases} \qquad (7.1)$$

(Wright and Barlow, 1975). ν_{turn} is the frequency where the wind becomes partially optically thick, and is determined by the radius of the inner boundary of the ionized envelope. High turnover frequencies indicate more compact inner boundaries. When

the wind becomes fully optically thick at very low frequencies the spectrum follows the typical $F_\nu \propto \nu^2$ spectrum expected for optically thick thermal emission.

For a fully ionized wind with a constant mass-loss rate we expect $\alpha = 2$ and the spectral dependence of free-free emission is

$$F_{\nu,ff} = \begin{cases} F_{\nu,turn} \left(\frac{\nu}{\nu_{turn}}\right)^{-0.1} & \nu \geq \nu_{turn} \\ F_{\nu,turn} \left(\frac{\nu}{\nu_{turn}}\right)^{0.6} & \nu < \nu_{turn} \end{cases}. \qquad (7.2)$$

Steeper density profiles may lead to steeper spectral dependences below the turnover frequency (e.g., Plambeck et al., 1995). Here, for simplicity, we adopt the solution for a fully ionized wind with a constant mass-loss rate. Many of our sources show evidence for a free-free turnover (see Figure 7.4), so we adopt a model including a turnover in the spectrum.

At higher frequencies, dust emission is expected to dominate. The differences in the expected spectral slopes between dust and free-free emission allows us to characterize each separately by observing our targets at a range of wavelengths. For each of our detected sources we fit a simple model to the known radio, millimeter, and sub-millimeter photometry:

$$F_\nu = F_{\nu,ff} + F_{\nu,dust,230GHz} \left(\frac{\nu}{230\text{GHz}}\right)^{2+\beta}. \qquad (7.3)$$

Here we assume $\beta = 0.7$, consistent with previous studies of protoplanetary disks in other star forming regions (e.g., Rodmann et al., 2006; Ricci et al., 2010a,b).

We fit the SED of each source by searching a grid over a large range of parameter space of ν_{turn}, $F_{\nu,turn}$, and $F_{\nu,dust,230GHz}$ for a minimum in χ^2. We then use a second, finely spaced, grid search based on the initial search to find the best χ^2 fit.

ν_{turn}, $F_{\nu,turn}$ and $F_{\nu,dust,230GHz}$ are left as free parameters in the grid search. If a source has no submillimeter detections ($\geq$ 90 GHz; Eisner et al., 2008; Mann and Williams, 2010; Mann et al., 2014), we assume that $F_{\nu,dust,230GHz} = 0$. In that case we also require $5.5\text{GHz} \leq \nu_{turn} \leq 22\text{GHz}$, because outside of this range we cannot constrain ν_{turn}. If a source does have sbmillimeter detections we only require $5.5\text{GHz} \leq \nu_{turn}$.
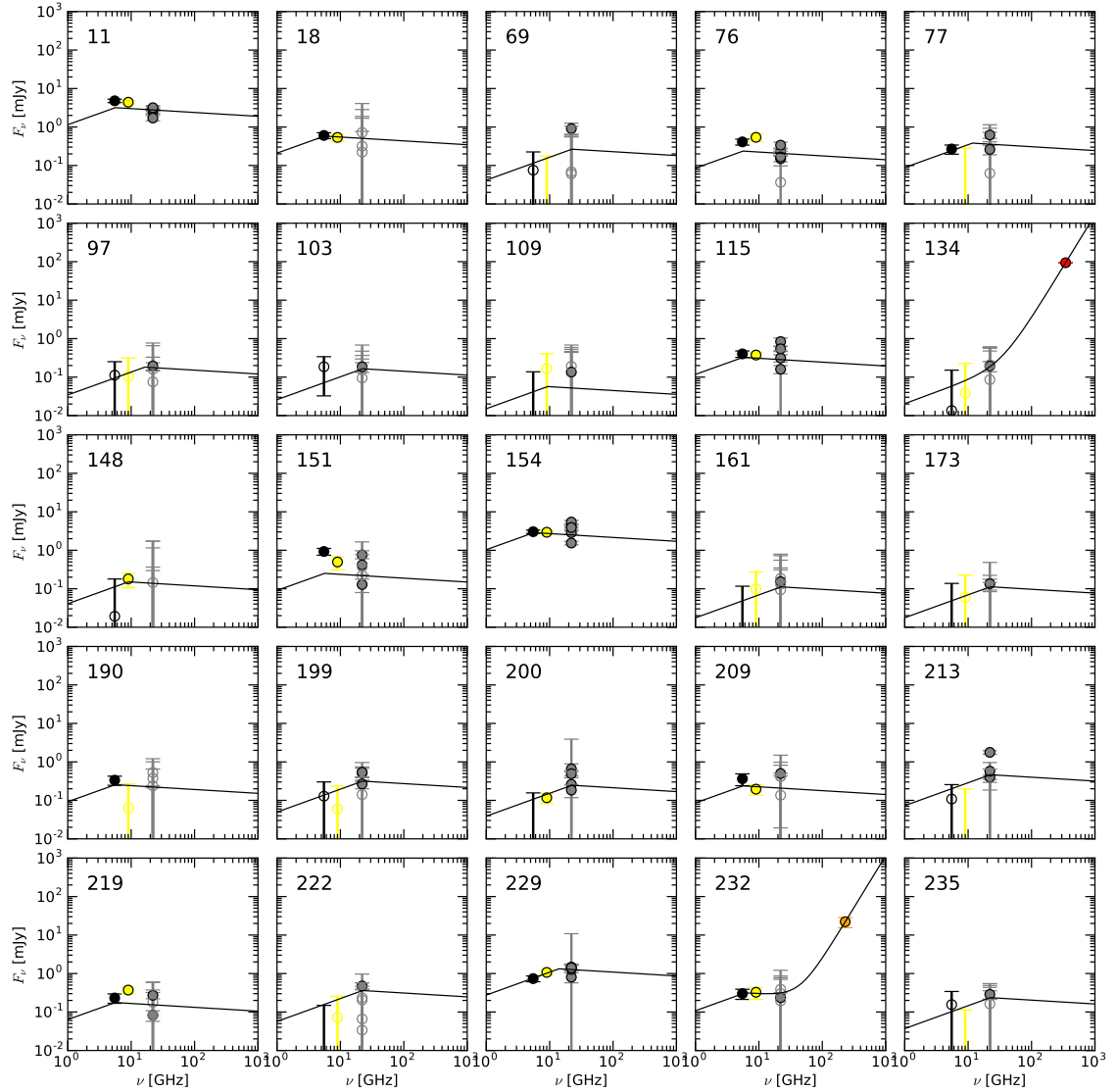
Figure 7.4: The millimeter and radio SEDs for all of the sources detected in our maps. We also show the best fit dust + free-free emission model for each source, as described in Section 3.2. Black, yellow and grey points are the 6 cm, 3.6 cm, and 1.3 cm flux measurements for objects detected in our maps. Circles with colored faces indicate that the source was detected by our search routines, while open face circles are fluxes measured in an aperture around a known source position. Orange data points are 3mm, 1.3 mm, and 870 μm fluxes from Eisner et al. (2008, and references therein). Green data points are 870 μm fluxes from Mann and Williams (2010), and red data points are 870 μm fluxes from Mann et al. (2014). The fluxes shown here are all measured with one of the SMA, CARMA, ALMA, OVRO, or the VLA. This figure is continued at the end of the text.

Sources 281, 391, 416, 423, 430, 433, 442, 512, 516, 537, 564, and 595 are all extended sources that are marginally resolved by our 3.6 cm and 6 cm maps, as well as in our B-configuration 1.3 cm observations. In our A-configuration 1.3 cm observations, however, these sources are very well resolved. In fact, they are so well resolved that much or all of the emission from the source is resolved out. As such we exclude the A-configuration flux measurements from our SED fitting, as flux variations are likely due to structure being resolved out rather than actual variability.

Some of our sources are variable across our multiple epochs of 1.3 cm data (see Section 4.2). We account for this variability in our modeling by including the measured flux at each epoch and allowing the variability to influence the uncertainty of our parameter estimation. Sources that are more variable will also have more uncertainty in model fits.

We list the parameters of our best fit models to each source detected in our maps in Table 7.3. The photometry, along with the best fit model, for each source is plotted in Figure 7.4.

The origin of the radiation ionizing these sources has been the subject of much debate. Early radio studies of the region disagreed as to whether these sources were externally ionized by radiation from θ^1 Ori C or ionized internally by a young massive star, and as to whether these objects are dense neutral condensations or protoplanetary disks (e.g., Garay et al., 1987; Churchwell et al., 1987), although these studies are complicated by the fact that only projected, and not actual, distances from θ^1 Ori C are known. Since these early studies, *HST* imaging (e.g., O'Dell et al., 1993) and detailed modeling of those images (e.g. Henney and Arthur, 1998) has favored protoplanetary disks ionized by θ^1 Ori C.

Free-free emission powered by ionizing radiation from θ^1 Ori C should decrease with increasing separation from θ^1 Ori C. We show the measured flux versus distance in the left panel of Figure 7.5. For most sources there is a trend of decreasing radio flux with increasing separation, suggesting that they are exhibiting free-free emission from gas ionized by θ^1 Ori C. We also find that the difference in their 1.3 cm and
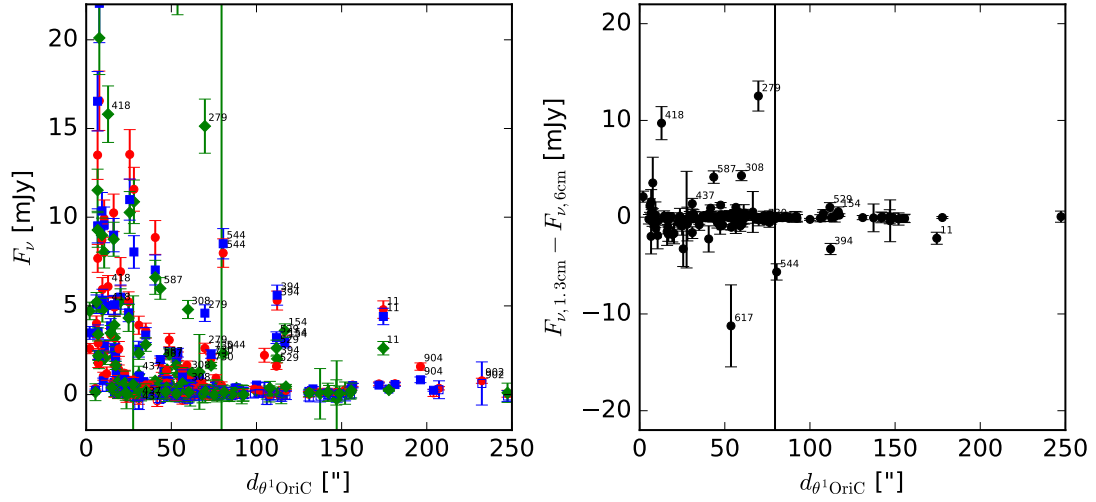
Figure 7.5: (left) The measured radio flux of each of our detected objects at 1.3 cm (green diamonds), 3.6 cm (blue squares), and 6 cm (red circles) as a function of projected distance from θ^1 Ori C. (right) Difference in measured 1.3 cm and 6 cm fluxes as a function of projected distance from θ^1 Ori C. With the exception of a few outliers, we find that radio fluxes for our targets decrease with increasing projected separation, as we would expect for free-free emission driven by the powerful ionizing radiation of θ^1 Ori C. This is also consistent with the difference in 1.3 cm and 6 cm fluxes, which falls near zero for most sources. Optically thin free-free emission is expected to have a roughly flat spectrum at these wavelengths, so we would expect the differences in those measurements to fall near zero. We label the significant outliers with the source ID for reference in future sections.

6 cm flux is close to zero, as expected for optically thin free-free emission, which has a roughly flat spectrum (see the right panel of Figure 7.5). We note that here we report projected distances. Actual separations are greater than or equal to this number. We discuss the outliers of these trends below, in Section 4.3.

For this study, we are only concerned with whether these sources are emitting thermal free-free emission or not so that we can characterize the emission and remove it from dust emission for disk mass studies, but on the surface Figure 5 would seem to suggest that these sources are externally ionized by θ^1 Ori C. The detailed structure of these compact objects is beyond the scope of this paper, as the radio emission can be well characterized without that knowledge, but we will revisit the subject in

a more detailed study in the future.

7.4 Discussion

7.4.1 Comparison with Previous Radio Surveys

Many compact radio sources have previously been identified at a range of wavelengths in the ONC through VLA surveys of the region. The earliest searches for compact radio sources in the ONC were conducted primarily at 20 cm, 6 cm, 2 cm, and 1.3 cm (e.g., Garay et al., 1987; Churchwell et al., 1987; Felli et al., 1993a,b). These surveys were state of the art at the time, with rms as low as 0.18 mJy beam^{-1} at 2 cm (Churchwell et al., 1987; Felli et al., 1993a), 0.23 mJy beam^{-1} at 6 cm (Felli et al., 1993b), or 1.0 mJy beam^{-1} at 1.3 cm (Garay et al., 1987). These searches identified 49 compact radio sources in the ONC.

A more recent survey mapped a 4' × 4' region of the the ONC at 3.6 cm using the VLA. This survey achieved a sensitivity of 0.03 mJy beam^{-1} and uncovered 77 compact radio sources (Zapata et al., 2004a). Of these 77 sources, 38 were previously known from the earlier studies mentioned above, while 39 were new centimeter detections. Zapata et al. (2004b) also mapped a 30" × 30" region in OMC-1 South at 1.3 cm with the VLA. They achieved an rms of 0.07 mJy beam^{-1}, but due to the limited area of their maps only detected 11 sources.

A recent survey mapped out a large region encompassing λ Ori, Lynds 1622, NGC 2068, NGC 2071, NGC 2023, NGC 2024, σ Ori, the ONC, and Lynds 1641 with the VLA at 4.5 GHz and 7.5 GHz with a 60 μJy sensitivity (Kounkel et al., 2014). They found > 350 sources over the area of their map, 54 of which overlap with the area we survey. The majority of their detected sources also have spectral indices consistent with flat spectra.

Here we compare these previous surveys with our own JVLA maps. In Figure 7.6 we plot the distribution of fluxes for compact sources detected in our maps as well as the distribution of fluxes for previously identified compact radio sources at the same wavelength. The most extensive existing studies at 1.3 cm are limited
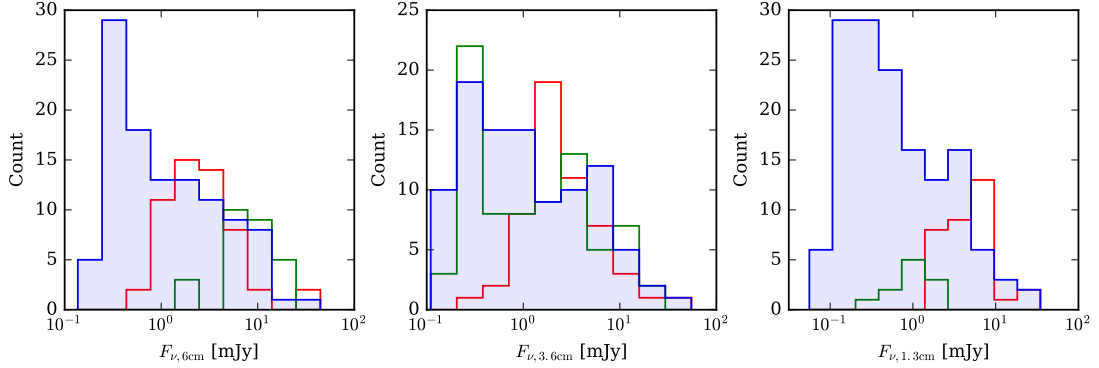
Figure 7.6: Histograms of the fluxes of sources detected in each of our maps. We also show a histogram of the compact radio sources detected in previous studies. Blue shows the histogram of detected sources from this work. Green shows the histograms of detected sources from Felli et al. (1993b) (6 cm), Zapata et al. (2004a) (3.6 cm), and Zapata et al. (2004b) (1.3 cm). Red shows the 4.5 GHz (6 cm) and 7.5 GHz (3.6 cm) detections from Kounkel et al. (2014), and the 2 cm detections from Felli et al. (1993a). We do not show the Forbrich et al. (2016) 6 cm sample, which includes 477 sources fainter than 0.3 mJy.

by either survey area or sensitivity so we also compare our 1.3 cm detections with previous 2 cm detections.

Of the 49 compact radio sources detected by initial surveys (e.g. Garay et al., 1987; Churchwell et al., 1987; Felli et al., 1993a,b), we have detected 37 in our maps. We have also recovered 64 of the 77 sources detected by Zapata et al. (2004a), 9 of the 11 sources found by Zapata et al. (2004b), 42 of the 54 sources found by Kounkel et al. (2014), and 144 of the 556 sources found by Forbrich et al. (2016). We detect 29 of the 35 sources that were previously detected at 2 cm. We also report the detection of 135 sources that have not previously been detected at 1.3 cm, 34 at 3.6 cm, 4 at 6 cm, and 26 sources that have not previously been detected at any radio wavelengths. The sources that were previously detected, but that we do not detect in our maps, are likely variable given the deeper sensitivity in our JVLA data.

7.4.2 Variability

Previous radio studies of the ONC explored multiple epochs of data to search for evidence of source variability. Felli et al. (1993b) monitored the ONC at 2 cm and 6 cm for a period of 7 months and found 13 sources to be variable over that time with flux variability of $20 - 80\%$. Zapata et al. (2004a) tracked the ONC at 3.6 cm over four years, and identified 36 sources that are time variable by more than 30%. More recently, Kounkel et al. (2014) mapped a large region of the Gould Belt at 4.5 GHz and 7.5 GHz over three epochs each separated by a month, and found 32 variable sources in the ONC. Futhermore, Rivilla et al. (2015) studied a field in the ONC at 0.7 cm and 0.9 cm and found 19 sources which are variable over long-term (monthly) timescales, and 5 sources which are variable on short timescales (hours to days). Moreover, very short timescale radio flares have been observed towards a number of pre-main sequence stars (e.g., Bower et al., 2003; Forbrich et al., 2008; Rivilla et al., 2015)

Here we compare previously measured fluxes for detected compact radio sources with the fluxes in our maps. Time-baselines are $\sim$10 years at 1.3 cm and 3.6 cm and $\gtrsim$20 years at 6 cm, and we cannot characterize shorter timescales for variability. We thus seek to identify sources that may not have been detected as variable in previous, shorter time-baseline studies (Felli et al., 1993b; Zapata et al., 2004a). We also use our multiple epochs of 1.3 cm data to search for variability on timescales of $\sim$ 7 months, between November 10, 2013 to May 3, 2014.

As we discussed earlier, Sources 281, 391, 416, 423, 430, 433, 442, 512, 516, 537, 564, and 595 are very well resolved with the A-configuration at 1.3 cm. As such we exclude these sources from our variability considerations at 1.3 cm, as flux variations may be due to structure being resolved out rather than actual variability.

We define a variable source as one for which the flux measurements are 3σ discrepant from one epoch to the next, at any observed wavelength. ΔF/F quantifies how variable a source is, where F is the mean flux of the source and ΔF is the standard deviation of the fluxes. We show the results of this search in Table 7.4.

For the sources detected in Zapata et al. (2004a) and Zapata et al. (2004b) we include a 10% uncertainty on the flux on top of the uncertainties they quote to account for a systematic flux calibration uncertainty across the datasets.

At 1.3 cm we find 30 sources that show some indication of variability, with $\Delta F/F$ ranging from 20-900%. At 3.6 cm we identify 32 sources whose fluxes are variable, including 3 sources not identified as variable in Zapata et al. (2004a), because they were too faint to be detected in individual epochs. The variability, as defined by $\Delta F/F$, of these sources ranges from 20-200%. Finally, at 6 cm we identify 5 variable sources with $\Delta F/F$ ranging from 50-100%.

There were 13 sources detected by previous radio surveys of the ONC (e.g. Felli et al., 1993a,b). Most of those sources were not detected in the same bands as our observations, and so they are excluded from our variability analysis. However, the 5 variable sources with 6 cm fluxes from Felli et al. (1993b) were undetected in our maps, and have $\Delta F/F$ ranging from 50-100%. Given the high fluxes of the remainder of the sources, we would have expected to detect them in our maps, so those sources likely have similarly high variability amplitudes.

In all, we find that 55 of our sources are variable at one or more wavelengths. Of the variable sources, 11 are characterized as variable at multiple wavelengths. 20 are found to be variable at one wavelength but not another, although many of our constraints on $\Delta F/F$ are not strong. The remaining sources could only be analyzed at a single wavelength.

We show the location of each variable source in the right panel of Figure 7.1, with the strength of the variability ($\Delta F/F$) represented by the size of the plot symbol. We find that variability amplitude does not follow the same trend as free-free flux, with variability decreasing with increased separation from θ^1 Ori C. Instead we find sources which are significantly variable out to large radii. Some of the most variable objects can be found at large separations.

Variability of radio emission from these sources is likely to arise from a few different mechanisms. It may be the result of gyrosynchrotron emission produced by magnetospheric activity in young stars (e.g., Feigelson and Montmerle, 1999).

These flares may be the result of magnetic reconnections on the protostellar surface, which would produce radio flares on the timescales of minutes (e.g Dulk, 1985; Bower et al., 2003; Forbrich et al., 2008). Interactions between the magnetic fields of the protostar and its disk could also produce flares on the timescales similar to the rotation periods of young stars, which are typically days to weeks in the ONC (e.g. Shu et al., 1997; Forbrich et al., 2006; Rodríguez-Ledesma et al., 2009).

Free-free emission may also be variable if the density distribution of material being ionized is non-uniform causing the amount of ionized material to vary, or if the incident ionizing radiation is varying. Studies have found that O-type stars have winds that exhibit cyclical variability on timescales of hours to days (see review by Fullerton, 2003). The visible, UV and X-ray intensity of θ^1 Ori C varies with a period of 15.4 days (e.g., Stahl et al., 1993, 1996; Caillault et al., 1994; Walborn and Nichols, 1994), so the ionization level and therefore free-free flux might be expected to vary on a similar timescale. The ionized region, however, is likely to be many light days across or larger, so this variability may be washed out.

Inhomogeneities in the disk are unlikely to be brought into the ionized region on timescales shorter than the dynamical timescale. For disks, the dynamical timescale varies depending on location in the disk and the mass of the central star (e.g., Kenyon, 2001). Inner disk radii for young stars are found to be on the order of $0.1 - 1$ AU (e.g., Eisner et al., 2007), so the smallest dynamical timescales we can expect are on the order of weeks to half a year. Photoevaporation in disks tends to produce winds at radii larger than the critical radius, where the photoionized material has sufficient velocity to escape. For ionization by EUV photons this tends to occur at radii of $\gtrsim 5$ AU (e.g., Hollenbach et al., 1994; Gorti and Hollenbach, 2009b), corresponding to dynamical timescales of a few years. Non-uniformities in the disk are therefore likely to cause longer term variability in the free-free emission.

Aside from the timescale of variability, the SED of the source at each epoch might be used to distinguish between free-free and synchrotron emission. As described in Section 3.2, free-free emission is characterized by a flat spectrum with $F_\nu \propto \nu^{-0.1}$. Gyrosynchrotron emission however, is expected to have a spectral index

that is significantly negative, typically $F_\nu \propto \nu^{-0.7}$. We discuss constraints on the nature of some of these sources in Section 4.3. Further studies with concurrent flux measurements at multiple wavelengths, however, are needed to fully distinguish between these sources of emission.

Here we do not have simultaneous flux measurements at all bands for each epoch of data, so it is difficult to constrain the spectral index of the emission at each epoch. There are, however, a few sources which change flux significantly between the 1.3 cm observations on March 3 and March 7 2014. For example, on March 3, Source 529 had a 1.3 cm flux of 7 mJy, but on March 7 it was down to a flux of 4.5 mJy. By May 7th the flux was all the way down at 0.5 mJy. Such an extreme change in flux may be indicative of gyrosynchrotron emission from a magnetic flare. Source 544 also shows a similar pattern. Source 587 has a flux of 1.7 mJy on March 3, but on March 7 it's flux increased significantly to 22 mJy, again possibly indicative of a magnetic flare. For most sources, however, we do not have sufficient time resolution to distinguish between daily, weekly, or even longer variability timescales.

7.4.3   Nature of Detected Sources

We detected emission in at least one of our maps from 67 *HST* identified proplyds (Ricci et al., 2008; Mann and Williams, 2010; Mann et al., 2014). Furthermore, we have detected radio emission towards 120 sources that have been identified by near-infrared imaging (Hillenbrand and Carpenter, 2000). We also detect radio emission from 2 sources dubbed 'MM' by Eisner et al. (2008), indicating that they have previously only been detected at wavelengths longer than 1 mm. Finally, we have detected 51 sources that are not associated with a known proplyd or near-infrared detected source.

The majority of our targets, including all of the sources identified as proplyds, are well fit by our free-free and dust emission model, in agreement with previous conclusions that these objects are disks with winds driven by photoevaporation (e.g., Churchwell et al., 1987; Henney and Arthur, 1998). We detect a turnover in the free-free emission spectrum for 40 objects, as evidenced by $5.5\text{GHz} < \nu_{turn} <$

22GHz. There are at least 3 sources (Sources 374, 465, 473) that might even have $\nu_{turn} > 22$GHz, indicating that our maps are insufficient to fully characterize their emission. With such high turnover frequencies, these objects must have small inner boundaries to their ionized envelopes and are likely very compact and dense. Further short wavelength observations are necessary to better constrain the free-free emission spectrum.

Some sources have SEDs that appear to be fitted well by our free-free + dust model with some variability included. Fluxes at all three wavelengths were measured concurrently on March 3, 2014, and if we just consider those flux measurements, all of our sources are fitted well by free-free emission models. Without simultaneous 3.6 cm and 6 cm measurements for the other 1.3 cm epochs it is impossible to say whether the SEDs at those epochs remain consistent with free-free emission, although it seems probable.

Below we split the sources whose SEDs are not fitted well by our model and therefore are not indicative of being free-free emission, or do not follow the expected trend of decreasing centimeter flux with increasing separation from θ^1 Ori C:

Strong Free-Free Sources

Source 418 is θ^1 Ori A, a binary system with a B0.5 primary star and a low-mass companion, possibly a T Tauri star (Levato and Abt, 1976; Bossi et al., 1989), which is known to be highly variable (e.g., Felli et al., 1993b). Rivilla et al. (2015) suggest that this variability may be twofold, (i) variations in free-free opacity from a stellar wind from the interactions with the companion, and (ii) variations in the non-thermal emission from stellar activity related to the distance between to binary, similar to the case of WR 140 (e.g., Williams et al., 1990). Rivilla et al. (2015) suggest that while the former mechanism may be present, the latter is required to explain previous observations.

Sources 279 and 308 each have radio spectra that are steeper than $\nu^{0.6}$. Source 279 is the Becklin-Neugebauer Object, and is thought to be a runaway B star, ejected from a system with Source I (our Source 308) in an explosive event 500 years ago

(e.g., Plambeck et al., 1995; Gómez et al., 2008; Plambeck et al., 2013). The BN Object has a spectral dependence of $\nu^{1.3}$ below 100 GHz, above which it flattens, and is suggested to be free-free emission from a dense, hypercompact HII region. Source I has a spectral dependence of ν^2 and is most easily explained by H^- free-free emission in a disk (e.g., Plambeck et al., 2013). Both sources have massive stars driving ionizing circumstellar material and driving the free free emission we detect, explaining their significant fluxes despite their distance from θ^1 Ori C.

Dust-Only Sources

Sources 134, 236, 246, and 301 have millimeter (850 μm or 1.3mm) detections and are detected at 1.3 cm in our maps, but are undetected at 3.6 cm and 6 cm. The SEDs for all of these sources are well fit by a model that is predominantly dust emission at 1.3 cm (and perhaps a minor contribution from free-free emission). Sources 236 and 246 are identified by Eisner et al. (2008) as "MM" objects (MM21 and MM8 respectively), which lack near-IR counterparts. Source 301 is also identified by Eisner et al. (2008) as LMLA 162. All three of those sources (236, 246, and 301) are among the most massive known sources in the ONC (> 0.2 $M_\odot$ Eisner et al., 2008). They are likely highly embedded young objects, and may be candidate Class 0 or I objects as suggested by Eisner et al. (2008).

Non-Thermal Radio Sources

Sources 11 and 617 each have spectra with steep negative spectral indices (see Figure 7.5), which may indicate that they are emitting synchrotron radiation. Source 11 is not associated with any previous detections in our reference catalogs, and is found to be variable at 3.6 cm. Source 617 has previously been detected, and is commonly referred to as F (e.g., Churchwell et al., 1987; Garay et al., 1987; Felli et al., 1993a). It has previously been found to experience radio flares on timescales as short as hours and possibly as long as months (Rivilla et al., 2015).

Sources 154, 394, 437, 440, 529, 544, 587, and 730 are highly variable

sources, showing significant changes in flux over just a few days between our observations on March 3, 2014 and March 7, 2014. All are significant outliers in Figure 7.5. Source 154 has previously been identified as A (e.g., Churchwell et al., 1987; Garay et al., 1987; Felli et al., 1993a), and Zapata et al. (2004a) find the source to show large percentages of circular polarization, and suggest that the emission may be gyrosynchrotron in nature. Felli et al. (1993b) also classify Source 587, also known as G, as a non-thermal variable emitter. All of these sources are associated with infrared detected objects (Hillenbrand and Carpenter, 2000). These sources may be indicative of radio flares of gyrosynchrotron emission, but further observations with concurrent flux measurements at multiple wavelengths are needed to confirm this.

Source 903 is located far from θ^1 Ori C, and is only detected at 6 cm, but it has a high flux given it's significant separation (see Figure 7.5). It is out of the field of view of our 1.3 cm data, and right on the edge of our 3.6 cm map, but undetected. It is associated with the proplyd 281-306, which is a disk seen only in silhouette with HST (Ricci et al., 2008). Radio emission from this source may be attributed to magnetic activity from the young star or free-free emission from material ionized by the star itself, as it is likely too far to be material ionized by θ^1 Ori C.

Source 904 is also located far from θ^1 Ori C, with a high flux given it's separation (Figure 7.5), and is outside the field of view of our 1.3 cm map. It's 6 cm and 3.6 cm fluxes are consistent with free-free emission, but do show indications that the spectral index may be significantly negative. It is unassociated with any previous catalog.

Extragalactic Sources

Given the large survey area of our maps, it is possible that some of our detections are extragalactic in nature. Following Fomalont et al. (1991), at 6 cm we would expect the number of extragalactic contaminants greater than 156 μJy (our 6σ threshold) in our 109 arcmin^2 survey area to be 6.5 ± 2.3. At 3.6 cm, using Fomalont et al. (2002), we estimate 1.1 ± 0.2 extragalactic sources in our 70 arcmin^2 survey area to above 216 μJy. No similar survey exists at 1.3 cm, so we use the 3.6 cm numbers

to estimate that in our 1.3 cm map we would expect 1.8 ± 0.2 contaminants in our 34 arcmin^2 survey area above 72 μJy. As most of these sources show non-thermal emission with negative spectral indices at these wavelengths (Condon, 1992) they should be fainter at 1.3 cm than at 3.6 cm and therefore we would expect the contamination at 1.3 cm to be even smaller than this.

7.4.4 Free-free Contamination of Sub-millimeter Dust Masses

At submillimeter, millimeter and radio wavelengths, the light emitted by dust grains is expected to be largely optically thin and the flux is directly proportional to the amount of dust present (e.g., Beckwith et al., 1990). As such, submillimeter flux measurements of protoplanetary disks are commonly used to measure the mass of those disks (e.g., Andrews and Williams, 2005; Eisner et al., 2008; Mann and Williams, 2010; Andrews et al., 2013; Mann et al., 2014). A number of previous surveys across millimeter and submillimeter wavelengths have employed this method to measure disk masses for protoplanetary disks in the ONC (e.g., Mundy et al., 1995; Bally et al., 1998b; Williams et al., 2005; Eisner and Carpenter, 2006; Eisner et al., 2008; Mann and Williams, 2010; Mann et al., 2014).

The proplyds, however, are located near the Trapezium cluster of young massive stars that are photoevaporating the disks (e.g., Churchwell et al., 1987). The ionized material produced in the proplyds emits free-free emission, which can be bright at the same wavelengths used to measure disk masses. In order to accurately measure disk masses, it is therefore important to separate the dust and free-free contributions to sub-millimeter and millimeter fluxes. This is particularly true with the advent of ALMA, which will detect disks in the ONC much fainter than those that have been previously detected.

In this work we characterized the free-free emission from a collection of compact radio sources in the ONC. In Table 7.3 we use the best fit free-free emission spectrum model from Section 3.2 to calculate the expected free-free flux at all ALMA bands. This table can be used to correct measured millimeter fluxes for free-free contamination, and accurately measure the sub-millimeter dust flux and thereby the

dust mass.

For most sources this extrapolation provides a good estimate of the free-free contribution of the source at ALMA wavelengths. This is not true, however, of sources for which the model fit is poor as was discussed in the previous section. Furthermore, the extrapolation to ALMA bands for sources whose turnover frequency is designated as > 22 GHz is also very uncertain. Many of these sources were only detected at 1.3 cm, and a few have radio photometry that is best fit by a $\nu^{0.6}$ power law. Our extrapolation for these sources assumes $\nu_{turn} = 22$ GHz, but if $\nu_{turn} > 22$ GHz the free-free flux at ALMA bands would be greater than our current prediction. Further radio or millimeter observations are necessary to constrain ν_{turn} before accurate ALMA free-free fluxes can be predicted.

Variability is also a significant source of uncertainty in determining how well free-free emission from disks can be constrained and removed from disk mass measurements, if the free-free flux to dust flux ratio is large. For example, the measured 230 GHz flux of Source 439 is 8.8 mJy and the model free-free flux at 230 GHz is 2.8 mJy, with a variability of 24%. So free-free emission makes up $32\pm 8\%$ of the total 230 GHz flux. Source 466, however, has a measured 230 GHz flux of 7.7 mJy, 0.3 mJy of which is due to free free emission with 50.8% variability, so the free-free emission makes up $5\pm 2\%$ of that flux. Because of the smaller free-free flux to total flux ratio of Source 466, the dust flux can be better constrained, even though Source 466 is more variable.

ALMA, however, will be able to detect disks which are much fainter than has previously been possible, For these sources, variability may be a significant problem. Source 469 has a 230 GHz free-free flux of 0.33 mJy with a variability of 108%. Although it has no previous millimeter detections, if it were found to have a millimeter flux of 0.5 mJy, the dust mass calculation would be highly uncertain because the free-free flux would make up $65\pm70\%$ of the total 230 GHz flux.

An accurate estimate of the uncertainty associated with variability of our sources, however, likely requires further monitoring of the sources to characterize the timescale and amplitude of the variability. Sources with significant variability

may even require concurrent millimeter and radio flux measurements in order to measure the free-free contribution to millimeter flux measurements.

While not important for some objects, the correction for free-free emission is often crucial for correctly measuring disk mass. For example, the free-free emission from sources 391, 408, 416, 418, 421, 423, 430, 438, 439, 442, 446, 460, 465, 484, 491, 494, 499, 512, 516, 518, 535, 537, 555, 564, 605, 612 and 617 contributes >50% of the measured 3 mm fluxes. Free-free emission also contributes >40% of the measured 1.3 mm fluxes for sources 408, 416, 418, 421, 423, 438, 442, 460, 465, 484, 491, 494, 499, 516, 518, 535, 564 and 617 and >30% of the measured 850 μm fluxes for sources 408, 421, 423, 438, 460, 465, 484, 491, 494, 499 and 617. Without these corrections, disk mass estimates from these sub-millimeter bands would be off by a significant amount.

7.4.5 Future Work

While our radio dataset is tremendously useful for finding radio sources and characterizing their free-free emission for ALMA disk mass studies in the ONC, the data also has a number of other applications which we will explore in future work.

Due to the high resolution of our maps, particularly at 1.3 cm, many of the sources detected in our maps are well resolved. The morphologies of these objects show interesting features, particularly when matched up with high resolution HST images of the proplyds. For many sources structure in HST maps is well matched with features in our maps.

Furthermore, we can use resolved images to measure mass loss rates for the protoplanetary disks. The free-free emission we detect here originates from ionized cocoons of gas which are flowing away from their associated disks under the intense radiation pressure from the star θ^1 Ori C. The flux of this free free emission coupled with measured sizes of these cocoons of gas is sufficient to measure disk mass-loss rates. Mass loss rates have previously been measured for a handful of disks in the ONC (e.g., Churchwell et al., 1987), but the improved sensitivity and resolution of our maps will allow us to make this measurement for many more sources.

7.5   Conclusions

We have produced new high spatial resolution maps of the Orion Nebula at 1.3 cm, 3.6 cm and 6 cm with significantly improved sensitivities compared with previous radio studies of the region, using the JVLA. In these maps we search for compact ($\lesssim 2$") radio sources, and use these detections to constrain the properties of free-free emission from protoplanetary disks in the ONC. Free-free emission is emitted from the ionized winds driven by the nearby massive star θ^1 Ori C. Constraints on this free-free emission are crucial for studies aiming to measure disk masses for the proplyds from sub-millimeter fluxes.

We detect 144 sources at 1.3 cm, 98 sources at 3.6 cm, and 108 sources at 6 cm, for a total of 175 unique sources. Of these 175 detections, 149 have previously been detected at radio wavelengths, 67 are associated with *HST* detected proplyds, 120 with near-infrared detected YSOs, 40 with sources detected previously at millimeter wavelengths, and 11 are detected for the first time at any wavelength.

For each source detected in our maps we report its position and flux, as measured by fitting a gaussian to the source, in Table 7.2. For previously identified sources not detected in one or more of our maps we also report the integrated flux in an 1" aperture measured towards the source. This information is presented in an extended version of Table 7.2 that is available in the online materials.

We fit each of our source spectra with a combined dust + free-free emission model. The majority of our targets are fitted well by this dust + free-free model, with many showing evidence for a turnover in the free-free emission. Further studies of free-free emission may benefit from longer wavelength flux measurements to better constrain the free-free turnover. Four of our detected sources (134, 236, 246, and 301) have SEDs that are consistent with being produced entirely by dust emission and are likely highly embedded young objects. We also detect the Becklin-Neugebauer Object, it's alleged counterpart Source I, and θ^1 Ori A.

Many of our sources have previously measured radio fluxes, so we can investigate variability. We find that 30 sources are variable at 1.3 cm, 32 at 3.6 cm, and 5 at

6 cm. 55 of our detected sources are variable at one or more wavelengths. For sources that are variable we define a metric, $\Delta F/F$, to quantify the variability, and find that $\Delta F/F \approx 20 - 900\%$ for our targets. 13 are variable at $> 100\%$, suggesting that any sub-millimeter measurements will be very uncertain. The time sampling is, however, poor, so more dedicated monitoring of our targets is necessary for better understanding this variability.

Finally, the free-free emission properties derived from our modeling can be extrapolated to sub-millimeter wavelengths to estimate the free-free contribution to sub-millimeter fluxes. This is necessary for correctly distinguishing dust emission and free-free emission at sub-millimeter wavelengths, particularly when sub-millimeter fluxes are used to calculate disk dust masses. This will be crucial for future studies of dust emission from protoplanetary disks in the ONC with ALMA. We provide free-free flux estimates for each detected source at each ALMA band in Table 7.3. Variability is a significant source of uncertainty in correcting millimeter flux measurements for free-free emission if the free-free flux to dust flux ratio is large, so understanding this variability is an important future direction.

In the future we will use this dataset to study the morphologies of the sources resolved in our high resolution VLA maps, particularly as compared with HST images of the proplyds. We will also measure the rate at which material is being photoevaporated and lost from the disks of these sources under the intense radiation and winds from θ^1 Ori C and the Trapezium Cluster, and therefore derive disk lifetimes for the protoplanetary disks in the ONC.

Table 7.2. Source Detections, Identifications and Fluxes

ID	Proplyd Name	HC00 ID	GMR ID	Z04a ID	Other Names	R.A. [J2000]	Dec [J2000]	$F_{\nu,6cm}$ [mJy]	$F_{\nu,3.6cm}$ [mJy]	$F_{\nu,1.3cm,1}$ [mJy][a]	$F_{\nu,1.3cm,2}$ [mJy][a]	$F_{\nu,1.3cm,3}$ [mJy]	$F_{\nu,1.3cm,4}$ [mJy][a]	$F_{\nu,1.3cm,mean}$ [mJy][a]
1	4538-311	—	—	—	—	5h34m53.79s	-5d23m10.73s	0.015 ± 0.567	···	···	···	···	···	···
2	—	—	—	—	—	5h34m55.97s	-5d23m13.00s	0.269 ± 0.338	···	···	···	···	···	···
3	4582-635	—	—	—	—	5h34m58.16s	-5d26m35.13s	-0.245 ± 0.409	···	···	···	···	···	···
4	005-514	—	—	—	—	5h35m00.47s	-5d25m14.34s	0.114 ± 0.233	···	···	···	···	···	···
5	006-439	—	—	—	—	5h35m00.58s	-5d24m38.79s	-0.008 ± 0.229	-0.049 ± 1.203	···	···	···	···	···
6	016-149	—	—	—	—	5h35m01.60s	-5d21m49.35s	-0.262 ± 0.274	-0.149 ± 0.884	···	···	···	···	···
7	038-627	—	—	—	—	5h35m04.19s	-5d26m27.89s	-0.061 ± 0.237	···	···	···	···	···	···
8	044-527	—	—	—	—	5h35m04.42s	-5d25m27.40s	0.006 ± 0.174	-0.091 ± 0.609	···	···	···	···	···
9	—	—	—	—	—	5h35m04.55s	-5d20m13.90s	0.255 ± 0.314	-0.843 ± 1.131	···	···	···	···	···
10	046-245	—	—	—	—	5h35m04.63s	-5d22m44.85s	0.022 ± 0.173	0.039 ± 0.368	···	···	···	0.126 ± 0.936	···
11	—	—	—	1	—	5h35m04.86s	-5d23m02.61s	4.790 ± 0.492	4.404 ± 0.463	2.643 ± 0.415	2.990 ± 0.426	3.169 ± 0.425	1.712 ± 0.262	2.554 ± 0.367
12	049-143	—	—	—	—	5h35m04.94s	-5d21m42.99s	0.095 ± 0.225	0.135 ± 0.444	···	···	···	···	···
13	053-717	—	—	—	—	5h35m05.40s	-5d27m16.99s	0.080 ± 0.254	···	···	···	···	···	···
14	057-419	—	—	—	—	5h35m05.73s	-5d24m18.55s	-0.098 ± 0.220	0.160 ± 0.331	0.116 ± 0.743	-0.019 ± 0.814	-0.064 ± 0.538	0.003 ± 0.178	-0.048 ± 0.267
15	061-401	—	—	—	—	5h35m06.09s	-5d24m00.60s	0.022 ± 0.176	-0.055 ± 0.350	-0.049 ± 0.680	-0.020 ± 0.643	-0.192 ± 0.472	0.021 ± 0.159	-0.029 ± 0.240
16	—	508	—	—	—	5h35m06.18s	-5d22m12.40s	-0.054 ± 0.183	0.181 ± 0.342	0.426 ± 3.794	-0.605 ± 3.254	-0.499 ± 1.532	-0.017 ± 1.483	-0.208 ± 0.854
17	—	601	—	—	—	5h35m06.21s	-5d21m35.90s	-0.068 ± 0.190	0.092 ± 0.367	···	-0.117 ± 2.957	-0.334 ± 2.154	···	-0.617 ± 1.151
18	—	538	—	—	—	5h35m06.28s	-5d22m02.63s	0.604 ± 0.105	0.536 ± 0.118	0.722 ± 3.353	0.170 ± 2.730	0.223 ± 1.664	0.318 ± 1.368	-0.061 ± 0.831
19	—	509	—	—	—	5h35m06.35s	-5d22m11.60s	0.015 ± 0.169	-0.058 ± 0.293	-0.187 ± 2.417	0.164 ± 0.948	-0.020 ± 1.658	-0.356 ± 1.323	0.425 ± 0.730
20	—	321	—	—	—	5h35m06.44s	-5d23m15.30s	0.052 ± 0.161	-0.086 ± 0.314	0.113 ± 1.030	-0.023 ± 2.732	0.057 ± 0.640	0.028 ± 0.228	0.093 ± 0.302
21	—	526	—	—	—	5h35m06.45s	-5d22m07.60s	0.038 ± 0.211	0.292 ± 0.343	-0.462 ± 2.676	···	0.499 ± 1.407	0.026 ± 1.409	0.290 ± 0.756
22	—	636	—	—	—	5h35m06.46s	-5d21m18.80s	0.022 ± 0.222	-0.261 ± 0.429	···	···	···	···	···
23	—	99	—	—	—	5h35m06.53s	-5d24m41.50s	-0.021 ± 0.152	0.114 ± 0.343	0.239 ± 0.837	0.092 ± 0.747	0.072 ± 0.649	-0.092 ± 0.178	-0.178 ± 0.289
24	—	116	—	—	—	5h35m06.53s	-5d24m33.30s	0.043 ± 0.147	0.099 ± 0.295	-0.052 ± 0.760	-0.074 ± 0.848	-0.088 ± 0.528	0.002 ± 0.185	-0.137 ± 0.242
25	—	742	—	—	—	5h35m06.54s	-5d22m28.60s	0.027 ± 0.193	0.014 ± 0.336	-0.804 ± 2.140	0.598 ± 2.413	-0.216 ± 1.313	-0.072 ± 0.753	-0.140 ± 0.605
26	—	60	—	—	—	5h35m06.55s	-5d25m01.70s	0.011 ± 0.163	-0.125 ± 0.423	-0.520 ± 1.617	0.179 ± 1.364	0.067 ± 0.872	-0.021 ± 0.305	-0.044 ± 0.446
27	066-652	—	—	—	—	5h35m06.59s	-5d26m51.99s	-0.017 ± 0.238	0.009 ± 0.999	···	···	···	···	···
28	—	741	—	—	—	5h35m06.67s	-5d22m44.60s	0.055 ± 0.164	0.084 ± 0.282	0.285 ± 1.806	0.340 ± 1.635	-0.072 ± 1.031	0.260 ± 0.586	0.319 ± 0.534
29	—	521	—	—	—	5h35m06.89s	-5d22m09.30s	0.018 ± 0.190	0.084 ± 0.344	0.366 ± 2.157	-0.163 ± 2.072	0.034 ± 1.167	-0.469 ± 0.989	0.026 ± 0.597
30	069-601	—	—	—	—	5h35m06.91s	-5d26m00.60s	-0.030 ± 0.165	0.186 ± 0.533	···	···	···	···	···
31	—	497	—	—	—	5h35m07.04s	-5d22m16.90s	0.035 ± 0.174	-0.020 ± 0.333	-0.164 ± 1.928	-0.081 ± 1.748	-0.248 ± 1.108	0.520 ± 0.872	0.025 ± 0.577
32	—	64	—	—	—	5h35m07.06s	-5d25m00.90s	-0.094 ± 0.178	0.067 ± 0.342	0.236 ± 1.232	-0.420 ± 1.245	-0.151 ± 0.882	-0.069 ± 0.290	-0.034 ± 0.383
33	—	715	—	—	—	5h35m07.17s	-5d24m45.80s	0.074 ± 0.169	0.008 ± 0.304	-0.163 ± 0.841	-0.219 ± 0.777	0.045 ± 0.582	-0.121 ± 0.222	-0.250 ± 0.303
34	072-135	603	—	—	—	5h35m07.21s	-5d21m34.42s	0.111 ± 0.193	-0.037 ± 0.330	1.628 ± 2.702	-0.884 ± 2.385	0.318 ± 1.816	0.024 ± 1.193	0.223 ± 0.751
35	—	534	—	—	—	5h35m07.24s	-5d22m03.90s	0.002 ± 0.198	0.094 ± 0.281	-0.475 ± 1.748	-0.068 ± 1.281	0.075 ± 0.995	-0.044 ± 0.742	0.038 ± 0.494

Table 7.2 (cont'd)

ID	Proplyd Name	HC00 ID	GMR ID	Z04a ID	Other Names	R.A. [J2000]	Dec [J2000]	$F_{\nu,6cm}$ [mJy]	$F_{\nu,3.6cm}$ [mJy]	$F_{\nu,1.3cm,1}$[a] [mJy]	$F_{\nu,1.3cm,2}$[a] [mJy]	$F_{\nu,1.3cm,3}$[a] [mJy]	$F_{\nu,1.3cm,4}$[a] [mJy]	$F_{\nu,1.3cm,mean}$[a] [mJy]
36	073-227	467	–	–	–	5h35m07.27s	-5d22m26.58s	0.057 ± 0.187	0.119 ± 0.299	0.243 ± 1.646	−0.155 ± 1.259	−0.071 ± 0.990	−0.206 ± 0.790	0.075 ± 0.444
37	–	459	–	–	–	5h35m07.39s	-5d22m29.00s	0.033 ± 0.175	-0.016 ± 0.281	-0.047 ± 1.333	−0.029 ± 1.240	−0.062 ± 0.849	0.187 ± 0.677	−0.031 ± 0.446
38	–	1	–	–	–	5h35m07.41s	-5d25m48.20s	0.001 ± 0.158	-0.038 ± 0.457	...	...	...	...	...
39	–	718	–	–	–	5h35m07.52s	-5d21m45.90s	0.021 ± 0.200	-0.182 ± 0.316	0.676 ± 1.776	−0.464 ± 1.411	−0.200 ± 1.067	−0.125 ± 0.898	−0.005 ± 0.551
40	–	777	–	–	–	5h35m07.57s	-5d22m00.50s	0.021 ± 0.177	-0.040 ± 0.257	-0.352 ± 1.642	−0.446 ± 1.263	0.027 ± 0.836	0.364 ± 0.809	0.122 ± 0.401
41	–	175	–	–	–	5h35m07.64s	-5d24m00.80s	0.089 ± 0.168	0.174 ± 0.218	0.006 ± 0.491	−0.025 ± 0.462	0.144 ± 0.350	−0.046 ± 0.137	−0.122 ± 0.189
42	–	85	–	–	–	5h35m07.71s	-5d24m53.00s	0.001 ± 0.151	-0.177 ± 0.338	-0.233 ± 0.861	0.083 ± 0.918	0.087 ± 0.639	−0.059 ± 0.192	−0.145 ± 0.301
43	–	667	–	–	–	5h35m07.74s	-5d21m01.50s	0.029 ± 0.210	-0.038 ± 0.381	...	...	...	...	...
44	–	625	–	–	–	5h35m07.74s	-5d21m27.10s	-0.029 ± 0.208	0.086 ± 0.424	-0.541 ± 2.599	−0.427 ± 2.418	−0.156 ± 1.226	−0.479 ± 1.062	−0.084 ± 0.726
45	–	670	–	–	–	5h35m07.84s	-5d21m00.40s	-0.056 ± 0.218	-0.038 ± 0.379	...	...	...	...	...
46	–	639	–	–	–	5h35m07.95s	-5d21m17.20s	-0.078 ± 0.220	-0.019 ± 0.367	-0.763 ± 3.085	−0.279 ± 2.775	0.624 ± 1.847	−0.149 ± 1.322	−0.295 ± 0.896
47	–	711	–	–	–	5h35m08.05s	-5d21m17.80s	-0.113 ± 0.233	0.097 ± 0.361	-0.698 ± 3.107	−0.345 ± 2.838	−0.149 ± 1.584	0.382 ± 1.563	−0.260 ± 0.804
48	–	743	–	–	–	5h35m08.10s	-5d23m15.20s	-0.079 ± 0.166	0.131 ± 0.239	-0.156 ± 0.569	−0.093 ± 0.598	0.177 ± 0.440	0.024 ± 0.178	0.022 ± 0.228
49	–	433	–	–	–	5h35m08.11s	-5d22m37.50s	-0.050 ± 0.201	-0.114 ± 0.231	0.088 ± 1.139	0.028 ± 0.942	−0.038 ± 0.659	0.137 ± 0.476	0.009 ± 0.321
50	–	166	–	–	–	5h35m08.23s	-5d24m03.30s	0.125 ± 0.157	-0.086 ± 0.232	0.027 ± 0.454	0.005 ± 0.434	−0.064 ± 0.339	0.015 ± 0.145	0.074 ± 0.166
51	–	693	–	–	–	5h35m08.23s	-5d20m46.90s	-0.097 ± 0.233	0.136 ± 0.412	...	...	...	...	...
52	–	400	–	–	–	5h35m08.24s	-5d22m52.80s	0.155 ± 0.161	0.048 ± 0.252	0.111 ± 0.962	−0.127 ± 0.780	−0.017 ± 0.577	0.294 ± 0.331	0.218 ± 0.268
53	–	725	–	–	–	5h35m08.27s	-5d23m07.80s	0.048 ± 0.172	0.061 ± 0.233	-0.162 ± 0.786	−0.060 ± 0.647	−0.006 ± 0.505	0.030 ± 0.209	0.038 ± 0.225
54	–	115	–	–	–	5h35m08.31s	-5d24m35.00s	-0.024 ± 0.167	0.052 ± 0.251	0.109 ± 0.616	−0.083 ± 0.616	−0.031 ± 0.430	−0.005 ± 0.140	−0.017 ± 0.210
55	–	740	–	–	–	5h35m08.32s	-5d21m02.40s	0.092 ± 0.230	0.036 ± 0.436	...	...	0.115 ± 2.149	−0.232 ± 1.577	0.314 ± 1.429
56	–	749	–	–	–	5h35m08.34s	-5d23m21.90s	-0.035 ± 0.167	0.198 ± 0.206	0.085 ± 0.560	0.034 ± 0.528	0.090 ± 0.457	−0.034 ± 0.142	−0.010 ± 0.237
57	–	454	–	–	–	5h35m08.42s	-5d22m30.30s	-0.059 ± 0.163	-0.141 ± 0.222	-0.281 ± 0.875	0.111 ± 0.877	−0.129 ± 0.587	0.106 ± 0.497	0.073 ± 0.297
58	–	634	–	–	–	5h35m08.43s	-5d21m19.80s	0.158 ± 0.210	0.048 ± 0.329	0.637 ± 2.122	−0.550 ± 2.156	−0.284 ± 1.242	0.537 ± 1.054	0.000 ± 0.608
59	–	353	–	–	–	5h35m08.44s	-5d23m05.00s	0.143 ± 0.186	0.197 ± 0.228	0.062 ± 0.773	0.069 ± 0.705	0.191 ± 0.554	0.015 ± 0.248	0.218 ± 0.276
60	–	100	–	–	–	5h35m08.53s	-5d24m41.70s	-0.028 ± 0.144	0.127 ± 0.284	-0.093 ± 0.647	0.073 ± 0.568	0.157 ± 0.456	−0.008 ± 0.157	0.040 ± 0.210
61	–	37	–	–	–	5h35m08.54s	-5d25m18.10s	-0.054 ± 0.141	0.033 ± 0.303	-0.006 ± 2.074	0.009 ± 1.935	0.190 ± 1.316	−0.004 ± 0.392	−0.076 ± 0.603
62	–	102	–	–	–	5h35m08.58s	-5d24m40.40s	0.020 ± 0.140	0.100 ± 0.260	-0.034 ± 0.626	0.132 ± 0.563	0.016 ± 0.478	−0.043 ± 0.157	−0.038 ± 0.217
63	–	290	–	–	–	5h35m08.62s	-5d23m24.40s	0.081 ± 0.170	-0.166 ± 0.252	-0.014 ± 0.550	0.090 ± 0.590	0.075 ± 0.423	−0.046 ± 0.186	−0.051 ± 0.190
64	–	382	–	–	–	5h35m08.74s	-5d22m56.70s	0.093 ± 0.159	0.019 ± 0.220	0.120 ± 0.750	0.200 ± 0.727	0.261 ± 0.468	0.018 ± 0.302	0.100 ± 0.248
65	–	455	–	–	–	5h35m08.93s	-5d22m30.00s	-0.101 ± 0.168	0.131 ± 0.280	-0.046 ± 0.706	0.119 ± 0.787	−0.186 ± 0.561	0.264 ± 0.580	−0.021 ± 0.271
66	090-326	724	–	–	–	5h35m09.03s	-5d23m26.25s	-0.103 ± 0.177	-0.080 ± 0.223	-0.074 ± 0.585	−0.005 ± 0.522	−0.055 ± 0.380	−0.045 ± 0.174	−0.006 ± 0.214
67	–	716	–	–	–	5h35m09.03s	-5d23m26.00s	-0.053 ± 0.145	0.030 ± 0.285	0.835 ± 2.727	−0.073 ± 2.716	−0.407 ± 1.609	−0.159 ± 0.458	−0.182 ± 0.813
68	–	717	–	–	–	5h35m09.20s	-5d25m31.90s	0.042 ± 0.174	-0.090 ± 0.296	...	...	0.357 ± 1.886	−0.170 ± 0.622	0.109 ± 0.900
69	–	592	–	–	–	5h35m09.35s	-5d21m41.52s	0.076 ± 0.149	-0.069 ± 0.246	0.060 ± 0.990	−0.299 ± 0.934	−0.131 ± 0.706	0.069 ± 0.574	0.907 ± 0.354
70	–	674	–	–	–	5h35m09.49s	-5d20m58.80s	-0.024 ± 0.231	0.037 ± 0.379	...	−0.620 ± 2.911	0.382 ± 1.919	−0.145 ± 1.734	0.198 ± 0.808

Table 7.2 (cont'd)

ID	Proplyd Name	HC00 ID	GMR ID	Z04a ID	Other Names	R.A. [J2000]	Dec [J2000]	$F_{\nu,6cm}$ [mJy]	$F_{\nu,3.6cm}$ [mJy]	$F_{\nu,1.3cm,1}$[a] [mJy]	$F_{\nu,1.3cm,2}$[a] [mJy]	$F_{\nu,1.3cm,3}$[a] [mJy]	$F_{\nu,1.3cm,4}$[a] [mJy]	$F_{\nu,1.3cm,mean}$[a] [mJy]
71	—	579	—	—	—	5h35m09.53s	-5d21m48.10s	-0.121 ± 0.161	-0.049 ± 0.271	0.038 ± 0.731	0.166 ± 0.671	0.052 ± 0.566	0.161 ± 0.554	0.221 ± 0.276
72	093-822	—	—	—	—	5h35m09.59s	-5d28m22.92s	-0.017 ± 0.348	...	...	...	...	...	...
73	—	186	—	—	—	5h35m09.68s	-5d23m55.90s	-0.019 ± 0.147	-0.010 ± 0.204	0.117 ± 0.469	0.007 ± 0.446	0.076 ± 0.343	-0.013 ± 0.122	0.075 ± 0.167
74	—	627	—	—	—	5h35m09.70s	-5d21m24.90s	0.035 ± 0.177	-0.000 ± 0.302	-0.283 ± 1.434	-0.650 ± 1.193	-0.604 ± 0.794	-0.264 ± 0.801	-0.271 ± 0.434
75	—	748	—	—	—	5h35m09.70s	-5d21m52.10s	0.017 ± 0.188	0.096 ± 0.299	0.124 ± 0.697	0.075 ± 0.675	-0.057 ± 0.481	0.159 ± 0.465	0.163 ± 0.293
76	—	283	—	—	—	5h35m09.77s	-5d23m26.89s	0.410 ± 0.072	0.538 ± 0.118	0.233 ± 0.048	0.337 ± 0.065	0.167 ± 0.069	0.037 ± 0.147	0.150 ± 0.025
77	—	621	—	2	—	5h35m09.77s	-5d21m28.29s	0.268 ± 0.072	-0.034 ± 0.320	0.063 ± 1.083	-0.251 ± 1.178	0.618 ± 0.112	-0.283 ± 0.695	0.261 ± 0.072
78	—	722	—	—	—	5h35m09.79s	-5d24m06.70s	-0.028 ± 0.158	-0.008 ± 0.235	-0.005 ± 0.446	-0.009 ± 0.324	-0.005 ± 0.291	-0.056 ± 0.124	-0.052 ± 0.133
79	099-339	243	—	—	—	5h35m09.90s	-5d23m38.50s	-0.027 ± 0.163	0.067 ± 0.197	-0.234 ± 0.454	0.023 ± 0.435	-0.080 ± 0.377	0.033 ± 0.133	-0.053 ± 0.184
80	—	630	—	—	—	5h35m09.90s	-5d21m22.50s	-0.001 ± 0.199	0.064 ± 0.263	0.226 ± 1.337	0.035 ± 1.171	-0.226 ± 0.875	0.025 ± 0.836	-0.187 ± 0.490
81	—	723	—	—	—	5h35m09.91s	-5d24m10.50s	0.050 ± 0.149	-0.009 ± 0.226	-0.080 ± 0.503	0.030 ± 0.460	0.066 ± 0.346	0.005 ± 0.105	0.059 ± 0.199
82	—	588	—	—	—	5h35m09.93s	-5d21m43.40s	0.004 ± 0.178	-0.130 ± 0.271	-0.068 ± 0.749	0.038 ± 0.764	-0.256 ± 0.485	-0.124 ± 0.481	-0.292 ± 0.307
83	—	179	—	—	—	5h35m09.94s	-5d23m59.00s	-0.071 ± 0.150	0.130 ± 0.219	-0.090 ± 0.453	-0.028 ± 0.414	0.071 ± 0.344	-0.012 ± 0.136	-0.026 ± 0.183
84	—	62	—	—	—	5h35m10.03s	-5d25m01.50s	-0.019 ± 0.166	-0.046 ± 0.243	-0.195 ± 1.167	0.530 ± 1.128	0.141 ± 0.685	-0.022 ± 0.243	0.060 ± 0.447
85	—	173	—	—	—	5h35m10.04s	-5d24m02.00s	-0.021 ± 0.147	0.139 ± 0.192	0.135 ± 0.411	-0.128 ± 0.410	0.042 ± 0.365	-0.014 ± 0.112	-0.009 ± 0.166
86	—	26	—	—	—	5h35m10.08s	-5d25m31.50s	0.009 ± 0.172	0.084 ± 0.272	...	...	0.171 ± 2.139	-0.189 ± 0.710	-0.013 ± 1.019
87	102-233	445	—	—	—	5h35m10.14s	-5d22m32.72s	0.106 ± 0.173	0.112 ± 0.199	0.171 ± 0.539	0.274 ± 0.525	-0.038 ± 0.419	0.008 ± 0.461	0.165 ± 0.196
88	102-021	—	—	—	—	5h35m10.19s	-5d20m20.99s	0.131 ± 0.248	0.251 ± 0.517	...	...	...	...	...
89	—	671	—	—	—	5h35m10.20s	-5d21m00.40s	0.025 ± 0.192	-0.293 ± 0.364	-0.462 ± 2.560	-0.738 ± 2.363	0.720 ± 1.405	0.531 ± 1.337	0.047 ± 0.719
90	102-322	305	—	—	—	5h35m10.21s	-5d23m21.58s	0.052 ± 0.176	-0.036 ± 0.206	-0.098 ± 0.606	-0.065 ± 0.508	0.087 ± 0.382	-0.029 ± 0.198	-0.094 ± 0.206
91	—	553	—	—	—	5h35m10.27s	-5d21m57.20s	-0.141 ± 0.174	-0.017 ± 0.242	-0.034 ± 0.579	-0.014 ± 0.519	0.000 ± 0.395	-0.160 ± 0.438	0.099 ± 0.203
92	—	320	—	—	—	5h35m10.27s	-5d23m16.40s	0.042 ± 0.172	-0.010 ± 0.222	0.104 ± 0.600	-0.045 ± 0.552	0.076 ± 0.428	0.013 ± 0.234	-0.094 ± 0.202
93	—	144	—	—	—	5h35m10.31s	-5d24m17.50s	0.055 ± 0.154	-0.016 ± 0.170	-0.122 ± 0.473	-0.176 ± 0.493	-0.041 ± 0.381	-0.064 ± 0.129	-0.126 ± 0.192
94	—	647	—	—	—	5h35m10.32s	-5d21m13.10s	-0.206 ± 0.197	-0.036 ± 0.293	-0.553 ± 1.511	-0.183 ± 1.522	-0.005 ± 1.113	0.027 ± 0.885	0.177 ± 0.382
95	—	90	—	—	—	5h35m10.38s	-5d24m51.60s	0.067 ± 0.162	-0.061 ± 0.204	-0.150 ± 0.895	-0.168 ± 0.831	-0.177 ± 0.567	-0.002 ± 0.201	-0.179 ± 0.346
96	—	374	—	—	—	5h35m10.39s	-5d22m59.80s	-0.040 ± 0.166	-0.036 ± 0.189	0.103 ± 0.575	-0.073 ± 0.670	-0.022 ± 0.423	-0.043 ± 0.305	-0.074 ± 0.194
97	—	—	—	—	—	5h35m10.43s	-5d24m30.30s	0.112 ± 0.139	0.103 ± 0.211	0.160 ± 0.607	0.075 ± 0.580	-0.075 ± 0.405	-0.010 ± 0.155	0.194 ± 0.043
98	—	605	—	—	—	5h35m10.43s	-5d21m34.60s	0.088 ± 0.183	-0.005 ± 0.270	-0.234 ± 0.817	0.053 ± 0.765	-0.127 ± 0.650	-0.374 ± 0.689	-0.128 ± 0.314
99	—	466	—	—	—	5h35m10.45s	-5d22m27.30s	-0.048 ± 0.165	0.086 ± 0.179	0.045 ± 0.508	0.017 ± 0.508	-0.099 ± 0.414	0.006 ± 0.398	-0.122 ± 0.201
100	—	570	—	—	—	5h35m10.47s	-5d21m49.60s	0.026 ± 0.193	0.109 ± 0.243	-0.024 ± 0.679	0.159 ± 0.622	0.203 ± 0.462	-0.268 ± 0.473	-0.061 ± 0.233
101	—	612	—	—	—	5h35m10.47s	-5d21m32.50s	0.056 ± 0.195	-0.047 ± 0.272	-0.050 ± 0.969	-0.075 ± 0.776	-0.379 ± 0.619	0.036 ± 0.625	-0.097 ± 0.286
102	—	417	—	3	—	5h35m10.49s	-5d22m45.75s	0.062 ± 0.132	0.153 ± 0.232	-0.035 ± 0.533	0.041 ± 0.519	-0.082 ± 0.399	-0.029 ± 0.396	0.077 ± 0.212
103	—	—	—	—	—	5h35m10.51s	-5d22m25.01s	0.186 ± 0.154	-0.337 ± 0.210	0.154 ± 0.526	-0.017 ± 0.489	0.185 ± 0.052	-0.027 ± 0.393	0.095 ± 0.201
104	—	8	—	—	—	5h35m10.52s	-5d25m44.60s	-0.071 ± 0.163	-0.166 ± 0.326	...	...	...	...	...
105	—	500	—	—	—	5h35m10.54s	-5d22m16.60s	0.008 ± 0.161	0.044 ± 0.200	-0.027 ± 0.506	-0.169 ± 0.470	0.091 ± 0.433	-0.252 ± 0.399	-0.146 ± 0.208

185

Table 7.2 (cont'd)

ID	Proplyd Name	HC00 ID	GMR ID	Z04a ID	Other Names	R.A. [J2000]	Dec [J2000]	$F_{\nu,6cm}$ [mJy]	$F_{\nu,3.6cm}$ [mJy]	$F_{\nu,1.3cm,1}$[a] [mJy]	$F_{\nu,1.3cm,2}$[a] [mJy]	$F_{\nu,1.3cm,3}$[a] [mJy]	$F_{\nu,1.3cm,4}$[a] [mJy]	$F_{\nu,1.3cm,mean}$[a] [mJy]
106	106-417	146	–	–	–	5h35m10.55s	-5d24m16.75s	0.009 ± 0.149	−0.071 ± 0.196	0.047 ± 0.443	−0.003 ± 0.443	0.016 ± 0.377	−0.023 ± 0.118	−0.010 ± 0.171
107	–	421	–	–	–	5h35m10.58s	-5d22m44.80s	0.084 ± 0.130	−0.004 ± 0.214	0.004 ± 0.572	0.040 ± 0.529	0.043 ± 0.411	−0.071 ± 0.426	0.025 ± 0.219
108	106-156	554	–	–	–	5h35m10.58s	-5d21m56.27s	0.196 ± 0.199	0.118 ± 0.260	0.145 ± 0.615	0.123 ± 0.522	0.013 ± 0.441	0.369 ± 0.485	0.238 ± 0.260
109	–	385	–	–	–	5h35m10.62s	-5d22m56.06s	−0.028 ± 0.165	0.167 ± 0.239	−0.109 ± 0.634	−0.138 ± 0.577	−0.031 ± 0.494	0.191 ± 0.397	0.135 ± 0.545
110	–	2	–	–	–	5h35m10.63s	-5d25m48.10s	0.016 ± 0.171	0.003 ± 0.305	· · ·	· · ·	· · ·	· · ·	· · ·
111	–	363	–	–	–	5h35m10.65s	-5d23m03.40s	0.162 ± 0.133	−0.200 ± 0.193	0.030 ± 0.657	−0.081 ± 0.560	0.094 ± 0.393	−0.053 ± 0.301	−0.034 ± 0.218
112	–	260	–	–	–	5h35m10.69s	-5d23m32.80s	0.033 ± 0.165	0.084 ± 0.241	0.069 ± 0.673	0.121 ± 0.462	−0.020 ± 0.398	0.012 ± 0.170	−0.081 ± 0.216
113	–	489	–	–	–	5h35m10.71s	-5d22m20.30s	−0.029 ± 0.139	0.196 ± 0.212	0.148 ± 0.522	0.219 ± 0.456	0.079 ± 0.397	0.094 ± 0.472	0.095 ± 0.168
114	–	392	–	–	–	5h35m10.73s	-5d22m54.50s	0.046 ± 0.146	0.161 ± 0.199	−0.127 ± 0.561	0.159 ± 0.526	−0.163 ± 0.437	−0.068 ± 0.354	0.019 ± 0.202
115	–	224	–	4	–	5h35m10.73s	-5d23m44.67s	0.401 ± 0.077	0.374 ± 0.067	0.160 ± 0.038	0.004 ± 0.481	0.313 ± 0.066	0.543 ± 0.083	0.838 ± 0.202
116	–	576	–	–	–	5h35m10.82s	-5d21m48.90s	−0.027 ± 0.149	0.279 ± 0.245	0.201 ± 0.608	0.042 ± 0.566	−0.085 ± 0.470	0.169 ± 0.525	0.190 ± 0.207
117	–	426	–	–	–	5h35m10.85s	-5d22m40.80s	0.066 ± 0.160	−0.108 ± 0.196	0.062 ± 0.544	−0.066 ± 0.556	0.023 ± 0.335	0.170 ± 0.383	−0.018 ± 0.220
118	–	529	–	–	–	5h35m10.88s	-5d22m06.00s	−0.022 ± 0.167	0.060 ± 0.218	−0.080 ± 0.476	−0.022 ± 0.471	0.087 ± 0.399	0.025 ± 0.435	−0.058 ± 0.216
119	109-246	416	–	–	–	5h35m10.90s	-5d22m46.38s	0.088 ± 0.159	0.037 ± 0.234	0.077 ± 0.535	0.100 ± 0.558	0.032 ± 0.441	0.021 ± 0.449	0.170 ± 0.228
120	109-327	286	–	–	–	5h35m10.95s	-5d23m26.58s	0.132 ± 0.172	−0.002 ± 0.207	0.310 ± 0.595	0.420 ± 0.573	0.225 ± 0.411	0.212 ± 0.202	0.462 ± 0.205
121	–	93	–	–	–	5h35m10.95s	-5d24m48.80s	−0.047 ± 0.117	0.108 ± 0.223	−0.092 ± 0.998	0.089 ± 0.809	−0.113 ± 0.620	0.130 ± 0.212	0.065 ± 0.316
122	–	582	–	–	–	5h35m10.97s	-5d21m46.40s	−0.122 ± 0.175	0.055 ± 0.262	0.258 ± 0.667	0.074 ± 0.569	0.076 ± 0.483	−0.071 ± 0.492	0.259 ± 0.253
123	–	473	–	–	–	5h35m10.99s	-5d22m24.80s	0.006 ± 0.152	0.015 ± 0.207	−0.061 ± 0.437	−0.180 ± 0.463	−0.055 ± 0.400	−0.104 ± 0.356	0.022 ± 0.177
124	–	415	–	–	–	5h35m11.04s	-5d22m46.70s	−0.006 ± 0.159	−0.022 ± 0.210	−0.102 ± 0.568	−0.047 ± 0.505	−0.065 ± 0.368	0.217 ± 0.434	−0.079 ± 0.189
125	–	329	–	–	–	5h35m11.09s	-5d23m14.70s	0.026 ± 0.150	0.187 ± 0.197	−0.288 ± 0.612	0.034 ± 0.640	0.003 ± 0.402	−0.050 ± 0.285	−0.186 ± 0.226
126	–	111	–	–	–	5h35m11.15s	-5d24m36.50s	−0.034 ± 0.175	−0.079 ± 0.185	0.016 ± 0.740	−0.033 ± 0.722	−0.008 ± 0.517	0.034 ± 0.191	−0.063 ± 0.244
127	–	24	–	–	–	5h35m11.16s	-5d25m32.30s	−0.104 ± 0.134	0.171 ± 0.223	· · ·	· · ·	−1.142 ± 1.779	0.120 ± 0.654	0.014 ± 0.867
128	–	434	–	–	–	5h35m11.20s	-5d22m37.80s	0.045 ± 0.159	0.012 ± 0.209	0.053 ± 0.461	0.026 ± 0.514	−0.061 ± 0.361	0.103 ± 0.417	0.110 ± 0.185
129	–	515	–	–	–	5h35m11.21s	-5d22m10.80s	−0.023 ± 0.147	−0.160 ± 0.199	0.052 ± 0.534	0.202 ± 0.449	−0.024 ± 0.420	0.008 ± 0.440	0.007 ± 0.185
130	–	148	–	–	–	5h35m11.27s	-5d24m16.50s	−0.031 ± 0.147	−0.013 ± 0.180	−0.125 ± 0.567	0.073 ± 0.557	−0.007 ± 0.409	−0.129 ± 0.166	−0.183 ± 0.184
131	–	666	–	–	–	5h35m11.29s	-5d21m03.10s	−0.057 ± 0.219	0.028 ± 0.282	−1.066 ± 1.890	−0.197 ± 1.818	−0.167 ± 1.384	0.264 ± 1.233	−0.061 ± 0.659
132	114-426	127	–	–	–	5h35m11.32s	-5d24m26.54s	0.056 ± 0.167	−0.017 ± 0.196	0.172 ± 0.647	0.045 ± 0.708	0.096 ± 0.432	−0.018 ± 0.200	0.004 ± 0.220
133	–	643	–	–	–	5h35m11.32s	-5d21m15.60s	−0.020 ± 0.191	0.057 ± 0.293	0.006 ± 1.324	−0.022 ± 1.203	−0.284 ± 0.822	0.213 ± 0.724	0.017 ± 0.386
134	113-438	105	–	–	–	5h35m11.32s	-5d24m38.22s	0.014 ± 0.138	0.038 ± 0.188	−0.183 ± 0.764	−0.101 ± 0.663	0.086 ± 0.529	0.195 ± 0.057	0.210 ± 0.267
135	–	559	–	–	–	5h35m11.37s	-5d21m54.00s	0.024 ± 0.176	0.126 ± 0.223	0.150 ± 0.605	−0.159 ± 0.503	−0.089 ± 0.409	0.104 ± 0.458	−0.089 ± 0.213
136	–	750	–	–	–	5h35m11.42s	-5d21m44.60s	0.129 ± 0.161	0.060 ± 0.251	0.138 ± 0.627	−0.102 ± 0.634	0.178 ± 0.466	−0.169 ± 0.462	−0.067 ± 0.264
137	–	203	–	–	–	5h35m11.48s	-5d23m52.10s	−0.037 ± 0.147	−0.004 ± 0.196	0.070 ± 0.552	−0.356 ± 0.537	0.070 ± 0.360	0.023 ± 0.178	0.079 ± 0.183
138	–	720	–	–	–	5h35m11.51s	-5d23m05.80s	−0.065 ± 0.156	0.033 ± 0.232	0.320 ± 1.558	−0.158 ± 1.726	−0.101 ± 0.925	−0.098 ± 0.328	−0.058 ± 0.407
139	–	656	–	–	–	5h35m11.51s	-5d21m06.40s	−0.040 ± 0.195	−0.024 ± 0.305	0.145 ± 1.691	0.440 ± 1.820	−0.159 ± 1.121	0.079 ± 0.999	0.265 ± 0.538
140	–	69	–	–	–	5h35m11.54s	-5d25m00.00s	0.094 ± 0.136	−0.037 ± 0.234	−0.578 ± 1.138	0.035 ± 1.235	0.064 ± 0.773	−0.012 ± 0.311	−0.214 ± 0.369

186

Table 7.2 (cont'd)

ID	Proplyd Name	HC00 ID	GMR ID	Z04a ID	Other Names	R.A. [J2000]	Dec [J2000]	$F_{\nu,6cm}$ [mJy]	$F_{\nu,3.6cm}$ [mJy]	$F_{\nu,1.3cm,1}$ [mJy] [a]	$F_{\nu,1.3cm,2}$ [mJy] [a]	$F_{\nu,1.3cm,3}$ [mJy] [a]	$F_{\nu,1.3cm,4}$ [mJy] [a]	$F_{\nu,1.3cm,mean}$ [mJy] [a]
141	—	94	—	—	—	5h35m11.56s	-5d24m48.20s	-0.092 ± 0.152	0.093 ± 0.216	-0.173 ± 0.944	-0.062 ± 0.870	0.114 ± 0.600	-0.008 ± 0.200	0.047 ± 0.301
142	—	404	—	—	—	5h35m11.63s	-5d22m51.70s	-0.084 ± 0.168	-0.016 ± 0.178	-0.032 ± 0.572	0.165 ± 0.531	0.140 ± 0.346	0.178 ± 0.436	0.112 ± 0.188
143	—	709	—	—	—	5h35m11.63s	-5d22m46.10s	-0.014 ± 0.173	0.064 ± 0.225	-0.239 ± 0.473	-0.111 ± 0.533	0.068 ± 0.421	-0.123 ± 0.423	-0.165 ± 0.190
144	117-421	140	—	—	—	5h35m11.65s	-5d24m21.55s	-0.018 ± 0.130	0.015 ± 0.190	-0.062 ± 0.594	-0.016 ± 0.549	0.069 ± 0.484	-0.076 ± 0.180	-0.027 ± 0.261
145	—	767	—	—	—	5h35m11.68s	-5d23m36.00s	-0.068 ± 0.150	0.226 ± 0.211	0.032 ± 0.689	-0.310 ± 0.548	-0.122 ± 0.429	0.083 ± 0.219	0.006 ± 0.182
146	—	238	—	—	—	5h35m11.72s	-5d23m40.50s	0.006 ± 0.147	-0.087 ± 0.176	-0.184 ± 0.596	-0.160 ± 0.576	0.286 ± 0.422	0.012 ± 0.190	-0.085 ± 0.207
147	—	539	—	—	—	5h35m11.72s	-5d22m03.10s	0.075 ± 0.156	-0.018 ± 0.226	-0.012 ± 0.474	-0.047 ± 0.467	-0.026 ± 0.391	0.134 ± 0.477	-0.007 ± 0.207
148	—	44	—	—	—	5h35m11.73s	-5d25m12.86s	0.019 ± 0.160	0.180 ± 0.073	-0.016 ± 1.732	-0.277 ± 2.013	0.145 ± 1.010	-0.043 ± 0.339	-0.155 ± 0.521
149	—	267	—	—	—	5h35m11.73s	-5d23m30.50s	-0.104 ± 0.177	0.198 ± 0.199	-0.003 ± 0.758	-0.007 ± 0.535	0.030 ± 0.441	0.072 ± 0.243	0.040 ± 0.231
150	—	257	—	—	—	5h35m11.73s	-5d23m33.50s	0.096 ± 0.196	-0.074 ± 0.192	0.268 ± 0.733	-0.262 ± 0.542	-0.123 ± 0.439	0.091 ± 0.195	0.173 ± 0.209
151	117-352	205	—	5	—	5h35m11.74s	-5d23m51.63s	0.929 ± 0.187	0.496 ± 0.184	0.224 ± 0.552	0.377 ± 0.594	0.129 ± 0.049	0.416 ± 0.185	0.754 ± 0.894
152	—	611	—	—	—	5h35m11.77s	-5d21m32.80s	-0.071 ± 0.190	-0.010 ± 0.249	0.137 ± 0.808	-0.272 ± 0.753	0.347 ± 0.587	0.146 ± 0.576	0.016 ± 0.207
153	—	555	—	—	—	5h35m11.79s	-5d21m55.60s	-0.023 ± 0.151	-0.076 ± 0.261	0.068 ± 0.552	-0.125 ± 0.481	0.165 ± 0.341	-0.107 ± 0.494	0.071 ± 0.206
154	—	573	A	6	—	5h35m11.81s	-5d21m49.24s	3.039 ± 0.316	2.935 ± 0.302	4.304 ± 0.441	5.418 ± 0.551	1.540 ± 0.168	3.899 ± 0.447	2.872 ± 0.292
155	—	672	—	—	—	5h35m11.86s	-5d21m00.30s	0.174 ± 0.189	-0.016 ± 0.294	-0.895 ± 2.113	-0.202 ± 1.897	0.635 ± 1.189	-0.332 ± 0.950	-0.250 ± 0.659
156	—	664	—	—	—	5h35m11.90s	-5d21m03.40s	0.006 ± 0.242	-0.003 ± 0.296	0.300 ± 1.806	0.115 ± 1.864	0.103 ± 1.177	0.055 ± 1.078	0.013 ± 0.550
157	119-340	—	—	—	—	5h35m11.90s	-5d23m39.70s	0.029 ± 0.158	-0.123 ± 0.171	-0.287 ± 0.621	-0.052 ± 0.602	0.293 ± 0.438	0.071 ± 0.214	0.012 ± 0.213
158	—	708	—	—	—	5h35m11.92s	-5d22m50.90s	0.016 ± 0.178	0.011 ± 0.190	-0.301 ± 0.564	-0.123 ± 0.523	0.212 ± 0.466	-0.007 ± 0.376	-0.002 ± 0.213
159	—	569	—	—	—	5h35m11.93s	-5d21m50.10s	-0.037 ± 0.155	-0.123 ± 0.240	-0.008 ± 0.638	-0.114 ± 0.648	0.170 ± 0.480	0.199 ± 0.494	0.132 ± 0.267
160	—	536	—	—	—	5h35m11.94s	-5d22m04.10s	-0.122 ± 0.196	0.064 ± 0.199	0.115 ± 0.506	-0.070 ± 0.496	0.041 ± 0.324	0.030 ± 0.451	-0.016 ± 0.223
161	—	395	—	—	—	5h35m11.98s	-5d22m54.13s	-0.044 ± 0.160	0.099 ± 0.177	0.185 ± 0.604	0.094 ± 0.626	0.132 ± 0.420	-0.046 ± 0.394	0.153 ± 0.157
162	—	772	—	—	—	5h35m11.98s	-5d22m08.00s	-0.072 ± 0.157	0.123 ± 0.206	-0.166 ± 0.495	0.098 ± 0.488	0.053 ± 0.351	-0.063 ± 0.439	-0.092 ± 0.209
163	121-1925	—	—	—	—	5h35m12.09s	-5d19m24.80s	0.022 ± 0.283	-0.052 ± 0.903	$\cdots$	$\cdots$	$\cdots$	$\cdots$	$\cdots$
164	—	95	—	—	—	5h35m12.12s	-5d24m48.00s	-0.024 ± 0.125	-0.029 ± 0.183	-0.174 ± 0.984	-0.324 ± 1.005	-0.120 ± 0.549	0.100 ± 0.242	0.017 ± 0.324
165	121-434	117	—	—	—	5h35m12.12s	-5d24m33.85s	0.060 ± 0.122	0.162 ± 0.170	-0.083 ± 0.828	0.108 ± 0.696	0.080 ± 0.485	-0.012 ± 0.229	-0.017 ± 0.245
166	—	746	—	—	—	5h35m12.14s	-5d21m48.50s	-0.089 ± 0.165	0.060 ± 0.221	-0.067 ± 0.620	0.020 ± 0.578	-0.092 ± 0.452	-0.222 ± 0.479	0.051 ± 0.255
167	—	263	—	—	—	5h35m12.15s	-5d23m32.00s	-0.149 ± 0.150	0.047 ± 0.182	-0.255 ± 0.725	0.146 ± 0.715	0.082 ± 0.470	-0.129 ± 0.264	-0.112 ± 0.209
168	—	747	—	—	—	5h35m12.16s	-5d21m53.80s	-0.050 ± 0.154	0.136 ± 0.219	0.015 ± 0.544	-0.218 ± 0.572	-0.157 ± 0.438	0.291 ± 0.428	0.060 ± 0.208
169	—	88	—	—	—	5h35m12.17s	-5d24m52.20s	-0.034 ± 0.147	-0.033 ± 0.175	0.181 ± 1.181	-0.053 ± 0.952	-0.264 ± 0.645	-0.025 ± 0.279	-0.218 ± 0.329
170	—	751	—	—	—	5h35m12.20s	-5d22m30.80s	-0.036 ± 0.160	-0.006 ± 0.187	0.144 ± 0.422	-0.224 ± 0.496	-0.077 ± 0.403	0.111 ± 0.502	-0.181 ± 0.187
171	—	77	—	—	—	5h35m12.21s	-5d24m56.50s	-0.111 ± 0.140	-0.024 ± 0.176	-0.383 ± 1.199	0.260 ± 1.255	0.125 ± 0.581	0.040 ± 0.280	0.041 ± 0.320
172	—	72	—	—	—	5h35m12.25s	-5d24m58.80s	-0.078 ± 0.160	-0.021 ± 0.208	-0.090 ± 1.331	-0.418 ± 1.124	0.157 ± 0.797	-0.001 ± 0.281	-0.122 ± 0.347
173	—	752	—	—	—	5h35m12.27s	-5d22m26.96s	-0.031 ± 0.169	0.060 ± 0.168	-0.041 ± 0.524	0.135 ± 0.042	-0.168 ± 0.391	-0.245 ± 0.390	-0.103 ± 0.187
174	—	698	—	—	—	5h35m12.28s	-5d20m45.20s	0.061 ± 0.216	-0.028 ± 0.337	$\cdots$	$\cdots$	-0.019 ± 2.334	-0.013 ± 1.811	-0.118 ± 1.203
175	—	215	—	—	—	5h35m12.28s	-5d23m48.10s	-0.083 ± 0.177	-0.026 ± 0.232	-0.446 ± 0.668	-0.009 ± 0.654	0.250 ± 0.400	-0.026 ± 0.236	-0.156 ± 0.227

Table 7.2 (cont'd)

ID	Proplyd Name	HC00 ID	GMR ID	Z04a ID	Other Names	R.A. [J2000]	Dec [J2000]	$F_{\nu,6cm}$ [mJy]	$F_{\nu,3.6cm}$ [mJy]	$F_{\nu,1.3cm,1}$ [mJy] [a]	$F_{\nu,1.3cm,2}$ [mJy] [a]	$F_{\nu,1.3cm,3}$ [mJy] [a]	$F_{\nu,1.3cm,4}$ [mJy] [a]	$F_{\nu,1.3cm,mean}$ [mJy] [a]
176	—	762	—	—	—	5h35m12.37s	-5d21m54.80s	0.075 ± 0.167	−0.076 ± 0.211	0.191 ± 0.501	0.001 ± 0.566	0.185 ± 0.387	0.329 ± 0.373	0.154 ± 0.204
177	124-132	616	—	—	—	5h35m12.38s	-5d21m31.49s	0.076 ± 0.169	−0.005 ± 0.223	0.056 ± 0.840	0.134 ± 0.871	−0.113 ± 0.556	0.283 ± 0.532	0.082 ± 0.316
178	—	206	—	—	—	5h35m12.39s	-5d23m51.70s	−0.017 ± 0.175	0.023 ± 0.222	0.193 ± 0.645	−0.129 ± 0.613	0.222 ± 0.451	0.052 ± 0.257	0.107 ± 0.245
179	—	692	—	—	—	5h35m12.40s	-5d20m47.90s	0.046 ± 0.196	0.045 ± 0.304	⋯	⋯	0.262 ± 2.116	−0.690 ± 1.990	−0.695 ± 0.992
180	—	753	—	—	—	5h35m12.43s	-5d22m08.70s	0.071 ± 0.175	0.085 ± 0.193	0.096 ± 0.520	−0.218 ± 0.537	0.115 ± 0.384	−0.293 ± 0.443	−0.144 ± 0.193
181	—	761	—	—	—	5h35m12.46s	-5d21m37.80s	0.038 ± 0.162	−0.066 ± 0.202	0.069 ± 0.651	−0.126 ± 0.644	0.063 ± 0.529	0.030 ± 0.501	0.025 ± 0.246
182	—	169	—	—	—	5h35m12.47s	-5d24m03.70s	0.036 ± 0.207	0.050 ± 0.174	−0.064 ± 0.685	−0.168 ± 0.644	−0.232 ± 0.497	0.008 ± 0.255	0.144 ± 0.201
183	—	106	—	—	—	5h35m12.49s	-5d24m38.10s	−0.019 ± 0.156	−0.061 ± 0.171	0.052 ± 0.825	0.191 ± 0.855	0.055 ± 0.456	−0.052 ± 0.233	−0.046 ± 0.279
184	—	368	33	—	—	5h35m12.56s	-5d23m02.04s	−0.165 ± 0.156	0.106 ± 0.210	0.119 ± 0.693	0.140 ± 0.621	−0.025 ± 0.456	−0.068 ± 0.362	−0.222 ± 0.233
185	—	228	—	—	—	5h35m12.60s	-5d23m44.20s	0.057 ± 0.187	−0.009 ± 0.192	−0.156 ± 0.703	0.034 ± 0.723	0.024 ± 0.415	−0.062 ± 0.283	−0.241 ± 0.242
186	—	696	—	—	—	5h35m12.65s	-5d20m47.30s	0.084 ± 0.181	−0.087 ± 0.311	⋯	⋯	1.223 ± 2.178	−0.688 ± 1.982	−0.459 ± 1.057
187	—	609	—	—	—	5h35m12.67s	-5d21m33.40s	0.039 ± 0.186	−0.029 ± 0.270	−0.160 ± 0.687	0.310 ± 0.865	0.158 ± 0.597	0.007 ± 0.606	0.200 ± 0.286
188	—	770	—	—	—	5h35m12.68s	-5d21m47.60s	−0.070 ± 0.164	0.065 ± 0.192	0.152 ± 0.591	0.403 ± 0.656	0.042 ± 0.509	0.131 ± 0.448	0.236 ± 0.192
189	—	128	—	—	—	5h35m12.70s	-5d24m26.50s	−0.034 ± 0.140	−0.028 ± 0.179	−0.239 ± 0.747	−0.008 ± 0.712	−0.008 ± 0.470	−0.122 ± 0.232	−0.111 ± 0.214
190	—	–	—	—	—	5h35m12.72s	-5d23m53.09s	0.336 ± 0.090	0.064 ± 0.201	0.529 ± 0.680	0.376 ± 0.630	0.237 ± 0.415	−0.074 ± 0.285	−0.018 ± 0.255
191	—	712	—	—	—	5h35m12.77s	-5d21m58.90s	−0.064 ± 0.142	0.112 ± 0.225	−0.199 ± 0.592	−0.059 ± 0.604	−0.052 ± 0.417	0.195 ± 0.409	0.066 ± 0.232
192	—	706	—	—	—	5h35m12.79s	-5d21m57.90s	0.008 ± 0.176	−0.028 ± 0.202	−0.025 ± 0.505	0.075 ± 0.570	−0.181 ± 0.453	0.090 ± 0.439	−0.022 ± 0.215
193	—	699	—	—	—	5h35m12.83s	-5d20m43.60s	0.098 ± 0.209	−0.000 ± 0.396	⋯	⋯	0.291 ± 2.280	⋯	0.494 ± 1.260
194	—	606	—	—	—	5h35m12.85s	-5d21m33.90s	−0.064 ± 0.196	0.086 ± 0.245	0.030 ± 0.875	−0.141 ± 0.789	0.038 ± 0.603	0.062 ± 0.630	0.122 ± 0.293
195	—	659	—	—	—	5h35m12.86s	-5d21m05.00s	0.134 ± 0.193	−0.045 ± 0.286	0.059 ± 1.972	−0.013 ± 1.500	0.280 ± 1.156	0.541 ± 0.939	0.417 ± 0.519
196	—	608	—	—	—	5h35m12.89s	-5d21m33.70s	−0.002 ± 0.185	−0.266 ± 0.244	−0.029 ± 0.712	−0.038 ± 0.787	−0.300 ± 0.652	0.102 ± 0.567	−0.232 ± 0.227
197	—	84	—	—	—	5h35m12.90s	-5d24m54.40s	−0.025 ± 0.144	−0.004 ± 0.201	0.301 ± 0.925	0.249 ± 0.874	−0.150 ± 0.644	0.091 ± 0.247	0.004 ± 0.308
198	—	74	—	—	—	5h35m12.95s	-5d24m58.00s	0.120 ± 0.151	0.042 ± 0.167	−0.028 ± 0.892	−0.161 ± 1.021	0.216 ± 0.642	−0.142 ± 0.290	0.039 ± 0.272
199	—	–	—	—	—	5h35m12.97s	-5d23m30.01s	0.129 ± 0.173	0.060 ± 0.177	0.142 ± 0.820	−0.417 ± 0.827	0.267 ± 0.067	0.535 ± 0.146	0.526 ± 0.216
200	—	–	—	7	—	5h35m12.99s	-5d23m55.01s	−0.039 ± 0.195	0.117 ± 0.034	0.261 ± 3.633	−0.120 ± 0.677	0.185 ± 0.067	0.492 ± 0.105	0.660 ± 0.228
201	—	683	—	—	—	5h35m13.02s	-5d20m52.90s	0.032 ± 0.201	0.060 ± 0.268	1.492 ± 3.327	0.930 ± 3.637	0.261 ± 1.773	−0.809 ± 1.569	0.201 ± 0.866
202	—	544	—	—	—	5h35m13.03s	-5d22m01.00s	0.070 ± 0.163	0.013 ± 0.196	0.120 ± 0.546	−0.064 ± 0.536	0.180 ± 0.460	−0.118 ± 0.432	0.091 ± 0.201
203	—	505	—	—	—	5h35m13.05s	-5d22m15.20s	0.058 ± 0.152	−0.044 ± 0.184	0.028 ± 0.498	0.231 ± 0.472	−0.120 ± 0.376	−0.016 ± 0.449	0.025 ± 0.213
204	131-046	–	—	—	—	5h35m13.05s	-5d20m45.79s	−0.060 ± 0.219	−0.028 ± 0.354	⋯	⋯	−0.638 ± 2.384	0.979 ± 1.666	0.159 ± 1.348
205	—	562	—	—	—	5h35m13.06s	-5d21m53.20s	−0.013 ± 0.150	0.051 ± 0.233	0.181 ± 0.517	−0.087 ± 0.627	0.092 ± 0.382	−0.054 ± 0.436	0.006 ± 0.222
206	—	599	—	—	—	5h35m13.07s	-5d21m39.00s	0.015 ± 0.166	−0.048 ± 0.257	0.175 ± 0.764	−0.077 ± 0.689	0.189 ± 0.453	−0.141 ± 0.439	−0.035 ± 0.263
207	—	402	—	—	—	5h35m13.09s	-5d22m53.20s	0.001 ± 0.161	0.005 ± 0.183	0.097 ± 0.658	0.258 ± 0.616	−0.049 ± 0.436	−0.055 ± 0.400	−0.099 ± 0.220
208	—	648	—	—	—	5h35m13.11s	-5d21m13.40s	−0.085 ± 0.163	−0.005 ± 0.230	0.198 ± 1.430	−0.242 ± 1.300	0.049 ± 0.898	0.137 ± 0.796	−0.012 ± 0.441
209	131-247	707	—	8	—	5h35m13.11s	-5d22m47.23s	0.364 ± 0.124	0.196 ± 0.058	0.417 ± 0.562	−0.188 ± 0.618	0.420 ± 0.400	0.136 ± 0.368	0.498 ± 0.995
210	—	87	—	—	—	5h35m13.13s	-5d24m53.00s	−0.004 ± 0.126	−0.120 ± 0.191	−0.123 ± 0.791	0.199 ± 0.907	0.505 ± 0.614	−0.043 ± 0.264	0.054 ± 0.323

Table 7.2 (cont'd)

ID	Proplyd Name	HC00 ID	GMR ID	Z04a ID	Other Names	R.A. [J2000]	Dec [J2000]	$F_{\nu,6cm}$ [mJy]	$F_{\nu,3.6cm}$ [mJy]	$F_{\nu,1.3cm,1}$[a] [mJy]	$F_{\nu,1.3cm,2}$[a] [mJy]	$F_{\nu,1.3cm,3}$[a] [mJy]	$F_{\nu,1.3cm,4}$[a] [mJy]	$F_{\nu,1.3cm,mean}$[a] [mJy]
211	—	487	—	—	—	5h35m13.18s	-5d22m21.20s	0.014 ± 0.169	-0.115 ± 0.198	-0.137 ± 0.505	-0.044 ± 0.587	-0.078 ± 0.406	0.096 ± 0.522	0.050 ± 0.190
212	—	721	—	—	—	5h35m13.18s	-5d24m24.90s	0.057 ± 0.160	-0.008 ± 0.190	0.006 ± 0.750	-0.160 ± 0.591	0.154 ± 0.434	-0.181 ± 0.228	-0.000 ± 0.196
213	—	—	Q	9	—	5h35m13.21s	-5d22m54.82s	0.108 ± 0.148	0.005 ± 0.193	-0.023 ± 0.674	-0.307 ± 0.601	1.769 ± 0.187	0.574 ± 0.388	0.399 ± 0.048
214	—	80	—	—	—	5h35m13.21s	-5d24m55.50s	-0.030 ± 0.130	-0.018 ± 0.179	0.325 ± 0.957	-0.274 ± 1.043	0.049 ± 0.599	0.075 ± 0.271	0.115 ± 0.285
215	—	682	—	—	—	5h35m13.22s	-5d20m52.80s	-0.025 ± 0.169	0.002 ± 0.279	-0.260 ± 2.713	-0.709 ± 3.659	-0.218 ± 1.781	-0.001 ± 1.761	0.457 ± 0.894
216	—	190	—	—	—	5h35m13.23s	-5d23m55.50s	-0.113 ± 0.179	-0.095 ± 0.184	-0.395 ± 0.701	0.027 ± 0.587	-0.227 ± 0.437	-0.233 ± 0.343	-0.182 ± 0.231
217	132-1832	—	—	—	—	5h35m13.24s	-5d18m32.95s	0.198 ± 0.462	...	...	...	...	...	...
218	132-042	—	—	—	—	5h35m13.24s	-5d20m41.94s	-0.073 ± 0.182	0.065 ± 0.366	...	...	...	...	...
219	—	523	—	—	—	5h35m13.24s	-5d22m09.82s	0.232 ± 0.063	0.371 ± 0.066	0.271 ± 0.050	0.082 ± 0.506	-0.048 ± 0.421	0.179 ± 0.421	0.082 ± 0.025
220	—	301	—	—	—	5h35m13.26s	-5d23m22.80s	-0.021 ± 0.205	-0.052 ± 0.215	-0.885 ± 0.798	0.036 ± 0.646	0.154 ± 0.486	0.277 ± 0.383	0.183 ± 0.267
221	—	380	—	—	—	5h35m13.29s	-5d22m57.90s	0.062 ± 0.149	0.034 ± 0.167	0.302 ± 0.710	0.044 ± 0.609	0.008 ± 0.459	-0.190 ± 0.390	0.008 ± 0.200
222	—	—	—	—	—	5h35m13.29s	-5d23m29.68s	-0.016 ± 0.165	0.071 ± 0.185	0.234 ± 0.734	0.475 ± 0.098	0.034 ± 0.542	0.066 ± 0.331	0.205 ± 0.261
223	133-353	199	—	—	—	5h35m13.31s	-5d23m53.08s	0.158 ± 0.187	0.057 ± 0.190	0.001 ± 0.748	0.372 ± 0.712	0.075 ± 0.461	0.067 ± 0.340	0.052 ± 0.222
224	—	572	—	—	—	5h35m13.33s	-5d21m49.90s	0.028 ± 0.153	-0.035 ± 0.220	0.031 ± 0.553	-0.031 ± 0.701	-0.190 ± 0.485	-0.245 ± 0.526	-0.081 ± 0.251
225	—	471	—	—	—	5h35m13.37s	-5d22m26.20s	0.089 ± 0.141	0.014 ± 0.190	-0.147 ± 0.567	0.190 ± 0.648	-0.146 ± 0.381	-0.224 ± 0.445	-0.175 ± 0.244
226	—	685	—	—	—	5h35m13.38s	-5d20m51.60s	0.031 ± 0.192	-0.133 ± 0.340	...	...	0.088 ± 1.792	-0.222 ± 1.848	0.176 ± 0.864
227	—	198	—	—	—	5h35m13.38s	-5d23m53.20s	-0.033 ± 0.231	-0.011 ± 0.173	-0.634 ± 0.641	0.149 ± 0.667	-0.041 ± 0.461	-0.065 ± 0.329	-0.357 ± 0.243
228	—	273	—	—	—	5h35m13.41s	-5d23m29.30s	0.121 ± 0.176	0.211 ± 0.176	-0.430 ± 0.682	0.555 ± 0.751	0.269 ± 0.524	0.201 ± 0.360	0.009 ± 0.256
229	—	—	—	10	—	5h35m13.41s	-5d24m11.22s	0.738 ± 0.126	1.068 ± 0.151	0.805 ± 0.232	1.285 ± 9.551	1.465 ± 0.300	1.410 ± 0.217	1.432 ± 0.232
230	—	653	—	—	—	5h35m13.44s	-5d21m07.40s	0.117 ± 0.196	-0.021 ± 0.289	0.401 ± 2.123	0.015 ± 1.938	-0.201 ± 1.271	0.395 ± 0.972	-0.302 ± 0.544
231	—	240	—	—	—	5h35m13.45s	-5d23m40.40s	-0.065 ± 0.196	0.132 ± 0.184	-0.905 ± 0.670	0.205 ± 0.700	-0.029 ± 0.404	0.030 ± 0.354	-0.312 ± 0.251
232	135-220	495	—	—	—	5h35m13.53s	-5d22m19.63s	0.301 ± 0.089	0.325 ± 0.113	0.195 ± 0.511	-0.215 ± 0.530	0.391 ± 0.469	0.303 ± 0.474	0.235 ± 0.979
233	—	266	—	—	—	5h35m13.53s	-5d23m30.90s	-0.087 ± 0.183	-0.261 ± 0.189	-0.122 ± 0.712	-0.430 ± 0.752	-0.009 ± 0.532	-0.046 ± 0.450	-0.083 ± 0.240
234	—	360	—	—	—	5h35m13.53s	-5d23m04.50s	0.067 ± 0.176	0.054 ± 0.197	-0.650 ± 0.678	0.000 ± 0.757	0.047 ± 0.488	0.038 ± 0.378	-0.118 ± 0.245
235	—	178	—	—	—	5h35m13.55s	-5d23m59.67s	0.155 ± 0.186	-0.069 ± 0.182	-0.300 ± 0.735	-0.059 ± 0.607	0.287 ± 0.070	0.163 ± 0.327	-0.025 ± 0.237
236	—	—	—	—	MM21	5h35m13.56s	-5d23m59.10s	-0.318 ± 0.220	-0.125 ± 0.182	0.731 ± 0.176	0.762 ± 0.137	0.563 ± 0.112	0.726 ± 0.148	0.723 ± 0.104
237	—	—	—	—	—	5h35m13.57s	-5d23m55.81s	-0.001 ± 0.213	-0.195 ± 0.209	0.342 ± 0.094	0.356 ± 0.093	0.358 ± 0.083	0.344 ± 0.090	0.375 ± 0.082
238	—	192	—	—	—	5h35m13.59s	-5d23m55.29s	2.155 ± 0.246	2.363 ± 0.247	2.305 ± 0.246	1.521 ± 0.176	0.575 ± 0.087	0.402 ± 0.101	0.751 ± 0.082
239	—	132	—	—	—	5h35m13.61s	-5d24m25.80s	0.099 ± 0.136	-0.107 ± 0.174	0.176 ± 0.686	-0.134 ± 0.608	0.023 ± 0.443	0.001 ± 0.232	-0.060 ± 0.218
240	—	633	—	—	—	5h35m13.62s	-5d21m21.10s	-0.046 ± 0.181	0.048 ± 0.239	0.319 ± 1.226	0.032 ± 1.106	0.023 ± 0.719	-0.200 ± 0.650	0.130 ± 0.351
241	136-1955	—	—	—	—	5h35m13.62s	-5d19m55.04s	-0.081 ± 0.258	0.007 ± 0.570	...	...	...	...	...
242	—	—	—	—	—	5h35m13.63s	-5d24m09.19s	-0.043 ± 0.171	0.082 ± 0.173	-0.138 ± 0.633	0.374 ± 0.665	0.133 ± 0.452	-0.210 ± 0.279	0.187 ± 0.041
243	—	—	—	—	MM22	5h35m13.65s	-5d23m54.94s	-0.071 ± 0.235	0.045 ± 0.218	0.288 ± 0.780	0.236 ± 0.555	0.297 ± 0.434	-0.210 ± 0.443	-0.085 ± 0.336
244	—	222	—	—	—	5h35m13.68s	-5d23m45.40s	-0.097 ± 0.220	-0.404 ± 0.168	-0.413 ± 0.607	-0.633 ± 0.710	-0.224 ± 0.442	0.028 ± 0.381	0.151 ± 0.242
245	—	719	—	—	—	5h35m13.70s	-5d25m31.90s	0.070 ± 0.140	0.025 ± 0.180	-0.003 ± 1.277	-0.060 ± 1.185	0.503 ± 0.723	-0.014 ± 0.257	0.192 ± 0.403

Table 7.2 (cont'd)

ID	Proplyd Name	HC00 ID	GMR ID	Z04a ID	Other Names	R.A. [J2000]	Dec [J2000]	$F_{\nu,6cm}$ [mJy]	$F_{\nu,3.6cm}$ [mJy]	$F_{\nu,1.3cm,1}$ [mJy] [a]	$F_{\nu,1.3cm,2}$ [mJy] [a]	$F_{\nu,1.3cm,3}$ [mJy] [a]	$F_{\nu,1.3cm,4}$ [mJy] [a]	$F_{\nu,1.3cm,mean}$ [mJy] [a]
246	–	–	–	–	MM8	5h35m13.71s	-5d23m46.89s	0.173 ± 0.242	−0.094 ± 0.176	0.240 ± 0.063	0.379 ± 0.118	0.259 ± 0.078	0.480 ± 0.189	0.657 ± 0.184
247	–	602	–	–	–	5h35m13.73s	-5d21m35.83s	−0.032 ± 0.148	−0.140 ± 0.239	0.073 ± 0.738	−0.074 ± 0.887	−0.032 ± 0.521	0.022 ± 0.546	0.204 ± 0.077
248	–	483	–	–	–	5h35m13.75s	-5d22m22.00s	−0.079 ± 0.145	0.061 ± 0.183	−0.161 ± 0.745	0.248 ± 0.637	0.207 ± 0.450	−0.051 ± 0.467	0.115 ± 0.230
249	–	–	–	–	MM13	5h35m13.75s	-5d24m07.74s	−0.007 ± 0.133	0.123 ± 0.188	0.275 ± 0.705	−0.234 ± 0.588	−0.012 ± 0.406	0.201 ± 0.337	0.468 ± 0.220
250	–	499	–	–	–	5h35m13.78s	-5d22m17.40s	−0.074 ± 0.166	0.103 ± 0.223	−0.112 ± 0.504	0.469 ± 0.585	−0.177 ± 0.424	−0.243 ± 0.396	−0.221 ± 0.251
251	138-207	703	–	–	–	5h35m13.80s	-5d22m07.02s	−0.069 ± 0.161	−0.056 ± 0.187	−0.001 ± 0.541	0.116 ± 0.531	0.109 ± 0.495	−0.048 ± 0.390	0.060 ± 0.022
252	–	548	–	–	–	5h35m13.80s	-5d21m59.67s	0.006 ± 0.168	0.192 ± 0.218	−0.370 ± 0.654	0.440 ± 0.570	0.143 ± 0.495	−0.028 ± 0.441	0.186 ± 0.074
253	–	242	–	–	–	5h35m13.80s	-5d23m40.12s	0.094 ± 0.193	−0.271 ± 0.177	−0.387 ± 0.749	0.198 ± 0.070	0.143 ± 0.050	−0.107 ± 0.386	0.185 ± 0.051
254	–	541	–	–	–	5h35m13.81s	-5d22m02.80s	0.137 ± 0.164	−0.073 ± 0.232	0.019 ± 0.617	0.342 ± 0.509	0.021 ± 0.455	−0.052 ± 0.398	−0.029 ± 0.232
255	–	525	–	–	–	5h35m13.83s	-5d22m09.10s	0.009 ± 0.159	−0.048 ± 0.194	−0.382 ± 0.522	−0.081 ± 0.536	0.136 ± 0.358	−0.112 ± 0.418	−0.009 ± 0.253
256	–	254	–	–	–	5h35m13.86s	-5d23m35.00s	0.051 ± 0.196	−0.004 ± 0.194	−0.138 ± 0.631	−0.240 ± 0.734	0.352 ± 0.488	0.103 ± 0.368	0.335 ± 0.225
257	–	–	–	–	–	5h35m13.88s	-5d23m57.21s	0.138 ± 0.224	0.180 ± 0.205	0.364 ± 0.090	0.157 ± 0.046	0.198 ± 0.055	−0.211 ± 0.406	0.230 ± 0.050
258	–	130	–	–	–	5h35m13.88s	-5d24m26.20s	−0.004 ± 0.154	0.105 ± 0.172	−0.057 ± 0.512	0.347 ± 0.533	−0.116 ± 0.397	−0.146 ± 0.225	−0.297 ± 0.224
259	–	–	–	–	–	5h35m13.93s	-5d24m09.41s	−0.128 ± 0.188	−0.267 ± 0.198	−0.212 ± 0.616	0.355 ± 0.076	0.367 ± 0.085	0.099 ± 0.270	0.010 ± 0.244
260	–	134	–	–	–	5h35m13.93s	-5d24m25.50s	0.085 ± 0.140	−0.030 ± 0.191	−0.052 ± 0.524	0.035 ± 0.590	−0.116 ± 0.388	0.067 ± 0.287	−0.080 ± 0.204
261	139-320	314	–	–	–	5h35m13.93s	-5d23m20.16s	0.309 ± 0.086	0.295 ± 0.086	−0.104 ± 0.698	0.413 ± 0.920	0.140 ± 0.454	0.232 ± 0.403	0.377 ± 0.288
262	–	–	–	–	–	5h35m13.93s	-5d24m09.49s	0.344 ± 0.130	0.168 ± 0.055	0.476 ± 0.179	0.225 ± 0.078	0.236 ± 0.092	0.518 ± 0.139	0.684 ± 0.135
263	–	451	–	–	–	5h35m13.97s	-5d22m31.90s	0.012 ± 0.142	0.117 ± 0.195	0.183 ± 0.507	0.274 ± 0.610	−0.031 ± 0.475	0.192 ± 0.364	0.212 ± 0.189
264	–	–	–	–	–	5h35m13.97s	-5d22m36.79s	−0.157 ± 0.151	−0.025 ± 0.212	0.163 ± 0.683	0.180 ± 0.561	0.143 ± 0.432	0.265 ± 0.392	0.137 ± 0.043
265	–	–	–	–	–	5h35m13.97s	-5d24m09.84s	−0.049 ± 0.188	0.172 ± 0.043	0.205 ± 0.062	0.166 ± 0.053	0.189 ± 0.051	0.093 ± 0.312	0.140 ± 0.032
266	–	552	–	–	–	5h35m13.98s	-5d21m58.00s	0.051 ± 0.171	−0.122 ± 0.218	0.090 ± 0.558	−0.088 ± 0.566	−0.013 ± 0.440	0.078 ± 0.426	0.042 ± 0.215
267	–	629	–	–	–	5h35m13.98s	-5d21m23.30s	−0.021 ± 0.141	−0.005 ± 0.241	−0.286 ± 1.289	−0.137 ± 1.012	0.167 ± 0.772	−0.024 ± 0.702	−0.072 ± 0.438
268	–	–	–	–	MM23	5h35m14.00s	-5d22m45.04s	0.114 ± 0.158	−0.075 ± 0.185	0.143 ± 0.696	0.334 ± 0.644	0.053 ± 0.460	0.142 ± 0.366	0.039 ± 0.242
269	–	760	–	–	–	5h35m14.01s	-5d21m51.90s	−0.024 ± 0.164	−0.130 ± 0.219	−0.017 ± 0.722	−0.132 ± 0.650	−0.004 ± 0.456	−0.101 ± 0.382	−0.168 ± 0.240
270	–	–	–	11	–	5h35m14.01s	-5d22m23.29s	0.416 ± 0.170	0.341 ± 0.107	−0.393 ± 0.923	0.146 ± 0.740	0.570 ± 0.616	0.012 ± 0.473	0.489 ± 0.346
271	–	–	–	–	–	5h35m14.03s	-5d23m29.91s	−0.053 ± 0.180	−0.028 ± 0.178	−0.101 ± 0.644	0.514 ± 0.098	−0.129 ± 0.466	0.086 ± 0.399	0.002 ± 0.236
272	140-1952	247	–	–	–	5h35m14.05s	-5d23m38.50s	0.058 ± 0.181	−0.087 ± 0.207	0.231 ± 0.718	0.548 ± 0.642	0.222 ± 0.461	−0.236 ± 0.370	0.005 ± 0.222
273	–	–	–	–	–	5h35m14.05s	-5d19m51.90s	0.100 ± 0.268	0.143 ± 0.600	...	...	...	...	...
274	–	704	–	–	–	5h35m14.06s	-5d22m05.70s	0.046 ± 0.152	−0.112 ± 0.199	0.046 ± 0.560	0.332 ± 0.568	−0.033 ± 0.407	−0.131 ± 0.409	−0.022 ± 0.220
275	–	–	31	–	–	5h35m14.06s	-5d23m51.30s	0.052 ± 0.362	0.012 ± 0.244	−0.317 ± 0.549	0.452 ± 0.632	0.123 ± 0.467	−0.068 ± 0.396	−0.164 ± 0.300
276	141-520	36	–	–	–	5h35m14.06s	-5d25m20.50s	0.153 ± 0.121	0.146 ± 0.215	0.016 ± 0.799	0.058 ± 0.840	−0.172 ± 0.635	0.152 ± 0.216	0.133 ± 0.290
277	–	438	R	–	–	5h35m14.07s	-5d22m36.63s	0.105 ± 0.193	−0.086 ± 0.193	0.356 ± 0.594	0.252 ± 0.542	−0.508 ± 0.368	−0.001 ± 0.321	0.025 ± 0.216
278	–	705	B	–	–	5h35m14.09s	-5d22m23.08s	−0.045 ± 0.166	−0.036 ± 0.250	−0.692 ± 0.933	−0.170 ± 0.913	−0.206 ± 0.642	0.008 ± 0.481	−0.294 ± 0.582
279	–	779	–	12	–	5h35m14.11s	-5d22m22.67s	2.611 ± 0.285	4.593 ± 0.469	15.747 ± 1.596	14.092 ± 1.425	11.914 ± 1.200	20.249 ± 2.038	13.658 ± 1.370
280	–	–	–	13	–	5h35m14.14s	-5d23m56.75s	0.499 ± 0.167	0.732 ± 0.150	0.660 ± 0.124	0.637 ± 0.113	0.579 ± 0.094	0.846 ± 0.175	0.834 ± 0.133

190

Table 7.2 (cont'd)

ID	Proplyd Name	HC00 ID	GMR ID	Z04a ID	Other Names	R.A. [J2000]	Dec [J2000]	$F_{\nu,6cm}$ [mJy]	$F_{\nu,3.6cm}$ [mJy]	$F_{\nu,1.3cm,1}$[a] [mJy]	$F_{\nu,1.3cm,2}$[a] [mJy]	$F_{\nu,1.3cm,3}$[a] [mJy]	$F_{\nu,1.3cm,4}$[a] [mJy]	$F_{\nu,1.3cm,mean}$[a] [mJy]
281	142-301	371	C	14	–	5h35m14.16s	-5d23m01.29s	8.857 ± 0.954	7.024 ± 0.846	1.292 ± 4.658	1.124 ± 5.151	1.629 ± 0.503	6.611 ± 0.958	3.556 ± 0.840
282	–	67	–	–	–	5h35m14.18s	-5d25m00.70s	0.025 ± 0.127	-0.051 ± 0.209	-0.164 ± 0.695	0.174 ± 0.586	-0.153 ± 0.485	-0.129 ± 0.195	-0.096 ± 0.209
283	–	–	–	–	–	5h35m14.18s	-5d26m20.96s	0.614 ± 0.094	0.565 ± 0.099	...	...	0.590 ± 2.325	0.219 ± 0.855	0.291 ± 1.141
284	–	–	–	–	–	5h35m14.22s	-5d22m25.91s	0.055 ± 0.144	-0.078 ± 0.227	-0.043 ± 0.625	0.341 ± 0.176	0.182 ± 0.047	0.085 ± 0.336	0.223 ± 0.044
285	–	690	–	–	–	5h35m14.28s	-5d20m48.50s	-0.034 ± 0.187	-0.173 ± 0.283	...	...	0.525 ± 1.674	...	-0.357 ± 1.385
286	143-425	135	–	–	–	5h35m14.28s	-5d24m24.72s	0.293 ± 0.088	0.088 ± 0.193	-0.088 ± 0.586	-0.042 ± 0.611	0.016 ± 0.356	0.518 ± 0.240	0.329 ± 0.107
287	–	–	–	15	–	5h35m14.28s	-5d23m53.01s	0.910 ± 0.345	0.522 ± 0.282	0.610 ± 0.593	0.452 ± 0.601	0.393 ± 0.365	0.736 ± 0.445	0.998 ± 0.224
288	–	361	–	–	–	5h35m14.29s	-5d23m04.30s	0.147 ± 0.228	0.097 ± 0.228	0.451 ± 0.747	0.451 ± 0.871	-0.087 ± 0.542	-0.096 ± 0.389	0.277 ± 0.297
289	–	–	–	–	–	5h35m14.30s	-5d22m36.73s	-0.049 ± 0.168	-0.006 ± 0.201	-0.292 ± 0.675	0.253 ± 0.050	0.129 ± 0.430	-0.100 ± 0.390	0.165 ± 0.031
290	–	458	–	–	–	5h35m14.31s	-5d22m30.70s	0.120 ± 0.144	0.111 ± 0.172	0.104 ± 0.555	-0.147 ± 0.700	-0.059 ± 0.350	0.118 ± 0.386	0.169 ± 0.247
291	–	537	–	–	–	5h35m14.31s	-5d22m04.40s	-0.005 ± 0.148	0.055 ± 0.159	-0.115 ± 0.541	-0.051 ± 0.638	-0.028 ± 0.409	-0.045 ± 0.360	0.078 ± 0.193
292	–	–	–	–	–	5h35m14.31s	-5d22m42.03s	-0.006 ± 0.149	0.077 ± 0.187	-0.166 ± 0.517	0.259 ± 0.608	0.067 ± 0.425	0.159 ± 0.358	0.272 ± 0.331
293	–	345	–	–	–	5h35m14.32s	-5d23m08.30s	-0.025 ± 0.190	0.017 ± 0.219	-0.189 ± 0.747	0.168 ± 0.760	-0.019 ± 0.504	0.008 ± 0.429	0.131 ± 0.260
294	–	–	–	16	–	5h35m14.34s	-5d23m17.42s	0.114 ± 0.204	0.181 ± 0.048	-0.261 ± 0.760	0.039 ± 0.785	-0.124 ± 0.597	0.476 ± 0.134	0.613 ± 0.250
295	144-522	33	–	–	–	5h35m14.34s	-5d25m22.40s	0.205 ± 0.144	0.023 ± 0.201	0.378 ± 0.918	-0.081 ± 0.719	0.089 ± 0.589	0.080 ± 0.222	0.252 ± 0.266
296	–	42	–	–	–	5h35m14.35s	-5d25m15.80s	-0.055 ± 0.135	-0.025 ± 0.202	-0.292 ± 0.741	0.061 ± 0.710	-0.131 ± 0.479	-0.012 ± 0.192	-0.016 ± 0.282
297	–	448	–	17	–	5h35m14.36s	-5d22m32.80s	1.653 ± 0.238	1.197 ± 0.239	0.379 ± 0.115	0.257 ± 0.083	0.573 ± 1.616	1.105 ± 0.275	1.426 ± 0.418
298	–	399	–	–	–	5h35m14.37s	-5d22m54.10s	0.066 ± 0.168	0.271 ± 0.192	-0.728 ± 0.683	-0.505 ± 0.719	0.338 ± 0.504	-0.377 ± 0.395	-0.646 ± 0.337
299	–	439	–	–	–	5h35m14.37s	-5d22m36.10s	0.047 ± 0.154	0.116 ± 0.192	0.036 ± 0.689	0.188 ± 0.628	0.070 ± 0.458	-0.047 ± 0.377	0.022 ± 0.226
300	–	391	–	–	–	5h35m14.39s	-5d22m55.70s	-0.048 ± 0.170	-0.221 ± 0.219	0.488 ± 0.708	0.168 ± 0.713	-0.031 ± 0.510	-0.157 ± 0.461	0.119 ± 0.257
301	–	–	–	–	LMLA162	5h35m14.39s	-5d23m50.84s	-0.354 ± 0.315	0.072 ± 0.246	0.549 ± 0.118	0.539 ± 0.130	0.489 ± 0.104	0.666 ± 0.168	0.642 ± 0.108
302	–	258	–	–	–	5h35m14.40s	-5d23m33.70s	-0.095 ± 0.209	0.281 ± 0.206	0.377 ± 0.623	0.580 ± 0.826	0.005 ± 0.455	0.220 ± 0.439	0.324 ± 0.283
303	–	300	–	–	–	5h35m14.40s	-5d23m23.10s	0.037 ± 0.207	0.205 ± 0.219	-0.310 ± 0.679	-0.115 ± 0.837	0.317 ± 0.500	-0.043 ± 0.383	-0.133 ± 0.313
304	–	–	–	–	–	5h35m14.40s	-5d22m30.40s	0.199 ± 0.163	0.074 ± 0.204	1.015 ± 0.665	0.357 ± 0.513	0.224 ± 0.470	0.269 ± 0.406	0.388 ± 0.633
305	–	63	–	–	–	5h35m14.46s	-5d25m02.21s	0.178 ± 0.068	0.153 ± 0.185	0.153 ± 0.654	0.101 ± 0.533	-0.026 ± 0.450	-0.008 ± 0.193	-0.042 ± 0.245
306	–	759	–	–	–	5h35m14.50s	-5d22m29.40s	0.005 ± 0.160	0.129 ± 0.180	-0.119 ± 0.633	-0.048 ± 0.559	0.102 ± 0.442	0.061 ± 0.429	-0.059 ± 0.340
307	–	–	H	18	–	5h35m14.50s	-5d22m38.70s	1.707 ± 0.189	1.815 ± 0.196	1.256 ± 0.151	1.145 ± 0.143	1.416 ± 0.156	2.684 ± 0.317	1.692 ± 0.182
308	–	–	I	19	–	5h35m14.52s	-5d22m30.61s	0.502 ± 0.092	1.192 ± 0.145	4.399 ± 0.485	4.523 ± 0.485	3.919 ± 0.422	6.337 ± 0.663	4.804 ± 0.496
309	–	530	–	–	–	5h35m14.53s	-5d22m06.60s	0.062 ± 0.174	-0.060 ± 0.197	-0.111 ± 0.700	0.298 ± 0.627	-0.022 ± 0.498	0.193 ± 0.377	0.011 ± 0.214
310	–	189	–	–	–	5h35m14.53s	-5d23m56.00s	0.115 ± 0.267	0.087 ± 0.228	0.345 ± 0.537	0.451 ± 0.538	0.267 ± 0.468	0.258 ± 0.369	0.331 ± 0.271
311	–	193	–	–	–	5h35m14.53s	-5d23m55.10s	-0.116 ± 0.346	-0.039 ± 0.288	0.488 ± 0.562	0.197 ± 0.545	0.353 ± 0.422	0.129 ± 0.436	0.582 ± 0.245
312	–	364	–	–	–	5h35m14.54s	-5d23m03.70s	-0.103 ± 0.204	0.127 ± 0.188	-0.292 ± 0.696	-0.249 ± 0.829	0.268 ± 0.463	0.031 ± 0.415	-0.362 ± 0.310
313	–	–	–	–	–	5h35m14.55s	-5d23m15.99s	0.196 ± 0.214	-0.153 ± 0.167	0.070 ± 0.777	0.315 ± 0.856	0.878 ± 0.115	-0.040 ± 0.433	0.243 ± 0.044
314	–	209	–	–	–	5h35m14.57s	-5d23m50.80s	0.044 ± 0.281	0.036 ± 0.207	-0.115 ± 0.592	-0.373 ± 0.586	-0.158 ± 0.389	-0.012 ± 0.389	-0.024 ± 0.252
315	–	–	–	–	–	5h35m14.57s	-5d22m31.29s	-0.031 ± 0.150	0.019 ± 0.212	0.497 ± 0.096	0.542 ± 0.093	0.667 ± 0.095	0.060 ± 0.352	0.432 ± 0.061

Table 7.2 (cont'd)

ID	Proplyd Name	HC00 ID	GMR ID	Z04a ID	Other Names	R.A. [J2000]	Dec [J2000]	$F_{\nu,6cm}$ [mJy]	$F_{\nu,3.6cm}$ [mJy]	$F_{\nu,1.3cm,1}$ [mJy] [a]	$F_{\nu,1.3cm,2}$ [mJy] [a]	$F_{\nu,1.3cm,3}$ [mJy] [a]	$F_{\nu,1.3cm,4}$ [mJy] [a]	$F_{\nu,1.3cm,mean}$ [mJy] [a]
316	–	–	–	–	–	5h35m14.61s	-5d22m21.04s	0.640 ± 0.166	0.246 ± 0.186	0.352 ± 0.677	−0.090 ± 0.650	0.177 ± 0.474	0.509 ± 0.449	0.627 ± 0.253
317	–	–	–	–	MM24	5h35m14.62s	-5d22m28.94s	−0.016 ± 0.168	−0.046 ± 0.230	0.069 ± 0.634	0.049 ± 0.605	0.069 ± 0.514	0.064 ± 0.478	0.123 ± 0.261
318	146-201	545	–	–	–	5h35m14.62s	-5d22m00.97s	0.102 ± 0.146	−0.113 ± 0.228	0.088 ± 0.711	0.399 ± 0.634	0.216 ± 0.443	0.178 ± 0.345	0.162 ± 0.224
319	–	443	–	–	–	5h35m14.66s	-5d22m33.76s	−0.023 ± 0.173	0.223 ± 0.064	0.413 ± 0.615	−0.073 ± 0.569	0.321 ± 0.065	0.136 ± 0.415	0.141 ± 0.032
320	–	276	–	–	–	5h35m14.66s	-5d23m28.70s	−0.318 ± 0.271	−0.193 ± 0.247	−0.158 ± 0.699	−0.326 ± 0.719	0.017 ± 0.504	−0.207 ± 0.410	−0.092 ± 0.328
321	–	756	–	–	–	5h35m14.67s	-5d22m38.60s	0.046 ± 0.164	−0.035 ± 0.202	−0.022 ± 0.624	0.346 ± 0.731	−0.266 ± 0.378	−0.039 ± 0.359	−0.050 ± 0.251
322	–	369	–	–	–	5h35m14.67s	-5d23m01.90s	0.101 ± 0.196	0.157 ± 0.186	0.187 ± 0.684	−0.055 ± 0.828	−0.410 ± 0.452	0.146 ± 0.369	0.153 ± 0.293
323	–	575	–	–	–	5h35m14.69s	-5d21m49.50s	0.060 ± 0.149	−0.009 ± 0.243	0.164 ± 0.701	0.290 ± 0.772	−0.056 ± 0.535	0.085 ± 0.391	0.097 ± 0.261
324	–	757	–	–	–	5h35m14.69s	-5d22m38.20s	−0.012 ± 0.156	0.140 ± 0.192	0.706 ± 0.732	0.370 ± 0.612	0.022 ± 0.440	0.126 ± 0.349	0.407 ± 0.262
325	–	–	–	–	–	5h35m14.69s	-5d22m11.00s	−0.114 ± 0.160	−0.075 ± 0.181	−0.092 ± 0.717	0.197 ± 0.649	0.215 ± 0.048	0.139 ± 0.361	0.189 ± 0.042
326	–	411	–	–	–	5h35m14.70s	-5d22m49.40s	−0.180 ± 0.176	0.061 ± 0.191	−0.199 ± 0.661	−0.142 ± 0.723	0.497 ± 0.466	0.083 ± 0.365	−0.029 ± 0.234
327	–	755	–	–	–	5h35m14.71s	-5d22m35.50s	−0.127 ± 0.158	−0.022 ± 0.187	−0.057 ± 0.569	0.303 ± 0.603	0.019 ± 0.387	0.042 ± 0.361	0.074 ± 0.255
328	–	657	–	–	–	5h35m14.72s	-5d21m06.30s	−0.035 ± 0.188	0.112 ± 0.285	0.441 ± 2.975	0.822 ± 2.707	0.177 ± 1.414	0.201 ± 1.010	0.617 ± 0.622
329	–	465	–	–	–	5h35m14.73s	-5d22m29.80s	−0.013 ± 0.162	−0.094 ± 0.210	−0.493 ± 0.698	−0.546 ± 0.562	0.276 ± 0.418	0.187 ± 0.384	−0.167 ± 0.268
330	–	464	–	–	–	5h35m14.73s	-5d22m29.82s	−0.008 ± 0.157	−0.094 ± 0.239	0.225 ± 0.055	0.259 ± 0.057	0.344 ± 0.451	0.184 ± 0.411	0.153 ± 0.036
331	147-323	302	–	20	–	5h35m14.73s	-5d23m22.95s	0.733 ± 0.260	−0.129 ± 0.214	0.236 ± 0.750	0.029 ± 0.890	0.520 ± 0.499	0.237 ± 0.440	0.730 ± 0.301
332	–	–	–	–	–	5h35m14.80s	-5d22m30.68s	0.058 ± 0.175	0.024 ± 0.199	0.099 ± 0.652	0.366 ± 0.111	0.260 ± 0.057	0.139 ± 0.413	0.384 ± 0.080
333	148-305	–	–	22	–	5h35m14.81s	-5d23m04.80s	0.349 ± 0.092	0.350 ± 0.110	−0.153 ± 0.705	0.380 ± 0.843	−0.012 ± 0.431	0.284 ± 0.353	−0.130 ± 0.266
334	–	220	–	–	–	5h35m14.82s	-5d23m46.50s	0.293 ± 0.261	0.427 ± 0.213	0.191 ± 0.484	0.295 ± 0.583	−0.354 ± 0.414	−0.021 ± 0.362	−0.001 ± 0.219
335	–	773	–	–	–	5h35m14.82s	-5d22m23.20s	0.017 ± 0.151	0.051 ± 0.182	0.186 ± 0.572	0.135 ± 0.662	0.183 ± 0.420	−0.225 ± 0.398	0.018 ± 0.225
336	–	324	–	–	–	5h35m14.84s	-5d23m16.00s	−0.009 ± 0.232	0.009 ± 0.206	−0.565 ± 0.702	0.360 ± 0.898	0.229 ± 0.488	−0.071 ± 0.429	−0.058 ± 0.333
337	–	771	–	–	–	5h35m14.86s	-5d22m44.10s	−0.104 ± 0.166	−0.100 ± 0.158	0.442 ± 0.627	−0.182 ± 0.612	0.021 ± 0.451	0.034 ± 0.385	0.066 ± 0.233
338	–	453	–	–	–	5h35m14.87s	-5d22m31.70s	0.049 ± 0.169	0.029 ± 0.199	0.432 ± 0.629	0.263 ± 0.651	−0.043 ± 0.470	0.022 ± 0.364	0.382 ± 0.265
339	–	714	–	–	–	5h35m14.88s	-5d23m05.10s	−0.133 ± 0.220	−0.276 ± 0.204	0.417 ± 0.684	−0.569 ± 0.898	−0.304 ± 0.430	0.019 ± 0.399	−0.137 ± 0.282
340	–	157	–	–	–	5h35m14.90s	-5d24m11.80s	0.129 ± 0.181	0.132 ± 0.170	−0.260 ± 0.437	−0.220 ± 0.455	−0.376 ± 0.397	−0.023 ± 0.265	0.039 ± 0.191
341	–	–	D	21	–	5h35m14.90s	-5d22m25.41s	0.812 ± 0.113	0.768 ± 0.097	0.687 ± 0.106	0.516 ± 0.087	1.772 ± 0.190	1.856 ± 0.241	1.320 ± 0.150
342	–	431	–	–	–	5h35m14.92s	-5d22m39.10s	−0.089 ± 0.149	−0.088 ± 0.180	0.031 ± 0.629	−0.101 ± 0.731	−0.229 ± 0.441	0.141 ± 0.310	0.133 ± 0.248
343	–	154	–	–	–	5h35m14.93s	-5d24m12.90s	−0.067 ± 0.210	−0.129 ± 0.156	−0.237 ± 0.453	−0.105 ± 0.488	−0.109 ± 0.395	−0.026 ± 0.262	−0.301 ± 0.193
344	149-329	275	–	23	–	5h35m14.93s	-5d23m29.02s	−0.162 ± 0.272	0.346 ± 0.079	−1.197 ± 0.686	0.781 ± 0.806	−0.129 ± 0.396	0.057 ± 0.417	0.244 ± 1.448
345	–	245	–	–	–	5h35m14.95s	-5d23m39.30s	0.209 ± 0.248	0.260 ± 0.219	−0.304 ± 0.656	−0.697 ± 0.650	−0.514 ± 0.427	−0.075 ± 0.423	−0.120 ± 0.270
346	–	673	–	–	–	5h35m14.96s	-5d21m00.80s	0.053 ± 0.192	−0.132 ± 0.296	···	···	−0.112 ± 1.785	0.557 ± 1.430	0.361 ± 0.898
347	–	147	–	–	–	5h35m14.97s	-5d24m17.20s	−0.194 ± 0.192	−0.101 ± 0.172	0.160 ± 0.501	−0.241 ± 0.521	−0.122 ± 0.377	−0.066 ± 0.216	−0.264 ± 0.185
348	–	546	–	–	–	5h35m15.00s	-5d22m00.00s	−0.073 ± 0.159	0.113 ± 0.210	−0.089 ± 0.695	−0.088 ± 0.696	−0.064 ± 0.433	−0.119 ± 0.316	−0.034 ± 0.255
349	–	334	–	–	–	5h35m15.00s	-5d23m14.30s	−0.011 ± 0.235	−0.059 ± 0.190	−0.401 ± 0.636	−0.194 ± 0.916	−0.240 ± 0.497	0.215 ± 0.442	−0.235 ± 0.293
350	150-147	581	–	–	–	5h35m15.01s	-5d21m47.37s	−0.031 ± 0.177	0.014 ± 0.247	−0.301 ± 0.930	−0.138 ± 0.817	−0.079 ± 0.563	−0.018 ± 0.353	−0.250 ± 0.266

Table 7.2 (cont'd)

ID	Proplyd Name	HC00 ID	GMR ID	Z04a ID	Other Names	R.A. [J2000]	Dec [J2000]	$F_{\nu,6cm}$ [mJy]	$F_{\nu,3.6cm}$ [mJy]	$F_{\nu,1.3cm,1}$[a] [mJy]	$F_{\nu,1.3cm,2}$[a] [mJy]	$F_{\nu,1.3cm,3}$[a] [mJy]	$F_{\nu,1.3cm,4}$[a] [mJy]	$F_{\nu,1.3cm,mean}$[a] [mJy]
351	—	684	—	—	—	5h35m15.02s	-5d20m52.60s	0.015 ± 0.194	0.047 ± 0.269	...	...	-0.453 ± 1.750	...	-0.070 ± 1.188
352	150-231	456	—	—	—	5h35m15.03s	-5d22m31.15s	0.192 ± 0.176	0.050 ± 0.167	0.220 ± 0.609	0.028 ± 0.619	0.293 ± 0.378	0.259 ± 0.406	0.362 ± 0.233
353	—	373	—	—	—	5h35m15.04s	-5d23m01.10s	-0.061 ± 0.160	0.186 ± 0.203	-0.470 ± 0.704	-0.180 ± 0.837	-0.086 ± 0.497	-0.145 ± 0.356	-0.370 ± 0.255
354	—	195	—	—	—	5h35m15.04s	-5d23m54.50s	0.112 ± 0.481	-0.218 ± 0.402	-0.222 ± 0.600	-0.273 ± 0.478	0.124 ± 0.357	-0.177 ± 0.546	-0.104 ± 0.277
355	—	298	—	—	—	5h35m15.07s	-5d23m23.40s	0.095 ± 0.240	-0.040 ± 0.219	-0.136 ± 0.617	-0.482 ± 0.812	-0.010 ± 0.550	-0.356 ± 0.419	-0.657 ± 0.330
356	—	744	—	—	—	5h35m15.07s	-5d24m22.10s	0.132 ± 0.161	-0.066 ± 0.171	0.134 ± 0.531	0.337 ± 0.390	0.222 ± 0.335	-0.103 ± 0.235	0.007 ± 0.162
357	—	—	—	24	—	5h35m15.07s	-5d23m52.96s	0.420 ± 0.408	0.648 ± 0.408	0.231 ± 0.569	0.290 ± 0.517	-0.181 ± 0.363	0.219 ± 0.395	0.152 ± 0.329
358	—	—	—	25	—	5h35m15.15s	-5d23m53.63s	0.649 ± 0.495	0.457 ± 0.405	0.159 ± 0.644	0.053 ± 0.602	0.623 ± 0.424	-0.074 ± 0.408	-0.061 ± 0.276
359	—	149	—	—	—	5h35m15.16s	-5d24m17.10s	0.258 ± 0.174	-0.031 ± 0.189	-0.424 ± 0.479	0.223 ± 0.540	0.143 ± 0.338	-0.013 ± 0.198	0.012 ± 0.176
360	—	219	—	—	—	5h35m15.16s	-5d23m46.70s	0.225 ± 0.309	0.591 ± 0.328	-0.278 ± 0.525	0.672 ± 0.540	0.252 ± 0.402	0.154 ± 0.391	0.503 ± 0.296
361	—	—	—	—	—	5h35m15.16s	-5d22m17.37s	0.132 ± 0.154	0.018 ± 0.184	-0.703 ± 0.670	0.109 ± 0.638	0.199 ± 0.518	0.040 ± 0.343	0.289 ± 0.096
362	—	694	—	—	—	5h35m15.17s	-5d20m48.20s	0.021 ± 0.189	0.090 ± 0.313	...	...	...	...	...
363	—	359	—	—	—	5h35m15.18s	-5d23m05.00s	-0.030 ± 0.183	-0.107 ± 0.208	0.036 ± 0.713	-0.640 ± 0.822	0.148 ± 0.508	0.174 ± 0.401	0.242 ± 0.292
364	—	—	—	26	—	5h35m15.18s	-5d24m03.61s	0.098 ± 0.245	-0.002 ± 0.238	0.085 ± 0.529	0.479 ± 0.475	0.213 ± 0.344	0.069 ± 0.374	0.362 ± 0.245
365	—	—	—	27	—	5h35m15.19s	-5d23m32.55s	0.609 ± 0.355	0.480 ± 0.284	0.187 ± 0.588	0.638 ± 0.715	0.002 ± 0.427	0.653 ± 0.418	1.366 ± 0.327
366	—	687	—	—	—	5h35m15.20s	-5d20m51.40s	-0.007 ± 0.192	0.071 ± 0.318	...	...	...	...	...
367	—	398	—	—	—	5h35m15.20s	-5d22m54.40s	-0.103 ± 0.178	-0.050 ± 0.187	-0.138 ± 0.738	-0.554 ± 0.639	-0.049 ± 0.462	0.105 ± 0.386	0.053 ± 0.275
368	152-738	—	—	—	—	5h35m15.21s	-5d27m37.85s	-0.042 ± 0.209	-0.110 ± 0.406	...	...	...	...	...
369	—	478	—	—	—	5h35m15.21s	-5d22m24.10s	0.085 ± 0.173	0.083 ± 0.197	0.184 ± 0.678	-0.093 ± 0.580	0.005 ± 0.440	0.008 ± 0.402	0.134 ± 0.192
370	—	437	—	—	—	5h35m15.21s	-5d22m36.70s	-0.006 ± 0.158	0.082 ± 0.177	-0.474 ± 0.586	0.085 ± 0.556	0.208 ± 0.324	-0.044 ± 0.350	-0.111 ± 0.213
371	152-319	318	—	28	—	5h35m15.21s	-5d23m18.80s	1.412 ± 0.257	0.895 ± 0.176	0.006 ± 0.658	0.815 ± 1.146	0.346 ± 0.519	0.272 ± 0.473	0.551 ± 0.337
372	—	211	—	—	—	5h35m15.25s	-5d23m49.80s	0.183 ± 0.396	0.045 ± 0.242	0.655 ± 0.513	1.095 ± 0.601	-0.092 ± 0.328	0.295 ± 0.379	0.862 ± 0.232
373	—	—	28	—	—	5h35m15.26s	-5d23m47.26s	0.527 ± 0.364	0.378 ± 0.283	-0.252 ± 0.566	-0.327 ± 0.534	0.749 ± 0.388	0.375 ± 0.393	0.493 ± 0.283
374	—	386	—	29	—	5h35m15.26s	-5d22m56.88s	-0.117 ± 0.148	0.131 ± 0.042	0.446 ± 0.617	0.078 ± 0.820	0.267 ± 0.077	0.195 ± 0.343	0.215 ± 0.089
375	—	558	—	—	—	5h35m15.27s	-5d21m55.70s	-0.066 ± 0.159	0.108 ± 0.187	0.098 ± 0.702	0.051 ± 0.714	0.064 ± 0.447	-0.069 ± 0.323	0.140 ± 0.269
376	—	624	—	—	—	5h35m15.30s	-5d21m28.80s	-0.048 ± 0.166	-0.009 ± 0.266	-0.058 ± 1.311	0.314 ± 1.309	-0.106 ± 0.773	0.060 ± 0.491	0.063 ± 0.397
377	—	299	—	—	—	5h35m15.30s	-5d23m23.20s	0.229 ± 0.235	0.200 ± 0.181	0.902 ± 0.634	0.407 ± 0.704	-0.166 ± 0.520	0.177 ± 0.456	0.600 ± 0.295
378	—	—	—	—	—	5h35m15.31s	-5d22m04.76s	0.105 ± 0.140	-0.014 ± 0.223	0.130 ± 0.665	0.075 ± 0.642	0.081 ± 0.487	0.151 ± 0.355	0.132 ± 0.036
379	—	739	—	—	—	5h35m15.32s	-5d20m55.00s	-0.044 ± 0.170	-0.019 ± 0.346	...	...	0.267 ± 2.545	0.425 ± 1.527	-0.545 ± 1.422
380	—	476	—	—	—	5h35m15.33s	-5d22m25.00s	0.815 ± 0.127	0.611 ± 0.094	0.446 ± 0.094	-0.040 ± 0.576	0.179 ± 0.447	-0.020 ± 0.369	0.100 ± 0.029
381	—	504	—	—	—	5h35m15.35s	-5d22m15.60s	0.035 ± 0.167	0.032 ± 0.201	-0.088 ± 0.628	0.189 ± 0.587	-0.038 ± 0.513	-0.051 ± 0.379	-0.097 ± 0.247
382	—	310	—	—	—	5h35m15.36s	-5d23m21.39s	0.064 ± 0.215	0.160 ± 0.048	0.150 ± 0.744	0.199 ± 0.065	0.208 ± 0.078	0.083 ± 0.462	0.227 ± 0.080
383	154-324	297	—	30	—	5h35m15.36s	-5d23m24.12s	0.604 ± 0.133	0.693 ± 0.125	0.348 ± 0.097	0.389 ± 0.150	0.634 ± 0.124	0.444 ± 0.135	0.515 ± 0.119
384	154-225	475	—	31	—	5h35m15.37s	-5d22m25.36s	0.100 ± 0.148	0.242 ± 0.078	0.535 ± 0.637	-0.163 ± 0.598	0.067 ± 0.443	0.162 ± 0.373	-0.044 ± 0.182
385	—	261	—	—	—	5h35m15.38s	-5d23m33.40s	0.190 ± 0.322	0.085 ± 0.212	-0.252 ± 0.656	-0.150 ± 0.676	0.046 ± 0.478	-0.347 ± 0.398	-0.516 ± 0.272

Table 7.2 (cont'd)

ID	Proplyd Name	HC00 ID	GMR ID	Z04a ID	Other Names	R.A. [J2000]	Dec [J2000]	$F_{\nu,6cm}$ [mJy]	$F_{\nu,3.6cm}$ [mJy]	$F_{\nu,1.3cm,1}$ [mJy] [a]	$F_{\nu,1.3cm,2}$ [mJy] [a]	$F_{\nu,1.3cm,3}$ [mJy] [a]	$F_{\nu,1.3cm,4}$ [mJy] [a]	$F_{\nu,1.3cm,mean}$ [mJy] [a]
386	154-240	–	–	32	–	5h35m15.40s	-5d22m40.06s	1.292 ± 0.214	1.293 ± 0.265	0.760 ± 0.606	0.414 ± 0.612	0.498 ± 0.429	0.500 ± 0.319	1.373 ± 0.509
387	–	646	–	–	–	5h35m15.41s	-5d21m14.00s	-0.055 ± 0.160	-0.033 ± 0.250	0.042 ± 2.507	0.359 ± 2.419	-0.490 ± 1.212	0.142 ± 0.852	0.073 ± 0.567
388	–	600	–	–	–	5h35m15.41s	-5d21m39.50s	-0.098 ± 0.155	0.043 ± 0.215	-0.644 ± 0.913	-0.197 ± 0.985	0.047 ± 0.675	-0.011 ± 0.426	0.055 ± 0.334
389	–	223	–	33	–	5h35m15.45s	-5d23m45.55s	0.496 ± 0.136	0.471 ± 0.095	0.168 ± 0.524	-0.155 ± 0.519	0.480 ± 0.119	0.355 ± 0.113	0.556 ± 0.146
390	–	413	–	–	–	5h35m15.51s	-5d22m48.45s	-0.003 ± 0.182	0.040 ± 0.196	0.467 ± 0.624	0.225 ± 0.628	0.165 ± 0.491	0.042 ± 0.270	0.226 ± 0.253
391	155-338	251	14	34	–	5h35m15.53s	-5d23m37.39s	6.927 ± 0.797	5.496 ± 0.681	1.386 ± 3.206	2.316 ± 1.007	2.311 ± 0.707	5.248 ± 0.715	4.678 ± 0.894
392	–	327	–	–	–	5h35m15.54s	-5d23m15.80s	0.222 ± 0.281	-0.081 ± 0.246	-0.470 ± 0.714	-0.320 ± 0.957	0.055 ± 0.509	-0.367 ± 0.487	-0.838 ± 0.327
393	–	419	–	–	–	5h35m15.55s	-5d22m46.40s	0.138 ± 0.186	-0.030 ± 0.164	-0.157 ± 0.687	0.197 ± 0.670	0.169 ± 0.049	0.064 ± 0.321	0.124 ± 0.052
394	–	43	–	–	–	5h35m15.56s	-5d25m14.15s	5.301 ± 0.535	5.605 ± 0.565	4.650 ± 0.474	1.264 ± 0.139	1.903 ± 0.199	0.669 ± 0.098	1.578 ± 0.162
395	–	274	–	–	–	5h35m15.56s	-5d23m29.60s	0.094 ± 0.306	0.344 ± 0.274	0.454 ± 0.705	-0.667 ± 0.739	0.554 ± 0.448	-0.060 ± 0.399	0.468 ± 0.278
396	–	4	–	–	–	5h35m15.56s	-5d25m46.80s	-0.057 ± 0.145	-0.012 ± 0.160	-0.056 ± 0.919	-0.107 ± 0.825	0.125 ± 0.548	0.012 ± 0.241	0.068 ± 0.315
397	–	378	–	–	–	5h35m15.60s	-5d22m58.90s	-0.013 ± 0.185	0.029 ± 0.212	-0.429 ± 0.611	-0.241 ± 0.695	0.068 ± 0.444	-0.220 ± 0.318	-0.237 ± 0.284
398	–	172	–	–	–	5h35m15.62s	-5d24m03.10s	-0.010 ± 0.282	0.123 ± 0.209	0.187 ± 0.448	0.449 ± 0.520	-0.186 ± 0.354	0.220 ± 0.276	0.485 ± 0.192
399	–	–	–	36	–	5h35m15.63s	-5d23m10.51s	0.985 ± 0.739	1.355 ± 0.336	-0.155 ± 0.718	0.932 ± 0.861	-0.161 ± 0.527	0.261 ± 0.470	0.369 ± 0.399
400	–	–	–	35	–	5h35m15.63s	-5d23m31.51s	0.488 ± 0.234	0.586 ± 0.303	-0.417 ± 0.647	-0.114 ± 0.714	-0.467 ± 0.404	0.116 ± 0.394	-0.186 ± 0.330
401	–	389	–	–	–	5h35m15.64s	-5d22m56.45s	-0.019 ± 0.208	0.192 ± 0.044	0.209 ± 0.070	-0.502 ± 0.806	0.024 ± 0.477	-0.027 ± 0.338	0.123 ± 0.048
402	–	46	–	–	–	5h35m15.67s	-5d25m10.50s	0.050 ± 0.141	0.038 ± 0.151	-0.185 ± 0.466	0.050 ± 0.411	0.083 ± 0.341	0.024 ± 0.147	0.027 ± 0.210
403	–	246	–	–	–	5h35m15.68s	-5d23m39.10s	-0.147 ± 0.219	-0.156 ± 0.200	-0.321 ± 0.616	-0.494 ± 0.617	-0.183 ± 0.407	0.108 ± 0.385	-0.080 ± 0.224
404	–	23	–	–	–	5h35m15.68s	-5d25m33.30s	0.001 ± 0.145	0.083 ± 0.158	-0.026 ± 0.688	-0.052 ± 0.556	0.148 ± 0.455	-0.030 ± 0.201	-0.119 ± 0.234
405	–	236	–	–	–	5h35m15.70s	-5d23m41.90s	0.162 ± 0.228	-0.153 ± 0.207	-0.391 ± 0.549	-0.258 ± 0.728	-0.194 ± 0.379	0.181 ± 0.401	0.656 ± 0.263
406	–	–	29	–	–	5h35m15.72s	-5d23m12.54s	-0.018 ± 0.310	0.046 ± 0.232	0.515 ± 0.632	0.927 ± 1.004	0.570 ± 0.685	0.249 ± 0.449	0.526 ± 0.639
407	–	–	32	–	–	5h35m15.73s	-5d23m02.33s	-0.005 ± 0.243	-0.061 ± 0.199	-0.466 ± 0.802	0.532 ± 0.727	0.008 ± 0.497	0.033 ± 0.301	-0.090 ± 0.308
408	157-323	307	26	37	–	5h35m15.73s	-5d23m22.51s	2.421 ± 0.295	2.774 ± 0.316	1.940 ± 0.364	1.360 ± 0.350	1.673 ± 0.230	2.958 ± 0.438	2.310 ± 0.364
409	–	248	–	–	–	5h35m15.76s	-5d23m38.38s	0.024 ± 0.252	0.017 ± 0.219	0.138 ± 0.460	0.163 ± 0.634	0.127 ± 0.043	-0.067 ± 0.349	0.072 ± 0.025
410	–	158	–	–	–	5h35m15.77s	-5d24m11.50s	0.057 ± 0.230	0.115 ± 0.199	0.023 ± 0.471	0.345 ± 0.399	0.076 ± 0.277	-0.054 ± 0.272	-0.100 ± 0.186
411	–	–	11	–	–	5h35m15.77s	-5d23m22.80s	-0.142 ± 0.256	-0.326 ± 0.283	0.401 ± 1.009	0.444 ± 0.876	-0.465 ± 0.552	1.272 ± 0.467	0.102 ± 0.489
412	–	598	–	–	–	5h35m15.77s	-5d21m39.80s	0.020 ± 0.166	0.027 ± 0.239	-0.024 ± 0.904	-0.019 ± 0.819	-0.101 ± 0.628	0.011 ± 0.436	-0.027 ± 0.316
413	–	344	25	38	–	5h35m15.77s	-5d23m09.89s	2.490 ± 0.308	2.610 ± 0.278	2.344 ± 0.254	2.404 ± 0.271	3.608 ± 0.371	0.922 ± 0.203	1.427 ± 0.152
414	–	–	–	39	–	5h35m15.79s	-5d23m23.96s	0.346 ± 0.277	0.567 ± 0.283	-0.033 ± 0.800	0.281 ± 0.983	1.202 ± 0.471	0.075 ± 0.426	1.197 ± 0.379
415	–	137	–	–	–	5h35m15.79s	-5d24m24.70s	0.003 ± 0.139	-0.095 ± 0.158	-0.567 ± 0.418	-0.154 ± 0.397	0.082 ± 0.326	-0.154 ± 0.210	-0.451 ± 0.185
416	158-327	287	13	40	–	5h35m15.80s	-5d23m26.55s	9.918 ± 1.052	9.568 ± 1.005	2.948 ± 1.240	5.809 ± 1.462	4.426 ± 0.813	8.033 ± 0.899	7.292 ± 1.116
417	–	340	–	–	–	5h35m15.81s	-5d23m12.00s	0.111 ± 0.305	0.275 ± 0.282	0.168 ± 0.836	0.452 ± 0.994	0.201 ± 0.581	0.441 ± 0.454	0.641 ± 0.808
418	–	336	12	41	–	5h35m15.83s	-5d23m14.17s	6.089 ± 0.621	5.018 ± 0.507	2.665 ± 0.282	40.855 ± 4.090	20.736 ± 2.081	5.124 ± 0.538	9.655 ± 0.972
419	–	635	–	–	–	5h35m15.84s	-5d21m21.20s	0.022 ± 0.158	-0.010 ± 0.269	-0.377 ± 1.637	0.586 ± 1.790	0.130 ± 1.002	-0.002 ± 0.554	0.206 ± 0.428
420	–	420	–	–	–	5h35m15.84s	-5d22m45.90s	-0.092 ± 0.167	-0.205 ± 0.177	0.226 ± 0.644	0.185 ± 0.588	0.016 ± 0.425	0.049 ± 0.257	0.006 ± 0.262

Table 7.2 (cont'd)

ID	Proplyd Name	HC00 ID	GMR ID	Z04a ID	Other Names	R.A. [J2000]	Dec [J2000]	$F_{\nu,6cm}$ [mJy]	$F_{\nu,3.6cm}$ [mJy]	$F_{\nu,1.3cm,1}$ [mJy] [a]	$F_{\nu,1.3cm,2}$ [mJy] [a]	$F_{\nu,1.3cm,3}$ [mJy] [a]	$F_{\nu,1.3cm,4}$ [mJy] [a]	$F_{\nu,1.3cm,mean}$ [mJy] [a]
421	158-323	306	–	42	–	5h35m15.84s	-5d23m22.49s	8.726 ± 0.896	10.344 ± 1.049	7.469 ± 0.846	8.504 ± 0.937	9.550 ± 0.998	10.725 ± 1.100	8.700 ± 0.918
422	–	342	–	–	–	5h35m15.85s	-5d23m11.00s	-0.163 ± 0.326	0.027 ± 0.218	-0.256 ± 0.583	-0.487 ± 1.072	-0.118 ± 0.706	0.085 ± 0.349	-0.052 ± 0.553
423	158-326	291	10	43	–	5h35m15.85s	-5d23m25.57s	5.929 ± 0.668	5.325 ± 0.612	0.785 ± 0.910	0.754 ± 0.991	1.799 ± 0.582	4.762 ± 0.670	4.546 ± 0.802
424	–	370	–	–	–	5h35m15.88s	-5d23m01.99s	0.523 ± 0.151	0.336 ± 0.098	0.315 ± 0.612	0.425 ± 0.756	-0.388 ± 0.448	-0.202 ± 0.355	-0.261 ± 0.300
425	–	447	–	–	–	5h35m15.89s	-5d22m33.20s	0.080 ± 0.165	0.048 ± 0.202	0.098 ± 0.647	-0.237 ± 0.596	0.065 ± 0.418	0.012 ± 0.304	0.076 ± 0.211
426	–	122	–	–	–	5h35m15.90s	-5d24m31.20s	0.118 ± 0.177	0.078 ± 0.167	-0.129 ± 0.474	-0.153 ± 0.370	-0.018 ± 0.307	0.014 ± 0.192	-0.163 ± 0.150
427	159-338	250	24	44	–	5h35m15.91s	-5d23m37.98s	1.779 ± 0.225	2.118 ± 0.241	1.240 ± 0.202	1.335 ± 0.239	1.725 ± 0.238	2.010 ± 0.238	1.912 ± 0.226
428	159-418	145	–	–	–	5h35m15.91s	-5d24m17.78s	0.716 ± 0.172	0.431 ± 0.101	0.253 ± 0.476	0.195 ± 0.072	0.216 ± 0.379	0.435 ± 0.093	0.779 ± 0.183
429	159-221	490	–	–	–	5h35m15.94s	-5d22m21.07s	0.092 ± 0.159	0.202 ± 0.207	0.480 ± 0.665	0.318 ± 0.610	0.133 ± 0.383	-0.097 ± 0.311	0.336 ± 0.274
430	159-350	213	9	45	–	5h35m15.95s	-5d23m49.81s	11.575 ± 1.237	8.040 ± 0.917	3.238 ± 0.821	3.416 ± 0.727	3.754 ± 0.669	10.868 ± 1.229	7.929 ± 1.488
431	–	769	–	–	–	5h35m15.96s	-5d22m41.10s	0.042 ± 0.177	-0.012 ± 0.211	-0.213 ± 0.557	-0.220 ± 0.617	0.056 ± 0.404	-0.000 ± 0.357	0.433 ± 0.272
432	–	304	–	–	–	5h35m15.97s	-5d23m22.70s	-0.040 ± 0.213	0.023 ± 0.227	0.302 ± 0.768	-0.379 ± 0.731	0.824 ± 0.472	-0.285 ± 0.428	-0.326 ± 0.391
433	160-353	202	–	46	–	5h35m16.00s	-5d23m52.97s	3.910 ± 0.509	2.561 ± 0.445	0.194 ± 0.094	0.754 ± 0.438	0.624 ± 0.862	2.313 ± 0.325	2.394 ± 0.732
434	–	651	–	–	–	5h35m16.00s	-5d21m09.87s	0.294 ± 0.074	0.319 ± 0.131	-0.636 ± 3.359	-0.154 ± 2.808	0.056 ± 1.481	0.234 ± 0.797	0.339 ± 0.628
435	–	584	–	–	–	5h35m16.01s	-5d21m47.00s	0.109 ± 0.161	-0.136 ± 0.238	-0.188 ± 0.865	-0.065 ± 0.927	-0.025 ± 0.610	-0.031 ± 0.348	-0.187 ± 0.325
436	–	565	–	–	–	5h35m16.01s	-5d21m53.10s	-0.023 ± 0.171	0.043 ± 0.179	-0.186 ± 0.761	0.010 ± 0.673	0.291 ± 0.529	0.031 ± 0.289	0.073 ± 0.275
437	–	–	23	47	–	5h35m16.04s	-5d23m53.09s	-0.274 ± 0.273	-0.571 ± 0.271	-0.522 ± 0.629	-0.253 ± 0.568	-0.403 ± 0.373	3.644 ± 0.383	3.134 ± 0.438
438	161-324	296	8	48	–	5h35m16.07s	-5d23m24.38s	4.004 ± 0.427	5.095 ± 0.522	4.510 ± 0.496	5.194 ± 0.567	5.619 ± 0.579	5.881 ± 0.618	4.814 ± 0.500
439	–	350	15	49	–	5h35m16.07s	-5d23m07.07s	4.956 ± 0.538	5.031 ± 0.534	2.076 ± 0.460	3.217 ± 0.624	3.026 ± 0.445	4.159 ± 0.503	3.528 ± 0.499
440	–	–	–	–	–	5h35m16.08s	-5d23m53.44s	0.427 ± 0.095	1.050 ± 0.129	1.533 ± 0.167	0.088 ± 0.470	-0.253 ± 0.509	-0.356 ± 0.318	0.263 ± 0.044
441	–	401	–	–	–	5h35m16.08s	-5d22m54.10s	-0.021 ± 0.188	0.098 ± 0.252	0.432 ± 0.572	0.140 ± 0.685	-0.357 ± 0.471	0.124 ± 0.261	0.316 ± 0.256
442	161-328	285	22	50	–	5h35m16.08s	-5d23m27.84s	2.290 ± 0.301	2.202 ± 0.285	0.686 ± 37.210	-0.111 ± 0.752	1.132 ± 0.291	1.783 ± 0.321	1.991 ± 0.364
443	–	159	–	–	–	5h35m16.10s	-5d24m11.50s	0.503 ± 0.237	0.430 ± 0.205	-0.195 ± 0.421	-0.125 ± 0.429	-0.268 ± 0.357	0.101 ± 0.278	0.177 ± 0.197
444	–	303	–	51	–	5h35m16.10s	-5d23m23.11s	0.347 ± 0.118	0.244 ± 0.068	-0.187 ± 0.744	0.045 ± 0.835	0.163 ± 0.051	0.322 ± 0.374	0.331 ± 0.376
445	–	354	–	–	–	5h35m16.11s	-5d23m06.80s	-0.197 ± 0.240	-0.070 ± 0.262	0.008 ± 0.809	-0.396 ± 0.799	-0.685 ± 0.532	-0.433 ± 0.383	-0.433 ± 0.419
446	161-314	335	–	–	–	5h35m16.11s	-5d23m14.31s	1.035 ± 0.225	0.776 ± 0.153	0.191 ± 0.741	0.409 ± 0.922	-0.020 ± 0.517	0.116 ± 0.417	0.463 ± 0.383
447	–	511	–	–	–	5h35m16.12s	-5d22m12.50s	-0.094 ± 0.160	-0.024 ± 0.166	-0.143 ± 0.664	-0.449 ± 0.562	0.219 ± 0.431	0.100 ± 0.251	-0.212 ± 0.210
448	–	393	–	–	–	5h35m16.14s	-5d22m55.20s	0.377 ± 0.192	-0.014 ± 0.239	0.078 ± 0.622	-0.311 ± 0.599	-0.163 ± 0.436	0.246 ± 0.265	0.326 ± 0.257
449	–	768	–	–	–	5h35m16.14s	-5d22m45.10s	0.065 ± 0.198	0.025 ± 0.201	-0.112 ± 0.536	-0.029 ± 0.624	-0.062 ± 0.472	-0.045 ± 0.282	-0.302 ± 0.232
450	–	520	–	–	–	5h35m16.18s	-5d22m11.30s	0.177 ± 0.150	0.234 ± 0.201	-0.136 ± 0.619	0.304 ± 0.588	0.041 ± 0.484	0.171 ± 0.320	0.122 ± 0.209
451	–	650	–	–	–	5h35m16.19s	-5d21m10.90s	-0.075 ± 0.146	0.136 ± 0.257	0.614 ± 3.111	-0.917 ± 2.366	0.101 ± 1.310	0.104 ± 0.767	0.114 ± 0.632
452	162-133	615	–	–	–	5h35m16.19s	-5d21m32.39s	0.120 ± 0.150	-0.142 ± 0.249	-0.172 ± 1.205	-0.170 ± 1.170	0.284 ± 0.764	-0.173 ± 0.382	0.040 ± 0.438
453	–	78	–	–	–	5h35m16.20s	-5d24m56.40s	0.114 ± 0.131	0.030 ± 0.144	0.004 ± 0.472	-0.127 ± 0.437	0.061 ± 0.345	0.081 ± 0.157	0.040 ± 0.179
454	–	435	–	–	–	5h35m16.20s	-5d22m37.50s	-0.198 ± 0.215	-0.203 ± 0.187	-0.366 ± 0.556	0.328 ± 0.608	-0.032 ± 0.423	-0.096 ± 0.284	-0.223 ± 0.249
455	–	710	–	–	–	5h35m16.22s	-5d24m56.00s	0.087 ± 0.155	0.027 ± 0.155	-0.004 ± 0.370	0.116 ± 0.354	0.005 ± 0.377	-0.065 ± 0.159	-0.135 ± 0.149

Table 7.2 (cont'd)

ID	Proplyd Name	HC00 ID	GMR ID	Z04a ID	Other Names	R.A. [J2000]	Dec [J2000]	$F_{\nu,6cm}$ [mJy]	$F_{\nu,3.6cm}$ [mJy]	$F_{\nu,1.3cm,1}$ [mJy][a]	$F_{\nu,1.3cm,2}$ [mJy][a]	$F_{\nu,1.3cm,3}$ [mJy][a]	$F_{\nu,1.3cm,4}$ [mJy][a]	$F_{\nu,1.3cm,mean}$ [mJy][a]
456	–	758	–	–	–	5h35m16.24s	-5d22m24.30s	-0.041 ± 0.168	-0.019 ± 0.193	0.216 ± 0.647	0.085 ± 0.633	0.358 ± 0.432	0.004 ± 0.249	0.273 ± 0.212
457	–	317	–	–	–	5h35m16.24s	-5d23m19.10s	-0.020 ± 0.207	-0.030 ± 0.223	0.622 ± 0.604	-0.027 ± 0.944	0.084 ± 0.456	-0.238 ± 0.429	-0.482 ± 0.322
458	163-210	522	–	–	–	5h35m16.28s	-5d22m10.42s	-0.089 ± 0.153	-0.066 ± 0.213	0.058 ± 0.612	-0.018 ± 0.538	-0.224 ± 0.420	0.027 ± 0.295	-0.005 ± 0.207
459	–	652	–	–	–	5h35m16.29s	-5d21m09.20s	-0.151 ± 0.156	0.015 ± 0.271	-1.320 ± 3.143	0.855 ± 2.933	0.126 ± 1.491	-0.519 ± 0.751	0.021 ± 0.859
460	163-317	322	7	52	–	5h35m16.29s	-5d23m16.59s	7.680 ± 0.788	9.512 ± 0.961	7.866 ± 0.855	9.154 ± 0.997	9.613 ± 0.989	10.848 ± 1.106	8.911 ± 0.926
461	163-026	–	–	–	–	5h35m16.31s	-5d20m25.24s	0.020 ± 0.210	0.003 ± 0.389	$\cdots$	$\cdots$	$\cdots$	$\cdots$	$\cdots$
462	–	479	–	–	–	5h35m16.31s	-5d22m24.00s	0.018 ± 0.143	0.144 ± 0.191	-0.244 ± 0.617	0.244 ± 0.575	0.106 ± 0.361	0.039 ± 0.262	0.153 ± 0.240
463	163-222	488	–	–	–	5h35m16.31s	-5d22m21.55s	0.136 ± 0.164	0.026 ± 0.207	0.439 ± 0.682	0.281 ± 0.659	0.218 ± 0.401	0.172 ± 0.286	0.144 ± 0.236
464	–	738	–	–	–	5h35m16.32s	-5d20m59.00s	-0.000 ± 0.184	0.117 ± 0.264	$\cdots$	$\cdots$	0.401 ± 2.233	0.088 ± 1.135	0.602 ± 1.182
465	163-323	–	16	53	–	5h35m16.33s	-5d23m22.60s	2.591 ± 0.286	3.475 ± 0.360	4.343 ± 0.463	4.935 ± 0.521	4.895 ± 0.503	5.061 ± 0.534	4.339 ± 0.443
466	163-249	412	–	54	–	5h35m16.34s	-5d22m49.10s	0.661 ± 0.126	0.727 ± 0.136	0.381 ± 0.130	0.327 ± 0.085	0.423 ± 0.166	0.390 ± 0.098	0.675 ± 0.179
467	–	292	–	–	–	5h35m16.35s	-5d23m25.30s	-0.133 ± 0.195	-0.008 ± 0.194	-0.601 ± 0.648	-0.047 ± 0.716	-0.441 ± 0.516	-0.075 ± 0.387	0.049 ± 0.294
468	164-511	50	–	–	–	5h35m16.36s	-5d25m09.65s	0.020 ± 0.122	0.043 ± 0.209	0.163 ± 0.499	-0.067 ± 0.471	0.052 ± 0.333	0.010 ± 0.143	-0.075 ± 0.157
469	–	171	–	–	–	5h35m16.38s	-5d24m03.37s	0.428 ± 0.130	0.340 ± 0.072	0.191 ± 0.054	0.166 ± 0.328	2.317 ± 0.238	0.597 ± 0.316	0.595 ± 0.066
470	–	485	–	–	–	5h35m16.38s	-5d22m22.30s	-0.076 ± 0.172	0.117 ± 0.207	-0.134 ± 0.527	-0.165 ± 0.549	0.007 ± 0.457	-0.192 ± 0.307	-0.151 ± 0.241
471	–	112	–	–	–	5h35m16.39s	-5d24m37.20s	0.094 ± 0.150	-0.014 ± 0.160	0.201 ± 0.354	-0.070 ± 0.425	-0.044 ± 0.312	0.075 ± 0.181	0.112 ± 0.156
472	–	571	–	–	–	5h35m16.39s	-5d21m50.60s	0.048 ± 0.149	0.111 ± 0.253	-0.042 ± 0.809	-0.005 ± 0.747	0.129 ± 0.528	0.023 ± 0.281	-0.018 ± 0.284
473	–	–	K	55	–	5h35m16.40s	-5d22m35.32s	0.161 ± 0.208	0.870 ± 0.203	1.315 ± 0.154	1.488 ± 0.181	1.422 ± 0.168	1.359 ± 0.174	1.462 ± 0.164
474	–	341	–	–	–	5h35m16.41s	-5d23m11.50s	0.094 ± 0.186	0.072 ± 0.205	-0.352 ± 0.561	0.217 ± 0.940	0.051 ± 0.491	0.014 ± 0.303	0.075 ± 0.313
475	–	514	–	–	–	5h35m16.43s	-5d22m12.20s	0.020 ± 0.149	-0.049 ± 0.182	0.093 ± 0.666	0.143 ± 0.611	0.219 ± 0.448	0.122 ± 0.297	0.212 ± 0.236
476	–	309	–	–	–	5h35m16.47s	-5d23m22.80s	0.113 ± 0.177	0.013 ± 0.227	-0.485 ± 0.649	-0.627 ± 0.850	0.254 ± 0.414	-0.099 ± 0.335	0.005 ± 0.307
477	165-235	442	–	56	–	5h35m16.48s	-5d22m35.49s	0.649 ± 0.207	0.417 ± 0.127	0.067 ± 0.526	0.387 ± 0.538	0.266 ± 0.451	0.183 ± 0.248	0.234 ± 0.301
478	–	390	–	–	–	5h35m16.49s	-5d22m56.50s	0.030 ± 0.192	0.070 ± 0.220	0.221 ± 0.623	-0.193 ± 0.642	0.089 ± 0.429	0.097 ± 0.249	0.159 ± 0.234
479	165-254	745	–	–	–	5h35m16.55s	-5d22m53.70s	-0.095 ± 0.187	0.072 ± 0.195	-0.024 ± 0.691	-0.312 ± 0.627	-0.013 ± 0.490	0.176 ± 0.292	0.131 ± 0.238
480	165-519	40	–	–	–	5h35m16.58s	-5d25m17.77s	0.066 ± 0.133	0.083 ± 0.183	0.129 ± 0.473	0.185 ± 0.386	-0.007 ± 0.340	-0.014 ± 0.164	0.082 ± 0.201
481	166-406	165	–	–	–	5h35m16.58s	-5d24m06.05s	0.158 ± 0.211	-0.041 ± 0.192	0.134 ± 0.047	-0.219 ± 0.431	0.249 ± 0.302	0.441 ± 0.256	0.598 ± 0.185
482	–	644	–	–	–	5h35m16.59s	-5d21m15.60s	0.053 ± 0.157	-0.024 ± 0.277	-0.276 ± 2.337	0.185 ± 2.200	-0.718 ± 1.243	-0.126 ± 0.513	-0.310 ± 0.544
483	166-250	–	–	57	–	5h35m16.60s	-5d22m50.37s	0.427 ± 0.108	0.506 ± 0.120	0.351 ± 0.568	0.143 ± 0.619	0.272 ± 0.097	0.242 ± 0.073	0.445 ± 0.137
484	166-316	325	21	58	–	5h35m16.62s	-5d23m16.15s	1.758 ± 0.232	2.227 ± 0.250	1.954 ± 0.229	2.177 ± 0.307	2.330 ± 0.257	2.407 ± 0.284	2.081 ± 0.230
485	–	126	–	–	–	5h35m16.63s	-5d24m28.10s	0.113 ± 0.168	-0.040 ± 0.176	-0.070 ± 0.381	0.212 ± 0.398	-0.018 ± 0.309	-0.017 ± 0.194	0.105 ± 0.172
486	–	620	–	–	–	5h35m16.64s	-5d21m30.90s	-0.064 ± 0.160	-0.022 ± 0.227	-0.129 ± 1.205	-0.116 ± 1.195	0.198 ± 0.693	-0.090 ± 0.394	0.161 ± 0.386
487	–	567	–	–	–	5h35m16.65s	-5d21m52.70s	-0.076 ± 0.156	-0.000 ± 0.194	0.034 ± 0.701	-0.137 ± 0.697	0.145 ± 0.507	-0.068 ± 0.252	-0.090 ± 0.252
488	–	280	–	–	–	5h35m16.66s	-5d23m28.90s	0.009 ± 0.240	0.024 ± 0.224	-0.463 ± 0.654	-0.080 ± 0.670	1.012 ± 0.400	-0.107 ± 0.375	-0.315 ± 0.276
489	–	293	–	–	–	5h35m16.73s	-5d23m25.20s	0.075 ± 0.193	-0.175 ± 0.300	-0.218 ± 0.650	-0.135 ± 0.788	-0.658 ± 0.435	-0.215 ± 0.429	-0.411 ± 0.372
490	167-231	457	–	–	–	5h35m16.74s	-5d22m31.30s	-0.132 ± 0.190	0.034 ± 0.217	0.078 ± 0.591	-0.007 ± 0.605	0.183 ± 0.402	0.049 ± 0.252	0.093 ± 0.242

Table 7.2 (cont'd)

ID	Proplyd Name	HC00 ID	GMR ID	Z04a ID	Other Names	R.A. [J2000]	Dec [J2000]	$F_{\nu,6cm}$ [mJy]	$F_{\nu,3.6cm}$ [mJy]	$F_{\nu,1.3cm,1}$[a] [mJy]	$F_{\nu,1.3cm,2}$[a] [mJy]	$F_{\nu,1.3cm,3}$[a] [mJy]	$F_{\nu,1.3cm,4}$[a] [mJy]	$F_{\nu,1.3cm,mean}$[a] [mJy]
491	167-317	323	6	59	—	5h35m16.76s	-5d23m16.49s	16.563 ± 1.673	22.058 ± 2.218	17.198 ± 1.812	20.801 ± 2.164	21.385 ± 2.174	22.660 ± 2.280	18.481 ± 1.888
492	—	170	—	—	—	5h35m16.77s	-5d24m04.28s	0.421 ± 0.105	0.410 ± 0.090	0.193 ± 0.050	0.139 ± 0.040	0.593 ± 0.081	0.620 ± 0.102	0.611 ± 0.097
493	—	—	5	—	—	5h35m16.77s	-5d23m26.51s	0.070 ± 0.205	-0.181 ± 0.271	0.762 ± 0.806	0.548 ± 0.730	-0.151 ± 0.468	0.299 ± 0.389	0.361 ± 0.533
494	168-328	284	17	60	—	5h35m16.77s	-5d23m28.09s	2.894 ± 0.324	3.554 ± 0.373	2.876 ± 0.328	3.124 ± 0.343	3.687 ± 0.387	3.921 ± 0.426	3.363 ± 0.354
495	—	518	—	—	—	5h35m16.78s	-5d22m11.70s	0.108 ± 0.140	0.085 ± 0.227	-0.047 ± 0.622	-0.194 ± 0.575	-0.002 ± 0.383	0.058 ± 0.239	0.088 ± 0.247
496	—	—	—	—	—	5h35m16.81s	-5d22m34.71s	0.142 ± 0.168	-0.123 ± 0.189	-0.058 ± 0.540	-0.113 ± 0.655	-0.068 ± 0.431	-0.003 ± 0.237	0.230 ± 0.251
497	168-235	120	—	—	—	5h35m16.82s	-5d24m32.20s	-0.083 ± 0.164	-0.068 ± 0.166	0.240 ± 0.345	-0.194 ± 0.352	-0.128 ± 0.318	0.057 ± 0.168	0.197 ± 0.141
498	—	235	—	—	—	5h35m16.84s	-5d23m42.30s	0.058 ± 0.176	0.220 ± 0.209	1.224 ± 0.565	0.343 ± 0.470	0.054 ± 0.392	-0.075 ± 0.306	0.489 ± 0.246
499	168-326	289	20	61	—	5h35m16.85s	-5d23m26.28s	13.503 ± 1.372	16.537 ± 1.675	9.008 ± 0.950	10.444 ± 1.091	10.821 ± 1.102	17.633 ± 1.797	9.694 ± 0.997
500	—	349	—	—	—	5h35m16.87s	-5d23m07.10s	0.084 ± 0.161	0.036 ± 0.216	0.824 ± 0.572	0.118 ± 0.656	-0.373 ± 0.442	-0.010 ± 0.260	0.127 ± 0.237
501	169-338	—	—	62	—	5h35m16.89s	-5d23m38.09s	0.320 ± 0.079	0.360 ± 0.072	0.499 ± 0.144	0.352 ± 0.197	0.338 ± 0.082	0.190 ± 0.329	0.494 ± 0.138
502	—	484	—	—	—	5h35m16.90s	-5d22m22.50s	0.085 ± 0.171	0.093 ± 0.180	0.031 ± 0.544	0.004 ± 0.537	0.011 ± 0.396	-0.103 ± 0.224	-0.019 ± 0.256
503	—	441	—	—	—	5h35m16.91s	-5d22m35.20s	-0.011 ± 0.193	0.034 ± 0.208	0.151 ± 0.457	0.082 ± 0.670	-0.043 ± 0.430	0.055 ± 0.209	0.212 ± 0.217
504	—	397	—	—	—	5h35m16.91s	-5d22m55.10s	0.123 ± 0.189	0.008 ± 0.167	0.225 ± 0.529	0.337 ± 0.615	-0.026 ± 0.407	0.032 ± 0.230	0.343 ± 0.232
505	—	—	M	—	—	5h35m16.92s	-5d23m58.27s	-0.173 ± 0.299	-0.056 ± 0.275	-0.105 ± 0.461	0.067 ± 0.431	-0.734 ± 0.380	-0.093 ± 0.306	0.016 ± 0.223
506	—	494	—	—	—	5h35m16.94s	-5d22m20.70s	-0.043 ± 0.179	-0.088 ± 0.185	-0.230 ± 0.552	0.224 ± 0.621	0.026 ± 0.371	0.057 ± 0.250	-0.161 ± 0.236
507	—	—	27	—	—	5h35m16.94s	-5d23m16.01s	0.023 ± 0.187	-0.029 ± 0.190	-1.409 ± 0.702	-0.199 ± 0.835	-0.958 ± 0.407	0.173 ± 0.364	0.171 ± 0.311
508	—	524	—	—	—	5h35m16.94s	-5d22m09.90s	-0.062 ± 0.183	0.139 ± 0.221	0.319 ± 0.576	0.128 ± 0.600	0.223 ± 0.375	-0.081 ± 0.277	-0.022 ± 0.224
509	—	675	—	—	—	5h35m16.95s	-5d20m59.90s	0.057 ± 0.198	-0.039 ± 0.285	⋯	⋯	-0.185 ± 1.932	0.174 ± 0.916	0.784 ± 1.112
510	—	3	—	—	—	5h35m16.95s	-5d25m47.10s	0.005 ± 0.138	-0.071 ± 0.162	0.154 ± 0.731	0.085 ± 0.716	-0.089 ± 0.535	0.055 ± 0.202	0.018 ± 0.256
511	—	182	—	—	—	5h35m16.97s	-5d23m59.67s	0.517 ± 0.245	0.263 ± 0.262	0.676 ± 0.465	0.563 ± 0.405	0.219 ± 0.278	0.661 ± 0.319	1.142 ± 0.247
512	170-249	414	E	63	—	5h35m16.97s	-5d22m48.72s	3.607 ± 0.421	3.355 ± 0.420	1.031 ± 0.581	1.721 ± 3.648	1.351 ± 69.472	2.820 ± 0.382	3.231 ± 0.661
513	—	587	—	—	—	5h35m16.98s	-5d21m45.40s	-0.005 ± 0.174	0.028 ± 0.213	0.095 ± 0.801	0.132 ± 0.825	-0.070 ± 0.541	-0.209 ± 0.282	-0.121 ± 0.276
514	—	623	—	—	—	5h35m16.98s	-5d21m29.40s	-0.022 ± 0.147	-0.009 ± 0.257	0.071 ± 1.320	-0.052 ± 1.270	0.072 ± 0.672	-0.116 ± 0.391	-0.046 ± 0.392
515	170-301	375	—	—	—	5h35m16.98s	-5d23m00.99s	0.381 ± 0.118	0.328 ± 0.099	-0.171 ± 0.682	0.004 ± 0.669	0.297 ± 0.430	0.083 ± 0.248	0.382 ± 0.158
516	170-337	252	4	64	—	5h35m16.98s	-5d23m36.98s	10.244 ± 1.059	8.989 ± 0.939	3.676 ± 0.974	3.863 ± 0.774	5.147 ± 0.709	8.758 ± 0.958	7.599 ± 0.926
517	—	450	—	—	—	5h35m17.01s	-5d22m33.10s	-0.093 ± 0.186	-0.032 ± 0.203	-0.106 ± 0.601	-0.150 ± 0.561	-0.037 ± 0.421	-0.171 ± 0.256	-0.300 ± 0.215
518	171-334	259	3	65	—	5h35m17.07s	-5d23m34.03s	3.369 ± 0.356	3.874 ± 0.407	2.884 ± 0.416	3.201 ± 0.444	3.733 ± 0.426	3.865 ± 0.429	3.660 ± 0.407
519	171-340	244	—	66	—	5h35m17.07s	-5d23m39.78s	2.574 ± 0.419	0.780 ± 0.370	0.141 ± 0.524	0.647 ± 0.579	0.705 ± 0.389	0.898 ± 0.382	1.537 ± 1.354
520	—	631	—	—	—	5h35m17.07s	-5d21m23.70s	0.030 ± 0.163	0.052 ± 0.245	0.060 ± 1.562	-0.509 ± 1.466	-0.380 ± 0.940	0.031 ± 0.365	-0.005 ± 0.398
521	—	410	—	—	—	5h35m17.12s	-5d22m50.10s	-0.139 ± 0.223	-0.265 ± 0.206	-0.159 ± 0.546	0.032 ± 0.616	-0.266 ± 0.444	0.039 ± 0.225	-0.116 ± 0.284
522	—	75	—	—	—	5h35m17.12s	-5d24m58.70s	0.057 ± 0.121	-0.012 ± 0.143	0.002 ± 0.411	-0.057 ± 0.387	0.017 ± 0.323	0.041 ± 0.143	-0.078 ± 0.162
523	—	517	—	—	—	5h35m17.13s	-5d22m11.90s	-0.130 ± 0.230	-0.085 ± 0.230	0.114 ± 0.607	-0.033 ± 0.581	0.147 ± 0.473	0.205 ± 0.228	0.250 ± 0.220
524	171-434	118	—	—	—	5h35m17.13s	-5d24m34.53s	-0.095 ± 0.151	0.130 ± 0.045	-0.020 ± 0.405	0.212 ± 0.336	-0.011 ± 0.287	0.070 ± 0.144	0.039 ± 0.141
525	—	107	—	—	—	5h35m17.15s	-5d24m39.00s	0.111 ± 0.140	-0.028 ± 0.191	-0.167 ± 0.426	0.034 ± 0.365	-0.127 ± 0.275	0.071 ± 0.168	0.094 ± 0.150

Table 7.2 (cont'd)

ID	Proplyd Name	HC00 ID	GMR ID	Z04a ID	Other Names	R.A. [J2000]	Dec [J2000]	$F_{\nu,6cm}$ [mJy]	$F_{\nu,3.6cm}$ [mJy]	$F_{\nu,1.3cm,1}$ [a] [mJy]	$F_{\nu,1.3cm,2}$ [a] [mJy]	$F_{\nu,1.3cm,3}$ [a] [mJy]	$F_{\nu,1.3cm,4}$ [a] [mJy]	$F_{\nu,1.3cm,mean}$ [a] [mJy]
526	–	315	–	–	–	5h35m17.16s	-5d23m20.40s	-0.145 ± 0.221	-0.161 ± 0.196	0.336 ± 0.636	0.125 ± 0.642	-0.387 ± 0.398	0.095 ± 0.352	0.386 ± 0.242
527	–	661	–	–	–	5h35m17.22s	-5d21m05.40s	0.071 ± 0.144	0.129 ± 0.295	0.785 ± 3.297	0.287 ± 3.344	0.122 ± 1.848	-0.217 ± 0.658	-0.255 ± 0.797
528	172-028	–	–	–	–	5h35m17.22s	-5d20m27.84s	-0.159 ± 0.210	0.098 ± 0.382	$\cdots$	$\cdots$	$\cdots$	$\cdots$	$\cdots$
529	–	618	–	–	–	5h35m17.22s	-5d21m31.70s	1.598 ± 0.179	3.208 ± 0.329	6.968 ± 0.719	4.538 ± 0.480	0.470 ± 0.583	-0.131 ± 0.334	1.254 ± 0.132
530	–	–	–	67	–	5h35m17.23s	-5d23m26.55s	1.181 ± 0.374	0.414 ± 0.236	1.425 ± 0.643	0.804 ± 0.695	0.356 ± 0.417	0.727 ± 0.383	1.345 ± 0.297
531	–	330	–	–	–	5h35m17.24s	-5d23m16.60s	0.019 ± 0.184	0.000 ± 0.220	0.404 ± 0.620	0.369 ± 0.672	-0.006 ± 0.501	-0.048 ± 0.289	0.144 ± 0.242
532	–	138	–	–	–	5h35m17.27s	-5d24m24.20s	-0.128 ± 0.154	0.066 ± 0.159	0.075 ± 0.427	0.113 ± 0.372	-0.064 ± 0.287	0.111 ± 0.149	0.090 ± 0.184
533	–	9	–	–	–	5h35m17.29s	-5d25m45.20s	-0.015 ± 0.141	0.047 ± 0.156	0.093 ± 0.750	0.067 ± 0.626	0.021 ± 0.485	-0.011 ± 0.184	0.073 ± 0.232
534	–	–	–	–	–	5h35m17.32s	-5d22m34.90s	-0.166 ± 0.203	-0.252 ± 0.214	-0.238 ± 0.567	0.254 ± 0.519	-0.002 ± 0.454	0.036 ± 0.228	0.085 ± 0.303
535	173-341	239	–	68	–	5h35m17.33s	-5d23m41.42s	1.201 ± 0.168	0.860 ± 0.130	0.589 ± 2.773	0.606 ± 0.163	0.513 ± 0.106	0.785 ± 0.163	0.760 ± 0.159
536	–	493	–	–	–	5h35m17.34s	-5d22m21.20s	-0.026 ± 0.151	0.069 ± 0.219	0.241 ± 0.536	-0.155 ± 0.556	-0.102 ± 0.419	0.054 ± 0.222	0.142 ± 0.233
537	173-236	440	L	69	–	5h35m17.35s	-5d22m35.93s	3.073 ± 0.376	2.332 ± 0.311	1.436 ± 3.520	0.985 ± 0.559	1.094 ± 1.498	2.269 ± 0.308	2.741 ± 0.524
538	–	640	–	–	–	5h35m17.36s	-5d21m17.90s	-0.039 ± 0.156	-0.076 ± 0.261	-0.171 ± 1.841	0.032 ± 1.763	-0.022 ± 0.939	0.135 ± 0.429	-0.018 ± 0.488
539	–	10	–	–	–	5h35m17.37s	-5d25m44.82s	0.074 ± 0.159	-0.041 ± 0.176	0.148 ± 0.686	0.129 ± 0.668	0.095 ± 0.548	0.051 ± 0.171	0.058 ± 0.019
540	174-305	362	–	–	–	5h35m17.38s	-5d23m04.88s	0.112 ± 0.185	0.045 ± 0.201	0.306 ± 0.575	0.497 ± 0.499	0.218 ± 0.435	-0.074 ± 0.232	-0.063 ± 0.216
541	–	422	–	–	–	5h35m17.38s	-5d22m45.80s	0.024 ± 0.160	-0.025 ± 0.209	0.128 ± 0.523	-0.121 ± 0.586	-0.012 ± 0.379	0.180 ± 0.215	0.377 ± 0.253
542	174-414	153	–	–	–	5h35m17.38s	-5d24m13.90s	0.130 ± 0.171	0.029 ± 0.172	0.260 ± 0.317	-0.062 ± 0.407	0.118 ± 0.326	0.086 ± 0.237	0.132 ± 0.176
543	–	180	–	–	–	5h35m17.39s	-5d24m00.30s	-0.179 ± 0.190	0.137 ± 0.180	0.229 ± 0.448	0.348 ± 0.462	0.126 ± 0.349	0.068 ± 0.264	0.264 ± 0.176
544	–	540	–	–	–	5h35m17.39s	-5d22m03.61s	7.978 ± 0.803	8.504 ± 0.854	6.535 ± 0.660	3.429 ± 0.355	0.168 ± 0.045	0.183 ± 0.063	1.292 ± 0.139
545	–	237	–	–	–	5h35m17.41s	-5d23m41.80s	0.178 ± 0.186	0.307 ± 0.202	0.241 ± 0.517	0.495 ± 0.550	0.716 ± 0.375	0.104 ± 0.319	0.620 ± 0.260
546	–	313	–	70	–	5h35m17.47s	-5d23m21.08s	0.490 ± 0.129	0.424 ± 0.090	0.430 ± 0.100	0.313 ± 0.093	0.354 ± 0.073	0.576 ± 0.792	0.317 ± 0.063
547	–	150	–	–	–	5h35m17.48s	-5d24m17.40s	0.131 ± 0.166	0.037 ± 0.177	0.032 ± 0.368	-0.142 ± 0.408	-0.030 ± 0.346	-0.033 ± 0.185	-0.097 ± 0.146
548	175-251	406	–	–	–	5h35m17.49s	-5d22m51.35s	0.531 ± 0.133	-0.001 ± 0.189	0.364 ± 0.587	0.270 ± 0.585	0.040 ± 0.431	0.139 ± 0.215	0.251 ± 0.149
549	–	658	–	–	–	5h35m17.52s	-5d21m06.41s	0.115 ± 0.187	-0.088 ± 0.326	-0.815 ± 3.094	1.051 ± 2.507	0.385 ± 0.134	-0.126 ± 0.601	-0.273 ± 0.778
550	175-355	194	–	–	–	5h35m17.54s	-5d23m55.07s	-0.140 ± 0.171	0.178 ± 0.198	-0.064 ± 0.440	-0.361 ± 0.473	0.275 ± 0.330	-0.018 ± 0.246	-0.024 ± 0.175
551	175-543	12	–	–	–	5h35m17.54s	-5d25m42.89s	0.062 ± 0.158	-0.002 ± 0.128	-0.012 ± 0.847	-0.307 ± 0.602	-0.121 ± 0.460	0.032 ± 0.177	-0.117 ± 0.230
552	–	550	–	–	–	5h35m17.55s	-5d22m00.30s	0.030 ± 0.161	0.104 ± 0.245	-0.160 ± 0.647	0.224 ± 0.661	0.006 ± 0.440	0.079 ± 0.210	-0.017 ± 0.231
553	–	586	–	–	–	5h35m17.56s	-5d21m45.60s	-0.000 ± 0.171	-0.023 ± 0.232	0.428 ± 0.705	-0.098 ± 0.756	0.166 ± 0.469	0.214 ± 0.253	0.207 ± 0.272
554	–	388	–	–	–	5h35m17.56s	-5d22m56.80s	0.045 ± 0.190	-0.106 ± 0.177	-0.014 ± 0.486	0.212 ± 0.513	0.061 ± 0.380	-0.038 ± 0.209	-0.085 ± 0.215
555	176-325	295	2	71	–	5h35m17.56s	-5d23m24.87s	4.931 ± 0.516	5.062 ± 0.530	2.949 ± 0.482	3.051 ± 0.434	4.034 ± 0.470	5.111 ± 0.567	4.469 ± 0.525
556	–	469	–	–	–	5h35m17.58s	-5d22m27.80s	0.062 ± 0.203	0.140 ± 0.218	0.179 ± 0.465	0.254 ± 0.473	0.139 ± 0.384	-0.072 ± 0.219	-0.116 ± 0.216
557	–	162	–	–	–	5h35m17.58s	-5d24m09.00s	0.113 ± 0.177	-0.095 ± 0.165	0.048 ± 0.415	-0.191 ± 0.481	0.027 ± 0.315	-0.052 ± 0.212	-0.156 ± 0.163
558	–	513	–	–	–	5h35m17.62s	-5d22m12.60s	-0.051 ± 0.151	-0.230 ± 0.219	0.056 ± 0.487	0.030 ± 0.542	0.131 ± 0.379	-0.081 ± 0.193	-0.331 ± 0.212
559	–	563	–	–	–	5h35m17.62s	-5d21m53.90s	-0.042 ± 0.168	0.101 ± 0.246	0.007 ± 0.713	-0.042 ± 0.659	-0.111 ± 0.475	-0.054 ± 0.240	-0.166 ± 0.246
560	–	–	–	–	–	5h35m17.64s	-5d19m56.41s	0.356 ± 0.093	0.273 ± 0.503	$\cdots$	$\cdots$	$\cdots$	$\cdots$	$\cdots$

198

Table 7.2 (cont'd)

ID	Proplyd Name	HC00 ID	GMR ID	Z04a ID	Other Names	R.A. [J2000]	Dec [J2000]	$F_{\nu,6cm}$ [mJy]	$F_{\nu,3.6cm}$ [mJy]	$F_{\nu,1.3cm,1}$[a] [mJy]	$F_{\nu,1.3cm,2}$[a] [mJy]	$F_{\nu,1.3cm,3}$[a] [mJy]	$F_{\nu,1.3cm,4}$[a] [mJy]	$F_{\nu,1.3cm,mean}$[a] [mJy]
561	176-252	405	–	–	–	5h35m17.65s	-5d22m51.68s	-0.002 ± 0.183	0.029 ± 0.205	-0.147 ± 0.541	-0.059 ± 0.542	0.164 ± 0.382	0.099 ± 0.236	0.081 ± 0.230
562	–	527	–	–	–	5h35m17.66s	-5d22m07.90s	0.100 ± 0.170	-0.053 ± 0.219	0.149 ± 0.546	0.043 ± 0.580	0.008 ± 0.461	-0.001 ± 0.194	-0.067 ± 0.227
563	–	47	–	–	–	5h35m17.66s	-5d25m10.70s	0.018 ± 0.142	0.014 ± 0.168	-0.011 ± 0.525	0.090 ± 0.395	0.019 ± 0.320	0.076 ± 0.139	0.090 ± 0.170
564	177-341W	241	1	72	–	5h35m17.68s	-5d23m40.89s	13.538 ± 1.400	10.992 ± 1.159	2.802 ± 5.098	4.251 ± 1.347	4.883 ± 0.985	10.267 ± 1.178	8.002 ± 1.133
565	177-454	86	–	–	–	5h35m17.69s	-5d24m54.10s	0.014 ± 0.158	0.089 ± 0.169	0.223 ± 0.392	0.141 ± 0.392	0.017 ± 0.273	0.077 ± 0.159	0.204 ± 0.150
566	177-541	14	–	–	–	5h35m17.71s	-5d25m40.83s	0.067 ± 0.133	0.040 ± 0.183	0.117 ± 0.683	-0.008 ± 0.641	0.084 ± 0.459	-0.014 ± 0.180	0.105 ± 0.227
567	177-341E	–	–	–	–	5h35m17.73s	-5d23m41.10s	0.243 ± 0.206	-0.062 ± 0.269	-0.461 ± 0.803	-0.185 ± 0.639	-0.897 ± 0.526	0.285 ± 0.363	-0.354 ± 0.510
568	177-444	98	–	–	–	5h35m17.74s	-5d24m43.78s	0.077 ± 0.128	-0.067 ± 0.150	-0.131 ± 0.371	0.150 ± 0.378	-0.027 ± 0.303	0.023 ± 0.124	0.009 ± 0.143
569	–	333	–	–	–	5h35m17.74s	-5d23m14.90s	-0.102 ± 0.141	-0.026 ± 0.175	-0.109 ± 0.586	0.375 ± 0.567	0.107 ± 0.374	-0.106 ± 0.290	-0.105 ± 0.220
570	–	462	–	–	–	5h35m17.76s	-5d22m31.00s	0.101 ± 0.176	0.179 ± 0.220	0.054 ± 0.598	0.291 ± 0.572	0.052 ± 0.383	0.071 ± 0.206	0.160 ± 0.210
571	–	234	–	–	–	5h35m17.77s	-5d23m42.60s	0.407 ± 0.208	-0.029 ± 0.225	-0.232 ± 0.512	0.219 ± 0.534	1.216 ± 0.419	0.344 ± 0.360	0.863 ± 0.297
572	–	230	–	–	–	5h35m17.79s	-5d23m44.20s	0.176 ± 0.224	-0.324 ± 0.185	0.232 ± 0.600	0.020 ± 0.536	-0.361 ± 0.350	0.276 ± 0.305	0.353 ± 0.244
573	178-441	104	–	–	–	5h35m17.82s	-5d24m41.08s	0.034 ± 0.146	-0.040 ± 0.136	-0.008 ± 0.406	-0.241 ± 0.407	-0.034 ± 0.297	0.108 ± 0.134	0.170 ± 0.151
574	–	124	–	–	–	5h35m17.82s	-5d24m30.60s	-0.016 ± 0.127	0.046 ± 0.155	0.146 ± 0.419	-0.164 ± 0.404	0.101 ± 0.322	-0.053 ± 0.163	-0.124 ± 0.143
575	–	332	–	–	–	5h35m17.82s	-5d23m15.60s	0.074 ± 0.149	-0.107 ± 0.211	-0.086 ± 0.575	-0.078 ± 0.647	0.323 ± 0.393	-0.210 ± 0.250	-0.402 ± 0.252
576	–	496	–	–	–	5h35m17.83s	-5d22m19.60s	0.066 ± 0.173	-0.017 ± 0.207	-0.258 ± 0.523	0.029 ± 0.430	-0.016 ± 0.369	-0.118 ± 0.205	-0.110 ± 0.238
577	178-258	383	–	–	–	5h35m17.84s	-5d22m58.18s	0.002 ± 0.178	0.013 ± 0.188	0.087 ± 0.552	-0.106 ± 0.577	0.363 ± 0.324	0.114 ± 0.178	0.442 ± 0.225
578	–	681	–	–	–	5h35m17.86s	-5d20m54.10s	-0.046 ± 0.204	0.096 ± 0.345	$\cdots$	$\cdots$	0.192 ± 2.939	-0.180 ± 1.120	-0.328 ± 1.401
579	–	367	–	–	–	5h35m17.87s	-5d23m03.10s	0.015 ± 0.143	-0.109 ± 0.176	-0.552 ± 0.537	-0.375 ± 0.557	-0.032 ± 0.386	-0.118 ± 0.228	-0.403 ± 0.250
580	–	542	–	–	–	5h35m17.88s	-5d22m03.00s	-0.112 ± 0.161	0.059 ± 0.198	0.019 ± 0.616	-0.206 ± 0.556	-0.370 ± 0.461	-0.032 ± 0.224	-0.058 ± 0.251
581	–	–	–	–	–	5h35m17.89s	-5d18m35.10s	0.120 ± 0.418	$\cdots$	$\cdots$	$\cdots$	$\cdots$	$\cdots$	$\cdots$
582	–	566	–	–	–	5h35m17.90s	-5d21m53.40s	0.042 ± 0.145	-0.097 ± 0.207	0.153 ± 0.618	-0.251 ± 0.692	-0.061 ± 0.428	-0.047 ± 0.204	-0.077 ± 0.220
583	179-056	679	–	–	–	5h35m17.92s	-5d20m55.47s	-0.103 ± 0.157	0.088 ± 0.322	$\cdots$	$\cdots$	0.477 ± 2.630	-0.131 ± 0.989	0.961 ± 1.377
584	–	56	–	–	–	5h35m17.94s	-5d25m06.50s	0.051 ± 0.185	-0.018 ± 0.172	0.326 ± 0.442	-0.031 ± 0.404	0.065 ± 0.316	0.141 ± 0.152	0.281 ± 0.165
585	–	689	–	–	–	5h35m17.95s	-5d20m49.30s	-0.069 ± 0.189	0.049 ± 0.350	$\cdots$	$\cdots$	$\cdots$	$\cdots$	$\cdots$
586	–	35	–	–	–	5h35m17.95s	-5d25m21.30s	0.011 ± 0.134	0.050 ± 0.179	0.137 ± 0.430	0.003 ± 0.476	-0.045 ± 0.378	0.042 ± 0.164	0.059 ± 0.173
587	–	425	G	73	–	5h35m17.95s	-5d22m45.45s	1.839 ± 0.209	1.971 ± 0.207	1.731 ± 0.183	22.228 ± 2.225	1.552 ± 0.164	1.022 ± 0.134	3.384 ± 0.344
588	–	21	–	–	–	5h35m17.96s	-5d25m34.10s	0.004 ± 0.161	0.044 ± 0.163	0.328 ± 0.650	-0.002 ± 0.610	-0.033 ± 0.373	0.047 ± 0.173	0.061 ± 0.226
589	179-354	764	–	–	–	5h35m17.96s	-5d23m53.55s	0.158 ± 0.179	-0.036 ± 0.192	0.388 ± 0.488	-0.139 ± 0.549	0.081 ± 0.371	0.200 ± 0.225	0.166 ± 0.197
590	–	256	–	–	–	5h35m17.97s	-5d23m35.50s	0.073 ± 0.178	0.154 ± 0.186	-0.652 ± 0.602	-0.096 ± 0.594	0.222 ± 0.405	-0.054 ± 0.327	-0.199 ± 0.232
591	–	676	–	–	–	5h35m17.98s	-5d20m59.60s	-0.047 ± 0.175	0.251 ± 0.294	$\cdots$	$\cdots$	-0.204 ± 2.343	0.144 ± 0.738	0.184 ± 1.019
592	–	501	–	–	–	5h35m18.03s	-5d22m18.20s	0.075 ± 0.151	0.151 ± 0.212	-0.089 ± 0.459	-0.003 ± 0.526	0.176 ± 0.424	-0.005 ± 0.214	0.042 ± 0.200
593	–	535	–	–	–	5h35m18.03s	-5d22m05.50s	0.066 ± 0.163	0.058 ± 0.219	0.207 ± 0.631	0.326 ± 0.553	0.083 ± 0.397	-0.067 ± 0.208	0.056 ± 0.253
594	–	174	–	–	–	5h35m18.04s	-5d24m03.10s	0.012 ± 0.179	-0.191 ± 0.178	0.105 ± 0.388	0.324 ± 0.416	-0.042 ± 0.313	0.095 ± 0.253	0.201 ± 0.221
595	180-331	271	19	74	–	5h35m18.05s	-5d23m30.74s	5.230 ± 0.562	4.608 ± 0.497	1.291 ± 0.385	1.772 ± 0.446	2.446 ± 0.425	4.319 ± 0.757	3.948 ± 0.585

Table 7.2 (cont'd)

ID	Proplyd Name	HC00 ID	GMR ID	Z04a ID	Other Names	R.A. [J2000]	Dec [J2000]	$F_{\nu,6cm}$ [mJy]	$F_{\nu,3.6cm}$ [mJy]	$F_{\nu,1.3cm,1}$[a] [mJy]	$F_{\nu,1.3cm,2}$[a] [mJy]	$F_{\nu,1.3cm,3}$[a] [mJy]	$F_{\nu,1.3cm,4}$[a] [mJy]	$F_{\nu,1.3cm,mean}$[a] [mJy]
596	—	594	—	—	—	5h35m18.05s	-5d21m41.20s	0.045 ± 0.152	-0.119 ± 0.244	0.002 ± 0.932	-0.300 ± 0.803	0.055 ± 0.517	-0.096 ± 0.234	-0.372 ± 0.284
597	—	177	—	—	—	5h35m18.08s	-5d24m01.20s	0.138 ± 0.179	0.128 ± 0.149	0.064 ± 0.479	-0.047 ± 0.475	0.155 ± 0.328	-0.020 ± 0.251	0.089 ± 0.173
598	—	372	—	—	—	5h35m18.08s	-5d23m01.80s	-0.007 ± 0.148	0.036 ± 0.196	0.230 ± 0.602	-0.097 ± 0.592	-0.080 ± 0.391	-0.045 ± 0.223	-0.175 ± 0.232
599	181-247	418	—	—	—	5h35m18.09s	-5d22m47.16s	0.248 ± 0.194	0.130 ± 0.211	0.371 ± 0.488	0.150 ± 0.519	-0.023 ± 0.430	0.275 ± 0.156	0.129 ± 0.362
600	181-825	—	—	—	—	5h35m18.10s	-5d28m25.04s	0.085 ± 0.271	0.250 ± 0.633	⋯	⋯	⋯	⋯	⋯
601	—	253	N	—	—	5h35m18.19s	-5d23m36.08s	0.099 ± 0.194	-0.091 ± 0.179	0.636 ± 0.558	-0.182 ± 0.624	0.121 ± 0.363	-0.222 ± 0.364	-0.444 ± 0.253
602	182-316	269	—	—	—	5h35m18.19s	-5d23m31.53s	0.027 ± 0.201	0.059 ± 0.262	-0.217 ± 0.575	0.198 ± 0.542	-0.058 ± 0.416	0.048 ± 0.357	0.104 ± 0.247
603	—	221	—	—	—	5h35m18.21s	-5d23m46.30s	0.013 ± 0.194	-0.274 ± 0.158	0.203 ± 0.503	-0.058 ± 0.484	-0.093 ± 0.376	-0.246 ± 0.270	-0.206 ± 0.208
604	—	125	—	—	—	5h35m18.22s	-5d24m30.30s	-0.081 ± 0.143	-0.009 ± 0.152	0.146 ± 0.426	0.043 ± 0.418	-0.003 ± 0.270	0.010 ± 0.157	-0.113 ± 0.151
605	182-413	774	O	—	—	5h35m18.23s	-5d24m12.83s	1.379 ± 0.283	0.990 ± 0.405	0.592 ± 0.449	0.040 ± 0.458	0.615 ± 0.320	0.684 ± 0.358	1.232 ± 2.864
606	—	19	—	—	—	5h35m18.23s	-5d25m35.20s	0.028 ± 0.155	-0.093 ± 0.177	-0.221 ± 0.506	0.179 ± 0.567	-0.170 ± 0.435	-0.088 ± 0.167	-0.236 ± 0.213
607	—	533	—	—	—	5h35m18.24s	-5d22m06.30s	0.027 ± 0.143	-0.046 ± 0.194	0.163 ± 0.505	0.161 ± 0.514	-0.188 ± 0.399	-0.011 ± 0.176	0.032 ± 0.213
608	—	331	—	75	—	5h35m18.25s	-5d23m15.63s	0.827 ± 0.132	0.676 ± 0.109	0.374 ± 0.159	0.379 ± 24.250	0.488 ± 0.161	0.683 ± 0.158	0.945 ± 0.223
609	—	348	—	—	—	5h35m18.28s	-5d23m07.50s	-0.032 ± 0.157	-0.043 ± 0.181	0.102 ± 0.574	0.296 ± 0.651	0.169 ± 0.375	0.048 ± 0.231	-0.117 ± 0.214
610	183-439	109	—	—	—	5h35m18.29s	-5d24m38.88s	0.111 ± 0.145	0.043 ± 0.147	0.084 ± 0.417	0.198 ± 0.407	0.022 ± 0.282	0.001 ± 0.145	0.028 ± 0.152
611	—	735	—	—	—	5h35m18.30s	-5d21m49.50s	0.024 ± 0.167	-0.014 ± 0.230	-0.037 ± 0.681	0.247 ± 0.652	-0.160 ± 0.524	0.077 ± 0.219	0.047 ± 0.262
612	183-419	143	—	—	—	5h35m18.32s	-5d24m19.19s	0.361 ± 0.149	0.078 ± 0.149	0.292 ± 0.457	0.298 ± 0.411	0.171 ± 0.272	0.334 ± 0.208	0.536 ± 0.153
613	—	108	—	—	—	5h35m18.33s	-5d24m38.90s	-0.109 ± 0.152	-0.075 ± 0.124	0.084 ± 0.414	-0.161 ± 0.370	0.063 ± 0.308	0.043 ± 0.146	0.062 ± 0.168
614	—	66	—	—	—	5h35m18.33s	-5d25m02.70s	0.059 ± 0.163	-0.003 ± 0.166	0.006 ± 0.387	0.043 ± 0.398	0.088 ± 0.307	-0.002 ± 0.143	0.118 ± 0.172
615	183-405	168	—	—	—	5h35m18.34s	-5d24m04.88s	0.085 ± 0.175	-0.080 ± 0.176	0.036 ± 0.498	0.048 ± 0.467	0.059 ± 0.315	-0.044 ± 0.234	-0.039 ± 0.164
616	184-427	423	—	—	—	5h35m18.36s	-5d24m26.87s	0.314 ± 0.081	0.256 ± 0.078	0.167 ± 0.466	0.141 ± 0.415	0.109 ± 0.296	0.205 ± 0.061	0.317 ± 0.585
617	—	436	F	76	—	5h35m18.37s	-5d22m37.44s	35.026 ± 3.504	36.419 ± 3.643	28.544 ± 2.856	27.765 ± 2.778	29.440 ± 2.945	14.539 ± 1.456	18.683 ± 1.870
618	—	131	—	—	—	5h35m18.38s	-5d24m26.80s	-0.207 ± 0.144	-0.108 ± 0.182	0.028 ± 0.478	0.067 ± 0.432	0.135 ± 0.294	-0.145 ± 0.175	-0.181 ± 0.174
619	—	589	—	—	—	5h35m18.38s	-5d21m44.20s	0.082 ± 0.138	0.157 ± 0.257	0.275 ± 0.811	-0.231 ± 0.636	0.062 ± 0.549	-0.037 ± 0.254	-0.065 ± 0.252
620	—	430	—	—	—	5h35m18.40s	-5d22m40.00s	-0.077 ± 0.190	-0.248 ± 0.275	-0.107 ± 0.568	-0.122 ± 0.720	0.140 ± 0.512	0.033 ± 0.236	0.483 ± 0.381
621	—	—	—	—	—	5h35m18.41s	-5d22m38.55s	-0.152 ± 0.193	0.024 ± 0.318	0.196 ± 0.051	0.302 ± 0.771	-0.308 ± 0.604	-0.096 ± 0.196	0.140 ± 0.598
622	184-520	38	—	—	—	5h35m18.44s	-5d25m19.30s	-0.014 ± 0.145	0.068 ± 0.172	0.176 ± 0.472	-0.239 ± 0.410	-0.097 ± 0.360	0.010 ± 0.142	0.036 ± 0.212
623	—	163	—	—	—	5h35m18.48s	-5d24m07.00s	0.166 ± 0.156	0.008 ± 0.150	-0.258 ± 0.428	0.132 ± 0.456	-0.033 ± 0.382	0.131 ± 0.222	0.088 ± 0.160
624	—	278	—	—	—	5h35m18.50s	-5d23m29.30s	-0.018 ± 0.194	-0.105 ± 0.233	0.557 ± 0.587	-0.339 ± 0.567	0.270 ± 0.373	0.030 ± 0.274	0.358 ± 0.268
625	—	185	—	—	—	5h35m18.51s	-5d23m57.80s	-0.084 ± 0.152	0.162 ± 0.171	0.093 ± 0.446	-0.197 ± 0.494	0.091 ± 0.294	-0.054 ± 0.237	-0.164 ± 0.182
626	—	765	—	—	—	5h35m18.53s	-5d23m47.90s	0.069 ± 0.161	-0.088 ± 0.175	-0.020 ± 0.462	-0.081 ± 0.520	0.117 ± 0.353	0.031 ± 0.260	0.063 ± 0.193
627	—	384	—	—	—	5h35m18.53s	-5d22m58.10s	0.032 ± 0.167	-0.063 ± 0.171	-0.205 ± 0.506	0.029 ± 0.549	0.132 ± 0.405	-0.019 ± 0.221	-0.126 ± 0.255
628	—	578	—	—	—	5h35m18.54s	-5d21m50.10s	-0.036 ± 0.172	0.028 ± 0.220	0.283 ± 0.649	0.103 ± 0.662	0.107 ± 0.517	-0.012 ± 0.179	0.226 ± 0.247
629	—	463	—	—	—	5h35m18.58s	-5d22m31.00s	0.130 ± 0.166	0.004 ± 0.223	0.016 ± 0.542	0.190 ± 0.520	-0.106 ± 0.356	0.078 ± 0.208	0.222 ± 0.286
630	—	583	—	—	—	5h35m18.60s	-5d21m47.70s	-0.035 ± 0.151	-0.010 ± 0.234	-0.047 ± 0.758	0.102 ± 0.660	0.184 ± 0.520	-0.012 ± 0.228	0.088 ± 0.231

Table 7.2 (cont'd)

ID	Proplyd Name	HC00 ID	GMR ID	Z04a ID	Other Names	R.A. [J2000]	Dec [J2000]	$F_{\nu,6cm}$ [mJy]	$F_{\nu,3.6cm}$ [mJy]	$F_{\nu,1.3cm,1}$ [mJy] [a]	$F_{\nu,1.3cm,2}$ [mJy] [a]	$F_{\nu,1.3cm,3}$ [mJy] [a]	$F_{\nu,1.3cm,4}$ [mJy] [a]	$F_{\nu,1.3cm,mean}$ [mJy] [a]
631		—	—	—	—	5h35m18.67s	-5d20m33.10s	-0.058 ± 0.229	-0.136 ± 0.399	...	...	...	...	...
632	187-314	337	—	—	—	5h35m18.67s	-5d23m14.01s	0.088 ± 0.177	-0.002 ± 0.174	0.237 ± 0.601	0.357 ± 0.557	0.102 ± 0.418	0.172 ± 0.213	0.412 ± 0.227
633	—	191	—	—	—	5h35m18.68s	-5d23m56.50s	-0.091 ± 0.150	-0.007 ± 0.155	0.074 ± 0.460	-0.239 ± 0.470	0.067 ± 0.352	0.062 ± 0.230	0.096 ± 0.178
634	—	713	—	—	—	5h35m18.71s	-5d22m56.90s	0.019 ± 0.150	-0.114 ± 0.191	0.027 ± 0.510	0.130 ± 0.573	-0.060 ± 0.342	-0.091 ± 0.204	-0.082 ± 0.251
635	—	543	—	—	—	5h35m18.76s	-5d22m02.20s	-0.030 ± 0.180	-0.097 ± 0.217	0.096 ± 0.514	-0.127 ± 0.562	-0.098 ± 0.408	-0.030 ± 0.169	0.116 ± 0.231
636	—	482	—	—	—	5h35m18.85s	-5d22m23.10s	0.024 ± 0.158	0.130 ± 0.233	0.014 ± 0.478	0.123 ± 0.439	0.028 ± 0.312	0.092 ± 0.174	0.063 ± 0.226
637	—	595	—	—	—	5h35m18.86s	-5d21m41.30s	0.021 ± 0.166	0.014 ± 0.245	0.063 ± 0.696	0.112 ± 0.785	-0.018 ± 0.653	0.042 ± 0.226	0.042 ± 0.266
638	189-329	282	—	—	—	5h35m18.88s	-5d23m28.88s	-0.074 ± 0.221	-0.113 ± 0.192	0.227 ± 0.572	0.007 ± 0.560	-0.086 ± 0.392	-0.189 ± 0.310	-0.173 ± 0.243
639	—	352	—	—	—	5h35m18.88s	-5d23m07.20s	0.079 ± 0.150	0.122 ± 0.193	0.035 ± 0.570	-0.071 ± 0.641	0.049 ± 0.409	-0.102 ± 0.200	0.006 ± 0.228
640	—	151	—	—	—	5h35m18.89s	-5d24m17.50s	0.100 ± 0.125	-0.030 ± 0.152	-0.056 ± 0.519	0.054 ± 0.414	0.074 ± 0.333	-0.012 ± 0.172	-0.028 ± 0.188
641	—	695	—	—	—	5h35m18.93s	-5d20m48.60s	-0.016 ± 0.184	-0.203 ± 0.291	...	...	...	...	...
642	—	686	—	—	—	5h35m18.96s	-5d20m52.20s	-0.025 ± 0.171	0.145 ± 0.310	...	...	0.038 ± 2.346	0.397 ± 1.014	0.774 ± 1.110
643	—	498	—	—	—	5h35m18.96s	-5d22m18.80s	0.233 ± 0.144	-0.018 ± 0.224	-0.170 ± 0.457	0.183 ± 0.536	-0.040 ± 0.374	-0.038 ± 0.177	-0.159 ± 0.192
644	—	655	—	—	—	5h35m18.97s	-5d21m07.80s	0.005 ± 0.191	-0.118 ± 0.309	0.429 ± 2.538	0.154 ± 2.416	0.413 ± 1.510	0.068 ± 0.519	-0.259 ± 0.755
645	—	311	—	—	—	5h35m18.97s	-5d23m22.00s	-0.096 ± 0.140	-0.078 ± 0.208	-0.526 ± 0.589	0.163 ± 0.612	-0.144 ± 0.429	-0.082 ± 0.216	-0.216 ± 0.206
646	190-251	409	—	—	—	5h35m19.04s	-5d22m50.67s	0.130 ± 0.158	-0.008 ± 0.259	0.092 ± 0.494	0.085 ± 0.562	0.267 ± 0.421	-0.073 ± 0.197	0.144 ± 0.246
647	—	65	—	—	—	5h35m19.04s	-5d25m03.00s	-0.032 ± 0.159	-0.154 ± 0.167	0.305 ± 0.485	0.051 ± 0.480	0.117 ± 0.344	-0.087 ± 0.158	-0.026 ± 0.173
648	—	351	—	—	—	5h35m19.07s	-5d23m07.50s	-0.134 ± 0.149	0.207 ± 0.210	0.118 ± 0.569	-0.159 ± 0.606	0.064 ± 0.414	0.017 ± 0.216	-0.140 ± 0.229
649	191-350	214	—	—	—	5h35m19.07s	-5d23m49.67s	1.325 ± 0.255	0.417 ± 0.170	0.277 ± 0.470	0.309 ± 0.484	0.185 ± 0.069	0.428 ± 0.190	0.803 ± 2.760
650	—	357	—	—	—	5h35m19.11s	-5d23m06.30s	0.084 ± 0.165	0.142 ± 0.195	-0.068 ± 0.502	0.374 ± 0.612	-0.200 ± 0.328	0.013 ± 0.179	0.058 ± 0.200
651	—	288	—	—	—	5h35m19.12s	-5d23m27.10s	0.036 ± 0.158	0.088 ± 0.177	-0.343 ± 0.667	0.112 ± 0.575	-0.031 ± 0.357	-0.014 ± 0.283	-0.211 ± 0.223
652	191-232	—	—	—	—	5h35m19.13s	-5d22m31.20s	-0.066 ± 0.183	-0.081 ± 0.221	0.151 ± 0.442	-0.078 ± 0.491	-0.017 ± 0.382	0.089 ± 0.195	0.174 ± 0.229
653	—	444	—	—	—	5h35m19.14s	-5d22m34.60s	-0.045 ± 0.147	-0.027 ± 0.183	-0.034 ± 0.456	0.005 ± 0.543	-0.083 ± 0.403	0.000 ± 0.168	-0.028 ± 0.211
654	—	591	—	—	—	5h35m19.16s	-5d21m43.70s	-0.144 ± 0.159	0.103 ± 0.218	0.242 ± 0.816	-0.014 ± 0.719	0.112 ± 0.513	0.034 ± 0.230	0.010 ± 0.262
655	—	408	—	—	—	5h35m19.22s	-5d22m50.70s	0.016 ± 0.180	-0.138 ± 0.219	-0.075 ± 0.502	0.020 ± 0.538	-0.073 ± 0.403	-0.030 ± 0.183	-0.193 ± 0.233
656	—	776	—	—	—	5h35m19.27s	-5d20m49.90s	-0.031 ± 0.209	0.056 ± 0.352	...	...	...	0.390 ± 0.781	...
657	—	691	—	—	—	5h35m19.27s	-5d20m49.50s	-0.061 ± 0.176	-0.266 ± 0.371	...	...	...	...	...
658	—	356	—	—	—	5h35m19.39s	-5d23m06.49s	0.220 ± 0.165	0.214 ± 0.174	0.188 ± 0.638	0.095 ± 0.632	-0.031 ± 0.430	0.248 ± 0.073	0.238 ± 0.225
659	—	13	—	—	—	5h35m19.40s	-5d25m42.40s	0.052 ± 0.155	-0.002 ± 0.195	0.020 ± 0.803	0.004 ± 0.711	-0.040 ± 0.495	0.101 ± 0.200	0.068 ± 0.308
660	—	491	—	—	—	5h35m19.47s	-5d22m21.80s	0.068 ± 0.176	0.134 ± 0.230	-0.052 ± 0.537	-0.108 ± 0.478	-0.050 ± 0.351	0.038 ± 0.187	-0.028 ± 0.207
661	—	665	—	—	—	5h35m19.51s	-5d21m04.50s	-0.116 ± 0.174	-0.186 ± 0.284	-0.099 ± 2.642	-0.668 ± 3.141	-0.188 ± 1.562	0.005 ± 0.512	-0.112 ± 0.843
662	—	728	—	—	—	5h35m19.51s	-5d23m39.70s	0.040 ± 0.163	-0.102 ± 0.168	-0.703 ± 0.665	0.112 ± 0.626	0.150 ± 0.395	-0.166 ± 0.226	-0.389 ± 0.228
663	—	580	—	—	—	5h35m19.55s	-5d21m49.20s	-0.008 ± 0.164	-0.012 ± 0.230	0.060 ± 0.754	-0.081 ± 0.688	-0.107 ± 0.489	0.005 ± 0.195	-0.167 ± 0.252
664	—	188	—	—	—	5h35m19.62s	-5d23m57.30s	-0.022 ± 0.151	-0.035 ± 0.147	-0.144 ± 0.496	0.019 ± 0.538	-0.014 ± 0.349	0.048 ± 0.203	0.031 ± 0.167
665	—	54	—	—	—	5h35m19.62s	-5d25m07.78s	-0.062 ± 0.160	-0.033 ± 0.144	0.121 ± 0.481	0.325 ± 0.061	-0.178 ± 0.291	0.080 ± 0.172	0.056 ± 0.013

Table 7.2 (cont'd)

ID	Proplyd Name	HC00 ID	GMR ID	Z04a ID	Other Names	R.A. [J2000]	Dec [J2000]	$F_{\nu,6cm}$ [mJy]	$F_{\nu,3.6cm}$ [mJy]	$F_{\nu,1.3cm,1}$[a] [mJy]	$F_{\nu,1.3cm,2}$[a] [mJy]	$F_{\nu,1.3cm,3}$[a] [mJy]	$F_{\nu,1.3cm,4}$[a] [mJy]	$F_{\nu,1.3cm,mean}$[a] [mJy]
666	–	366	–	–	–	5h35m19.63s	-5d23m03.60s	0.060 ± 0.148	−0.056 ± 0.200	−0.099 ± 0.548	0.013 ± 0.584	0.010 ± 0.395	0.101 ± 0.169	0.110 ± 0.205
667	–	123	–	–	–	5h35m19.64s	-5d24m31.60s	0.040 ± 0.157	0.077 ± 0.156	0.018 ± 0.504	−0.099 ± 0.461	0.054 ± 0.345	0.084 ± 0.203	0.086 ± 0.162
668	197-427	133	P	–	–	5h35m19.65s	-5d24m26.47s	0.521 ± 0.196	0.105 ± 0.157	0.240 ± 0.431	0.338 ± 0.497	0.247 ± 0.353	0.413 ± 0.152	0.563 ± 1034.349
669	197-427	103	–	–	–	5h35m19.66s	-5d24m42.20s	0.177 ± 0.156	0.069 ± 0.168	−0.094 ± 0.458	0.157 ± 0.416	−0.150 ± 0.379	−0.007 ± 0.173	−0.017 ± 0.187
670	–	59	–	–	–	5h35m19.68s	-5d25m05.20s	0.097 ± 0.156	0.022 ± 0.159	0.088 ± 0.594	−0.057 ± 0.566	−0.010 ± 0.349	−0.007 ± 0.154	−0.084 ± 0.207
671	–	446	–	–	–	5h35m19.66s	-5d22m34.20s	0.032 ± 0.139	0.000 ± 0.226	0.005 ± 0.456	0.090 ± 0.602	−0.050 ± 0.350	0.091 ± 0.162	0.145 ± 0.241
672	198-222	492	–	–	–	5h35m19.82s	-5d22m21.62s	0.403 ± 0.106	0.248 ± 0.234	0.098 ± 0.467	0.079 ± 0.493	0.300 ± 0.370	0.227 ± 0.187	0.243 ± 0.223
673	–	654	–	–	–	5h35m19.84s	-5d21m08.00s	0.023 ± 0.207	0.120 ± 0.297	−0.627 ± 2.969	−0.456 ± 2.546	0.078 ± 1.457	−0.260 ± 0.580	−0.465 ± 0.625
674	198-448	96	–	–	–	5h35m19.84s	-5d24m47.86s	0.310 ± 0.144	0.031 ± 0.174	0.357 ± 0.455	0.011 ± 0.492	−0.175 ± 0.345	0.122 ± 0.168	0.184 ± 0.172
675	–	210	–	–	–	5h35m19.86s	-5d23m51.60s	0.145 ± 0.155	0.120 ± 0.148	0.231 ± 0.561	0.229 ± 0.537	0.033 ± 0.373	−0.096 ± 0.210	−0.118 ± 0.176
676	–	531	–	–	–	5h35m19.90s	-5d22m07.30s	−0.003 ± 0.153	−0.010 ± 0.224	0.189 ± 0.518	0.119 ± 0.595	0.060 ± 0.471	0.103 ± 0.192	0.092 ± 0.191
677	–	176	–	–	–	5h35m19.93s	-5d24m02.60s	0.132 ± 0.171	−0.278 ± 0.155	0.185 ± 0.446	0.137 ± 0.481	0.236 ± 0.354	0.106 ± 0.182	0.139 ± 0.182
678	–	564	–	–	–	5h35m19.97s	-5d21m54.00s	0.020 ± 0.156	−0.023 ± 0.253	0.006 ± 0.618	−0.087 ± 0.665	0.136 ± 0.439	−0.044 ± 0.174	0.075 ± 0.221
679	–	452	–	–	–	5h35m19.98s	-5d22m32.80s	0.058 ± 0.177	−0.026 ± 0.202	−0.276 ± 0.563	0.169 ± 0.558	0.196 ± 0.415	0.019 ± 0.198	−0.020 ± 0.212
680	–	766	–	–	–	5h35m20.00s	-5d23m28.80s	0.050 ± 0.163	−0.054 ± 0.177	0.092 ± 0.598	0.224 ± 0.550	0.034 ± 0.349	−0.008 ± 0.207	0.051 ± 0.211
681	–	34	–	–	–	5h35m20.03s	-5d25m22.40s	0.083 ± 0.158	0.023 ± 0.147	−0.009 ± 0.730	−0.017 ± 0.615	0.125 ± 0.400	−0.060 ± 0.162	0.009 ± 0.227
682	–	474	–	–	–	5h35m20.03s	-5d22m26.50s	0.049 ± 0.189	0.150 ± 0.241	0.161 ± 0.494	−0.130 ± 0.538	0.085 ± 0.470	−0.039 ± 0.149	−0.032 ± 0.233
683	–	17	–	–	–	5h35m20.05s	-5d25m37.70s	0.103 ± 0.132	−0.110 ± 0.160	−0.155 ± 0.737	0.266 ± 0.712	−0.128 ± 0.461	0.052 ± 0.190	0.082 ± 0.222
684	200-106	660	–	–	–	5h35m20.06s	-5d21m05.88s	0.119 ± 0.152	−0.107 ± 0.323	−0.979 ± 2.983	−0.498 ± 2.854	−0.331 ± 1.585	0.087 ± 0.652	0.451 ± 2.704
685	–	45	–	–	–	5h35m20.06s	-5d25m14.30s	0.059 ± 0.163	0.046 ± 0.155	0.210 ± 0.580	−0.072 ± 0.487	0.021 ± 0.436	−0.039 ± 0.158	−0.029 ± 0.196
686	–	700	–	–	–	5h35m20.09s	-5d20m43.90s	0.049 ± 0.186	0.000 ± 0.387	⋯	⋯	⋯	⋯	⋯
687	–	365	–	–	–	5h35m20.13s	-5d23m04.50s	−0.058 ± 0.141	−0.168 ± 0.175	−0.125 ± 0.590	0.114 ± 0.570	−0.035 ± 0.437	0.122 ± 0.182	0.251 ± 0.227
688	–	613	–	–	–	5h35m20.14s	-5d21m33.70s	0.028 ± 0.161	−0.063 ± 0.255	0.206 ± 1.176	−0.013 ± 1.155	0.037 ± 0.774	0.059 ± 0.230	0.226 ± 0.325
689	201-534	25	–	–	–	5h35m20.15s	-5d25m33.87s	0.049 ± 0.139	−0.013 ± 0.178	−0.009 ± 0.669	0.161 ± 0.741	−0.155 ± 0.442	0.051 ± 0.167	0.036 ± 0.230
690	202-228	468	–	–	–	5h35m20.16s	-5d22m28.31s	0.045 ± 0.153	−0.011 ± 0.238	0.163 ± 0.571	0.203 ± 0.426	−0.179 ± 0.409	0.170 ± 0.060	0.043 ± 0.214
691	–	–	–	–	–	5h35m20.17s	-5d26m39.13s	0.093 ± 0.198	0.244 ± 0.056	⋯	0.384 ± 2.994	0.274 ± 1.505	0.091 ± 0.610	0.169 ± 0.825
692	–	346	–	–	–	5h35m20.18s	-5d23m08.50s	−0.172 ± 0.139	0.141 ± 0.189	0.043 ± 0.611	0.094 ± 0.625	−0.066 ± 0.466	−0.047 ± 0.176	0.027 ± 0.195
693	–	678	–	–	–	5h35m20.22s	-5d20m56.80s	0.541 ± 0.094	0.504 ± 0.123	⋯	⋯	0.313 ± 2.423	0.228 ± 0.988	0.289 ± 1.132
694	–	697	–	–	–	5h35m20.27s	-5d20m47.40s	0.018 ± 0.208	0.134 ± 0.344	⋯	⋯	⋯	⋯	⋯
695	203-504	61	–	–	–	5h35m20.28s	-5d25m04.03s	0.364 ± 0.101	0.144 ± 0.176	−0.030 ± 0.604	0.183 ± 0.441	0.224 ± 0.431	0.163 ± 0.179	0.261 ± 0.184
696	203-506	57	–	–	–	5h35m20.31s	-5d25m05.57s	0.167 ± 0.136	0.173 ± 0.179	0.234 ± 0.675	−0.242 ± 0.543	−0.015 ± 0.463	−0.036 ± 0.180	−0.008 ± 0.216
697	–	727	–	–	–	5h35m20.36s	-5d25m25.70s	0.015 ± 0.139	−0.028 ± 0.155	−0.033 ± 0.716	−0.329 ± 0.670	−0.033 ± 0.466	0.044 ± 0.162	−0.084 ± 0.228
698	–	510	–	–	–	5h35m20.40s	-5d22m13.70s	−0.060 ± 0.139	−0.136 ± 0.243	−0.102 ± 0.565	−0.083 ± 0.582	0.137 ± 0.428	−0.034 ± 0.178	−0.082 ± 0.233
699	–	279	–	–	–	5h35m20.43s	-5d23m29.70s	0.142 ± 0.164	0.148 ± 0.211	−0.123 ± 0.589	0.035 ± 0.659	0.173 ± 0.375	0.073 ± 0.198	0.079 ± 0.222
700	205-330	277	–	–	–	5h35m20.47s	-5d23m29.80s	0.271 ± 0.146	0.292 ± 0.179	−0.017 ± 0.611	0.040 ± 0.521	0.353 ± 0.393	0.032 ± 0.204	0.299 ± 1.013

Table 7.2 (cont'd)

ID	Proplyd Name	HC00 ID	GMR ID	Z04a ID	Other Names	R.A. [J2000]	Dec [J2000]	$F_{\nu,6cm}$ [mJy]	$F_{\nu,3.6cm}$ [mJy]	$F_{\nu,1.3cm,1}$ [mJy] [a]	$F_{\nu,1.3cm,2}$ [mJy] [a]	$F_{\nu,1.3cm,3}$ [mJy] [a]	$F_{\nu,1.3cm,4}$ [mJy] [a]	$F_{\nu,1.3cm,mean}$ [mJy] [a]
701	–	272	–	–	–	5h35m20.50s	-5d23m31.10s	0.098 ± 0.169	-0.066 ± 0.184	-0.184 ± 0.687	0.281 ± 0.539	-0.228 ± 0.365	0.140 ± 0.189	0.022 ± 0.181
702	–	308	–	–	–	5h35m20.52s	-5d23m23.00s	0.024 ± 0.144	0.044 ± 0.156	-0.238 ± 0.614	0.201 ± 0.601	-0.016 ± 0.403	0.048 ± 0.200	-0.179 ± 0.182
703	205-052	688	–	–	–	5h35m20.52s	-5d20m52.03s	0.021 ± 0.196	-0.005 ± 0.376	$\cdots$	$\cdots$	$\cdots$	$\cdots$	$\cdots$
704	205-421	141	–	–	–	5h35m20.54s	-5d24m20.97s	0.160 ± 0.156	-0.152 ± 0.162	0.108 ± 0.561	0.084 ± 0.447	0.125 ± 0.378	0.085 ± 0.176	0.091 ± 0.169
705	–	596	–	–	–	5h35m20.54s	-5d21m41.00s	0.068 ± 0.169	0.157 ± 0.239	0.279 ± 0.918	0.040 ± 0.993	0.009 ± 0.657	-0.007 ± 0.270	0.010 ± 0.297
706	–	701	–	–	–	5h35m20.58s	-5d20m43.20s	-0.077 ± 0.189	-0.016 ± 0.393	$\cdots$	$\cdots$	$\cdots$	$\cdots$	$\cdots$
707	–	632	–	–	–	5h35m20.59s	-5d21m22.90s	-0.046 ± 0.182	-0.096 ± 0.312	-0.169 ± 1.800	-0.409 ± 1.683	-0.384 ± 1.014	0.083 ± 0.392	0.090 ± 0.466
708	–	396	–	–	–	5h35m20.63s	-5d22m55.70s	0.059 ± 0.145	0.161 ± 0.196	0.042 ± 0.683	0.138 ± 0.586	-0.054 ± 0.441	0.053 ± 0.179	0.065 ± 0.211
709	–	429	–	–	–	5h35m20.64s	-5d22m41.20s	-0.109 ± 0.153	0.000 ± 0.185	-0.113 ± 0.496	0.123 ± 0.555	-0.170 ± 0.380	-0.092 ± 0.175	-0.110 ± 0.204
710	–	424	–	–	–	5h35m20.64s	-5d22m45.60s	0.128 ± 0.171	0.149 ± 0.206	-0.027 ± 0.561	0.162 ± 0.558	-0.068 ± 0.329	0.139 ± 0.209	0.060 ± 0.204
711	206-446	97	–	–	–	5h35m20.66s	-5d24m46.67s	2.217 ± 0.391	0.478 ± 0.207	0.449 ± 0.551	0.516 ± 0.567	0.194 ± 0.395	0.458 ± 0.175	1.014 ± 0.209
712	–	49	–	–	–	5h35m20.67s	-5d25m10.80s	-0.107 ± 0.135	0.031 ± 0.140	-0.109 ± 0.668	-0.052 ± 0.593	0.248 ± 0.439	0.033 ± 0.158	0.044 ± 0.217
713	–	207	–	–	–	5h35m20.68s	-5d23m53.20s	-0.011 ± 0.136	0.097 ± 0.199	0.293 ± 0.524	-0.177 ± 0.520	-0.071 ± 0.371	0.007 ± 0.176	-0.001 ± 0.173
714	–	461	–	–	–	5h35m20.72s	-5d22m31.50s	-0.038 ± 0.168	0.013 ± 0.212	-0.046 ± 0.585	-0.054 ± 0.542	0.058 ± 0.444	-0.041 ± 0.179	-0.137 ± 0.248
715	–	590	–	–	–	5h35m20.73s	-5d21m44.34s	0.237 ± 0.067	-0.031 ± 0.250	0.353 ± 0.100	1.316 ± 0.173	0.240 ± 0.067	0.135 ± 0.234	0.218 ± 0.033
716	–	560	–	–	–	5h35m20.77s	-5d21m55.20s	-0.117 ± 0.171	0.037 ± 0.229	-0.167 ± 0.804	0.102 ± 0.670	0.093 ± 0.468	0.045 ± 0.212	0.102 ± 0.265
717	–	732	–	–	–	5h35m20.77s	-5d22m39.50s	-0.059 ± 0.156	-0.075 ± 0.225	0.183 ± 0.624	0.052 ± 0.444	0.034 ± 0.464	0.097 ± 0.159	0.321 ± 0.241
718	–	731	–	–	–	5h35m20.79s	-5d22m36.30s	0.158 ± 0.132	0.089 ± 0.195	-0.208 ± 0.578	-0.182 ± 0.632	-0.080 ± 0.414	-0.074 ± 0.210	-0.248 ± 0.206
719	208-122	637	–	–	–	5h35m20.84s	-5d21m21.47s	-0.026 ± 0.170	0.030 ± 0.305	0.009 ± 1.771	0.176 ± 1.953	0.373 ± 1.078	-0.007 ± 0.432	0.031 ± 0.501
720	–	622	–	–	–	5h35m20.84s	-5d21m30.10s	-0.073 ± 0.163	0.009 ± 0.215	-0.363 ± 1.480	-0.136 ± 1.269	-0.146 ± 0.816	0.217 ± 0.378	-0.110 ± 0.430
721	–	649	–	–	–	5h35m20.85s	-5d21m13.70s	-0.188 ± 0.198	-0.022 ± 0.321	0.698 ± 2.589	0.025 ± 2.781	-0.382 ± 1.476	0.087 ± 0.499	0.375 ± 0.690
722	–	22	–	–	–	5h35m20.90s	-5d25m34.50s	-0.047 ± 0.150	-0.036 ± 0.166	0.024 ± 0.852	-0.057 ± 0.778	0.238 ± 0.503	-0.015 ± 0.172	0.025 ± 0.219
723	–	312	–	–	–	5h35m20.92s	-5d23m21.80s	0.049 ± 0.137	0.193 ± 0.157	-0.084 ± 0.644	0.123 ± 0.627	-0.270 ± 0.382	-0.135 ± 0.206	-0.258 ± 0.173
724	–	574	–	–	–	5h35m20.93s	-5d21m50.90s	0.106 ± 0.141	0.143 ± 0.247	-0.030 ± 0.908	-0.076 ± 0.720	-0.096 ± 0.575	0.132 ± 0.232	0.083 ± 0.279
725	209-151	–	–	–	–	5h35m21.00s	-5d21m52.30s	0.130 ± 0.142	0.272 ± 0.262	-0.034 ± 0.788	-0.103 ± 0.797	-0.149 ± 0.580	-0.018 ± 0.237	-0.001 ± 0.315
726	–	196	–	–	–	5h35m21.02s	-5d23m55.70s	0.057 ± 0.163	-0.146 ± 0.149	0.205 ± 0.461	-0.101 ± 0.486	-0.005 ± 0.345	0.051 ± 0.139	0.133 ± 0.187
727	–	486	–	–	–	5h35m21.02s	-5d22m22.90s	0.083 ± 0.179	0.043 ± 0.210	-0.219 ± 0.720	0.082 ± 0.549	0.118 ± 0.429	0.104 ± 0.198	-0.023 ± 0.238
728	–	403	–	–	–	5h35m21.02s	-5d22m54.30s	-0.038 ± 0.145	0.045 ± 0.211	-0.041 ± 0.643	-0.164 ± 0.522	-0.098 ± 0.386	-0.045 ± 0.156	-0.162 ± 0.203
729	210-225	477	–	–	–	5h35m21.03s	-5d22m25.25s	0.087 ± 0.163	0.073 ± 0.243	0.483 ± 0.648	0.170 ± 0.581	0.091 ± 0.449	-0.012 ± 0.184	0.059 ± 0.211
730	–	217	30	77	–	5h35m21.05s	-5d23m49.03s	2.031 ± 0.217	2.282 ± 0.237	2.712 ± 0.280	0.683 ± 0.098	2.420 ± 0.248	0.996 ± 0.117	1.373 ± 0.140
731	–	680	–	–	–	5h35m21.11s	-5d20m55.50s	0.164 ± 0.205	0.161 ± 0.428	$\cdots$	$\cdots$	$\cdots$	$\cdots$	$\cdots$
732	–	729	–	–	–	5h35m21.12s	-5d22m50.20s	0.035 ± 0.141	-0.172 ± 0.202	-0.259 ± 0.625	-0.327 ± 0.627	0.155 ± 0.483	-0.074 ± 0.167	0.013 ± 0.215
733	212-557	–	–	–	–	5h35m21.15s	-5d25m57.04s	-0.022 ± 0.157	0.008 ± 0.181	-0.159 ± 0.806	0.143 ± 0.807	0.124 ± 0.540	0.068 ± 0.189	0.051 ± 0.286
734	–	264	–	–	–	5h35m21.18s	-5d23m33.10s	0.025 ± 0.158	0.030 ± 0.190	0.148 ± 0.601	-0.001 ± 0.586	-0.129 ± 0.379	-0.022 ± 0.177	-0.023 ± 0.190
735	212-400	184	–	–	–	5h35m21.19s	-5d24m00.15s	-0.032 ± 0.161	0.002 ± 0.158	0.153 ± 0.423	0.053 ± 0.432	-0.023 ± 0.382	-0.033 ± 0.131	-0.016 ± 0.178

Table 7.2 (cont'd)

ID	Proplyd Name	HC00 ID	GMR ID	Z04a ID	Other Names	R.A. [J2000]	Dec [J2000]	$F_{\nu,6cm}$ [mJy]	$F_{\nu,3.6cm}$ [mJy]	$F_{\nu,1.3cm,1}$[a] [mJy]	$F_{\nu,1.3cm,2}$[a] [mJy]	$F_{\nu,1.3cm,3}$[a] [mJy]	$F_{\nu,1.3cm,4}$[a] [mJy]	$F_{\nu,1.3cm,mean}$[a] [mJy]
736	–	551	–	–	–	5h35m21.23s	-5d22m00.30s	0.072 ± 0.157	−0.046 ± 0.219	−0.049 ± 0.612	0.198 ± 0.821	0.184 ± 0.538	0.044 ± 0.202	0.086 ± 0.273
737	212-260	381	–	–	–	5h35m21.25s	-5d22m59.49s	0.079 ± 0.133	0.057 ± 0.237	−0.497 ± 0.593	−0.200 ± 0.643	0.588 ± 0.083	−0.066 ± 0.171	0.114 ± 0.029
738	–	326	–	–	–	5h35m21.25s	-5d23m16.80s	0.008 ± 0.161	−0.018 ± 0.184	−0.026 ± 0.623	0.079 ± 0.562	0.076 ± 0.472	−0.022 ± 0.160	−0.186 ± 0.188
739	–	734	–	–	–	5h35m21.28s	-5d22m09.10s	−0.089 ± 0.180	−0.005 ± 0.264	−0.322 ± 0.686	−0.135 ± 0.731	−0.016 ± 0.620	−0.149 ± 0.181	−0.131 ± 0.251
740	213-533	27	–	–	–	5h35m21.29s	-5d25m33.11s	0.057 ± 0.156	−0.037 ± 0.186	−0.101 ± 0.798	−0.118 ± 0.594	0.025 ± 0.475	0.041 ± 0.158	0.047 ± 0.254
741	–	79	–	–	–	5h35m21.30s	-5d24m57.35s	0.073 ± 0.137	0.067 ± 0.182	0.087 ± 0.641	0.261 ± 0.598	0.100 ± 0.439	−0.086 ± 0.170	−0.072 ± 0.225
742	–	507	–	–	–	5h35m21.30s	-5d22m15.70s	−0.012 ± 0.174	0.051 ± 0.245	−0.097 ± 0.727	−0.164 ± 0.630	0.083 ± 0.489	−0.062 ± 0.185	−0.058 ± 0.256
743	213-346	225	–	–	–	5h35m21.31s	-5d23m46.05s	0.085 ± 0.162	−0.169 ± 0.149	0.161 ± 0.488	−0.148 ± 0.486	0.261 ± 0.338	−0.013 ± 0.157	−0.020 ± 0.179
744	–	160	–	–	–	5h35m21.33s	-5d24m11.40s	0.018 ± 0.173	0.147 ± 0.190	0.143 ± 0.500	0.019 ± 0.425	0.169 ± 0.373	0.046 ± 0.136	0.089 ± 0.149
745	–	20	–	–	–	5h35m21.35s	-5d25m35.00s	0.038 ± 0.137	−0.010 ± 0.167	−0.153 ± 0.692	−0.017 ± 0.682	−0.094 ± 0.499	−0.090 ± 0.151	−0.105 ± 0.222
746	–	229	–	–	–	5h35m21.37s	-5d23m45.40s	0.048 ± 0.151	−0.014 ± 0.175	0.087 ± 0.534	0.073 ± 0.435	0.065 ± 0.363	−0.008 ± 0.164	0.118 ± 0.177
747	–	532	–	–	–	5h35m21.39s	-5d22m07.40s	−0.021 ± 0.168	−0.007 ± 0.239	0.300 ± 0.743	−0.071 ± 0.734	0.065 ± 0.489	−0.003 ± 0.241	−0.083 ± 0.256
748	215-652	–	–	–	–	5h35m21.45s	-5d26m52.40s	−0.074 ± 0.167	−0.069 ± 0.226	−0.002 ± 3.102	1.402 ± 2.474	−0.450 ± 1.551	0.389 ± 0.510	0.490 ± 0.730
749	215-317	328	–	–	–	5h35m21.50s	-5d23m16.71s	0.100 ± 0.135	0.013 ± 0.160	−0.402 ± 0.620	−0.119 ± 0.592	0.310 ± 0.388	0.129 ± 0.173	0.038 ± 0.227
750	215-106	663	–	–	–	5h35m21.56s	-5d21m05.60s	0.111 ± 0.167	−0.020 ± 0.361	⋯	⋯	1.089 ± 2.160	0.156 ± 0.816	0.280 ± 1.207
751	216-541	15	–	–	–	5h35m21.60s	-5d25m40.65s	0.009 ± 0.135	0.058 ± 0.158	0.014 ± 0.750	0.112 ± 0.704	−0.021 ± 0.408	−0.069 ± 0.163	−0.053 ± 0.219
752	216-715	–	–	–	–	5h35m21.62s	-5d27m14.65s	0.014 ± 0.177	0.069 ± 0.297	⋯	⋯	⋯	⋯	⋯
753	–	294	–	–	–	5h35m21.63s	-5d23m25.80s	−0.042 ± 0.145	0.031 ± 0.180	−0.126 ± 0.674	0.399 ± 0.573	0.016 ± 0.401	−0.038 ± 0.139	−0.168 ± 0.205
754	–	516	–	–	–	5h35m21.64s	-5d22m12.70s	−0.061 ± 0.168	0.014 ± 0.261	0.164 ± 0.693	−0.044 ± 0.583	0.076 ± 0.550	−0.091 ± 0.194	−0.012 ± 0.269
755	–	31	–	–	–	5h35m21.66s	-5d25m26.50s	−0.016 ± 0.156	0.015 ± 0.176	0.146 ± 0.689	−0.111 ± 0.653	−0.243 ± 0.445	0.034 ± 0.175	0.047 ± 0.241
756	–	255	–	–	–	5h35m21.67s	-5d21m47.40s	0.044 ± 0.148	−0.074 ± 0.268	0.251 ± 1.117	0.144 ± 0.812	0.071 ± 0.702	0.034 ± 0.258	0.118 ± 0.364
757	–	585	–	–	–	5h35m21.68s	-5d21m47.20s	0.076 ± 0.159	−0.060 ± 0.255	0.507 ± 0.967	0.066 ± 1.175	0.066 ± 0.654	−0.157 ± 0.282	−0.163 ± 0.351
758	–	730	–	–	–	5h35m21.71s	-5d22m38.30s	0.149 ± 0.165	0.037 ± 0.242	0.014 ± 0.699	−0.175 ± 0.614	0.171 ± 0.477	−0.021 ± 0.188	−0.246 ± 0.264
759	–	218	–	–	–	5h35m21.73s	-5d23m48.40s	−0.016 ± 0.130	−0.079 ± 0.162	0.194 ± 0.454	−0.016 ± 0.420	0.079 ± 0.377	0.003 ± 0.119	0.087 ± 0.183
760	218-339	249	–	–	–	5h35m21.77s	-5d23m39.40s	0.174 ± 0.057	0.186 ± 0.202	0.056 ± 0.553	0.220 ± 0.551	0.016 ± 0.354	0.176 ± 0.151	0.182 ± 0.201
761	218-354	204	–	–	–	5h35m21.80s	-5d23m53.90s	0.107 ± 0.152	0.166 ± 0.192	0.035 ± 0.509	0.041 ± 0.521	−0.039 ± 0.337	0.142 ± 0.129	0.202 ± 0.183
762	–	343	–	–	–	5h35m21.80s	-5d23m10.70s	−0.015 ± 0.167	0.062 ± 0.166	−0.019 ± 0.685	−0.026 ± 0.627	0.028 ± 0.471	−0.017 ± 0.165	−0.046 ± 0.245
763	218-529	30	–	–	–	5h35m21.83s	-5d25m28.43s	−0.002 ± 0.141	−0.071 ± 0.194	−0.194 ± 0.692	0.045 ± 0.580	0.036 ± 0.418	0.002 ± 0.159	−0.049 ± 0.248
764	–	432	–	–	–	5h35m21.83s	-5d22m40.30s	0.070 ± 0.135	−0.032 ± 0.218	−0.291 ± 0.686	−0.033 ± 0.745	0.242 ± 0.526	0.105 ± 0.180	0.285 ± 0.235
765	218-306	358	–	–	–	5h35m21.84s	-5d23m06.48s	0.262 ± 0.147	0.124 ± 0.224	−0.030 ± 0.632	−0.015 ± 0.697	0.147 ± 0.457	0.082 ± 0.190	−0.025 ± 0.234
766	–	528	–	–	–	5h35m21.86s	-5d22m08.40s	0.021 ± 0.161	−0.029 ± 0.274	0.224 ± 0.749	−0.211 ± 0.697	−0.135 ± 0.608	−0.179 ± 0.228	0.040 ± 0.261
767	–	197	–	–	–	5h35m21.89s	-5d23m55.50s	0.044 ± 0.150	−0.204 ± 0.201	0.069 ± 0.421	0.146 ± 0.497	−0.177 ± 0.357	0.108 ± 0.116	0.315 ± 0.175
768	–	355	–	–	–	5h35m21.89s	-5d23m07.20s	−0.144 ± 0.155	−0.036 ± 0.190	−0.344 ± 0.617	−0.077 ± 0.722	0.016 ± 0.476	0.107 ± 0.177	0.245 ± 0.219
769	–	136	–	–	–	5h35m21.98s	-5d24m26.10s	−0.068 ± 0.119	−0.129 ± 0.160	0.155 ± 0.409	0.041 ± 0.486	0.186 ± 0.384	−0.013 ± 0.130	0.173 ± 0.188
770	–	91	–	–	–	5h35m21.99s	-5d24m53.30s	0.142 ± 0.177	0.009 ± 0.166	0.252 ± 0.679	0.064 ± 0.613	0.134 ± 0.410	0.013 ± 0.172	0.078 ± 0.233

Table 7.2 (cont'd)

ID	Proplyd Name	HC00 ID	GMR ID	Z04a ID	Other Names	R.A. [J2000]	Dec [J2000]	$F_{\nu,6cm}$ [mJy]	$F_{\nu,3.6cm}$ [mJy]	$F_{\nu,1.3cm,1}$ [mJy] [a]	$F_{\nu,1.3cm,2}$ [mJy] [a]	$F_{\nu,1.3cm,3}$ [mJy] [a]	$F_{\nu,1.3cm,4}$ [mJy] [a]	$F_{\nu,1.3cm,mean}$ [mJy] [a]
771	221-433	121	–	–	–	5h35m22.09s	-5d24m32.88s	0.349 ± 0.151	0.378 ± 0.204	−0.030 ± 0.512	0.407 ± 0.488	0.218 ± 0.379	0.134 ± 0.158	0.270 ± 0.189
772	–	142	–	–	–	5h35m22.12s	-5d24m20.20s	0.010 ± 0.137	−0.058 ± 0.153	−0.212 ± 0.477	−0.143 ± 0.501	0.010 ± 0.346	−0.023 ± 0.115	−0.035 ± 0.198
773	–	55	–	–	–	5h35m22.12s	-5d25m07.60s	0.047 ± 0.148	0.179 ± 0.156	−0.012 ± 0.766	−0.140 ± 0.592	−0.058 ± 0.443	−0.079 ± 0.165	−0.130 ± 0.230
774	–	449	–	–	–	5h35m22.13s	-5d22m34.10s	0.076 ± 0.164	0.021 ± 0.213	−0.041 ± 0.815	−0.404 ± 0.877	0.224 ± 0.543	−0.035 ± 0.182	−0.107 ± 0.293
775	–	512	–	–	–	5h35m22.16s	-5d22m13.50s	−0.021 ± 0.147	−0.019 ± 0.263	0.036 ± 0.891	0.155 ± 0.895	0.005 ± 0.573	−0.131 ± 0.190	−0.000 ± 0.294
776	–	139	–	–	–	5h35m22.19s	-5d24m24.90s	−0.030 ± 0.125	0.021 ± 0.174	−0.024 ± 0.471	−0.014 ± 0.514	−0.050 ± 0.353	−0.010 ± 0.146	0.027 ± 0.194
777	–	503	–	–	–	5h35m22.25s	-5d22m17.40s	0.083 ± 0.121	0.034 ± 0.253	−0.084 ± 0.845	−0.087 ± 0.897	−0.002 ± 0.711	−0.084 ± 0.232	−0.112 ± 0.284
778	–	593	–	–	–	5h35m22.29s	-5d21m42.60s	0.017 ± 0.153	0.062 ± 0.273	−0.187 ± 1.534	0.109 ± 1.584	−0.117 ± 0.947	0.062 ± 0.323	0.141 ± 0.465
779	223-414	155	–	–	–	5h35m22.33s	-5d24m14.33s	0.256 ± 0.073	0.067 ± 0.200	0.343 ± 0.419	0.093 ± 0.428	0.096 ± 0.335	0.050 ± 0.140	0.173 ± 0.196
780	–	733	–	–	–	5h35m22.33s	-5d22m13.10s	−0.146 ± 0.156	−0.069 ± 0.221	−0.093 ± 0.857	−0.178 ± 0.852	0.111 ± 0.551	0.053 ± 0.233	0.308 ± 0.294
781	224-728	–	–	–	–	5h35m22.37s	-5d27m28.40s	0.093 ± 0.191	−0.117 ± 0.353	⋯	⋯	⋯	⋯	⋯
782	–	53	–	–	–	5h35m22.41s	-5d25m09.50s	0.148 ± 0.162	0.044 ± 0.176	−0.007 ± 0.590	0.144 ± 0.584	0.023 ± 0.467	0.000 ± 0.158	0.095 ± 0.238
783	–	156	–	–	–	5h35m22.43s	-5d24m13.40s	−0.056 ± 0.166	0.078 ± 0.152	0.142 ± 0.480	0.032 ± 0.436	0.011 ± 0.354	−0.010 ± 0.124	−0.028 ± 0.172
784	–	549	–	–	–	5h35m22.46s	-5d22m01.20s	0.059 ± 0.152	−0.043 ± 0.241	0.241 ± 1.045	−0.035 ± 1.328	−0.220 ± 0.833	−0.155 ± 0.267	−0.047 ± 0.377
785	–	11	–	–	–	5h35m22.47s	-5d25m45.20s	0.024 ± 0.182	−0.047 ± 0.209	0.204 ± 0.550	−0.018 ± 0.506	0.202 ± 0.399	−0.046 ± 0.162	−0.065 ± 0.184
786	–	376	–	–	–	5h35m22.49s	-5d23m01.94s	0.107 ± 0.158	−0.009 ± 0.208	−0.337 ± 0.838	0.174 ± 0.055	−0.012 ± 0.458	0.057 ± 0.155	0.094 ± 0.248
787	–	200	–	–	–	5h35m22.54s	-5d23m54.80s	0.040 ± 0.163	−0.162 ± 0.189	0.104 ± 0.422	0.017 ± 0.403	0.150 ± 0.362	0.047 ± 0.108	0.090 ± 0.174
788	–	233	–	–	–	5h35m22.55s	-5d23m43.70s	0.145 ± 0.121	−0.082 ± 0.182	0.097 ± 0.564	−0.160 ± 0.452	0.048 ± 0.395	0.020 ± 0.148	0.190 ± 0.189
789	–	604	–	–	–	5h35m22.64s	-5d21m37.50s	0.017 ± 0.152	0.124 ± 0.315	−0.028 ± 2.321	−0.155 ± 2.062	−0.432 ± 1.322	0.102 ± 0.454	0.034 ± 0.618
790	–	597	–	–	–	5h35m22.71s	-5d21m41.20s	0.208 ± 0.160	0.168 ± 0.265	−0.236 ± 2.048	−0.257 ± 1.818	0.006 ± 1.139	−0.270 ± 0.440	−0.197 ± 0.524
791	–	58	–	–	–	5h35m22.73s	-5d25m05.80s	0.063 ± 0.142	0.058 ± 0.141	−0.031 ± 0.621	0.016 ± 0.627	0.065 ± 0.402	0.006 ± 0.146	0.021 ± 0.213
792	–	556	–	–	–	5h35m22.76s	-5d21m57.70s	−0.055 ± 0.164	−0.050 ± 0.268	−0.509 ± 1.299	−0.231 ± 1.343	−0.587 ± 0.981	0.015 ± 0.375	−0.407 ± 0.498
793	–	339	–	–	–	5h35m22.80s	-5d23m13.40s	−0.030 ± 0.156	0.032 ± 0.210	0.613 ± 0.706	0.044 ± 0.598	0.070 ± 0.495	0.018 ± 0.154	0.089 ± 0.225
794	228-548	5	–	–	–	5h35m22.83s	-5d25m47.65s	0.018 ± 0.171	0.030 ± 0.168	−0.034 ± 0.506	0.304 ± 0.477	0.111 ± 0.401	−0.016 ± 0.138	0.028 ± 0.224
795	–	472	–	–	–	5h35m22.84s	-5d22m27.00s	0.025 ± 0.145	−0.013 ± 0.242	−0.224 ± 0.951	0.026 ± 1.046	−0.075 ± 0.687	−0.272 ± 0.281	−0.351 ± 0.322
796	–	82	–	–	–	5h35m22.88s	-5d24m57.65s	0.072 ± 0.169	−0.020 ± 0.175	0.017 ± 0.696	0.149 ± 0.682	−0.060 ± 0.436	−0.016 ± 0.145	−0.023 ± 0.208
797	–	428	–	–	–	5h35m22.97s	-5d22m41.60s	−0.068 ± 0.121	−0.138 ± 0.200	−0.204 ± 1.075	−0.243 ± 0.984	−0.257 ± 0.630	0.181 ± 0.249	0.043 ± 0.342
798	230-536	18	–	–	–	5h35m23.03s	-5d25m36.25s	−0.026 ± 0.151	0.063 ± 0.180	−0.005 ± 0.481	−0.054 ± 0.487	0.140 ± 0.386	−0.055 ± 0.120	−0.023 ± 0.213
799	231-460	754	–	–	–	5h35m23.04s	-5d24m59.88s	0.139 ± 0.160	0.048 ± 0.166	0.125 ± 0.659	0.238 ± 0.637	−0.154 ± 0.473	−0.019 ± 0.144	−0.001 ± 0.222
800	–	73	–	–	–	5h35m23.05s	-5d25m00.20s	0.191 ± 0.169	0.047 ± 0.170	0.222 ± 0.567	−0.203 ± 0.673	−0.153 ± 0.472	0.008 ± 0.161	−0.071 ± 0.200
801	231-838	–	–	–	–	5h35m23.10s	-5d28m37.34s	−0.053 ± 0.341	0.139 ± 0.982	⋯	⋯	⋯	⋯	⋯
802	–	216	–	–	–	5h35m23.15s	-5d23m49.30s	0.003 ± 0.134	−0.004 ± 0.174	0.051 ± 0.488	0.136 ± 0.432	−0.010 ± 0.375	0.022 ± 0.134	0.082 ± 0.180
803	231-502	68	–	–	–	5h35m23.16s	-5d25m02.25s	−0.046 ± 0.139	0.042 ± 0.165	−0.081 ± 0.552	0.005 ± 0.619	−0.031 ± 0.439	0.023 ± 0.155	0.149 ± 0.215
804	–	470	–	–	–	5h35m23.19s	-5d22m28.40s	−0.017 ± 0.141	−0.021 ± 0.269	0.892 ± 1.267	−0.394 ± 1.281	0.050 ± 0.761	−0.191 ± 0.310	−0.488 ± 0.390
805	–	778	–	–	–	5h35m23.19s	-5d23m58.30s	0.019 ± 0.114	−0.090 ± 0.178	−0.066 ± 0.432	0.109 ± 0.449	−0.087 ± 0.322	0.058 ± 0.117	−0.004 ± 0.180

Table 7.2 (cont'd)

ID	Proplyd Name	HC00 ID	GMR ID	Z04a ID	Other Names	R.A. [J2000]	Dec [J2000]	$F_{\nu,6cm}$ [mJy]	$F_{\nu,3.6cm}$ [mJy]	$F_{\nu,1.3cm,1}$ [a] [mJy]	$F_{\nu,1.3cm,2}$ [a] [mJy]	$F_{\nu,1.3cm,3}$ [a] [mJy]	$F_{\nu,1.3cm,4}$ [a] [mJy]	$F_{\nu,1.3cm,mean}$ [a] [mJy]
806	—	607	—	—	—	5h35m23.22s	-5d21m35.90s	-0.061 ± 0.163	0.008 ± 0.328	-0.316 ± 2.821	0.124 ± 2.807	0.102 ± 1.579	-0.031 ± 0.569	-0.186 ± 0.753
807	232-453	92	—	—	—	5h35m23.23s	-5d24m52.85s	-0.026 ± 0.142	-0.031 ± 0.173	-0.227 ± 0.593	-0.001 ± 0.613	0.058 ± 0.439	-0.062 ± 0.158	-0.104 ± 0.237
808	—	164	—	—	—	5h35m23.26s	-5d24m07.40s	-0.098 ± 0.143	0.042 ± 0.185	0.111 ± 0.543	-0.120 ± 0.400	-0.002 ± 0.341	0.028 ± 0.113	0.025 ± 0.187
809	—	763	—	—	—	5h35m23.31s	-5d25m05.80s	0.041 ± 0.157	0.053 ± 0.179	-0.078 ± 0.664	0.020 ± 0.564	0.041 ± 0.428	0.024 ± 0.140	-0.002 ± 0.242
810	—	316	—	—	—	5h35m23.34s	-5d23m20.80s	0.108 ± 0.156	0.037 ± 0.202	0.096 ± 0.692	-0.156 ± 0.592	0.032 ± 0.410	0.004 ± 0.161	-0.039 ± 0.218
811	—	628	—	—	—	5h35m23.34s	-5d21m25.50s	0.020 ± 0.165	0.209 ± 0.407			0.777 ± 2.332	-0.210 ± 0.844	0.300 ± 1.090
812	—	736	—	—	—	5h35m23.34s	-5d20m48.10s	-0.005 ± 0.187	0.187 ± 0.494	$\cdots$	$\cdots$	$\cdots$	$\cdots$	$\cdots$
813	—	669	—	—	—	5h35m23.36s	-5d21m03.70s	-0.039 ± 0.201	0.114 ± 0.473	$\cdots$	$\cdots$	$\cdots$	$\cdots$	$\cdots$
814	234-853	—	—	—	—	5h35m23.40s	-5d28m53.19s	0.133 ± 0.395	-0.093 ± 1.075	$\cdots$	$\cdots$	$\cdots$	$\cdots$	$\cdots$
815	—	677	—	—	—	5h35m23.44s	-5d21m00.00s	-0.018 ± 0.185	0.004 ± 0.413	$\cdots$	$\cdots$	$\cdots$	$\cdots$	$\cdots$
816	—	—	—	—	—	5h35m23.49s	-5d20m01.60s	0.184 ± 0.271	-0.413 ± 0.970	$\cdots$	$\cdots$	$\cdots$	$\cdots$	$\cdots$
817	—	89	—	—	—	5h35m23.54s	-5d24m54.30s	0.049 ± 0.155	-0.177 ± 0.158	-0.053 ± 0.629	0.089 ± 0.575	0.080 ± 0.387	-0.021 ± 0.156	-0.038 ± 0.207
818	—	212	—	—	—	5h35m23.54s	-5d23m51.00s	0.087 ± 0.143	-0.088 ± 0.181	-0.098 ± 0.477	0.061 ± 0.388	0.056 ± 0.317	0.077 ± 0.135	0.071 ± 0.189
819	236-527	32	—	—	—	5h35m23.60s	-5d25m26.52s	-0.019 ± 0.149	0.025 ± 0.152	-0.012 ± 0.462	0.012 ± 0.455	0.064 ± 0.368	0.045 ± 0.132	0.073 ± 0.208
820	—	281	—	—	—	5h35m23.64s	-5d23m29.90s	-0.002 ± 0.152	0.021 ± 0.199	0.006 ± 0.599	0.070 ± 0.498	-0.028 ± 0.367	-0.053 ± 0.136	-0.149 ± 0.190
821	—	270	—	—	—	5h35m23.66s	-5d23m31.96s	-0.015 ± 0.136	-0.072 ± 0.222	-0.001 ± 0.534	-0.226 ± 0.512	-0.178 ± 0.461	0.917 ± 0.107	1.326 ± 0.270
822	237-627	—	—	—	—	5h35m23.66s	-5d26m27.15s	0.069 ± 0.178	0.053 ± 0.224	-0.553 ± 0.725	0.127 ± 0.688	-0.112 ± 0.489	0.107 ± 0.180	0.070 ± 0.246
823	—	227	—	—	—	5h35m23.66s	-5d23m46.40s	-0.053 ± 0.142	-0.104 ± 0.177	0.152 ± 0.434	-0.076 ± 0.433	-0.108 ± 0.380	-0.008 ± 0.138	0.035 ± 0.160
824	—	645	—	—	—	5h35m23.67s	-5d21m16.40s	0.052 ± 0.175	-0.144 ± 0.426	$\cdots$	$\cdots$	$\cdots$	$\cdots$	$\cdots$
825	—	81	—	—	—	5h35m23.68s	-5d24m57.40s	0.035 ± 0.143	-0.091 ± 0.183	0.372 ± 0.566	0.033 ± 0.594	-0.086 ± 0.394	-0.036 ± 0.154	0.035 ± 0.201
826	—	519	—	—	—	5h35m23.69s	-5d22m12.80s	0.037 ± 0.185	-0.063 ± 0.244	0.047 ± 1.978	-0.140 ± 1.685	-0.052 ± 1.129	0.137 ± 0.438	0.440 ± 0.553
827	—	319	—	—	—	5h35m23.72s	-5d23m19.90s	0.108 ± 0.130	-0.191 ± 0.244	-0.118 ± 0.667	-0.117 ± 0.621	-0.023 ± 0.459	-0.023 ± 0.162	-0.141 ± 0.233
828	238-334	262	—	—	—	5h35m23.80s	-5d23m34.30s	-0.060 ± 0.132	0.066 ± 0.214	-0.026 ± 0.553	0.007 ± 0.521	0.114 ± 0.392	0.066 ± 0.147	0.126 ± 0.228
829	—	152	—	—	—	5h35m23.81s	-5d24m16.80s	-0.065 ± 0.144	-0.157 ± 0.174	0.103 ± 0.467	-0.009 ± 0.476	0.031 ± 0.361	-0.010 ± 0.136	-0.024 ± 0.207
830	239-334	—	—	—	—	5h35m23.86s	-5d23m34.05s	-0.064 ± 0.165	-0.026 ± 0.169	0.069 ± 0.469	-0.167 ± 0.515	-0.151 ± 0.387	-0.027 ± 0.152	-0.041 ± 0.215
831	—	265	—	—	—	5h35m23.89s	-5d23m33.30s	-0.004 ± 0.168	0.017 ± 0.212	0.024 ± 0.545	0.224 ± 0.572	-0.072 ± 0.437	0.078 ± 0.153	0.079 ± 0.206
832	—	641	—	—	—	5h35m23.89s	-5d21m18.70s	0.011 ± 0.153	-0.035 ± 0.367	$\cdots$	$\cdots$	$\cdots$	$\cdots$	$\cdots$
833	—	379	—	—	—	5h35m23.92s	-5d23m00.50s	-0.020 ± 0.151	0.071 ± 0.219	0.088 ± 0.913	-0.122 ± 0.948	0.276 ± 0.572	-0.010 ± 0.206	0.039 ± 0.309
834	—	662	—	—	—	5h35m23.93s	-5d21m06.40s	0.079 ± 0.171	0.049 ± 0.463	$\cdots$	$\cdots$	$\cdots$	$\cdots$	$\cdots$
835	239-510	52	—	—	—	5h35m23.99s	-5d25m09.92s	0.245 ± 0.093	-0.002 ± 0.184	0.181 ± 0.615	0.001 ± 0.603	0.042 ± 0.406	0.140 ± 0.044	0.185 ± 0.168
836	240-314	338	—	—	—	5h35m24.02s	-5d23m13.88s	0.209 ± 0.137	0.177 ± 0.201	0.036 ± 0.841	0.066 ± 0.676	-0.051 ± 0.545	0.197 ± 0.175	0.365 ± 0.238
837	—	619	—	—	—	5h35m24.11s	-5d21m32.80s	-0.001 ± 0.165	0.023 ± 0.379	$\cdots$	$\cdots$	-0.360 ± 2.444	-0.201 ± 1.054	-0.209 ± 1.106
838	—	506	—	—	—	5h35m24.12s	-5d22m16.40s	-0.031 ± 0.181	-0.032 ± 0.296	0.147 ± 2.316	0.620 ± 2.176	0.246 ± 1.190	0.083 ± 0.459	0.457 ± 0.601
839	—	561	—	—	—	5h35m24.13s	-5d21m55.70s	0.019 ± 0.147	0.097 ± 0.322	-1.026 ± 3.137	0.648 ± 3.005	0.406 ± 1.458	0.073 ± 0.640	-0.004 ± 0.815
840	242-519	41	—	—	—	5h35m24.24s	-5d25m18.75s	0.117 ± 0.167	0.131 ± 0.183	-0.101 ± 0.475	0.093 ± 0.439	0.046 ± 0.324	0.066 ± 0.141	0.161 ± 0.205

Table 7.2 (cont'd)

ID	Proplyd Name	HC00 ID	GMR ID	Z04a ID	Other Names	R.A. [J2000]	Dec [J2000]	$F_{\nu,6cm}$ [mJy]	$F_{\nu,3.6cm}$ [mJy]	$F_{\nu,1.3cm,1}$ [mJy] [a]	$F_{\nu,1.3cm,2}$ [mJy] [a]	$F_{\nu,1.3cm,3}$ [mJy] [a]	$F_{\nu,1.3cm,4}$ [mJy] [a]	$F_{\nu,1.3cm,mean}$ [mJy] [a]
841	—	460	—	—	—	5h35m24.35s	-5d22m32.40s	-0.085 ± 0.138	0.213 ± 0.258	-0.288 ± 2.114	0.648 ± 2.188	-0.195 ± 1.032	0.121 ± 0.353	0.013 ± 0.572
842	244-440	110	—	—	—	5h35m24.44s	-5d24m39.86s	0.148 ± 0.208	0.093 ± 0.209	0.152 ± 0.678	0.115 ± 0.536	0.123 ± 0.038	0.024 ± 0.174	0.229 ± 1.142
843	—	201	—	—	—	5h35m24.45s	-5d23m55.00s	-0.027 ± 0.152	0.022 ± 0.177	0.019 ± 0.544	-0.012 ± 0.442	0.062 ± 0.402	0.030 ± 0.129	0.071 ± 0.185
844	245-632	—	—	—	—	5h35m24.45s	-5d26m31.55s	0.096 ± 0.206	-0.039 ± 0.244	-0.142 ± 0.710	-0.205 ± 0.680	0.196 ± 0.539	0.083 ± 0.149	0.033 ± 0.252
845	—	183	—	—	—	5h35m24.47s	-5d24m01.10s	-0.032 ± 0.180	-0.087 ± 0.191	0.046 ± 0.481	0.151 ± 0.434	-0.112 ± 0.377	-0.076 ± 0.130	-0.071 ± 0.183
846	245-1910	—	—	—	—	5h35m24.48s	-5d19m09.84s	-0.004 ± 0.362	...	...	...	...	...	...
847	—	626	—	—	—	5h35m24.49s	-5d21m30.00s	0.124 ± 0.179	-0.167 ± 0.389	...	...	...	...	...
848	245-502	71	—	—	—	5h35m24.52s	-5d25m01.60s	0.356 ± 0.088	0.328 ± 0.101	0.063 ± 0.612	0.122 ± 0.531	0.157 ± 0.419	0.275 ± 0.070	0.531 ± 0.467
849	—	407	—	—	—	5h35m24.60s	-5d22m52.00s	-0.014 ± 0.159	0.018 ± 0.215	0.099 ± 1.550	-0.522 ± 1.352	-0.297 ± 0.824	0.054 ± 0.319	-0.269 ± 0.427
850	—	668	—	—	—	5h35m24.63s	-5d21m04.40s	-0.091 ± 0.175	0.185 ± 0.486	...	...	...	...	...
851	—	427	—	—	—	5h35m24.66s	-5d22m42.60s	-0.093 ± 0.175	0.239 ± 0.268	-0.091 ± 1.848	0.628 ± 1.929	0.315 ± 1.027	0.207 ± 0.356	0.480 ± 0.515
852	247-436	119	—	—	—	5h35m24.70s	-5d24m35.72s	0.107 ± 0.142	0.062 ± 0.203	-0.245 ± 0.653	0.266 ± 0.610	0.085 ± 0.461	-0.113 ± 0.142	-0.081 ± 0.200
853	—	101	—	—	—	5h35m24.70s	-5d24m44.20s	0.062 ± 0.145	-0.024 ± 0.179	-0.059 ± 0.722	-0.249 ± 0.639	0.184 ± 0.424	0.019 ± 0.146	0.043 ± 0.222
854	—	113	—	—	—	5h35m24.73s	-5d24m38.50s	-0.106 ± 0.141	0.076 ± 0.203	0.106 ± 0.558	-0.016 ± 0.540	-0.169 ± 0.401	0.077 ± 0.147	0.054 ± 0.209
855	—	617	—	—	—	5h35m24.74s	-5d21m34.00s	0.067 ± 0.191	0.215 ± 0.431	...	...	...	...	...
856	—	557	—	—	—	5h35m24.84s	-5d21m57.80s	-0.086 ± 0.168	-0.004 ± 0.336	...	...	0.275 ± 2.827	0.224 ± 1.025	-0.137 ± 1.192
857	—	51	—	—	—	5h35m24.89s	-5d25m10.20s	-0.021 ± 0.155	0.058 ± 0.184	0.072 ± 0.622	0.163 ± 0.490	-0.111 ± 0.434	-0.032 ± 0.115	-0.070 ± 0.201
858	—	181	—	—	—	5h35m24.96s	-5d24m01.50s	0.018 ± 0.192	0.069 ± 0.182	-0.003 ± 0.513	-0.135 ± 0.492	0.020 ± 0.413	0.024 ± 0.146	0.075 ± 0.203
859	250-439	114	—	—	—	5h35m25.03s	-5d24m38.50s	0.100 ± 0.156	0.048 ± 0.160	0.067 ± 0.776	0.080 ± 0.578	0.008 ± 0.479	0.132 ± 0.038	0.019 ± 0.243
860	—	387	—	—	—	5h35m25.06s	-5d22m58.60s	-0.016 ± 0.164	0.021 ± 0.236	0.017 ± 1.307	0.012 ± 1.376	-0.172 ± 0.737	0.158 ± 0.266	0.154 ± 0.428
861	—	208	—	—	—	5h35m25.08s	-5d23m53.80s	-0.011 ± 0.166	-0.148 ± 0.235	-0.047 ± 0.542	-0.183 ± 0.568	0.026 ± 0.401	-0.031 ± 0.152	-0.080 ± 0.197
862	—	226	—	—	—	5h35m25.09s	-5d23m46.76s	0.137 ± 0.042	-0.182 ± 0.177	-0.009 ± 0.544	0.108 ± 0.032	0.101 ± 0.377	0.133 ± 0.042	0.147 ± 0.050
863	—	481	—	—	—	5h35m25.14s	-5d22m25.20s	0.009 ± 0.158	0.056 ± 0.305	...	...	-0.151 ± 1.991	-0.184 ± 0.715	0.454 ± 0.902
864	252-457	83	—	—	—	5h35m25.22s	-5d24m57.27s	0.017 ± 0.140	-0.015 ± 0.156	0.216 ± 0.571	-0.032 ± 0.601	-0.156 ± 0.557	-0.065 ± 0.139	-0.078 ± 0.198
865	—	167	—	—	—	5h35m25.27s	-5d24m06.50s	-0.072 ± 0.141	-0.148 ± 0.215	0.073 ± 0.578	0.160 ± 0.489	-0.086 ± 0.396	0.021 ± 0.158	0.017 ± 0.209
866	—	29	—	—	—	5h35m25.35s	-5d25m29.50s	0.087 ± 0.179	0.057 ± 0.192	0.085 ± 0.451	0.012 ± 0.459	0.024 ± 0.355	0.033 ± 0.126	0.067 ± 0.198
867	254-412	161	—	—	—	5h35m25.37s	-5d24m11.45s	-0.084 ± 0.167	-0.050 ± 0.191	-0.250 ± 0.562	-0.142 ± 0.595	-0.094 ± 0.475	-0.024 ± 0.151	-0.155 ± 0.214
868	—	231	—	—	—	5h35m25.39s	-5d23m45.80s	-0.078 ± 0.149	-0.016 ± 0.196	0.026 ± 0.626	0.082 ± 0.533	0.101 ± 0.421	0.103 ± 0.148	0.177 ± 0.226
869	—	268	—	—	—	5h35m25.43s	-5d23m33.40s	-0.044 ± 0.154	0.035 ± 0.224	0.097 ± 0.730	0.307 ± 0.660	-0.066 ± 0.508	0.091 ± 0.165	0.089 ± 0.254
870	—	577	—	—	—	5h35m25.44s	-5d21m51.50s	0.089 ± 0.184	-0.051 ± 0.184	...	...	...	...	...
871	—	775	—	—	—	5h35m25.45s	-5d21m51.50s	0.047 ± 0.178	0.027 ± 0.343	...	...	...	...	...
872	—	614	—	—	—	5h35m25.48s	-5d21m34.50s	0.034 ± 0.186	-0.014 ± 0.428	...	...	...	...	...
873	—	610	—	—	—	5h35m25.49s	-5d21m35.60s	-0.034 ± 0.161	-0.010 ± 0.429	...	...	...	...	...
874	255-512	48	—	—	—	5h35m25.53s	-5d25m11.77s	-0.082 ± 0.148	0.116 ± 0.194	0.079 ± 0.523	-0.156 ± 0.517	0.011 ± 0.458	0.045 ± 0.133	0.066 ± 0.185
875	—	568	—	—	—	5h35m25.56s	-5d21m54.00s	0.070 ± 0.162	0.112 ± 0.379	...	...	...	...	...

Table 7.2 (cont'd)

ID	Proplyd Name	HC00 ID	GMR ID	Z04a ID	Other Names	R.A. [J2000]	Dec [J2000]	$F_{\nu,6cm}$ [mJy]	$F_{\nu,3.6cm}$ [mJy]	$F_{\nu,1.3cm,1}$[a] [mJy]	$F_{\nu,1.3cm,2}$[a] [mJy]	$F_{\nu,1.3cm,3}$[a] [mJy]	$F_{\nu,1.3cm,4}$[a] [mJy]	$F_{\nu,1.3cm,mean}$[a] [mJy]
876	–	70	–	–	–	5h35m25.67s	-5d25m02.60s	-0.042 ± 0.143	-0.082 ± 0.212	-0.122 ± 0.707	-0.011 ± 0.567	0.079 ± 0.470	-0.050 ± 0.146	-0.108 ± 0.227
877	–	726	–	–	–	5h35m25.67s	-5d25m43.50s	0.009 ± 0.150	-0.001 ± 0.193	0.019 ± 0.428	-0.064 ± 0.397	-0.003 ± 0.323	0.028 ± 0.103	0.007 ± 0.175
878	–	129	–	–	–	5h35m25.70s	-5d24m28.60s	-0.095 ± 0.151	-0.014 ± 0.192	-0.188 ± 0.561	-0.245 ± 0.632	-0.068 ± 0.469	-0.017 ± 0.161	-0.048 ± 0.212
879	–	347	–	–	–	5h35m25.72s	-5d23m09.40s	0.064 ± 0.160	0.057 ± 0.255	0.051 ± 1.162	0.123 ± 1.137	0.128 ± 0.790	-0.016 ± 0.250	0.047 ± 0.424
880	–	547	–	–	–	5h35m25.86s	-5d22m01.90s	0.113 ± 0.164	-0.029 ± 0.389	$\cdots$	$\cdots$	$\cdots$	$\cdots$	$\cdots$
881	–	7	–	–	–	5h35m25.96s	-5d25m47.60s	-0.061 ± 0.136	-0.036 ± 0.203	0.020 ± 0.420	-0.004 ± 0.471	0.088 ± 0.358	0.012 ± 0.128	0.014 ± 0.169
882	–	6	–	–	–	5h35m26.02s	-5d25m47.70s	0.066 ± 0.171	0.052 ± 0.218	-0.284 ± 0.422	0.031 ± 0.398	0.039 ± 0.372	-0.027 ± 0.109	-0.088 ± 0.184
883	–	638	–	–	–	5h35m26.07s	-5d21m21.10s	-0.013 ± 0.165	-0.107 ± 0.545	$\cdots$	$\cdots$	$\cdots$	$\cdots$	$\cdots$
884	–	16	–	–	–	5h35m26.16s	-5d25m39.40s	0.110 ± 0.175	-0.027 ± 0.223	0.051 ± 0.507	0.148 ± 0.480	0.021 ± 0.341	-0.000 ± 0.128	0.042 ± 0.174
885	–	394	–	–	–	5h35m26.16s	-5d22m57.10s	-0.048 ± 0.196	0.147 ± 0.293	0.383 ± 2.151	0.130 ± 1.980	0.020 ± 1.025	-0.166 ± 0.399	-0.028 ± 0.635
886	262-521	39	–	–	–	5h35m26.18s	-5d25m20.44s	0.077 ± 0.190	-0.126 ± 0.179	0.212 ± 0.498	-0.093 ± 0.562	-0.017 ± 0.435	0.030 ± 0.120	0.018 ± 0.195
887	–	502	–	–	–	5h35m26.24s	-5d22m19.50s	0.045 ± 0.141	0.057 ± 0.294	$\cdots$	$\cdots$	$\cdots$	$\cdots$	$\cdots$
888	–	642	–	–	–	5h35m26.26s	-5d21m18.90s	0.035 ± 0.211	0.056 ± 0.581	$\cdots$	$\cdots$	$\cdots$	$\cdots$	$\cdots$
889	–	737	–	–	–	5h35m26.29s	-5d20m59.70s	0.139 ± 0.182	0.005 ± 0.717	$\cdots$	$\cdots$	$\cdots$	$\cdots$	$\cdots$
890	–	702	–	–	–	5h35m26.36s	-5d25m40.10s	-0.070 ± 0.179	0.071 ± 0.221	0.019 ± 0.445	-0.021 ± 0.482	0.157 ± 0.344	0.033 ± 0.117	0.042 ± 0.173
891	–	76	–	–	–	5h35m26.40s	-5d25m00.72s	0.297 ± 0.065	0.312 ± 0.074	0.277 ± 0.077	0.252 ± 0.077	0.171 ± 0.064	0.236 ± 0.055	0.372 ± 0.122
892	–	377	–	–	–	5h35m26.41s	-5d23m02.40s	-0.041 ± 0.163	0.008 ± 0.286	0.584 ± 2.092	0.406 ± 1.932	0.273 ± 1.179	0.021 ± 0.442	0.395 ± 0.582
893	264-532	28	–	–	–	5h35m26.42s	-5d25m31.60s	-0.124 ± 0.196	-0.039 ± 0.195	-0.074 ± 0.586	0.050 ± 0.424	0.131 ± 0.389	0.054 ± 0.134	0.132 ± 0.178
894	–	480	–	–	–	5h35m26.46s	-5d22m25.80s	0.034 ± 0.167	0.094 ± 0.318	$\cdots$	$\cdots$	$\cdots$	$\cdots$	$\cdots$
895	–	232	–	–	–	5h35m26.50s	-5d23m45.00s	-0.058 ± 0.137	-0.037 ± 0.244	0.059 ± 0.936	0.046 ± 0.850	0.036 ± 0.557	0.071 ± 0.234	0.246 ± 0.308
896	266-558	–	–	–	–	5h35m26.62s	-5d25m57.84s	-0.072 ± 0.165	0.049 ± 0.239	-0.027 ± 0.508	0.026 ± 0.465	0.006 ± 0.352	0.004 ± 0.150	0.001 ± 0.182
897	–	–	–	–	–	5h35m27.44s	-5d26m28.14s	0.047 ± 0.194	-0.081 ± 0.304	0.093 ± 0.854	0.075 ± 0.818	0.087 ± 0.658	0.255 ± 0.061	0.003 ± 0.320
898	281-306	–	–	–	–	5h35m28.13s	-5d23m06.45s	0.112 ± 0.157	0.150 ± 0.417	$\cdots$	$\cdots$	-0.242 ± 2.576	-0.020 ± 0.780	-0.486 ± 1.107
899	282-614	–	–	–	–	5h35m28.20s	-5d26m14.20s	-0.069 ± 0.210	-0.053 ± 0.340	0.320 ± 0.964	0.215 ± 0.854	0.038 ± 0.586	0.067 ± 0.228	0.039 ± 0.351
900	282-458	–	–	–	–	5h35m28.20s	-5d24m58.19s	0.304 ± 0.172	0.176 ± 0.259	0.415 ± 1.329	0.250 ± 1.098	-0.008 ± 0.763	0.124 ± 0.254	0.251 ± 0.390
901	284-439	–	–	–	–	5h35m28.40s	-5d24m38.69s	0.011 ± 0.175	-0.050 ± 0.259	0.218 ± 2.121	0.005 ± 1.790	-0.300 ± 1.109	0.169 ± 0.384	0.173 ± 0.570
902	–	–	–	–	–	5h35m28.55s	-5d20m56.59s	0.779 ± 0.143	0.626 ± 1.216	$\cdots$	$\cdots$	$\cdots$	$\cdots$	$\cdots$
903	294-606	–	–	–	–	5h35m29.48s	-5d26m06.63s	0.200 ± 0.233	-0.016 ± 0.333	0.114 ± 1.401	0.121 ± 1.302	-0.003 ± 0.892	-0.062 ± 0.256	-0.133 ± 0.426
904	–	–	–	–	–	5h35m29.59s	-5d23m12.13s	1.579 ± 0.207	0.833 ± 0.161	$\cdots$	$\cdots$	$\cdots$	$\cdots$	$\cdots$
905	304-539	–	–	–	–	5h35m30.41s	-5d25m38.63s	0.045 ± 0.257	0.023 ± 0.361	0.123 ± 2.366	0.037 ± 2.095	0.054 ± 1.289	0.153 ± 0.427	0.319 ± 0.579
906	314-816	–	–	–	–	5h35m31.40s	-5d28m16.48s	-0.211 ± 0.548	$\cdots$	$\cdots$	$\cdots$	$\cdots$	$\cdots$	$\cdots$
907	321-602	–	–	–	–	5h35m32.10s	-5d26m01.94s	-0.088 ± 0.258	0.062 ± 0.527	$\cdots$	$\cdots$	$\cdots$	$\cdots$	$\cdots$
908	332-405	–	–	–	–	5h35m33.19s	-5d24m04.74s	0.039 ± 0.212	-0.342 ± 0.591	$\cdots$	$\cdots$	$\cdots$	$\cdots$	$\cdots$
909	353-130	–	–	–	–	5h35m35.32s	-5d21m29.59s	-0.047 ± 0.345	$\cdots$	$\cdots$	$\cdots$	$\cdots$	$\cdots$	$\cdots$

[a]Subscript 1 indicates the 1.3 cm data were taken on Nov 10, 2013, 2 on Mar. 3, 2014, 3 on Mar. 7, 2014, 4 on May 3, 2014, and mean indicates the image from the combined 1.3 cm tracks.

Table 7.3. Free-free Emission Model Parameters and ALMA Band Fluxes for Detected Sources

ID	$\nu_{\rm turn}$ [GHz]	$F_{\nu,\,\rm turn}$ [mJy]	$F_{\nu,\rm dust,230GHz}$ [mJy]	$F_{\nu,\rm Band\ 1}$ [a] [mJy]	$F_{\nu,\rm Band\ 2}$ [a] [mJy]	$F_{\nu,\rm Band\ 3}$ [a] [mJy]	$F_{\nu,\rm Band\ 4}$ [a] [mJy]	$F_{\nu,\rm Band\ 5}$ [a] [mJy]	$F_{\nu,\rm Band\ 6}$ [a] [mJy]	$F_{\nu,\rm Band\ 7}$ [a] [mJy]	$F_{\nu,\rm Band\ 8}$ [a] [mJy]	$F_{\nu,\rm Band\ 9}$ [a] [mJy]	$F_{\nu,\rm Band\ 10}$ [a] [mJy]
11	< 5.5	3.188 ± 0.161	$\cdots$	2.65	2.44	2.39	2.29	2.23	2.19	2.11	2.05	1.98	1.93
18	< 5.5	0.582 ± 0.078	$\cdots$	0.48	0.45	0.44	0.42	0.41	0.40	0.38	0.37	0.36	0.35
69	> 22.0	0.265 ± 0.181	$\cdots$	0.25	0.23	0.23	0.22	0.21	0.21	0.20	0.20	0.19	0.18
76	< 5.5	0.237 ± 0.021	$\cdots$	0.20	0.18	0.18	0.17	0.17	0.16	0.16	0.15	0.15	0.14
77	11.477 ± 6.002	0.382 ± 0.055	$\cdots$	0.34	0.31	0.31	0.30	0.29	0.28	0.27	0.26	0.25	0.25
97	16.116 ± 8.250	0.182 ± 0.040	$\cdots$	0.17	0.16	0.15	0.15	0.14	0.14	0.13	0.13	0.13	0.12
103	> 22.0	0.165 ± 0.048	$\cdots$	0.16	0.15	0.14	0.14	0.13	0.13	0.13	0.12	0.12	0.11
109	9.152 ± 8.250	0.057 ± 0.090	$\cdots$	0.05	0.05	0.04	0.04	0.04	0.04	0.04	0.04	0.04	0.04
115	< 5.5	0.327 ± 0.028	$\cdots$	0.27	0.25	0.24	0.24	0.23	0.23	0.22	0.21	0.20	0.20
134	300.000 ± 59.025	0.625 ± 0.191	31.179 ± 0.067	0.77	0.71	0.70	0.67	0.65	0.64	0.62	0.60	0.58	0.56
148	8.897 ± 6.799	0.151 ± 0.067	$\cdots$	0.13	0.12	0.12	0.11	0.11	0.11	0.11	0.10	0.10	0.10
151	< 5.5	0.251 ± 0.049	$\cdots$	0.21	0.19	0.19	0.18	0.18	0.17	0.17	0.16	0.16	0.15
154	< 5.5	2.878 ± 0.122	$\cdots$	2.39	2.20	2.15	2.07	2.01	1.98	1.90	1.85	1.79	1.74
161	> 22.0	0.112 ± 0.108	$\cdots$	0.11	0.10	0.10	0.09	0.09	0.09	0.09	0.08	0.08	0.08
173	> 22.0	0.113 ± 0.039	$\cdots$	0.11	0.10	0.10	0.09	0.09	0.09	0.09	0.08	0.08	0.08
190	< 5.5	0.256 ± 0.072	$\cdots$	0.21	0.20	0.19	0.18	0.18	0.18	0.17	0.16	0.16	0.15
199	> 22.0	0.317 ± 0.056	$\cdots$	0.30	0.28	0.27	0.26	0.25	0.25	0.24	0.23	0.23	0.22
200	> 22.0	0.248 ± 0.039	$\cdots$	0.24	0.22	0.21	0.20	0.20	0.20	0.19	0.18	0.18	0.17
209	< 5.5	0.239 ± 0.053	$\cdots$	0.20	0.18	0.18	0.17	0.17	0.16	0.16	0.15	0.15	0.14
213	> 22.0	0.465 ± 0.044	$\cdots$	0.44	0.41	0.40	0.38	0.37	0.37	0.35	0.34	0.33	0.32
219	< 5.5	0.177 ± 0.022	$\cdots$	0.15	0.14	0.13	0.13	0.12	0.12	0.12	0.11	0.11	0.11
222	> 22.0	0.362 ± 0.080	$\cdots$	0.35	0.32	0.31	0.30	0.29	0.29	0.28	0.27	0.26	0.25
229	13.758 ± 2.391	1.328 ± 0.094	$\cdots$	1.21	1.11	1.09	1.05	1.02	1.00	0.96	0.94	0.90	0.88
232	5.899 ± 2.239	0.313 ± 0.069	21.865 ± 6.394	0.26	0.24	0.24	0.23	0.22	0.22	0.21	0.20	0.20	0.19
235	> 22.0	0.237 ± 0.061	$\cdots$	0.23	0.21	0.20	0.20	0.19	0.19	0.18	0.18	0.17	0.16
236	89.990 ± 20.480	0.874 ± 0.128	157.197 ± 11.932	0.96	0.88	0.87	0.83	0.81	0.80	0.76	0.74	0.72	0.70
237	> 22.0	0.346 ± 0.038	$\cdots$	0.33	0.30	0.30	0.29	0.28	0.27	0.26	0.26	0.25	0.24
238	< 5.5	0.973 ± 0.052	$\cdots$	0.81	0.74	0.73	0.70	0.68	0.67	0.64	0.63	0.60	0.59
242	> 22.0	0.173 ± 0.039	$\cdots$	0.17	0.15	0.15	0.14	0.14	0.14	0.13	0.13	0.12	0.12
246	300.000 ± 57.149	0.065 ± 0.011	273.937 ± 17.585	0.08	0.07	0.07	0.07	0.07	0.07	0.06	0.06	0.06	0.06
247	> 22.0	0.168 ± 0.071	$\cdots$	0.16	0.15	0.14	0.14	0.13	0.13	0.13	0.12	0.12	0.12
251	> 22.0	0.058 ± 0.021	$\cdots$	0.06	0.05	0.05	0.05	0.05	0.05	0.04	0.04	0.04	0.04
252	> 22.0	0.177 ± 0.067	$\cdots$	0.17	0.16	0.15	0.15	0.14	0.14	0.13	0.13	0.13	0.12
253	> 22.0	0.161 ± 0.031	$\cdots$	0.15	0.14	0.14	0.13	0.13	0.13	0.12	0.12	0.12	0.11
257	12.493 ± 8.250	0.219 ± 0.028	$\cdots$	0.20	0.18	0.18	0.17	0.17	0.16	0.16	0.15	0.15	0.14

Table 7.3 (cont'd)

ID	ν_{turn} [GHz]	$F_{\nu,turn}$ [mJy]	$F_{\nu,dust,230GHz}$ [mJy]	$F_{\nu,Band\,1}$ [a] [mJy]	$F_{\nu,Band\,2}$ [a] [mJy]	$F_{\nu,Band\,3}$ [a] [mJy]	$F_{\nu,Band\,4}$ [a] [mJy]	$F_{\nu,Band\,5}$ [a] [mJy]	$F_{\nu,Band\,6}$ [a] [mJy]	$F_{\nu,Band\,7}$ [a] [mJy]	$F_{\nu,Band\,8}$ [a] [mJy]	$F_{\nu,Band\,9}$ [a] [mJy]	$F_{\nu,Band\,10}$ [a] [mJy]
259	> 22.0	0.301 ± 0.052	$\cdots$	0.29	0.26	0.26	0.25	0.24	0.24	0.23	0.22	0.21	0.21
261	< 5.5	0.309 ± 0.063	$\cdots$	0.26	0.24	0.23	0.22	0.22	0.21	0.20	0.20	0.19	0.19
262	> 22.0	0.340 ± 0.042	$\cdots$	0.32	0.30	0.29	0.28	0.27	0.27	0.26	0.25	0.24	0.24
264	> 22.0	0.130 ± 0.040	$\cdots$	0.12	0.11	0.11	0.11	0.10	0.10	0.10	0.10	0.09	0.09
265	9.963 ± 4.865	0.175 ± 0.021	$\cdots$	0.15	0.14	0.14	0.13	0.13	0.13	0.12	0.12	0.12	0.11
270	< 5.5	0.372 ± 0.087	$\cdots$	0.31	0.28	0.28	0.27	0.26	0.26	0.25	0.24	0.23	0.22
271	> 22.0	0.343 ± 0.079	$\cdots$	0.33	0.30	0.30	0.28	0.28	0.27	0.26	0.25	0.24	0.24
279	> 22.0	9.579 ± 0.397	$\cdots$	9.14	8.42	8.23	7.91	7.68	7.58	7.27	7.08	6.83	6.65
280	9.415 ± 2.894	0.734 ± 0.052	$\cdots$	0.64	0.59	0.58	0.56	0.54	0.53	0.51	0.50	0.48	0.47
281	< 5.5	6.976 ± 0.479	$\cdots$	5.80	5.34	5.22	5.01	4.87	4.80	4.61	4.49	4.33	4.21
283	< 5.5	0.602 ± 0.068	$\cdots$	0.50	0.46	0.45	0.43	0.42	0.41	0.40	0.39	0.37	0.36
284	> 22.0	0.203 ± 0.030	$\cdots$	0.19	0.18	0.17	0.17	0.16	0.16	0.15	0.15	0.14	0.14
286	5.820 ± 3.860	0.304 ± 0.063	$\cdots$	0.25	0.23	0.23	0.22	0.21	0.21	0.20	0.20	0.19	0.18
287	< 5.5	0.813 ± 0.138	$\cdots$	0.68	0.62	0.61	0.58	0.57	0.56	0.54	0.52	0.50	0.49
289	> 22.0	0.184 ± 0.026	$\cdots$	0.18	0.16	0.16	0.15	0.15	0.15	0.14	0.14	0.13	0.13
292	> 22.0	0.111 ± 0.128	$\cdots$	0.11	0.10	0.10	0.09	0.09	0.09	0.08	0.08	0.08	0.08
294	> 22.0	0.358 ± 0.064	$\cdots$	0.34	0.31	0.31	0.30	0.29	0.28	0.27	0.26	0.26	0.25
297	< 5.5	0.588 ± 0.068	$\cdots$	0.49	0.45	0.44	0.42	0.41	0.40	0.39	0.38	0.36	0.35
301	22.608 ± 6.489	0.379 ± 0.053	103.200 ± 6.964	0.36	0.33	0.33	0.31	0.30	0.30	0.29	0.28	0.27	0.26
304	> 22.0	0.337 ± 0.168	$\cdots$	0.32	0.30	0.29	0.28	0.27	0.27	0.26	0.25	0.24	0.23
305	< 5.5	0.149 ± 0.058	$\cdots$	0.12	0.11	0.11	0.11	0.10	0.10	0.10	0.10	0.09	0.09
307	< 5.5	1.678 ± 0.073	$\cdots$	1.39	1.28	1.26	1.21	1.17	1.16	1.11	1.08	1.04	1.01
308	> 22.0	2.589 ± 0.129	$\cdots$	2.47	2.28	2.23	2.14	2.08	2.05	1.97	1.91	1.85	1.80
313	> 22.0	0.308 ± 0.039	$\cdots$	0.29	0.27	0.26	0.25	0.25	0.24	0.23	0.23	0.22	0.21
315	> 22.0	0.489 ± 0.039	$\cdots$	0.47	0.43	0.42	0.40	0.39	0.39	0.37	0.36	0.35	0.34
316	< 5.5	0.495 ± 0.108	$\cdots$	0.41	0.38	0.37	0.36	0.35	0.34	0.33	0.32	0.31	0.30
319	8.897 ± 4.245	0.195 ± 0.027	$\cdots$	0.17	0.16	0.15	0.15	0.14	0.14	0.14	0.13	0.13	0.12
325	> 22.0	0.193 ± 0.030	$\cdots$	0.18	0.17	0.17	0.16	0.15	0.15	0.15	0.14	0.14	0.13
330	> 22.0	0.191 ± 0.026	$\cdots$	0.18	0.17	0.16	0.16	0.15	0.15	0.14	0.14	0.14	0.13
331	25.930 ± 26.573	0.481 ± 0.189	7.114 ± 2.139	0.47	0.43	0.42	0.40	0.39	0.39	0.37	0.36	0.35	0.34
332	> 22.0	0.303 ± 0.042	$\cdots$	0.29	0.27	0.26	0.25	0.24	0.24	0.23	0.22	0.22	0.21
333	< 5.5	0.320 ± 0.068	$\cdots$	0.27	0.25	0.24	0.23	0.22	0.22	0.21	0.21	0.20	0.19
341	6.705 ± 2.443	0.921 ± 0.049	$\cdots$	0.78	0.72	0.70	0.68	0.66	0.65	0.62	0.60	0.58	0.57
344	8.897 ± 3.322	0.288 ± 0.072	$\cdots$	0.25	0.23	0.23	0.22	0.21	0.21	0.20	0.19	0.19	0.18
361	> 22.0	0.237 ± 0.081	$\cdots$	0.23	0.21	0.20	0.20	0.19	0.19	0.18	0.18	0.17	0.16

Table 7.3 (cont'd)

ID	$\nu_{\rm turn}$ [GHz]	$F_{\nu,{\rm turn}}$ [mJy]	$F_{\nu,{\rm dust,230GHz}}$ [mJy]	$F_{\nu,{\rm Band\,1}}$ [a] [mJy]	$F_{\nu,{\rm Band\,2}}$ [a] [mJy]	$F_{\nu,{\rm Band\,3}}$ [a] [mJy]	$F_{\nu,{\rm Band\,4}}$ [a] [mJy]	$F_{\nu,{\rm Band\,5}}$ [a] [mJy]	$F_{\nu,{\rm Band\,6}}$ [a] [mJy]	$F_{\nu,{\rm Band\,7}}$ [a] [mJy]	$F_{\nu,{\rm Band\,8}}$ [a] [mJy]	$F_{\nu,{\rm Band\,9}}$ [a] [mJy]	$F_{\nu,{\rm Band\,10}}$ [a] [mJy]
371	< 5.5	0.936 ± 0.126	...	0.78	0.72	0.70	0.67	0.65	0.64	0.62	0.60	0.58	0.57
374	> 22.0	0.228 ± 0.044	...	0.22	0.20	0.20	0.19	0.18	0.18	0.17	0.17	0.16	0.16
378	> 22.0	0.131 ± 0.035	...	0.13	0.12	0.11	0.11	0.11	0.10	0.10	0.10	0.09	0.09
380	< 5.5	0.226 ± 0.028	...	0.19	0.17	0.17	0.16	0.16	0.16	0.15	0.15	0.14	0.14
382	15.230 ± 6.019	0.216 ± 0.036	...	0.20	0.18	0.18	0.17	0.17	0.16	0.16	0.15	0.15	0.14
383	< 5.5	0.569 ± 0.050	...	0.47	0.44	0.43	0.41	0.40	0.39	0.38	0.37	0.35	0.34
384	8.897 ± 3.860	0.193 ± 0.064	...	0.17	0.15	0.15	0.15	0.14	0.14	0.13	0.13	0.13	0.12
386	< 5.5	1.120 ± 0.132	...	0.93	0.86	0.84	0.80	0.78	0.77	0.74	0.72	0.69	0.68
389	< 5.5	0.496 ± 0.056	...	0.41	0.38	0.37	0.36	0.35	0.34	0.33	0.32	0.31	0.30
391	< 5.5	6.005 ± 0.405	9.481 ± 1.367	4.99	4.59	4.49	4.31	4.19	4.13	3.97	3.87	3.73	3.63
393	> 22.0	0.144 ± 0.034	...	0.14	0.13	0.12	0.12	0.12	0.11	0.11	0.11	0.10	0.10
394	< 5.5	1.507 ± 0.074	...	1.25	1.15	1.13	1.08	1.05	1.04	1.00	0.97	0.94	0.91
399	< 5.5	0.710 ± 0.201	...	0.59	0.54	0.53	0.51	0.50	0.49	0.47	0.46	0.44	0.43
401	8.897 ± 3.322	0.173 ± 0.030	...	0.15	0.14	0.14	0.13	0.13	0.12	0.12	0.12	0.11	0.11
408	< 5.5	2.352 ± 0.125	0.418 ± 0.099	1.95	1.80	1.76	1.69	1.64	1.62	1.56	1.51	1.46	1.42
409	> 22.0	0.085 ± 0.021	...	0.08	0.07	0.07	0.07	0.07	0.07	0.06	0.06	0.06	0.06
413	< 5.5	2.122 ± 0.097	...	1.76	1.62	1.59	1.52	1.48	1.46	1.40	1.37	1.32	1.28
416	< 5.5	9.716 ± 0.397	5.518 ± 0.130	8.07	7.43	7.27	6.98	6.78	6.69	6.42	6.25	6.03	5.87
418	< 5.5	4.931 ± 0.222	3.744 ± 1.957	4.10	3.77	3.69	3.54	3.44	3.40	3.26	3.17	3.06	2.98
421	6.910 ± 1.017	10.001 ± 0.292	2.955 ± 0.098	8.50	7.83	7.66	7.35	7.14	7.04	6.76	6.59	6.35	6.18
423	< 5.5	5.603 ± 0.279	2.307 ± 0.100	4.66	4.29	4.19	4.03	3.91	3.86	3.70	3.61	3.48	3.38
424	< 5.5	0.327 ± 0.077	...	0.27	0.25	0.24	0.23	0.23	0.22	0.22	0.21	0.20	0.20
427	6.114 ± 1.027	1.903 ± 0.093	...	1.60	1.47	1.44	1.38	1.34	1.32	1.27	1.24	1.19	1.16
428	< 5.5	0.422 ± 0.050	...	0.35	0.32	0.32	0.30	0.29	0.29	0.28	0.27	0.26	0.25
430	< 5.5	10.314 ± 0.598	23.822 ± 1.580	8.57	7.89	7.72	7.41	7.20	7.10	6.82	6.64	6.40	6.23
433	< 5.5	2.953 ± 0.237	...	2.45	2.26	2.21	2.12	2.06	2.03	1.95	1.90	1.83	1.78
434	6.518 ± 2.374	0.326 ± 0.067	...	0.28	0.25	0.25	0.24	0.23	0.23	0.22	0.21	0.21	0.20
437	> 22.0	0.940 ± 0.173	...	0.90	0.83	0.81	0.78	0.75	0.74	0.71	0.70	0.67	0.65
438	9.965 ± 1.275	5.543 ± 0.195	0.472 ± 0.099	4.89	4.50	4.40	4.23	4.11	4.05	3.89	3.79	3.65	3.55
439	< 5.5	4.060 ± 0.209	5.918 ± 2.089	3.37	3.11	3.04	2.92	2.83	2.80	2.68	2.61	2.52	2.45
440	6.114 ± 1.677	0.453 ± 0.041	...	0.38	0.35	0.34	0.33	0.32	0.32	0.30	0.29	0.28	0.28
442	< 5.5	2.245 ± 0.154	1.546 ± 0.099	1.87	1.72	1.68	1.61	1.57	1.55	1.48	1.44	1.39	1.36
444	< 5.5	0.233 ± 0.041	...	0.19	0.18	0.17	0.17	0.16	0.16	0.15	0.15	0.14	0.14
446	< 5.5	0.768 ± 0.114	0.867 ± 0.198	0.64	0.59	0.57	0.55	0.54	0.53	0.51	0.49	0.48	0.46
460	8.431 ± 1.331	9.970 ± 0.287	1.876 ± 0.098	8.65	7.96	7.79	7.48	7.26	7.16	6.88	6.70	6.46	6.29

Table 7.3 (cont'd)

ID	$\nu_{\rm turn}$ [GHz]	$F_{\nu,\rm turn}$ [mJy]	$F_{\nu,\rm dust,230GHz}$ [mJy]	$F_{\nu,\rm Band\ 1}$[a] [mJy]	$F_{\nu,\rm Band\ 2}$[a] [mJy]	$F_{\nu,\rm Band\ 3}$[a] [mJy]	$F_{\nu,\rm Band\ 4}$[a] [mJy]	$F_{\nu,\rm Band\ 5}$[a] [mJy]	$F_{\nu,\rm Band\ 6}$[a] [mJy]	$F_{\nu,\rm Band\ 7}$[a] [mJy]	$F_{\nu,\rm Band\ 8}$[a] [mJy]	$F_{\nu,\rm Band\ 9}$[a] [mJy]	$F_{\nu,\rm Band\ 10}$[a] [mJy]
465	15.529 ± 1.806	4.832 ± 0.172	0.956 ± 0.100	4.46	4.10	4.01	3.85	3.74	3.69	3.54	3.45	3.33	3.24
466	< 5.5	0.506 ± 0.049	11.191 ± 0.622	0.42	0.39	0.38	0.36	0.35	0.35	0.33	0.33	0.31	0.31
469	11.806 ± 5.083	0.439 ± 0.037	$\cdots$	0.39	0.36	0.35	0.34	0.33	0.33	0.31	0.31	0.29	0.29
473	> 22.0	1.386 ± 0.071	$\cdots$	1.32	1.22	1.19	1.14	1.11	1.10	1.05	1.02	0.99	0.96
477	< 5.5	0.431 ± 0.093	$\cdots$	0.36	0.33	0.32	0.31	0.30	0.30	0.28	0.28	0.27	0.26
481	> 22.0	0.165 ± 0.043	$\cdots$	0.16	0.15	0.14	0.14	0.13	0.13	0.13	0.12	0.12	0.11
483	< 5.5	0.375 ± 0.048	$\cdots$	0.31	0.29	0.28	0.27	0.26	0.26	0.25	0.24	0.23	0.23
484	9.467 ± 1.636	2.352 ± 0.104	0.621 ± 0.131	2.06	1.90	1.86	1.78	1.73	1.71	1.64	1.60	1.54	1.50
491	8.464 ± 0.970	21.520 ± 0.450	3.717 ± 0.131	18.67	17.19	16.81	16.14	15.69	15.47	14.85	14.46	13.94	13.57
492	< 5.5	0.335 ± 0.028	$\cdots$	0.28	0.26	0.25	0.24	0.23	0.23	0.22	0.22	0.21	0.20
494	8.041 ± 1.374	3.658 ± 0.141	1.536 ± 0.099	3.16	2.91	2.84	2.73	2.65	2.62	2.51	2.45	2.36	2.30
499	< 5.5	12.669 ± 0.414	5.062 ± 0.157	10.53	9.69	9.48	9.10	8.84	8.72	8.38	8.16	7.86	7.65
501	10.543 ± 3.632	0.421 ± 0.045	$\cdots$	0.37	0.34	0.34	0.32	0.31	0.31	0.30	0.29	0.28	0.27
511	20.248 ± 5.492	0.699 ± 0.128	$\cdots$	0.66	0.61	0.60	0.57	0.56	0.55	0.53	0.51	0.49	0.48
512	< 5.5	3.496 ± 0.231	4.317 ± 0.622	2.91	2.67	2.62	2.51	2.44	2.41	2.31	2.25	2.17	2.11
515	< 5.5	0.349 ± 0.068	$\cdots$	0.29	0.27	0.26	0.25	0.24	0.24	0.23	0.22	0.22	0.21
516	< 5.5	9.614 ± 0.386	5.804 ± 0.124	7.99	7.36	7.19	6.91	6.71	6.62	6.36	6.19	5.97	5.81
518	6.979 ± 1.091	3.902 ± 0.163	2.128 ± 0.132	3.32	3.06	2.99	2.87	2.79	2.75	2.64	2.57	2.48	2.41
519	< 5.5	1.147 ± 0.178	10.800 ± 0.162	0.95	0.88	0.86	0.82	0.80	0.79	0.76	0.74	0.71	0.69
524	8.897 ± 5.539	0.109 ± 0.039	$\cdots$	0.09	0.09	0.09	0.08	0.08	0.08	0.08	0.07	0.07	0.07
529	6.715 ± 1.156	1.796 ± 0.101	$\cdots$	1.52	1.40	1.37	1.32	1.28	1.26	1.21	1.18	1.14	1.11
530	19.098 ± 5.097	0.981 ± 0.162	$\cdots$	0.92	0.85	0.83	0.80	0.78	0.76	0.73	0.71	0.69	0.67
535	< 5.5	0.830 ± 0.063	0.787 ± 0.297	0.69	0.63	0.62	0.60	0.58	0.57	0.55	0.53	0.51	0.50
537	< 5.5	2.728 ± 0.187	8.006 ± 0.628	2.27	2.09	2.04	1.96	1.90	1.88	1.80	1.76	1.69	1.65
539	> 22.0	0.058 ± 0.018	$\cdots$	0.06	0.05	0.05	0.05	0.05	0.05	0.04	0.04	0.04	0.04
544	< 5.5	0.374 ± 0.039	$\cdots$	0.31	0.29	0.28	0.27	0.26	0.26	0.25	0.24	0.23	0.23
546	< 5.5	0.412 ± 0.038	$\cdots$	0.34	0.32	0.31	0.30	0.29	0.28	0.27	0.27	0.26	0.25
548	< 5.5	0.316 ± 0.083	$\cdots$	0.26	0.24	0.24	0.23	0.22	0.22	0.21	0.20	0.20	0.19
549	> 22.0	0.313 ± 0.118	$\cdots$	0.30	0.28	0.27	0.26	0.25	0.25	0.24	0.23	0.22	0.22
555	< 5.5	4.579 ± 0.206	7.897 ± 2.061	3.81	3.50	3.43	3.29	3.20	3.15	3.03	2.95	2.84	2.77
560	$\cdots$	0.337 ± 0.087	$\cdots$	0.29	0.27	0.26	0.25	0.25	0.24	0.23	0.23	0.22	0.21
564	< 5.5	11.794 ± 0.484	6.237 ± 0.160	9.80	9.02	8.82	8.47	8.23	8.12	7.80	7.59	7.32	7.12
587	< 5.5	1.806 ± 0.083	$\cdots$	1.50	1.38	1.35	1.30	1.26	1.24	1.19	1.16	1.12	1.09
595	< 5.5	4.907 ± 0.308	$\cdots$	4.08	3.75	3.67	3.53	3.43	3.38	3.24	3.16	3.04	2.96
599	< 5.5	0.225 ± 0.100	7.456 ± 2.401	0.19	0.17	0.17	0.16	0.16	0.15	0.15	0.14	0.14	0.14

Table 7.3 (cont'd)

ID	ν_{turn} [GHz]	$F_{\nu,turn}$ [mJy]	$F_{\nu,dust,230GHz}$ [mJy]	$F_{\nu,Band\ 1}$[a] [mJy]	$F_{\nu,Band\ 2}$[a] [mJy]	$F_{\nu,Band\ 3}$[a] [mJy]	$F_{\nu,Band\ 4}$[a] [mJy]	$F_{\nu,Band\ 5}$[a] [mJy]	$F_{\nu,Band\ 6}$[a] [mJy]	$F_{\nu,Band\ 7}$[a] [mJy]	$F_{\nu,Band\ 8}$[a] [mJy]	$F_{\nu,Band\ 9}$[a] [mJy]	$F_{\nu,Band\ 10}$[a] [mJy]
605	< 5.5	0.912 ± 0.159	4.238 ± 0.490	0.76	0.70	0.68	0.66	0.64	0.63	0.60	0.59	0.57	0.55
608	< 5.5	0.718 ± 0.063	$\cdots$	0.60	0.55	0.54	0.52	0.50	0.49	0.47	0.46	0.45	0.43
612	18.297 ± 10.071	0.403 ± 0.088	1.965 ± 0.491	0.38	0.35	0.34	0.33	0.32	0.31	0.30	0.29	0.28	0.27
616	< 5.5	0.266 ± 0.043	$\cdots$	0.22	0.20	0.20	0.19	0.19	0.18	0.18	0.17	0.17	0.16
617	< 5.5	24.441 ± 0.958	0.000 ± 0.230	20.31	18.70	18.29	17.56	17.06	16.83	16.16	15.73	15.17	14.76
621	> 22.0	0.167 ± 0.048	$\cdots$	0.16	0.15	0.14	0.14	0.13	0.13	0.13	0.12	0.12	0.12
649	< 5.5	0.344 ± 0.064	$\cdots$	0.29	0.26	0.26	0.25	0.24	0.24	0.23	0.22	0.21	0.21
658	7.298 ± 8.250	0.260 ± 0.065	$\cdots$	0.22	0.20	0.20	0.19	0.19	0.18	0.18	0.17	0.17	0.16
665	> 22.0	0.067 ± 0.013	$\cdots$	0.06	0.06	0.06	0.06	0.05	0.05	0.05	0.05	0.05	0.05
668	< 5.5	0.323 ± 0.093	19.229 ± 0.624	0.27	0.25	0.24	0.23	0.23	0.22	0.21	0.21	0.20	0.20
672	< 5.5	0.340 ± 0.079	$\cdots$	0.28	0.26	0.25	0.24	0.24	0.23	0.22	0.22	0.21	0.21
674	< 5.5	0.173 ± 0.080	5.458 ± 0.662	0.14	0.13	0.13	0.12	0.12	0.12	0.11	0.11	0.11	0.10
684	< 5.5	0.077 ± 0.101	$\cdots$	0.06	0.06	0.06	0.06	0.05	0.05	0.05	0.05	0.05	0.05
690	> 22.0	0.151 ± 0.053	$\cdots$	0.14	0.13	0.13	0.12	0.12	0.12	0.11	0.11	0.11	0.10
691	9.152 ± 4.050	0.240 ± 0.054	$\cdots$	0.21	0.19	0.19	0.18	0.18	0.17	0.17	0.16	0.16	0.15
693	< 5.5	0.534 ± 0.075	$\cdots$	0.44	0.41	0.40	0.38	0.37	0.37	0.35	0.34	0.33	0.32
695	< 5.5	0.288 ± 0.073	$\cdots$	0.24	0.22	0.22	0.21	0.20	0.20	0.19	0.19	0.18	0.17
700	< 5.5	0.233 ± 0.094	$\cdots$	0.19	0.18	0.17	0.17	0.16	0.16	0.15	0.15	0.14	0.14
711	< 5.5	0.751 ± 0.108	20.984 ± 0.658	0.62	0.57	0.56	0.54	0.52	0.52	0.50	0.48	0.47	0.45
715	7.508 ± 4.446	0.284 ± 0.028	$\cdots$	0.24	0.22	0.22	0.21	0.20	0.20	0.19	0.19	0.18	0.18
730	< 5.5	1.433 ± 0.064	$\cdots$	1.19	1.10	1.07	1.03	1.00	0.99	0.95	0.92	0.89	0.87
737	> 22.0	0.158 ± 0.027	$\cdots$	0.15	0.14	0.14	0.13	0.13	0.12	0.12	0.12	0.11	0.11
760	5.977 ± 2.824	0.182 ± 0.051	2.172 ± 0.231	0.15	0.14	0.14	0.13	0.13	0.13	0.12	0.12	0.11	0.11
779	< 5.5	0.206 ± 0.058	$\cdots$	0.17	0.16	0.15	0.15	0.14	0.14	0.14	0.13	0.13	0.12
786	> 22.0	0.152 ± 0.048	$\cdots$	0.15	0.13	0.13	0.13	0.12	0.12	0.12	0.11	0.11	0.11
821	> 22.0	0.733 ± 0.086	$\cdots$	0.70	0.64	0.63	0.60	0.59	0.58	0.56	0.54	0.52	0.51
835	< 5.5	0.171 ± 0.040	$\cdots$	0.14	0.13	0.13	0.12	0.12	0.12	0.11	0.11	0.11	0.10
842	< 5.5	0.134 ± 0.040	$\cdots$	0.11	0.10	0.10	0.10	0.09	0.09	0.09	0.09	0.08	0.08
848	< 5.5	0.334 ± 0.050	$\cdots$	0.28	0.26	0.25	0.24	0.23	0.23	0.22	0.22	0.21	0.20
859	20.210 ± 8.250	0.130 ± 0.036	$\cdots$	0.12	0.11	0.11	0.11	0.10	0.10	0.10	0.10	0.09	0.09
862	< 5.5	0.136 ± 0.021	$\cdots$	0.11	0.10	0.10	0.10	0.09	0.09	0.09	0.09	0.08	0.08
891	< 5.5	0.287 ± 0.029	$\cdots$	0.24	0.22	0.21	0.21	0.20	0.20	0.19	0.18	0.18	0.17
897	> 22.0	0.237 ± 0.057	$\cdots$	0.23	0.21	0.20	0.20	0.19	0.19	0.18	0.18	0.17	0.16
902	$\cdots$	0.740 ± 0.135	$\cdots$	0.65	0.59	0.58	0.56	0.54	0.53	0.51	0.50	0.48	0.47
904	$\cdots$	1.102 ± 0.125	$\cdots$	0.96	0.89	0.87	0.83	0.81	0.80	0.77	0.75	0.72	0.70

[a]Band 1 = 35 GHz, Band 2 = 80 GHz, Band 3 = 100 GHz, Band 4 = 150 GHz, Band 5 = 200 GHz, Band 6 = 230 GHz, Band 7 = 345 GHz, Band 8 = 450 GHz, Band 9 = 650 GHz, Band 10 = 850 GHz
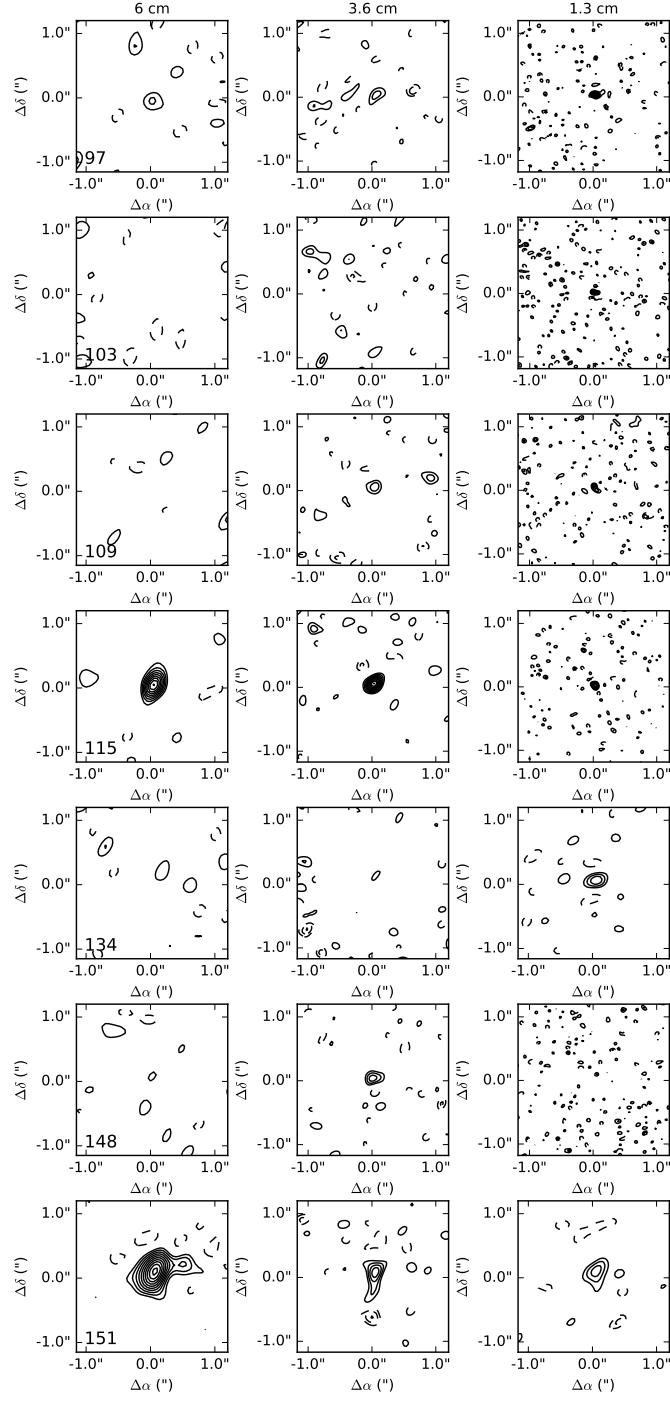
213

Table 7.4.   Variability of ONC Sources

| ID	1.3 cm Variable?	$(\Delta F/F)_{1.3cm}$	3.6 cm Variable?	$(\Delta F/F)_{3.6cm}$	6 cm Variable?	$(\Delta F/F)_{6cm}$
11	N	$\cdots$	Y	20 ± 28	–	$\cdots$
76	N	$\cdots$	–	$\cdots$	–	$\cdots$
77	N	$\cdots$	Y	144 ± 25	–	$\cdots$
102	–	$\cdots$	N	$\cdots$	–	$\cdots$
103	N	$\cdots$	–	$\cdots$	–	$\cdots$
115	Y	78 ± 102	N	$\cdots$	–	$\cdots$
134	N	$\cdots$	–	$\cdots$	–	$\cdots$
151	N	$\cdots$	N	$\cdots$	–	$\cdots$
154	Y	37 ± 10	Y	152 ± 3	–	$\cdots$
173	N	$\cdots$	–	$\cdots$	–	$\cdots$
199	N	$\cdots$	–	$\cdots$	–	$\cdots$
200	N	$\cdots$	Y	71 ± 7	–	$\cdots$
209	–	$\cdots$	N	$\cdots$	–	$\cdots$
213	Y	158 ± 68	Y	77 ± 29	–	$\cdots$
219	N	$\cdots$	–	$\cdots$	–	$\cdots$
222	N	$\cdots$	–	$\cdots$	–	$\cdots$
229	Y	29 ± 574	N	$\cdots$	–	$\cdots$
235	N	$\cdots$	–	$\cdots$	–	$\cdots$
236	N	$\cdots$	–	$\cdots$	–	$\cdots$
237	N	$\cdots$	–	$\cdots$	–	$\cdots$
238	Y	64 ± 9	–	$\cdots$	–	$\cdots$
243	N	$\cdots$	–	$\cdots$	–	$\cdots$
246	Y	45 ± 22	–	$\cdots$	–	$\cdots$
253	N	$\cdots$	–	$\cdots$	–	$\cdots$
257	Y	122 ± 72	–	$\cdots$	–	$\cdots$
259	Y	125 ± 74	–	$\cdots$	–	$\cdots$
262	N	$\cdots$	–	$\cdots$	–	$\cdots$
265	Y	129 ± 21	–	$\cdots$	–	$\cdots$
270	–	$\cdots$	N	$\cdots$	–	$\cdots$
271	N	$\cdots$	–	$\cdots$	–	$\cdots$
275	–	$\cdots$	–	$\cdots$	Y	100 ± 4
278	–	$\cdots$	–	$\cdots$	N	$\cdots$
279	Y	20 ± 26	N	$\cdots$	–	$\cdots$
280	N	$\cdots$	N	$\cdots$	–	$\cdots$
281	–	$\cdots$	Y	28 ± 12	N	$\cdots$
284	N	$\cdots$	–	$\cdots$	–	$\cdots$
286	N	$\cdots$	–	$\cdots$	–	$\cdots$
287	N	$\cdots$	N	$\cdots$	–	$\cdots$
289	N	$\cdots$	–	$\cdots$	–	$\cdots$
294	N	$\cdots$	Y	52 ± 22	–	$\cdots$
297	N	$\cdots$	Y	25 ± 21	–	$\cdots$
301	Y	29 ± 27	–	$\cdots$	–	$\cdots$
307	Y	38 ± 19	Y	67 ± 8	N	$\cdots$
308	Y	19 ± 30	Y	38 ± 14	–	$\cdots$
313	N	$\cdots$	–	$\cdots$	–	$\cdots$
315	N	$\cdots$	–	$\cdots$	–	$\cdots$
319	N	$\cdots$	–	$\cdots$	–	$\cdots$
325	N	$\cdots$	–	$\cdots$	–	$\cdots$
330	N	$\cdots$	–	$\cdots$	–	$\cdots$
331	–	$\cdots$	N	$\cdots$	–	$\cdots$
332	N	$\cdots$	–	$\cdots$	–	$\cdots$
333	–	$\cdots$	N	$\cdots$	–	$\cdots$

Table 7.4 (cont'd)

ID	1.3 cm Variable?	$(\Delta F/F)_{1.3cm}$	3.6 cm Variable?	$(\Delta F/F)_{3.6cm}$	6 cm Variable?	$(\Delta F/F)_{6cm}$
341	Y	51 ± 10	Y	55 ± 13	N	$\cdots$
344	–	$\cdots$	N	$\cdots$	–	$\cdots$
357	–	$\cdots$	N	$\cdots$	–	$\cdots$
358	–	$\cdots$	N	$\cdots$	–	$\cdots$
364	–	$\cdots$	Y	73 ± 16	–	$\cdots$
365	–	$\cdots$	N	$\cdots$	–	$\cdots$
371	–	$\cdots$	N	$\cdots$	–	$\cdots$
373	–	$\cdots$	–	$\cdots$	Y	91 ± 7
374	N	$\cdots$	N	$\cdots$	–	$\cdots$
380	N	$\cdots$	–	$\cdots$	–	$\cdots$
382	N	$\cdots$	–	$\cdots$	–	$\cdots$
383	N	$\cdots$	Y	39 ± 17	–	$\cdots$
384	–	$\cdots$	N	$\cdots$	–	$\cdots$
386	–	$\cdots$	Y	36 ± 20	–	$\cdots$
389	N	$\cdots$	Y	70 ± 4	–	$\cdots$
391	–	$\cdots$	N	$\cdots$	N	$\cdots$
393	N	$\cdots$	–	$\cdots$	–	$\cdots$
394	Y	72 ± 9	–	$\cdots$	–	$\cdots$
399	–	$\cdots$	N	$\cdots$	–	$\cdots$
400	–	$\cdots$	Y	60 ± 16	–	$\cdots$
401	N	$\cdots$	–	$\cdots$	–	$\cdots$
407	–	$\cdots$	–	$\cdots$	Y	101 ± 3
408	N	$\cdots$	Y	31 ± 21	N	$\cdots$
409	N	$\cdots$	–	$\cdots$	–	$\cdots$
411	–	$\cdots$	–	$\cdots$	N	$\cdots$
413	Y	41 ± 14	Y	23 ± 15	N	$\cdots$
414	–	$\cdots$	N	$\cdots$	–	$\cdots$
416	–	$\cdots$	N	$\cdots$	N	$\cdots$
418	Y	88 ± 5	Y	63 ± 10	–	$\cdots$
421	N	$\cdots$	N	$\cdots$	–	$\cdots$
423	–	$\cdots$	N	$\cdots$	N	$\cdots$
427	N	$\cdots$	Y	33 ± 13	–	$\cdots$
428	N	$\cdots$	–	$\cdots$	–	$\cdots$
430	–	$\cdots$	N	$\cdots$	N	$\cdots$
433	–	$\cdots$	Y	39 ± 13	–	$\cdots$
437	Y	284 ± 45	Y	215 ± 46	N	$\cdots$
438	N	$\cdots$	N	$\cdots$	N	$\cdots$
439	Y	24 ± 32	N	$\cdots$	N	$\cdots$
440	Y	299 ± 89	–	$\cdots$	–	$\cdots$
442	–	$\cdots$	Y	29 ± 17	–	$\cdots$
444	N	$\cdots$	N	$\cdots$	–	$\cdots$
460	N	$\cdots$	N	$\cdots$	N	$\cdots$
465	N	$\cdots$	N	$\cdots$	–	$\cdots$
466	N	$\cdots$	Y	51 ± 13	–	$\cdots$
469	Y	108 ± 21	–	$\cdots$	–	$\cdots$
473	N	$\cdots$	Y	55 ± 11	–	$\cdots$
477	–	$\cdots$	Y	60 ± 16	–	$\cdots$
481	N	$\cdots$	–	$\cdots$	–	$\cdots$
483	N	$\cdots$	N	$\cdots$	–	$\cdots$
484	N	$\cdots$	N	$\cdots$	–	$\cdots$
491	N	$\cdots$	N	$\cdots$	N	$\cdots$
492	Y	57 ± 13	–	$\cdots$	–	$\cdots$

Table 7.4 (cont'd)

ID	1.3 cm Variable?	$(\Delta F/F)_{1.3cm}$	3.6 cm Variable?	$(\Delta F/F)_{3.6cm}$	6 cm Variable?	$(\Delta F/F)_{6cm}$
493	–	$\cdots$	–	$\cdots$	Y	102 ± 3
494	N	$\cdots$	N	$\cdots$	–	$\cdots$
499	Y	28 ± 22	N	$\cdots$	–	$\cdots$
501	N	$\cdots$	N	$\cdots$	–	$\cdots$
512	–	$\cdots$	Y	27 ± 22	N	$\cdots$
516	–	$\cdots$	N	$\cdots$	N	$\cdots$
518	N	$\cdots$	N	$\cdots$	N	$\cdots$
519	–	$\cdots$	N	$\cdots$	–	$\cdots$
529	Y	99 ± 11	–	$\cdots$	–	$\cdots$
530	–	$\cdots$	N	$\cdots$	–	$\cdots$
535	N	$\cdots$	Y	31 ± 19	–	$\cdots$
537	–	$\cdots$	N	$\cdots$	–	$\cdots$
544	Y	102 ± 4	–	$\cdots$	–	$\cdots$
546	N	$\cdots$	N	$\cdots$	–	$\cdots$
549	N	$\cdots$	–	$\cdots$	–	$\cdots$
555	N	$\cdots$	N	$\cdots$	N	$\cdots$
564	–	$\cdots$	N	$\cdots$	N	$\cdots$
587	Y	136 ± 3	Y	69 ± 6	–	$\cdots$
595	–	$\cdots$	N	$\cdots$	N	$\cdots$
599	N	$\cdots$	–	$\cdots$	–	$\cdots$
605	N	$\cdots$	–	$\cdots$	–	$\cdots$
608	N	$\cdots$	Y	38 ± 18	–	$\cdots$
616	N	$\cdots$	–	$\cdots$	–	$\cdots$
617	Y	24 ± 14	Y	49 ± 12	–	$\cdots$
621	N	$\cdots$	–	$\cdots$	–	$\cdots$
649	N	$\cdots$	–	$\cdots$	–	$\cdots$
658	N	$\cdots$	–	$\cdots$	–	$\cdots$
665	N	$\cdots$	–	$\cdots$	–	$\cdots$
668	N	$\cdots$	–	$\cdots$	–	$\cdots$
690	N	$\cdots$	–	$\cdots$	–	$\cdots$
715	Y	92 ± 24	–	$\cdots$	–	$\cdots$
730	Y	51 ± 9	Y	50 ± 6	Y	47 ± 11
737	Y	905 ± 487	–	$\cdots$	–	$\cdots$
760	N	$\cdots$	–	$\cdots$	–	$\cdots$
786	N	$\cdots$	–	$\cdots$	–	$\cdots$
821	N	$\cdots$	–	$\cdots$	–	$\cdots$
835	N	$\cdots$	–	$\cdots$	–	$\cdots$
842	N	$\cdots$	–	$\cdots$	–	$\cdots$
848	N	$\cdots$	–	$\cdots$	–	$\cdots$
859	N	$\cdots$	–	$\cdots$	–	$\cdots$
862	N	$\cdots$	–	$\cdots$	–	$\cdots$
891	N	$\cdots$	–	$\cdots$	–	$\cdots$
897	N	$\cdots$	–	$\cdots$	–	$\cdots$

Figure 7.7: *Continued*
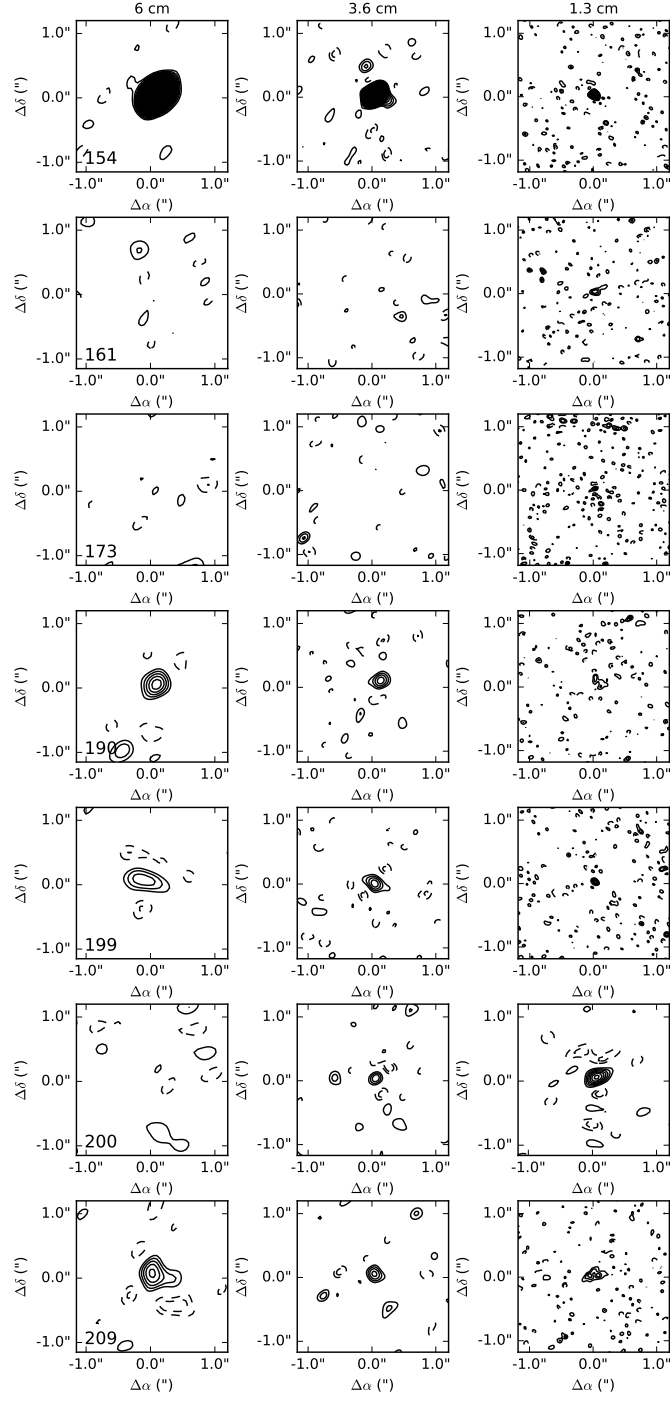
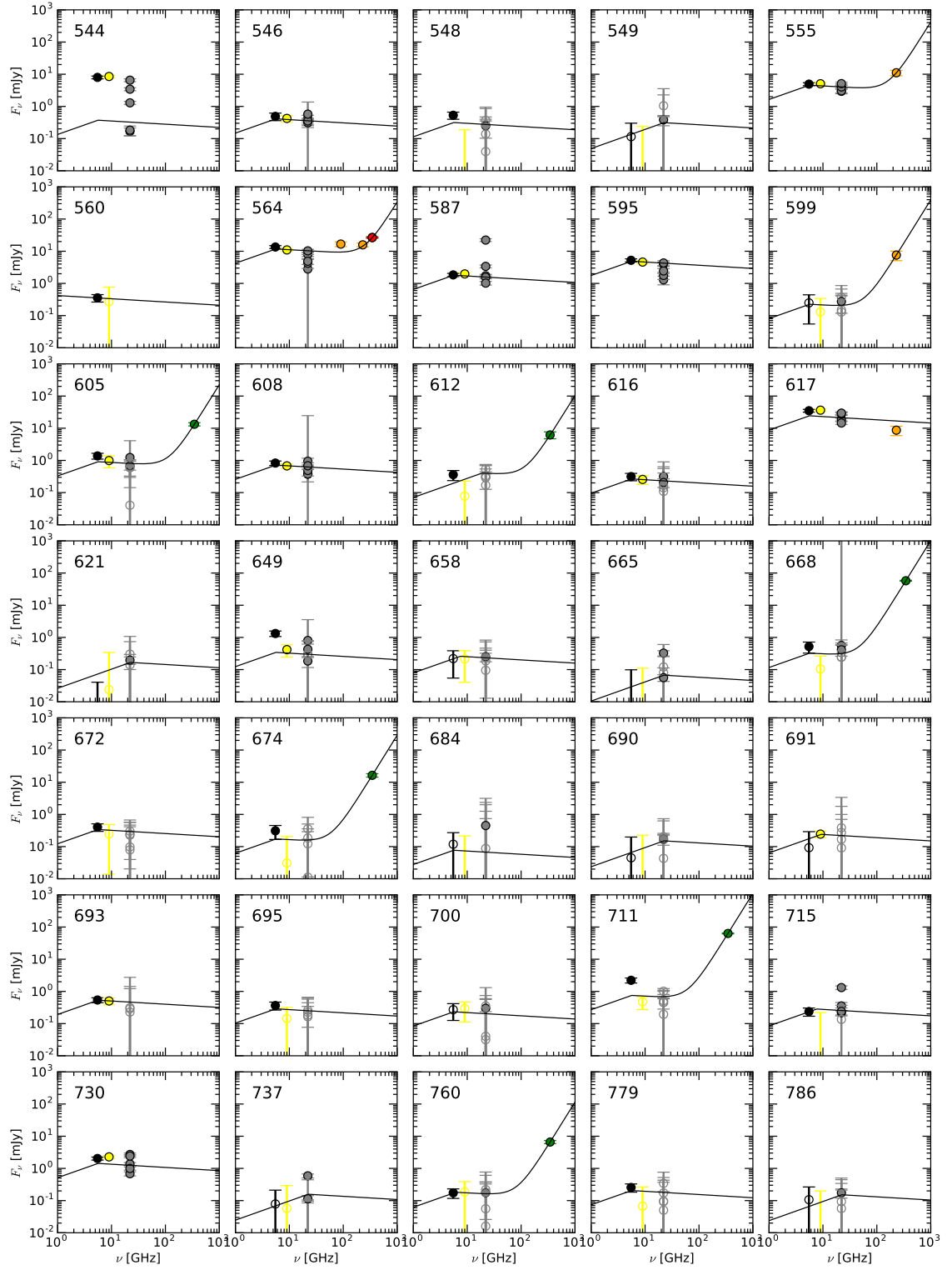Figure 7.8: *Continued*
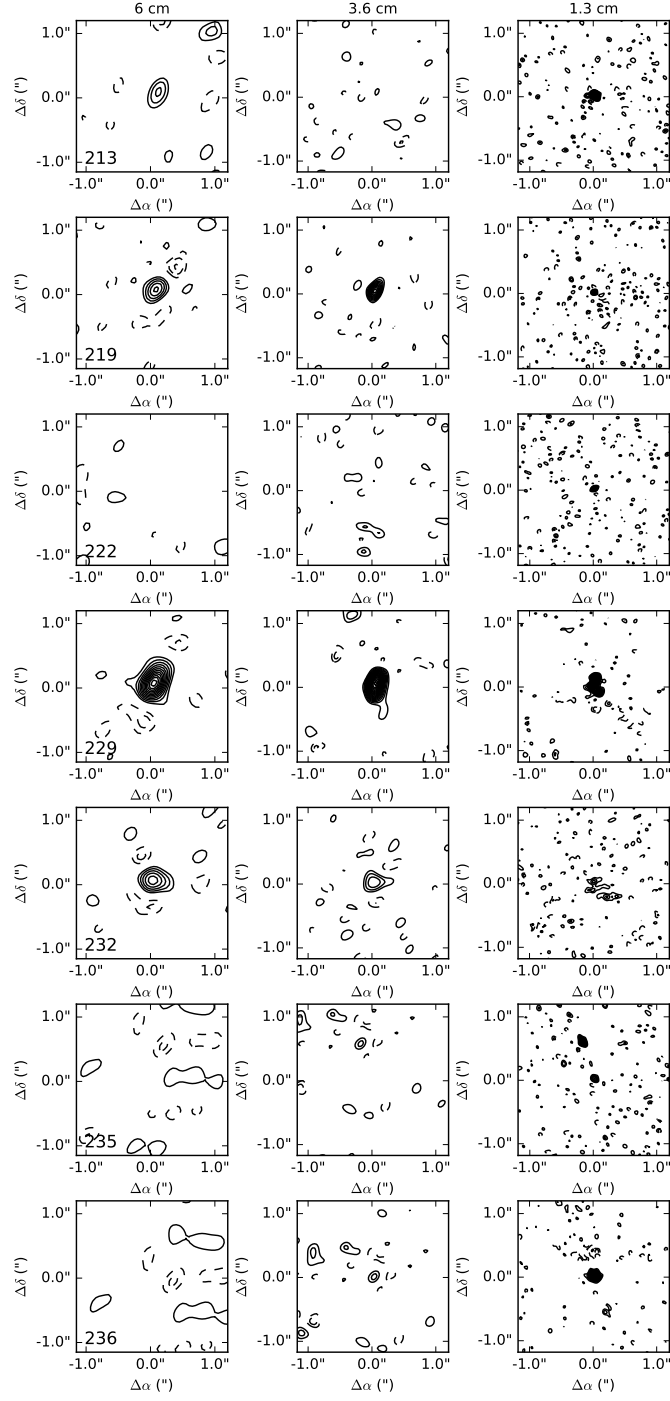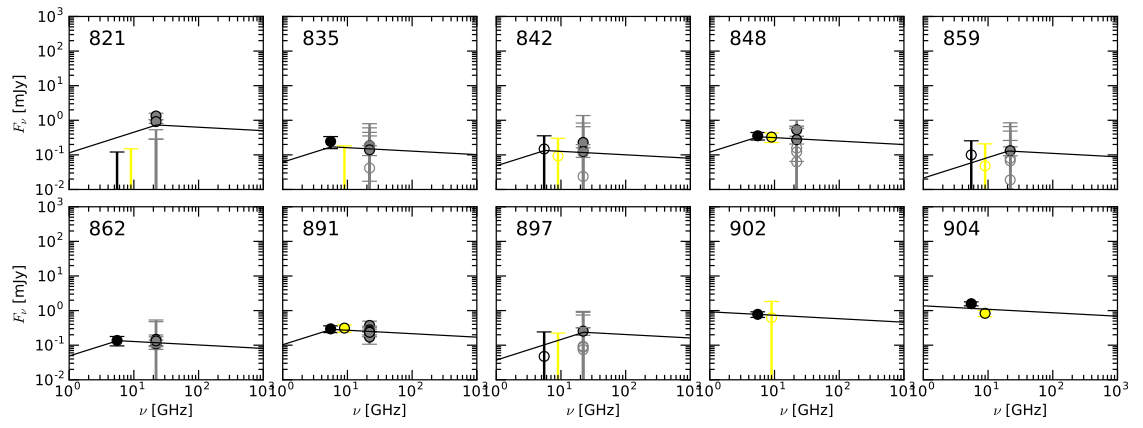
Figure 7.9: *Continued*
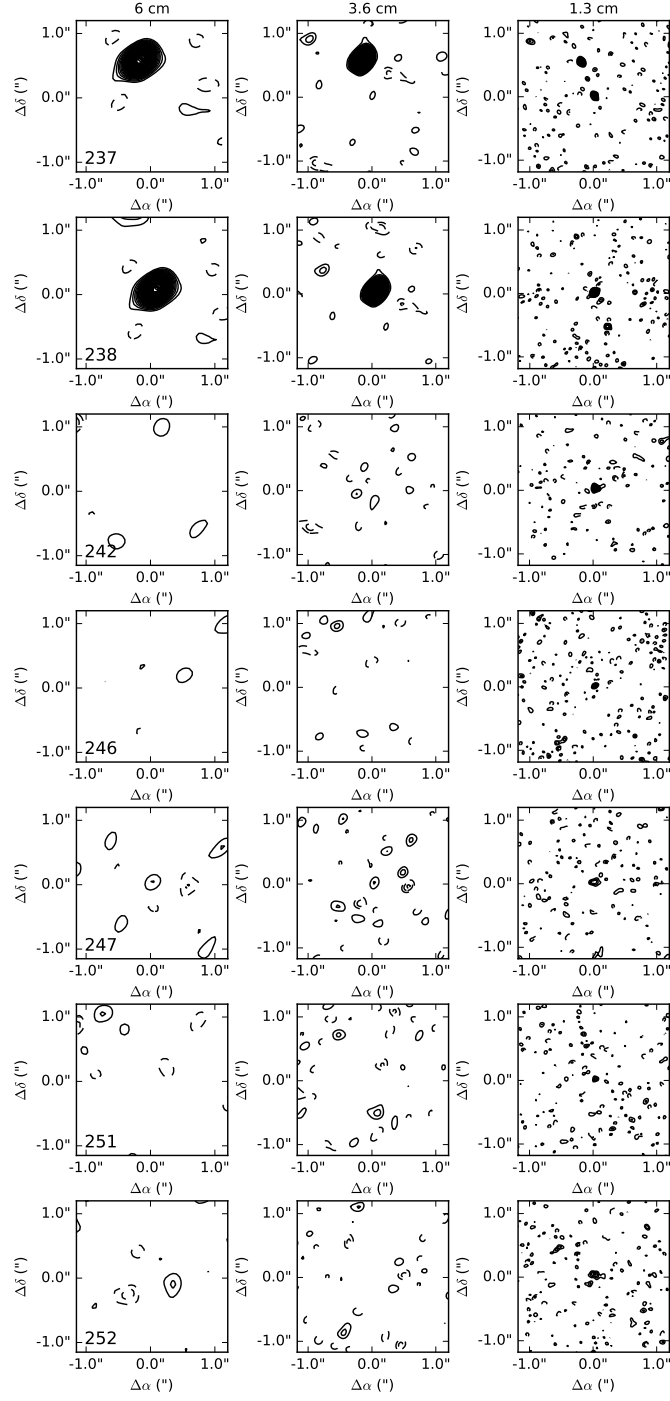
Figure 7.10: *Continued*
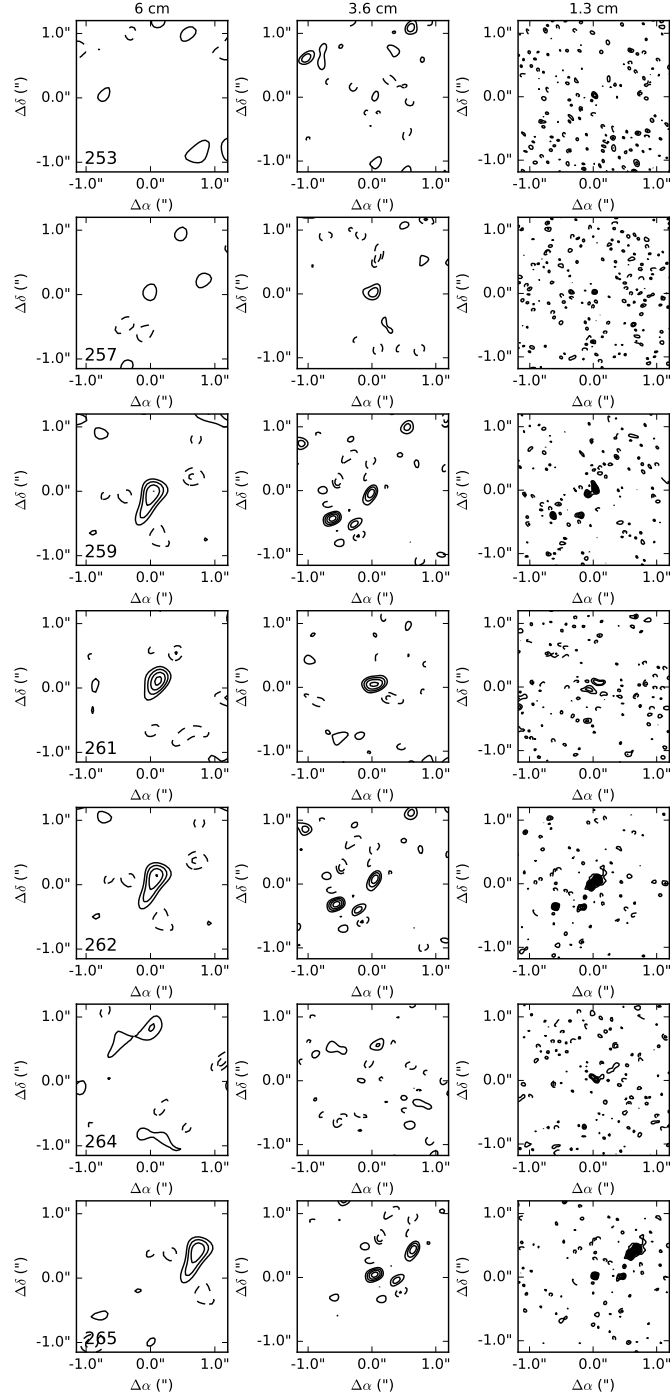
Figure 7.11: *Continued*
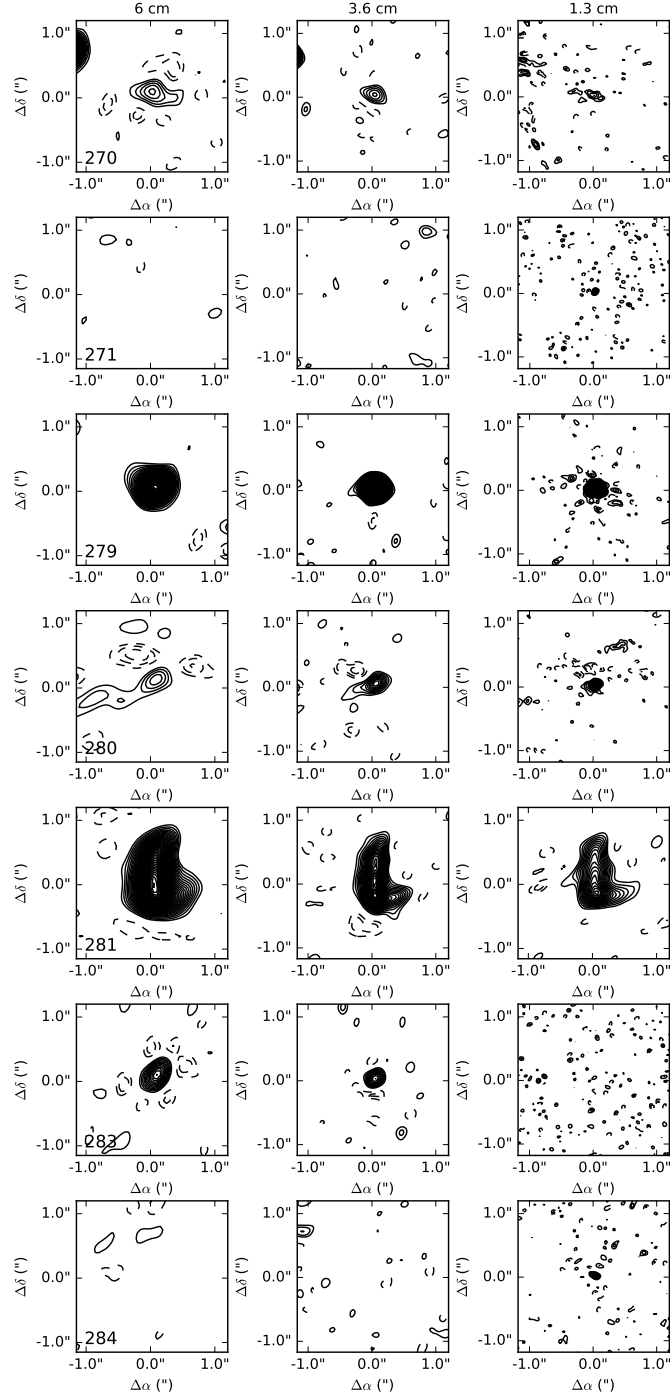
Figure 7.12: *Continued*
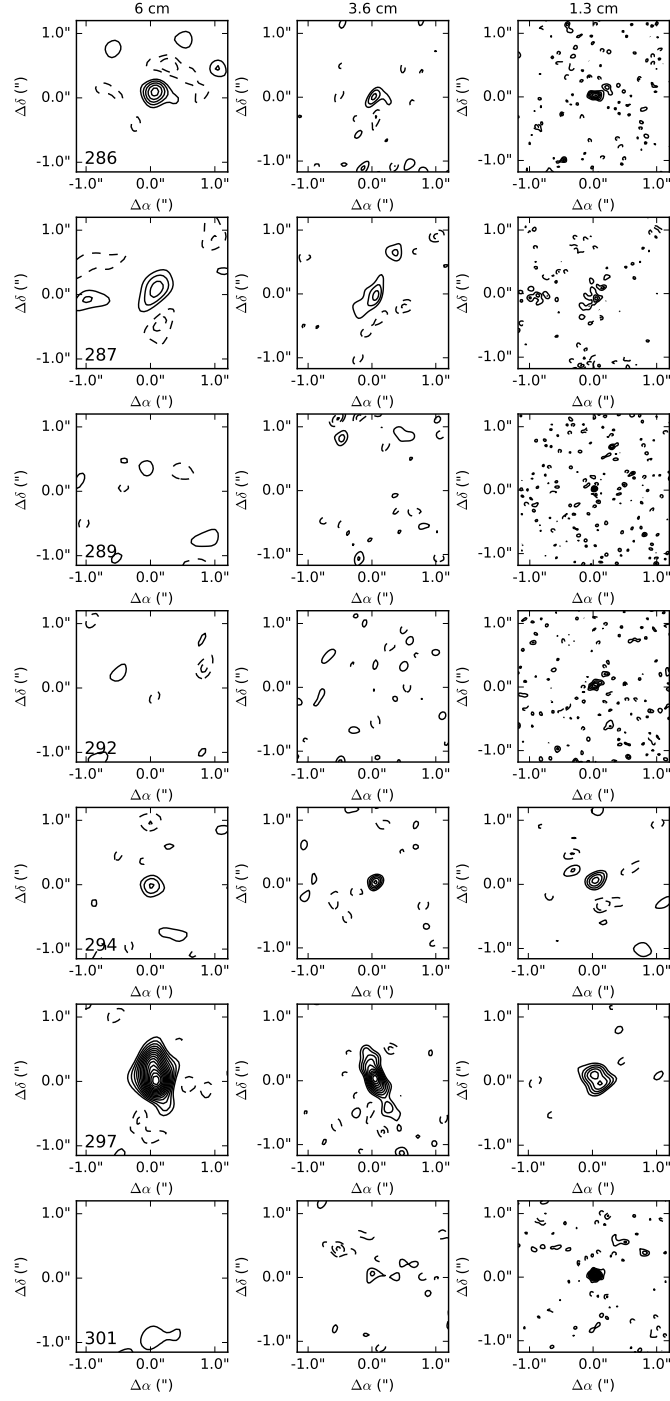
Figure 7.13: *Continued*
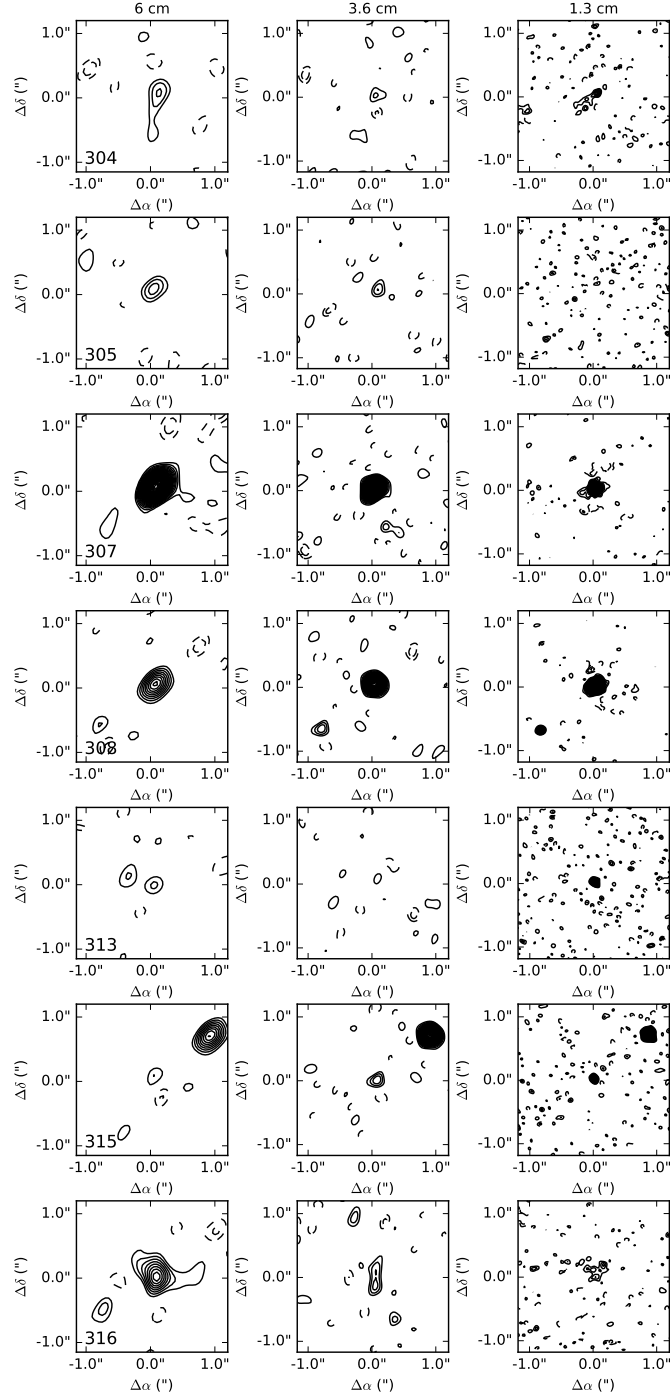
Figure 7.14: *Continued*
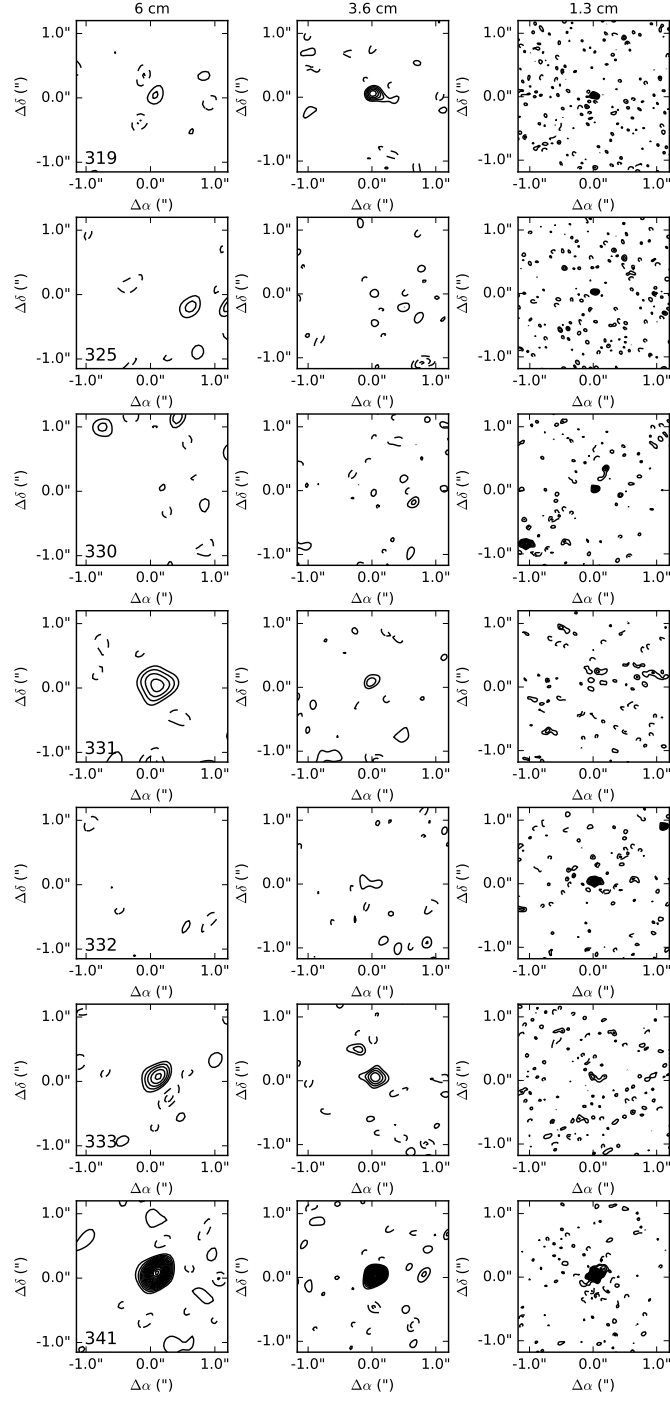
Figure 7.15: *Continued*
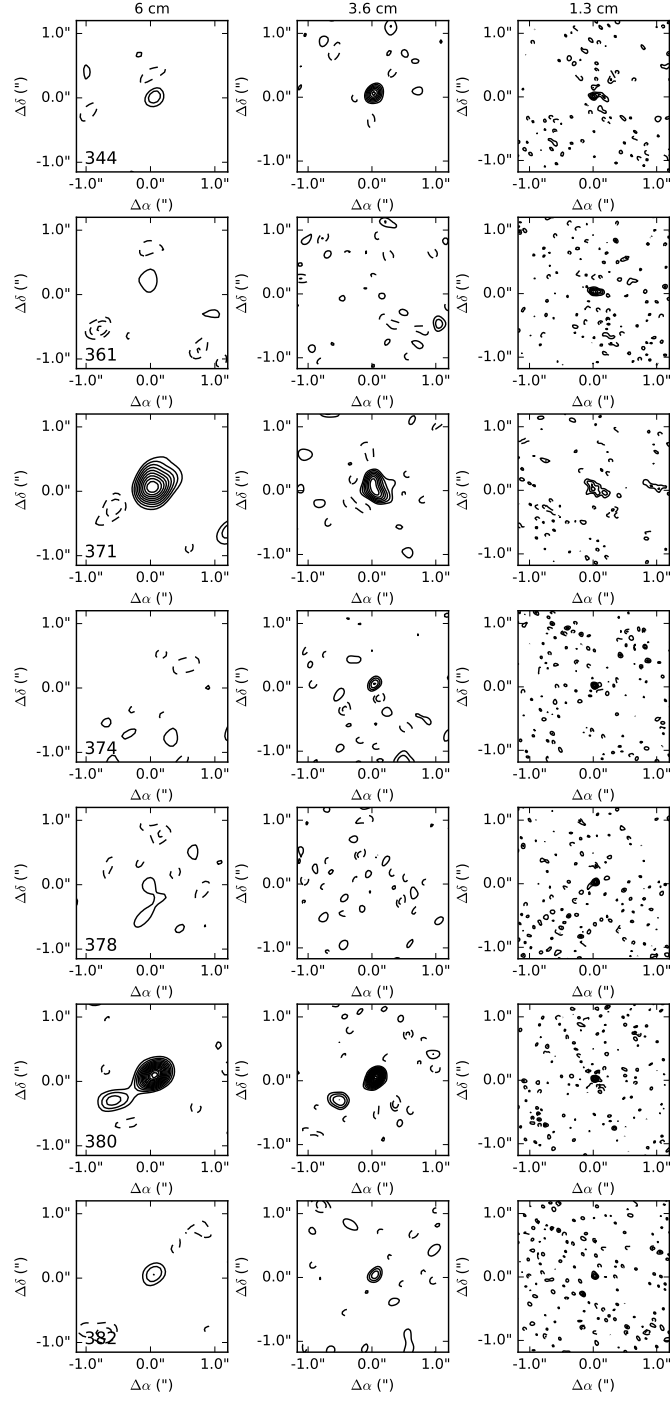
Figure 7.16: *Continued*
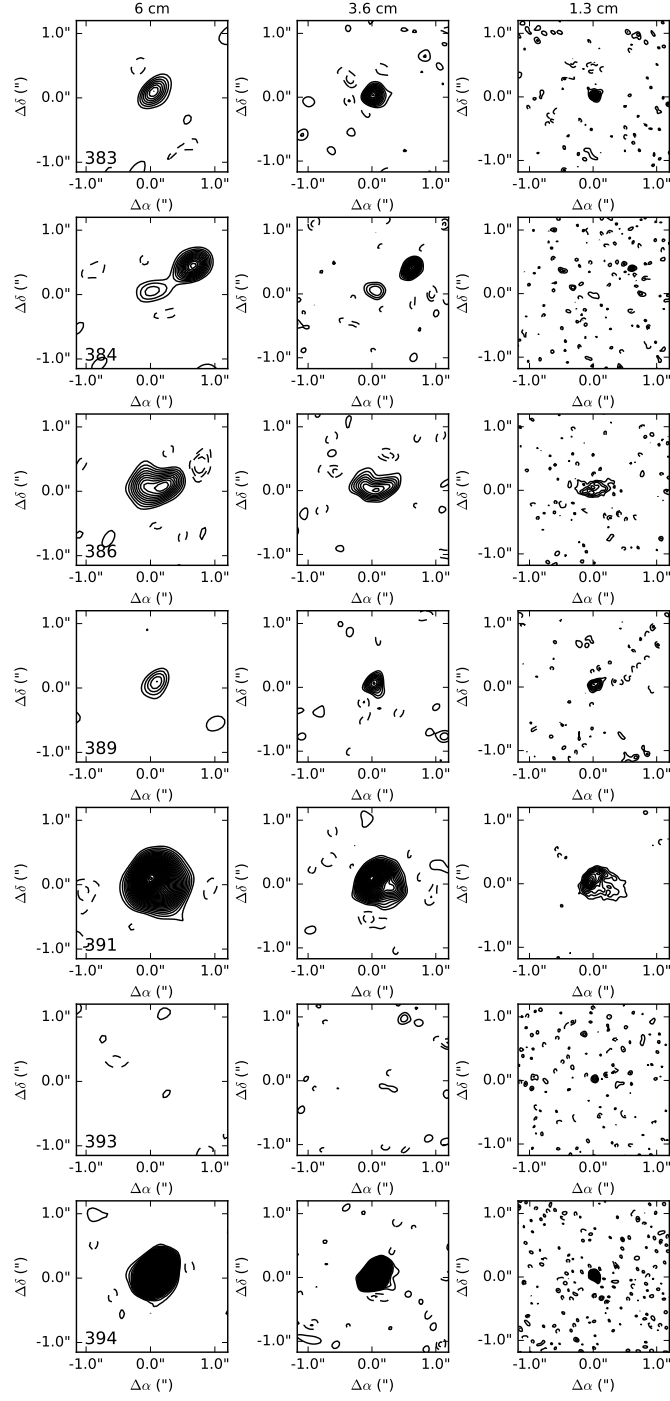
Figure 7.17: *Continued*
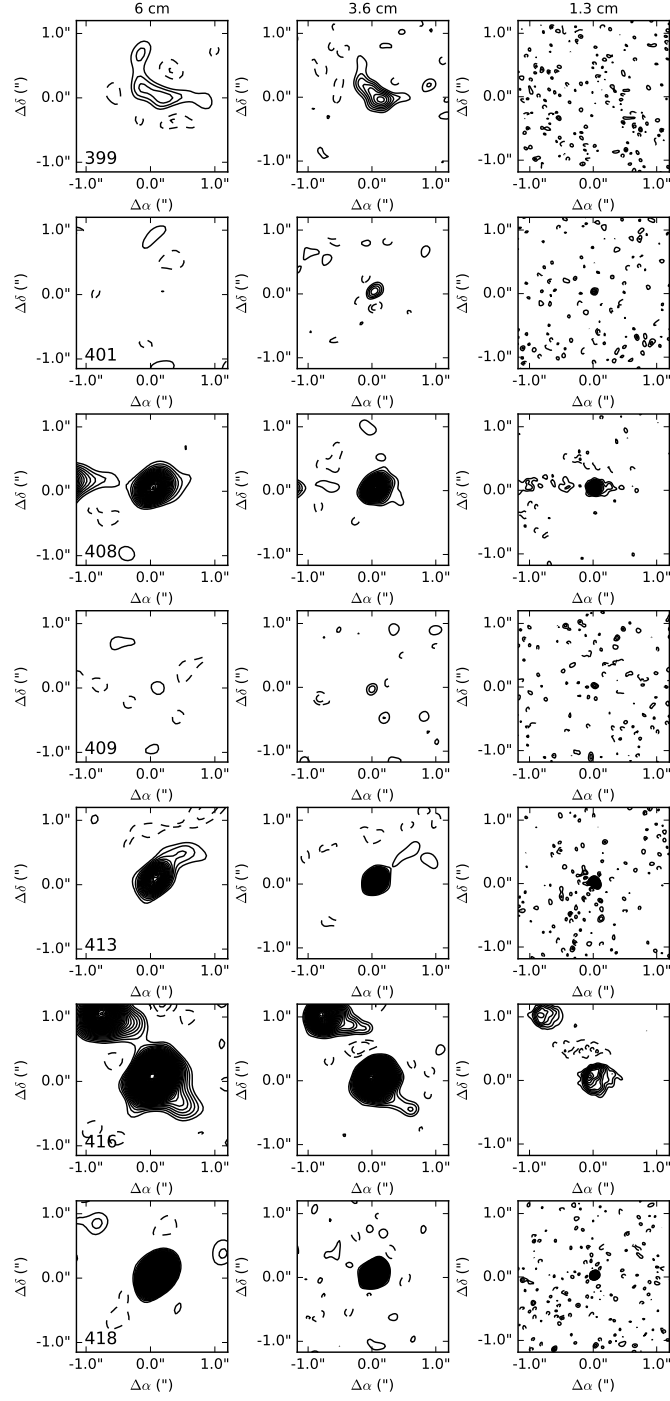
Figure 7.18: *Continued*
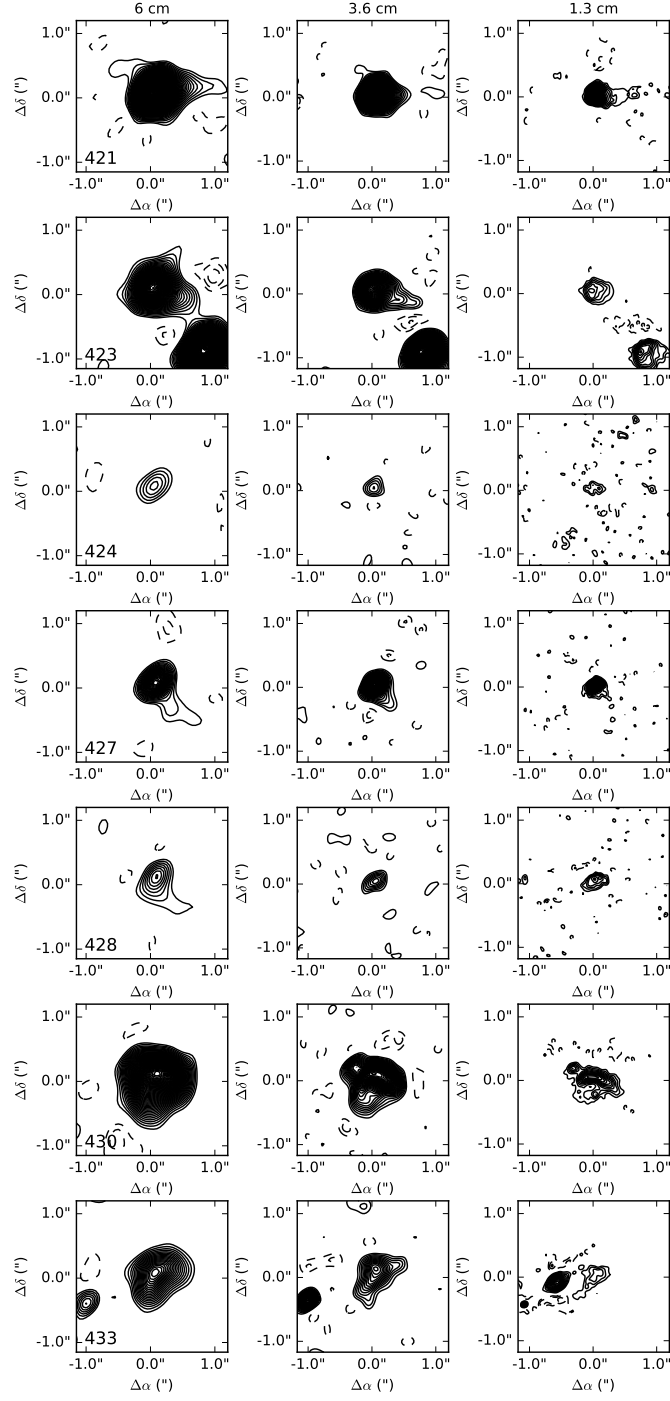
Figure 7.19: *Continued*
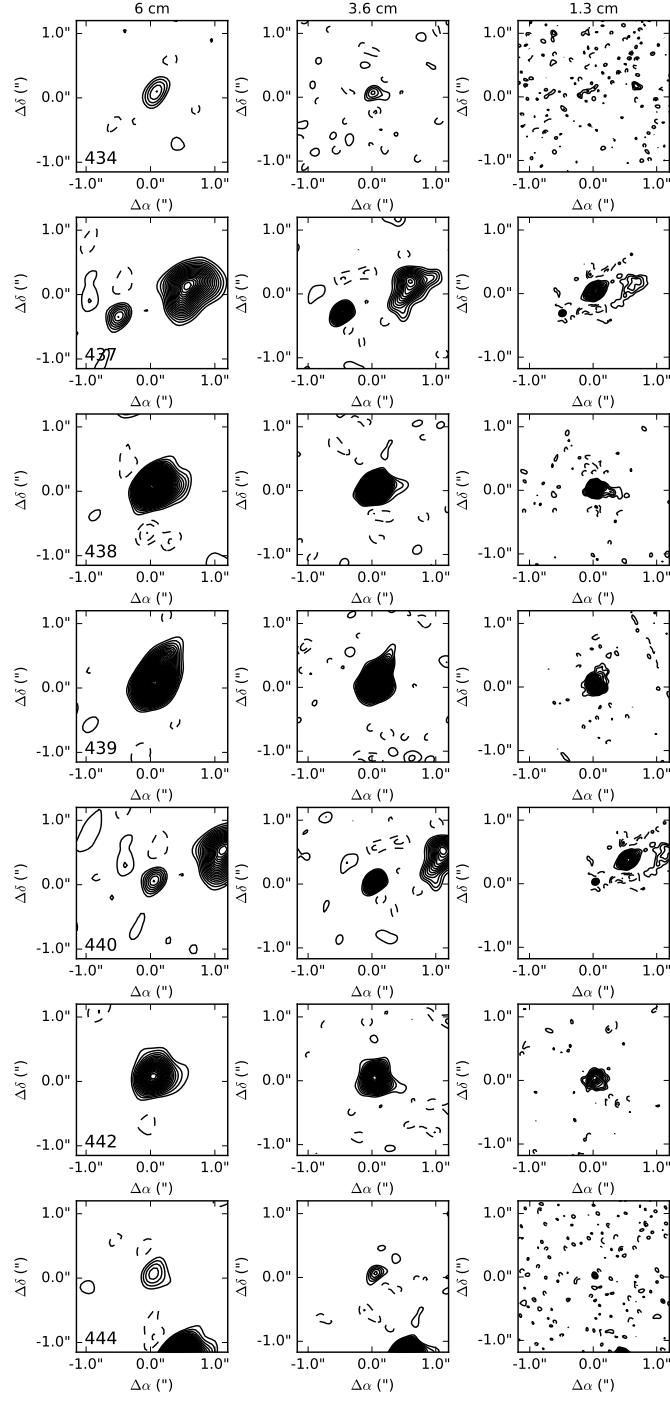
Figure 7.20: *Continued*
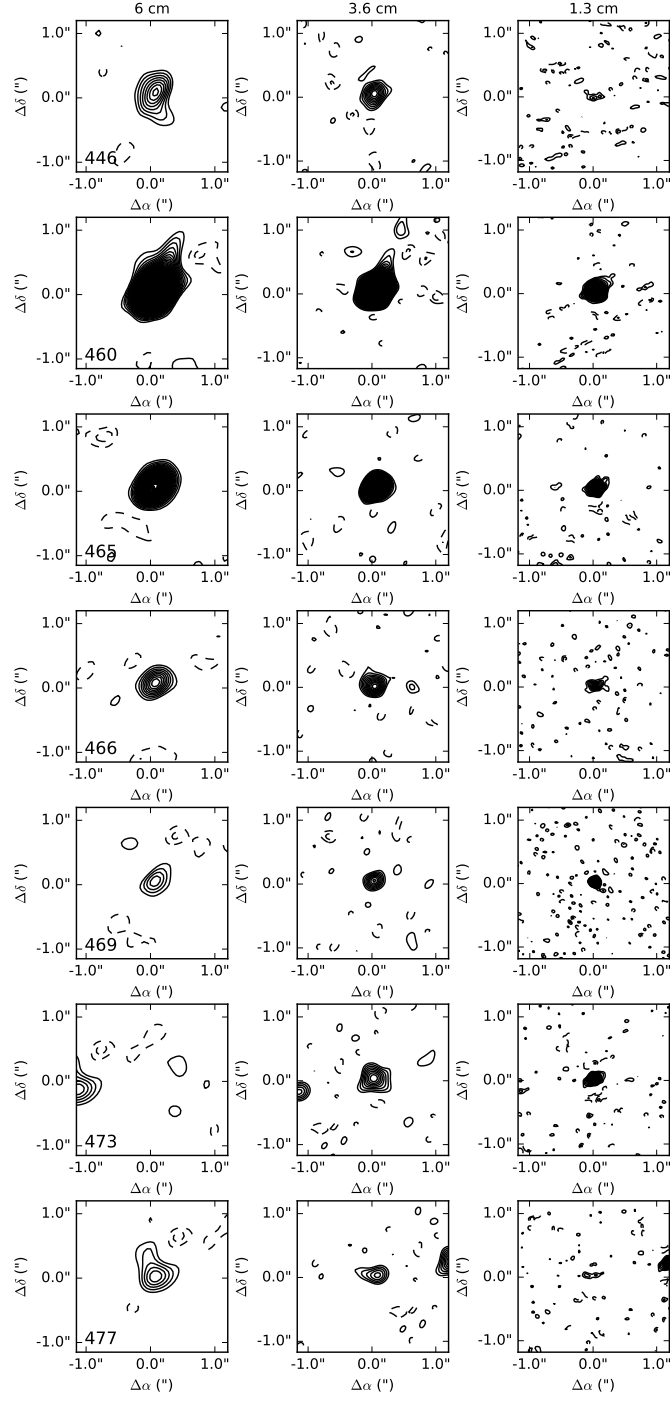
Figure 7.21: *Continued*
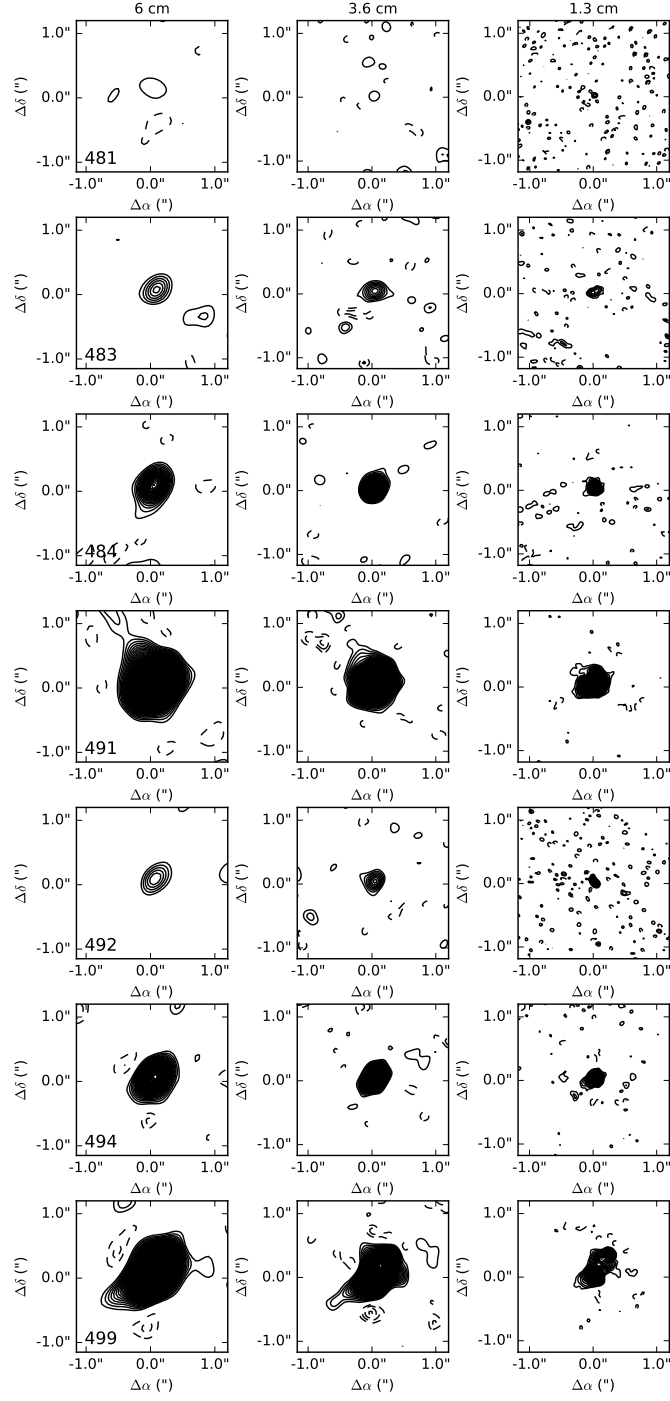
Figure 7.22: *Continued*
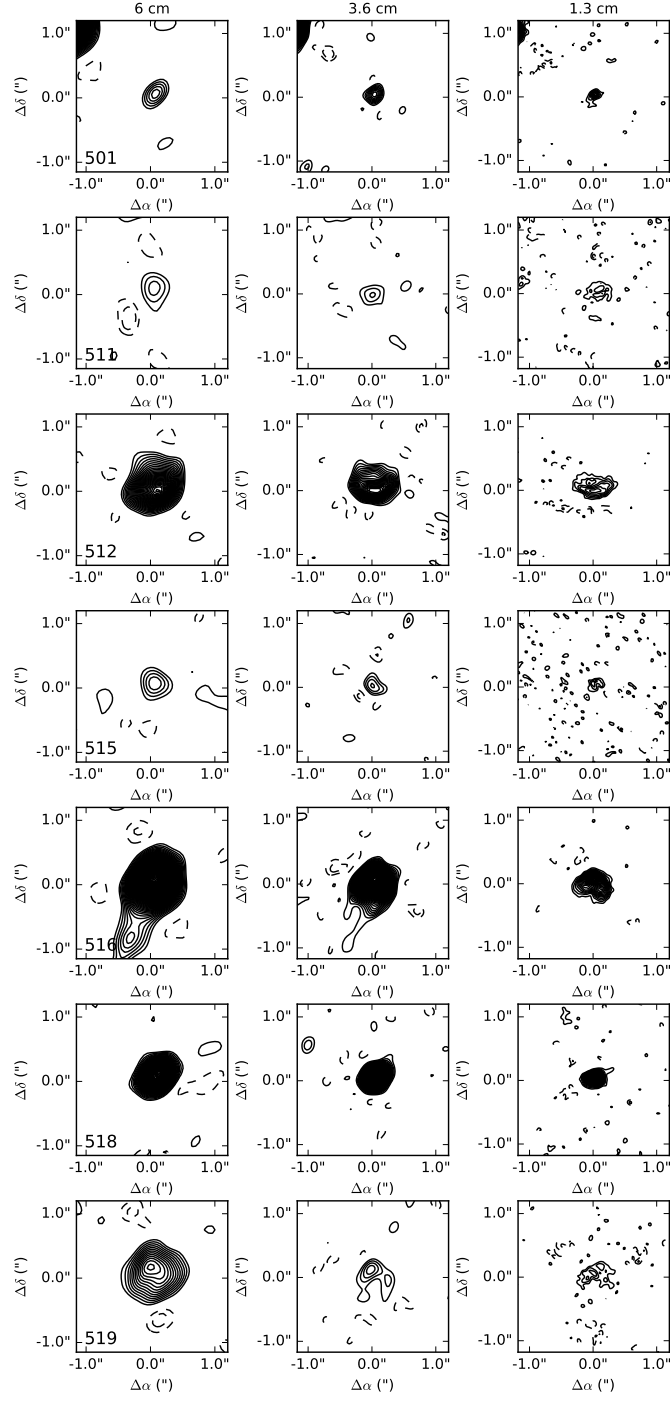
Figure 7.23: *Continued*
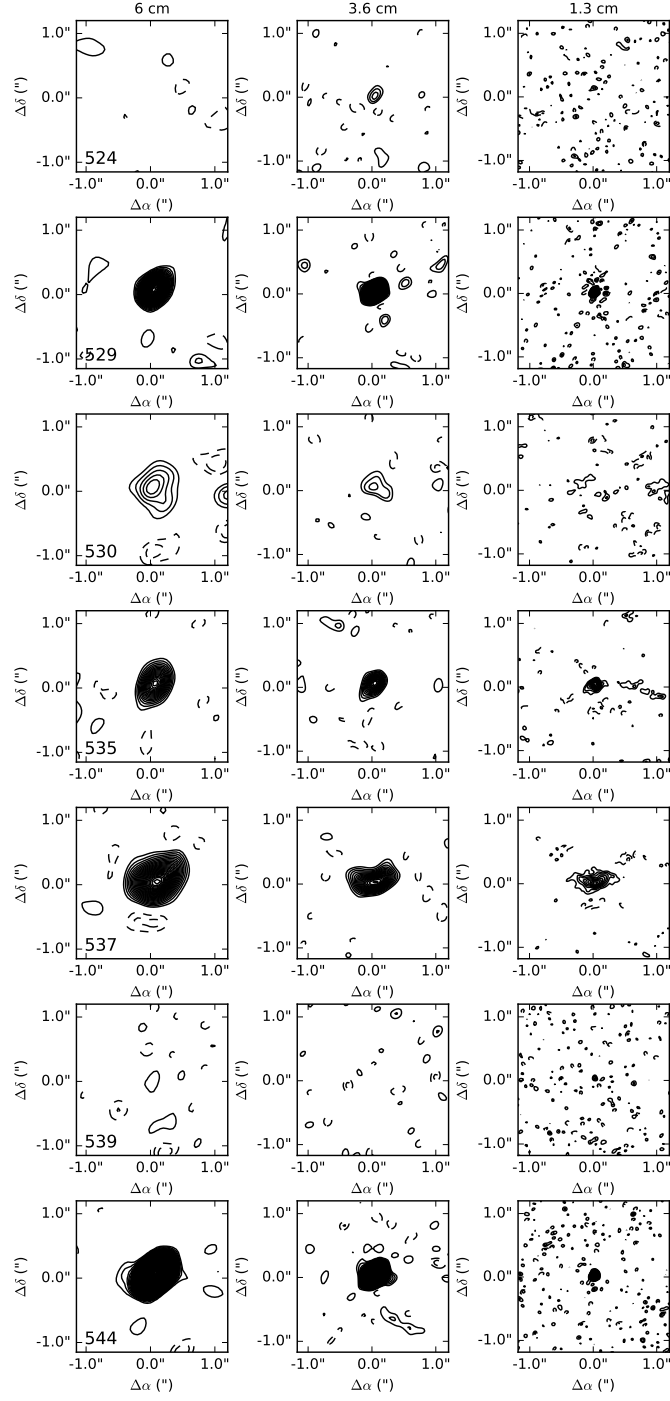
Figure 7.24: *Continued*
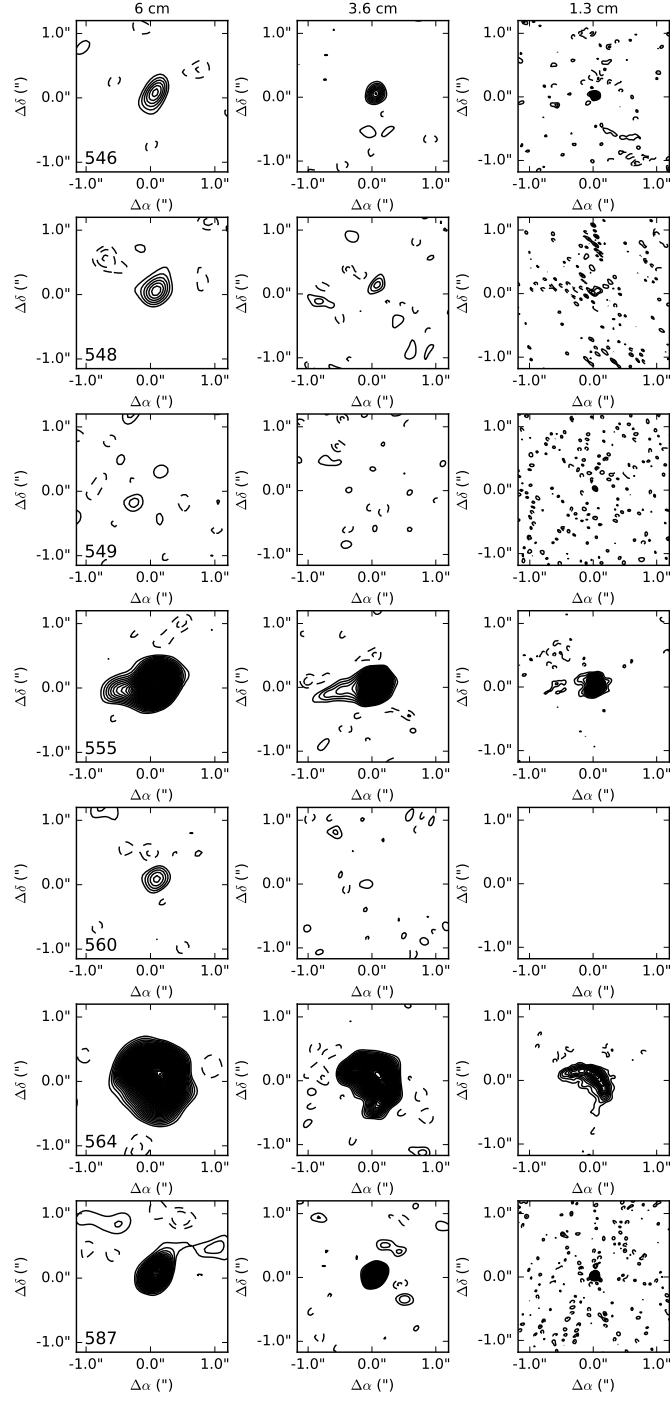
Figure 7.25: *Continued*
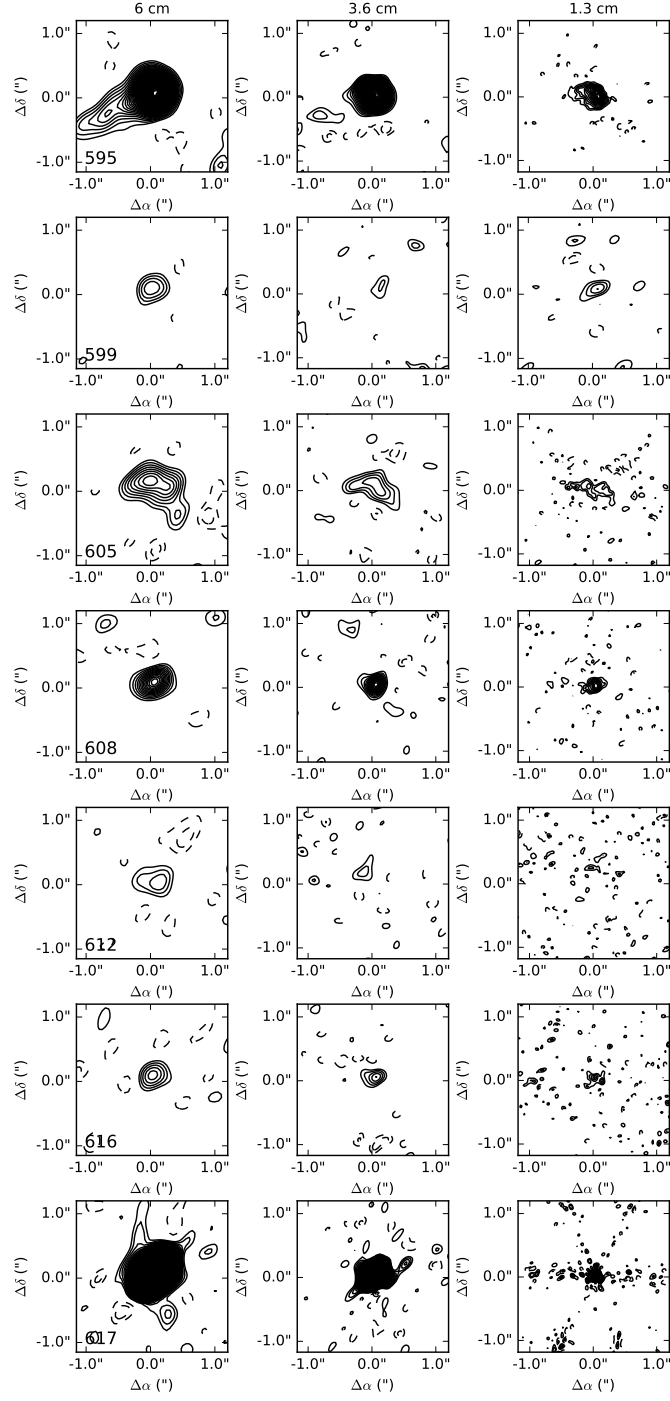
Figure 7.26: *Continued*
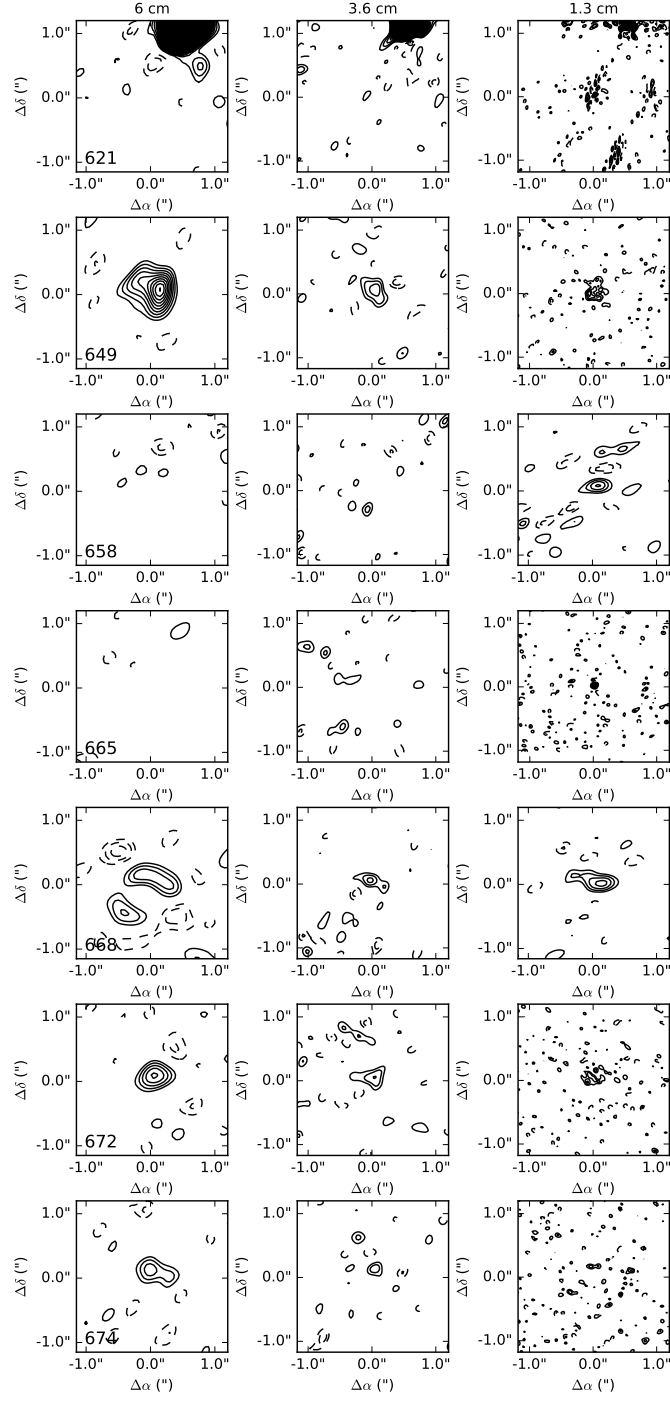
Figure 7.27: *Continued*
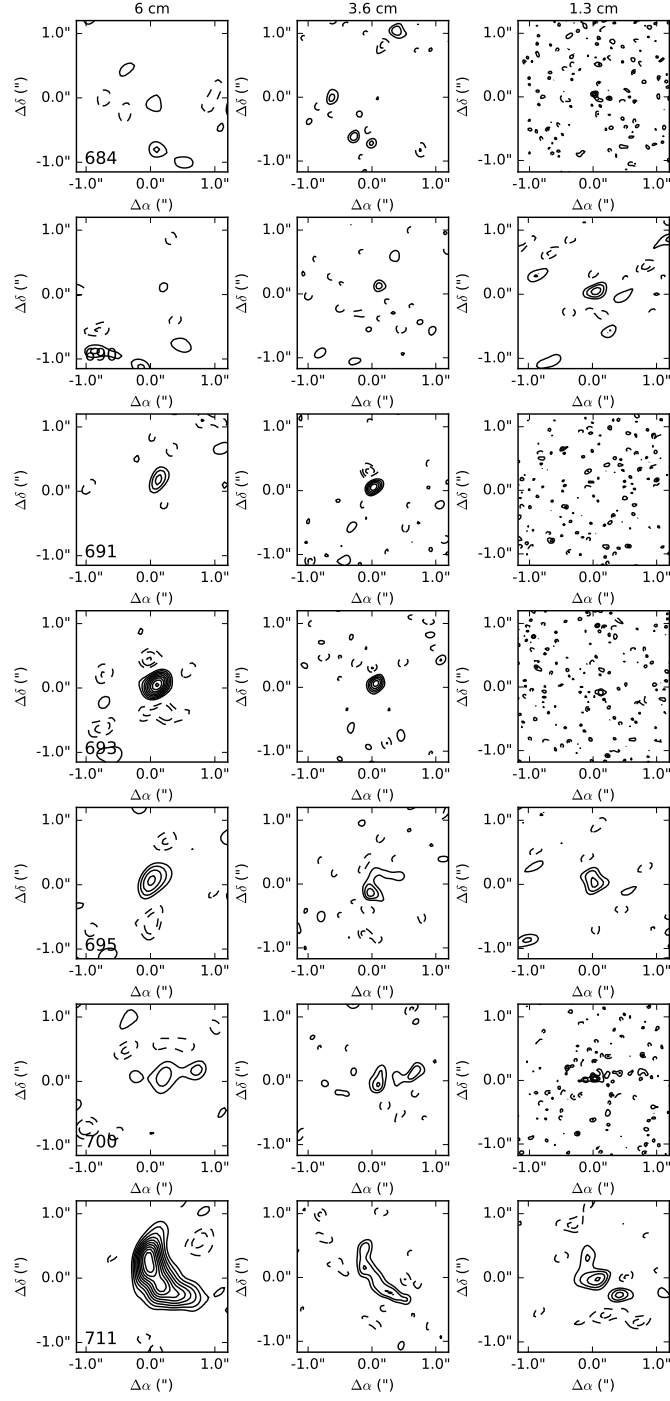
Figure 7.28: *Continued*
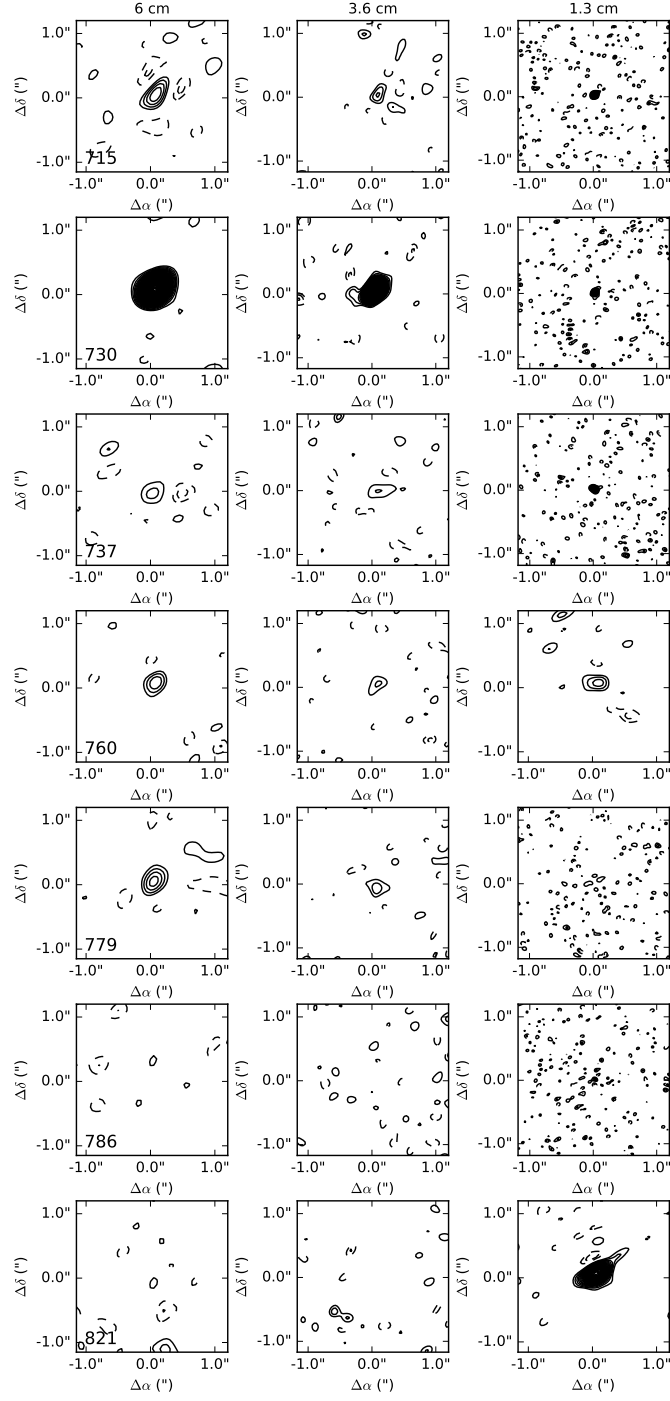
Figure 7.29: *Continued*
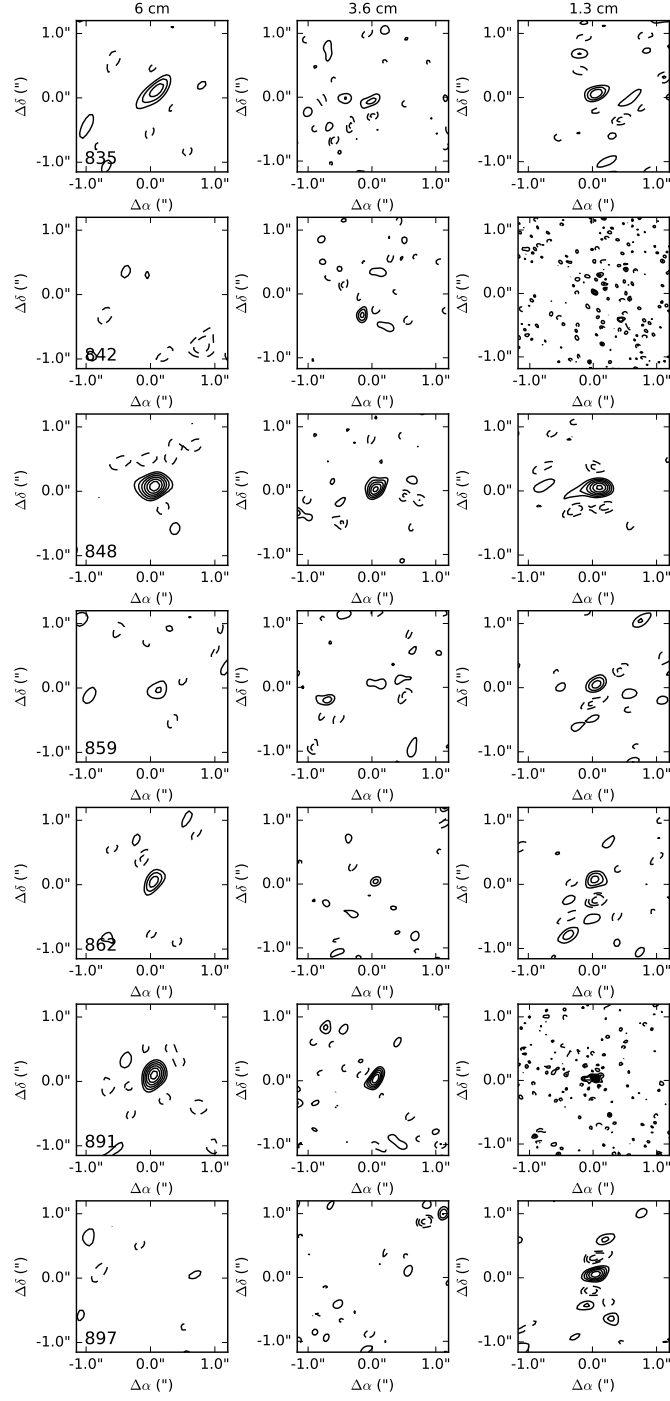
Figure 7.30: *Continued*
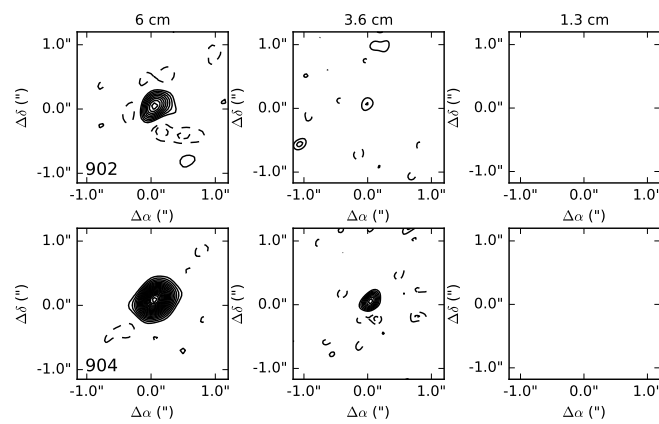
Figure 7.31: *Continued*
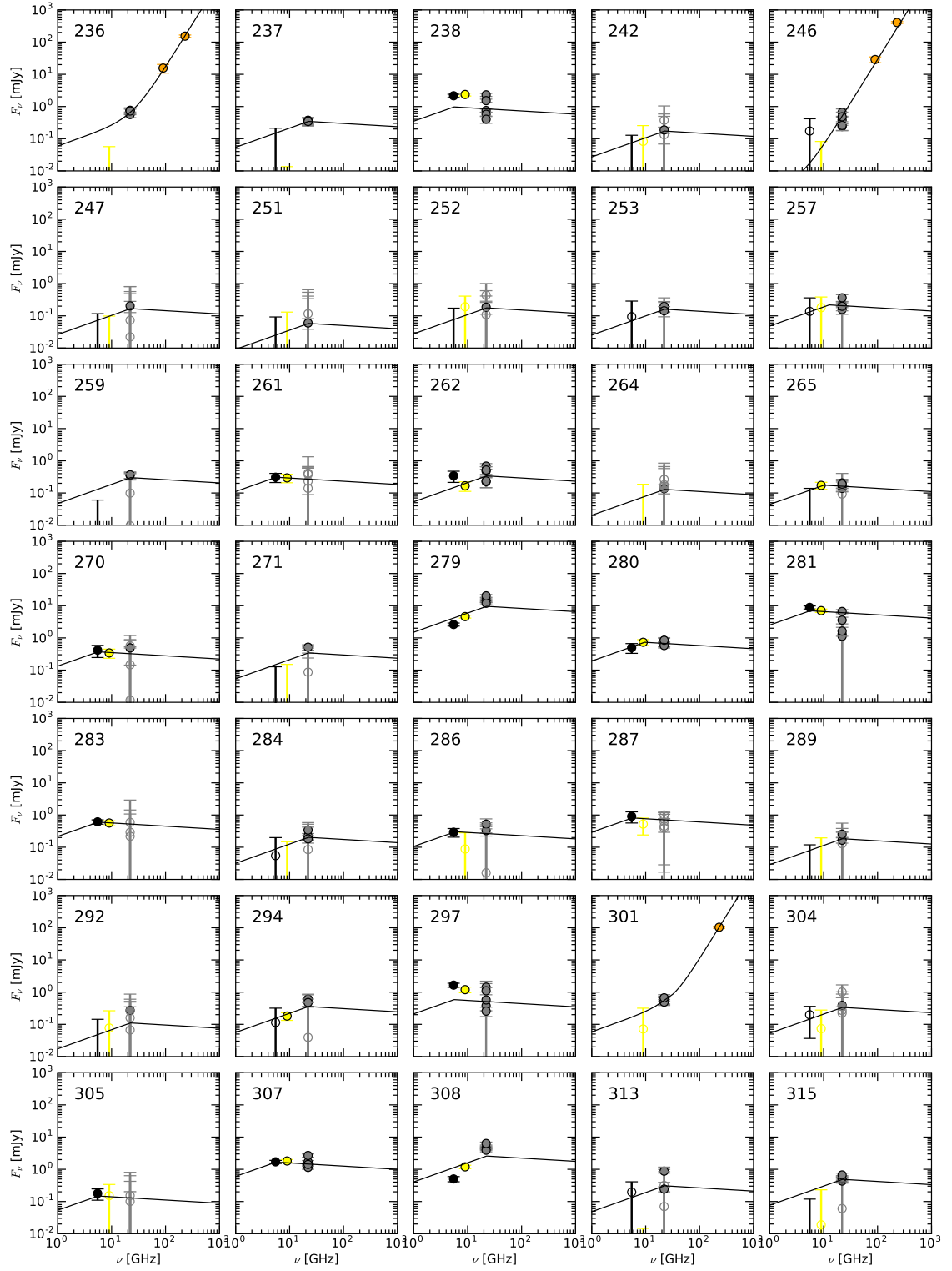
Figure 7.32: *Continued*
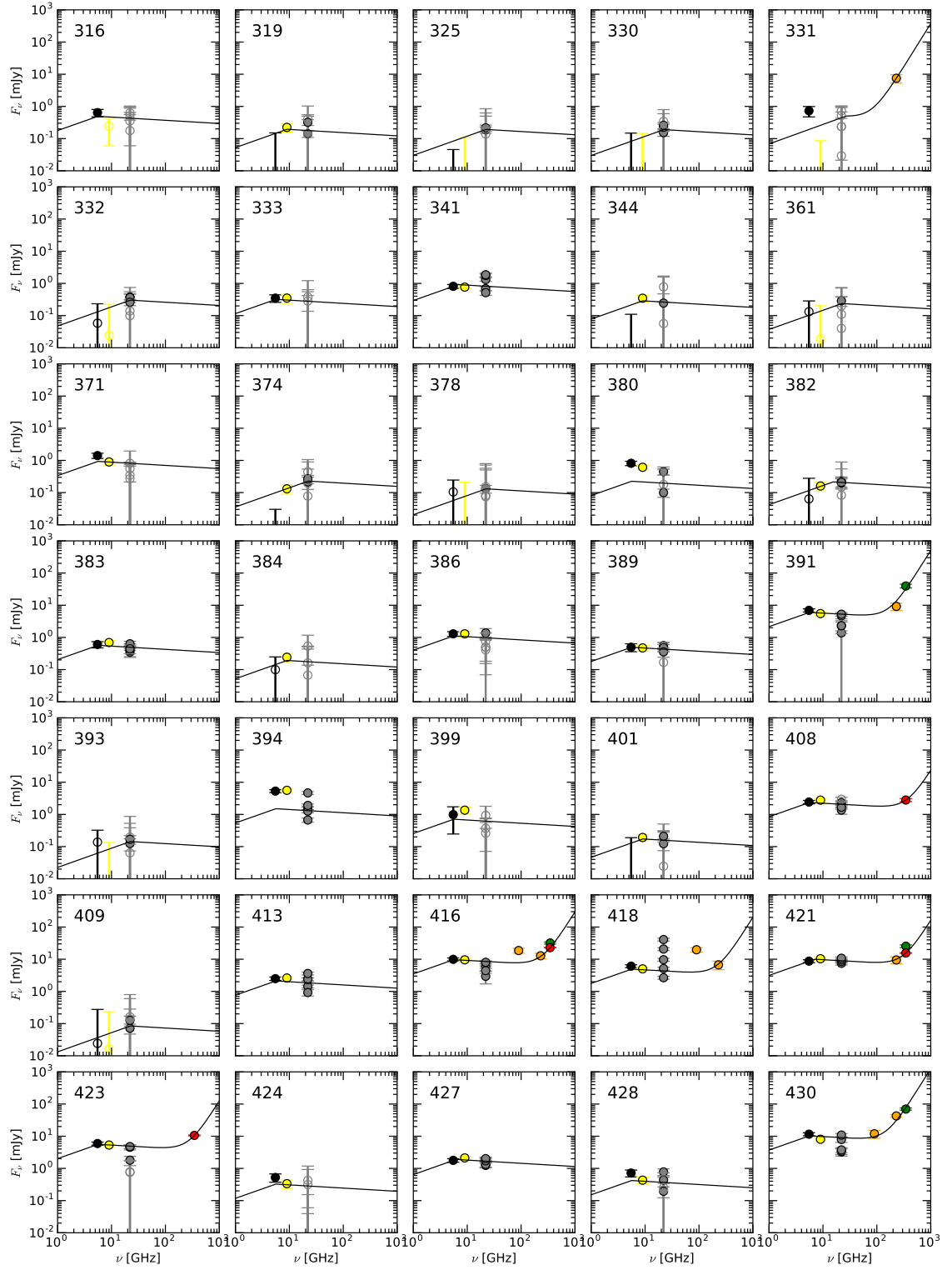
Figure 7.33: *Continued*
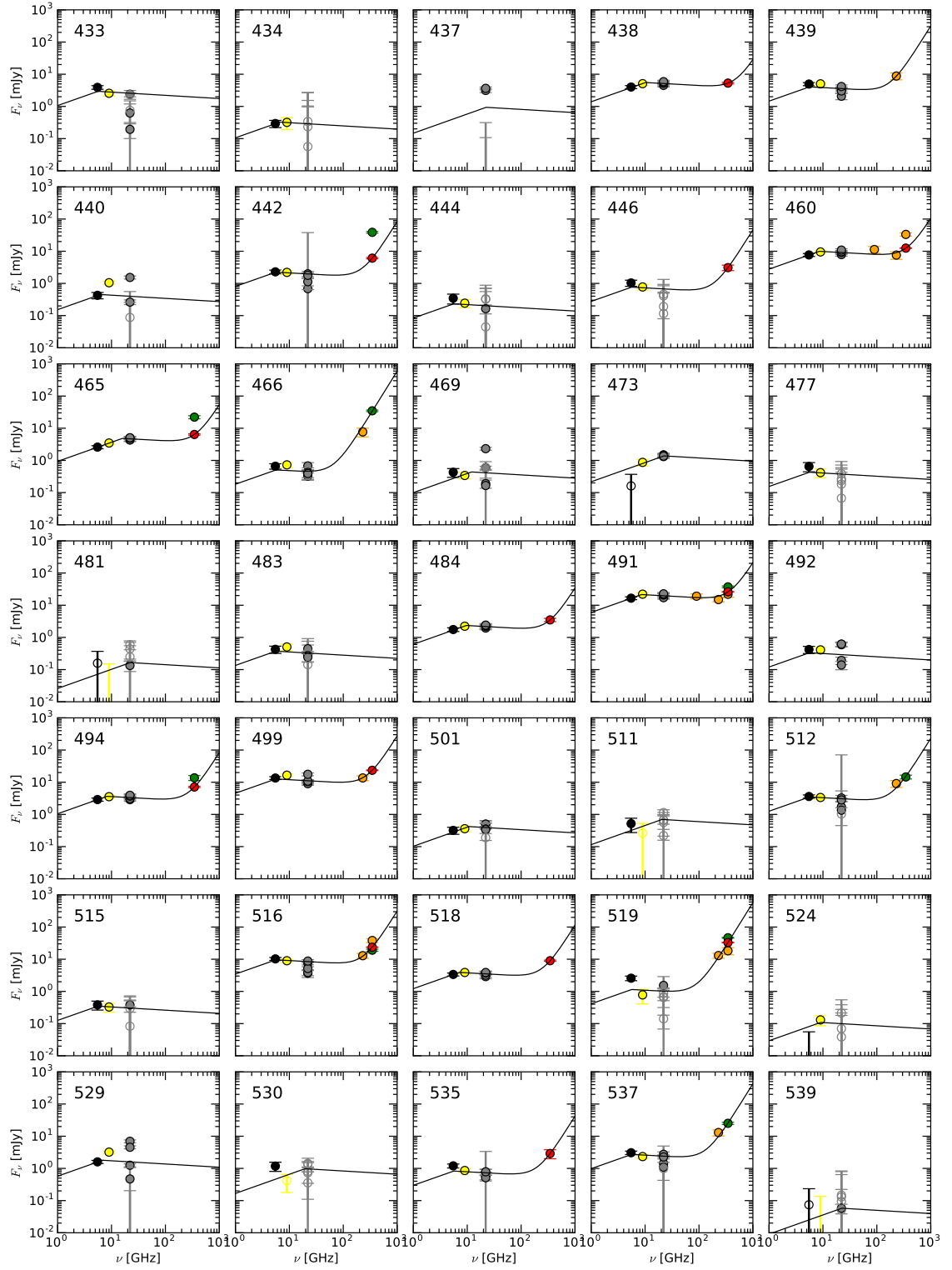
Figure 7.34: *Continued*

Figure 7.35: *Continued*

Figure 7.36: *Continued*

CHAPTER 8

CONCLUSION

8.1   Summary of Thesis Work and Conclusions

In summary, I have carried out a survey of 10 of 12 protostars that are consistently identified as Class I across multiple independent surveys with the goal of characterizing their structure and disk masses. I find that Class I disks in Taurus are, on average, more massive than the older Class II disks in the same region, which is likely an indication that dust grain processing occurs between the Class I and Class II stages. It remains unclear, however, whether Class I disks have enough mass on average to form giant planets. If this is the case, it may be that planet formation is already underway, even at the early ages probed by Class I protostars. In this scenario, Class 0 disks, if such disks are common, may be a better representation of the initial mass budget of disks for forming planets.

Of course, what a typical exoplanetary system looks like, and therefore how much mass is needed to form it, remains an open question. When I started this thesis, the majority of known planets were massive, Jupiter-like planets and our own Solar System was the best characterized system. While the latter remains true, the *Kepler* mission has led to the discovery of thousands of planets and planet candidates that have updated our picture of typical exoplanetary systems since that time. Studies of the planets found by the *Kepler* mission have suggested that Neptune-like planets may be much more common than Jupiter-like planets (e.g. Malhotra, 2015), a result that is also corroborated by microlensing surveys (e.g. Clanton and Gaudi, 2014). Although *Kepler* primarily probes close-in planets, if these results extend to large orbital radii then the amount of matter needed to form giant planets may need to be revised. Still, Neptune and Uranus require a similar amount of mass as Jupiter to form (e.g. Weidenschilling, 1977; Desch, 2007), and these estimates still assume

a relatively efficient planet formation process.

Taurus is a region of low mass star formation, with stars that are typically less massive than our own Sun (e.g. Andrews et al., 2013). Studies have shown that the frequency of Jupiter-mass planets is correlated with stellar mass, with frequencies as low as 3% for M stars (e.g. Johnson et al., 2010; Clanton and Gaudi, 2014). As most of the young stars studied in Taurus by Andrews et al. (2013) are indeed low-mass stars, this may ease tensions with the number of disks that have enough mass to form Jupiter-mass planets. Neptune- and Uranus-mass planets, though, are found to be much more common around M stars and may still require a large amount of material to form. My study was done in Taurus because it is nearby and easy to study, but larger samples with a significant number of Sun-like protostars are needed to better understand whether their disks can account for the $\sim 20\%$ of Sun-like stars with Jupiter-mass planets (Cumming et al., 2008).

The lower occurrence rate of Jupiter-mass planets around low mass stars may ease tensions between the number of protoplanetary disks in Taurus that have sufficient mass to form Jupiter-like planets and the occurrence rates of Jupiter-mass planets. However, it remains the case that the early Solar nebula must have had a significant amount of mass present, and we also know that Jupiter-mass or larger planets are formed in exoplanetary systems. As of yet, very few protoplanetary disks have been found with sufficient mass to form a planetary system like our own, although my work suggests we may have not yet identified disks with the majority of their material in a pristine state. Further constraints on the initial mass budget for forming planets in disks will therefore help us to understand how common planetary systems like our own are.

Perhaps more excitingly, I have found several interesting Class I disks from an ongoing survey of Class I disks in ρ Ophiuchus that could be already in the process of forming planets. WL 17 has a compact ($R_{\mathrm{disk}} \sim 25$ AU) disk that has a large cavity ($R_{\mathrm{cav}} \sim 12$ AU) that is depleted of dust, which may be an indication that multiple massive planets are forming and have cleared out the disk. Moreover, GY 91's disk is found to have three narrow gaps in it's disk that may be produced by young

Saturn-mass planets. Although these features cannot yet be definitively shown to be produced by planets, the presence of such features is likely an indication that the processes that govern planet formation are all already underway, even at these early ages. If planets are indeed forming in these disks, they would place strong limits on the timescales of giant planet formation.

Finally, while Class II disks masses have been well studied for many star-forming regions, one aspect of these studies that has not received much attention is the contribution from free-free emission that may contaminate disk mass studies of rich clusters at millimeter wavelengths. These clusters are important for studying the typical mode of star formation, and they are similar to the environment that our Solar System may have formed in. In these regions, ionizing radiation from young, massive stars can photoevaporate the protoplanetary disks around nearby stars, and the resulting outflow of ionized material can emit strongly in free-free emission at radio wavelengths. I have carried out a large survey with the updated VLA to map the Orion Nebula at 1.3 cm, 3.6 cm, and 6 cm to search for signs of photoevaporating disks and to characterize their free-free emission spectra. These measurements will be crucial for ongoing and future disk mass surveys for disks in the ONC.

8.2   Future Directions

While some progress has been made towards understanding disk structures and masses during the Class I stage, there remain a number of open questions. Class I disks are, on average, more massive than Class II disks, but it remains unknown whether their disk masses are correlated with protostellar mass, as is found for Class II disks (Andrews et al., 2013; Pascucci et al., 2016; Barenfeld et al., 2016; Ansdell et al., 2016). Moreover, it has been suggested that the disk mass stellar mass relation steepens with age, but it is unknown whether this remains true for the youngest disks, or what the initial disk-mass-stellar-mass scaling relationship is (Pascucci et al., 2016). Also, if Class I disks do not have enough matter to form giant planets, the Class 0 disk mass distribution may be the best representation of
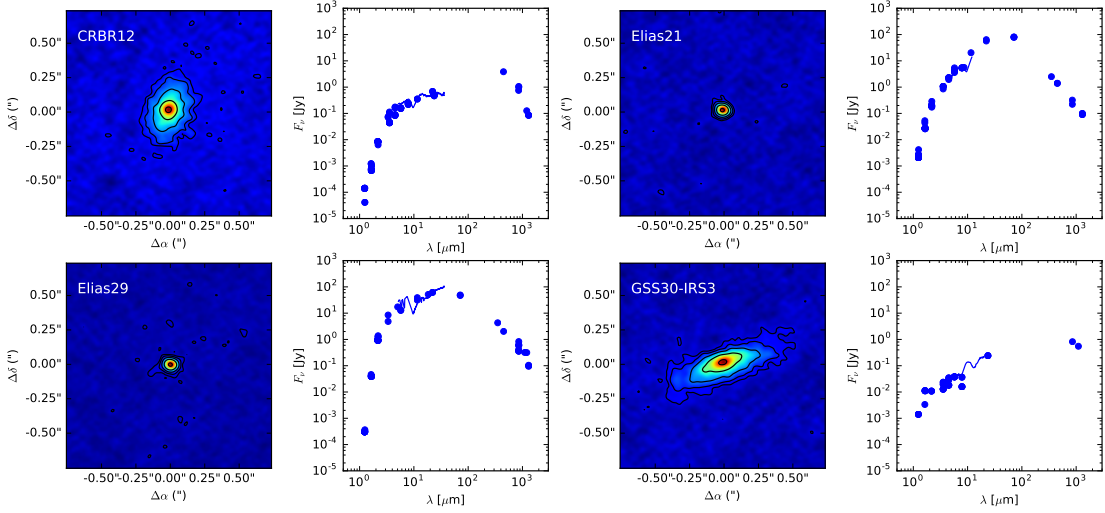
Figure 8.1: Four sources from my sample of Class I protostars in ρ Ophiuchus that have been imaged with ALMA. We also show the broadband SED for each source.

the initial disk mass budget.

With the high sensitivity afforded by ALMA, detecting and spatially resolving protoplanetary disks in large samples is easier than ever before. I have already collected data for a preliminary sample of Class I protostars in the ρ Ophiuchus star forming region (see Figures 8.1 and 8.2 for some initial results) to expand our sample of measured Class I disk masses. Initial results from this survey confirm our findings that Class I disks are on average more massive than Class II disks (see Figure 8.3). The median Class I disk mass is also higher in Ophiuchus than in Taurus ($M_{\mathrm{disk,Oph}} \sim 0.035$ $\mathrm{M}_\odot$), but perhaps still too low for Class I disks to be on average massive enough to form giant planets. In future observations this sample will be expanded to every Class I protostar in ρ Ophiuchus with a known spectral type in order to investigate the Class I disk mass-protostellar mass relation. I will also expand the sample to include measurements of the Class 0 disk mass distribution, as it may be a better representation of the initial mass budget for forming planets.

More excitingly, perhaps, is the possibility that planet formation is already underway during the Class I stage, and yet little is known about the conditions and distributions of solid and gaseous materials in these early disks. While there has
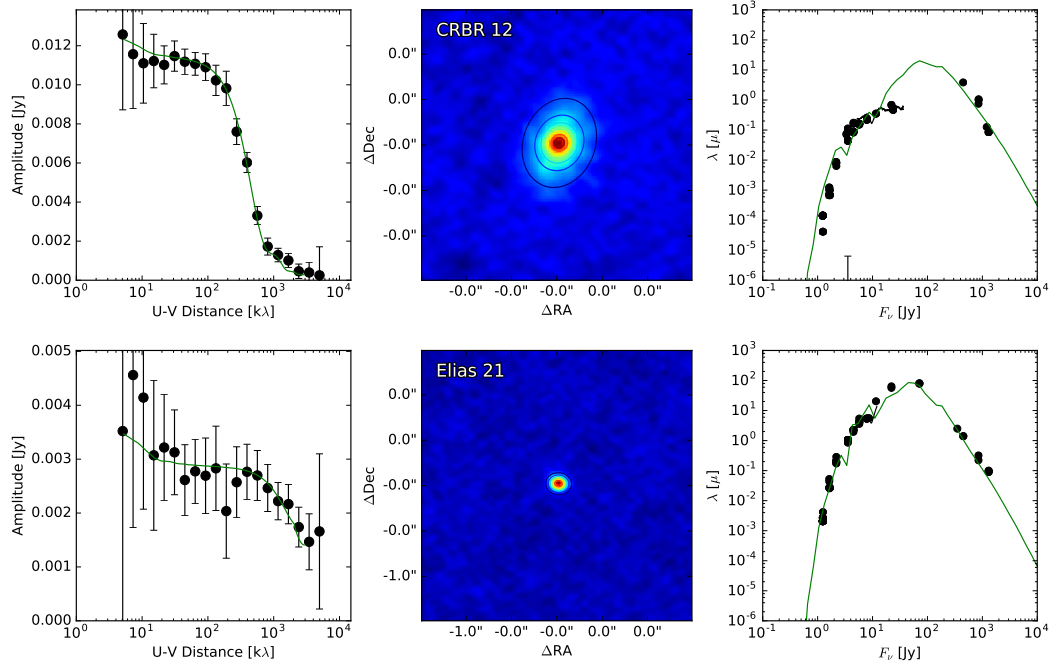
Figure 8.2: Example fits for two of the Class I sources in my ρ Ophiuchus sample. The left panels show the ALMA 3 mm visibilities and the central panel shows the 3 mm images. On the right we show the broadband SED from the literature. In all three columns we show the current best-fit model in comparison with the data.

been some evidence of dust grain growth in the disks and perhaps envelopes of Class 0/I protostars (Shirley et al., 2011; Miotello et al., 2014), the sample is limited in size and only includes low spatial resolution observations. My ALMA survey of Class I disks in ρ Ophiuchus includes disk observations at both 870 μm and 3 mm, which can be used to measure dust grain growth in Class I disks and determine how far along grain growth is at these early times for a much larger sample. Furthermore, these observations have resolved the disks at both wavelengths, and so it is possible to search for evidence of radial variations in maximum dust grain sizes, as has been found for Class II disks (Pérez et al., 2012, 2015).

Whether planets themselves are the underlying reason for the features seen in WL 17 and GY 91 is also still unknown. The current datasets have insufficient information to constrain whether the features are, in fact, caused by planets, and if they are, to place strong constraints on their masses. Observations of the gas
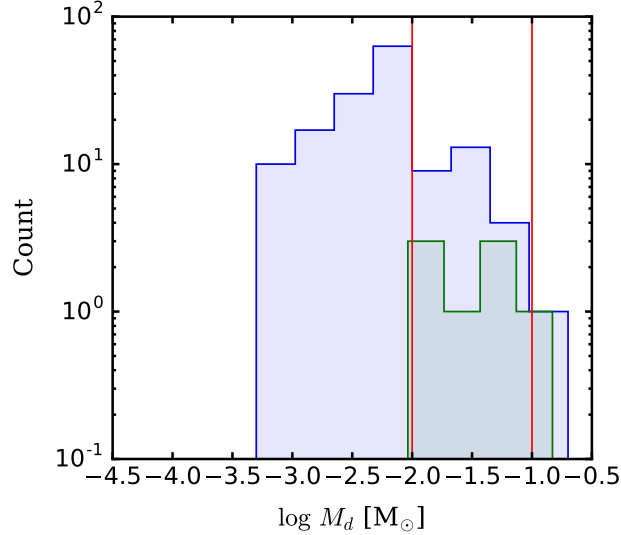
Figure 8.3: Histograms of the disk masses of Class I (*green*) sources from our ρ Ophiuchus ALMA sample and Class II (*blue*) sources in Ophiuchus from Andrews and Williams (2007). The red lines show the range of lower limits for the Minimum Mass Solar Nebula (e.g. Weidenschilling 1977). Although this is still preliminary, we find that our Class I disks, on average, are more massive than the Class II disks. This is in agreement with our results from Taurus protoplanetary disks (see Chapter 3).

in WL 17's disk can be a powerful way to distinguish between possible causes of cavities (de Juan Ovelar et al., 2013; van der Marel et al., 2015), and may help to determine whether the locations of snow lines are coincident with disk gaps (e.g. van't Hoff et al., 2017). Moreover, observations of disk gaps in gas are the best way to constrain the masses of planets sculpting the gas (Fung et al., 2014; Kanagawa et al., 2015; Dong and Fung, 2017). It may even be possible to directly image disks around forming protoplanets in disk gaps with ALMA, and thereby show definitively that planets are carving these gaps and holes (Eisner, 2015; Zhu et al., 2016). It also remains unclear how common these features are, but larger and higher spatial resolution surveys will help to answer this question.

Since the advent of ALMA, our understanding of the structure of protoplanetary disks and the planets that are forming in them has been moving at a breakneck pace. And yet, while much has been learned about protoplanetary disks, our understand-

ing of the planet formation properties of the youngest disks still largely remain a mystery. This thesis indicates that young disks are where the beginnings of planet formation may be happening, and in the next decade ALMA will be able to study these systems in much greater detail.

REFERENCES

Abt, H. A. and S. G. Levy (1976). Multiplicity among solar-type stars. *ApJS*, **30**, pp. 273–306. doi:10.1086/190363.

Adams, F. C. (2010). The Birth Environment of the Solar System. *ARA&A*, **48**, pp. 47–85. doi:10.1146/annurev-astro-081309-130830.

Adams, F. C., C. J. Lada, and F. H. Shu (1987). Spectral evolution of young stellar objects. *ApJ*, **312**, pp. 788–806. doi:10.1086/164924.

Alexander, R. D., M. M. Casali, P. André, P. Persi, and C. Eiroa (2003). ISOCAM-CVF spectroscopy of the circumstellar environment of young stellar objects. *A&A*, **401**, pp. 613–624. doi:10.1051/0004-6361:20030158.

Alexander, R. D., C. J. Clarke, and J. E. Pringle (2006). Photoevaporation of protoplanetary discs - I. Hydrodynamic models. *MNRAS*, **369**, pp. 216–228. doi:10.1111/j.1365-2966.2006.10293.x.

Alibert, Y., C. Mordasini, W. Benz, and C. Winisdoerffer (2005). Models of giant planet formation with migration and disc evolution. *A&A*, **434**, pp. 343–353. doi:10.1051/0004-6361:20042032.

Allen, A., Z.-Y. Li, and F. H. Shu (2003). Collapse of Magnetized Singular Isothermal Toroids. II. Rotation and Magnetic Braking. *ApJ*, **599**, pp. 363–379. doi:10.1086/379243.

Allen, L. E., P. C. Myers, J. Di Francesco, R. Mathieu, H. Chen, and E. Young (2002). Hubble Space Telescope/NICMOS Imaging Survey of the Ophiuchus (Lynds 1688) Cluster. *ApJ*, **566**, pp. 993–1004. doi:10.1086/338128.

ALMA Partnership, C. L. Brogan, L. M. Pérez, T. R. Hunter, W. R. F. Dent, A. S. Hales, R. E. Hills, S. Corder, E. B. Fomalont, C. Vlahakis, Y. Asaki, D. Barkats, A. Hirota, J. A. Hodge, C. M. V. Impellizzeri, R. Kneissl, E. Liuzzo, R. Lucas, N. Marcelino, S. Matsushita, K. Nakanishi, N. Phillips, A. M. S. Richards, I. Toledo, R. Aladro, D. Broguiere, J. R. Cortes, P. C. Cortes, D. Espada, F. Galarza, D. Garcia-Appadoo, L. Guzman-Ramirez, E. M. Humphreys, T. Jung, S. Kameno, R. A. Laing, S. Leon, G. Marconi, A. Mignano, B. Nikolic, L.-A. Nyman, M. Radiszcz, A. Remijan, J. A. Rodón, T. Sawada, S. Takahashi, R. P. J. Tilanus, B. Vila Vilaro, L. C. Watson, T. Wiklind, E. Akiyama, E. Chapillon, I. de Gregorio-Monsalvo, J. Di Francesco, F. Gueth, A. Kawamura, C.-F. Lee, Q. Nguyen Luong, J. Mangum, V. Pietu, P. Sanhueza, K. Saigo, S. Takakuwa,

C. Ubach, T. van Kempen, A. Wootten, A. Castro-Carrizo, H. Francke, J. Gallardo, J. Garcia, S. Gonzalez, T. Hill, T. Kaminski, Y. Kurono, H.-Y. Liu, C. Lopez, F. Morales, K. Plarre, G. Schieven, L. Testi, L. Videla, E. Villard, P. Andreani, J. E. Hibbard, and K. Tatematsu (2015). The 2014 ALMA Long Baseline Campaign: First Results from High Angular Resolution Observations toward the HL Tau Region. *ApJ*, **808**, L3. doi:10.1088/2041-8205/808/1/L3.

Alves de Oliveira, C. and M. Casali (2008). Deep near-IR variability survey of pre-main-sequence stars in ρ Ophiuchi. *A&A*, **485**, pp. 155–166. doi:10.1051/0004-6361:20079146.

Andre, P. and T. Montmerle (1994a). From T Tauri stars to protostars: Circumstellar material and young stellar objects in the rho Ophiuchi cloud. *ApJ*, **420**, pp. 837–862. doi:10.1086/173608.

Andre, P. and T. Montmerle (1994b). From T Tauri stars to protostars: Circumstellar material and young stellar objects in the rho Ophiuchi cloud. *ApJ*, **420**, pp. 837–862. doi:10.1086/173608.

Andre, P., D. Ward-Thompson, and M. Barsony (1993). Submillimeter continuum observations of Rho Ophiuchi A - The candidate protostar VLA 1623 and prestellar clumps. *ApJ*, **406**, pp. 122–141. doi:10.1086/172425.

Andrews, S. M. (2015). Observations of Solids in Protoplanetary Disks. *PASP*, **127**, p. 961. doi:10.1086/683178.

Andrews, S. M., M. C. Liu, J. P. Williams, and K. N. Allers (2008). Submillimeter Observations of the Young Low-Mass Object IRAS 04158+2805. *ApJ*, **685**, 1039-1045. doi:10.1086/591417.

Andrews, S. M., K. A. Rosenfeld, A. L. Kraus, and D. J. Wilner (2013). The Mass Dependence between Protoplanetary Disks and their Stellar Hosts. *ApJ*, **771**, 129. doi:10.1088/0004-637X/771/2/129.

Andrews, S. M., K. A. Rosenfeld, D. J. Wilner, and M. Bremer (2011a). A Closer Look at the LkCa 15 Protoplanetary Disk. *ApJ*, **742**, L5. doi:10.1088/2041-8205/742/1/L5.

Andrews, S. M. and J. P. Williams (2005). Circumstellar Dust Disks in Taurus-Auriga: The Submillimeter Perspective. *ApJ*, **631**, pp. 1134–1160. doi:10.1086/432712.

Andrews, S. M. and J. P. Williams (2007). A Submillimeter View of Circumstellar Dust Disks in ρ Ophiuchi. *ApJ*, **671**, pp. 1800–1812. doi:10.1086/522885.

Andrews, S. M., D. J. Wilner, C. Espaillat, A. M. Hughes, C. P. Dullemond, M. K. McClure, C. Qi, and J. M. Brown (2011b). Resolved Images of Large Cavities in Protoplanetary Transition Disks. *ApJ*, **732**, 42. doi:10.1088/0004-637X/732/1/42.

Andrews, S. M., D. J. Wilner, A. M. Hughes, C. Qi, and C. P. Dullemond (2009). Protoplanetary Disk Structures in Ophiuchus. *ApJ*, **700**, pp. 1502–1523. doi:10.1088/0004-637X/700/2/1502.

Andrews, S. M., D. J. Wilner, A. M. Hughes, C. Qi, and C. P. Dullemond (2010). Protoplanetary Disk Structures in Ophiuchus. II. Extension to Fainter Sources. *ApJ*, **723**, pp. 1241–1254. doi:10.1088/0004-637X/723/2/1241.

Andrews, S. M., D. J. Wilner, Z. Zhu, T. Birnstiel, J. M. Carpenter, L. M. Pérez, X.-N. Bai, K. I. Öberg, A. M. Hughes, A. Isella, and L. Ricci (2016). Ringed Substructure and a Gap at 1 au in the Nearest Protoplanetary Disk. *ApJ*, **820**, L40. doi:10.3847/2041-8205/820/2/L40.

Ansdell, M., J. P. Williams, C. F. Manara, A. Miotello, S. Facchini, N. van der Marel, L. Testi, and E. F. van Dishoeck (2017). An ALMA Survey of Protoplanetary Disks in the σ Orionis Cluster. *AJ*, **153**, 240. doi:10.3847/1538-3881/aa69c0.

Ansdell, M., J. P. Williams, N. van der Marel, J. M. Carpenter, G. Guidi, M. Hogerheijde, G. S. Mathews, C. F. Manara, A. Miotello, A. Natta, I. Oliveira, M. Tazzari, L. Testi, E. F. van Dishoeck, and S. E. van Terwisga (2016). ALMA Survey of Lupus Protoplanetary Disks. I. Dust and Gas Masses. *ApJ*, **828**, 46. doi:10.3847/0004-637X/828/1/46.

Armitage, P. J. (2011). Dynamics of Protoplanetary Disks. *ARA&A*, **49**, pp. 195–236. doi:10.1146/annurev-astro-081710-102521.

Armitage, P. J., J. A. Eisner, and J. B. Simon (2016). Prompt Planetesimal Formation beyond the Snow Line. *ApJ*, **828**, L2. doi:10.3847/2041-8205/828/1/L2.

Aso, Y., N. Ohashi, K. Saigo, S. Koyamatsu, Y. Aikawa, M. Hayashi, M. N. Machida, M. Saito, S. Takakuwa, K. Tomida, K. Tomisaka, and H.-W. Yen (2015). ALMA Observations of the Transition from Infall Motion to Keplerian Rotation around the Late-phase Protostar TMC-1A. *ApJ*, **812**, 27. doi:10.1088/0004-637X/812/1/27.

Avenhaus, H., S. P. Quanz, H. M. Schmid, M. R. Meyer, A. Garufi, S. Wolf, and C. Dominik (2014). Structures in the Protoplanetary Disk of HD142527 Seen in Polarized Scattered Light. *ApJ*, **781**, 87. doi:10.1088/0004-637X/781/2/87.

Bae, J., Z. Zhu, and L. Hartmann (2017). On the formation of multiple concentric rings and gaps in protoplanetary disks. *ArXiv e-prints*.

Balbus, S. A. and J. F. Hawley (1991). A powerful local shear instability in weakly magnetized disks. I - Linear analysis. II - Nonlinear evolution. *ApJ*, **376**, pp. 214–233. doi:10.1086/170270.

Bally, J., R. S. Sutherland, D. Devine, and D. Johnstone (1998a). Externally Illuminated Young Stellar Environments in the Orion Nebula: Hubble Space Telescope Planetary Camera and Ultraviolet Observations. *AJ*, **116**, pp. 293–321. doi:10.1086/300399.

Bally, J., L. Testi, A. Sargent, and J. Carlstrom (1998b). Disk Mass Limits and Lifetimes of Externally Irradiated Young Stellar Objects Embedded in the Orion Nebula. *AJ*, **116**, pp. 854–859. doi:10.1086/300469.

Banzatti, A., P. Pinilla, L. Ricci, K. M. Pontoppidan, T. Birnstiel, and F. Ciesla (2015). Direct Imaging of the Water Snow Line at the Time of Planet Formation using Two ALMA Continuum Bands. *ApJ*, **815**, L15. doi:10.1088/2041-8205/815/1/L15.

Baraffe, I., D. Homeier, F. Allard, and G. Chabrier (2015). New evolutionary models for pre-main sequence and main sequence low-mass stars down to the hydrogen-burning limit. *A&A*, **577**, A42. doi:10.1051/0004-6361/201425481.

Barenfeld, S. A., J. M. Carpenter, L. Ricci, and A. Isella (2016). ALMA Observations of Circumstellar Disks in the Upper Scorpius OB Association. *ApJ*, **827**, 142. doi:10.3847/0004-637X/827/2/142.

Barge, P. and J. Sommeria (1995). Did planet formation begin inside persistent gaseous vortices? *A&A*, **295**, pp. L1–L4.

Barsony, M. (1994). Class 0 Protostars. In Clemens, D. P. and R. Barvainis (eds.) *Clouds, Cores, and Low Mass Stars*, volume 65 of *Astronomical Society of the Pacific Conference Series*, p. 197.

Barsony, M., K. E. Haisch, K. A. Marsh, and C. McCarthy (2012). A Significant Population of Candidate New Members of the ρ Ophiuchi Cluster. *ApJ*, **751**, 22. doi:10.1088/0004-637X/751/1/22.

Barsony, M. and S. J. Kenyon (1992). On the origin of submillimeter emission from young stars in Taurus-Auriga. *ApJ*, **384**, pp. L53–L57. doi:10.1086/186260.

Barsony, M., S. J. Kenyon, E. A. Lada, and P. J. Teuben (1997). A Near-Infrared Imaging Survey of the ρ Ophiuchi Cloud Core. *ApJS*, **112**, pp. 109–191. doi:10.1086/313029.

Bate, M. R., I. A. Bonnell, C. J. Clarke, S. H. Lubow, G. I. Ogilvie, J. E. Pringle, and C. A. Tout (2000). Observational implications of precessing protostellar discs and jets. *MNRAS*, **317**, pp. 773–781. doi:10.1046/j.1365-8711.2000.03648.x.

Bate, M. R. and A. Burkert (1997). Resolution requirements for smoothed particle hydrodynamics calculations with self-gravity. *MNRAS*, **288**, pp. 1060–1072.

Beck, T. L., J. S. Bary, and P. J. McGregor (2010). Spatially Extended Brackett Gamma Emission in the Environments of Young Stars. *ApJ*, **722**, pp. 1360–1372. doi:10.1088/0004-637X/722/2/1360.

Beckwith, S. V. W. and A. I. Sargent (1991). Particle emissivity in circumstellar disks. *ApJ*, **381**, pp. 250–258. doi:10.1086/170646.

Beckwith, S. V. W., A. I. Sargent, R. S. Chini, and R. Guesten (1990). A survey for circumstellar disks around young stellar objects. *AJ*, **99**, pp. 924–945. doi:10.1086/115385.

Begemann, B., J. Dorschner, T. Henning, H. Mutschke, and E. Thamm (1994). A laboratory approach to the interstellar sulfide dust problem. *ApJ*, **423**, pp. L71–L74. doi:10.1086/187238.

Bell, C. P. M., T. Naylor, N. J. Mayne, R. D. Jeffries, and S. P. Littlefair (2013). Pre-main-sequence isochrones - II. Revising star and planet formation time-scales. *MNRAS*, **434**, pp. 806–831. doi:10.1093/mnras/stt1075.

Bergin, E. A., F. Du, L. I. Cleeves, G. A. Blake, K. Schwarz, R. Visser, and K. Zhang (2016). Hydrocarbon Emission Rings in Protoplanetary Disks Induced by Dust Evolution. *ApJ*, **831**, 101. doi:10.3847/0004-637X/831/1/101.

Bertin, E. (2006). Automatic Astrometric and Photometric Calibration with SCAMP. In Gabriel, C., C. Arviset, D. Ponz, and S. Enrique (eds.) *Astronomical Data Analysis Software and Systems XV*, volume 351 of *Astronomical Society of the Pacific Conference Series*, p. 112.

Bertin, E. and S. Arnouts (1996). SExtractor: Software for source extraction. *A&AS*, **117**, pp. 393–404.

Birnstiel, T., S. M. Andrews, and B. Ercolano (2012). Can grain growth explain transition disks? *A&A*, **544**, A79. doi:10.1051/0004-6361/201219262.

Bjorkman, J. E. and K. Wood (2001). Radiative Equilibrium and Temperature Correction in Monte Carlo Radiation Transfer. *ApJ*, **554**, pp. 615–623. doi:10.1086/321336.

Blum, J. and G. Wurm (2008). The Growth Mechanisms of Macroscopic Bodies in Protoplanetary Disks. *ARA&A*, **46**, pp. 21–56. doi:10.1146/annurev.astro.46.060407.145152.

Bohren, C. F. and D. R. Huffman (1983). *Absorption and scattering of light by small particles.* Wiley, New York, NY.

Bonnell, I. A. (1994). A New Binary Formation Mechanism. *MNRAS*, **269**, pp. 837–848.

Bonnell, I. A. and M. R. Bate (1994a). Massive Circumbinary Discs and the Formation of Multiple Systems. *MNRAS*, **269**, pp. L45–L48.

Bonnell, I. A. and M. R. Bate (1994b). The Formation of Close Binary Systems. *MNRAS*, **271**, pp. 999–1004.

Bontemps, S., P. Andre, S. Terebey, and S. Cabrit (1996). Evolution of outflow activity around low-mass embedded young stellar objects. *A&A*, **311**, pp. 858–872.

Boogert, A. C. A., M. R. Hogerheijde, C. Ceccarelli, A. G. G. M. Tielens, E. F. van Dishoeck, G. A. Blake, W. B. Latter, and F. Motte (2002). The Environment and Nature of the Class I Protostar Elias 29: Molecular Gas Observations and the Location of Ices. *ApJ*, **570**, pp. 708–723. doi:10.1086/339627.

Boogert, A. C. A., K. M. Pontoppidan, F. Lahuis, J. K. Jørgensen, J.-C. Augereau, G. A. Blake, T. Y. Brooke, J. Brown, C. P. Dullemond, N. J. Evans, II, V. Geers, M. R. Hogerheijde, J. Kessler-Silacci, C. Knez, P. Morris, A. Noriega-Crespo, F. L. Schöier, E. F. van Dishoeck, L. E. Allen, P. M. Harvey, D. W. Koerner, L. G. Mundy, P. C. Myers, D. L. Padgett, A. I. Sargent, and K. R. Stapelfeldt (2004). Spitzer Space Telescope Spectroscopy of Ices toward Low-Mass Embedded Protostars. *ApJS*, **154**, pp. 359–362. doi:10.1086/422556.

Boss, A. P. (2003). Rapid Formation of Outer Giant Planets by Disk Instability. *ApJ*, **599**, pp. 577–581. doi:10.1086/379163.

Boss, A. P. (2011). Formation of Giant Planets by Disk Instability on Wide Orbits Around Protostars with Varied Masses. *ApJ*, **731**, 74. doi:10.1088/0004-637X/731/1/74.

Boss, A. P. and P. Bodenheimer (1979). Fragmentation in a rotating protostar - A comparison of two three-dimensional computer codes. *ApJ*, **234**, pp. 289–295. doi:10.1086/157497.

Bossi, M., A. Gaspani, M. Scardia, and M. Tadini (1989). Orionis A - A pre-main sequence low Q binary system? *A&A*, **222**, pp. 117–120.

Bower, G. C., R. L. Plambeck, A. Bolatto, N. McCrady, J. R. Graham, I. de Pater, M. C. Liu, and F. K. Baganoff (2003). A Giant Outburst at Millimeter Wavelengths in the Orion Nebula. *ApJ*, **598**, pp. 1140–1150. doi:10.1086/379101.

Brinch, C., A. Crapsi, M. R. Hogerheijde, and J. K. Jørgensen (2007a). Structure and dynamics of the class I young stellar object L1489 IRS. *A&A*, **461**, pp. 1037–1047. doi:10.1051/0004-6361:20065473.

Brinch, C., A. Crapsi, J. K. Jørgensen, M. R. Hogerheijde, and T. Hill (2007b). A deeply embedded young protoplanetary disk around L1489 IRS observed by the Submillimeter Array. *A&A*, **475**, pp. 915–923. doi:10.1051/0004-6361:20078249.

Brown, J. M., G. A. Blake, C. Qi, C. P. Dullemond, D. J. Wilner, and J. P. Williams (2009). Evidence for Dust Clearing Through Resolved Submillimeter Imaging. *ApJ*, **704**, pp. 496–502. doi:10.1088/0004-637X/704/1/496.

Brown, J. M., G. J. Herczeg, K. M. Pontoppidan, and E. F. van Dishoeck (2012). A 30 AU Radius CO Gas Hole in the Disk around the Herbig Ae Star Oph IRS 48. *ApJ*, **744**, 116. doi:10.1088/0004-637X/744/2/116.

Bryden, G., X. Chen, D. N. C. Lin, R. P. Nelson, and J. C. B. Papaloizou (1999). Tidally Induced Gap Formation in Protostellar Disks: Gap Clearing and Suppression of Protoplanetary Growth. *ApJ*, **514**, pp. 344–367. doi:10.1086/306917.

Burkert, A., M. R. Bate, and P. Bodenheimer (1997). Protostellar fragmentation in a power-law density distribution. *MNRAS*, **289**, pp. 497–504.

Caillault, J.-P., M. Gagné, and J. R. Stauffer (1994). ROSAT HRI observations of hot stars in the Orion Nebula. *ApJ*, **432**, pp. 386–391. doi:10.1086/174576.

Cameron, A. G. W. (1962). The formation of the sun and planets. , **1**, pp. 13–69. doi:10.1016/0019-1035(62)90005-2.

Cameron, A. G. W. (1978). Physics of the primitive solar accretion disk. *Moon and Planets*, **18**, pp. 5–40. doi:10.1007/BF00896696.

Casassus, S., G. van der Plas, S. P. M, W. R. F. Dent, E. Fomalont, J. Hagelberg, A. Hales, A. Jordán, D. Mawet, F. Ménard, A. Wootten, D. Wilner, A. M. Hughes, M. R. Schreiber, J. H. Girard, B. Ercolano, H. Canovas, P. E. Román, and V. Salinas (2013). Flows of gas through a protoplanetary gap. *Nature*, **493**, pp. 191–194. doi:10.1038/nature11769.

Cassen, P. and A. Moosman (1981). On the formation of protostellar disks. , **48**, pp. 353–376. doi:10.1016/0019-1035(81)90051-8.

Chandler, C. J., M. Barsony, and T. J. T. Moore (1998). The circumstellar envelopes around three protostars in Taurus. *MNRAS*, **299**, pp. 789–798. doi:10.1046/j. 1365-8711.1998.01818.x.

Chandler, C. J. and J. S. Richer (2000). The Structure of Protostellar Envelopes Derived from Submillimeter Continuum Images. *ApJ*, **530**, pp. 851–866. doi: 10.1086/308401.

Chandler, C. J., S. Terebey, M. Barsony, T. J. T. Moore, and T. N. Gautier (1996). Compact Outflows Associated with TMC-1 and TMC-1A. *ApJ*, **471**, p. 308. doi:10.1086/177971.

Chen, H., P. C. Myers, E. F. Ladd, and D. O. S. Wood (1995). Bolometric temperature and young stars in the Taurus and Ophiuchus complexes. *ApJ*, **445**, pp. 377–392. doi:10.1086/175703.

Chiang, E. and G. Laughlin (2013). The minimum-mass extrasolar nebula: in situ formation of close-in super-Earths. *MNRAS*, **431**, pp. 3444–3455. doi:10.1093/ mnras/stt424.

Chiang, E. I. and P. Goldreich (1997). Spectral Energy Distributions of T Tauri Stars with Passive Circumstellar Disks. *ApJ*, **490**, p. 368. doi:10.1086/304869.

Chiang, E. I. and P. Goldreich (1999). Spectral Energy Distributions of Passive T Tauri Disks: Inclination. *ApJ*, **519**, pp. 279–284. doi:10.1086/307351.

Choi, M., K. Tatematsu, and M. Kang (2010). Kinematics of the Ammonia Disk Around the Protostar NGC 1333 IRAS 4A2. *ApJ*, **723**, pp. L34–L37. doi:10. 1088/2041-8205/723/1/L34.

Churchwell, E., M. Felli, D. O. S. Wood, and M. Massi (1987). Solar system-sized condensations in the Orion Nebula. *ApJ*, **321**, pp. 516–529. doi:10.1086/165648.

Cieza, L. A., D. L. Padgett, L. E. Allen, C. E. McCabe, T. Y. Brooke, S. J. Carey, N. L. Chapman, M. Fukagawa, T. L. Huard, A. Noriga-Crespo, D. E. Peterson, and L. M. Rebull (2009). Primordial Circumstellar Disks in Binary Systems: Evidence for Reduced Lifetimes. *ApJ*, **696**, pp. L84–L88. doi:10.1088/0004-637X/ 696/1/L84.

Clampin, M., J. E. Krist, D. R. Ardila, D. A. Golimowski, G. F. Hartig, H. C. Ford, G. D. Illingworth, F. Bartko, N. Benítez, J. P. Blakeslee, R. J. Bouwens, T. J. Broadhurst, R. A. Brown, C. J. Burrows, E. S. Cheng, N. J. G. Cross, P. D. Feldman, M. Franx, C. Gronwall, L. Infante, R. A. Kimble, M. P. Lesser, A. R. Martel, F. Menanteau, G. R. Meurer, G. K. Miley, M. Postman, P. Rosati, M. Sirianni, W. B. Sparks, H. D. Tran, Z. I. Tsvetanov, R. L. White, and W. Zheng

(2003). Hubble Space Telescope ACS Coronagraphic Imaging of the Circumstellar Disk around HD 141569A. *AJ*, **126**, pp. 385–392. doi:10.1086/375460.

Clanton, C. and B. S. Gaudi (2014). Synthesizing Exoplanet Demographics from Radial Velocity and Microlensing Surveys. II. The Frequency of Planets Orbiting M Dwarfs. *ApJ*, **791**, 91. doi:10.1088/0004-637X/791/2/91.

Clark, B. G. (1980). An efficient implementation of the algorithm 'CLEAN'. *A&A*, **89**, p. 377.

Clarke, C. J., A. Gendrin, and M. Sotomayor (2001). The dispersal of circumstellar discs: the role of the ultraviolet switch. *MNRAS*, **328**, pp. 485–491. doi:10.1046/j.1365-8711.2001.04891.x.

Code, A. D. and B. A. Whitney (1995). Polarization from scattering in blobs. *ApJ*, **441**, pp. 400–407. doi:10.1086/175363.

Codella, C., S. Cabrit, F. Gueth, L. Podio, S. Leurini, R. Bachiller, A. Gusdorf, B. Lefloch, B. Nisini, M. Tafalla, and W. Yvart (2014). The ALMA view of the protostellar system HH212. The wind, the cavity, and the disk. *A&A*, **568**, L5. doi:10.1051/0004-6361/201424103.

Cohen, M., J. H. Bieging, and P. R. Schwartz (1982). VLA observations of mass loss from T Tauri stars. *ApJ*, **253**, pp. 707–715. doi:10.1086/159671.

Condon, J. J. (1992). Radio emission from normal galaxies. *ARA&A*, **30**, pp. 575–611. doi:10.1146/annurev.aa.30.090192.003043.

Connelley, M. S. and T. P. Greene (2010). A Near-infrared Spectroscopic Survey of Class I Protostars. *AJ*, **140**, pp. 1214–1240. doi:10.1088/0004-6256/140/5/1214.

Cornwell, T. J. (1988). Radio-interferometric imaging of very large objects. *A&A*, **202**, pp. 316–321.

Crapsi, A., E. F. van Dishoeck, M. R. Hogerheijde, K. M. Pontoppidan, and C. P. Dullemond (2008). Characterizing the nature of embedded young stellar objects through silicate, ice and millimeter observations. *A&A*, **486**, pp. 245–254. doi:10.1051/0004-6361:20078589.

Cumming, A., R. P. Butler, G. W. Marcy, S. S. Vogt, J. T. Wright, and D. A. Fischer (2008). The Keck Planet Search: Detectability and the Minimum Mass and Orbital Period Distribution of Extrasolar Planets. *PASP*, **120**, pp. 531–554. doi:10.1086/588487.

Cuzzi, J. N. and K. J. Zahnle (2004). Material Enhancement in Protoplanetary Nebulae by Particle Drift through Evaporation Fronts. *ApJ*, **614**, pp. 490–496. doi:10.1086/423611.

D'Alessio, P., N. Calvet, and L. Hartmann (2001). Accretion Disks around Young Objects. III. Grain Growth. *ApJ*, **553**, pp. 321–334. doi:10.1086/320655.

Dawson, R. I., R. A. Murray-Clay, and D. C. Fabrycky (2011). On the Misalignment of the Directly Imaged Planet β Pictoris b with the System's Warped Inner Disk. *ApJ*, **743**, L17. doi:10.1088/2041-8205/743/1/L17.

de Juan Ovelar, M., M. Min, C. Dominik, C. Thalmann, P. Pinilla, M. Benisty, and T. Birnstiel (2013). Imaging diagnostics for transitional discs. *A&A*, **560**, A111. doi:10.1051/0004-6361/201322218.

Dent, W. R. F., H. E. Matthews, and D. Ward-Thompson (1998). The submillimetre colour of young stellar objects. *MNRAS*, **301**, pp. 1049–1063. doi:10.1046/j.1365-8711.1998.02091.x.

Desch, S. J. (2007). Mass Distribution and Planet Formation in the Solar Nebula. *ApJ*, **671**, pp. 878–893. doi:10.1086/522825.

Dittrich, K., H. Klahr, and A. Johansen (2013). Gravoturbulent Planetesimal Formation: The Positive Effect of Long-lived Zonal Flows. *ApJ*, **763**, 117. doi:10.1088/0004-637X/763/2/117.

Dodson-Robinson, S. E. and C. Salyk (2011). Transitional Disks as Signposts of Young, Multiplanet Systems. *ApJ*, **738**, 131. doi:10.1088/0004-637X/738/2/131.

Dohnanyi, J. S. (1969). Collisional Model of Asteroids and Their Debris. *J. Geophys. Res.*, **74**, p. 2531. doi:10.1029/JB074i010p02531.

Dong, R. and J. Fung (2017). What is the Mass of a Gap-opening Planet? *ApJ*, **835**, 146. doi:10.3847/1538-4357/835/2/146.

Dong, R., Z. Zhu, and B. Whitney (2015). Observational Signatures of Planets in Protoplanetary Disks I. Gaps Opened by Single and Multiple Young Planets in Disks. *ApJ*, **809**, 93. doi:10.1088/0004-637X/809/1/93.

Doppmann, G. W., T. P. Greene, K. R. Covey, and C. J. Lada (2005). The Physical Natures of Class I and Flat-Spectrum Protostellar Photospheres: A Near-Infrared Spectroscopic Study. *AJ*, **130**, pp. 1145–1170. doi:10.1086/431954.

Doppmann, G. W., J. R. Najita, and J. S. Carr (2008). Stellar and Circumstellar Properties of the Pre-Main-Sequence Binary GV Tau from Infrared Spectroscopy. *ApJ*, **685**, pp. 298–312. doi:10.1086/590328.

Draine, B. T. (2003). Scattering by Interstellar Dust Grains. II. X-Rays. *ApJ*, **598**, pp. 1026–1037. doi:10.1086/379123.

Draine, B. T. (2006). On the Submillimeter Opacity of Protoplanetary Disks. *ApJ*, **636**, pp. 1114–1120. doi:10.1086/498130.

Drążkowska, J. and C. P. Dullemond (2014). Can dust coagulation trigger streaming instability? *A&A*, **572**, A78. doi:10.1051/0004-6361/201424809.

Duffell, P. C. and A. I. MacFadyen (2013). Gap Opening by Extremely Low-mass Planets in a Viscous Disk. *ApJ*, **769**, 41. doi:10.1088/0004-637X/769/1/41.

Dulk, G. A. (1985). Radio emission from the sun and stars. *ARA&A*, **23**, pp. 169–224. doi:10.1146/annurev.aa.23.090185.001125.

Dullemond, C. P. (2012). RADMC-3D: A multi-purpose radiative transfer tool. Astrophysics Source Code Library.

Dullemond, C. P. and C. Dominik (2005). Dust coagulation in protoplanetary disks: A rapid depletion of small grains. *A&A*, **434**, pp. 971–986. doi:10.1051/0004-6361: 20042080.

Dunham, M. M., L. E. Allen, N. J. Evans, II, H. Broekhoven-Fiene, L. A. Cieza, J. Di Francesco, R. A. Gutermuth, P. M. Harvey, J. Hatchell, A. Heiderman, T. L. Huard, D. Johnstone, J. M. Kirk, B. C. Matthews, J. F. Miller, D. E. Peterson, and K. E. Young (2015). Young Stellar Objects in the Gould Belt. *ApJS*, **220**, 11. doi:10.1088/0067-0049/220/1/11.

Dunham, M. M., E. I. Vorobyov, and H. G. Arce (2014). On the reliability of proto-stellar disc mass measurements and the existence of fragmenting discs. *MNRAS*, **444**, pp. 887–901. doi:10.1093/mnras/stu1511.

Dutrey, A., S. Guilloteau, G. Duvert, L. Prato, M. Simon, K. Schuster, and F. Menard (1996). Dust and gas distribution around T Tauri stars in Taurus-Auriga. I. Interferometric 2.7mm continuum and ˆ13ˆCO J=1-0 observations. *A&A*, **309**, pp. 493–504.

Dzib, S. A., L. Loinard, A. J. Mioduszewski, L. F. Rodríguez, G. N. Ortiz-León, G. Pech, J. L. Rivera, R. M. Torres, A. F. Boden, L. Hartmann, N. J. Evans, II, C. Briceño, and J. Tobin (2013). The Gould's Belt Very Large Array Survey. I. The Ophiuchus Complex. *ApJ*, **775**, 63. doi:10.1088/0004-637X/775/1/63.

Eisloffel, J., R. Mundt, T. P. Ray, and L. F. Rodriguez (2000). Collimation and Propagation of Stellar Jets. *Protostars and Planets IV*, p. 815.

Eisner, J. A. (2012). Disk Masses at the End of the Main Accretion Phase: CARMA Observations and Multi-wavelength Modeling of Class I Protostars. *ApJ*, **755**, 23. doi:10.1088/0004-637X/755/1/23.

Eisner, J. A. (2015). Spectral Energy Distributions of Accreting Protoplanets. *ApJ*, **803**, L4. doi:10.1088/2041-8205/803/1/L4.

Eisner, J. A., J. M. Bally, A. Ginsburg, and P. D. Sheehan (2016). Protoplanetary Disks in the Orion OMC1 Region Imaged with ALMA. *ApJ*, **826**, 16. doi: 10.3847/0004-637X/826/1/16.

Eisner, J. A. and J. M. Carpenter (2006). Massive Protoplanetary Disks in the Trapezium Region. *ApJ*, **641**, pp. 1162–1171. doi:10.1086/500637.

Eisner, J. A., L. A. Hillenbrand, J. M. Carpenter, and S. Wolf (2005). Constraining the Evolutionary Stage of Class I Protostars: Multiwavelength Observations and Modeling. *ApJ*, **635**, pp. 396–421. doi:10.1086/497161.

Eisner, J. A., L. A. Hillenbrand, R. J. White, J. S. Bloom, R. L. Akeson, and C. H. Blake (2007). Near-Infrared Interferometric, Spectroscopic, and Photometric Monitoring of T Tauri Inner Disks. *ApJ*, **669**, pp. 1072–1084. doi:10.1086/521874.

Eisner, J. A., R. L. Plambeck, J. M. Carpenter, S. A. Corder, C. Qi, and D. Wilner (2008). *ApJ*, **683**, p. 304.

Enoch, M. L., N. J. Evans, II, A. I. Sargent, and J. Glenn (2009). Properties of the Youngest Protostars in Perseus, Serpens, and Ophiuchus. *ApJ*, **692**, 973. doi:10.1088/0004-637X/692/2/973.

Enoch, M. L., N. J. Evans, II, A. I. Sargent, J. Glenn, E. Rosolowsky, and P. Myers (2008). The Mass Distribution and Lifetime of Prestellar Cores in Perseus, Serpens, and Ophiuchus. *ApJ*, **684**, 1240-1259. doi:10.1086/589963.

Espaillat, C., N. Calvet, P. D'Alessio, J. Hernández, C. Qi, L. Hartmann, E. Furlan, and D. M. Watson (2007). On the Diversity of the Taurus Transitional Disks: UX Tauri A and LkCa 15. *ApJ*, **670**, pp. L135–L138. doi:10.1086/524360.

Espaillat, C., J. Muzerolle, J. Najita, S. Andrews, Z. Zhu, N. Calvet, S. Kraus, J. Hashimoto, A. Kraus, and P. D'Alessio (2014). An Observational Perspective of Transitional Disks. *Protostars and Planets VI*, pp. 497–520. doi:10.2458/azu_uapress_9780816531240-ch022.

Evans, N. J., II, M. M. Dunham, J. K. Jørgensen, M. L. Enoch, B. Merín, E. F. van Dishoeck, J. M. Alcalá, P. C. Myers, K. R. Stapelfeldt, T. L. Huard, L. E. Allen, P. M. Harvey, T. van Kempen, G. A. Blake, D. W. Koerner, L. G. Mundy,

D. L. Padgett, and A. I. Sargent (2009). The Spitzer c2d Legacy Results: Star-Formation Rates and Efficiencies; Evolution and Lifetimes. *ApJS*, **181**, 321-350. doi:10.1088/0067-0049/181/2/321.

Fedele, D., M. Carney, M. R. Hogerheijde, C. Walsh, A. Miotello, P. Klaassen, S. Bruderer, T. Henning, and E. F. van Dishoeck (2017). ALMA unveils rings and gaps in the protoplanetary system ¡ASTROBJ¿HD 169142¡/ASTROBJ¿: signatures of two giant protoplanets. *A&A*, **600**, A72. doi:10.1051/0004-6361/201629860.

Feigelson, E. D. and T. Montmerle (1999). High-Energy Processes in Young Stellar Objects. *ARA&A*, **37**, pp. 363–408. doi:10.1146/annurev.astro.37.1.363.

Felli, M., E. Churchwell, T. L. Wilson, and G. B. Taylor (1993a). The radio continuum morphology of the Orion Nebula - From 10 arcmin to 0.1 arcsec Resolution. *A&AS*, **98**, pp. 137–164.

Felli, M., G. B. Taylor, M. Catarzi, E. Churchwell, and S. Kurtz (1993b). The Orion Radio Zoo Revisited - Source Variability. *A&AS*, **101**, p. 127.

Flaherty, K. M., A. M. Hughes, K. A. Rosenfeld, S. M. Andrews, E. Chiang, J. B. Simon, S. Kerzner, and D. J. Wilner (2015). Weak Turbulence in the HD 163296 Protoplanetary Disk Revealed by ALMA CO Observations. *ApJ*, **813**, 99. doi:10.1088/0004-637X/813/2/99.

Flock, M., J. P. Ruge, N. Dzyurkevich, T. Henning, H. Klahr, and S. Wolf (2015). Gaps, rings, and non-axisymmetric structures in protoplanetary disks. From simulations to ALMA observations. *A&A*, **574**, A68. doi:10.1051/0004-6361/201424693.

Fomalont, E. B., K. I. Kellermann, R. B. Partridge, R. A. Windhorst, and E. A. Richards (2002). The Microjansky Sky at 8.4 GHz. *AJ*, **123**, pp. 2402–2416. doi:10.1086/339308.

Fomalont, E. B., R. A. Windhorst, J. A. Kristian, and K. I. Kellerman (1991). The micro-Jansky radio source population at 5 GHz. *AJ*, **102**, pp. 1258–1277. doi:10.1086/115952.

Forbrich, J., K. M. Menten, and M. J. Reid (2008). A 1.3 cm wavelength radio flare from a deeply embedded source in the Orion BN/KL region. *A&A*, **477**, pp. 267–272. doi:10.1051/0004-6361:20078070.

Forbrich, J., T. Preibisch, and K. M. Menten (2006). Radio and X-ray variability of young stellar objects in the Coronet cluster. *A&A*, **446**, pp. 155–170. doi:10.1051/0004-6361:20052871.

Forbrich, J., V. M. Rivilla, K. M. Menten, M. J. Reid, C. J. Chandler, U. Rau, S. Bhatnagar, S. J. Wolk, and S. Meingast (2016). The Population of Compact Radio Sources in the Orion Nebula Cluster. *ArXiv e-prints*.

Foreman-Mackey, D., D. W. Hogg, D. Lang, and J. Goodman (2013). emcee: The MCMC Hammer. *PASP*, **125**, p. 306. doi:10.1086/670067.

Fuente, A., J. Cernicharo, and M. Agúndez (2012). Warm HCN in the Planet Formation Zone of GV Tau N. *ApJ*, **754**, L6. doi:10.1088/2041-8205/754/1/L6.

Fukagawa, M., M. Hayashi, M. Tamura, Y. Itoh, S. S. Hayashi, Y. Oasa, T. Takeuchi, J.-i. Morino, K. Murakawa, S. Oya, T. Yamashita, H. Suto, S. Mayama, T. Naoi, M. Ishii, T.-S. Pyo, T. Nishikawa, N. Takato, T. Usuda, H. Ando, M. Iye, S. M. Miyama, and N. Kaifu (2004). Spiral Structure in the Circumstellar Disk around AB Aurigae. *ApJ*, **605**, pp. L53–L56. doi:10.1086/420699.

Fullerton, A. W. (2003). Cyclical Wind Variability from O-Type Stars. In Balona, L. A., H. F. Henrichs, and R. Medupe (eds.) *Magnetic Fields in O, B and A Stars: Origin and Connection to Pulsation, Rotation and Mass Loss*, volume 305 of *Astronomical Society of the Pacific Conference Series*, p. 333.

Fung, J., J.-M. Shi, and E. Chiang (2014). How Empty are Disk Gaps Opened by Giant Planets? *ApJ*, **782**, 88. doi:10.1088/0004-637X/782/2/88.

Furlan, E., M. McClure, N. Calvet, L. Hartmann, P. D'Alessio, W. J. Forrest, D. M. Watson, K. I. Uchida, B. Sargent, J. D. Green, and T. L. Herter (2008). Spitzer IRS Spectra and Envelope Models of Class I Protostars in Taurus. *ApJS*, **176**, 184-215. doi:10.1086/527301.

Galli, D. and F. H. Shu (1993a). Collapse of Magnetized Molecular Cloud Cores. I. Semianalytical Solution. *ApJ*, **417**, p. 220. doi:10.1086/173305.

Galli, D. and F. H. Shu (1993b). Collapse of Magnetized Molecular Cloud Cores. II. Numerical Results. *ApJ*, **417**, p. 243. doi:10.1086/173306.

Garay, G., J. M. Moran, and M. J. Reid (1987). Compact continuum radio sources in the Orion Nebula. *ApJ*, **314**, pp. 535–550. doi:10.1086/165084.

Garufi, A., S. P. Quanz, H. Avenhaus, E. Buenzli, C. Dominik, F. Meru, M. R. Meyer, P. Pinilla, H. M. Schmid, and S. Wolf (2013). Small vs. large dust grains in transitional disks: do different cavity sizes indicate a planet?. SAO 206462 (HD 135344B) in polarized light with VLT/NACO. *A&A*, **560**, A105. doi:10.1051/0004-6361/201322429.

Gibb, E. L., K. A. Van Brunt, S. D. Brittain, and T. W. Rettig (2007). Warm HCN, C_2H_2, and CO in the Disk of GV Tau. *ApJ*, **660**, pp. 1572–1579. doi: 10.1086/513502.

Gibb, E. L., K. A. Van Brunt, S. D. Brittain, and T. W. Rettig (2008). Erratum: "Warm HCN, C_2H_2, and CO in the Disk of GV Tau" (¡A href="/abs/2007ApJ...660.1572G"¿ApJ, 660, 1572 [2007]¡/A¿). *ApJ*, **686**, pp. 748–748. doi:10.1086/591644.

Glauser, A. M., F. Ménard, C. Pinte, G. Duchêne, M. Güdel, J.-L. Monin, and D. L. Padgett (2008). Multiwavelength studies of the gas and dust disc of IRAS 04158+2805. *A&A*, **485**, pp. 531–540. doi:10.1051/0004-6361:20065685.

Goldreich, P. and S. Tremaine (1980). Disk-satellite interactions. *ApJ*, **241**, pp. 425–441. doi:10.1086/158356.

Gómez, L., L. F. Rodríguez, L. Loinard, S. Lizano, C. Allen, A. Poveda, and K. M. Menten (2008). Monitoring the Large Proper Motions of Radio Sources in the Orion BN/KL Region. *ApJ*, **685**, pp. 333–343. doi:10.1086/590229.

Gomez, M., B. A. Whitney, and S. J. Kenyon (1997). A survey of optical and near-infrared jets in taurus embedded sources. *AJ*, **114**, p. 1138. doi:10.1086/118545.

Gorti, U. and D. Hollenbach (2009a). Photoevaporation of Circumstellar Disks By Far-Ultraviolet, Extreme-Ultraviolet and X-Ray Radiation from the Central Star. *ApJ*, **690**, pp. 1539–1552. doi:10.1088/0004-637X/690/2/1539.

Gorti, U. and D. Hollenbach (2009b). Photoevaporation of Circumstellar Disks By Far-Ultraviolet, Extreme-Ultraviolet and X-Ray Radiation from the Central Star. *ApJ*, **690**, pp. 1539–1552. doi:10.1088/0004-637X/690/2/1539.

Grady, C. A., T. Muto, J. Hashimoto, M. Fukagawa, T. Currie, B. Biller, C. Thalmann, M. L. Sitko, R. Russell, J. Wisniewski, R. Dong, J. Kwon, S. Sai, J. Hornbeck, G. Schneider, D. Hines, A. Moro Martín, M. Feldt, T. Henning, J.-U. Pott, M. Bonnefoy, J. Bouwman, S. Lacour, A. Mueller, A. Juhász, A. Crida, G. Chauvin, S. Andrews, D. Wilner, A. Kraus, S. Dahm, T. Robitaille, H. Jang-Condell, L. Abe, E. Akiyama, W. Brandner, T. Brandt, J. Carson, S. Egner, K. B. Follette, M. Goto, O. Guyon, Y. Hayano, M. Hayashi, S. Hayashi, K. Hodapp, M. Ishii, M. Iye, M. Janson, R. Kandori, G. Knapp, T. Kudo, N. Kusakabe, M. Kuzuhara, S. Mayama, M. McElwain, T. Matsuo, S. Miyama, J.-I. Morino, T. Nishimura, T.-S. Pyo, G. Serabyn, H. Suto, R. Suzuki, M. Takami, N. Takato, H. Terada, D. Tomono, E. Turner, M. Watanabe, T. Yamada, H. Takami, T. Usuda, and M. Tamura (2013). Spiral Arms in the Asymmetrically Illuminated Disk of MWC 758 and Constraints on Giant Planets. *ApJ*, **762**, 48. doi: 10.1088/0004-637X/762/1/48.

Gramajo, L. V., B. A. Whitney, M. Gómez, and T. P. Robitaille (2010). Combined Analysis of Images and Spectral Energy Distributions of Taurus Protostars. *AJ*, **139**, pp. 2504–2524. doi:10.1088/0004-6256/139/6/2504.

Gramajo, L. V., B. A. Whitney, S. J. Kenyon, M. Gómez, and K. M. Merrill (2007). High Spatial Resolution Near-Infrared Images of Taurus Protostars. *AJ*, **133**, pp. 1911–1926. doi:10.1086/512608.

Greene, T. P., B. A. Wilking, P. Andre, E. T. Young, and C. J. Lada (1994). Further mid-infrared study of the rho Ophiuchi cloud young stellar population: Luminosities and masses of pre-main-sequence stars. *ApJ*, **434**, pp. 614–626. doi:10.1086/174763.

Greene, T. P. and E. T. Young (1992). Near-infrared observations of young stellar objects in the Rho Ophiuchi dark cloud. *ApJ*, **395**, pp. 516–528. doi:10.1086/171672.

Guilloteau, S., A. Dutrey, V. Piétu, and Y. Boehler (2011). A dual-frequency sub-arcsecond study of proto-planetary disks at mm wavelengths: first evidence for radial variations of the dust properties. *A&A*, **529**, A105. doi:10.1051/0004-6361/201015209.

Gutermuth, R. A., S. T. Megeath, P. C. Myers, L. E. Allen, J. L. Pipher, and G. G. Fazio (2009). A Spitzer Survey of Young Stellar Clusters Within One Kiloparsec of the Sun: Cluster Core Extraction and Basic Structural Analysis. *ApJS*, **184**, pp. 18–83. doi:10.1088/0067-0049/184/1/18.

Haisch, K. E., Jr., E. A. Lada, and C. J. Lada (2001). Disk Frequencies and Lifetimes in Young Clusters. *ApJ*, **553**, pp. L153–L156. doi:10.1086/320685.

Harsono, D., J. K. Jørgensen, E. F. van Dishoeck, M. R. Hogerheijde, S. Bruderer, M. V. Persson, and J. C. Mottram (2014). Rotationally-supported disks around Class I sources in Taurus: disk formation constraints. *A&A*, **562**, A77. doi:10.1051/0004-6361/201322646.

Hayashi, C. (1981). Structure of the Solar Nebula, Growth and Decay of Magnetic Fields and Effects of Magnetic and Turbulent Viscosities on the Nebula. *Progress of Theoretical Physics Supplement*, **70**, pp. 35–53. doi:10.1143/PTPS.70.35.

Hendler, N. P., G. D. Mulders, I. Pascucci, A. Greenwood, I. Kamp, T. Henning, F. Ménard, W. R. F. Dent, and N. J. Evans, II (2017). Hints for Small Disks around Very Low Mass Stars and Brown Dwarfs. *ApJ*, **841**, 116. doi:10.3847/1538-4357/aa71b8.

Henney, W. J. and S. J. Arthur (1998). Modeling the Brightness Profiles of the Orion Proplyds. *AJ*, **116**, pp. 322–335. doi:10.1086/300433.

Hernández, J., L. Hartmann, N. Calvet, R. D. Jeffries, R. Gutermuth, J. Muzerolle, and J. Stauffer (2008). A Spitzer View of Protoplanetary Disks in the γ Velorum Cluster. *ApJ*, **686**, 1195-1208. doi:10.1086/591224.

Hildebrand, R. H. (1983). The Determination of Cloud Masses and Dust Characteristics from Submillimetre Thermal Emission. *QJRAS*, **24**, p. 267.

Hillenbrand, L. A. and J. M. Carpenter (2000). Constraints on the Stellar/Substellar Mass Function in the Inner Orion Nebula Cluster. *ApJ*, **540**, pp. 236–254. doi:10.1086/309309.

Hogerheijde, M. R. and G. Sandell (2000). Testing Envelope Models of Young Stellar Objects with Submillimeter Continuum and Molecular-Line Observations. *ApJ*, **534**, pp. 880–893. doi:10.1086/308795.

Hogerheijde, M. R., E. F. van Dishoeck, G. A. Blake, and H. J. van Langevelde (1997). Tracing the Envelopes around Embedded Low-Mass Young Stellar Objects with HCO + and Millimeter-Continuum Observations. *ApJ*, **489**, p. 293. doi:10.1086/304755.

Hogerheijde, M. R., E. F. van Dishoeck, G. A. Blake, and H. J. van Langevelde (1998). Envelope Structure on 700 AU Scales and the Molecular Outflows of Low-Mass Young Stellar Objects. *ApJ*, **502**, pp. 315–336. doi:10.1086/305885.

Hollenbach, D., D. Johnstone, S. Lizano, and F. Shu (1994). Photoevaporation of disks around massive stars and application to ultracompact H II regions. *ApJ*, **428**, pp. 654–669. doi:10.1086/174276.

Hoyle, F. (1960). The Origin of the Solar Nebula. *QJRAS*, **1**, p. 28.

Huang, J., K. I. Öberg, C. Qi, Y. Aikawa, S. M. Andrews, K. Furuya, V. V. Guzmán, R. A. Loomis, E. F. van Dishoeck, and D. J. Wilner (2017). An ALMA Survey of DCN/H^{13}CN and DCO$^+$/H^{13}CO$^+$ in Protoplanetary Disks. *ApJ*, **835**, 231. doi:10.3847/1538-4357/835/2/231.

Hudgins, D. M., S. A. Sandford, L. J. Allamandola, and A. G. G. M. Tielens (1993). Mid- and far-infrared spectroscopy of ices - Optical constants and integrated absorbances. *ApJS*, **86**, pp. 713–870. doi:10.1086/191796.

Hughes, A. M., D. J. Wilner, N. Calvet, P. D'Alessio, M. J. Claussen, and M. R. Hogerheijde (2007). An Inner Hole in the Disk around TW Hydrae Resolved in 7 mm Dust Emission. *ApJ*, **664**, pp. 536–542. doi:10.1086/518885.

Isella, A., G. Guidi, L. Testi, S. Liu, H. Li, S. Li, E. Weaver, Y. Boehler, J. M. Carperter, I. De Gregorio-Monsalvo, C. F. Manara, A. Natta, L. M. Pérez, L. Ricci, A. Sargent, M. Tazzari, and N. Turner (2016). Ringed Structures of the HD 163296 Protoplanetary Disk Revealed by ALMA. *Phys. Rev. Lett.*, **117**, p. 251101. doi:10.1103/PhysRevLett.117.251101.

Isella, A., A. Natta, D. Wilner, J. M. Carpenter, and L. Testi (2010). Millimeter Imaging of MWC 758: Probing the Disk Structure and Kinematics. *ApJ*, **725**, pp. 1735–1741. doi:10.1088/0004-637X/725/2/1735.

Isella, A., L. M. Pérez, J. M. Carpenter, L. Ricci, S. Andrews, and K. Rosenfeld (2013). An Azimuthal Asymmetry in the LkHα 330 Disk. *ApJ*, **775**, 30. doi:10.1088/0004-637X/775/1/30.

Jayawardhana, R., L. Hartmann, and N. Calvet (2001). Infall Models of Class 0 Protostars. *ApJ*, **548**, pp. 310–317. doi:10.1086/318650.

Johansen, A. and A. Youdin (2007). Protoplanetary Disk Turbulence Driven by the Streaming Instability: Nonlinear Saturation and Particle Concentration. *ApJ*, **662**, pp. 627–641. doi:10.1086/516730.

Johansen, A., A. Youdin, and H. Klahr (2009). Zonal Flows and Long-lived Axisymmetric Pressure Bumps in Magnetorotational Turbulence. *ApJ*, **697**, pp. 1269–1289. doi:10.1088/0004-637X/697/2/1269.

Johansen, A., A. N. Youdin, and Y. Lithwick (2012). Adding particle collisions to the formation of asteroids and Kuiper belt objects via streaming instabilities. *A&A*, **537**, A125. doi:10.1051/0004-6361/201117701.

Johnson, J. A., K. M. Aller, A. W. Howard, and J. R. Crepp (2010). Giant Planet Occurrence in the Stellar Mass-Metallicity Plane. *PASP*, **122**, p. 905. doi:10.1086/655775.

Johnstone, D., C. D. Wilson, G. Moriarty-Schieven, G. Joncas, G. Smith, E. Gregersen, and M. Fich (2000). Large-Area Mapping at 850 Microns. II. Analysis of the Clump Distribution in the ρ Ophiuchi Molecular Cloud. *ApJ*, **545**, pp. 327–339. doi:10.1086/317790.

Jørgensen, J. K., D. Johnstone, H. Kirk, P. C. Myers, L. E. Allen, and Y. L. Shirley (2008). Current Star Formation in the Ophiuchus and Perseus Molecular Clouds: Constraints and Comparisons from Unbiased Submillimeter and Mid-Infrared Surveys. II. *ApJ*, **683**, 822-843. doi:10.1086/589956.

Jørgensen, J. K., E. F. van Dishoeck, R. Visser, T. L. Bourke, D. J. Wilner, D. Lommen, M. R. Hogerheijde, and P. C. Myers (2009). PROSAC: a submillimeter

array survey of low-mass protostars. II. The mass evolution of envelopes, disks, and stars from the Class 0 through I stages. *A&A*, **507**, pp. 861–879. doi: 10.1051/0004-6361/200912325.

Kanagawa, K. D., T. Muto, H. Tanaka, T. Tanigawa, T. Takeuchi, T. Tsukagoshi, and M. Momose (2015). Mass Estimates of a Giant Planet in a Protoplanetary Disk from the Gap Structures. *ApJ*, **806**, L15. doi:10.1088/2041-8205/806/1/L15.

Kenyon, S. J. (2001). Dynamical Evolution of Protoplanetary Disks. In Woodward, C. E., M. D. Bicay, and J. M. Shull (eds.) *Tetons 4: Galactic Structure, Stars and the Interstellar Medium*, volume 231 of *Astronomical Society of the Pacific Conference Series*, p. 594.

Kenyon, S. J., N. Calvet, and L. Hartmann (1993). The embedded young stars in the Taurus-Auriga molecular cloud. I - Models for spectral energy distributions. *ApJ*, **414**, pp. 676–694. doi:10.1086/173114.

Kenyon, S. J. and L. Hartmann (1987). Spectral energy distributions of T Tauri stars - Disk flaring and limits on accretion. *ApJ*, **323**, pp. 714–733. doi:10.1086/165866.

Kenyon, S. J. and L. Hartmann (1995). Pre-Main-Sequence Evolution in the Taurus-Auriga Molecular Cloud. *ApJS*, **101**, p. 117. doi:10.1086/192235.

Kim, K. H., D. M. Watson, P. Manoj, E. Furlan, J. Najita, W. J. Forrest, B. Sargent, C. Espaillat, N. Calvet, K. L. Luhman, M. K. McClure, J. D. Green, and S. T. Harrold (2009). Mid-Infrared Spectra of Transitional Disks in the Chamaeleon I Cloud. *ApJ*, **700**, pp. 1017–1025. doi:10.1088/0004-637X/700/2/1017.

Koresko, C. D., G. A. Blake, M. E. Brown, A. I. Sargent, and D. W. Koerner (1999). Imaging the Haro 6-10 Infrared Companion. *ApJ*, **525**, pp. L49–L52. doi:10.1086/312333.

Kounkel, M., L. Hartmann, L. Loinard, A. J. Mioduszewski, S. A. Dzib, G. N. Ortiz-León, L. F. Rodríguez, G. Pech, J. L. Rivera, R. M. Torres, A. F. Boden, N. J. Evans, II, C. Briceño, and J. Tobin (2014). The Gould's Belt Very Large Array Survey. III. The Orion Region. *ApJ*, **790**, 49. doi:10.1088/0004-637X/790/1/49.

Kratter, K. M., R. A. Murray-Clay, and A. N. Youdin (2010). The Runts of the Litter: Why Planets Formed Through Gravitational Instability Can Only Be Failed Binary Stars. *ApJ*, **710**, pp. 1375–1386. doi:10.1088/0004-637X/710/2/1375.

Kraus, A. L. and M. J. Ireland (2012). LkCa 15: A Young Exoplanet Caught at Formation? *ApJ*, **745**, 5. doi:10.1088/0004-637X/745/1/5.

Kuiper, G. P. (1951). On the Origin of the Solar System. *Proceedings of the National Academy of Science*, **37**, pp. 1–14. doi:10.1073/pnas.37.1.1.

Lada, C. J. (1987). Star formation - From OB associations to protostars. In Peimbert, M. and J. Jugaku (eds.) *Star Forming Regions*, volume 115 of *IAU Symposium*, pp. 1–17.

Lada, C. J. and E. A. Lada (2003). Embedded Clusters in Molecular Clouds. *ARA&A*, **41**, pp. 57–115. doi:10.1146/annurev.astro.41.011802.094844.

Lada, C. J. and B. A. Wilking (1984). The nature of the embedded population in the Rho Ophiuchi dark cloud - Mid-infrared observations. *ApJ*, **287**, pp. 610–621. doi:10.1086/162719.

Ladd, E. F., F. C. Adams, G. A. Fuller, P. C. Myers, S. Casey, J. A. Davidson, D. A. Harper, and R. Padman (1991). Far-infrared and submillimeter wavelength observations of star-forming dense cores. II - Images. *ApJ*, **382**, pp. 555–569. doi:10.1086/170742.

Lambrechts, M. and A. Johansen (2012). Rapid growth of gas-giant cores by pebble accretion. *A&A*, **544**, A32. doi:10.1051/0004-6361/201219127.

Laughlin, G. and P. Bodenheimer (1994). Nonaxisymmetric evolution in protostellar disks. *ApJ*, **436**, pp. 335–354. doi:10.1086/174909.

Lebouteiller, V., D. J. Barry, C. Goes, G. C. Sloan, H. W. W. Spoon, D. W. Weedman, J. Bernard-Salas, and J. R. Houck (2015). CASSIS: The Cornell Atlas of Spitzer/Infrared Spectrograph Sources. II. High-resolution Observations. *ApJS*, **218**, 21. doi:10.1088/0067-0049/218/2/21.

Lebouteiller, V., D. J. Barry, H. W. W. Spoon, J. Bernard-Salas, G. C. Sloan, J. R. Houck, and D. W. Weedman (2011). CASSIS: The Cornell Atlas of Spitzer/Infrared Spectrograph Sources. *ApJS*, **196**, 8. doi:10.1088/0067-0049/196/1/8.

Lee, C.-F. (2010). A Change of Rotation Profile in the Envelope in the HH 111 Protostellar System: A Transition to a Disk? *ApJ*, **725**, pp. 712–720. doi:10.1088/0004-637X/725/1/712.

Lefevre, J., J. Bergeat, and J.-Y. Daniel (1982). Numerical simulation of radiative transfer in circumstellar dust shells. I - Spherical shells. *A&A*, **114**, pp. 341–346.

Lefevre, J., J.-Y. Daniel, and J. Bergeat (1983). Numerical simulation of radiative transfer in circumstellar dust shells. II - Ellipsoidal shells. *A&A*, **121**, pp. 51–58.

Leinert, C., T. L. Beck, S. Ligori, M. Simon, J. Woitas, and R. R. Howell (2001). The near-infrared and ice-band variability of Haro 6-10. *A&A*, **369**, pp. 215–221. doi:10.1051/0004-6361:20010111.

Leinert, C. and M. Haas (1989). Detection of an infrared companion to Haro 6-10. *ApJ*, **342**, pp. L39–L42. doi:10.1086/185479.

Levato, H. and H. A. Abt (1976). Spectral types in the Orion nebula cluster. *PASP*, **88**, pp. 712–714. doi:10.1086/130015.

Levison, H. F., A. Morbidelli, R. Gomes, and D. Backman (2007). Planet Migration in Planetesimal Disks. *Protostars and Planets V*, pp. 669–684.

Li, Z.-Y., R. Krasnopolsky, and H. Shang (2011). Non-ideal MHD Effects and Magnetic Braking Catastrophe in Protostellar Disk Formation. *ApJ*, **738**, 180. doi:10.1088/0004-637X/738/2/180.

Li, Z.-Y., R. Krasnopolsky, and H. Shang (2013). Does Magnetic-field-Rotation Misalignment Solve the Magnetic Braking Catastrophe in Protostellar Disk Formation? *ApJ*, **774**, 82. doi:10.1088/0004-637X/774/1/82.

Lin, D. N. C., P. Bodenheimer, and D. C. Richardson (1996). Orbital migration of the planetary companion of 51 Pegasi to its present location. *Nature*, **380**, pp. 606–607. doi:10.1038/380606a0.

Lin, D. N. C. and J. C. B. Papaloizou (1993). On the tidal interaction between protostellar disks and companions. In Levy, E. H. and J. I. Lunine (eds.) *Protostars and Planets III*, pp. 749–835.

Lindberg, J. E., J. K. Jørgensen, C. Brinch, T. Haugbølle, E. A. Bergin, D. Harsono, M. V. Persson, R. Visser, and S. Yamamoto (2014). ALMA observations of the kinematics and chemistry of disc formation. *A&A*, **566**, A74. doi:10.1051/0004-6361/201322651.

Lissauer, J. J. (1993). Planet formation. *ARA&A*, **31**, pp. 129–174. doi:10.1146/annurev.aa.31.090193.001021.

Lommen, D., J. K. Jørgensen, E. F. van Dishoeck, and A. Crapsi (2008). SMA observations of young disks: separating envelope, disk, and stellar masses in class I YSOs. *A&A*, **481**, pp. 141–147. doi:10.1051/0004-6361:20077543.

Loomis, R. A., K. I. Öberg, S. M. Andrews, and M. A. MacGregor (2017). A Multiringed, Modestly Inclined Protoplanetary Disk around AA Tau. *ApJ*, **840**, 23. doi:10.3847/1538-4357/aa6c63.

Looney, L. W., L. G. Mundy, and W. J. Welch (2000). Unveiling the Circumstellar Envelope and Disk: A Subarcsecond Survey of Circumstellar Structures. *ApJ*, **529**, pp. 477–498. doi:10.1086/308239.

Lucas, P. W. and P. F. Roche (1997). Butterfly star in Taurus: structures of young stellar objects. *MNRAS*, **286**, pp. 895–919. doi:10.1093/mnras/286.4.895.

Lucy, L. B. (1999). Computing radiative equilibria with Monte Carlo techniques. *A&A*, **344**, pp. 282–288.

Luhman, K. L. (2006). The Spatial Distribution of Brown Dwarfs in Taurus. *ApJ*, **645**, pp. 676–687. doi:10.1086/504073.

Lynden-Bell, D. and J. E. Pringle (1974). The evolution of viscous discs and the origin of the nebular variables. *MNRAS*, **168**, pp. 603–637. doi:10.1093/mnras/168.3.603.

Malhotra, R. (2015). The Mass Distribution Function of Planets. *ApJ*, **808**, 71. doi:10.1088/0004-637X/808/1/71.

Mamajek, E. E. (2008). On the distance to the Ophiuchus star-forming region. *Astronomische Nachrichten*, **329**, p. 10. doi:10.1002/asna.200710827.

Mamajek, E. E. (2009). Initial Conditions of Planet Formation: Lifetimes of Primordial Disks. In Usuda, T., M. Tamura, and M. Ishii (eds.) *American Institute of Physics Conference Series*, volume 1158 of *American Institute of Physics Conference Series*, pp. 3–10. doi:10.1063/1.3215910.

Mann, R. K., J. Di Francesco, D. Johnstone, S. M. Andrews, J. P. Williams, J. Bally, L. Ricci, A. M. Hughes, and B. C. Matthews (2014). ALMA Observations of the Orion Proplyds. *ApJ*, **784**, 82. doi:10.1088/0004-637X/784/1/82.

Mann, R. K. and J. P. Williams (2009). The Circumstellar Disk Mass Distribution in the Orion Trapezium Cluster. *ApJ*, **694**, pp. L36–L40. doi:10.1088/0004-637X/694/1/L36.

Mann, R. K. and J. P. Williams (2010). A Submillimeter Array Survey of Protoplanetary Disks in the Orion Nebula Cluster. *ApJ*, **725**, pp. 430–442. doi:10.1088/0004-637X/725/1/430.

Mathis, J. S., W. Rumpl, and K. H. Nordsieck (1977). The size distribution of interstellar grains. *ApJ*, **217**, pp. 425–433. doi:10.1086/155591.

McCaughrean, M. J. and C. R. O'Dell (1996). Direct Imaging of Circumstellar Disks in the Orion Nebula. *AJ*, **111**, p. 1977. doi:10.1086/117934.

McClure, M. (2009). Observational 5-20 μm Interstellar Extinction Curves Toward Star-Forming Regions Derived From Spitzer IRS Spectra. *ApJ*, **693**, pp. L81–L85. doi:10.1088/0004-637X/693/2/L81.

McClure, M. K., E. Furlan, P. Manoj, K. L. Luhman, D. M. Watson, W. J. Forrest, C. Espaillat, N. Calvet, P. D'Alessio, B. Sargent, J. J. Tobin, and H.-F. Chiang (2010). The Evolutionary State of the Pre-main Sequence Population in Ophiuchus: A Large Infrared Spectrograph Survey. *ApJS*, **188**, pp. 75–122. doi:10.1088/0067-0049/188/1/75.

Mellon, R. R. and Z.-Y. Li (2008). Magnetic Braking and Protostellar Disk Formation: The Ideal MHD Limit. *ApJ*, **681**, 1356-1376. doi:10.1086/587542.

Menard, F., J.-L. Monin, F. Angelucci, and D. Rouan (1993). Disks around pre-main-sequence binary systems - The case of Haro 6-10. *ApJ*, **414**, pp. L117–L120. doi:10.1086/187010.

Merín, B., J. M. Brown, I. Oliveira, G. J. Herczeg, E. F. van Dishoeck, S. Bottinelli, N. J. Evans, II, L. Cieza, L. Spezzi, J. M. Alcalá, P. M. Harvey, G. A. Blake, A. Bayo, V. G. Geers, F. Lahuis, T. Prusti, J.-C. Augereau, J. Olofsson, F. M. Walter, and K. Chiu (2010). A Spitzer c2d Legacy Survey to Identify and Characterize Disks with Inner Dust Holes. *ApJ*, **718**, 1200-1223. doi:10.1088/0004-637X/718/2/1200.

Min, M., C. P. Dullemond, C. Dominik, A. de Koter, and J. W. Hovenier (2009). Radiative transfer in very optically thick circumstellar disks. *A&A*, **497**, pp. 155–166. doi:10.1051/0004-6361/200811470.

Miotello, A., L. Testi, G. Lodato, L. Ricci, G. Rosotti, K. Brooks, A. Maury, and A. Natta (2014). Grain growth in the envelopes and disks of Class I protostars. *A&A*, **567**, A32. doi:10.1051/0004-6361/201322945.

Miotello, A., E. F. van Dishoeck, J. P. Williams, M. Ansdell, G. Guidi, M. Hogerheijde, C. F. Manara, M. Tazzari, L. Testi, N. van der Marel, and S. van Terwisga (2017). Lupus disks with faint CO isotopologues: low gas/dust or high carbon depletion? *A&A*, **599**, A113. doi:10.1051/0004-6361/201629556.

Mizuno, H. (1980). Formation of the Giant Planets. *Progress of Theoretical Physics*, **64**, pp. 544–557. doi:10.1143/PTP.64.544.

Mizuno, H., K. Nakazawa, and C. Hayashi (1978). Instability of a gaseous envelope surrounding a planetary core and formation of giant planets. *Progress of Theoretical Physics*, **60**, pp. 699–710. doi:10.1143/PTP.60.699.

Moran, J. M., G. Garay, M. J. Reid, R. Genzel, and P. T. P. Ho (1982). Compact continuum radio sources in the Orion Nebula. *Annals of the New York Academy of Sciences*, **395**, pp. 204–208. doi:10.1111/j.1749-6632.1982.tb43395.x.

Moriarty-Schieven, G. H., P. G. Wannier, J. Keene, and M. Tamura (1994). Circumprotostellar environments. 2: Envelopes, activity, and evolution. *ApJ*, **436**, pp. 800–806. doi:10.1086/174956.

Motte, F. and P. André (2001a). The circumstellar environment of low-mass protostars: A millimeter continuum mapping survey. *A&A*, **365**, pp. 440–464. doi:10.1051/0004-6361:20000072.

Motte, F. and P. André (2001b). The circumstellar environment of low-mass protostars: A millimeter continuum mapping survey. *A&A*, **365**, pp. 440–464. doi:10.1051/0004-6361:20000072.

Motte, F., P. Andre, and R. Neri (1998). The initial conditions of star formation in the rho Ophiuchi main cloud: wide-field millimeter continuum mapping. *A&A*, **336**, pp. 150–172.

Mouillet, D., J. D. Larwood, J. C. B. Papaloizou, and A. M. Lagrange (1997). A planet on an inclined orbit as an explanation of the warp in the Beta Pictoris disc. *MNRAS*, **292**, p. 896. doi:10.1093/mnras/292.4.896.

Movsessian, T. A. and T. Y. Magakian (1999). Herbig-Haro jet in the Haro 6-10 system. *A&A*, **347**, pp. 266–271.

Mundy, L. G., L. W. Looney, and E. A. Lada (1995). Constraints on Circumstellar Disk Masses in the Trapezium Cluster. *ApJ*, **452**, p. L137. doi:10.1086/309734.

Murillo, N. M., S.-P. Lai, S. Bruderer, D. Harsono, and E. F. van Dishoeck (2013). A Keplerian disk around a Class 0 source: ALMA observations of VLA1623A. *A&A*, **560**, A103. doi:10.1051/0004-6361/201322537.

Muto, T., C. A. Grady, J. Hashimoto, M. Fukagawa, J. B. Hornbeck, M. Sitko, R. Russell, C. Werren, M. Curé, T. Currie, N. Ohashi, Y. Okamoto, M. Momose, M. Honda, S. Inutsuka, T. Takeuchi, R. Dong, L. Abe, W. Brandner, T. Brandt, J. Carson, S. Egner, M. Feldt, T. Fukue, M. Goto, O. Guyon, Y. Hayano, M. Hayashi, S. Hayashi, T. Henning, K. W. Hodapp, M. Ishii, M. Iye, M. Janson, R. Kandori, G. R. Knapp, T. Kudo, N. Kusakabe, M. Kuzuhara, T. Matsuo, S. Mayama, M. W. McElwain, S. Miyama, J.-I. Morino, A. Moro-Martin, T. Nishimura, T.-S. Pyo, E. Serabyn, H. Suto, R. Suzuki, M. Takami, N. Takato, H. Terada, C. Thalmann, D. Tomono, E. L. Turner, M. Watanabe, J. P. Wisniewski, T. Yamada, H. Takami, T. Usuda, and M. Tamura (2012). Discovery of

Small-scale Spiral Structures in the Disk of SAO 206462 (HD 135344B): Implications for the Physical State of the Disk from Spiral Density Wave Theory. *ApJ*, **748**, L22. doi:10.1088/2041-8205/748/2/L22.

Muzerolle, J., L. E. Allen, S. T. Megeath, J. Hernández, and R. A. Gutermuth (2010). A Spitzer Census of Transitional Protoplanetary Disks with AU-scale Inner Holes. *ApJ*, **708**, pp. 1107–1118. doi:10.1088/0004-637X/708/2/1107.

Myers, P. C., G. A. Fuller, R. D. Mathieu, C. A. Beichman, P. J. Benson, R. E. Schild, and J. P. Emerson (1987). Near-infrared and optical observations of IRAS sources in and near dense cores. *ApJ*, **319**, pp. 340–357. doi:10.1086/165458.

Myers, P. C. and E. F. Ladd (1993). Bolometric temperatures of young stellar objects. *ApJ*, **413**, pp. L47–L50. doi:10.1086/186956.

Najita, J. R., S. E. Strom, and J. Muzerolle (2007). Demographics of transition objects. *MNRAS*, **378**, pp. 369–378. doi:10.1111/j.1365-2966.2007.11793.x.

Natta, A., L. Testi, and S. Randich (2006). Accretion in the ρ-Ophiuchi pre-main sequence stars. *A&A*, **452**, pp. 245–252. doi:10.1051/0004-6361:20054706.

O'Dell, C. R. and Z. Wen (1994). Postrefurbishment mission Hubble Space Telescope images of the core of the Orion Nebula: Proplyds, Herbig-Haro objects, and measurements of a circumstellar disk. *ApJ*, **436**, pp. 194–202. doi:10.1086/174892.

O'Dell, C. R., Z. Wen, and X. Hu (1993). Discovery of new objects in the Orion nebula on HST images - Shocks, compact sources, and protoplanetary disks. *ApJ*, **410**, pp. 696–700. doi:10.1086/172786.

Ohashi, N., M. Hayashi, P. T. P. Ho, M. Momose, M. Tamura, N. Hirano, and A. I. Sargent (1997). Rotation in the Protostellar Envelopes around IRAS 04169+2702 and IRAS 04365+2535: The Size Scale for Dynamical Collapse. *ApJ*, **488**, pp. 317–329. doi:10.1086/304685.

Ohashi, N., M. Hayashi, R. Kawabe, and M. Ishiguro (1996). The Nobeyama Millimeter Array Survey of Young Stellar Objects Associated with the Taurus Molecular Cloud. *ApJ*, **466**, p. 317. doi:10.1086/177512.

Okuzumi, S., M. Momose, S.-i. Sirono, H. Kobayashi, and H. Tanaka (2016). Sintering-induced Dust Ring Formation in Protoplanetary Disks: Application to the HL Tau Disk. *ApJ*, **821**, 82. doi:10.3847/0004-637X/821/2/82.

Ormel, C. W. and H. H. Klahr (2010). The effect of gas drag on the growth of protoplanets. Analytical expressions for the accretion of small bodies in laminar disks. *A&A*, **520**, A43. doi:10.1051/0004-6361/201014903.

Ortiz-León, G. N., L. Loinard, M. A. Kounkel, S. A. Dzib, A. J. Mioduszewski, L. F. Rodríguez, R. M. Torres, R. A. González-Lópezlira, G. Pech, J. L. Rivera, L. Hartmann, A. F. Boden, N. J. Evans, II, C. Briceño, J. J. Tobin, P. A. B. Galli, and D. Gudehus (2017). The Goulds Belt Distances Survey (GOBELINS). I. Trigonometric Parallax Distances and Depth of the Ophiuchus Complex. *ApJ*, **834**, 141. doi:10.3847/1538-4357/834/2/141.

Osorio, M., P. D'Alessio, J. Muzerolle, N. Calvet, and L. Hartmann (2003). A Comprehensive Study of the L1551 IRS 5 Binary System. *ApJ*, **586**, pp. 1148–1161. doi:10.1086/367695.

Ossenkopf, V. and T. Henning (1994). Dust opacities for protostellar cores. *A&A*, **291**, pp. 943–959.

Osterloh, M. and S. V. W. Beckwith (1995). Millimeter-wave continuum measurements of young stars. *ApJ*, **439**, pp. 288–302. doi:10.1086/175172.

Owen, J. E., B. Ercolano, C. J. Clarke, and R. D. Alexander (2010). Radiation-hydrodynamic models of X-ray and EUV photoevaporating protoplanetary discs. *MNRAS*, **401**, pp. 1415–1428. doi:10.1111/j.1365-2966.2009.15771.x.

Padgett, D. L., W. Brandner, K. R. Stapelfeldt, S. E. Strom, S. Terebey, and D. Koerner (1999). HUBBLE SPACE TELESCOPE/NICMOS Imaging of Disks and Envelopes around Very Young Stars. *AJ*, **117**, pp. 1490–1504. doi:10.1086/300781.

Padgett, D. L., L. M. Rebull, K. R. Stapelfeldt, N. L. Chapman, S.-P. Lai, L. G. Mundy, N. J. Evans, II, T. Y. Brooke, L. A. Cieza, W. J. Spiesman, A. Noriega-Crespo, C.-E. McCabe, L. E. Allen, G. A. Blake, P. M. Harvey, T. L. Huard, J. K. Jørgensen, D. W. Koerner, P. C. Myers, A. I. Sargent, P. Teuben, E. F. van Dishoeck, Z. Wahhaj, and K. E. Young (2008). The Spitzer c2d Survey of Large, Nearby, Interstellar Clouds. VII. Ophiuchus Observed with MIPS. *ApJ*, **672**, 1013-1037. doi:10.1086/523883.

Papaloizou, J. C. and G. J. Savonije (1991). Instabilities in self-gravitating gaseous discs. *MNRAS*, **248**, pp. 353–369. doi:10.1093/mnras/248.3.353.

Pascucci, I., L. Testi, G. J. Herczeg, F. Long, C. F. Manara, N. Hendler, G. D. Mulders, S. Krijt, F. Ciesla, T. Henning, S. Mohanty, E. Drabek-Maunder, D. Apai, L. Szucs, G. Sacco, and J. Olofsson (2016). A Steeper than Linear Disk Mass-Stellar Mass Scaling Relation. *ArXiv e-prints*.

Pérez, L. M., J. M. Carpenter, S. M. Andrews, L. Ricci, A. Isella, H. Linz, A. I. Sargent, D. J. Wilner, T. Henning, A. T. Deller, C. J. Chandler, C. P. Dullemond, J. Lazio, K. M. Menten, S. A. Corder, S. Storm, L. Testi, M. Tazzari, W. Kwon,

N. Calvet, J. S. Greaves, R. J. Harris, and L. G. Mundy (2016). Spiral density waves in a young protoplanetary disk. *Science*, **353**(6307), pp. 1519–1521. ISSN 0036-8075. doi:10.1126/science.aaf8296.

Pérez, L. M., J. M. Carpenter, C. J. Chandler, A. Isella, S. M. Andrews, L. Ricci, N. Calvet, S. A. Corder, A. T. Deller, C. P. Dullemond, J. S. Greaves, R. J. Harris, T. Henning, W. Kwon, J. Lazio, H. Linz, L. G. Mundy, A. I. Sargent, S. Storm, L. Testi, and D. J. Wilner (2012). Constraints on the Radial Variation of Grain Growth in the AS 209 Circumstellar Disk. *ApJ*, **760**, L17. doi:10.1088/2041-8205/760/1/L17.

Pérez, L. M., C. J. Chandler, A. Isella, J. M. Carpenter, S. M. Andrews, N. Calvet, S. A. Corder, A. T. Deller, C. P. Dullemond, J. S. Greaves, R. J. Harris, T. Henning, W. Kwon, J. Lazio, H. Linz, L. G. Mundy, L. Ricci, A. I. Sargent, S. Storm, M. Tazzari, L. Testi, and D. J. Wilner (2015). Grain Growth in the Circumstellar Disks of the Young Stars CY Tau and DoAr 25. *ApJ*, **813**, 41. doi:10.1088/0004-637X/813/1/41.

Pérez, L. M., A. Isella, J. M. Carpenter, and C. J. Chandler (2014). Large-scale Asymmetries in the Transitional Disks of SAO 206462 and SR 21. *ApJ*, **783**, L13. doi:10.1088/2041-8205/783/1/L13.

Perley, R., P. Napier, J. Jackson, B. Butler, B. Carlson, D. Fort, P. Dewdney, B. Clark, R. Hayward, S. Durand, M. Revnell, and M. McKinnon (2009). The Expanded Very Large Array. *IEEE Proceedings*, **97**, pp. 1448–1462. doi:10.1109/JPROC.2009.2015470.

Piétu, V., A. Dutrey, S. Guilloteau, E. Chapillon, and J. Pety (2006). Resolving the inner dust disks surrounding LkCa 15 and MWC 480 at mm wavelengths. *A&A*, **460**, pp. L43–L47. doi:10.1051/0004-6361:20065968.

Pinilla, P., T. Birnstiel, L. Ricci, C. P. Dullemond, A. L. Uribe, L. Testi, and A. Natta (2012). Trapping dust particles in the outer regions of protoplanetary disks. *A&A*, **538**, A114. doi:10.1051/0004-6361/201118204.

Plambeck, R. L., A. D. Bolatto, J. M. Carpenter, J. A. Eisner, J. W. Lamb, E. M. Leitch, D. P. Marrone, S. J. Muchovej, L. M. Pérez, M. W. Pound, P. J. Teuben, N. H. Volgenau, D. P. Woody, M. C. H. Wright, and B. A. Zauderer (2013). The Ionized Circumstellar Envelopes of Orion Source I and the Becklin-Neugebauer Object. *ApJ*, **765**, 40. doi:10.1088/0004-637X/765/1/40.

Plambeck, R. L., M. C. H. Wright, L. G. Mundy, and L. W. Looney (1995). Subarcsecond-Resolution 86 GHz Continuum Maps of Orion KL. *ApJ*, **455**, p. L189. doi:10.1086/309830.

Pollack, J. B., D. Hollenbach, S. Beckwith, D. P. Simonelli, T. Roush, and W. Fong (1994). Composition and radiative properties of grains in molecular clouds and accretion disks. *ApJ*, **421**, pp. 615–639. doi:10.1086/173677.

Pollack, J. B., O. Hubickyj, P. Bodenheimer, J. J. Lissauer, M. Podolak, and Y. Greenzweig (1996). Formation of the Giant Planets by Concurrent Accretion of Solids and Gas. , **124**, pp. 62–85. doi:10.1006/icar.1996.0190.

Pontoppidan, K. M., A. C. A. Boogert, H. J. Fraser, E. F. van Dishoeck, G. A. Blake, F. Lahuis, K. I. Öberg, N. J. Evans, II, and C. Salyk (2008). The c2d Spitzer Spectroscopic Survey of Ices around Low-Mass Young Stellar Objects. II. CO_2. *ApJ*, **678**, 1005-1031. doi:10.1086/533431.

Prato, L., K. E. Lockhart, C. M. Johns-Krull, and J. T. Rayner (2009). Stellar and Circumstellar Properties of Class I Protostars. *AJ*, **137**, pp. 3931–3941. doi:10.1088/0004-6256/137/4/3931.

Qi, C., P. D'Alessio, K. I. Öberg, D. J. Wilner, A. M. Hughes, S. M. Andrews, and S. Ayala (2011). Resolving the CO Snow Line in the Disk around HD 163296. *ApJ*, **740**, 84. doi:10.1088/0004-637X/740/2/84.

Quanz, S. P., A. Amara, M. R. Meyer, J. H. Girard, M. A. Kenworthy, and M. Kasper (2015). Confirmation and Characterization of the Protoplanet HD 100546 bDirect Evidence for Gas Giant Planet Formation at 50 AU. *ApJ*, **807**, 64. doi:10.1088/0004-637X/807/1/64.

Quillen, A. C., P. Varnière, I. Minchev, and A. Frank (2005). Driving Spiral Arms in the Circumstellar Disks of HD 100546 and HD 141569A. *AJ*, **129**, pp. 2481–2495. doi:10.1086/428954.

Raghavan, D., H. A. McAlister, T. J. Henry, D. W. Latham, G. W. Marcy, B. D. Mason, D. R. Gies, R. J. White, and T. A. ten Brummelaar (2010). A Survey of Stellar Families: Multiplicity of Solar-type Stars. *ApJS*, **190**, pp. 1–42. doi:10.1088/0067-0049/190/1/1.

Raymond, S. N. and C. Cossou (2014). No universal minimum-mass extrasolar nebula: evidence against in situ accretion of systems of hot super-Earths. *MNRAS*, **440**, pp. L11–L15. doi:10.1093/mnrasl/slu011.

Rebull, L. M., X. P. Koenig, D. L. Padgett, S. Terebey, P. M. McGehee, L. A. Hillenbrand, G. R. Knapp, D. Leisawitz, W. Liu, A. Noriega-Crespo, M. E. Ressler, K. R. Stapelfeldt, S. Fajardo-Acosta, and A. Mainzer (2011). New Young Star Candidates in the Taurus-Auriga Region as Selected from the Wide-Field Infrared Survey Explorer. *ApJS*, **196**, 4. doi:10.1088/0067-0049/196/1/4.

Regály, Z., A. Juhász, Z. Sándor, and C. P. Dullemond (2012). Possible planet-forming regions on submillimetre images. *MNRAS*, **419**, pp. 1701–1712. doi: 10.1111/j.1365-2966.2011.19834.x.

Reggiani, M., S. P. Quanz, M. R. Meyer, L. Pueyo, O. Absil, A. Amara, G. Anglada, H. Avenhaus, J. H. Girard, C. Carrasco Gonzalez, J. Graham, D. Mawet, F. Meru, J. Milli, M. Osorio, S. Wolff, and J.-M. Torrelles (2014). Discovery of a Companion Candidate in the HD 169142 Transition Disk and the Possibility of Multiple Planet Formation. *ApJ*, **792**, L23. doi:10.1088/2041-8205/792/1/L23.

Reipurth, B., L. F. Rodríguez, G. Anglada, and J. Bally (2004). Radio Continuum Jets from Protostellar Objects. *AJ*, **127**, pp. 1736–1746. doi:10.1086/381062.

Ricci, L., M. Robberto, and D. R. Soderblom (2008). The Hubble Space Telescope/Advanced Camera for Surveys Atlas of Protoplanetary Disks in the Great Orion Nebula. *AJ*, **136**, 2136. doi:10.1088/0004-6256/136/5/2136.

Ricci, L., L. Testi, A. Natta, and K. J. Brooks (2010a). Dust grain growth in ρ-Ophiuchi protoplanetary disks. *A&A*, **521**, A66. doi:10.1051/0004-6361/201015039.

Ricci, L., L. Testi, A. Natta, R. Neri, S. Cabrit, and G. J. Herczeg (2010b). Dust properties of protoplanetary disks in the Taurus-Auriga star forming region from millimeter wavelengths. *A&A*, **512**, A15. doi:10.1051/0004-6361/200913403.

Rivilla, V. M., C. J. Chandler, J. Sanz-Forcada, I. Jiménez-Serra, J. Forbrich, and J. Martín-Pintado (2015). Short- and Long-Term Radio Variability of Young Stars in The Orion Nebula Cluster and Molecular Cloud. *ApJ*, **808**, 146. doi: 10.1088/0004-637X/808/2/146.

Robitaille, T. P. (2010). On the modified random walk algorithm for Monte-Carlo radiation transfer. *A&A*, **520**, A70. doi:10.1051/0004-6361/201015025.

Robitaille, T. P. (2011). HYPERION: an open-source parallelized three-dimensional dust continuum radiative transfer code. *A&A*, **536**, A79. doi:10.1051/0004-6361/201117150.

Robitaille, T. P. (2017). A modular set of synthetic spectral energy distributions for young stellar objects. *A&A*, **600**, A11. doi:10.1051/0004-6361/201425486.

Robitaille, T. P., B. A. Whitney, R. Indebetouw, and K. Wood (2007). Interpreting Spectral Energy Distributions from Young Stellar Objects. II. Fitting Observed SEDs Using a Large Grid of Precomputed Models. *ApJS*, **169**, pp. 328–352. doi:10.1086/512039.

Robitaille, T. P., B. A. Whitney, R. Indebetouw, K. Wood, and P. Denzmore (2006). Interpreting Spectral Energy Distributions from Young Stellar Objects. I. A Grid of 200,000 YSO Model SEDs. *ApJS*, **167**, pp. 256–285. doi:10.1086/508424.

Roccatagliata, V., T. Ratzka, T. Henning, S. Wolf, C. Leinert, and J. Bouwman (2011). Multi-wavelength observations of the young binary system Haro 6-10: The case of misaligned discs. *A&A*, **534**, A33. doi:10.1051/0004-6361/201116805.

Rodmann, J., T. Henning, C. J. Chandler, L. G. Mundy, and D. J. Wilner (2006). Large dust particles in disks around T Tauri stars. *A&A*, **446**, pp. 211–221. doi:10.1051/0004-6361:20054038.

Rodríguez-Ledesma, M. V., R. Mundt, and J. Eislöffel (2009). Rotational studies in the Orion Nebula Cluster: from solar mass stars to brown dwarfs. *A&A*, **502**, pp. 883–904. doi:10.1051/0004-6361/200811427.

Ros, K. and A. Johansen (2013). Ice condensation as a planet formation mechanism. *A&A*, **552**, A137. doi:10.1051/0004-6361/201220536.

Rosenfeld, K. A., S. M. Andrews, D. J. Wilner, J. H. Kastner, and M. K. McClure (2013). The Structure of the Evolved Circumbinary Disk around V4046 Sgr. *ApJ*, **775**, 136. doi:10.1088/0004-637X/775/2/136.

Rosotti, G. P., A. Juhasz, R. A. Booth, and C. J. Clarke (2016). The minimum mass of detectable planets in protoplanetary discs and the derivation of planetary masses from high-resolution observations. *MNRAS*, **459**, pp. 2790–2805. doi:10.1093/mnras/stw691.

Safronov, V. S. and E. V. Zvjagina (1969). Relative Sizes of the Largest Bodies during the Accumulation of Planets. , **10**, pp. 109–115. doi:10.1016/0019-1035(69)90013-X.

Sallum, S., K. B. Follette, J. A. Eisner, L. M. Close, P. Hinz, K. Kratter, J. Males, A. Skemer, B. Macintosh, P. Tuthill, V. Bailey, D. Defrère, K. Morzinski, T. Rodigas, E. Spalding, A. Vaz, and A. J. Weinberger (2015). Accreting protoplanets in the LkCa 15 transition disk. *Nature*, **527**, pp. 342–344. doi:10.1038/nature15761.

Santiago-García, J., M. Tafalla, D. Johnstone, and R. Bachiller (2009). Shells, jets, and internal working surfaces in the molecular outflow from IRAS 04166+2706. *A&A*, **495**, pp. 169–181. doi:10.1051/0004-6361:200810739.

Schwarz, K. R., E. A. Bergin, L. I. Cleeves, G. A. Blake, K. Zhang, K. I. Öberg, E. F. van Dishoeck, and C. Qi (2016). The Radial Distribution of H_2 and CO in TW Hya as Revealed by Resolved ALMA Observations of CO Isotopologues. *ApJ*, **823**, 91. doi:10.3847/0004-637X/823/2/91.

Shakura, N. I. and R. A. Sunyaev (1973). Black holes in binary systems. Observational appearance. *A&A*, **24**, pp. 337–355.

Sheehan, P. D. and J. A. Eisner (2014). Constraining the Disk Masses of the Class I Binary Protostar GV Tau. *ApJ*, **791**, 19. doi:10.1088/0004-637X/791/1/19.

Sheehan, P. D. and J. A. Eisner (2017). WL 17: A Young Embedded Transition Disk. *ArXiv e-prints*.

Sheehan, P. D., J. A. Eisner, R. K. Mann, and J. P. Williams (2016). A VLA Survey for Faint Compact Radio Sources in the Orion Nebula Cluster. *ApJ*, **831**, 155. doi:10.3847/0004-637X/831/2/155.

Shirley, Y. L., B. S. Mason, J. G. Mangum, D. E. Bolin, M. J. Devlin, S. R. Dicker, and P. M. Korngut (2011). Mustang 3.3 mm Continuum Observations of Class 0 Protostars. *AJ*, **141**, 39. doi:10.1088/0004-6256/141/2/39.

Shu, F. H., F. C. Adams, and S. Lizano (1987). Star formation in molecular clouds - Observation and theory. *ARA&A*, **25**, pp. 23–81. doi:10.1146/annurev.aa.25. 090187.000323.

Shu, F. H., H. Shang, A. E. Glassgold, and T. Lee (1997). X-rays and fluctuating X-winds from protostars. *Science*, **277**, pp. 1475–1479. doi:10.1126/science.277. 5331.1475.

Siess, L., E. Dufour, and M. Forestini (2000). An internet server for pre-main sequence tracks of low- and intermediate-mass stars. *A&A*, **358**, pp. 593–599.

Simon, J. B. and P. J. Armitage (2014). Efficiency of Particle Trapping in the Outer Regions of Protoplanetary Disks. *ApJ*, **784**, 15. doi:10.1088/0004-637X/784/1/15.

Simon, J. B., P. J. Armitage, R. Li, and A. N. Youdin (2016). The Mass and Size Distribution of Planetesimals Formed by the Streaming Instability. I. The Role of Self-gravity. *ApJ*, **822**, 55. doi:10.3847/0004-637X/822/1/55.

Smith, N., J. Bally, R. Y. Shuping, M. Morris, and M. Kassis (2005). Thermal Dust Emission from Proplyds, Unresolved Disks, and Shocks in the Orion Nebula. *AJ*, **130**, pp. 1763–1777. doi:10.1086/432912.

Stahl, O., A. Kaufer, T. Rivinius, T. Szeifert, B. Wolf, T. Gaeng, C. A. Gummersbach, I. Jankovics, J. Kovacs, H. Mandel, M. W. Pakull, and J. Peitz (1996). Phase-locked photospheric and stellar-wind variations of ˆ1ˆOrionis C. *A&A*, **312**, pp. 539–548.

Stahl, O., B. Wolf, T. Gang, C. A. Gummersbach, A. Kaufer, J. Kovacs, H. Mandel, and T. Szeifert (1993). Periodic Spectral Variations of THETA-1-ORIONIS-C. *A&A*, **274**, p. L29.

Stanke, T., M. D. Smith, R. Gredel, and T. Khanzadyan (2006). An unbiased search for the signatures of protostars in the ρ Ophiuchi molecular cloud . II. Millimetre continuum observations. *A&A*, **447**, pp. 609–622. doi:10.1051/0004-6361: 20041331.

Stapelfeldt, K. R., J. E. Krist, F. Ménard, J. Bouvier, D. L. Padgett, and C. J. Burrows (1998). An Edge-On Circumstellar Disk in the Young Binary System HK Tauri. *ApJ*, **502**, pp. L65–L69. doi:10.1086/311479.

Stark, D. P., B. A. Whitney, K. Stassun, and K. Wood (2006). Near-Infrared Synthetic Images of Protostellar Disks and Envelopes. *ApJ*, **649**, pp. 900–913. doi:10.1086/506926.

Strom, K. M., J. Kepner, and S. E. Strom (1995). The evolutionary status of the stellar population in the rho Ophiuchi cloud core. *ApJ*, **438**, pp. 813–829. doi: 10.1086/175125.

Strom, K. M., S. E. Strom, S. Edwards, S. Cabrit, and M. F. Skrutskie (1989). Circumstellar material associated with solar-type pre-main-sequence stars - A possible constraint on the timescale for planet building. *AJ*, **97**, pp. 1451–1470. doi:10.1086/115085.

Tachibana, S., G. R. Huss, N. T. Kita, G. Shimoda, and Y. Morishita (2006). ^{60}Fe in Chondrites: Debris from a Nearby Supernova in the Early Solar System? *ApJ*, **639**, pp. L87–L90. doi:10.1086/503201.

Tafalla, M., J. Santiago, D. Johnstone, and R. Bachiller (2004). A highly collimated, extremely high velocity outflow in Taurus. *A&A*, **423**, pp. L21–L24. doi:10.1051/ 0004-6361:200400015.

Takakuwa, S., M. Saito, J. Lim, K. Saigo, T. K. Sridharan, and N. A. Patel (2012). A Keplerian Circumbinary Disk around the Protostellar System L1551 NE. *ApJ*, **754**, 52. doi:10.1088/0004-637X/754/1/52.

Tanaka, H., Y. Himeno, and S. Ida (2005). Dust Growth and Settling in Protoplanetary Disks and Disk Spectral Energy Distributions. I. Laminar Disks. *ApJ*, **625**, pp. 414–426. doi:10.1086/429658.

Terebey, S., F. H. Shu, and P. Cassen (1984). The collapse of the cores of slowly rotating isothermal clouds. *ApJ*, **286**, pp. 529–551. doi:10.1086/162628.

Tobin, J. J., L. Hartmann, H.-F. Chiang, D. J. Wilner, L. W. Looney, L. Loinard, N. Calvet, and P. D'Alessio (2012). A ~0.2-solar-mass protostar with a Keplerian disk in the very young L1527 IRS system. *Nature*, **492**, pp. 83–85. doi:10.1038/ nature11610.

Tobin, J. J., L. Hartmann, H.-F. Chiang, D. J. Wilner, L. W. Looney, L. Loinard, N. Calvet, and P. D'Alessio (2013). Modeling the Resolved Disk around the Class 0 Protostar L1527. *ApJ*, **771**, 48. doi:10.1088/0004-637X/771/1/48.

Tobin, J. J., L. W. Looney, D. J. Wilner, W. Kwon, C. J. Chandler, T. L. Bourke, L. Loinard, H.-F. Chiang, S. Schnee, and X. Chen (2015). A Sub-arcsecond Survey Toward Class 0 Protostars in Perseus: Searching for Signatures of Protostellar Disks. *ApJ*, **805**, 125. doi:10.1088/0004-637X/805/2/125.

Trotta, F., L. Testi, A. Natta, A. Isella, and L. Ricci (2013). Constraints on the radial distribution of the dust properties in the CQ Tauri protoplanetary disk. *A&A*, **558**, A64. doi:10.1051/0004-6361/201321896.

Ulrich, R. K. (1976). An infall model for the T Tauri phenomenon. *ApJ*, **210**, pp. 377–391. doi:10.1086/154840.

van der Marel, N., L. E. Kristensen, R. Visser, J. C. Mottram, U. A. Yıldız, and E. F. van Dishoeck (2013). Outflow forces of low-mass embedded objects in Ophiuchus: a quantitative comparison of analysis methods. *A&A*, **556**, A76. doi:10.1051/0004-6361/201220717.

van der Marel, N., E. F. van Dishoeck, S. Bruderer, L. Pérez, and A. Isella (2015). Gas density drops inside dust cavities of transitional disks around young stars observed with ALMA. *A&A*, **579**, A106. doi:10.1051/0004-6361/201525658.

van Dokkum, P. G. (2001). Cosmic-Ray Rejection by Laplacian Edge Detection. *PASP*, **113**, pp. 1420–1427. doi:10.1086/323894.

van Kempen, T. A., E. F. van Dishoeck, D. M. Salter, M. R. Hogerheijde, J. K. Jørgensen, and A. C. A. Boogert (2009). The nature of the Class I population in Ophiuchus as revealed through gas and dust mapping. *A&A*, **498**, pp. 167–194. doi:10.1051/0004-6361/200810445.

van't Hoff, M. L. R., C. Walsh, M. Kama, S. Facchini, and E. F. van Dishoeck (2017). Robustness of N_2H^+ as tracer of the CO snowline. *A&A*, **599**, A101. doi:10.1051/0004-6361/201629452.

Viana Almeida, P., C. Melo, N. C. Santos, P. Figueira, M. Sterzik, and J. F. Gameiro (2012). Finding proto-spectroscopic binaries. Precise multi-epoch radial velocities of seven protostars in ρ Ophiuchus. *A&A*, **539**, A62. doi:10.1051/0004-6361/ 201117703.

Walborn, N. R. and J. S. Nichols (1994). A large, periodic variation in the stellar wind of theta[1] Orionis C. *ApJ*, **425**, pp. L29–L32. doi:10.1086/187303.

Wang, L.-Y., H. Shang, Y.-N. Su, J. Santiago-García, M. Tafalla, Q. Zhang, N. Hirano, and C.-F. Lee (2014). Molecular Jet of IRAS 04166+2706. *ApJ*, **780**, 49. doi:10.1088/0004-637X/780/1/49.

Watson, D. M., F. Kemper, N. Calvet, L. D. Keller, E. Furlan, L. Hartmann, W. J. Forrest, C. H. Chen, K. I. Uchida, J. D. Green, B. Sargent, G. C. Sloan, T. L. Herter, B. R. Brandl, J. R. Houck, J. Najita, P. D'Alessio, P. C. Myers, D. J. Barry, P. Hall, and P. W. Morris (2004). Mid-infrared Spectra of Class I Protostars in Taurus. *ApJS*, **154**, pp. 391–395. doi:10.1086/422918.

Weidenschilling, S. J. (1977). *Ap&SS*, **51**, p. 153.

Weidenschilling, S. J. (1977). Aerodynamics of solid bodies in the solar nebula. *MNRAS*, **180**, pp. 57–70. doi:10.1093/mnras/180.1.57.

Whipple, F. L. (1972). On certain aerodynamic processes for asteroids and comets. In Elvius, A. (ed.) *From Plasma to Planet*, p. 211.

White, R. J. and L. A. Hillenbrand (2004). On the Evolutionary Status of Class I Stars and Herbig-Haro Energy Sources in Taurus-Auriga. *ApJ*, **616**, pp. 998–1032. doi:10.1086/425115.

Whitney, B. A., S. J. Kenyon, and M. Gómez (1997). Near-Infrared Imaging Polarimetry of Embedded Young Stars in the Taurus-Auriga Molecular Cloud. *ApJ*, **485**, pp. 703–734. doi:10.1086/304454.

Whitney, B. A., K. Wood, J. E. Bjorkman, and M. J. Wolff (2003). Two-dimensional Radiative Transfer in Protostellar Envelopes. I. Effects of Geometry on Class I Sources. *ApJ*, **591**, pp. 1049–1063. doi:10.1086/375415.

Wilking, B. A., M. Gagne, and L. E. Allen (2008). VizieR Online Data Catalog: JKH photometry in LDN 1688 (Wilking+, 2008). *VizieR Online Data Catalog*, **2289**, pp. 351–380.

Wilking, B. A. and C. J. Lada (1983). The discovery of new embedded sources in the centrally condensed core of the Rho Ophiuchi dark cloud - The formation of a bound cluster. *ApJ*, **274**, pp. 698–716. doi:10.1086/161482.

Wilking, B. A., M. R. Meyer, J. G. Robinson, and T. P. Greene (2005). Optical Spectroscopy of the Surface Population of the ρ Ophiuchi Molecular Cloud: The First Wave of Star Formation. *AJ*, **130**, pp. 1733–1751. doi:10.1086/432758.

Williams, J. P., S. M. Andrews, and D. J. Wilner (2005). The Masses of the Orion Proplyds from Submillimeter Dust Emission. *ApJ*, **634**, pp. 495–500. doi:10.1086/444493.

Williams, J. P. and W. M. J. Best (2014). A Parametric Modeling Approach to Measuring the Gas Masses of Circumstellar Disks. *ApJ*, **788**, 59. doi:10.1088/0004-637X/788/1/59.

Williams, P. M., K. A. van der Hucht, A. M. T. Pollock, D. R. Florkowski, H. van der Woerd, and W. M. Wamsteker (1990). Multi-frequency variations of the Wolf-Rayet system HD 193793. I - Infrared, X-ray and radio observations. *MNRAS*, **243**, pp. 662–684.

Witt, A. N. (1977). Multiple scattering in reflection nebulae. I - A Monte Carlo approach. *ApJS*, **35**, pp. 1–6. doi:10.1086/190463.

Wolf, S., D. L. Padgett, and K. R. Stapelfeldt (2003). The Circumstellar Disk of the Butterfly Star in Taurus. *ApJ*, **588**, pp. 373–386. doi:10.1086/374041.

Wolf, S., A. Schegerer, H. Beuther, D. L. Padgett, and K. R. Stapelfeldt (2008). Submillimeter Structure of the Disk of the Butterfly Star. *ApJ*, **674**, L101. doi:10.1086/529188.

Wright, A. E. and M. J. Barlow (1975). The radio and infrared spectrum of early-type stars undergoing mass loss. *MNRAS*, **170**, pp. 41–51.

Yen, H.-W., S. Takakuwa, N. Ohashi, and P. T. P. Ho (2013). Unveiling the Evolutionary Sequence from Infalling Envelopes to Keplerian Disks around Low-mass Protostars. *ApJ*, **772**, 22. doi:10.1088/0004-637X/772/1/22.

Youdin, A. N. and J. Goodman (2005). Streaming Instabilities in Protoplanetary Disks. *ApJ*, **620**, pp. 459–469. doi:10.1086/426895.

Young, C. H., Y. L. Shirley, N. J. Evans, II, and J. M. C. Rawlings (2003). Tracing the Mass during Low-Mass Star Formation. IV. Observations and Modeling of the Submillimeter Continuum Emission from Class I Protostars. *ApJS*, **145**, pp. 111–145. doi:10.1086/345341.

Yusef-Zadeh, F., M. Morris, and R. L. White (1984). Bipolar reflection nebulae - Monte Carlo simulations. *ApJ*, **278**, pp. 186–194. doi:10.1086/161780.

Zapata, L. A., L. F. Rodríguez, S. E. Kurtz, and C. R. O'Dell (2004a). Compact Radio Sources in Orion: New Detections, Time Variability, and Objects in OMC-1S. *AJ*, **127**, pp. 2252–2261. doi:10.1086/382715.

Zapata, L. A., L. F. Rodríguez, S. E. Kurtz, C. R. O'Dell, and P. T. P. Ho (2004b). A Cluster of 1.3 Centimeter Continuum Sources in OMC-1 South. *ApJ*, **610**, pp. L121–L124. doi:10.1086/423428.

Zhang, K., G. A. Blake, and E. A. Bergin (2015). Evidence of Fast Pebble Growth Near Condensation Fronts in the HL Tau Protoplanetary Disk. *ApJ*, **806**, L7. doi:10.1088/2041-8205/806/1/L7.

Zhu, Z., W. Ju, and J. M. Stone (2016). Shock-driven Accretion in Circumplanetary Disks: Observables and Satellite Formation. *ApJ*, **832**, 193. doi:10.3847/0004-637X/832/2/193.

Zhu, Z., R. P. Nelson, L. Hartmann, C. Espaillat, and N. Calvet (2011). Transitional and Pre-transitional Disks: Gap Opening by Multiple Planets? *ApJ*, **729**, 47. doi:10.1088/0004-637X/729/1/47.

Zhu, Z. and J. M. Stone (2014). Dust Trapping by Vortices in Transitional Disks: Evidence for Non-ideal Magnetohydrodynamic Effects in Protoplanetary Disks. *ApJ*, **795**, 53. doi:10.1088/0004-637X/795/1/53.

Zsom, A., C. W. Ormel, C. Güttler, J. Blum, and C. P. Dullemond (2010). The outcome of protoplanetary dust growth: pebbles, boulders, or planetesimals? II. Introducing the bouncing barrier. *A&A*, **513**, A57. doi:10.1051/0004-6361/200912976.